BINARY FLUID HEAT AND MASS EXCHANGE AT THE MICROSCALES IN INTERNAL AND EXTERNAL AMMONIA-WATER ABSORPTION

A Dissertation
Presented to
The Academic Faculty

by

Ananda Krishna Nagavarapu

In Partial Fulfillment
of the Requirements for the Degree
Doctor of Philosophy in Mechanical Engineering

Georgia Institute of Technology

December 2012

BINARY FLUID HEAT AND MASS EXCHANGE AT THE MICROSCALES IN INTERNAL AND EXTERNAL AMMONIA-WATER ABSORPTION

Approved by:

Dr. Srinivas Garimella, Adviser
George W. Woodruff School of Mechanical Engineering
Georgia Institute of Technology

Dr. Sheldon Jeter
George W. Woodruff School of Mechanical Engineering
Georgia Institute of Technology

Dr. Samuel Graham
George W. Woodruff School of Mechanical Engineering
Georgia Institute of Technology

Dr. William Koros
School of Chemical and Biomolecular Engineering
Georgia Institute of Technology

Dr. Thomas Fuller
School of Chemical and Biomolecular Engineering
Georgia Institute of Technology

Date Approved: August 7, 2012

To my family for their unconditional love and unwavering support

ACKNOWLEDGEMENTS

I would like to express my deepest gratitude to my adviser and mentor, Dr. Srinivas Garimella, for his guidance, support, and encouragement throughout my graduate education. Without the many long hours he devoted over several years, this work would not have been possible. I have always deeply valued his advice and hope this to be the beginning of a long association.

I would also like to thank all the current and past members of the Sustainable Thermal Systems Laboratory for their friendship and support. I would specially like to thank Christopher Keinath, Jared Delahanty, and Drs. Matthew Determan, Sangsoo Lee, and Lalit Bohra for their help and guidance in the development and operation of the various test facilities. Discussions and collaborations with them have often resulted in valuable insights that have helped address the various challenges faced throughout this work. I would also like to thank Michael Garrabrant and Stone Mountain Technologies Incorporated for their valuable inputs during the course of this study.

Finally, I would like to thank my Ph.D. committee members, Drs. Sheldon Jeter, Samuel Graham, William Koros, and Thomas Fuller for their valuable suggestions and patient perusal of my dissertation.

TABLE OF CONTENTS

LIST OF TABLES

LIST OF FIGURES

NOMENCLATURE

A	Area, m^2
$\overline{A}$	Average area, m^2
Ar	Archimedes number
COP	Coefficient of performance
Cp	Specific heat capacity, kJ kg^{-1} K^{-1}
$\tilde{C}p$	Molar specific heat, kJ $kmol^{-1}$ K^{-1}
C_T	Total molar concentration, kmol m^{-3}
D	Diameter, m
D_{aw}	Binary diffusion coefficient, m^2 s^{-1}
F_{ST}	Surface tension force, N
g	acceleration due to gravity, m s^{-2}
GAX	Generator-Absorber-Exchanger
Ga	Galileo number
Gr	Grashof number
h	Enthalpy, kJ kg^{-1}
HT	Heat transfer
I.D.	Inner diameter, m
Ja	Jakob number
k	Thermal conductivity, W m^{-1} K^{-1}
Ka	Kapitza number
l, L	Length, m
l'	Dimensionless length

$l_{semi,inf}$	Semi-infinite length, m
$LMTD$	Logarithmic mean temperature difference, K
m	Mass, kg
$\dot{m}$	Mass flow rate, kg s^{-1}
M	Molecular mass, kg $kmol^{-1}$
$\dot{n}$	Molar flux of species undergoing absorption, kmol m^{-2} s^{-1}
N	Number
$N_{drop,pr}$	Number of drops per row
$N_{drop,ps}$	Number of drops per second
$N_{tube,pr}$	Number of tubes per row
N_{row}	Number of rows
$N_{ch,ps}$	Number of channels per sheet
N_{shim}	Number of sheets
Nu	Nusselt number
O.D.	Outer diameter, m
P	Pressure, kPa
Per	Perimeter, m
Pr	Prandtl number
q	Quality
Q	Heat duty, kW
R	Thermal resistance, K W^{-1} or m^2 K W^{-1}
R_{gas}	Universal gas constant, kJ $kmol^{-1}$ K^{-1}
Ra	Rayleigh number

Re	Reynolds number
Sc	Schmidt number
Sh	Sherwood number
S_L	Longitudinal pitch, m
S_T	Transverse pitch, m
T	Temperature, ^oC
t	time, s
U	Overall heat transfer coefficient, W m^{-2} K^{-1}
UA	Overall heat transfer conductance, W K^{-1}
u	Velocity, m s^{-1}
$\overline{u}$	Average velocity, m s^{-1}
w	Width, m
We	Weber number
WR	Wetting ratio
x	Ammonia concentration (mass basis)
$\tilde{x}$	Ammonia concentration (molar basis)
y	Coordinate normal to tube surface, m
z	Concentration of condensing flux (mass basis)
$\tilde{z}$	Concentration of condensing flux (molar basis)

Greek Symbols

α	Heat transfer coefficient, W m^{-2} K^{-1}
β	Mass transfer coefficient, m s^{-1}
Γ	Linear mass flux, kg m^{-1} s^{-1}

Δ	Differential
η_f	Fin efficiency
η_T	Fin array efficiency
δ	Film thickness, m
λ	Droplet spacing, m
μ	Viscosity, kg m^{-1} s^{-1}
ϕ_T	Parameter for correction factor to heat transfer coefficient
ρ	Density, kg m^{-3}
σ	Surface tension, N m^{-2}
θ	Inclination angle
ζ	Coordinate in the axial direction

Subscripts/Superscripts

A	Ammonia
Abs	Absorber
abs	Absorption
avg	Average
bot	Bottom
bulk	Bulk
bubble	Bubble mode
CF	Coupling fluid
Cond	Condenser
Conc	Concentrated solution
cone	Conical section

ch	Channel
cr	Critical
Des	Desorber
Dil	Dilute
drop	Droplet
Evap	Evaporator
eff	Effective
falling-film	Falling-film mode
FA	Fin array
f/film	Solution film
fg	Latent (phase change)
feed	Feed region
hem	Hemispherical section
H2O	Water
i	Inner
in	Inlet
int	Interface
l	Liquid
max	Maximum
min	Minimum
NC	Natural convection
NH3	Ammonia
o	Outer

out	Outlet
pool	Solution pool
ratio	Ratio
Rect	Rectifier
Ref/ref	Refrigerant
reflux	Reflux
RPC	Refrigerant Pre-cooler
s	Coordinate in the circumferential direction
sat	Saturated
Sep	Separator
seg	Segment
SHX	Solution heat exchanger
sol	Solution
spread	Spread region
sub	Subcooling
T	Total
TA	Tube array
top	Top
tri	Triangular region
trap	Trapezoidal region
tube	Tube
vap	Vapor phase
W	Water

wall Wall

SUMMARY

An investigation of ammonia-water absorption at the microscales was conducted. The heat and mass transfer characteristics during absorption were studied for two absorption configurations: falling-film absorption around horizontal microchannel tube banks, and forced-convective absorption inside microscale channels. Falling-film absorption was investigated first, where a microchannel absorber was installed in a test facility replicating a single-effect ammonia-water absorption heat pump, and investigated over a range of concentrated solution flow rates (0.11 – 0.023 kg s^{-1}) and concentrations (40 – 55%), refrigerant fractions (15 – 40%), and coupling fluid inlet temperatures (20 – 40^{o}C). These operating conditions represent operation of the heat pump in both heating and cooling mode, over a range of capacities, and ambient conditions. The experimentally measured temperatures, pressures, and flow rates were analyzed to determine the state of the solution and vapor at various locations around the test loop, obtain the relevant component duties, and estimate the segmental absorption rates, and the overall and solution heat transfer coefficients. The microchannel falling-film absorber was found to transfer duties ranging between 2.89 – 10.09 kW in a compact envelope. The solution heat transfer coefficients were found to range between 1461 – 3430 W m^{-2} K^{-1}, and in general were found to increase with increase in the solution flow rate, the solution concentration, and the vapor flow rate.

A coupled hydrodynamic and heat and mass transfer model was developed to estimate the local absorption rates during falling-film absorption. In a horizontal tube absorber, solution transferred from one tube row to another as droplets. As these droplets fall on the tube, a film was formed which spread over the tube surface similar to a wave. The hydrodynamic model was developed which addressed the effects of these flow structures, and estimated the various flow characteristics such as droplet spacing, droplet evolution time, local film thickness, film spreading, and tube wetting ratio. These

estimates were coupled with the heat and mass transfer model to estimate the local absorption rates in each flow mode. Three regions in the absorber were considered for absorption of vapor: absorption at the solution pool, absorption into the droplets, and absorption into the film. Relevant concentration and temperature profiles were estimated in each region to calculate the local heat and mass transfer rates. Most of the absorption was found to occur in the film region, while up to ~ 7% of the absorption was found to occur in the droplet. The film Nusselt numbers were found to be affected by both the fluid and flow properties and a correlation was developed based on the solution Reynolds and Prandtl numbers, and vapor Reynolds number. This correlation can be used in conjunction with the coupled hydrodynamic and heat and mass transfer model to design microchannel falling-film absorbers.

Next, a complementary study of binary fluid coupled heat and mass transfer in internal microscale forced-convective absorption was conducted. A microscale heat and mass exchange miniaturization concept was presented, which consists of an array of alternating sheets with integral microscale features, enclosed between cover plates. These microscale features on the sheet include microchannel arrays for the flow of solution, vapor, and coupling fluid, and inlet and outlet headers for distribution of these fluids into the microchannel arrays. A segmental heat and mass transfer model was developed to obtain estimates of the miniaturization possible from the use of the above geometry for a hydronically cooled absorber. The model adapted the falling-film heat and mass transfer model to the forced-convective configuration, and predicted potential for the development of extremely small absorption system components.

Microscale absorber test sections were fabricated for two conditions: an absorber as part of a single-effect absorption chiller of cooling capacity 2.5 kW with a co-current desorber, and an absorber as part of a single-effect absorption chiller of cooling capacity 2 kW with a counter-current desorber. Photochemical etching was adopted to machine the microscale features on individual sheets, and diffusion bonding and vacuum brazing

were adopted to join the sheet array. These test sections were experimentally evaluated as a part of their corresponding chillers, where all the other absorption system components, were also designed and developed using similar microfabrication technologies. An absorption breadboard test facility was fabricated to install these absorption system components, and provide the necessary fluid streams at the realistic operating conditions.

The microscale forced-convective absorption test sections were tested over a range of solution and vapor flow rates, and the measured temperature, pressure, and flow rate data were analyzed to determine the state of the solution and vapor at various locations in the test loop, and calculate the relevant component duties. The absorber duty was found to range between 1.1 – 3.5 kW for the three test sections. A heat and mass transfer analysis on the test section estimated the solution heat transfer coefficients to range between 25.5 – 1138 W m^{-2} K^{-1}. Channel blockage during fabrication of the test sections was identified as a major issue in the operation of the absorber, and a revised sheet design was proposed to mitigate some of these problems.

Finally, a comparative assessment between the two absorption modes was conducted. Prototype miniaturized falling-film and forced-convective absorbers were designed for a representative absorber that is part of a 10.5 kW (3 RT) cooling capacity absorption chiller. While the local absorption rate and the required transfer area for complete absorption were different for the two modes, the overall trends were comparable. The overall volume of the microscale convective flow absorber was found to be nearly 8 times smaller than the microchannel falling-film absorber, but weigh nearly 1.6 times more. In general, the microscale forced-convective absorber was found to be suited for applications where space is at a premium, while the microchannel falling-film absorber was found to be suited for applications where component weight is critical. However, with improvement in the solution heat transfer process, the microscale forced-convective absorber can also be competitive in applications where component weight is critical.

CHAPTER 1. INTRODUCTION

Electrically driven vapor compression systems for space conditioning have lately been a cause for concern due to their contribution to high utility loads during peak hours. They also use synthetic refrigerants with potential adverse effects on the global climate. Absorption space-conditioning systems are environmentally benign alternatives and have the capability of being driven by waste heat. These systems have the potential for high coefficients of performance (*COP*s) through the use of increasingly complex thermodynamic cycles. However, a lack of practically feasible and economically viable compact heat and mass exchangers has thus far hindered the realization of the performance potential of these advanced cycles.

In particular, the success of the entire absorption cycle depends on the design of the absorber, which has been referred to as the "bottleneck" in the absorption heat pump (Beutler *et al.*, 1996). In the absorber, refrigerant vapor is absorbed into dilute solution with the release of a substantial amount of heat of absorption. In addition to the large heat transfer resistances, the absorber also experiences large mass transfer resistances due to the adverse concentration gradients during the phase change of the binary mixture working fluid. A lack of understanding of the inherently coupled heat and mass transfer phenomena during the absorption process has resulted in the use of poor designs, often employing inappropriate and oversized heat exchangers. This limitation becomes increasingly significant when attempting to implement absorption technology in the small capacity residential, mobile, and light-commercial markets where compact heat and mass exchangers are essential. The use of microchannels that facilitate high heat and mass transfer rates to develop absorption heat pump components can successfully address their limitations, and make them competitive for several of these applications. However, a good understanding of the binary fluid heat and mass transfer processes at the microscales is critical for the deployment of these technologies.

1.1. Absorption heat pump

Fig. 1.1 shows a schematic of a typical single-effect ammonia-water absorption heat pump (Bohra, 2007). It consists of five major components: the absorber, desorber, rectifier, condenser, and evaporator. Additionally, two recuperative heat exchangers, the solution heat exchanger and refrigerant pre-cooler, are also used, which facilitate internal heat exchange and increase the cycle *COP*. The working fluid in an absorption cycle is typically a binary mixture, where one component acts as the absorbent and the other component as the refrigerant. Two working fluid pairs have typically been used in the development of these cycles due to their favorable properties: water-LiBr, and ammonia-water. In water-LiBr absorption systems, the absorbent is aqueous LiBr while the refrigerant is water. These systems are typically suitable only for air-conditioning applications, because operation at temperatures lower than 0^{o}C is not possible due to

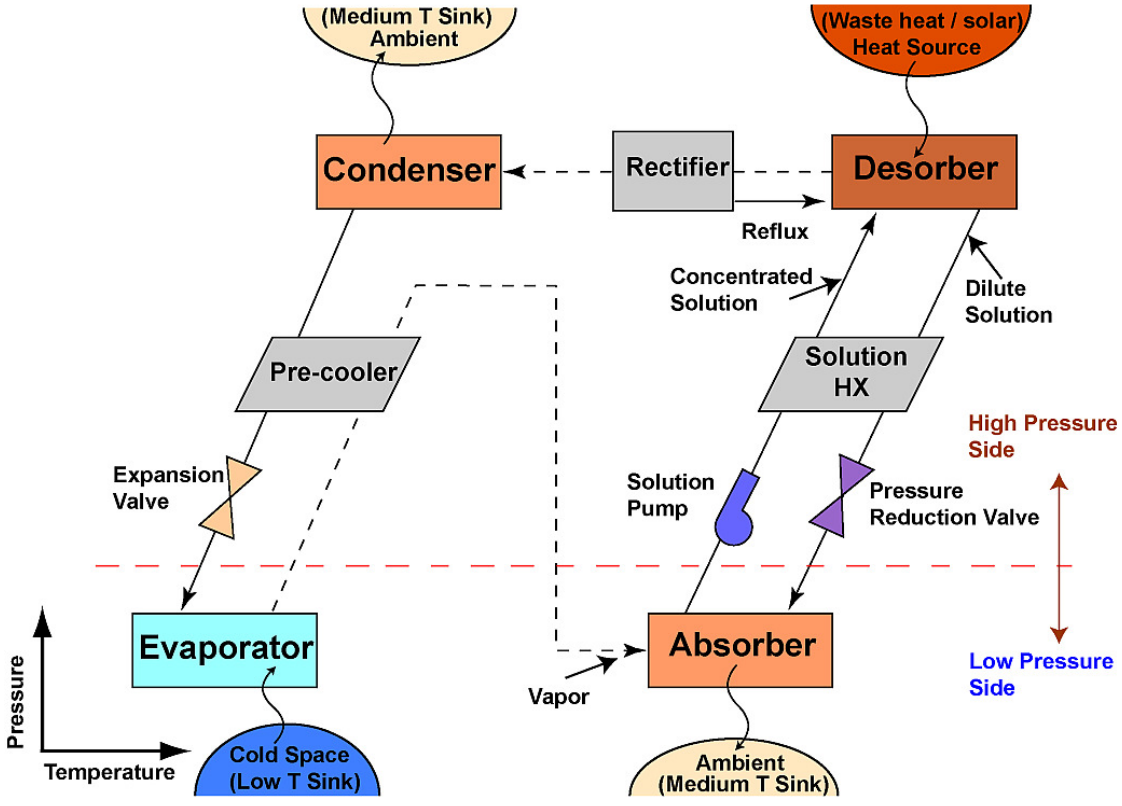

Fig. 1.1 Schematic of a single-effect ammonia-water absorption heat pump

freezing of water. In ammonia-water systems, water is the absorbent while ammonia is the refrigerant. These systems can be used for refrigeration, space-conditioning and cooling, and water heating applications because of the much lower freezing temperature (-77.65^{o}C) of ammonia. However, they are more complicated because an additional rectifier component is necessary to increase the concentration of the refrigerant vapor generated in the desorber.

The single-effect ammonia-water absorption cycle operates between two nominal pressure levels: the high pressure level of the desorber, the rectifier, and the condenser, and the low pressure level of the absorber and the evaporator. The cycle can be operated in both cooling and heating modes. In cooling mode operation (shown schematically in Fig. 1.1), the desired cooling (for space-conditioning) is achieved at the evaporator, and the medium temperature heat is rejected in the absorber and the condenser. In heating mode operation, the desired heating (for space-conditioning or water heating) is achieved at the condenser and absorber, and the low temperature heat is gained at the evaporator. High-pressure refrigerant vapor exiting the rectifier is condensed in the condenser. The condensed refrigerant is further subcooled in the refrigerant pre-cooler by the cooler low-pressure refrigerant exiting the evaporator. The subcooled high-pressure refrigerant is expanded to the low pressure using an expansion device, and flows through the evaporator, where it receives the low-temperature heat input. The refrigerant vapor leaving the evaporator is further heated in the refrigerant pre-cooler before entering the absorber. At the absorber, the refrigerant vapor is absorbed into the dilute solution returning from the desorber.

Dilute solution here refers to the ammonia-water solution that has a lower concentration of ammonia, sometimes referred to as the weak solution. This dilute solution is generated when the refrigerant is desorbed from the concentrated solution in the desorber. Concentrated solution here refers to the ammonia-water solution that has a higher concentration of ammonia, sometimes referred to as the strong solution. The

concentrated solution leaving the absorber at the low pressure is pumped to the desorber at the high pressure by the solution pump. Using a pump, instead of the compressor needed in vapor-compression systems, significantly reduces the required electrical work input to the system. Before entering the desorber, the concentrated solution recuperates heat from the dilute solution stream leaving the desorber in the solution heat exchanger.

The heat input required to drive the system is supplied at the desorber to generate vapor from the concentrated solution. The resulting dilute solution is routed back to the absorber via the solution heat exchanger. Since the absorbent water is a volatile component, the generated vapor stream in the desorber contains some water in addition to ammonia. The concentration of ammonia in the vapor stream is increased in the rectifier where some amount of water is preferentially condensed out, and the reflux is routed back to the desorber. The higher purity refrigerant vapor leaving the rectifier is introduced into the condenser, and the cycle is repeated.

It should be noted that while the refrigerant is mostly ammonia, it still contains some amount of water, which causes temperature glides during the phase-change process in the evaporator and condenser. These temperature glides can be particularly detrimental in the evaporator, where a rise in temperature as the evaporation proceeds leads to a decrease in the temperature difference needed for evaporation, thereby leaving some of the refrigerant in the liquid phase and decreasing the possible cooling load. Thus, it is important to minimize the water content in the refrigerant stream.

1.2. Absorber

During phase change of a binary mixture working fluid in the absorber, non-equilibrium conditions exist in the vapor and liquid bulk, while equilibrium exists at the vapor-liquid interface. The temperature and concentration in vapor and liquid bulk are different from those at the interface, resulting in temperature and concentration gradients in the respective phases that act as the driving potential for heat and mass transfer. During

absorption, the working fluid undergoes significant temperature and concentration glides, which often result in establishment of unfavorable gradients between the bulk and interface in the respective phases for heat and mass transfer (for example low driving concentration gradient in the vapor, or low temperature gradient in the liquid bulk.) Furthermore, the phase change process at the vapor-liquid interface is associated with the release of a substantial amount of heat. All these factors necessitate a large transfer area for the absorption process. Thus, the absorber is typically one of the biggest components in the heat pump. Several configurations for this component have been proposed in the literature. The two most commonly used configurations are falling-film absorbers, and bubble and forced-convective absorbers. Fig. 1.2 shows a schematic of a horizontal tube falling-film absorber (Meacham, 2002). In this absorber configuration, dilute solution

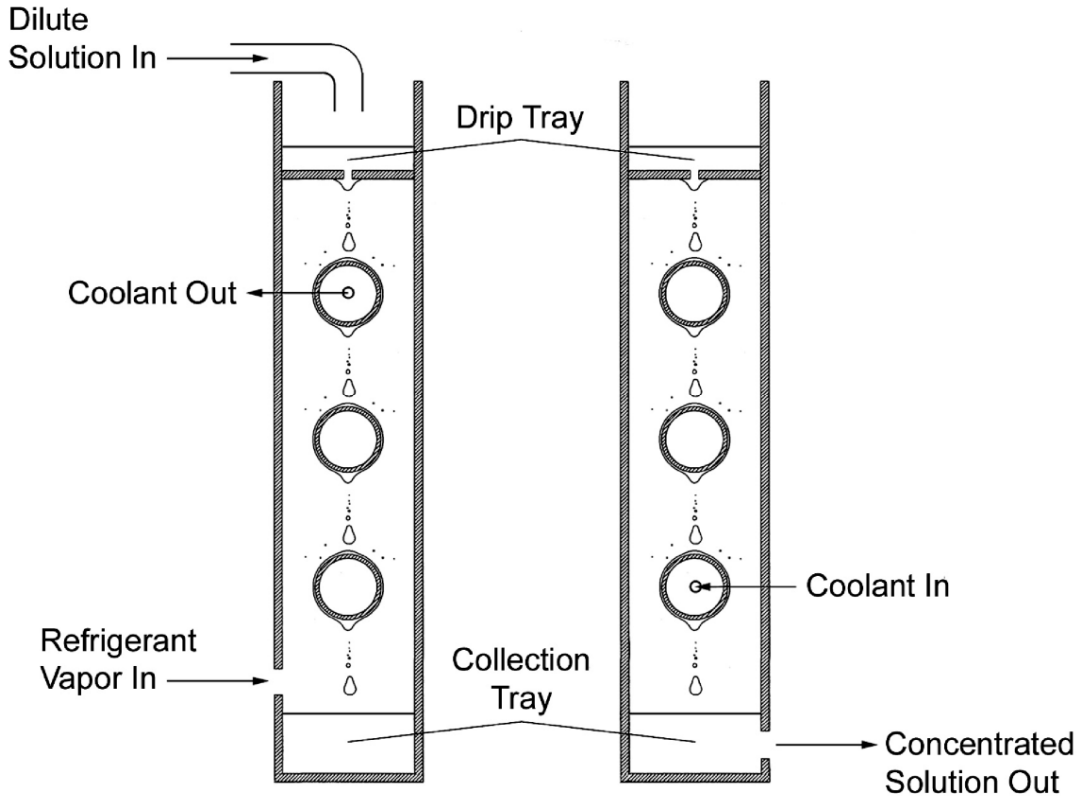

Fig. 1.2 Schematic of a falling-film absorber (Meacham, 2002)

flows as a film on the outside of a tube bank due to gravity, absorbing the refrigerant vapor, while the heat of absorption is removed by the coupling fluid circulated on the inside of this tube. The vapor can flow co-current or counter-current to the solution flow, or be introduced as a relatively quiescent vapor in the absorber shell. The falling-film flow configuration can also be achieved using a variety of different geometries including vertical columns and flat plates, in addition to the horizontal tube configuration shown here. Due to the formation of a thin film, large heat transfer coefficients can be achieved on the solution side with negligible pressure drops. However, the overall heat transfer resistance in such tube banks is usually dominated by the large thermal resistance on the coupling-fluid side, resulting in poor overall performance of the component.

Fig. 1.3 shows a schematic of a typical vertical tube bubble and forced-convective absorber (Meacham, 2002). In this absorber, vapor and solution are in convective flow on the inside of the tube, while the heat of absorption is removed by the coupling fluid circulated on the outside of the tube. Due to flooding concerns, the vapor flow is typically co-current to the solution flow, except at very low vapor flow rates, where flooding in a counterflow orientation would not be a major concern. Bubble and forced-convective configuration can be achieved using a variety of geometries including U-tubes and flat plate heat exchangers, in addition to the vertical tube configuration shown here. The presence of the vapor in bubble form can reduce the mass transfer resistance by increasing the interfacial transfer area. However, the overall heat transfer resistance is often still high due to low heat transfer coefficients on both the solution and coupling-fluid sides, resulting in poor overall performance of the component.

1.3. Research issues

Absorption systems have been in use for a long time (since the 1850s) (Herold *et al.*, 1996). However, there has been a lack of understanding of the inherently complex, coupled heat and mass transfer processes associated with vapor absorption with the

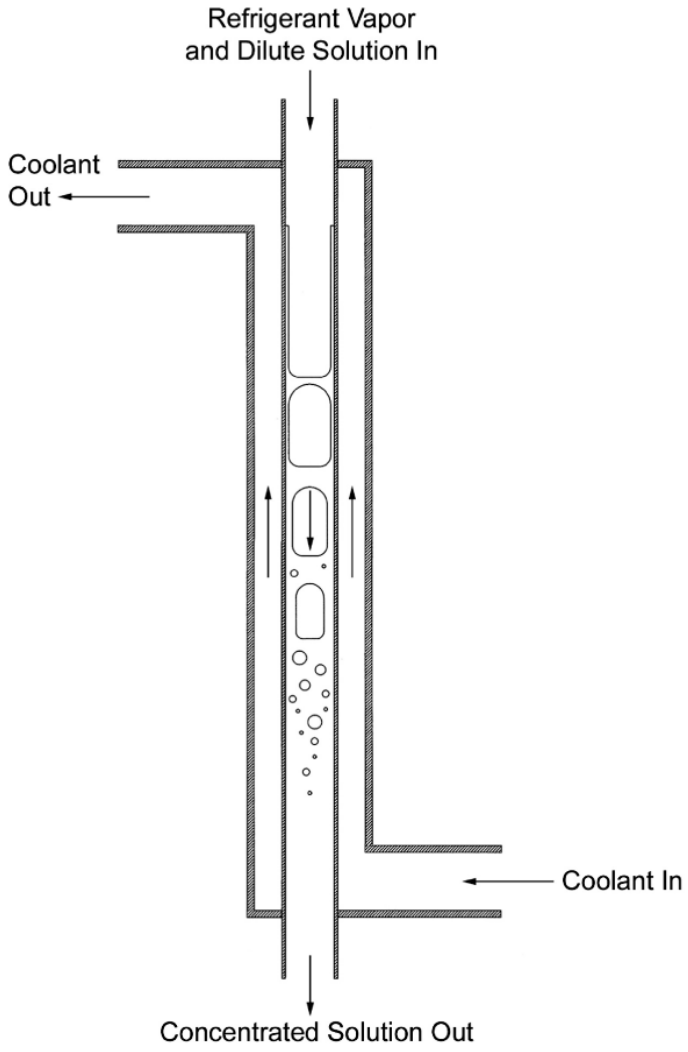

Fig. 1.3 Schematic of a bubble and convective-flow absorber (Meacham, 2002)

release of large latent heat loads. This is particularly true for the ammonia-water fluid pair where the volatile absorbent presents heat and mass transfer resistances across respective temperature and concentration gradients in both liquid and vapor phases. Analysis of the heat and mass transfer process, and quantification of each of these resistances is a challenging task. This is further complicated by the flow mechanisms observed during solution and vapor flow inside the absorber. For example, in falling-film absorption over horizontal tubes, mechanisms such as waves and evolving droplets are

observed over the tube surface, which can significantly affect the concentration and temperature profiles and as a result, the absorption process.

Most absorption models in the literature are often too simplistic, employing assumptions that are unrealistic (Killion and Garimella, 2001). This results in oversized or inappropriately sized components, which in turn yields low overall system performance. Thus, absorption systems have been restricted to larger industrial applications, where space and weight are not major constraints. Development of realistic models that can accurately capture the fluid flow, and heat and mass transfer mechanisms is important to achieve optimal performance of absorption heat pumps. In addition, for entry into residential, mobile, and light-commercial applications, development of compact high performance heat and mass exchangers is critical. The use of microchannels that facilitate high heat and mass transfer rates to develop absorption heat pump components can address some of these limitations. The development of such components requires a good understanding of the binary mixture heat and mass transfer at the microscales, which is a significant deficiency in the literature, as will be shown in the next chapter.

1.4. Scope of present research

The principal objective of this study is to investigate heat and mass transfer phenomena in the ammonia-water fluid pair at the microscales, and improve the understanding of the absorption process. Both absorption modes are experimentally and analytically studied in microscale geometries: falling-film absorption over microchannel tube banks, and forced-convective flow absorption inside microscale channels. The ammonia-water fluid pair is chosen for two reasons. As previously noted, ammonia-water absorption heat pumps can be operated at temperatures lower than 0^{o}C, without any risk of freezing. Additionally, the refrigerant in a water-LiBr absorption heat pump is water, which has a very high specific volume in the vapor phase. Routing large volumetric flows

of this vapor through microchannels can result in pressure drops that are beyond acceptable system limits.

It should be noted that in an actual heat pump, the absorber operating conditions are significantly influenced by other absorption system components, and thus an accurate and representative experimental investigation of the absorber must consider these effects. Therefore, to account for these influences, two complete single-effect ammonia-water absorption heat pump test facilities were designed and fabricated to study absorber test sections developed for both falling-film, and bubble and forced-convective absorption modes. Experiments are conducted over a wide range of operating conditions representing operation of the heat pump in both cooling and heating modes, over a range of cooling and heating capacities.

Absorption heat and mass transfer strongly depends on the local solution and vapor conditions, which vary along the flow path inside the absorber. Obtaining local level results and variations within components, while functioning in a realistic absorption system, has not thus far been addressed in the literature. Therefore, this study aims to understand the local phenomena inside the absorber, and estimate the corresponding heat and mass transfer rates from the experimental investigations, while considering the local temperature and concentration profiles, and the fluid flow structures. Furthermore, these investigations are conducted on a fully functional absorption chiller. Based on these insights, models for fluid flow and heat and mass transfer that can be used to design miniaturized components for both falling-film absorption and forced-convective flow absorption configurations are developed. The study concludes with a comparison between the two absorption flow configurations, and recommendations for their application in future miniaturization efforts.

1.5. Dissertation organization

This dissertation is organized as follows:

- Chapter 2 provides a summary of the literature on the analytical, numerical, experimental, and miniaturization studies on both falling-film, and bubble and forced-convective mode absorption.
- Chapter 3 describes the development of an absorption heat pump test facility for investigation of a microchannel falling-film absorber, and the summary of the experimental procedures and the matrix of tests conducted.
- Chapter 4 describes the data analysis procedures to estimate the state of the fluid streams at various locations in the test facility, and the analysis of the overall heat and mass transfer rates inside the absorber.
- Chapter 5 describes the development of a hydrodynamic model to analyze the flow of solution over microchannel tube banks, and a heat and mass transfer model to analyze the absorption process in each flow mechanism.
- Chapter 6 presents the development of a microscale heat and mass exchanger using a convective flow configuration, and a heat and mass transfer model for absorber applications. This chapter also presents the design and fabrication of 3 microscale absorption test sections.
- Chapter 7 describes the development of a breadboard test facility to investigate the absorption test sections as part of a single-effect ammonia-water absorption heat pump. This chapter also describes the experimental investigations on these test sections, and the subsequent system and component level analysis.
- Chapter 8 presents a comparative assessment between the falling-film and forced-convective flow absorption modes in terms of the possible heat and mass transfer rates within similar envelopes, fabrication, and packaging characteristics.

- Chapter 9 summarizes the important conclusions of this study and provides recommendations for future work in this area.

CHAPTER 2. LITERATURE REVIEW

Absorption cycles have been studied extensively since the late 1800s (Herold *et al.*, 1996). Because the present study focuses on the ammonia-water absorption, a significant portion of the literature presented in this review is pertinent to the ammonia-water fluid pair, and particularly the absorber component. However, some studies relevant to the absorber configuration and fluid flow regimes are also discussed. The review is categorized into three sections: studies relevant to falling-film absorption, studies relevant to bubble and convective mode absorption, and studies examining both absorption configurations. Falling-film, and bubble and convective mode absorption studies are further categorized into three subsections: analytical and numerical studies, experimental studies, and miniaturization studies. This summary of prior work is followed by a summary of the deficiencies in literature, the need for further research, and the objectives of the present study. A summary of the reviewed literature in tabular form is also presented at the end of the chapter.

2.1. Falling-film mode absorption

As discussed in the previous chapter, during falling-film absorption, dilute solution flows downward due to gravity as a thin film on a cooled wall while absorbing vapor. Several geometries have been studied in the literature both analytically and experimentally, including vertical and horizontal tubes, coiled tubes, and flat plates. A summary of these studies is included below.

2.1.1. Analytical and numerical studies

Some general assumptions have been made in most analytical and numerical studies reported in the literature. These common assumptions are listed below for brevity, followed by a discussion of specific aspects of each study separately.

- Steady-state absorption

- Constant pressure across the absorption domain
- Presence of non-condensable gases ignored
- Thermodynamic equilibrium at the vapor-liquid interface
- No direct heat transfer between vapor and coupling fluid
- Mass transfer only due to concentration gradient

Additionally for falling-film absorption, most studies in the literature assume that the film is laminar, and the transfer surface is completely wet. Studies that do not make some of the above listed assumptions are identified individually below.

One of the earlier studies on the coupled heat and mass transfer associated with ammonia-water absorption was conducted by Ruhemann (1947), who studied falling-film absorption on coiled-tube heat exchangers. In his absorber, solution and vapor flowed downward on the outside of the tube surface, while the heat of absorption was removed by the coupling fluid circulated on the inside of the tubes. He considered three separate zones for absorption: the vapor zone, the liquid zone, and the coupling fluid zone. He simplified the energy balance and heat and mass transport equations to develop three ordinary differential equations for the coupling fluid and solution temperatures and the solution mass flow rate as a function of location in the absorber. He observed that while the equation for solution mass flow rate involved the mass transfer coefficient and the equation for coupling fluid temperature involved the overall heat transfer coefficient, the equation for solution temperature involved both these coefficients, indicating the coupled nature of the heat and mass transfer process. He further considered two scenarios: one with large overall heat transfer coefficient and small mass transfer coefficient, and the other with small overall heat transfer coefficient and large mass transfer coefficient, and noted that for the same absorption duties, the required transfer areas were about the same, but the solution outlet conditions were significantly different. In addition, the temperature profiles inside the absorber were found to be different, with a spike in temperature observed in the second scenario. This spike was attributed to inefficient removal of heat

from the system due to lower heat transfer rates. It was also noted that the “effective” overall heat transfer coefficients (neglecting mass transfer) for the two scenarios were vastly different, and therefore he argued that considering only one of the two transport processes can result in appreciable error in absorber design.

Perez-Blanco (1988) developed a simplified model for the falling-film absorption process in ammonia-water absorbers to identify the important characteristics relevant to the development of compact absorbers. He applied Fick’s law of diffusion to estimate mass transfer rate in an infinitesimal volume, and determined the mass transfer coefficient from the Penetration theory (Higbie, 1935). Heat transfer in the liquid phase was assumed to be driven by conduction, and mass, species, and energy balance equations were solved to determine the solution and vapor states, and absorption rates in successive control volumes. The model was validated by comparing model predictions with experiments conducted on a coiled-tube absorber of tube diameter 12.7 mm (0.5’’) and coil diameter 82.6 mm (3.25’’). He observed that the model predicted the experimentally measured outlet conditions within an uncertainty of 10%. It should be noted that only two experiments were reported in this article, and the author states that this comparison was preliminary. It should also be noted that the model does not consider the possibility of local desorption of water, a phenomenon which was later reported by other investigators. A parametric study was conducted for two representative cases: low solution concentration and high solution temperature representative of more complex cycles (Generator-Absorber Heat Exchange - GAX cycle), and high solution concentration and low solution temperature representative of refrigeration and air-conditioning systems (single-effect cycle). For both cases, the absorption process was enhanced with increase in the falling-film mass transfer coefficient and decrease in solution mass flux. Additionally, for the second case, the coupling fluid heat transfer coefficient was found to influence the absorption process significantly, because the driving temperature differences were lower. Perez-Blanco recommended periodic mixing

of the film, use of surface additives for enhanced mass transfer, and the use of special surfaces to enhance mixing of the film at the vapor-liquid interface to ensure better mass transfer in the falling film.

Price and Bell (1974) developed a design methodology based on the Colburn-Drew equations (Colburn and Drew, 1937) for condensation of binary mixtures, and compared it with predictions from an earlier approximate method (Bell and Ghaly, 1972). It should be noted that while their formulation is only applicable for the design of condensers, several models for ammonia-water absorbers discussed here are extensions of this formulation of the absorption process. Price and Bell argued that while the vapor and liquid phases in a binary mixture are expected to be in equilibrium with each other at the vapor-liquid interface, concentration differences are expected in the bulk due to presence of a second condensing component. To model the condensation of binary mixtures, they considered the liquid film to be well mixed, and considered the resistance to vapor heat and mass transfer to extend only to the laminar boundary of the vapor-film adjacent to the vapor-liquid interface. Mass transfer in the vapor film, sensible cooling of the vapor bulk, and latent heat of condensation at the interface were considered in each segment of the binary mixture condenser. Correlations were used to estimate the relevant heat and mass transfer coefficients. They considered two fluid pairs, methanol-water and n-butane-n-octane, as two representative cases where the temperature glide during condensation is relatively small or relatively large, respectively. They observed that for the methanol-water mixture, the vapor resistance was relatively low and the predicted heat exchange area did not change significantly with the choice of correlation for vapor heat transfer coefficient, and compared reasonably well with the predictions from the approximate method. However, for n-butane and n-octane mixture, the vapor heat and mass transfer resistance was found to be significant, and their predicted heat exchange area differed significantly from the predictions of the approximate method. They also noted that the vapor bulk temperature was higher than the interface temperature, and the

vapor bulk concentration was found to continuously increase along the condenser length, indicating that the less volatile component condensed first. It should be noted that the ammonia-water mixture undergoes temperature glides in excess of 30^{o}C during the absorption process, and is expected to see trends similar to the latter representative case.

Based on this study, Kang and Christensen (1994) developed a heat and mass transfer model for the design of a vertically fluted tube, hydronically cooled absorber for an ammonia-water GAX absorber. Solution and vapor flowed in a counter-current configuration on the inside of the fluted tubes with an outer diameter of 33 mm, while exchanging heat with the coupling fluid circulated on the outside of the tubes. Their one-dimensional segmental model considered three different regions of absorption: vapor bulk, vapor-liquid interface, and liquid film, to account for the latent heat of absorption at the interface and the sensible cooling of both, the vapor and solution bulk. Similar to the model developed by Price and Bell (1974), they considered the solution to be well mixed, and utilized correlations from the literature for heat and mass transfer coefficients in the vapor and solution. They observed that the mass transfer resistance in the vapor and the heat transfer resistance on the coupling fluid side were the dominant resistances during absorption. Furthermore, they observed local desorption of water (while ammonia was being absorbed) at certain segments of the absorber. In these segments, vapor mass transfer rate is high, resulting in a large amount of heat released at the vapor-liquid interface. However, the overall heat transfer coefficient is not large enough to transfer all the heat generated at the interface to the coupling fluid, resulting in local desorption of water. The authors estimated that seven fluted tubes of length 1.075 m were needed to transfer 23.75 kW of heat in the GAX absorber.

The same authors extended the above heat and mass transfer model to study ammonia-water absorption in a spirally coiled fluted tube absorber with a porous medium (Kang and Christensen, 1995). The porous medium, which was on the outside of the tube, was assumed to contain the complete liquid film, the vapor-liquid interface, and a part of

the vapor flow. They argued that presence of a porous medium enhances wetting of the tube wall, and reduces the possibility of flooding by constraining the flow of solution. In addition to the three regions of absorption considered previously, an additional single-phase vapor region located inside the porous medium was considered. A previous study by Kang *et al.* (1994) analyzed the absorption process on smooth tubes with a porous medium. In comparison, the absorber configuration in this study was found to be nearly 28% smaller in size for the same overall performance, which was attributed to the higher coupling fluid heat transfer coefficient for fluted tubes. In addition, it was found that as the ratio of the outer envelope diameter to inner bore diameter increased, the absorber size decreased, which was attributed to enhancement of the coupling fluid heat transfer coefficient. Thus, they concluded that the absorption process was limited by the coupling fluid heat transfer coefficient. They also examined the effects of the ratio of thermal conductivity of the porous matrix (k_P) to that of the liquid (k_{sol}) on the absorption rate, and found that the absorption rate did not increase significantly for values of k_p/k_{sol} greater than 10.

Based on these studies, Kang *et al.* (1997) developed a generalized model to design all absorption system components. They utilized this model to design a desorber where the solution and vapor are in counter-current flow configuration. The vapor bulk temperature was found to be always higher than the solution temperature throughout the desorber, and higher than even the heating fluid temperature at the top of the desorber. This was attributed to the poor heat transfer rate in the vapor phase, where the generated vapor is not effectively cooled by the counter-current solution. They noted that the vapor phase heat transfer coefficient was, therefore, more important in desorber design than in absorber design. They further developed a composite map that provides insight into the mass transfer phenomena in each component of the absorption heat pump. For the absorption process, they noted that, $\tilde{z}$, the molar concentration of the condensing flux, was related to the bulk and interface vapor molar concentrations, $\tilde{x}_{vap,bulk}$ and $\tilde{x}_{vap,int}$,

respectively, such that $\tilde{z} > \tilde{x}_{\text{vap,bulk}} > \tilde{x}_{\text{vap,int}}$. Similarly, they noted that for the desorption process, $\tilde{z} > \tilde{x}_{\text{vap,int}} > \tilde{x}_{\text{vap,bulk}}$, rectification process $\tilde{z} < \tilde{x}_{\text{sol}}$, condensation process $\tilde{x}_{\text{sol}} < \tilde{z} < \tilde{x}_{\text{vap,bulk}}$, and evaporation process $\tilde{x}_{\text{sol}} < \tilde{z} < \tilde{x}_{\text{vap,int}}$, where $\tilde{x}_{\text{sol}}$ is the solution concentration. The direction of mass transfer of ammonia and water should the same for the rectifier, evaporator, and the condenser. For the absorber and the desorber however, transfer of water can be in either direction. They concluded by noting that the coupling fluid heat transfer resistance was the dominant resistance in most of the system components. It should be noted that in the above discussed studies, correlations from the literature were used to estimate the local heat and mass transfer coefficients in the solution and the vapor. These correlations were not developed for the ammonia-water fluid pair and are not always representative of the geometry under consideration.

Other authors have conducted computational studies on falling-film absorption. One such study was conducted by Wassenaar and Segal (1999) who developed a 2D model, based on the Navier-Stokes equations for mass, momentum, and energy applied to both the vapor and liquid phases. They also made several simplifying assumptions like assuming constant properties for the different fluids, and neglecting changes in mass flow rate of the fluid streams in each segment. It should be noted that these assumptions are not valid, particularly in ammonia-water absorption; however, they do facilitate the development of a simpler model. They applied their model to a flat plate heat exchanger with channels of width and length 5 mm and 1 m, respectively, for different vapor-liquid flow configurations (co-current and counter-current). They observed that irrespective of what the flow configuration was, the velocity vectors of the vapor near the vapor-liquid interface always had similar profiles. This was explained by the no-slip boundary condition applied at the vapor-liquid interface, which forces the local vapor velocity to be equal to the falling-film velocity, irrespective of the overall flow configuration. The authors also observed that convection was more dominant than diffusion, but this

dominance decreased with a decrease in channel width. Furthermore, the difference in the performance of the absorber for the different flow configurations was less than 4% for channel widths greater than 5 mm. However, the counter-flow configuration outperformed the co-flow configuration for smaller channel widths, but also presented a higher risk of flooding.

Another numerical study was conducted by Gommed *et al.* (2001) who studied ammonia-water absorption in laminar falling films in the absorber configuration previously studied by Kang and Christensen (1994). They applied the finite volume method to solve five partial differential equations setup from the mass, momentum, species, and energy conservation laws to estimate the pressure, temperature, concentration, and radial and axial velocities. Their model assumes the geometry to be axisymmetric and updates the state dependent properties along the flow. However, to simplify the problem, these properties were assumed to be constant in the radial direction at any given location. They observed that the temperature profile in the solution developed quickly into a nearly linear profile, indicating that the heat transfer process in the liquid film is conduction dominated. The vapor temperature and concentration profiles were found to undergo a sharp change near the interface, before gradually attaining a near constant value towards the vapor bulk, indicating the presence of a thin vapor film region between the vapor-liquid interface and the vapor bulk. A concentration gradient was also observed in the solution film. Confirming the observations of the previous authors (Kang and Christensen, 1994, 1995), they also noted that the rate of absorption decreased along the tube length as the driving potential (the concentration difference between the vapor and the liquid) decreased. They also studied the influence of transport properties on the absorption process, and noted that the vapor diffusion coefficient has a very slight effect on the absorption process. In general, decreasing the vapor flow rate in the absorber resulted in a reduction in the absorption rate, and an increase in the solution thermal conductivity and diffusivity improved the absorption rate.

Chen and Christensen (2000) extended the dimensionless analysis previously developed for water-LiBr absorption (Conlisk, 1992) to ammonia-water absorption by accounting for the volatile nature of water as the absorbent in the NH_3-H_2O pair. To simplify their model, they considered the diffusion in the vapor phase to be negligible, and ignored shear between the liquid and vapor phases, which resulted in the decoupling of the vapor and liquid momentum equations. By further assuming nearly constant solution flow rate in each segment, relatively low liquid and vapor velocities, and slow changes in the bulk and interface concentrations, they conducted an order-of-magnitude analysis on the governing equations to yield linear partial differential equations in the liquid phase. The governing equations were solved by isolating the two non-homogenous boundary conditions (inlet subcooling and wall heat flux) into two separate problems. They concluded that any absorption process can be estimated as the linear combination of these two cases: subcooled absorption in the absence of cooling, and saturated absorption with wall cooling. They observed that adiabatic absorption with subcooled solution inlet resulted in an asymptotic decrease in the absorbed mass flux over the absorption length considered. However, saturated absorption with a cooled wall resulted in a continuous increase in the absorbed mass flux over the absorption length. They noted that during adiabatic absorption, the lower interface temperature leads to a high vapor interface concentration. This large gradient between the interface and the bulk vapor concentrations results in high absorption rates initially. However, as more ammonia moves into the liquid bulk, the absorption rate decreases due to the diminishing concentration gradient in the liquid phase, as well as increase in the interface temperature. During cooled absorption, the interface temperature is continuously cooled, resulting in an increase in the concentration gradient between the interface and bulk solution, leading to larger absorption mass fluxes. Based on a parametric study, they developed a correlation for heat transfer as a function of the ratio of the inlet subcooling and dimensionless wall heat flux, film thickness, thermal conductivity, and other flow

parameters. The heat transfer coefficient was found to decrease with increase in the inlet subcooling, and was generally found to be higher than those predicted based on a Nusselt type analysis. Finally, they recommended the use of passive mixing devices along the film that can trip the thermal and concentration boundary layers, and enhance the local heat and mass transfer rate.

Other work on ammonia-water falling-film absorption includes the study of absorption enhancement in the presence of a magnetic field (Xiaofeng *et al.*, 2007). They developed a mathematical model that included the force exerted by an external magnetic field as a body force in the momentum equation. The simplifying assumptions used include negligible heat conduction in the vapor phase, and uniform increase in coupling fluid temperature. Furthermore, mass transfer was considered only in the radial direction. They observed that the falling-film velocity and film thickness increased with an increase in the intensity of magnetic induction. These flow enhancements resulted in higher rates of absorption, indicating that the presence of a magnetic field along the flow direction enhances the absorption process. They also observed that the temperature of the solution remained relatively independent of the magnetic field, indicating that the magnetic field largely affected only the mass transfer process by influencing the momentum equation. An experimental study validating the above predictions was also conducted by the same authors, and will be discussed later.

The above studies all considered ammonia-water as the working fluid pair. The water-LiBr working fluid pair has traditionally received more attention because the absorption process is relatively simpler to model due to the absence of a second condensing component in the vapor phase (Killion and Garimella, 2001). While these studies are not directly relevant to the present work, some present the development of a more realistic analysis that captures the different flow characteristics observed during the absorption process. Such studies are discussed next.

Patnaik *et al.* (1993) developed a computational model for water-LiBr falling-film absorption on vertical single-tube absorbers, by considering the enhancement in the mass transfer rate in the liquid due to the wavy nature of the film. Correlations were used to estimate heat and mass transfer coefficients in the solution and coupling fluid, and design charts were developed for absorber sizing. For a given evaporator duty and selected solution and coupling fluid flow rates, these charts could be used to determine the absorber size, solution outlet temperature, concentration, and degree of subcooling at the solution outlet. They noted that for lower coupling fluid flow rates, the absorber performance did not vary appreciably with change in the solution flow rate, as the coupling fluid heat transfer resistance was the dominant transfer resistance. However, at higher coupling fluid flow rates, the degree of subcooling at the solution outlet increased, and vapor absorption rate decreased with decrease in the solution flow rate, indicating that the limiting resistance is now on the solution side.

In their later studies, the same researchers explored the characteristics of roll waves in falling-films and their effect on absorption. Patnaik and Perez-Blanco (1996a) developed approximate equations for flow in roll waves in falling films. They utilized the model developed by Brauner (1989) to estimate the dominant frequencies, film thickness, and average velocity in the roll wave. They then applied a parabolic profile to the longitudinal velocity in various segments of the wave (substrate, wave front, and wave back), and estimated the velocity in the transverse direction using the continuity equation. The plot of the film thickness as a function of time and location indicated a periodic rise and fall, representing a roll wave. The transverse velocity was found to undergo rapid fluctuations with both positive and negative values, indicating flow both away and towards the wall. Thus, rapid mixing of fluid is expected to occur due to the presence of these roll waves. They then applied this approximate velocity field to study absorption enhancement due to wavy films (Patnaik and Perez-Blanco, 1996b). Starting with the 2D unsteady species and energy equations, they developed two parabolic partial differential

equations, which were numerically solved in conjunction with the flow field estimated previously. At lower film Reynolds numbers, reasonable agreement was observed with experimental data, and with predictions from the Penetration theory (Higbie, 1935). However, at higher film Reynolds number, their model predicted significantly higher absorption rates in comparison to the Penetration theory (Higbie, 1935), indicating absorption enhancement due to roll waves. They observed that the temperature and concentration profiles underwent fluctuations in time at any location due to the presence of roll waves. Also, the concentration in the transverse direction also underwent a rapid drop due to the roll waves, which was identified as the cause for enhancement in the absorption rate. These fluctuations decayed to periodic fluctuations around a steady value for both concentration and temperature, and were found to be out of phase. The concentration boundary layer was found to reach the wall a certain distance below the top of the absorber, indicating that fully developed condition was achieved below this point. Additionally, two thermal boundary layers were found to exist in the film, one coming from the interface and the other from the wall. These boundary layers were quite close to each other and underwent fluctuations similar to the film thickness.

Other researchers studied the flow mechanisms observed during falling-film absorption around horizontal round tubes, and their effect on the absorption process. Kirby and Perez-Blanco (1994) presented a design model for horizontal tube water-LiBr absorbers by considering the different flow regimes observed during falling-film absorption (falling film, evolving droplet, and droplet free fall). They considered a representative droplet spaced uniformly along the horizontal tube, and developed equations to determine residence times in different flow regimes during absorption. Correlations from the literature were utilized to estimate heat and mass transfer rates in each flow regime. They observed that a significant amount of absorption occurred in the droplet mode, which was indicated by a change in the concentration of the solution between successive tube rows. This absorption process is adiabatic since the droplets are

not being actively cooled by the coupling fluid. They also observed that thinner films underwent a higher concentration change due to shorter distances for mass transfer in the liquid, but thicker films were able to absorb a higher amount of vapor due to a higher solution concentration for a larger section of the absorber. The contribution to absorption from the droplet free-fall regime was comparatively low due to the low residence time in this regime. In general, the authors observed that the absorption duty increased with increase in solution flow rate, coupling fluid flow rate, and absorption pressure.

Jeong and Garimella (2002) conducted a study on water-LiBr absorption on horizontal tubes. In addition to considering the above discussed flow regimes, the authors also explored the effects of wetting on tubes and solution flow rate on the absorption process. Absorption in the droplet mode was considered to be adiabatic, while the absorption in the film mode was cooled by the coupling fluid circulated in the tube. They assumed a linear temperature profile in the bulk of the film, except at the interface where the temperature rises rapidly to the interface temperature. Additionally, they also assumed a velocity profile for the film flow based on the relations developed by Nusselt (1916). The heat of absorption released at the interface was tracked through the film to the wall. Furthermore, a wetting ratio (ratio of the wet tube surface area to the total tube surface area) was defined to account for the effect of incomplete wetting on tubes. They presented the temperature and concentration profiles as a function of the angle from top of the tube, and noted that the absorption rate was low at the top and bottom of the tube due to the presence of a thick, warm liquid film formed by the impinging/evolving droplet that underwent adiabatic absorption previously. On the other hand, the absorption rate was high at the center of the tube due to the presence of a cool, thin film. In droplet mode absorption, they observed that vapor was initially found to absorb rapidly due to the presence of cool liquid supplied from the falling film. The absorption rate decreased as the droplet evolved further, with the contribution to absorption from the falling droplet being negligible in comparison to the other two regimes. The contribution to absorption

due to the droplet mode increased at the lower tube levels, and was more significant at higher solution flow rates. In general, the tubes at the higher levels absorbed more vapor due to favorable mass transfer conditions. Tube wetting was found to affect the absorption rate in film mode significantly, but had no significant effect on the absorption rate in droplet mode. They found that their predictions compared well with the experimental results presented by Nomura *et al.* (1994b). They recommended that the mass flux per tube in the absorber should between 0.02-0.04 kg m^{-1} s^{-1} to ensure good wetting and performance.

In a subsequent study, the same authors conducted a systematic investigation of the effects of tube diameter and pass arrangement on absorber performance (Jeong and Garimella, 2005). They considered three tube diameters A, B, and C of diameter 15.88, 6.35, and 3.175 mm, respectively, and analyzed absorbers of the same transfer area for different pass arrangements and for a range of solution flow mass fluxes (0.01-0.04 kg m^{-1} s^{-1}). They observed that for any tube diameter, the performance of the absorber did not vary much if the number of passes was greater than two. For passes less than or equal to two, the absorber performance was slightly lower, for which the authors presented a correction factor. They observed that the smaller tube diameters exhibited higher absorption rates, with absorbers made from tube B and C providing a 30 and 55% increase in overall cooling capacity, respectively. A sharp decrease in the performance of the absorber was observed when the coupling fluid heat transfer coefficient was less than 3000 W m^{-2} K^{-1}, which was attributed to the transition point where the coupling fluid resistance becomes important in the absorption process. They also noted that the absorption in droplet mode was proportional to the number of tubes, which in turn was inversely related to the tube diameter. Thus, as the tube diameter decreased, the absorption in droplet mode increased, while the absorption in the film was found to remain relatively constant.

Subramaniam and Garimella (2009) presented a detailed summary of the different visualization and numerical studies on water-LiBr absorption conducted by Garimella and coworkers. Killion and Garimella (2003) conducted an extensive study on flow mechanisms in falling films flowing over horizontal tube banks using high-speed flow visualization. They observed that at lower Reynolds numbers, typically observed during falling-film absorption, liquid moves from one tube row to another as droplets. Liquid was found to accumulate at certain sites on the tube, and then form droplets due to gravity. Quantitative measurements of the droplet volume and surface area were made as the droplet evolved on the underside of a tube. Both these parameters were found to increase to a maximum value just before droplet detachment and impact on the subsequent tube row, and satellite droplets were observed after droplet impact. The same authors later developed a 3D numerical model by considering the Navier-Stokes momentum equations and utilizing the volume of fluid (VOF) method to solve for the flow of solution around a horizontal tube, and development of a pendant droplet (Killion and Garimella, 2004b). They considered a computational domain extending to half the tube spacing on either side of a single tube in the vertical direction and half the distance between successive droplet sites in the horizontal direction. They observed that gravitational forces caused the solution to accumulate at the bottom of the tube, resulting in the creation of the droplet formation site. As the droplet grows, more of the fluid starts to move towards the lower regions of the droplet, resulting in the formation of a neck. The detachment of the droplet from the tube was dependent upon the spacing between the successive tube rows. Over time, the neck was found to get thinner, resulting in detachment of the droplet, followed by the formation of satellite droplets. Predictions for surface area and volume of the droplet from their simulations were found to compare very well with experiments after the volume of the droplet reached a value of 75 mm^3. A similar comparison was observed for satellite droplets after impact of the primary droplet.

Subramaniam and Garimella (2009) extended this model by incorporating the heat and mass transfer associated with water-LiBr absorption, by solving the 3D mass and species conservation equations in conjunction with the momentum equations. Their model was able to estimate local temperature and concentration values in the axial and circumferential direction, and along the thickness of the film. They observed that the solution, which was continuously cooled by coolant circulated on the inside of the tube, absorbed water vapor at a higher rate than the pendant droplet, which was largely adiabatic. Solution in the film right above the droplet was found to have a lower concentration than solution around the rest of the tube, which was attributed to the high local absorption rate from high local fluid velocity and low film thickness. Prior to droplet impact, the solution on the film was found to have significant temperature and concentration gradients along the film thickness due to poor local transport mechanisms. However, upon droplet impact, the resulting wave induced rapid mixing which resulted in a nearly uniform film temperature and concentration. The mixed film was found to have significantly higher heat and mass transfer rates. Finally, as a new droplet was being generated, the absorption rate was again found to decrease because the absorption in the droplet was largely adiabatic. About 4.4% of the total absorption was found to occur in the droplet mode. The authors, however, argued that the droplets are more important to the absorption process because they facilitate rapid mixing of the solution, which results in high film heat and mass transfer rates.

2.1.2. Experimental Studies

Experimental studies on falling-film heat and mass transfer are discussed next. Several of these studies are for the ammonia-water fluid pair during absorption. Additionally, studies that are relevant to some of the flow mechanisms observed in the present work have also been discussed. In most absorption studies, experiments are conducted on a single-pressure, bench-top test facility that consists of only the absorber,

or the absorber, desorber, and the solution heat exchanger, instead of a complete absorption chiller. It should be noted that these experiments do not always represent operation of the absorber under conditions observed during operation of absorption chillers.

One of the early experimental studies on falling-film absorption was conducted by Haselden and Malaty (1959), who considered ammonia-water absorption on the outside of a vertical tube. In their absorber, solution flowed downwards as a falling film and vapor flowed counter-current to the solution on the outside of the tube, while the heat of absorption was removed by the coupling fluid flowing vertically upward on the inside of the tube. The experiments were conducted at near-atmospheric pressure, and on a tube of outer diameter 0.0127 m. Solution was distributed uniformly over the vertical tube using a ferrule type funnel at the top of the absorber and the length of the absorber tube was varied by moving the solution collection chamber along the tube. The absorber assembly was housed inside a Pyrex pipe to enable visual access. Thermometers were used to estimate the inlet and outlet bulk temperatures of the solution, vapor, and coupling fluid, a manometer to measure the operating pressure, and rotameters to measure the flow rate of the different fluid streams. Bulk concentration of the solution was estimated by titration. The interface concentration was estimated by assuming that the interface was at equilibrium and at the solution bulk temperature. Experiments were conducted for a range of dilute solution flow rates (0.25-1.75 g s^{-1}), dilution solution concentrations (0-21%), and absorber lengths (0.15-2.1 m). They observed that the mass transfer coefficient, calculated using the solution interface and bulk concentrations, increased with increase in the solution average concentration and solution temperature, which was contradictory to the predictions from the Penetration theory (Higbie, 1935). They also did not observe a clear influence of the solution Reynolds number on the mass transfer coefficient. They observed an enhancement in the heat and mass transfer rate due to formation of ripples, which they attributed to an increase in the transfer area. For cases

where a surface additive (Teepol) was added to the solution to reduce the formation of ripples, the predictions from Penetration theory (Higbie, 1935) were comparable to the experimental results. Finally, they noted that the dominant resistance to heat transfer was on the coupling fluid side, and therefore the solution-side heat transfer coefficients could not be estimated accurately. The presence of air in the absorber was also found to lower the absorber performance by inhibiting the mass transfer process.

Palmer and Christensen (1996) conducted an experimental investigation on vertical fluted tube absorbers, and verified the heat and mass transfer model previously developed by Kang and Christensen (1994). Their absorber consisted of two co-axial tubes, a smooth outer tube and a fluted inner tube, sharing common headers at the end. Solution flowed as a falling film on the inside of the fluted tube absorbing the counter-current vapor, while the heat of absorption was removed by the coupling fluid flowing on the outside of the tube. Three proprietary inserts were placed at the center of these tubes to facilitate better heat and mass transfer. This absorber was installed in a single-pressure test facility consisting of the test absorber and a desorber, and investigated over a range of solution concentrations. They reported that their model predicted experimentally measured dilute solution concentration and temperature within ±2% for several test cases. It should be noted that the model was adjusted with a wetting factor obtained by matching of the measured and predicted dilute solution state at the inlet of the absorber. The absorber duty was predicted within ±20% of experimentally measured values; the higher discrepancy being attributed to heat losses from the absorber and surrounding tubing during experiments. They also noted that the concentration and temperature of the solution and vapor were found to decrease monotonically from top to the bottom of the absorber. The wetting of the fluted tube was predicted to be between 25-50% for all test cases, and found to increase with increase in solution concentration. They attributed this to the reduction in the solution surface tension, which improves spreading of solution.

Jeong *et al.* (1998) studied ammonia-water falling-film absorption on a coiled tube absorber, where solution and vapor flowed in counter-current configuration on the outside of the tubes, while coupling fluid flowed on the inside of the tubes. A stainless steel tube of outer diameter of 12.7 mm was wound in a coil of diameter 82.6 mm, and housed inside an outer shell to form the absorber. This absorber was installed in a single-pressure test facility where dilute solution and vapor were supplied from separate reservoirs. Experiments were conducted for dilute solution flow rate of 4.9-19.7 g s^{-1} at an inlet concentration of 1.2-2.2% and temperature of 66-69^{o}C, and vapor flow rate of 0.09-0.42 g s^{-1} at an inlet concentration of 63-77%. The coupling fluid inlet temperature was varied between 41-16^{o}C at a fixed flow rate of 27 g s^{-1}. It should be noted that these test conditions, particularly the solution concentrations, are not relevant to heat pump operation. To estimate the solution-side heat transfer coefficients, a 1D resistance network was developed and mass transfer effects were neglected. They observed that the solution-side heat transfer coefficient increased with increase in solution flow rate. They also noted that the heat transfer coefficients were higher for the falling film in the absence of absorption, which was attributed to uneven distribution or stagnation of the liquid film due to the vapor-liquid shear during absorption. To enhance the absorber performance, they recommended reducing the coil radius and increasing the number of turns in a coil, which would increase the solution flow rate per length of coil and therefore, increase the heat transfer coefficient. They also developed the following correlations for the solution-side heat transfer coefficient, with and without absorption.

$$Nu_{sol} = 0.00022 \cdot Re_{sol} \tag{2.1}$$

$$Nu_{sol} = 0.00035 \cdot Re_{sol} \tag{2.2}$$

Kang *et al.* (1999) studied falling-film absorption in a plate heat exchanger with offset strip fins, where the solution and vapor were in co-current flow configuration. This absorber was studied in a single pressure system, consisting of a generator and a

separator (used to separate the two-phase solution leaving the generator). The vapor separated in the separator, and dilute solution of known concentration from an external reservoir were routed to the absorber at the same pressure. As a result, the vapor temperature was much higher than the dilute solution. The authors conducted experiments at three different dilute solution concentrations (5, 10 and 15%), and for a range of vapor concentrations between 64.7-79.7%. It should be noted that the above concentrations and temperature are not representative of conditions observed during operation of an absorption heat pump. They described the absorption process to proceed as follows: as the vapor and solution enter the absorber, the concentration of vapor bulk is higher than the equilibrium concentration at the interface, leading to local rectification initially. Subsequently, as the vapor temperature decreases and concentration increases, the absorption process is initiated. They observed that both the heat and mass transfer rates increased with increase in solution inlet subcooling, and this effect was more pronounced on heat transfer. With increase in concentration difference between the solution and vapor, the mass transfer coefficient was found to increase while the heat transfer coefficient was found to decrease for the same solution flow rate and degree of subcooling. Finally, they noted that the Nusselt number had a stronger dependence on the falling-film Reynolds number in comparison to the vapor Reynolds number, contrary to the dependence of the Sherwood number on these parameters. The correlations for Nusselt and Sherwood numbers developed from this study based on solution and vapor Reynolds number, degree of inlet subcooling and concentration difference between the vapor and solution at the absorber inlet are given below.

$$Nu_{\text{sol}} = 0.853\times10^{-3}\cdot Re_{\text{sol}}^{1.518}\cdot Re_{\text{vap}}^{0.1759}\cdot\left(\frac{\Delta T_{\text{sub}}}{T_{\text{sol}}}\right)^{1.879}\cdot\left(\frac{\Delta x_{\text{vap-sol}}}{x_{\text{sol}}}\right)^{-0.5756} \tag{2.3}$$

$$Sh_{\text{sol}} = 0.6996\times10^{-7}\cdot Re_{\text{sol}}^{0.8874}\cdot Re_{\text{vap}}^{1.265}\cdot\left(\frac{\Delta T_{\text{sub}}}{T_{\text{sol}}}\right)^{0.8844}\cdot\left(\frac{\Delta x_{\text{vap-sol}}}{x_{\text{sol}}}\right)^{0.5304} \tag{2.4}$$

Hoffmann and Ziegler (1996) fabricated a single pressure test facility and developed a data reduction algorithm for falling-film ammonia-water absorption experiments over horizontal tube banks. Their test facility was designed to run tests over a wide range of solution and vapor flow rates, and concentrations, and consisted of an absorber, a generator, and a rectifier, all housed inside a cylindrical shell. The absorber consisted of 24 tubes in four passes with a total heat transfer area of 0.8 m^2. Local temperature, pressure, flow rate, and density measurements could be made for different fluid streams, and ports for visual access were available at strategic locations to observe the different flow regimes during operation. A data reduction algorithm was developed to estimate the state of the solution and vapor streams, which could in turn be used to estimate the local heat and mass transfer coefficients. However, no experimental data were reported in this paper.

Kwon and Jeong (2004) explored the effect of vapor flow direction on ammonia-water falling-film absorption by experimentally studying a helical coil absorber in a single-pressure system at three dilute solution concentrations (3%, 14% and 30%), four inlet temperatures (45, 50, 55, 60^{o}C), and over a range of solution flow rates per unit length (4.43-90.9 g s^{-1} m^{-1}). The helical coil considered had a tube diameter of 12.7 mm and a coil diameter of 82.6 mm, housed in an absorber chamber of diameter 114.3 mm and length of 600.6 mm, which included vapor flow passages. Dilute solution heated by an electric heater was supplied to the absorber from the bottom of a two-phase reservoir, while vapor was supplied from the top of the same reservoir. The concentration of the vapor generated in the supply tank ranged between 45.6-96.5%. They observed that the heat transfer rates increased with increase in the solution flow rate, which was attributed to the rapid mixing and corresponding enhancement in mass transfer rate. They also noted that the heat transfer rate at lower solution and vapor concentrations was higher for the parallel-flow configuration in comparison to the counter-current configuration. However, this difference became smaller as the concentration of the reservoir tank

increased, and was negligible for the highest concentration. They explained this by suggesting that at lower concentration, the specific volume of the vapor generated was larger, leading to higher vapor velocities and uneven solution distribution or stagnation (flooding). Thus, they concluded that the vapor-liquid shear plays a significant role in absorption rates, which is reflected in the correlations developed based on their data for parallel and counter-current flow configurations.

$$Nu_{\text{sol,parallel}} = 1.975\times10^{-3} \cdot Re_{\text{sol}}^{0.6895} \cdot \tau_{\text{vap}}^{0.0249} \tag{2.5}$$

$$Nu_{\text{sol,counter}} = 1.683\times10^{-4} \cdot Re_{\text{sol}}^{0.8672} \cdot \tau_{\text{vap}}^{0.3018} \tag{2.6}$$

It should be noted that the exponents of the shear stress terms are small (particularly for parallel-flow), and therefore, their influence on the Nusselt number is expected to be low. It is possible that the difference in the heat transfer coefficients for the two flow configurations may not be due to the influence of shear stress, but due to a combination of experimental uncertainties, non-equilibrium conditions in the vapor bulk, and subcooling of the solution bulk. This highlights the need to study absorption as a coupled heat and mass transfer process to accurately address all these influences.

Niu *et al.* (2010) experimentally studied the effect of an externally applied magnetic field on falling-film ammonia-water absorption on the outside of a 900 mm long vertical tube of diameter 25 mm housed inside an outer shell. Three copper magnetic coils placed on the outside of the shell were used to generate a magnetic field upon introduction of a direct current. The absorber was placed in a single-pressure test facility with dilute solution of known concentration introduced into the absorber from a reservoir, and pure ammonia introduced from an ammonia cylinder through a pressure regulating valve. Solution flow rates were measured in the solution lines, and thermocouples and pressure transducers were used to measure the local temperature and pressure at different locations on the test loop. The concentration of the concentrated solution leaving the absorber was estimated by measuring the density of the solution stream. They observed

that the concentration of the solution leaving the absorber increased with increase in magnetic field applied in the direction of the falling film. The opposite trend was observed if the magnetic field was reversed, which was consistent with the predictions from their previous numerical study (Xiaofeng *et al.*, 2007). Furthermore, the absorber duty was also found to increase with increase in magnetic field in the direction of flow. At any magnetic field intensity, absorber performance was found to decrease with increase in dilute solution concentration and coupling fluid temperature, and decrease in coupling fluid flow rate; a trend that is inherent to the properties of the fluid and the driving temperature difference, and not necessarily a result of an externally applied magnetic field.

Enhancement in absorption with nanoparticles was studied by Yang *et al.* (2011), who measured the effect of addition of surfactant sodium dodecyl benzene sulfonate (SDBS), and three nanoparticles: $ZnFe_2O_4$, Fe_2O_3, and Al_2O_3. They considered a vertical tubular absorber of 25 mm diameter with solution flowing as a falling film on the outside of the tube, and coupling fluid circulated on the inside of the tube. This absorber was installed in a single-pressure test facility where dilute solution and refrigerant vapor were supplied from two reservoirs, and experiments were conducted at a pressure 90 kPa. They observed that addition of surfactant SDBS decreased the absorption rate, which was attributed to an increase in the solution viscosity, which in turn increased the resistance to interfacial mass transfer. When nanoparticles were mixed with this surfactant to produce a stable mixture, the authors found the absorption rate to increase to a peak value, followed by a subsequent decrease with increase in mass fraction of nanoparticles. They suggested that there were two competing phenomena that caused this behavior: the use of SDBS decreases the absorption rate, but use of nanoparticles increases the absorption rate by enhancing the effective thermal conductivity and introducing micro-convection. Thus, an optimal nanoparticle mass fraction was observed. The enhancement was found to be higher for higher solution concentrations (an enhancement of nearly 70% was achieved

for 15% ammonia-water solution with Fe_2O_3 nanoparticles), and nanofluids made from Fe_2O_3 exhibited the highest increase in absorption rate among the three different nanoparticles considered in this study.

All the previous experimental studies were conducted on a single-pressure system with limited control over the absorber operating conditions. While the absorber pressure can be reasonably controlled, the resulting solution and vapor concentrations supplied from the desorber are not representative of heat pump operation. The study conducted by Lee *et al.* (2008a, b) is a notable exception where horizontal tube falling-film absorption was investigated in a two-pressure test facility replicating a single-effect ammonia-water absorption chiller, over a wide range of operating pressures, solution flow rates, and concentrations. The absorber tube array had 4 columns of 9.5 mm outer diameter tubes of length 0.29 m. Each column had 6 tubes with headers located at either end to facilitate a serpentine flow configuration for the coupling fluid. This absorber was placed inside a shell with an optical port to facilitate visual observation of the absorption process. In addition to system level temperature, pressure, and flow measurements, in-situ temperature measurements were also recorded during the absorption process at the tube level inside the absorber to monitor the progression of the absorption process. Experiments were conducted over dilute solution concentrations ranging from 5-40%, concentrated solution flow rate ranging from 0.019-0.034 kg s^{-1}, and absorber pressure ranging between 150 and 500 kPa, representing absorber operating conditions during chiller operation in refrigeration, cooling, and heating modes. They obtained solution-side heat transfer coefficients, and solution and vapor mass transfer coefficients from their data. The solution-side heat transfer coefficient was estimated to range between 923 and 2857 W m^{-2} K^{-1}, and increased with increase in solution flow rate and decrease in absorber pressure. The vapor mass transfer coefficient was estimated to vary between 0.0025 and 0.26 m s^{-1}, and was found to increase with decrease in pressure and increase in concentration, and was relatively independent of the solution flow rate. They also

found that the absorber pressure and solution concentration affected the liquid phase mass transfer coefficient. They conducted an extensive comparison with correlations available in the literature for falling-film heat and mass transfer coefficients, and found that most correlations did not compare well with their data. They argued that several of the correlations were not developed for the ammonia-water fluid pair, and those that were developed for this fluid pair were not based on experiments at realistic operating conditions and for geometries or flow mechanisms different from those observed in their study.

Bohra (2007) conducted a flow visualization and heat and mass transfer study on the horizontal tube absorber discussed above. High speed video of the solution flowing over the tube banks was taken, capturing the different flow mechanisms at the tube as well as at the tube-bank level. Solution flow between successive tube rows was found to be in droplet mode, which compared well with the transition criteria presented in the literature (Hu and Jacobi, 1996a; Mitrovic, 2005). He further observed that while the droplet mode was the dominant flow mode, the primary droplet never actually detached from the tube underside, which was attributed to the small spacing between successive tube rows (vertical pitch 20.1 mm). An edge-detection tool was used to estimate different parameters such as droplet size, spacing between droplets, droplet fall time, and found to compare reasonably with correlations in the literature (Yung *et al.*, 1980; Armbruster and Mitrovic, 1998). He also presented the progression of solution flow over a tube and noted that as the pendant droplet is formed, the film flow over the tube surface could be described as a stretched triangle previously reported by Killion and Garimella (2003). He suggested that this stretching film induces mixing and presents new surfaces for the absorption process. Characteristics of the evolving droplets were also studied where the primary droplet was found to grow rapidly upon receiving liquid from an impinging droplet originating on the upper tube. Formation of a liquid bridge was observed when the droplet came into contact with the subsequent tube row. Upon break up of this bridge,

a secondary (satellite) droplet was also observed. Significant interactions between axially adjacent droplet sites were also observed, along with axial movement of solution on the underside of the tubes, which affected the local film thicknesses, wetting behavior, and active heat transfer area of the tube. Bohra suggested that the absorber operating conditions played an important role in determining film and droplet behavior by affecting critical solution properties such as surface tension, which in turn affected the overall heat and mass transfer rates.

Based on these insights, Bohra *et al.* (2008) developed a segmental heat and mass transfer model that considered absorption in both falling-film and droplet mode flow. Temperatures measured at different locations in the tube bank were used to determine the local solution state in the bulk and at the interface. The vapor bulk inside the chamber was assumed to be quiescent, and vapor interface conditions were determined based on the solution interface conditions. Mass transfer was considered in both the vapor and the solution. The tubes were considered to be fully wet and the solution bulk was found to be subcooled throughout the absorber. Similar to the analysis conducted by Jeong and Garimella (2002), droplet mode absorption was modeled by considering an adiabatic primary droplet. The authors noted that for a majority of test conditions, the contribution from droplet mode to the overall absorption process was less than 6%, which is in contrast to what was observed for the water-LiBr fluid pair (Jeong and Garimella, 2002, 2005). The film heat transfer coefficient was found to range between 78 – 6116 W m^{-2} K^{-1}, the vapor mass transfer coefficient between 0.42 – 2.8 m s^{-1}, and solution mass transfer coefficient between 3.59×10^{-5} – 8.96×10^{-5} m s^{-1}. Based on their experimental data, the authors presented correlations for film Nusselt number, and vapor and solution Sherwood numbers.

$$Nu_{\text{film,seg}} = 7.589\times10^{-3} \cdot Re_{\text{sol,seg}}^{1.04} \cdot Pr_{\text{sol,seg}}^{0.46} \cdot \left(\frac{P_{\text{abs}}}{345} \right) \tag{2.7}$$

$$Sh_{vap} = 2.708\times10^{-11}\cdot\left(\frac{Gr_{vap}\times Sc_{vap}}{Ja_{vap}}\right)^{1.26}\cdot\left(\frac{Pr_{sol}}{Sc_{sol}}\right)^{-1.68}\cdot\left(\frac{\mu_{sol}-\mu_{vap}}{\mu_{vap}}\right)^{1.43} \quad (2.8)$$

$$Sh_{sol,seg} = 1.298\times10^{-4}\times Re_{sol,seg}^{0.57}\times Sc_{sol,seg}^{1.32}\times\left(\frac{P_{abs}}{345}\right)^{0.64} \quad (2.9)$$

Hu and Jacobi (1996a, b) conducted a detailed study on the flow characteristics and heat transfer in falling films on horizontal tubes for a variety of fluids. It should be noted that there was no phase change in this study; only sensible heat transfer was considered. Five tube diameters ranging from 9.5-22.2 mm were studied with different tube spacing, and solution linear mass flux was varied from 0 to 0.22 kg m^{-1} s^{-1}. For the study of flow characteristics, five fluids were considered: water, glycol, water-glycol, oil, and alcohol. They observed that as the solution flow rate increased, the flow between consecutive tube rows transitioned between three principal flow modes: droplet, jet, and sheet. In addition to these modes, they also observed two mixed modes: droplet-jet and jet-sheet. A hysteresis in the transition between each mode when the solution flow rate was being increased and decreased was also observed. Based on the different fluid and flow properties and geometric considerations, they argued that the flow transitions would depend upon the film Reynolds number, modified Galileo number, Ohnesorge number, and dimensionless tube spacing. In their experiments, they observed that the effect of the last two numbers were negligible, and therefore developed transition criteria and a map for flow transitions based on the film Reynolds number and Galileo number. They found that inertia effects dominated in the sheet mode, while gravity or surface tension effects dominated in droplet mode. Jets were formed due to a competition between these effects and viscous forces.

In a subsequent heat transfer study, Hu and Jacobi (1996b) considered three fluids (water, glycol, and glycol-water) in falling-film mode around the tube arrays discussed above. Several thermocouples were placed around the circumference of the tube and at different locations axially to measure local temperatures of the solution. Heat was

provided to the falling film by heaters placed on the tube surface. Local and average heat transfer coefficients were estimated using the measurements from these thermocouples. They observed that the local heat transfer rates varied significantly along the circumference of the tube for all flow modes. The heat transfer coefficient was found to be highest at the top of the tube because of the surface-normal velocities in the flow due to impact of fluid coming from the tube above. As the fluid flows around the tube circumference, a thermal boundary layer develops, resulting in a reduction in the local heat transfer coefficient. The heat transfer coefficients were found to reach a near-constant value towards the bottom of the tube. In the axial direction, the variation of local heat transfer coefficient was found to be negligible for sheet mode but significant for droplet and jet mode. For droplet and jet mode, locations between two active sites were found to exhibit high heat transfer coefficient values compared to locations close to the droplet/jet formation site, which were attributed to the low thickness of the film in the corresponding locations. The average Nusselt number was found to depend upon the film Reynolds number, Prandtl number, Archimedes number, and dimensionless tube spacing. They also found that the solution heat transfer coefficient was higher for smaller tube diameters. For smaller tubes, the developing boundary layer occupies a larger fraction of the total heat transfer area, resulting in higher average heat transfer coefficient and Nusselt numbers. Correlations were developed for the average Nusselt numbers for all three flow modes.

$$Nu_{\text{sheet}} = 2.194 \cdot Re_{\text{sol}}^{0.28} \cdot Pr_{\text{sol}}^{0.14} \cdot Ar_{\text{sol}}^{-0.20} \cdot \left(s/d\right)^{0.07} \tag{2.10}$$

$$Nu_{\text{jet}} = 1.378 \cdot Re_{\text{sol}}^{0.42} \cdot Pr_{\text{sol}}^{0.26} \cdot Ar_{\text{sol}}^{-0.23} \cdot \left(s/d\right)^{0.08} \tag{2.11}$$

$$Nu_{\text{drop}} = 0.113 \cdot Re_{\text{sol}}^{0.85} \cdot Pr_{\text{sol}}^{0.85} \cdot Ar_{\text{sol}}^{-0.27} \cdot \left(s/d\right)^{0.04} \tag{2.12}$$

2.1.3. Miniaturization Studies

Some of the early miniaturization attempts for falling-film ammonia-water absorbers were made by Christensen and co-workers. In addition to the vertically fluted tube absorbers (Kang and Christensen, 1994) discussed above, they also developed a corrugated and perforated plate-fin absorber (Christensen *et al.*, 1998). Garrabrant and Christensen (1997) presented the development of a prototype based on this concept. In this absorber concept, a perforated fin structure, folded like an accordion, was sandwiched between two end plates forming a structure similar to a corrugated sheet. Vapor flows upward through the perforations (pentagon shaped holes) in the corrugated fins, while solution flows downward over corrugated fins and through the perforations. Off-set strip fins were sandwiched between the end plate and the outer plate, forming channels to circulate coupling fluid flow for removal of the heat of absorption. Christensen and coworkers applied the heat and mass transfer model previously developed by Kang and Christensen (1994) to the new geometry, and developed an α-prototype absorber. In this prototype, the perforated fins (6-7 perforations per row) were fabricated from a 432 × 127 mm carbon steel sheet of thickness 0.25 mm. The solution and coupling fluid channels were machined in a 38.1 mm thick carbon steel sheet, and sealed on both ends with end plates. In the α-prototype, coupling fluid was circulated on only one side of the solution channels. This absorber was installed in a single-pressure test facility, which included a desorber and separator, and tested over a range of solution concentrations (13-41%), solution flow rates (4.16-11.8 g s^{-1}), and absorption duties (1.55-5.1 kW). Based on these experiments, they observed that the absorber performance depended upon the wetted fin area fraction, the fin efficiency, and the vapor mass transfer coefficient. They developed calibration curves for each of these parameters, such that the predictions from their models matched the experimental results. A β-prototype was developed next using methods closer to that of a production unit where coupling fluid channels were brazed on both sides of the solution channel, and the overall absorber size

was 432 × 127 × 31.8 mm. This absorber was tested over a range of solution flow rates and concentrations, resulting in absorber loads ranging from 1.47-2.93 kW, and yielding an overall heat transfer conductance value of 1829-2445 W/K. They also observed that the dominant resistance shifts from the coupling-fluid side to the solution side as the vapor flow rate decreases. Local desorption of water at the lower absorber levels was also reported for some conditions.

Another miniaturization study was conducted by Goel and Goswami (2005) who proposed using the space between successive tube rows of a horizontal-tube falling-film absorber by introducing a wire mesh that could guide the solution flow between tubes. They reasoned that the presence of this mesh increases the vapor-liquid interfacial area, and enhances the wetting and mixing characteristics of the absorber, leading to a reduction in the overall size of the absorber. A finite-difference method based heat and mass transfer model developed for the absorption process indicated nearly 25% reduction in size of the absorber due to the presence of the mesh. They observed that while the mesh increases the vapor-liquid interfacial area, it does not provide any additional cooling. Thus, the solution reaching the subsequent tube row is hotter in the presence of the mesh, which leads to favorable heat transfer conditions. The authors observed a saw-tooth profile for the solution temperature; the temperature decreased in cooled tube region, and increased in the mesh region. It should be noted that the presence of a mesh can inhibit formation of droplets, which might be detrimental to the absorption process, by inhibiting the intense mixing of the solution bulk on the tube surface that these droplets facilitate.

In a subsequent study, the same authors evaluated this design by conducting an experimental investigation on horizontal-tube absorbers with and without the mesh (Goel and Goswami, 2007). A four-pass arrangement was used with tubes of outer diameter 3.175 mm and length 98 mm, stacked in four tubes per row and fifteen rows per pass. An aluminum wire mesh (16 × 16 meshes in^{-2} or 24800 × 24800 meshes m^{-2}) was used to

connect successive tube rows. The overall absorber dimensions were 63.5 × 120 ×635 mm. This absorber was studied in a single-pressure test facility with a desorber and solution heat exchanger. The dilute solution and vapor volume flow rates were measured using a rotameter and a turbine flow meter, respectively, while temperatures were measured using T-type thermocouples. They observed that for similar operating conditions, the conventional absorber transferred a heat duty ranging from 3-3.8 kW while the mesh-enhanced absorber transferred a heat duty of 3.5-4.5 kW, an increase of 17-26%. They further observed that the absorber duty increased with an increase in the dilute solution flow rate. The overall heat transfer conductance (*UA*) values for the conventional and mesh-enhanced absorbers were found to vary from 0.34-0.5 kW K^{-1} and 0.48-0.62 kW K^{-1}, respectively, an average increase of 49%. They observed that the theoretical model developed in their previous study (Goel and Goswami, 2005) seemed to over-predict the number of rows required to transfer the same heat duty in comparison to experimental results. The theoretical model was able to predict 58% and 79% of the data points for conventional and mesh-enhanced absorber, respectively. The authors attributed the larger error in the conventional absorber predictions to their model formulation, which did not consider flow mechanisms such as droplet formation and impingement.

The above miniaturization studies attempted to enhance absorption rates by increasing the transfer area/volume ratio. Miniaturization studies conducted by Garimella and co-workers attempted to enhance the absorption rates by not only increasing this transfer area/volume ratio, but also by decreasing the coupling fluid- and solution/vapor-side heat and mass transfer resistances. Garimella (1999) developed a compact, microchannel based falling-film absorber for residential applications consisting of transversely alternating arrays of stacked microchannels. The liquid solution flows in falling-film mode on the outside of these tube rows, absorbing the vapor that flows upward in countercurrent fashion, while the heat of absorption is removed by the coupling fluid flowing through the microchannels. In addition to the high solution-side

heat transfer coefficients observed due to the thin film-flow over round tubes, he also noted that the tube-side heat transfer resistance was considerably reduced due to the high heat transfer coefficients observed in single-phase flow through the small hydraulic diameter microchannels. He observed that this design promotes high heat and mass transfer rates due to mechanisms such as countercurrent vapor-liquid flow, vapor shear, adiabatic absorption between tubes, species concentration redistribution at every row due to liquid droplet impingement, and significant interaction between vapor and liquid flows around adjacent tubes in the transverse and vertical directions. He developed a heat and mass transfer model based on the approach described by Price and Bell (1974) to design one such microchannel absorber for a 10.5 kW single-effect absorption chiller for residential applications by accounting for heat and mass transfer in both the vapor and liquid phases. The resulting absorber had an overall volume of 0.476 × 0.127 × 0.127 m and a transfer area of 1.9 m^2. He observed very high solution-side and coupling fluid-side heat transfer coefficients (2790 W m^{-2} K^{-1} and 1604 W m^{-2} K^{-1}, respectively), and attributed this to the microchannel geometry. He also observed higher absorption rates at the top of the absorber, which was attributed to the higher solution temperatures and lower solution concentrations at this location, which yield favorable heat and mass transfer rates. Local desorption of water, previously observed in literature (Kang and Christensen, 1994), was also reported in this study.

Meacham and Garimella (2002) experimentally demonstrated this heat and mass exchanger concept in an absorber application, in a single-pressure test facility consisting of a desorber and solution heat exchanger in addition to the absorber itself. A slightly modified microchannel array configuration of total transfer area 1.5 m^2 was fabricated and evaluated for a range of concentrated solution flow rates (0.011-0.036 kg s^{-1}). Temperatures and pressures were recorded at different locations in the loop, and mass flow rates of the dilute and concentrated solution streams were measured. In addition to the absorber coupling fluid flow rate, temperatures were measured at the inlet, outlet, and

at five different intermediate locations in the corresponding coolant headers in the absorber. They demonstrated absorption duties ranging from 5-16.23 kW, and estimated the overall and solution-side heat transfer coefficients to range from 130-400 W m^{-2} K^{-1} and 150-550 W m^{-2} K^{-1}, respectively. They also observed that these coefficients had a strong dependence on the solution flow rate and a relatively weaker dependence on the vapor fraction. Due to the laminar nature of the flow, the coolant heat transfer coefficient was constant at 2600 W m^{-2} K^{-1}. They noted that the absorber performance falls short of the earlier predictions (Garimella, 1999), which they attributed to three main reasons. Their absorber was about 27% smaller than the original design, resulting in lesser area for transfer. Secondly, the vapor entering the absorber was at a lower concentration than the design conditions, leading to poor mass transfer rates in the vapor phase. Finally, there was potential solution flow mal-distribution on the tube banks due to non-uniform flow from the solution distribution tray, which could significantly deteriorate the absorption performance.

To quantify this solution mal-distribution, Meacham and Garimella (2003) developed a segmental heat and mass transfer model based on the model previously presented by Garimella (1999). They also proposed an area effectiveness ratio $r = A_{eff}/A_{actual}$ to account for the underutilized area during the absorption process. They observed that the value for the effectiveness ratio varied between 0.22 and 0.31 for all the experimental data, indicating that a large portion of the absorber was not wet during the absorption process. They also noted higher heat transfer coefficients for the falling film than predicted by Garimella (1999), which was attributed to the higher local mass flux due to the lesser effective transfer area. They observed that the vapor temperature upon entering the absorber decreased due to sensible cooling with the liquid solution flowing downwards. However, about midway through the absorber, the vapor temperature started to rise due to sensible heating of the vapor with the heat of absorption generated at the vapor-liquid interface. The solution temperature was found to decrease continuously from

the top to the bottom of the absorber. Good comparison between measured and predicted coupling fluid temperatures and absorption duties was achieved for most test cases. Based on this study, the authors confirmed that the challenge of high coolant-side heat transfer resistance was addressed, and concluded that any improvement on the solution side, particularly addressing the flow mal-distribution issue, would significantly enhance the already miniaturized absorber.

Meacham and Garimella (2004) next developed and experimentally demonstrated a second generation absorber that had better flow distribution characteristics. Unlike the previous generation device, the successive tube arrays were oriented in the same direction in this absorber which facilitated optical access to visualize the flow during the absorption process. The total transfer area was significantly reduced to 0.456 m^2 (a 70% reduction from the first generation). This absorber was housed in a stainless steel shell with a large sight glass in the front and smaller sight glasses on the other three sides, to visualize the flow mechanisms during absorption using a high-speed video camera. Its performance was investigated over a range of solution flow rates (0.015 – 0.027 kg s^{-1}), and vapor fractions (15-30%) in a single-pressure test facility similar to the one described in Meacham and Garimella (2002). The absorber was found to transfer heat duties ranging from 4.5-15.1 kW, which is comparable to the performance of the original prototype, despite a significant reduction in the transfer area. The solution-side heat transfer coefficient was found to range from 638-1648 W m^{-2} K^{-1}, which is comparable to the predictions from Garimella (1999), and significantly higher than those observed in the original prototype (Meacham and Garimella, 2002). They attributed this to the superior flow distribution of the solution on the tube banks due to a revised channel configuration and drip tray design, which was confirmed by high-speed video of the absorption process. They also observed several flow mechanisms such as wavy film, evolving droplet, and droplet impact, and recommended the need to model these mechanisms accurately for effective design of absorption components.

Determan *et al.* (2004) investigated the microchannel array studied by Meacham and Garimella (2002, 2003) in a desorber application with a minor modification to the drip tray. The modified drip tray simultaneously facilitated distribution of solution around the tube banks and removal of vapor generated in the desorber through the vapor flow passages in the tray. This desorber was installed in a single-pressure test facility and studied over a range solution flow rates (0.019-0.035 kg s^{-1}). Desorption duties ranging from 5.4-17.5 kW were demonstrated, with the overall heat transfer coefficient and solution-side heat transfer coefficient ranging from 388-617 W m^{-2} K^{-1} and 659-1795 W m^{-2} K^{-1}, respectively. They reported that at lower solution flow rates, the heat transfer process was solution-side limited while at higher solution flow rates, the resistances on both the solution- and coupling-fluid sides were comparable. In a subsequent study, Determan and Garimella (2011) developed a segmental heat and mass transfer model for the desorption process, and estimated wetting ratios along the desorber height. Tube wetting was found to decrease from top to bottom of the array, which was attributed to the decreasing flow rate due to desorption and due to coalescence of solution and formation of rivulets as it flowed downwards in the bank. At the lowest tube rows, wetting was found to increase again, which was attributed to the lower solution flow rates in this region that form thinner films that spread more readily. The average wetting for all data points was found to range from 25-69%. Determan and Garimella also observed local rectification of vapor at the top levels of the desorber, where the vapor temperature was higher than the solution temperature, resulting in condensation of water out of the vapor stream. The predictions of the vapor outlet temperature compared reasonably well with the experimentally measured values.

A summary of the progression of these miniaturization efforts on falling-film ammonia-water absorption has been reported recently in Garimella *et al.* (2011). In addition, development and demonstration of a larger capacity (1.357 m^2 transfer area) third generation microchannel absorber with a revised drip tray for better flow

distribution and horizontally oriented shell for improved wetting characteristics due to decreased coalescence and rivulet formation in shorter tube banks, was also presented. This component was found to exhibit high solution-side heat transfer coefficients, and require fewer tube segments and braze joints per unit transfer area, making it a cheaper component to fabricate. Also, they suggested that the horizontal orientation of the component could represent a better aspect ratio, making it more favorable from a packaging perspective for some applications.

2.1.4. Summary of falling-film absorption

Table 2.1 shows a summary of the literature on falling-film ammonia-water absorption discussed above. While some of the early analytical models simplified the ammonia-water absorption process by ignoring the presence of water in the vapor phase, the more realistic studies adapted the methodology presented by Price and Bell (1974) for binary mixture condensation to the absorption process. These models could typically account for temperature and concentration gradients in the vapor and solution films at any intermediate location of the absorber, as well as for absorption and the corresponding temperature and concentration variation along the length of the absorber. They are particularly useful in sizing and designing absorbers, and provide useful insights into the absorption trends (such as local desorption of water), as well as predicting the limiting resistances during the absorption process. It should be noted that these studies utilize correlations from the literature to estimate the local heat and mass transfer coefficients, which can be a source of significant error because these correlations are often not applicable to the fluid pair being investigated and/or relevant to the geometry and operating conditions being studied (Kang and Christensen, 1994, 1995; Kang *et al.*, 1997; Garimella, 1999; Goel and Goswami, 2005). Numerical models were developed by considering the Navier-Stokes equations and applying simplifying assumptions such as constant properties, negligible vapor heat transfer, low solution and vapor velocities, and

negligible changes in flow rate over a control volume (Wassenaar and Segal, 1999; Chen and Christensen, 2000; Gommed *et al.*, 2001). While these assumptions might not be completely valid for the ammonia-water absorption process, the resulting models present some interesting trends of flow behavior near the vapor-liquid interface and heat and mass transfer mechanisms. It should be noted that almost all of the analytical and numerical studies on falling-film ammonia-water absorption make simplifying assumptions like laminar films and fully wet tube surfaces, which are not accurate in a realistic system. Studies on water-LiBr absorption, which is relatively simpler to model compared to ammonia-water absorption due to the absence of absorbent and the corresponding concentration gradients in the vapor phase, have focused on capturing these effects and have highlighted their importance (Patnaik *et al.*, 1993; Patnaik and Perez-Blanco, 1996b, a). Other research on water-LiBr absorption addressed the different flow regimes observed during flow of solution over cooled surfaces and reported significant influences of each regime (Kirby and Perez-Blanco, 1994; Jeong and Garimella, 2002, 2005; Subramaniam and Garimella, 2009).

Experimental studies on falling-film absorption have been conducted on a variety of geometries such as plain vertical tubes and vertically fluted tubes (Haselden and Malaty, 1959; Palmer and Christensen, 1996), coiled tube heat exchangers (Jeong *et al.*, 1998; Kwon and Jeong, 2004), plate heat exchangers (Kang *et al.*, 1999), and horizontal tube banks (Bohra, 2007; Bohra *et al.*, 2008; Lee *et al.*, 2008a, b). Several of these authors confirmed the existence of waves on the films and observed their influence on the absorption process. Furthermore, for horizontal tube banks, film and droplet flow regimes were observed and their influence on the hydrodynamics and heat and mass transfer were investigated (Hu and Jacobi, 1996a, b; Bohra, 2007; Bohra *et al.*, 2008). Correlations for Sherwood and Nusselt numbers were also developed, although the coupling of heat and mass transfer was not completely explored. It should be noted that most of these studies were conducted on single-pressure test facilities, where the supplied solution and vapor

were at conditions not representative of operation of an absorber in an absorption chiller (Haselden and Malaty, 1959; Jeong *et al.*, 1998; Kang *et al.*, 1999; Kwon and Jeong, 2004). Therefore, these correlations may not be applicable to realistic absorption processes. Other researchers studied the influence of magnetic fields (Niu *et al.*, 2010) and nanoparticles (Yang *et al.*, 2011) on the absorption process and reported conditions for performance enhancement.

Miniaturization efforts in falling-film absorption were focused on reducing the solution-side resistance or both solution- and coupling-fluid side resistances. Solution-side area was enhanced by using corrugated fins (Garrabrant and Christensen, 1997; Christensen *et al.*, 1998), and wire meshes between tube banks (Goel and Goswami, 2005, 2007). These concepts demonstrated significant improvement in the absorption process, but the limiting resistance was found to be on the coupling fluid side. To address this, a horizontal tube microchannel absorber concept was developed, which demonstrated high heat and mass transfer rates on the solution-side and low thermal resistance on the coupling fluid-side (Garimella, 1999). This concept was experimentally demonstrated as an absorber and as a desorber indicating the versatility of this concept (Garimella *et al.*, 2011).

2.2. Bubble and convective mode Absorption

In bubble and convective mode absorption, vapor is typically dispersed into the dilute solution in convective flow inside a tube or channel. The heat released during absorption is removed by coupling fluid circulated on the outside of the tube or channel. Several geometries for this flow configuration have been studied in the literature both analytically and experimentally, including vertical, horizontal, and U-shaped tubes, and flat plates. A summary of these studies follows.

2.2.1. Analytical and numerical studies

Similar to studies on falling-film absorption, several assumption have been made in most analytical and numerical studies on bubble and convective mode absorption. These assumptions are listed below.

- Steady-state absorption
- Constant pressure system
- Presence of non-condensable gases ignored
- Thermodynamic equilibrium at the vapor-liquid interface
- No direct heat transfer between vapor and coupling fluid
- Mass transfer only due to concentration gradient

In addition to the above assumptions, most studies on bubble mode absorption in the literature have neglected coalescence or break up of bubbles. Studies that do not make some of the above listed assumptions are identified individually below.

Herbine and Perez-Blanco (1995) developed a model for ammonia-water bubble absorption by solving for the bulk and interface temperatures and concentrations in both the liquid and vapor phases. The absorber they considered was a tall, concentric U-tube with solution and vapor flowing in a co-current configuration on the inside, and the coupling fluid on the outside of the inner tube, a configuration previously studied experimentally by Merrill *et al.* (1994). Resistance to mass transfer was neglected and correlations from the literature, developed for single-component fluids, were used to estimate heat and mass transfer rates in the solution. The bubble velocity was assumed to be a weighted sum of terminal and liquid bulk velocity, and a segmental approach was adopted, where segment lengths were equal to the distance traveled by a bubble over an infinitesimal time step such that the bubble velocity is nearly constant. They also defined an "extent to equilibrium" term which was used to account for the fractions of ammonia and water condensing at the interface. They observed that while the direction of mass

transfer for ammonia was always into the solution, water moved in either direction of the interface, indicating local desorption of water which was also reported by other researchers in falling-film absorption (Kang and Christensen, 1994; Garimella, 1999). This phenomenon was observed in the initial segments, and was attributed to the balance between heat transfer rate in the liquid phase and latent heat released due to phase change at the interface. The bubble diameter was found to increase initially, followed by a monotonic decrease, which was attributed to the direction of transfer of water at the interface. However, the concentration of the vapor bubble monotonically decreased along the absorber length, concluding with a segment where the vapor was pure water. It should be noted that this observation might be due to their assumption that neglected resistance to mass transfer in the vapor phase, resulting in the inability of the model to capture concentration gradients in the vapor phase.

Dence *et al.* (1996) presented the development of a bubble absorber with a helical bubble injector for GAX applications. The absorber was an annulus-shaped shell with vapor and solution flowing upwards, and coupling fluid flowing downwards in a counter-current flow configuration. While in their prototype design, the coupling fluid was simulated by using single-phase water, they suggested that in a GAX application, the coupling fluid can be concentrated solution undergoing desorption. They first developed a thermodynamic model to estimate the desired operating conditions for the component for a 6.7 kW GAX chiller, corresponding to an absorption duty of 4.7 kW. At design conditions, the dilute solution entered the absorber at a flow rate of 9.49×10^{-3} kg s^{-1} and concentration of 21%, while vapor entered the absorber at a flow rate of 1.91×10^{-3} kg s^{-1} and concentration of 86.6%. They next developed a design model by considering only heat transfer during the absorption process. They also suggested that to avoid dry out of the absorber walls, the diameter of the largest bubble should be smaller than the spacing between inner and outer walls of the annulus. They predicted a bubble diameter of 4 mm

at design conditions, and recommended a spacing of 8 mm. No information on the other dimensions in the absorber was reported.

Kang *et al.* (1998) extended their earlier design model (Kang and Christensen, 1994) to study bubble absorption in plate heat exchangers with an offset strip fin, by considering heat and mass transfer in both liquid and vapor phases. Solution and vapor were assumed to be in counter-current flow configuration, with solution flowing downwards, and correlations were used to estimate heat and mass transfer rates in both phases. Correlations were also used to estimate the bubble size and gas hold-up inside the absorber. A hydronically cooled absorber was designed for GAX systems by adopting a segmental approach. They observed that the solution bulk temperature closely followed the interface temperature, indicating low solution heat transfer resistance. A relatively larger temperature difference between the vapor bulk and interface indicated a higher vapor phase heat transfer resistance. The dominant heat transfer resistance however, was observed to be on the coupling fluid side. They also noted that the concentration difference between the vapor bulk and interface was much lower than the concentration difference between the solution bulk and interface, indicating higher mass transfer resistance in the solution. During the absorption process, they also noted local desorption of water, which is consistent with the observations of Herbine and Perez-Blanco (1995). Additionally, they observed that bubble size and gas hold-up decreased along the absorber length and attributed that to the reduction in vapor mass, which also resulted in a reduction of the overall mass transfer area.

Merrill and Perez-Blanco (1997) conducted a numerical study of the combined heat and mass transfer during ammonia-water bubble absorption, with a focus on modeling the behavior of a moving bubble injected into a subcooled liquid solution. They assumed the bubble to be spherical throughout the absorption process, with equal pressure on both sides of the bubble surface. Vapor temperature and concentration were assumed to be uniform, and inertial effects associated with liquid motion into the bubble

were neglected. Solution flow on the outside of the bubble was assumed to be irrotational with the radially inward velocity dependent only on absorption. They noted that their predictions compared reasonably well with analytical solutions for moving bubbles in well-mixed liquid for simpler cases that considered only mass transfer, or heat and mass transfer only in the vapor phase. In an absorber application, their model predicted that the concentration and thermal boundary layers were relatively thin and independent of the solution Peclet number. The largest temperature and concentration gradients were observed near the forward stagnation point of the bubble. They also observed that bubble collapse occurred in three distinct stages. During the first stage, the bubble diameter remained almost constant, which was explained by nearly equal transfer rate of ammonia into the bubble and water out of the bubble. In the second stage, the diameter underwent a steady decline due to steady absorption of both species, concluding with the third stage where the droplet collapsed rapidly. As the bubble collapsed, the heat transfer coefficient underwent a six fold increase, while the mass transfer coefficient doubled.

Lee *et al.* (2003) developed a numerical model to simulate the absorption process in an ammonia-water bubble absorber and compared their predictions with experimental results. Their model neglected mass transfer in the vapor phase and did not allow for local desorption of water. Correlations were used to estimate the bubble dynamics such as the bubble diameter, and heat and mass transfer coefficients in the liquid phase. To validate their model, they fabricated a single-pressure test facility with a 30 mm inner diameter vertical tubular absorber. Dilute solution was preheated to the desired temperature and introduced to the test section from a dilute solution reservoir, while the ammonia vapor was supplied to the test section from a separate ammonia cylinder through a pressure regulating valve. The absorber test section was not cooled by any external coupling fluid. Experiments were conducted for scenarios where solution and vapor were in both co-current, and counter-current flow configurations. They observed that their model compared reasonably well with experimental observations. They also

noted from their model that the absorption process depended strongly on the flow configuration, the coupling fluid temperature, and dilute solution concentration, temperature, and vapor flow rate. They noted that the counter-current flow configuration generally resulted in shorter absorber lengths, which can be attributed to more favorable heat and mass transfer gradients in comparison to the co-current configuration. It should be noted the vapor flow rate in the counter-current flow configuration was very low, and thus, no flooding and flow reversal was observed. Counter-current operation is typically not possible at higher vapor flow rates in bubble absorbers. They also noted that lower solution and coolant inlet temperature, and lower solution inlet concentration resulted in higher absorption rates and lower absorber lengths. Lower coupling fluid temperature presents more favorable heat transfer mechanisms, and lower solution temperature results in a higher amount of solution subcooling, both of which enhance the absorption process.

Fernández-Seara *et al.* (2005) presented an analysis of the heat and mass transfer associated with bubble absorption in vertical tubular ammonia-water absorbers by considering three flow regimes – churn flow, slug flow, and bubbly flow. These flow regimes were previously reported in an experimental study conducted by Ferreira *et al.* (1984). The absorber they considered was a shell-and-tube heat exchanger with 40 vertical tubes of outer diameter 25 mm and length 0.9 m. Vapor and solution were introduced at the bottom of these tubes through two separate nozzles, and coupling fluid was introduced at the top of the heat exchanger and flowed counter-current to the solution flow. They developed a mathematical model by accounting for heat and mass transfer in both the liquid and vapor phases. They utilized correlations in the literature and the Colburn-Drew equations (Colburn and Drew, 1937) to estimate the heat and mass transfer rates. They reported that churn flow was expected to be merely an entrance effect, and considered it to extend to a length equal to the bubble length at the entrance. This was followed by transition to slug flow. High absorption rates were observed in churn and slug flow regimes, which was attributed to higher heat and mass transfer

coefficients, as well as favorable temperature and concentration gradients in these regimes. Similar to the observations of Kang *et al.* (1998), these authors also reported that the interface temperature closely followed the liquid bulk temperature, indicating low heat transfer resistance in the liquid phase. These temperatures were found to fall rapidly in the churn flow regime, followed by a slight rise and gradual fall in the slug flow regime and in the subsequent bubble flow regime. The slight temperature rise was attributed to the different correlations used in each flow regime, while the rapid fall initially was attributed to high local heat transfer rate. The vapor bulk temperature was found to increase in the churn flow regime and initial segments of the slug flow regime, followed by a monotonic decline in later segments, indicating that some of the latent heat liberated at the interface propagated back to the vapor bulk. Local desorption of water initially was also reported. Based on a parametric study, they observed the existence of an optimum tube diameter for a given tube length. To determine the sensitivity of the absorption process to the heat and mass transfer coefficients, the authors applied multipliers to the relevant vapor and liquid transfer coefficients. They observed that while varying the vapor heat and mass transfer coefficients had no significant change in the absorber length, varying the solution heat and mass transfer coefficients, and the coupling fluid heat transfer coefficients significantly affected the absorption length, indicating that the enhancement of these parameters can result in smaller absorbers.

In a subsequent study, Fernández-Seara *et al.* (2007) extended their previous model to analyze the absorption process in air-cooled vertical tubular absorbers, where finned tube rows were arranged in a staggered configuration with cooling air in cross flow. Similar to their prior study, the authors considered three flow regimes: churn flow, slug flow, and bubbly flow. They observed that the required tube lengths for complete absorption were different for the tubes in different rows, and this length was found to increase in successive rows. This observation was attributed to the warmer inlet air conditions for the latter rows, resulting in longer absorption lengths. The temperature

profiles of the solution and vapor were found to be similar to those observed in their previous study (Fernández-Seara *et al.*, 2005). The cooling air temperature increased monotonically across the tube bank. Additionally, decreasing the fin spacing, which resulted in higher air-side heat transfer area, yielded smaller absorber lengths, indicating the limiting resistance was on the air side. As expected, they found that higher air flow rates and lower air inlet temperatures resulted in smaller absorber lengths due to favorable heat transfer conditions.

Elperin and Fominykh (2003) developed analytical expressions for concentration and temperature gradients during bubble formation and rise in a bubble absorber, by considering non-stationary convective diffusion and energy equations. They considered flows with large Peclet, Prandtl, and Schmidt numbers, and neglected the resistance to heat and mass transfer in the vapor phase. They considered mass transfer in four stages of bubble formation and rise: 1) mass transfer during bubble formation at the orifice described by unsteady convective diffusion, 2) mass transfer during accelerating motion of a bubble after detachment described by unsteady convective diffusion under unsteady flow conditions, 3) mass transfer in bubble with constant velocity described by unsteady diffusion under steady flow conditions, and 4) mass transfer during bubble rise with constant velocity described by steady diffusion under steady flow conditions. Velocity profiles of the solution from the corresponding hydrodynamic problem with zero mass flux at the interface were assumed to be applicable, and applied to the diffusion and energy equations. The resulting analytical expressions for dimensionless temperature and concentration gradients were found to be functions of bulk and interface concentrations, and thermal and concentration boundary layer thicknesses, indicating the coupled nature of heat and mass transfer during absorption. They simplified these expressions by considering the case of infinite dilution in the solution, and developed a correction factor for mass transfer for cases with finite concentration levels during isothermal absorption. They noted that the predictions for the residence times of the bubble in the liquid

compared reasonably with the experimental observation of Kang *et al.* (2002). In general, the residence time increased with increase in the initial bubble diameter and initial concentration of the dissolved gas in the liquid. They further defined a heat and mass transfer coupling parameter as the ratio of the Lewis number and the dimensionless heat of absorption, and noted that for smaller coupling parameter number values, mass transfer limited the absorption process. For larger coupling parameter numbers, the process was limited by heat transfer. Finally, the authors noted that absorption of gases like CO_2, H_2S, O_2, N_2, and Cl_2 in water was predicted reasonably well by the approximation of infinite dilution of absorbate, while absorption of gases like NH_3, SO_2, and HCl in water required the approximation of finite dilution of absorbate for reasonable predictions. This was attributed to the high solubility of these gases, where coupling between heat and mass transfer is more prominent.

2.2.2. Experimental studies

Ferreira *et al.* (1984) conducted a detailed experimental study of the ammonia-water absorption process in vertical tubular absorbers with solution and vapor flowing co-currently upwards. In addition to heat and mass transfer measurements, they also viewed the absorption process inside three glass tubes of diameters 10, 15, and 20 mm, and length of 1 m. The heat of absorption was removed by very cold methanol (-40^{o}C) circulated on the outside of the tube to compensate for the very low thermal conductivity of the glass. The absorber was installed in a single-pressure test facility, and solution and ammonia were supplied from two separate reservoirs. Temperatures and pressures were measured at various locations in the loop, and solution and coupling fluid flow rates were measured around the absorber test section. Experiments were conducted over a pressure range of 126-333 kPa, solution flow rate of 2.1-26.2 g s^{-1}, and vapor flow rate of 0.018-0.48 g s^{-1}. They observed three different flow regimes during the absorption process: froth flow (churn flow), slug flow, and bubbly flow. Froth flow was observed initially

when the vapor was introduced into the absorber, and extended to about 20% of the tube length. This was followed by slug flow which extended to about 65% of the tube length, concluding with bubble flow for the rest of the tube length. A large amount of absorption occurred in the slug flow region which not only extended over a large part of the absorber, but also had favorable temperature and concentration gradients and a thin liquid film next to the cooled wall, which facilitated high heat and mass transfer rates. They also developed a segmental model to estimate the heat and mass transfer rates during the absorption process. They assumed the vapor and liquid to have uniform concentration inside each segment, considered mass transfer in the liquid phase, and utilized mass, species, and energy conservation equations to determine absorption rates. They further assumed the heat and mass transfer coefficients to be constant throughout the absorption process, which were iteratively estimated by matching predicted outlet conditions to experimentally observed conditions. It should be noted that while this assumption is generally not valid, it is still a reasonable first attempt at characterizing the absorption process. They observed that as the vapor flow velocity increased, the necessary absorber tube length decreased. This was attributed to the more favorable mass transfer mechanism due to higher velocities. They also noted that the solution mass flow rate did not affect the necessary absorber tube length significantly. Based on their observations, the authors developed a correlation for Sherwood number as a function of the vapor Reynolds number, liquid Schmidt number, and ratio between the absorber height and diameter as follows:

$$Sh = exp^{0.863} \cdot Re_{vap}^{0.853} \cdot Sc_{sol}^{0.50} \cdot \left(\frac{z}{D} \right)^{-1.00} \tag{2.13}$$

In a subsequent study, Ferreira (1985) developed a more detailed heat and mass transfer model by solving the governing energy and species transport equations. He studied ammonia-lithium nitrate and ammonia-sodium thiocyanate absorption in vertical tubular absorbers in the test facility previously developed by Ferreira *et al.* (1984). In his

model, the energy and mass diffusion equations were considered in the liquid bulk and the interface, and heat transfer in the vapor phase was neglected. This resulted in two sets of non-linear partial differential equations at the interface and the liquid bulk, to which the finite difference method was applied to yield two sets of ordinary differential equations. Velocity profiles were assumed in the liquid regions of the flow. This model was applied to the data recorded from his experiments, and local heat and mass transfer coefficients were estimated, which were compared with the predictions from Nusselt (1916) and penetration (Higbie, 1935) theories. In comparison to the experimental results, he observed that Nusselt theory, which assumes constant interface conditions, under-predicted the overall heat transfer coefficient by nearly 40%. Similarly, the penetration theory, which assumes constant properties at the interface and liquid bulk, over-predicted the driving potential by nearly 10%. He reasoned that the absorption process is an inherently coupled heat and mass transfer process, and thus, the idealizations of the Nusselt and Penetration theories are not valid. However, he did note that in all experiments, the limiting resistance was on the coupling fluid side, and therefore, the overall absorber performance predictions were still acceptable for the conditions studied if the Nusselt or Penetration theories were used. Based on visual data, he also observed that the vapor bubbles resembled Taylor bubbles, and applied a potential flow solution to model the absorption process at the nose of the bubble. The absorption rate here was found to be nearly 75% of the absorption rate at other locations in the bubble, which was attributed to the flow mechanisms around the front end of the bubble.

Kang *et al.* (2002) conducted a visualization study of bubble behavior during absorption to study the effect of key parameters such as orifice diameter, bubble diameter, number of orifices, liquid concentration, and vapor velocity. Ammonia vapor was introduced from a separate cylinder into solution inside a transparent rectangular tube (80 mm length × 53.5 mm width × 300 mm height) via three orifices. The diameter of the orifices was varied between 3.0, 3.8, and 5.5 mm, and some of the orifices were

selectively closed to have one, two, or three orifices introducing ammonia into the test section. The concentration of the solution inside the test section was varied between 0, 10, and 20% of ammonia. Temperatures were measured at various locations inside the test section, and the initial and final mass of the test section was measured to estimate the mass of absorbed vapor. High-speed video of the absorption process was used to obtain estimates of the bubble diameter. For non-spherical bubbles, an equivalent diameter was considered. The time taken for absorption was also measured to estimate the absorption rate. They observed that the bubbles tended to be spherical in cases where surface tension forces dominated inertial forces. As the vapor velocities increased, inertial forces increased and the bubbles tended towards a hemispherical shape. They also observed that the initial bubble diameter increased with increase in the concentration of the dilute solution. As the driving concentration difference between the vapor and the solution decreased, the absorption rate decreased, leading to larger bubble diameters and longer residence time. Based on these observations, they suggested that the driving concentration difference plays a more important role than surface tension forces in determining the initial bubble diameter, indicating the inapplicability of most air-water or single-component studies to ammonia-water absorption. They also noted a transition vapor Reynolds number at which the rate of change of the initial bubble diameter with vapor Reynolds number underwent a marked change. This transition was considered to be driven by the balance between the internal absorption potential (due to concentration difference in the vapor and liquid phases), and the external absorption potential (vapor inlet mass flow rate) and the transition number was found to increase with increase in the solution concentration. The residence time of the bubbles were found to increase with increase in the initial bubble diameter and the liquid concentration, which was due to the reduction in absorption rate. In addition, as the orifice diameter increased, the bubble diameter increased. The number of orifices had little effect on the initial bubble diameter with the maximum difference being less than 10%. They compared their experimental

data with correlations from two previous studies (Akita and Yoshida, 1974; Bhavaraju *et al.*, 1978), and found both correlations to over-predict the data. Thus, they developed a correlation for the initial bubble diameter, which was a function of the vapor Reynolds number, Weber number, Buoyancy number, concentration difference between the vapor-liquid bulk, and the orifice diameter as follows.

$$\frac{d_{ib}}{d_o} = 12.0 \cdot Re_{vap}^{0.29} \cdot We_{vap}^{-2.53} \cdot \left(Bu_{vap} \times 10^6 \right)^{2.58} \cdot x_{vap\text{-}sol}^{-0.2} \tag{2.14}$$

Kim *et al.* (2003a, b) conducted an experimental study of ammonia-water absorption in a counter-current vertical slug flow absorber, where vapor entered at the bottom of a vertical Pyrex glass tube and moved upwards due to buoyancy, while solution flowed downward due to gravity. The test section had an inner diameter of 10 mm and length of 1500 mm. The heat of absorption was removed by coolant circulated in a coolant jacket on the outside of the tube. The jacket was divided into seven segments, with coupling fluid temperatures recorded at the inlet and exit of each of these segments. These temperatures were used to determine segmental absorption duty. The absorber wall, and solution and vapor inlet and outlet temperatures were also measured. The absorber was installed in a single-pressure system, and vapor ammonia and dilute solution were introduced from separate reservoirs. Mass flow rate and concentration of the concentrated solution exiting the test section were measured. Experiments were conducted for three dilute solution concentrations (2.5, 10.3 and 21.6%) over a range of flow rates (1.0 – 3.5 kg hr^{-1}), three different coolant inlet temperatures (20, 30, 40^oC) over a range of flow rates (0.08 - 0.4 L min^{-1}), and three different vapor flow rates (0.6, 0.9 and 1.2 kg hr^{-1}).

Kim *et al.* observed two flow patterns during the absorption process. In the initial stages the vapor-liquid mixture was observed to be in churn or frost (presumably implying froth) flow, in which the flow was wavy with several disturbances. Subsequently, the slug flow regime was observed with the formation of Taylor bubbles.

The length of these bubbles shortened as they progressed downstream. No discernible bubbly flow regime was observed.

They also developed a heat and mass transfer model to estimate the local heat and mass transfer coefficients during absorption (Kim *et al.*, 2003b). They utilized a drift flux model with Taylor bubbles to model the slug flow, and accounted for the interface area by accounting for the vapor slug and liquid plug sizes. Mass transfer was considered in both the phases, and the heat and mass transfer analogy was used to estimate the mass transfer coefficients from the heat transfer coefficients. Because pure ammonia was introduced into the absorber, the authors neglected the presence of water in the vapor bulk. It should however be noted that, while no water is present in the vapor phase initially, water might transfer from the liquid phase during subsequent stages of the absorption process, as previously reported by other researchers. They observed that the interface, liquid bulk, and vapor bulk temperatures monotonically decreased from top to the bottom of the absorber, with the interface temperature always higher than the liquid and the vapor bulk temperatures. Thus, the heat of absorption released at the interface was transferred to both the solution and the vapor. Their subsequent models (Kim *et al.*, 2003b) showed that the vapor bulk and the vapor interface concentrations are nearly equal throughout the whole absorption process, indicating that the mass transfer resistance in the vapor was negligible. A similar trend was observed with the vapor heat transfer coefficient, which was attributed to the use of heat and mass transfer analogy in the model. The mass transfer coefficient in the liquid phase was higher at the beginning of the absorption process and decreased along the absorber length. The higher mass transfer coefficients at the inlet were attributed to the churn flow in these regions, which facilitate intense mixing in the liquid phase. For lower vapor velocities, the mass transfer coefficient was found to monotonically decrease along the absorber length, but for the higher vapor velocities, the mass transfer coefficient was found to increase in the second segment followed by a monotonic decline. They suggested that for higher vapor

velocities, churn flow extended into the second segment, resulting in higher mass transfer coefficients. The liquid mass transfer coefficient was found to be relatively independent of the dilute solution concentration, coolant flow rate, and coolant inlet temperature. Finally, they observed that the experimental heat transfer coefficients compared well with the heat transfer coefficients predicted by Nusselt (1916) theory for the slug flow regime, although such a mechanism should not be applicable for slug flow. Experimental heat transfer coefficients, however, were higher than predictions from the Nusselt theory for churn flow, which was attributed to the very different flow mechanisms associated with this regime.

Lee *et al.* (2002b) studied absorption characteristics in a transparent, vertical cylindrical tube of diameter 0.03 m and height 1 m. Their test section had five equally spaced ports to facilitate sampling of solution, and provision for seven manometers and twelve thermocouples to measure the solution pressure and temperature at various locations. Adiabatic experiments were conducted over a range of vapor flow rates, with vapor flowing, co-current and counter-current to the solution supplied at concentrations of 20 and 30%. They observed that for lower vapor flow rates, the concentration of the solution above a height of 0.2 m remained almost constant, indicating rapid absorption at the bottom of the absorber. For the vapor and liquid co-current flow configuration, solution temperature was found to rise rapidly in the initial parts of the absorber, beyond which the temperature was found to be nearly constant. For the counter-current flow configuration, the temperature of the solution at the top of the absorber was nearly constant, while the temperature of the solution leaving the absorber increased with increasing vapor flow rates. Both these observations again indicate that a major portion of the absorption process was occurring at the bottom of the absorber, irrespective of the flow configuration. Confirming this observation, the authors reported that the gas holdup decreased along the absorber height, and the rate of this decrease was much higher towards the bottom of the absorber for both configurations.

In a subsequent study, Lee *et al.* (2002a) studied the heat transfer characteristics in four vertical tubular absorbers with diameters/heights of 30/700 mm, 30/400 mm, 20/700 mm, and 40/700 mm, respectively. These absorbers were cooled by the coupling fluid circulated on the outside, counter-current to the solution flow. Experiments were conducted over solution flow rates, temperatures, and concentrations ranging from 0.2-0.8 kg min^{-1}, 15-60^{o}C, and 0-28%, respectively. Ammonia vapor flow rate was varied from 1-9 l min^{-1}. They observed that heat transfer coefficient increased with increase in solution and vapor flow rates. As solution flow rate increased, the boundary layers became thinner, resulting in higher heat transfer rates. Similarly, as the vapor flow rate increased, the mixing in the solution due to formation of eddies resulted in an increase in the heat transfer rate. The solution heat transfer coefficient was found to decrease slightly with increase in solution concentration, which was attributed to the associated mass transfer phenomena, where ammonia rectification was possible at higher solution concentrations, resulting in lower heat transfer rates. They observed that smaller tube diameters resulted in higher heat transfer coefficients, and the counter-current flow configuration resulted in higher heat transfer rates in comparison to the co-current flow configuration due to increased shear and mixing between the vapor and liquid phases. Based on their data, the authors developed a correlation for the solution Nusselt number as a function of the solution and vapor Reynolds number, temperature and concentration difference between the vapor and dilute solution, and height and diameter of the absorber as follows.

$$Nu_{sol} = 1.487 \cdot Re_{sol}^{0.1760} \cdot Re_{vap}^{0.1866} \cdot \left(\frac{\Delta x}{x_{sol}}\right)^{0.6013} \cdot \left(\frac{\Delta T}{T_{sol}}\right)^{-0.1146} \cdot \left(\frac{H}{d}\right)^{0.2662} \qquad (2.15)$$

Lee *et al.* (2002d) conducted an experimental investigation of ammonia-water bubble absorption in a plate-type absorber, and studied the effects of the solution and vapor flow rates. Their absorber consisted of a single channel of dimensions 0.112 × 0.264 × 0.003 m^3 with coupling fluid circulated only on one wall. Solution and vapor

were in a counter-current flow orientation inside the absorber with solution flowing downwards. The absorber was installed in a single-pressure test facility with ammonia vapor and dilution solution supplied from two separate reservoirs. Experiments were conducted over a range of vapor flow rates (0-1.6×10^{-4} m^3 s^{-1}), solution flow rates (0-0.016 kg s^{-1}), and at two dilute solution concentrations (20 and 30%). Temperatures were measured at the inlet and outlet of the absorber, and at five intermediate locations in the test section. In the reduction of their data, they considered only the overall heat transfer coefficients, and neglected mass transfer in the vapor phase. They observed that the solution mass transfer coefficient was weakly influenced by the solution flow rate but strongly influenced by the vapor flow rate. A similar observation was previously reported by Kang *et al.* (1999) who studied falling-film absorption in similar geometries. The overall heat transfer coefficient was found to increase with increase in both, the solution and vapor flow rates. They suggested that an increase in solution flow rate resulted in an increase in the convective forces, resulting in higher heat transfer rates. Also, higher vapor flow rates resulted in increased "slugging" in the absorber, yielding favorable heat transfer mechanisms due to formation of a thin liquid film near the wall. The temperature of the solution was found to decrease from bottom to top of the absorber; the higher temperatures at the bottom were attributed to the increased absorption in this region. It should be noted that this result is contradictory to predictions from the heat and mass transfer model developed by Kang *et al.* (1998) who reported a monotonic increase in solution temperature from bottom to the top of the absorber. This difference can be attributed to the differences in the operating conditions of the two studies, thus highlighting the need for conducting experiments at realistic conditions. Based on their results, the authors developed correlations for the overall Nusselt number and liquid Sherwood number as a function of solution and vapor Reynolds number, and the temperature and concentration difference between the vapor and solution entering the absorber as follows.

$$Nu = 3.133 \cdot Re_{sol}^{0.2519} \cdot Re_{vap}^{0.2995} \cdot \left(\frac{\Delta x}{x_{sol}} \right)^{0.0864} \cdot \left(\frac{\Delta T}{T_{sol}} \right)^{0.0685} \quad (2.16)$$

$$Sh = 43.57 \cdot Re_{sol}^{0.0403} \cdot Re_{vap}^{0.2865} \cdot \left(\frac{\Delta x}{x_{sol}} \right)^{0.0462} \quad (2.17)$$

Cerezo *et al.* (2009) studied ammonia-water bubble mode absorption in similar geometries. They considered a corrugated plate heat exchanger with solution and vapor flowing vertically upwards in co-current configuration, cooled by coupling fluid circulated in two adjoining channels. The total transfer area of the absorber was 0.1 m^2. This absorber was installed in a single-pressure test facility where dilute solution and vapor ammonia were supplied from two independent reservoirs. A hydronically coupled heat exchanger was used to heat the dilute solution to the desired temperature, while the desired absorption pressure was achieved by regulating the vapor ammonia flow rate. The heat of absorption was removed using a coupling fluid loop, which in turn rejected heat to city water. The coupling fluid inlet temperature was adjusted using an immersion heater. Temperature and pressure measurements were taken at the inlet and outlet of all fluid streams flowing through the absorber, and mass flow rates of the dilute and concentrated solution were measured using high accuracy Coriolis flow meters. Experiments were conducted over a range of dilute solution concentrations (29-33%), flow rates (30-40 kg hr^{-1}), inlet temperatures (38-42^{o}C), absorber pressures (160-200 kPa), and coupling fluid flow rates (30-35^{o}C). The recorded data were analyzed to estimate absorption duties, and solution heat and mass transfer coefficients. The solution heat transfer coefficient was found to increase from 2.8-4.1 kW m^{-2} K^{-1} as the solution Reynolds number increased from 170-350. This trend was attributed to the thinner thermal boundary layers observed at higher flow rates. The solution heat transfer coefficients were also found to increase with decrease in solution concentration, which was attributed to the more favorable mass transfer mechanisms at low solution concentration. Absorption duties also followed an increasing trend with increasing solution flow rate, with the reported duties varying

between 0.4-1.5 kW. An increase of nearly 120% in the absorption duty was observed as the coupling fluid temperature decreased from 35 to 30°C, which was attributed to the more favorable temperature differences between the solution and the coupling fluid. The authors also reported that the solution heat transfer coefficient increased with increase in absorber pressure (an increase of about 85% when the pressure increased from 160 to 200 kPa), which was attributed to the larger pressure gradients between the vapor bulk and the interface. This observation highlights the importance of conducting experiments at realistic operating conditions. Finally, the authors also noted that the degree of subcooling of the concentrated solution leaving the absorber was low, which indicated optimal utilization of the absorption area.

In a subsequent study, Cerezo *et al.* (2010) utilized their previous experimental data (Cerezo *et al.*, 2009) to develop correlations for predicting solution Nusselt number and pressure drop. It should be noted that for pressure drop calculations, they modeled the two-phase solution flow as a single phase flow by developing an equivalent Darcy friction factor, although the bases for this development and its validity are not very clear. They also developed a heat and mass transfer model of the absorption process based on previous studies by Kang *et al.* (1998) and Herbine and Perez-Blanco (1995), and compared their experimental results with the predictions from this model. The model was found to generally under-predict the absorber performance in comparison to experimental results. The maximum error in the absorption duty and absorption mass flux was reported to be 11.1 and 28.4%, respectively. It should be noted that the authors did not present the coupling fluid heat transfer resistance values. If the dominant resistance to the absorption process lies on the coupling fluid side, the predictions of heat and mass transfer rates on the solution-side would have high uncertainties and the comparison would not be accurate.

Other researchers have studied the enhancement of ammonia-water bubble absorption with the use of nanoparticles (Kim *et al.*, 2006). They considered three

nanoparticles: Cu, CuO, and Al_2O_3, and measured the absorption rate in a solution pool of known solution concentration. Pure ammonia was supplied from a separate reservoir, and the absorption process was visualized using high-speed video. Experiments were conducted at a temperature of 20^{o}C, pressure of 100 kPa, and solution concentrations varying from 0.1-18.7%, with weight percentages of nanoparticles ranging from 0-0.1%. They observed that while the shape of the bubble formed in solution with nanoparticles was spherical, the shape of the bubble in pure solution was hemispherical. It is interesting to note that Kang *et al.* (2002) previously reported a hemispherical shape for bubbles with higher vapor velocities, which has been discussed above. Kim *et al.* also reported that presence of nanoparticles in the solution enhanced the absorption process, with the absorption rate increasing with increasing weight percentage of nanoparticles. Cu nanoparticles were observed to facilitate the highest absorption rates. They also defined an "effective absorption ratio" which was the ratio between the absorption rate with and without nanoparticles, and observed that this value increased with increasing solution concentration. The highest effective absorption ratio (a value of 3.21) was reported for solution with Cu nanoparticles of weight percentage 0.1%. The enhancement in absorption due to nanoparticles was explained as follows: nanoparticles adsorb ammonia at the interface, and physically migrate through the film layer to the liquid bulk, before desorbing the ammonia in the liquid bulk. It should be noted that the nanoparticles used in this study are generally reactive to ammonia-water solutions and so it is possible that this enhancement would not last over longer durations.

To address this issue, Ma *et al.* (2009) studied the enhancement of the absorption process with carbon nanotubes (CNTs). Their test facility was similar to the one developed by Kim *et al.* (2006), and experiments were conducted over a solution concentration range of 0-25% and nanotube weight percentage of 0-0.5%. The CNTs had a diameter of 20 nm and length of 5-10 μm. They observed that the effective absorption ratio was found to initially increase, followed by a decrease indicating an optimum

nanotube weight percentage. This trend was different from that reported by Kim *et al.* (2006), and was attributed to the fact that the previous study did not test for nanoparticles beyond the weight percentage of 0.1%. They attributed the enhancement in the absorption process to four factors. First, they noted that presence of nanoparticles induced microconvection, which resulted in higher heat and mass transfer rates. Second, introduction of nanoparticles in the fluid resulted in an increase in gas hold up which increased the absorption rate. Third, nanoparticles increased the thermal conductivity, which enhanced the heat transfer rate. And finally, nanoparticles induced a grazing effect where they enhanced the absorption process by adsorbing and desorbing ammonia from interface to the liquid bulk, as previous noted by Kim *et al.* (2006). They also explained the higher enhancement observed at higher solution concentration. As the solution concentration increased, the absorption rate decreased, resulting in higher disturbances between the vapor and liquid phases, which enhanced the movement of nanoparticles and effectively enhanced the absorption process.

2.2.3. Miniaturization studies

Early miniaturization efforts in bubble and convective mode absorption were conducted by Merrill *et al.* (1994), who conducted an experimental study on two generations of bubble absorbers designed for GAX systems. Their absorber was a tall, concentric U-tube with solution and vapor flowing in a co-current configuration on the inside, and the coolant removing the heat of absorption on the outside. The first generation absorber was fabricated from stainless steel with no surface enhancement, and was designed for an absorption duty of 2.6 kW. This absorber was installed in a single-pressure test facility, which included a desorber and a rectifier to condition the concentration of the vapor entering the absorber. Initial experiments indicated that the first generation absorber performed well below design. They attributed this to insufficient heat transfer area on both the solution- and coupling-fluid sides, and poor thermal

properties of stainless steel. To address these issues, the second generation absorber was fabricated from carbon steel, which has a higher thermal conductivity than stainless steel, and flow enhancement features were also installed on both the solution and coupling fluid sides. On the coupling fluid side, internal spacers were added, which could locally increase the heat transfer coefficient by increasing the local Reynolds number. On the solution side, the tube surface was roughened to ensure that the boundary layer was continuously tripped, leading to higher heat transfer coefficients. Analysis of the second generation absorber data showed a performance increase of almost three times compared to the first generation absorber, although the peak absorber duty was still below design. Based on these observations, they recommended that to improve the absorption process, the coolant-side heat transfer coefficient, and the overall heat and mass transfer areas should be increased. Also, they found that the vapor and liquid inlet mechanisms are critical to the absorber performance, with flow mal-distribution significantly hampering the absorber performance.

Chen *et al.* (2006) studied the performance of a novel hybrid hollow fiber membrane device acting as both an absorber and heat exchanger (HFMAE). Their absorber concept was similar to a shell-and-tube heat exchanger, where the tubes were fabricated from two types of hollow fibers – porous and non-porous. Coupling fluid was circulated through the non-porous fibers, while vapor was introduced into the solution flowing on the shell-side through porous fibers. The porous fibers were located closer to the center of the shell, while the non-porous fibers were located closer to the end of the shell. Baffles were used to redirect solution flow inside the shell and enhance mixing and contact between the vapor, solution, and cooled fiber walls. To study the performance of this concept, a heat and mass transfer model was developed which considered the transfer processes in both the liquid and the vapor phases, similar to the bubble absorber model developed by Kang *et al.* (2000). Colburn-Drew (1937) equations were applied in both the liquid and vapor phases, and correlations from the literature were used to estimate

heat and mass transfer rates. The effect of porous media on the transport of vapor was also considered. They compared the performance of the HFMAE to the previously investigated plate heat exchanger falling-film absorber (PHEFFA) (Kang *et al.*, 2000) by standardizing the coolant-side heat transfer area in both absorbers. The total volume occupied by HFMAE was found to be about 31% of the volume occupied by the PHEFFA, while the total mass transfer area was found to 4.3 times greater. The reduction in component size was attributed to the increased mass transfer area per unit volume, as the heat and mass transfer coefficients in both absorbers were found to be comparable. The concentration difference between solution interface and bulk was found to be higher for the HFMAE, also resulting in higher absorption rates. Furthermore, because vapor was introduced into the solution at several locations via the porous hollow fibers, the predicted temperature profiles of the different fluid streams in the two absorbers were significantly different. A parametric study indicated that the solution mass transfer coefficient was the most important parameter in the absorption process. Finally, they noted that when installed in an absorption chiller, the new absorber concept could increase the overall cycle *COP* by ~ 15%, although these predictions about system-level performance improvements must be borne out by system-level experiments or by accounting for the changes in the performance of the other components in the system. As their concept was able to transfer a higher absorption duty in the same overall volume, the absorption chiller could be operated at ~ 38% lower dilute solution flow rate, yielding higher concentration split between the dilute and concentrated solution lines, thereby resulting in higher *COP*s.

Constrained microscale-film ammonia-water bubble absorption was studied by Jenks and Narayanan (2008), who conducted an experimental study to examine the effect of channel geometry on absorber performance. They considered six different channel configurations, three smooth-bottom-walled channels and three structured-bottom-walled channels of width 20 mm and length 100 mm, respectively. The depth of the smooth

channels was varied between 150, 400 and 1500 µm. The three structured channels were: cross ribbed-bottom-walled channel of depth 400 µm, angled cross ribbed-bottom-walled channel of depth 400 µm, and stream-wise finned-bottom-walled channel of depth 150 µm. Dilute solution flowed in these channels while absorbing vapor introduced through a perforated plate at various locations along the absorber length, from a vapor chamber above the channel. The heat of absorption was removed by the coupling fluid circulated below the solution channel. This absorber was installed in a single-pressure test facility where dilute solution and ammonia vapor were introduced from separate reservoirs. Experiments were conducted at an absorber pressure of 400 kPa, for three vapor and solution flow rates at a dilute solution concentration of 15%, coupling fluid inlet temperature of 10.6^{o}C and flow rate of 269 g min^{-1}. They observed that for the smooth channels, at lower vapor fractions, the overall heat transfer coefficient decreased with increase in channel depth, while for higher vapor fraction, the overall heat transfer coefficients increased with increase in depth, reaching a maximum for the 400 µm channel, followed by a decrease for deeper channels. They noted that the mass transfer coefficient increased with increase in the vapor flow rate, while the heat transfer coefficient increased with decrease in channel depth. A combination of these two factors could be attributed to the existence of an optimum channel depth for given operating conditions. Additionally, the overall heat transfer coefficients for the 150 µm and 400 µm channels seemed to tend towards a limiting value as the solution flow rate was increased. They observed that for the structured-bottom-walled channels, the overall heat transfer coefficient decreased with increasing vapor flow rates at higher solution flow rates, the decrease being more dramatic at higher vapor flow rates. Among all the channels, the stream-wise finned channel exhibited the largest overall heat transfer coefficient. Based on these observations, they developed a graphical method to identify the desirable operating points for absorber design based on the geometries considered.

In a subsequent study, Cardenas and Narayanan (2010) developed a numerical model for ammonia-water absorption in a constrained microscale film in a 150 mm long channel of width 30 mm and depth 1 mm. Their model considered heat and mass transfer only in the liquid phase, and neglected diffusion of water back into the vapor phase during absorption. The absorber was divided into several segments, and the vapor bubbles entering from the previous segment were assumed to be either spherical or cylindrical, depending on their diameter. Vapor bubbles entering the segment from the vapor injection holes at the top were considered to be spherical. The diameter of these bubbles was estimated by matching the model results with those from the experiments. Correlations from the literature were used to determine the heat and mass transfer coefficients in the solution. Predictions of the absorber duty from the model compared reasonably with the experimental results, with a maximum deviation of 35% and mean deviation of 9%. They later conducted a parametric study to capture the influence of the dilute solution, vapor, and coupling fluid flow rates on the absorption process. As the dilute solution flow rate increased, the absorption rate was found to initially increase, followed by a subsequent decline at higher flow rates. At lower solution flow rates, the mass transfer coefficient increased with increase in flow rate, resulting in higher absorption rates. However, at higher solution flow rates, the residence time decreased, resulting in a decrease in the absorption rate. They also observed that the absorption rate initially increased, followed by a decrease with increase in the vapor flow rate. While the heat transfer coefficient increased with increase in vapor flow rate, at higher vapor flow rates, the resulting solution concentration was also higher, leading to smaller driving concentration differences, and resulting in a reduction of the absorption rate. Coupling fluid flow rate did not affect the absorption process noticeably, indicating that the process was mass transfer limited. The authors also studied the influence of channel aspect ratio, and noted that as the channel depth increased, the absorption process increased initially, followed by a decrease at larger depths. As the channel depth increased, the available

heat and mass transfer area increased, resulting in higher absorption rates. However, at larger channel depths, the heat and mass transfer coefficients decreased, resulting in lower absorption rates. This observation is consistent with the previous experimental study indicating the existence of an optimum channel geometry (Jenks and Narayanan, 2008).

Determan and Garimella (2010) presented the development of a miniaturized, monolithic absorption heat pump with a microscale convective flow absorber. This heat pump was fabricated by bonding multiple thin sheets of metal, each with integral microscale fluid channels and headers that form all the components of a heat pump. In the absorber, vapor and solution flowed in co-current configuration inside microchannels of hydraulic diameter 306 μm, with the heat of absorption removed by coupling fluid circulated on the sheets above and below. Vapor was distributed into each solution channel via individual vapor through-holes located near the entrance of each channel. The absorber was sized for a chiller of cooling capacity 300 W, driven by a desorber heat duty of 800 W, requiring a total of 40 sheets. The monolithic chiller had an envelope of 200 × 200 × 34 mm and weighed 7 kg. They demonstrated the feasibility of this miniaturization concept by fabricating a prototype chiller using photochemical etching to machine the microscale features, and diffusion bonding to seal the array of sheets, and experimentally investigating the chiller performance over a range of ambient conditions. At design conditions (Ambient temperature = 35^{o}C), the chiller was observed to deliver a cooling capacity of 230 W. At lower ambient temperatures, the absorption chiller was able to meet the target cooling capacities. The *COP* of the chiller varied from 0.25-0.43 over the range of experiments conducted.

2.2.4. Summary of bubble and convective mode absorption

Table 2.2 shows a summary of the literature presented on bubble and convective mode ammonia-water absorption. Similar to studies on falling-film absorption, while

early analytical models made several assumptions, such as neglecting mass transfer (Herbine and Perez-Blanco, 1995; Dence *et al.*, 1996), later models conducted a more realistic analyses by employing the Colburn-Drew (1937) equations to estimate mass transfer of both species (Kang *et al.*, 1998; Fernández-Seara *et al.*, 2005; Fernández-Seara *et al.*, 2007). Similar to models of falling-film absorption, these models could estimate local absorption rates, and map the corresponding temperature and concentration variations along the length of the absorber. They are useful in sizing and designing absorbers, and provide useful insights into trends (such as local desorption of water), as well as predicting the limiting resistances during absorption. However, as was the case with falling-film absorption models, these studies utilize correlations from the literature to estimate the local heat and mass transfer coefficients, which can be a source of significant error. In addition, such correlations were typically used to model the behavior of bubbles, and simplistic assumptions such as uniform bubble size were employed to close these models, which can be sources of error. To address this problem, several numerical and experimental studies were conducted to observe the bubble behavior during absorption (1984; Merrill and Perez-Blanco, 1997; Kang *et al.*, 2002; Elperin and Fominykh, 2003). Bubble collapse was found to occur in several stages, which depended upon the flow behavior and the associated heat and mass transfer. Other researchers attempted to develop numerical models for simultaneous heat and mass transfer, by employing simplifying assumptions like neglecting mass transfer in the vapor phase (Lee *et al.*, 2003), or considered specific situations involving large dimensionless numbers (Elperin and Fominykh, 2003).

Vertical tubular absorbers have been investigated experimentally, and several authors have identified distinct flow regimes during the absorption process: churn flow, slug flow, and bubbly flow (Ferreira *et al.*, 1984; Ferreira, 1985; Kim *et al.*, 2003b, a). These investigators found the absorption rate to be high in the churn flow regime, while the bulk of the absorption occurred in the slug flow regime. The bubbles resembled the

shape of a Taylor bubble, and these absorbers have been called slug flow absorbers. Another geometry studied is the plate type heat exchanger (Lee *et al.*, 2002d; Cerezo *et al.*, 2009; Cerezo *et al.*, 2010). Correlations have been developed for the Sherwood number, Nusselt number, and initial bubble diameter. It should be noted that during reduction of experimental data, these authors often neglected mass transfer in the vapor phase, or the coupling between heat and mass transfer (Lee *et al.*, 2002a; Lee *et al.*, 2002d). Other experimental studies investigated the influence of addition of nanoparticles on the absorption process, and reported the existence of optimum concentrations for absorption enhancement (Kim *et al.*, 2006; Ma *et al.*, 2009). Similar to most experimental studies on falling-film absorption, experiments in these studies were conducted on a single-pressure test facility under conditions that are dissimilar to those observed in a real system. Thus, several of these trends may not be relevant for heat pump applications.

Early miniaturization efforts in bubble and convective mode absorption included the development of concentric U-tube absorbers, where flow enhancements were used on both solution and coupling-fluid sides (Merrill *et al.*, 1994). Other researchers employed an innovative miniaturization concept by utilizing a hybrid hollow fiber membrane device acting as both an absorber and heat exchanger (Chen *et al.*, 2006). Constrained microscale-film absorbers were also investigated, where effect of channel dimensions on the absorption process was studied and existence of an optimal channel size was demonstrated (Jenks and Narayanan, 2008; Cardenas and Narayanan, 2010). Microscale convective flow absorbers were also developed as part of a compact monolithic heat pump (Determan and Garimella, 2010).

2.3. Comparative studies

While the above studies have exclusively focused on either falling-film or bubble and convective mode absorption, there have been a few studies that conducted a comparative assessment of the two absorption configurations. Kang *et al.* (2000)

analytically studied these configurations in an offset strip fin flat plate heat exchanger, similar to the absorber considered in their previous study (Kang *et al.*, 1999). They developed a model for the absorption process in both configurations by considering heat and mass transfer in the vapor and liquid phases. These models were similar to those presented in the literature previously (Kang and Christensen, 1994; Kang *et al.*, 1997; Garimella, 1999). Correlations for single component fluids were used to calculate heat and mass transfer coefficients in the vapor and liquid phases, and bubble dynamics in bubble mode absorption. They reported that the absorption rate during bubble mode was always higher than during falling-film mode, noting that a bubble absorber can be ~49% smaller than a falling-film absorber for the same absorption duty. Furthermore, the temperature profiles of the vapor bulk were completely different in the two cases, indicating that the coupled heat and mass transfer characteristics are fundamentally different for the two modes. To investigate the influence of various transport processes, they applied multipliers to the various transfer coefficients, and recorded their influence on the absorber size. They observed that heat transfer coefficient in the vapor, and mass transfer coefficient in both the vapor and solution significantly influenced falling-film absorption, and therefore the absorber size. Other the other hand, bubble absorption was significantly influenced by mass transfer coefficient in the solution, and heat transfer coefficient in the vapor. The significant increase in the vapor mass transfer area in bubble mode absorption, which resulted in lower vapor mass transfer resistance in comparison to falling-film absorption, was attributed to improved performance of the bubble absorber. Heat transfer resistance on the coupling fluid-side was found to be important for both absorption modes. For miniaturization, the authors recommended enhancement of heat transfer coefficients in falling-film absorption and enhancement of mass transfer coefficients in bubble mode absorption.

Lee *et al.* (2002c) experimentally studied the two absorption configurations in a flat plate absorber (11.2 × 26.4 × 3 mm) with solution and vapor flowing on one side of

the plate, and the heat of absorption removed by coupling fluid circulated on the other side of the plate. This absorber was installed in a single-pressure test facility, in which dilute solution and ammonia vapor were supplied from two different reservoirs, and tested over a range of dilute solution concentrations (0-30%), flow rates (0.1-0.9 kg min^{-1}), and vapor flow rates (1-9 l min^{-1}). Flow meters were used to measure the dilute solution and vapor flow rates, and K-type thermocouples were used to measure the temperature at various locations inside the absorber. They observed that both the heat and mass transfer coefficients increased with increase in solution flow rate for both absorption modes. In general, the mass transfer coefficients were higher for bubble mode absorption and resulted in higher absorption duties. The increase in heat transfer coefficient with solution flow rate was more pronounced at lower flow rates, which was attributed to the thinning of the thermal boundary layer. At lower vapor flow rates, the heat transfer coefficient was higher in falling-film absorption, but the difference decreased with increasing vapor flow rate. At very high vapor flow rates and very low solution flow rates, heat transfer coefficients in bubble mode absorption were higher than those for falling-film absorption. This trend was attributed to possible channeling of the solution at higher vapor flow rates, resulting in reduction in available area for heat transfer. They also noted differing trends in the temperature profiles where the solution temperature increased along the absorber height for falling-film absorption, but decreased slightly for bubble absorption. The Sherwood and Nusselt numbers were found to increase with increase in solution Reynolds number for both flow modes. The vapor Reynolds number had a similar influence on Sherwood number for both modes. However, the Nusselt number increased and decreased with increase in vapor Reynolds number in bubble and falling-film absorption configurations, respectively. The following correlations were developed based on these observations:

$$Nu_{\text{falling-film}} = 0.01369 \cdot Re_{\text{sol}}^{0.5103} \cdot Re_{\text{vap}}^{0.02461} \cdot \left(\frac{\Delta x}{x_{\text{sol}}} \right)^{0.1438} \cdot \left(\frac{\Delta T}{T_{\text{sol}}} \right)^{0.2977} \tag{2.18}$$

$$Sh_{\text{falling-film}} = 658.46 \cdot Re_{\text{sol}}^{0.0195} \cdot Re_{\text{vap}}^{0.9571} \cdot \left(\frac{\Delta x}{x_{\text{sol}}} \right)^{-0.0639} \tag{2.19}$$

$$Nu_{\text{bubble}} = 3.133 \cdot Re_{\text{sol}}^{0.2519} \cdot Re_{\text{vap}}^{0.2995} \cdot \left(\frac{\Delta x}{x_{\text{sol}}} \right)^{0.08636} \cdot \left(\frac{\Delta T}{T_{\text{sol}}} \right)^{0.06851} \tag{2.20}$$

$$Sh_{\text{bubble}} = 43.57 \cdot Re_{\text{vap}}^{0.0403} \cdot Re_{\text{gas}}^{0.2865} \cdot \left(\frac{\Delta x}{x_{\text{sol}}} \right)^{0.0462} \tag{2.21}$$

It should be noted that in several studies discussed above, parameters such as ($\Delta x/x$) and ($\Delta T/T$) have been used in Nusselt and Sherwood number correlations, although it is difficult to justify their physical significance. For example, it is unclear how dimensional temperature can influence a dimensionless parameter such as the Nusselt number. Furthermore, for conditions where the vapor inlet temperature is lower than the solution inlet temperature, these correlations predict irrational Nusselt numbers, which is not feasible in reality. Therefore, these correlations are generally only applicable to the narrow band of conditions that are investigated in the respective studies. Outside these ranges, their predictions are questionable.

Another comparative study was conducted by Castro *et al.* (2009), who studied the performance of air-cooled falling-film and bubble absorbers. The absorber was a fin and tube compact heat exchanger, with solution and vapor flowing on the inside of the vertical tubes, cooling air flowing in cross-flow on the outside (tube outer diameter 22 mm, fin pitch 5 mm, 24 tubes in 4 rows). They developed a model for falling-film absorption by assuming the solution flow to be axis-symmetric, and solving the 2D Navier-Stokes equations to account for mass, energy and species transport. Vapor heat and mass transfer coefficients were estimated from the Penetration theory (Higbie, 1935). Partial wetting of the tube surface was accounted for by utilizing the model developed by Mikielewicz and Moszynskl (1976). They compared the predictions of this model with results from experiments conducted on a single-pressure test facility that consisted of a generator and a rectifier, in addition to the air-cooled absorber. They observed that while

the model predictions compared reasonably well with experimental results, it generally over-predicted the concentration and under-predicted the temperature of the concentrated solution leaving the absorber, which was attributed to the 2D flow assumption employed to simplify their model. They also developed a model for bubble absorption using empirical correlations to estimate mass transfer coefficients, and the heat and mass transfer analogy to estimate heat transfer coefficients in the vapor and solution. A linear temperature profile was assumed inside the bubbles and bubble coalescence was ignored. The authors observed that while their model compared well qualitatively with the predictions of Herbine and Perez-Blanco (1995), there were some discrepancies, that were attributed to the different assumptions used in the two studies. Using these models, they conducted a parametric study on air and solution flow rate for both absorption modes. Bubble mode absorption was observed to significantly outperform falling-film absorption at low flow rates, which was attributed to wetting issues in falling-film absorption. As the solution flow rate increased, tube wetting increased, and the performance of both modes was comparable. In general, bubble absorption was found to be more efficient than falling-film absorption. In both flow configurations, the dominant resistance was on the air side due to low heat transfer coefficient of the cooling air. The arrangement of the tubes was found to have little influence on the overall absorption process, although higher air velocities, achieved for a narrower tube bank, yielded slightly better performance.

A summary of the comparative studies on falling-film and bubble and convective mode absorption is provided in Table 2.3.

2.4. Research needs

It can be concluded from the above review of the literature that absorption is governed by complex, coupled heat and mass transfer processes. In comparison to water-Lithium Bromide absorption, ammonia-water absorption is inherently more complex, due

to the presence of concentration gradients in both the liquid and the vapor phases, and has therefore received lesser attention in the past (Killion and Garimella, 2001). To model the ammonia-water absorption process, several simplifying assumptions have been made. For example some researchers neglected the resistance to heat and mass transfer in the vapor phase (Herbine and Perez-Blanco, 1995; Dence *et al.*, 1996; Chen and Christensen, 2000; Lee *et al.*, 2003; Xiaofeng *et al.*, 2007), while others assumed constant fluid properties (Wassenaar and Segal, 1999; Gommed *et al.*, 2001). Other simplifying assumptions include assumed temperature, concentration, and velocity profiles (Merrill and Perez-Blanco, 1997; Elperin and Fominykh, 2003). Additionally, most analytical studies utilize correlations developed for single-component fluids and are not applicable to binary mixtures or to the geometry and operating conditions under consideration (Kang and Christensen, 1994; Herbine and Perez-Blanco, 1995; Kang *et al.*, 1997; Kang *et al.*, 1998; Garimella, 1999; Fernández-Seara *et al.*, 2005; Goel and Goswami, 2005). Similarly, most ammonia-water falling-film absorption models neglect the presence of flow features such as roll waves and droplets (which have been explored previously for water-LiBr absorption), while uniform bubble size is a common assumption in ammonia-water bubble absorption models. Not surprisingly, the conclusions pertaining to the limiting transfer resistances from these studies have been conflicting. Liquid-phase mass transfer resistance is considered dominant in some studies (Perez-Blanco, 1988; Gommed *et al.*, 2001; Fernández-Seara *et al.*, 2005), while others have concluded that the vapor-phase mass transfer resistance was dominant (Kang and Christensen, 1994). Yet other studies concluded that the coupling-fluid side heat transfer resistance was the dominant absorption resistance (Haselden and Malaty, 1959; Kang and Christensen, 1995). It should be noted though, that these conclusions might not be so much conflicting as being limited in their extent of applicability.

Experimental studies have often been conducted on stand-alone, bench-top, single component, single-pressure test facilities where the absorbers are tested under conditions

that are not representative of space-conditioning systems, and influences of other absorption system components are not considered. In such test facilities, dilute solution and vapor are supplied to the absorber from separate reservoirs or directly from the desorber. However, in a typical absorption system, refrigerant generated at the desorber undergoes rectification, and expansion to a lower pressure, arriving at the absorber at a different pressure and concentration. The absorber operating conditions are influenced by condenser (heat rejection) and evaporator (cooling load) conditions that are determined by ambient and conditioned space conditions. Therefore, while these studies could be valid over their range of test conditions, they are not valid for a wide range of operating conditions that apply for absorption systems over the design range of heating and cooling mode operation. Examples of such studies include the study on falling-film ammonia-water absorption on vertical tubes (Haselden and Malaty, 1959) conducted at near atmospheric pressures, and helical coils (Kwon and Jeong, 2004) conducted at 17-193 kPa. Similarly studies on bubble mode ammonia-water absorption in vertical tubes (Ferreira *et al.*, 1984; Ferreira, 1985) were conducted at 120-370 kPa, and corrugated plate heat exchangers (Cerezo *et al.*, 2009; Cerezo *et al.*, 2010) were investigated at 160-200 kPa. It should be noted that typical absorber pressures during refrigeration, cooling, and heating mode operation are between 250-650 kPa. Other studies were conducted at unrealistic vapor and solution concentrations, in addition to the unrealistic absorber pressures, such as a vapor concentrations of 64.7-79.9% (Kang *et al.*, 1999), and vapor and solution concentrations of 63-77% and 1.2-2.2%, respectively (Jeong *et al.*, 1998). Also, these studies make several simplifying assumptions such as saturated liquid and vapor states, and neglecting the coupling between heat and mass transfer, while real systems vary significantly from these idealizations. In a typical heat pump application, the dilute solution entering the absorber is in a subcooled state, after exchanging heat with the concentrated solution in the solution heat exchanger. As the solution flows through the absorber, the solution bulk typically remains subcooled throughout the

absorption process. However, during experiments conducted on single-pressure test facilities, the solution is at near saturation conditions throughout the absorption process, which is not representative of realistic heat pump applications (Jeong *et al.*, 1998; Kang *et al.*, 1999; Kwon and Jeong, 2004). Furthermore, the driving temperature differences for heat exchange between the solution and coupling fluid streams in these experiments is higher than those observed in heat pump applications, and thus, the estimations of the heat transfer coefficients can often be inaccurate. Several miniaturization concepts have been proposed in the literature to develop compact heat and mass exchangers (Merrill *et al.*, 1994; Christensen *et al.*, 1998; Goel and Goswami, 2005, 2007; Jenks and Narayanan, 2008). While some of these concepts have yielded high heat and mass transfer rates, designs for use in residential and light commercial markets must necessarily attain these rates with simple and compact geometries. In addition, the flow mechanisms in these miniaturization geometries have not been considered in adequate detail.

Therefore, there is a need to develop a theory based, experimentally validated model that can capture the coupled heat and mass transfer processes during ammonia-water absorption in miniaturized components. This model should consider the different flow mechanisms encountered during phase change. In addition, both absorption modes traditionally investigated in the literature: falling-film, and bubble and convective mode absorption should be investigated. A comparison of the absorption process in these two modes is also necessary, to provide recommendations for the suitability of the different configurations for different applications and operating conditions.

2.5. Research objectives

The present study aims at improving the understanding of ammonia-water absorption in falling-film mode over horizontal microchannel tube bundles, and in

forced-convective mode during internal flow in microscale channels. The specific objectives of this study are as follows:

1. Experimentally investigate microchannel falling-film absorption at realistic operating conditions in a test facility replicating a single-effect ammonia-water absorption chiller. Understand the progression of the absorption process inside the absorber through in situ measurements.
2. Propose and refine a theory based model for heat and mass transfer based on the relevant flow mechanisms in falling-film absorption over horizontal tube bundles.
3. Conduct a complementary study of binary fluid coupled heat and mass transfer in internal microscale forced-convective absorption, with experimental demonstration in an absorption chiller test facility.
4. Conduct a comparative assessment of falling-film and forced-convective absorption at microscales and develop recommendations for future miniaturization efforts.

Table 2.1 Summary of studies on falling-film absorption

Literature	Study type/Fluid	Absorber/Flow	Specific Conditions	Key assumptions	Key conclusions
Ruhemann (1947)	Analytical/ NH_3-H_2O	• Coiled tube • Co-current solution-vapor flow	• P_{abs} = 196 kPa, $T_{sol,in}$ = 30°C, $x_{sol,in}$ = 9.5%, $x_{sol,out}$ = 19%, x_{vap} = 1	• 3 absorption zones • Laminar, 1D flow • Uniform wetting • Assumed overall $\alpha$and β	• Coupled nature of heat and mass transfer demonstrated • Choice of $\alpha$and β critical in prediction of absorber outlet conditions • Low α result in temperature spikes near top of absorber
Perez-Blanco (1988)	Analytical/ NH_3-H_2O	• Coiled tube, tube O.D. 12.7 mm, coil dia 82.6 mm • Counter-current solution-vapor flow	• P_{abs} = 481 kPa, $T_{sol,in}$ = 44-115°C, $x_{sol,in}$ = 5-45%, x_{vap} = 90-99.9%	• Laminar, 1D flow • Uniform wetting • Solution β_{sol} from Penetration theory • Only conduction in solution • Simplified model using mass, species and energy conservation • Fick's law of diffusion for mass transfer	• Reasonable comparison with preliminary experiments • Absorption rate increases with increase in β_{sol} and decrease in solution mass flux • α_{CF} important for single-effect cycle absorbers • Periodic mixing of solution recommended

Table 2.1 Continued…

Literature	Study type/Fluid	Absorber/Flow	Specific Conditions	Key assumptions	Key conclusions
Price and Bell (1974)	Analytical/ methanol-water, n-butane-n-octane	• Vertical tube, O.D. 25.2 mm • Co-current condensing flow	• Methanol-water: x_{mix} = 30%, P_{cond} = 101 kPa, $\dot{m}_{mix}$ = 0.04 kg s^{-1} • n-butane-n-octane: x_{mix} = 30%, P_{cond} = 138 kPa, $\dot{m}_{mix}$ = 0.1 kg s^{-1}	• Laminar, 1D flow • Liquid well mixed • Vapor mass transfer in thin vapor film • Correlations for heat and mass transfer in vapor and liquid phases • Colburn-Drew equations for vapor condensation	• When temperature glide is small: vapor mass transfer resistance negligible, reasonable comparison with approximate method • When temperature glide is large: vapor mass transfer resistance significant, deviation from approximate method • Less volatile component undergoes condensation first
Kang and Christensen (1994)	Analytical/ NH_3-H_2O	• Vertically fluted tube, O.D. 33 mm • Counter-current solution-vapor flow	• $T_{sol,in}$ = 79°C, $\dot{m}_{sol,in}$ = 0.054 kg s^{-1}, $x_{sol,in}$ = 32.3%, T_{vap} = 10°C, $\dot{m}_{vap,in}$ = 0.034 kg s^{-1}, x_v = 99.7%	• Solution well mixed • Vapor mass transfer in thin vapor film • Correlations for heat and mass transfer coefficients • Colburn-Drew equations for vapor condensation	• β_{vap} and α_{CF} limiting • Local desorption of water observed in initial absorber segments •

Table 2.1 Continued…

Literature	Study type/Fluid	Absorber/Flow	Specific Conditions	Key assumptions	Key conclusions
Kang and Christensen (1995)	Analytical/ NH_3-H_2O	• Coiled fluted tube with porous medium, O.D. 27.6 mm, coil 304.8 mm • Counter-current solution-vapor flow	• $T_{sol,in}$ = 79°C, $\dot{m}_{sol,in}$ = 0.054 kg s^{-1}, $x_{sol,in}$ = 32.3%, T_{vap} = 10°C, $\dot{m}_{vap}$ = 0.034 kg s^{-1}, x_{vap} = 99.7% • Porous media on outside of tube	• Solution, interface, and vapor film inside porous media • Solution well mixed • Correlations for heat and mass transfer coefficients • Colburn-Drew equations for vapor condensation	• 28% reduction in absorber size in comparison to smooth tubes • Absorption limited by coupling fluid heat transfer resistance • Absorption enhancement limited beyond thermal conductivity ratio of 10 (porous medium: solution)
Kang *et al.*(1997)	Analytical/ NH_3-H_2O	• Counter-current solution-vapor flow	• GAX conditions	• Solution well mixed • Correlations for heat and mass transfer coefficients • Colburn-Drew equations for vapor mass transfer	• Composite map for mass transfer in all absorption components developed • Mass transfer of ammonia and water in the same direction for evaporator, condenser, and rectifier • Desorption/absorption of water possible in absorber/desorber
Wassenaar and Segal (1999)	Numerical/ NH_3-H_2O	• Flat plate • Co-current and counter-current solution-vapor flow	• 2D flow	• 2D Navier-Stokes mass, momentum, and energy equations • Constant solution properties • No mass flow rate change in segment	• Vapor velocity vector near interface similar for all configurations • Convection dominant mass transfer mode for wider channels • Counter-current outperforms co-current for channel widths < 5 mm

Table 2.1 Continued…

Literature	Study type/Fluid	Absorber/Flow	Specific Conditions	Key assumptions	Key conclusions
Gommed *et al.* (2001)	Numerical/ NH_3-H_2O	• Vertically fluted tube, O.D. 33 mm • Counter-current solution-vapor flow	• P_{abs} = 600 kPa, $T_{sol,in}$ = 55°C, $\dot{m}_{sol,in}$ = 0.060 kg s^{-1}, $x_{sol,in}$ = 35%, T_{vap} = 10.9°C, $\dot{m}_{vap}$ = 0.015 kg s^{-1}, x_{vap} = 99.9% • 2D flow	• Constant solution properties in radial direction • Axi-symmetric flow • 2D mass, momentum, species, and energy conservation equations	• Nearly linear temperature profile in the solution • Presence of thin vapor film near interface confirmed • Absorption rate increased with increase in vapor flow rate, solution thermal conductivity, and diffusivity
Chen and Christensen (2000)	Numerical/ NH_3-H_2O	• Vertical wall • Counter-current solution-vapor flow	• 2D flow	• Vapor diffusion and interface shear neglected • Constant solution flow rate in segment • Low solution and vapor velocities • 2D mass, momentum, species, and energy conservation equations	• Absorption process linear combination of adiabatic absorption in subcooled solution and saturated absorption with wall cooling • Heat transfer coefficient greater than prediction from Nusselt analysis • Passive mixing devices recommended to enhance mixing and improve absorption process

Table 2.1 Continued…

Literature	Study type/Fluid	Absorber/Flow	Specific Conditions	Key assumptions	Key conclusions
Xiaofeng *et al.* (2007)	Numerical/ NH_3-H_2O	• Vertical tube • Co-current solution-vapor flow	• P_{abs} = 250 kPa, $T_{sol,in}$ = 35°C, $x_{sol,in}$ = 20%, B_{mag}= 0-3 Tesla • 2D flow	• Vapor heat transfer neglected • Coupling fluid temperature increase uniform • 2D Navier-Stokes momentum and energy equations with additional body force	• Absorption enhancement due to increased mass transfer resulting from increase in film velocity and thickness due to presence of magnetic field • Magnetic field has negligible effect on the heat transfer process
Patnaik *et al.* (1993)	Analytical/ H_2O-LiBr	• Vertical tube, O.D. 19.05 mm, length 1.524 m • Co-current solution-vapor flow	• P_{abs} = 1.2 kPa, $x_{sol,in}$ = 60%	• Correlations from literature to estimate local heat and mass transfer rate • 1D energy and mass conservation equation	• Wavy nature of film modeled • Design charts for absorber sizing developed • As coupling fluid flow rate increases, the limiting resistance to absorption shifts from coupling fluid side to the solution side

Table 2.1 Continued…

Literature	Study type/Fluid	Absorber/Flow	Specific Conditions	Key assumptions	Key conclusions
Patnaik and Perez-Blanco (1996b, a)	Analytical-Numerical/ H_2O-LiBr	• Vertical tube • Co-current solution-vapor flow	• 2D flow	• Parabolic profile for longitudinal velocity in wave • Dominant frequencies, film thickness, average roll velocity from Brauner (1989) • 2D unsteady momentum equation • 2D unsteady species and energy equations	• Approximate equations for flow inside roll wave developed, indicate rapid fluctuations in velocity in the transverse direction • At lower Reynolds number, reasonable comparison between model predictions and Penetration theory results. • Absorption rates predicted to be higher than Penetration theory results at higher Reynolds number due to formation of roll wave • Formation and growth of concentration and thermal boundary layer tracked
Kirby and Perez-Blanco (1994)	Analytical/ H_2O-LiBr	• Horizontal tube, O.D. 19 mm, length 0.28 m • Quiescent vapor	• P_{abs} = 0.75-0.95 kPa, $x_{sol,in}$ = 60-62%, $\dot{m}_{sol,in}$ = 0.006-0.04 kg s^{-1}	• Correlations from literature for heat and mass transfer coefficients, droplet size, and droplet spacing • Droplet absorption adiabatic • Falling film, evolving droplet, droplet free fall regimes considered	• Significant amount of absorption occurred in the droplet mode due to subcooled solution • Thinner films had higher absorption rates but thicker films absorbed more vapor • Absorption duty increases with increase in solution and coupling fluid flow rates

Table 2.1 Continued…

Literature	Study type/Fluid	Absorber/Flow	Specific Conditions	Key assumptions	Key conclusions
Jeong and Garimella (2002)	Analytical/ H_2O-LiBr	• Horizontal tube, O.D. 16 mm, length 0.2 m, 13 tube rows • Quiescent vapor	• P_{abs} = 0.9-1.4 kPa, $\Gamma_{sol,in}$ = 0.006-0.106 kg m^{-1} s^{-1} • 2D flow	• Linear temperature profile in solution bulk • Droplet absorption adiabatic • Wetting ratio defined • Falling film, evolving droplet, droplet free fall regimes considered • 2D Mass, species, energy conservation equations	• Low absorption rates at the top and bottom of tube due to thicker film • Droplet absorption higher at lower tube levels • Tube wetting has low influence on droplet mode absorption but significant influence of falling film absorption
Jeong and Garimella (2005)	Analytical/ H_2O-LiBr	• Horizontal tube, O.D. 15.88, 6.35, 3.175 mm • Quiescent vapor	• 2D flow	• Linear temperature profile in solution bulk • Droplet absorption adiabatic • Falling film, evolving droplet, droplet free fall regimes considered • 2D Mass, species, energy conservation equations	• No difference in absorber performance if number of passes > 2 • Coupling fluid heat transfer resistance important if α_{CF} < 3000 W m^{-2} K^{-1} • Droplet mode absorption greater for smaller tubes • Cooling capacity increased by 30 and 55% as the tube diameter was decreased from 15.88 mm to 6.35 and 3.175 mm, respectively

Table 2.1 Continued…

Literature	Study type/Fluid	Absorber/Flow	Specific Conditions	Key assumptions	Key conclusions
Subramaniam and Garimella (2009)	Computational / H_2O-LiBr	• Horizontal tube, O.D. 15.9 mm • Quiescent vapor	• $\Gamma_{sol,in}$ = 0.0086 kg m^{-1} s^{-1}, $T_{sol,in}$ = 40.5°C, $x_{sol,in}$ = 65% • 3D flow	• Equilibrium at the vapor liquid interface • 3D Navier-Stokes equations for mass, momentum, species, and energy equations • Volume of fluid (VOF) technique	• Only about 4.4% of the absorption occurs in the droplet mode, but droplet impact facilitates rapid mixing in the film resulting in rapid absorption • Adverse concentration and temperature gradients exist in the film right before droplet impact, and absorption rate is low •
Haselden and Malaty (1959)	Experimental / NH_3-H_2O	• Vertical tube, O.D. 12.7 mm, Length 0.15-2.1 m • Counter-current solution-vapor flow	• P_{abs} ≈ 101 kPa, $x_{sol,in}$ = 0-21%, $\dot{m}_{sol,in}$ = 0.25-1.75 kg s^{-1} • Pyrex glass outer shell to enable visualization • Single-pressure test facility	• Solution interface in equilibrium with vapor at solution bulk temperature	• Mass transfer trends different from predictions of Penetration theory • Mass transfer rate enhanced with formation of ripples on surface • Dominant resistance on coupling fluid side
Palmer and Christensen (1996)	Experimental / NH_3-H_2O	• Vertical fluted tube • Counter-current solution-vapor flow	• $x_{sol,out}$ = 18-38% • Single-pressure test facility • Solution flow on inside of tube	• Tube not fully wet	• Tube wetting varied between 25-50% and increased with solution concentration • Kang and Christensen (1994) model adjusted to predict experimental results

Table 2.1 Continued…

Literature	Study type/Fluid	Absorber/Flow	Specific Conditions	Key assumptions	Key conclusions
Jeong *et al.* (1998)	Experimental / NH_3-H_2O	• Coiled tube, O.D. 12.7 mm, Coil dia 82.6 mm • Counter-current solution-vapor flow	• $x_{sol,in}$ = 1.2-2.2%, $\dot{m}_{sol,in}$ = 4.9-19.7 g s^{-1}, x_{vap} = 63-77%, $\dot{m}_{vap,in}$ = 0.09-0.4 g s^{-1} • Single-pressure test facility	• Mass transfer neglected • 1-D resistance network	• Absorption inhibited heat transfer process by reducing wetting • α_{sol} increased with increase in solution flow rate • Absorber performance enhanced by reducing coil diameter and increasing number of turns
Kang *et al.* (1999)	Experimental / NH_3-H_2O	• Offset strip fin plate heat exchanger • Co-current solution-vapor flow	• $x_{sol,in}$ = 5-15%, $\dot{m}_{sol,in}$ = 4.0-10.2 g s^{-1}, $x_{vap,in}$ = 63-77%, $\dot{m}_{vap,in}$ = 0.62-0.9 g s^{-1} • Single-pressure test facility	• Coupling between heat and mass transfer neglected • 1-D resistance network	• Local rectification of vapor noted initially • Heat transfer rate increased with subcooling and decreased with solution-vapor concentration difference • Mass transfer rate increased with subcooling and solution-vapor concentration difference
Hoffman and Ziegler (1996)	Experimental / NH_3-H_2O	• Horizontal tube absorber • Counter-current solution-vapor flow	• Single-pressure test facility	• Coupling between heat and mass transfer neglected • 1-D resistance network	• Data reduction algorithm developed • No experimental data reported

Table 2.1 Continued…

Literature	Study type/Fluid	Absorber/Flow	Specific Conditions	Key assumptions	Key conclusions
Kwon and Jeong (2004)	Experimental / NH_3-H_2O	• Helical coil, O.D. 12.7 mm, Coil dia 82.6 mm • Co- and Counter-current solution-vapor flow	• $x_{sol,in}$ = 3-30%, $\Gamma_{sol,in}$ = 4.43-90.9 g m^{-1} s^{-1}, $T_{sol,in}$ = 45-60°C, $x_{vap,in}$ = 45.6-96.5% • Single-pressure test facility	• Mass transfer neglected • 1-D resistance network • Nusselt number dependent upon interfacial shear	• α_{sol} coefficient increased with increase in solution flow rate • Co-current configuration favorable at lower solution and vapor concentrations • Vapor-liquid shear at higher flow rates can cause uneven solution distribution and flooding
Niu *et al.* (2010)	Experimental / NH_3-H_2O	• Vertical tube, O.D. 25 mm, Length 900 mm • Counter-current solution-vapor flow	• $x_{sol,in}$ = 14.2-25.5%, $T_{sol,in}$ = 30°C • Single-pressure test facility • External magnetic field	• Heat and mass transfer coefficients not estimated	• Magnetic field in the direction of the solution flow enhanced absorption and vice versa • Absorption trends in presence of magnetic field similar to trends in absence of magnetic field
Yang *et al.* (2011)	Experimental / NH_3-H_2O	• Vertical tube, O.D. 25 mm, Length 1 m • Counter-current solution-vapor flow	• Single-pressure test facility • Surfactant and $ZnFeO_4$, Fe_2O_3, and Al_2O_3 nanoparticles	• Heat and mass transfer coefficients not estimated	• Surfactant reduced, while nanoparticles enhanced, absorption rate • Peak in absorption performance observed with increase in nanoparticle concentration • Maximum enhancement of nearly 70%

Table 2.1 Continued…

Literature	Study type/Fluid	Absorber/Flow	Specific Conditions	Key assumptions	Key conclusions
Lee *et al.* (2008a, b)	Experimental / NH_3-H_2O	• Horizontal tube bank, O.D. 9.5 mm, length 0.29 m • Quiescent vapor	• $x_{sol,in}$ = 5-40%, $\dot{m}_{sol,out}$ = 0.019-0.034 kg s^{-1}, P_{abs} = 150-500°C • Two-pressure test facility	• Saturated liquid and vapor assumptions during data reduction • Quiescent vapor	• In-situ measurements during falling-film absorption reported • α_{sol} increased with increase in solution flow and decrease in absorber pressure • β_{vap} increase with increase in concentration and decrease in absorber pressure
Bohra (2007)	Experimental / NH_3-H_2O	• Horizontal tube bank, O.D. 9.5 mm, length 0.29 m • Quiescent vapor	• $x_{sol,in}$ = 5-40%, $\dot{m}_{sol,out}$ = 0.019-0.034 kg s^{-1}, P_{abs} = 150-500°C • Two-pressure test facility	• Droplets assumed to be symmetric around the vertical axis	• Solution flow between successive rows in droplet mode • Primary droplet did not detach from tube before impact • Stretched triangular waves observed for film flow over tube
Bohra *et al.* (2008)	Experimental / NH_3-H_2O	• Horizontal tube bank, O.D. 9.5 mm, length 0.29 m • Quiescent vapor	• $x_{sol,in}$ = 5-40%, $\dot{m}_{sol,out}$ = 0.019-0.034 kg s^{-1}, P_{abs} = 150-500°C • Two-pressure test facility	• Fully wet tube surface • Quiescent vapor • 1-D resistance network	• Contribution to absorption from droplet mode under 6% • Heat and mass transfer considered in both vapor and liquid phases • Correlations developed based on Reynolds number, Prandtl number, and absorber pressure
Hu and Jacobi (1996a, b)	Experimental / water, glycol, water-glycol, oil, alcohol	• Horizontal tube, O.D. 9.5-22.2 mm • No vapor	• No phase-change • Single pressure test facility	• Fully wet tube surface • Phase-change neglected	• Three flow regimes observed: droplet mode, jet mode, sheet mode • Hysteresis observed for transition between flow modes • Local heat transfer coefficient varied significantly along the axis of the tube • Nusselt number correlated to Reynolds number, Prandtl number, Archimedes number, and tube spacing

Table 2.1 Continued…

Literature	Study type/Fluid	Absorber/Flow	Specific Conditions	Key assumptions	Key conclusions
Garrabrant and Christensen (1997)	Experimental / NH_3-H_2O	• Corrugated and perforated plate-fin absorber • Counter-current solution-vapor flow	• $x_{sol,in}$ = 13-41%, $\dot{m}_{sol,out}$ = 4.16-11.8 g s^{-1}, Q_{abs} = 1.55-5.1 kW • Single-pressure test facility	• Solution well mixed • Vapor mass transfer in thin vapor film • Correlations for heat and mass transfer coefficients	• Absorber performance depended upon wetted fin area, fin efficiency, and vapor mass transfer coefficient • Correction factors for correlations in literature developed for these parameters • Dominant resistance shifts from the coupling fluid side to solution side as vapor flow rate decreases •
Goel and Goswami (2005)	Analytical/ NH_3-H_2O	• Horizontal tube with wire mesh, O.D. 3.2 mm • Counter-current solution-vapor flow	• $x_{sol,in}$ = 25%, $\dot{m}_{sol,out}$ = 0.01 kg s^{-1}, $x_{vap,in}$ = 99.7%, $\dot{m}_{vap,in}$ = 0.0015 kg s^{-1}, P_{abs} = 300 kPa	• Fully wet tube surface and droplets neglected • Conduction in mesh neglected • Flooding neglected • Colburn-Drew equations for vapor condensation	• 25% reduction is size reported due to the presence of mesh between successive tube rows • Saw-tooth temperature profile observed indicating adiabatic absorption • Mesh might inhibit droplet formation and consequent mixing of the film flow
Goel and Goswami (2007)	Experimental / NH_3-H_2O	• Horizontal tube with wire mesh, O.D. 3.2 mm • Counter-current solution-vapor flow	• $x_{sol,in}$ = 30%, $\dot{m}_{sol,in}$ = 14.4 g s^{-1}, $x_{v,in}$ = 95.6%, P_{abs} = 281 kPa • Single-pressure test facility	• LMTD based on measured solution and coolant temperatures	• Mesh enhanced absorber transfers 17-26% higher absorption duty, and yields an average *UA* increase of 49% • Absorption duty increased with increase in solution flow rate • Previous mathematical model under-predicts absorber performance

Table 2.1 Continued…

Literature	Study type/Fluid	Absorber/Flow	Specific Conditions	Key assumptions	Key conclusions
Garimella (1999)	Analytical/ NH_3-H_2O	• Microchannel horizontal tube O.D. 1.587 mm, total area 1.9 m^2 • Counter-current solution-vapor flow	• $x_{sol,in}$ = 21%, $\dot{m}_{sol,in}$ = 0.0189 kg s^{-1}, $x_{vap,in}$ = 99.5%, $\dot{m}_{vap,in}$ = 0.0095 kg s^{-1}, P_{abs} = 510 kPa	• Solution well mixed • Fully wet tube surface • Vapor mass transfer in thin vapor film • Correlations for heat and mass transfer coefficients • Colburn-Drew equations for condensation of vapor	• Low coupling fluid heat transfer resistance due to use of microchannels • Species concentration redistribution due to droplet impingement • Absorption rates higher at the top of the absorber due to favorable conditions • Local desorption of water reported
Meacham and Garimella (2002)	Experimental / NH_3-H_2O	• Microchannel horizontal tube O.D. 1.575 mm, total area 1.5 m^2 • Counter-current solution-vapor flow	• $\dot{m}_{sol,in}$ = 0.011-0.036 kg s^{-1}, vapor fraction = 0-50%, Q_{abs} = 5-16.23 kW • Single-pressure test facility	• Tube surface assumed to be fully wet • LMTD based on saturated solution temperatures	• Overall and solution-side heat transfer coefficient ranged between 130-440 and 15-550 W m^{-2} K^{-1}, respectively • α_{sol} strongly dependent upon solution flow rate • Absorber performance lower than previous predictions
Meacham and Garimella (2003)	Analytical/ NH_3-H_2O	• Microchannel horizontal tube O.D. 1.575 mm, total area 1.5 m^2 • Counter-current solution-vapor flow	• $\dot{m}_{sol,in}$ = 0.011-0.036 kg s^{-1}, vapor fraction = 0-50%, Q_{abs} = 5-16.23 kW	• Tube surface not fully wet • Correlations for heat and mass transfer coefficients • Colburn-Drew equations for condensation of vapor	• Area effectiveness ratio defined and quantified – found to vary between 0.22-0.31 for all data points • Vapor underwent sensible cooling initially followed by sensible heating along the absorber height • Solution temperature found to increase along the absorber height

Table 2.1 Continued…

Literature	Study type/Fluid	Absorber/Flow	Specific Conditions	Key assumptions	Key conclusions
Meacham and Garimella (2004)	Experimental / NH_3-H_2O	• Microchannel horizontal tube O.D. 1.575 mm, total area 0.456 m^2 • Counter-current solution-vapor flow	• $\dot{m}_{sol,in}$ = 0.015-0.027 kg s^{-1}, vapor fraction = 15-30%, Q_{abs} = 4.5-15.1 kW • Single-pressure test facility	• Tube surface assumed to be fully wet • LMTD based on saturated solution temperatures	• Solution-side heat transfer coefficient ranged between 638-1648 W m^{-2} K^{-1} • Superior flow distribution visually confirmed due to better drip tray and tube spacing • Falling-film and droplet flow mechanisms observed
Determan *et al.* (2004), Determan and Garimella (2011)	Experimental / NH_3-H_2O	• Microchannel horizontal tube O.D. 1.575 mm, total area 1.5 m^2 • Counter-current solution-vapor flow	• $\dot{m}_{sol,in}$ = 0.019-0.035 kg s^{-1}, vapor fraction = 0-30%, Q_{abs} = 5.4-17.5 kW • Single-pressure test facility	• Tube surface not fully wet • Correlations for heat and mass transfer coefficients	• Overall and solution-side heat transfer coefficient ranged between 388-617 and 638-1648 W m^{-2} K^{-1}, respectively • Area effectiveness ratio defined and quantified – found to vary between 0.25-0.69 for all data points • Local rectification of vapor reported

Table 2.2 Summary of studies on bubble and convective mode absorption

Literature	Study type/Fluid	Absorber/Flow	Specific Conditions	Key assumptions	Key conclusions
Herbine and Perez-Blanco (1995)	Analytical/ NH_3-H_2O	• Concentric U-tube, Inner O.D. 12.7 mm, Outer O.D. 25.4 mm • Co-current solution-vapor flow	• P_{abs} = 501.8 kPa, $T_{sol,in}$ = 126.7°C, $x_{sol,in}$ = 7.3%, $\dot{m}_{sol,in}$ = 5.02 g s^{-1}, $T_{v,in}$ = 40°C, $x_{vap,in}$ = 99.4%, $\dot{m}_{vap,in}$ = 0.058 g s^{-1}	• Resistance to mass transfer neglected • Bubble velocity weighted sum of terminal and bulk velocity • Correlations for heat and mass transfer coefficients • "Extent of equilibrium" defined to estimate individual species absorption rates	• Local desorption of water reported • Bubble diameter found to increase initially followed by a decrease • Pure water in the bubble towards the end of absorption
Dence *et al.* (1996)	Analytical/ NH_3-H_2O	• Annulus shaped shell • Co-current solution-vapor flow	• Q_{abs} = 4.7 kW, $x_{sol,in}$ = 21%, $m_{sol,in}$ = 9.49 g s^{-1}, x_v = 86.6%, $\dot{m}_{vap,in}$ = 1.91 g s^{-1}	• Mass transfer neglected • Tube spacing greater than largest bubble diameter	• Largest bubble diameter of 4 mm predicted • Absorber designed to be installed directly in the desorber of a GAX cycle

Table 2.2 Continued…

Literature	Study type/Fluid	Absorber/Flow	Specific Conditions	Key assumptions	Key conclusions
Kang *et al.* (1998)	Analytical/ NH_3-H_2O	• Offset strip fin plate heat exchanger, channel 3.3 mm • Counter-current solution-vapor flow	• $T_{sol,in}$ = 65.9°C, $x_{sol,in}$ = 28.3%, $\dot{m}_{sol,in}$ = 17.8 g s^{-1}, $T_{vap,in}$ = 28.8°C, $x_{vap,in}$ = 98.3%, $\dot{m}_{vap,in}$ = 10.4 g s^{-1}	• Bubbles of uniform size and coalescence neglected • Correlations for heat and mass transfer coefficients • Colburn-Drew equations for condensation of vapor	• Solution bulk temperature closely followed the interface temperature • Dominant heat transfer resistance on the solution side • High mass transfer resistance on the solution side
Merrill and Perez-Blanco (1997)	Numerical/ NH_3-H_2O	• None • Counter-current solution-vapor flow	• P_{abs} = 501 kPa $T_{sol,in}$ = 127°C, $x_{sol,in}$ = 8%, $\dot{m}_{sol,in}$ = 4 g s^{-1}, $T_{vap,in}$ = 71°C, $x_{vap,in}$ = 92%, $\dot{m}_{vap,in}$ = 0.91 g s^{-1}	• Spherical bubble throughout absorption • Vapor temperature and concentration uniform • Irrotational flow around bubble	• Concentration and thermal boundary layers relatively thin and independent of *Pe* number • Largest temperature and concentration gradients near the forward stagnation point • Three stages of bubble collapse reported
Lee *et al.* (2003)	Numerical/ NH_3-H_2O	• Vertical tube, I.D. 30 mm • Co- and Counter-current solution-vapor flow	• $T_{sol,in}$ = 15°C, $x_{sol,in}$ = 0-28%, $\dot{m}_{sol,in}$ = 5 g s^{-1}, $\dot{m}_{vap,in}$ = 0.015-0.132 g s^{-1}	• Correlations for bubble dynamics • Vapor phase mass transfer neglected • Water desorption not considered	• Counter-current flow configuration resulted in shorter absorber lengths • Absorption process enhanced by low solution and coupling fluid inlet temperatures, and low solution inlet concentration

Table 2.2 Continued…

Literature	Study type/Fluid	Absorber/Flow	Specific Conditions	Key assumptions	Key conclusions
Fernandez-Seara *et al.* (2005)	Analytical/ NH_3-H_2O	• Vertical shell-and-tube, O.D. 25 mm, Length 0.9 m • Co-current solution-vapor flow	• P_{abs} = 200 kPa, $T_{sol,in}$ = 45°C, $x_{sol,in}$ = 22.5%, $\dot{m}_{sol,in}$ = 27.8 g s^{-1}, $T_{vap,in}$ = 10°C, $x_{vap,in}$ = 99.9%, $\dot{m}_{vap,in}$ = 4.17 g s^{-1}	• Three flow regimes considered • Correlations for heat and mass transfer coefficients • Bubble coalescence and break up neglected	• Churn flow entrance effect • High absorption rates in churn and slug flow regimes • Solution bulk temperature closely followed the interface temperature • Existence of an optimum tube diameter predicted
Fernandez-Seara *et al.* (2007)	Analytical/ NH_3-H_2O	• Vertical finned tube, O.D. 25 mm, Fin spacing 6 mm, 60 tubes • Co-current solution-vapor flow	• P_{abs} = 225 kPa, $T_{sol,in}$ = 50°C, $x_{sol,in}$ = 23.5%, $\dot{m}_{sol,in}$ = 37.5 g s^{-1}, $T_{vap,in}$ = 15°C, $x_{vap,in}$ = 99.5%, $\dot{m}_{vap,in}$ = 4.17 g s^{-1}	• Three flow regimes considered • Correlations for heat and mass transfer coefficients • Bubble coalescence and break up neglected	• Tube lengths required for complete absorption increased for successive rows • Decrease in fin spacing resulted in smaller absorber size • Higher air flow rate and higher degree of solution subcooling yielded favorable absorption rates
Elperin and Fominykh (2003)	Analytical/ NH_3-H_2O, CO_2-H_2O, H_2S-H_2O, O_2-H_2O, N_2-H_2O, SO_2-H_2O	• Vertical tube • Co-current solution-vapor flow	• $Pe >> 1$, $Pr >> 1$, $Sc >> 1$	• Behavior of a single bubble considered • 4 stages of mass transfer considered • Heat and mass transfer in vapor phase neglected • Velocity profiles superimposed from hydrodynamic solution	• Residence times increased with increase in initial bubble diameter, and initial solution concentration • Process was heat transfer and mass transfer limited for larger and smaller coupling parameter value, respectively

Table 2.2 Continued…

Literature	Study type/Fluid	Absorber/Flow	Specific Conditions	Key assumptions	Key conclusions
Ferreira *et al.* (1984)	Experimental / NH_3-H_2O	• Vertical tube, O.D. 10-20 mm, Length 1 m • Co-current solution-vapor flow	• P_{abs} = 126-333 kPa, $\dot{m}_{sol,in}$ = 2.1-26.2 g s^{-1}, $\dot{m}_{vap,in}$ = 0.018-0.48 g s^{-1} • Single-pressure test facility	• Vapor and liquid have uniform concentration • Heat and mass transfer coefficients constant	• Three flow regimes observed: froth flow, slug flow, bubble flow • Largest amount of absorption in the slug flow regime • Correlations for Sherwood number developed
Ferreira (1985)	Experimental / NH_3-$LiNO_3$, NH_3-SCN	• Vertical tube, O.D. 10-20 mm, Length 1 m • Co-current solution-vapor flow	• P_{abs} = 120-370 kPa, $\dot{m}_{sol,in}$ = 2-9.5 g s^{-1}, $x_{sol,in}$ = 35-45%, $T_{vap,in}$ = 15-30°C • Single-pressure test facility	• Heat transfer in the vapor phase neglected • Velocity profile assumed for the liquid	• Nusselt theory under-predicted the overall heat transfer coefficient by 40% • Penetration theory over-predicted the driving potential by 10% • Vapor bubbles resembled Taylor bubbles
Kang *et al.* (2002)	Experimental / NH_3-H_2O	• Vertical rectangular tube 80 × 53.5 × 300 mm • Solution pool	• $x_{sol,in}$ = 0-20%, x_{vap} = 0-100% • Single-pressure test facility	• Bubbles assumed to be axis-symmetric	• As vapor velocities increased, the bubbles tended to a hemispherical shape • Initial bubble diameter increased with increase in solution concentration • Bubble diameter increased with increase in orifice diameter

Table 2.2 Continued…

Literature	Study type/Fluid	Absorber/Flow	Specific Conditions	Key assumptions	Key conclusions
Kim *et al.* (2003b, a)	Experimental / NH_3-H_2O	• Vertical tube, I.D. 10 mm, Length 1.5 m • Counter-current solution-vapor flow	• $m_{sol,in}$ = 0.28-0.97 g s^{-1}, $x_{sol,in}$ = 2.5-21.6%, $T_{CF,in}$ = 20-40°C, $V_{CF,in}$ = 0.08-0.4 L min^{-1}, $\dot{m}_{vap,in}$ = 0.17-0.33 g s^{-1} • Single-pressure test facility	• Heat and mass transfer analogy applied • Presence of water in vapor neglected	• Two flow regimes observed: churn flow and slug flow • Taylor bubbles observed in slug flow • Interface temperature always higher than liquid and vapor bulk temperatures • Mass transfer resistance in the vapor bulk was negligible • β_{sol} relatively independent of solution concentration and coolant conditions
Lee *et al.* (2002b)	Experimental / NH_3-H_2O	• Vertical tube, I.D. 30 mm, Length 1 m • Co- and Counter-current solution-vapor flow	• $x_{sol,in}$ = 20-30%, $T_{sol,in}$ = 22°C, $V_{vap,in}$ = 1-9 L min^{-1} • Single-pressure test facility	• Heat transfer neglected	• Major portion of the absorption was found to occur at the bottom of the absorber for both co-current and counter-current configurations • Gas holdup decreased along the absorber height
Lee *et al.* (2002a)	Experimental / NH_3-H_2O	• Vertical tube, I.D. 20-40 mm, Length 0.4-0.7 m • Counter-current solution-vapor flow	• $\dot{m}_{sol,in}$ = 3.3-13.3 g s^{-1}, $x_{sol,in}$ = 0-28%, $T_{sol,in}$ = 15-60°C, $V_{vap,in}$ = 1-9 L min^{-1} • Single-pressure test facility	• Mass transfer neglected	• Heat transfer coefficient increased with increase in solution and vapor flow rate • Smaller tube diameters resulted in higher heat transfer coefficients • Correlation for Nusselt number developed

Table 2.2 Continued…

Literature	Study type/Fluid	Absorber/Flow	Specific Conditions	Key assumptions	Key conclusions
Lee *et al.* (2002d)	Experimental / NH_3-H_2O	• Flat plate absorber (0.112 × 0.264× 0.003 m^3) • Counter-current solution-vapor flow	• $\dot{m}_{sol,in}$ = 0-16 g s^{-1}, $x_{sol,in}$ = 20-30%, $V_{vap,in}$ = 0-0.16 L s^{-1} • Single-pressure test facility	• Mass transfer in vapor phase neglected	• Solution mass transfer coefficient strongly influenced by vapor flow rate and weakly influenced by solution flow rate • Solution temperature found to decrease from bottom to the top of the absorber
Cerezo *et al.* (2009)	Experimental / NH_3-H_2O	• Corrugated plate heat exchanger, total area 0.1 m^2 • Co-current solution-vapor flow	• $\dot{m}_{sol,in}$ = 8.3-11.1 g s^{-1}, $x_{sol,in}$ = 29-33%, $T_{sol,in}$ = 38-42°C, P_{abs} = 160-200 kPa, $T_{CF,in}$ = 30-35°C • Single-pressure test facility	• Mass transfer in vapor phase neglected	• Solution heat transfer coefficient varied between 2.8-4.1 kW m^{-2} K^{-1} • Absorption duty increased with increase in solution flow rate and decrease in coupling fluid temperature • Solution heat transfer coefficient increased with absorber pressure
Cerezo *et al.* (2010)	Experimental / NH_3-H_2O	• Corrugated plate heat exchanger, total area 0.1 m^2 • Co-current solution-vapor flow	• $\dot{m}_{sol,in}$ = 8.3-11.1 g s^{-1}, $x_{sol,in}$ = 29-33%, $T_{sol,in}$ = 38-42°C, P_{abs} = 160-200 kPa, $T_{CF,in}$ = 30-35°C • Single-pressure test facility	• Bubbles of uniform size and coalescence neglected • Correlations for heat and mass transfer coefficients	• Model under-predicted the performance of the absorber • Maximum error in the absorption duty and absorption mass flux equal to 11.1 and 28.4%
Kim *et al.* (2006)	Experimental / NH_3-H_2O, Cu, Cuo, Al_2O_3	• Rectangular chamber • Solution pool	• $x_{sol,in}$ = 0-18.7%, $T_{sol,in}$ = 20°C, P_{abs} = 100 kPa • Single-pressure test facility	• Bubble assumed to be axis-symmetric	• Bubbles found to be symmetric in the presence of nanoparticles • Absorption rate increased with increase in nanoparticle concentration • Highest enhancement observed for Cu nanoparticles

Table 2.2 Continued…

Literature	Study type/Fluid	Absorber/Flow	Specific Conditions	Key assumptions	Key conclusions
Ma *et al.* (2009)	Experimental / NH_3-H_2O, CNT	• Rectangular chamber • Solution pool	• $x_{sol,in}$ = 0-25%, $V_{v,in}$ = 0.175 m^3 h^{-1}, P_{abs} = 100 kPa • Single-pressure test facility	• Performance analyzed based on initial and final conditions	• Optimal CNT concentration observed for peak absorption performance • Absorption enhancement attributed to four factors • Enhancement higher at higher solution concentrations
Merrill *et al.* (1994)	Experimental / NH_3-H_2O	• Concentric U-tube, Inner O.D. 12.7 mm, Outer O.D. 25.4 mm • Co-current solution-vapor flow	• Q_{abs} = 2.6 kW • Single-pressure test facility	• Mass transfer neglected	• First generation absorber performed below design conditions due to insufficient heat transfer area • Flow enhancement in solution and coolant sides for second generation absorber • Dominant resistance found to be on the coupling fluid side
Chen *et al.* (2006)	Experimental / NH_3-H_2O	• Hollow fiber membrane device acting as an absorber and heat exchanger, O.D. 300 µm • Co-current solution-vapor flow	• P_{abs} = 480 kPa, $\dot{m}_{sol,in}$ = 9.78 g s^{-1}, $x_{sol,in}$ = 26.8%, $T_{sol,in}$ = 78.5°C, $\dot{m}_{vap,in}$ = 5.64 g s^{-1}, $x_{vap,in}$ = 99.8%, $T_{vap,in}$ = 31.6°C, $m_{c,in}$ = 15.4 g s^{-1}, $T_{CF,in}$ = 73.6°C	• Correlations for heat and mass transfer coefficients • Colburn-Drew equations for condensation of vapor	• Total volume of the HFMAE found to be nearly 31% of plate heat exchanger • Enhancement attributed to increased mass transfer area • Solution mass transfer found to be the limiting resistance of the absorption process • Overall cycle *COP* increase estimated to be ~ 15%

Table 2.2 Continued…

Literature	Study type/Fluid	Absorber/Flow	Specific Conditions	Key assumptions	Key conclusions
Jenks and Narayanan (2008)	Experimental / NH_3-H_2O	• Constrained microscale film, width 2 cm, depth 0.15-1.5 mm • Co-current solution-vapor flow	• P_{abs} = 400 kPa, $\dot{m}_{sol,in}$ = 0.16-0.5 g s^{-1}, $x_{sol,in}$ = 15%, $\dot{m}_{vap,in}$ = 0.016-0.05 g s^{-1}, $x_{vap,in}$ = 99.9%, $m_{CF,in}$ = 4.5 g s^{-1}, $T_{CF,in}$ = 10.6°C • Single-pressure test facility	• Mass transfer in vapor phase neglected	• Overall heat transfer coefficient reached a maximum value at depth of 400 µm • β_{sol} increased with increase in vapor flow rate • Existence of optimum channel depth reported
Cardenas and Narayanan (2010)	Numerical/ NH_3-H_2O	• Constrained microscale film, width 3 cm, depth 1 mm • Co-current solution-vapor flow	• P_{abs} = 400 kPa, $\dot{m}_{sol,in}$ = 0.16-0.5 g s^{-1}, $x_{sol,in}$ = 15%, $\dot{m}_{vap,in}$ = 0.016-0.05 g s^{-1}, $x_{vap,in}$ = 99.9%, $m_{CF,in}$ = 4.5 g s^{-1}, $T_{CF,in}$ = 10.6°C • Single-pressure test facility	• Bubble diameter assumed to match experimental results • Correlations for heat and mass transfer coefficients	• Model predictions compared reasonably with experiments with a maximum deviation of 35% • Absorption process was found to be mass transfer limited on the solution side • Confirmed the existence of optimal channel depth
Determan and Garimella (2010)	Experimental / NH_3-H_2O	• Microscale absorber, D_h = 306 µm • Co-current solution-vapor flow	• $T_{CF,in}$ = 20-35°C	• Conditions controlled by system operation	• Two-pressure system • Absorber part of a monolithic single-effect heat pump • Absorber design for a chiller cooling capacity of 300 W • 230 W cooling capacity demonstrated at design conditions • *COP* of chiller varied between 0.25-0.43

Table 2.3 Summary of comparative studies

Literature	Study type/ Fluid	Absorber/Flow	Specific Details	Key assumptions	Key conclusions
Kang *et al.* (2000)	Analytical/ NH_3-H_2O	• Offset strip fin plate heat exchanger • Counter-current solution-vapor flow	• P_{abs} = 557.2 kPa, $x_{sol,in}$ = 27.95%, $T_{sol,in}$ = 74.5°C, $x_{vap,in}$ = 98.7%, $T_{vap,in}$ = 12.2°C, $m_{c,in}$ = 0.378 kg s^{-1}, $T_{CF,in}$ = 46.4°C	• Vapor mass transfer in thin vapor film • Correlations for heat and mass transfer coefficients • Bubbles of uniform size • Colburn-Drew equations for condensation of vapor	• Bubble absorber ~ 49% smaller than falling-film absorber for same absorption • Falling-film absorption influenced strongly by α_{vap}, β_{vap} and β_{sol} • Bubble absorption influenced strongly by α_{vap} and β_{sol}
Lee *et al.* (2002c)	Experimental / NH_3-H_2O	• Flat plate absorber (11.2 × 26.4 × 3 mm) • Counter-current solution-vapor flow	• $x_{sol,in}$ = 0-30%, $\dot{m}_{sol,in}$ = 1.67-15 g s^{-1}, $V_{vap,in}$ = 1-9 l min^{-1} • Single-pressure test facility	• Coupling between heat and mass transfer neglected	• Mass transfer coefficient was higher in bubble mode than falling-film mode absorption • α_{sol} was higher for falling-film mode at lower vapor velocities • Correlations for heat and mass transfer coefficients developed
Castro *et al.* (2009)	Analytical / NH_3-H_2O	• Fin and tube compact heat exchanger, O.D 22 mm, fin pitch 5 mm • Co-current solution-vapor flow	• P_{abs} = 501 kPa, $x_{sol,in}$ = 7.3%, $T_{sol,in}$ = 126.7°C, $x_{vap,in}$ = 99.4%, $T_{vap,in}$ = 40°C, $m_{CF,in}$ = 1.25 kg s^{-1}	• Model from literature for tube wetting used • Uniform spherical bubbles • Linear temperature profile inside the bubble	• Falling-film absorption model over-predicted solution concentration and under-predicted solution temperature • Bubble absorption model predicted well with literature • Bubble absorption found to outperform falling-film absorption due to better wetting of tube surfaces • Dominant resistance in both modes on the air-side

CHAPTER 3. EXPERIMENTS: FALLING-FILM ABSORPTION

As outlined in the previous chapter, one of the objectives of this study is to propose and refine a theory based, experimentally validated heat and mass transfer model for falling-film ammonia-water absorption over horizontal microchannel tube bundles. For this purpose, a comprehensive experimental investigation of microchannel falling-film absorption was conducted first, where a microchannel absorber test section was studied over a range of solution and refrigerant flow rates, solution concentrations, and coupling fluid temperatures. This absorber was installed in a test facility replicating a single-effect ammonia-water absorption heat pump, and experiments were conducted for a heat pump operating in both cooling and heating modes. Solution and refrigerant flow rates were varied over ranges that represent operation of the chiller at different cooling/heating capacities, while coupling fluid temperatures were varied to represent operation at different ambient conditions. Similarly, solution concentrations were varied in controlled fashion to represent operation in cooling as well as heating modes. Such an investigation will present a thorough understanding of the operation of the absorber at realistic heat pump operating conditions. The measurements recorded at the system, component, and local level during these experiments will be used to develop a heat and mass transfer model for falling-film ammonia-water absorption over horizontal tube banks. Details of the test facility developed for these experiments, the microchannel absorber test section, and the experimental procedures and test matrix are discussed in this chapter. Analysis and development of the heat and mass transfer model based on this experimental investigation is discussed in subsequent chapters.

An existing single-effect ammonia-water absorption heat pump test facility was modified to experimentally investigate microchannel falling-film absorption. This test facility provides dilute solution and refrigerant vapor at realistic conditions to the microchannel absorber being investigated, over a wide range of heat pump operating

conditions (both cooling and heating mode.) All components of the absorption heat pump are hydronically coupled, and the desired operating conditions are achieved by controlling and adjusting the coupling fluids circulated through these components. This test facility was originally designed for investigation of falling-film absorption over large diameter horizontal tubes in a quiescent vapor ambient (Lee *et al.*, 2008a, b). Significant modifications to the facility were made to enable investigation of the microchannel absorber, which included installation of a larger evaporator for higher cooling capacities, installation of higher capacity pumps for higher fluid flow rates, and revised instrumentation for in-situ measurements. The following sections present the details of the modified test facility, the microchannel absorber test section, and the experimental procedures.

3.1. Test facility

A schematic and a photograph of the test facility are shown in Figs. 3.1 and 3.2, respectively. The test facility replicates a complete, single-effect, thermally activated absorption chiller including the absorber, desorber, condenser, evaporator, rectifier, solution heat exchanger, and refrigerant pre-cooler, together with coupling fluid loops and heat exchangers for the major externally coupled components. The system operates at two different nominal pressure levels: high pressure at the condenser, rectifier and desorber, and low pressure at the absorber and evaporator.

Concentrated solution from the absorber is pumped to the desorber, where a steam-heated desorber (coiled tube-in-tube heat exchanger, Model 00528, Exergy Inc.) generates a two-phase mixture of vapor and dilute solution. The temperature of the laboratory heating steam is varied by regulating the supply pressure using a pressure regulating valve (range 0-1825 kPa). Because the dilute solution and vapor generated at the desorber exit the component in a co-current flow configuration, a separator is used to separate the two fluid streams. The separator is an assembly of meshes and tubing inside

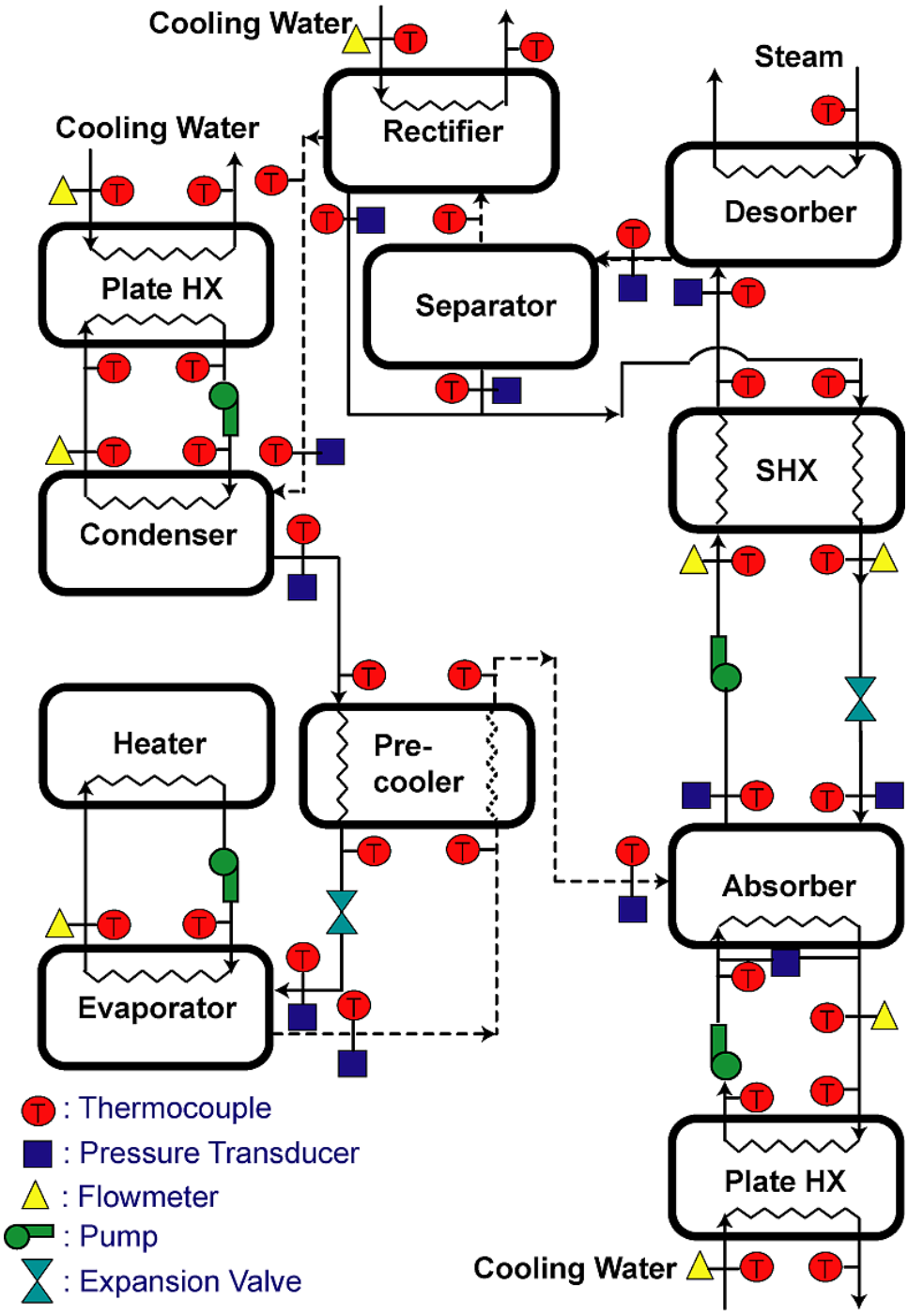

Fig. 3.1 Schematic of falling-film absorption test facility

a 0.3 m long, 0.15 m O.D., stainless steel flanged cylindrical shell. Two-phase solution entering the separator from the top is separated into the vapor and liquid phases, exiting from the top and bottom of the component, respectively. A level indicator (sight glass) is

used to monitor the fluid level in the separator. Thermocouples are used to measure the temperature of the various fluid streams entering and exiting the desorber and separator.

The dilute solution exiting the separator flows back to the absorber, exchanging heat with the concentrated solution from the absorber in the solution heat exchanger (shell-and-tube heat exchanger, Model 00256-3, Exergy Inc.) The vapor from the separator flows through a rectifier, where water is preferentially condensed out. The resulting ammonia-rich refrigerant vapor flows to the condenser, while the reflux solution mixes with the dilute solution returning from the separator. The rectifier (Rocky Research) is a 0.483 m long and 0.114 m diameter shell enclosing a helical coil of 12.7 mm tube diameter, with appropriate fill material in the space between the coil and the shell. The rectifier is directly cooled by laboratory chilled water/glycol coolant (supplied by a 50 RT Carrier AquaSnap chiller) and the flow rate controlled by a rotameter (Model VFB-85-EC and VFB-86-EC, Dwyer Instruments). The rectifier is installed at the highest point in the system, at a slight incline, which provides the necessary pressure gradient for flow of the reflux. Sight glasses are installed at the reflux outlet, and at the separator solution outlet to confirm only liquid is flowing through these streams. Thermocouples are used to measure the temperature of the various fluid streams entering and leaving the rectifier and the solution heat exchanger. It should be noted that the dashed lines in Fig. 3.1 indicate vapor flow, while the solid lines indicate solution flow.

The refrigerant vapor rejects heat to a water/glycol solution (50% by mass) circulated in the refrigerant condenser (shell-and-tube heat exchanger, Model 00677-3, Exergy Inc.) A centrifugal pump (Model TE-7-MD-HC, Little Giant), with an upstream expansion tank to provide necessary head, is used to circulate the water/glycol coupling fluid. The flow rate of the coupling fluid can be altered using a metering needle valve and measured using a Coriolis flow meter (CMF 100, Micromotion). The coupling fluid, in turn, transfers heat to the laboratory chilled water/glycol coolant in a plate heat exchanger (Supercharger Model UX-016-UJ-21, Tranter). The flow rate of the chilled water/glycol

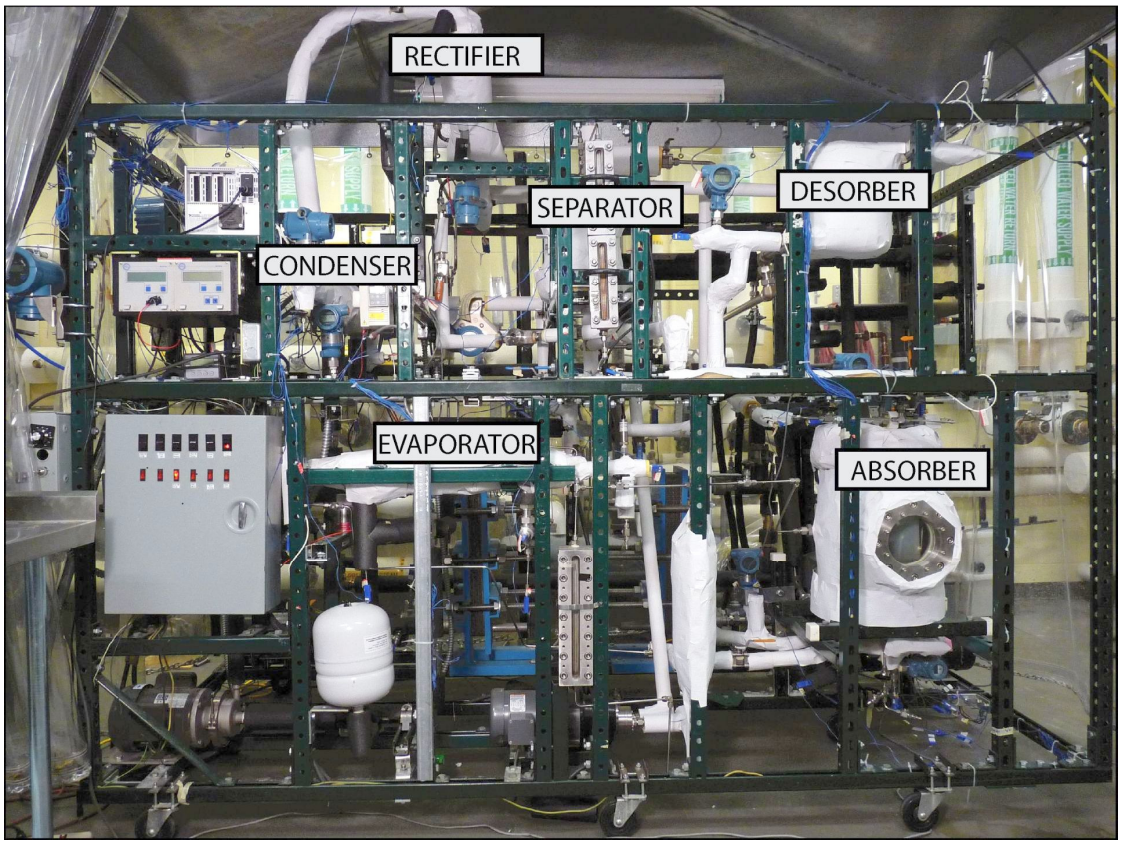

Fig. 3.2 Photograph of falling-film absorption test facility

coolant is measured using a rotameter (7530 7C-08, King Instrument Company). Thermocouples are used to measure the temperature of the refrigerant, coupling fluid, and chilled water/glycol coolant streams at the inlet and exit of the both the condenser and the plate heat exchanger.

A sight glass is used to confirm that the refrigerant exiting the condenser is completely condensed. The flow rate of this condensed refrigerant is measured using a Coriolis flow meter (CMF 010, Micromotion). The condensed high pressure refrigerant exiting the flow meter flows through the refrigerant pre-cooler (shell-and-tube heat exchanger, Model 00256-2, Energy Inc.) exchanging heat with the evaporated low pressure refrigerant exiting the evaporator. The cooled high pressure refrigerant is expanded to the low pressure through a needle valve (Model SS-4MG-MH, Swagelok.), upstream of the evaporator. A closed loop water/glycol solution (50% by mass) with two

5 kW electric heaters (Model L12X4B, Watlow) provide the heating load to the evaporator (shell-and-tube heat exchanger, Model 00677-3, Exergy Inc.) A centrifugal pump (Model AC4STS Series, Finish Thompson Pump), with an upstream expansion tank to provide necessary head, is used to circulate this coupling fluid. The flow rate of the coupling fluid can be altered using a metering needle valve and measured using a positive displacement flow meter (Model JVM 60KL, AW Company). Thermocouples are used to measure the temperature of the refrigerant and the coupling fluid at the inlet and exit of both the refrigerant pre-cooler and the evaporator. Vapor from the evaporator returns to the absorber via the refrigerant pre-cooler, where it is absorbed into the dilute solution to complete the cycle. The details of the construction of the absorber, installation, and coupling fluid are provided in the next section.

Concentrated solution leaving the absorber on the low pressure side is pumped to the high pressure side using a solution pump (variable frequency magnetic gear pump, Model TXS2.6 series, Tuthill). A concentrated solution tank is installed upstream of the solution pump to ensure that the pump never runs dry. A sight glass is installed in parallel to the solution tank to monitor the solution level. To achieve stable start up, a 6.35 mm tube connection is made between the absorber shell and the top of the concentrated solution tank, with quarter turn plug valves to open and close the connection. A similar connection is also made between the evaporator refrigerant inlet and the bottom of the concentrated solution tank. These connections are used to equalize pressure during start up, the procedure for which is discussed later. The flow rate of the concentrated solution is measured at the exit of the solution pump, while the flow rate of the dilute solution is measured upstream of the absorber using Coriolis flow meters (CMF 025, Micromotion). A summary of the system heat exchangers is provided in Table 3.1.

Table 3.1 Summary of heat exchangers in the falling-film absorption test facility

Component	Manufacturer (model)	Dimensions/Specifications	Operating Limits
Condenser/ Evaporator	Exergy, Inc. (Model 00677–3)	Stainless Steel Type: Shell–and–Tube Length: 0.5 m Shell O.D.: 76.2 mm Number of Tubes: 253 Tube O.D.: 3.2 mm Tube Wall Thickness: 0.32 mm Heat Transfer Area: 1.24 m^2	Pressure (MPa): Tube–side: 5.171 Shell–side: 3.447 Working Fluid Temperature: 427^oC
Desorber	Exergy, Inc. (Model 00528)	Type: Tube–in–Tube Material: Stainless Steel Length: 5.9 m Inner Tube O.D.: 12.7 mm Outer Tube O.D.: 25.4 mm Wall Thickness: 1.7 mm Heat Transfer Area: 0.23 m^2	Pressure (MPa): Tube–side: 31.026 Annulus–side: 13.790 Working Fluid Temperature: 427^oC
Rectifier	Rocky Research	Type: Shell–Coiled Tube Material: Carbon steel Shell Length: 0.48 m Shell O.D.: 0.11 m Coil O.D.: 12.7 mm	
Separator	In–House	Material: Stainless Steel Shell Length: 0.3 m Shell O.D.: 0.15 m Tube O.D.: 12.7 mm Tube Length: 0.15 m Number of Holes: 32 (1.6 mm) Pipe Nipples O.D.: 50 mm Pipe Nipples Length: 0.15 m Number of Holes: 56 (3.2 mm)	
Solution Heat Exchanger	Exergy Inc. (Model 00256–3)	Type: Shell–and–Tube Material: Stainless Steel Length: 0.38 m Shell O.D.: 38.1 mm Number of Tube: 55 Tube O.D.: 3.2 mm Tube Wall Thickness: 0.3 mm Heat Transfer Area: 0.20 m^2	Pressure (MPa): Tube–side: 8.274 Shell–side: 5.516 Working Fluid Temperature: 427^oC

Table 3.1 Continued…

Component	Manufacturer (model)	Dimensions/Specifications	Operating Limits
Refrigerant Pre–cooler	Exergy Inc. (Model 00256–2)	Type: Shell–and–Tube Material: Stainless Steel Length: 0.25 m Shell O.D.: 38.1 mm Number of Tube: 55 Tube O.D.: 3.2 mm Tube Wall Thickness: 0.3 mm Heat Transfer Area: 0.13 m^2	Pressure (MPa): Tube–side: 8.274 Shell–side: 5.516 Working Fluid Temperature: 427^oC
Absorber/ Condenser Plate Heat Exchanger	Tranter Inc. (Superchanger, Model UX–016–UJ–21)	Type: Plate Height: 0.774 m Length: 0.3 m Depth: 63 – 67.3 mm Heat Transfer Area: 1.65 m^2 Weight: 95.7 kg	Pressure (MPa): 1.034 Working Fluid Temperature: 93.3^oC

3.2. Microchannel falling-film absorber

The microchannel falling-film absorber is the main component investigated in this study. The absorber assembly consists of two major parts: the microchannel tube array and the outer shell. Dilute solution from the solution heat exchanger enters the outer shell, is distributed over the microchannel array where the absorption occurs, and the resulting concentrated solution is removed from the bottom of the outer shell and directed toward the solution tank. Details of this absorber component follow.

3.2.1. Absorber outer shell

The absorber outer shell is a flanged stainless steel 0.264 m inner diameter, 0.5 m length, Schedule 10 shell, with a large sight port (Fig. 3.3a) to enable viewing of the solution flow mechanisms. A B-weld sight glass (Pressure Products Company Inc.), consisting of a stainless steel body, cap, cap screws, compression ring, lens, lens packing, compression adjustment screws, and two cushioning gaskets is used to seal the large sight

port. The sight glass is 0.32 m in diameter and 89 mm in thickness with a tempered borosilicate glass that can withstand a maximum pressure of 2068 kPa. Three additional smaller sight ports at 90^{o} intervals are provided in the shell to enable viewing from different orientations (axial and transverse) as well as for illumination of the absorber. Each of these ports is equipped with a Bull's Eye NPT 38 mm sight glass (Pressure Products Inc.) rated for 4137 kPa. Teflon gaskets, compression rings, and O-rings are used for sealing in the sight glasses to ensure compatibility with ammonia.

The flanges at the top and bottom of the outer shell are used to facilitate connections between the inside of the absorber and the test facility. The tube array is mounted on the bottom flange. Refrigerant vapor inlet, concentrated solution outlet, coupling fluid inlet and outlet, and system charging ports are located on the bottom flange, while the dilute solution inlet port is located on the top flange.

3.2.2. Microchannel tube array

The tube array (Fig. 3.3b) consists of 1.575 mm OD, 0.2 mm wall tubes, sandblasted to facilitate surface wetting, with the straight section of each tube segment being 0.1397 m long. There are 20 rows of stainless steel tubes, with each row consisting of 33 tubes. Series flow between passes of the absorber is achieved by bending the tubes

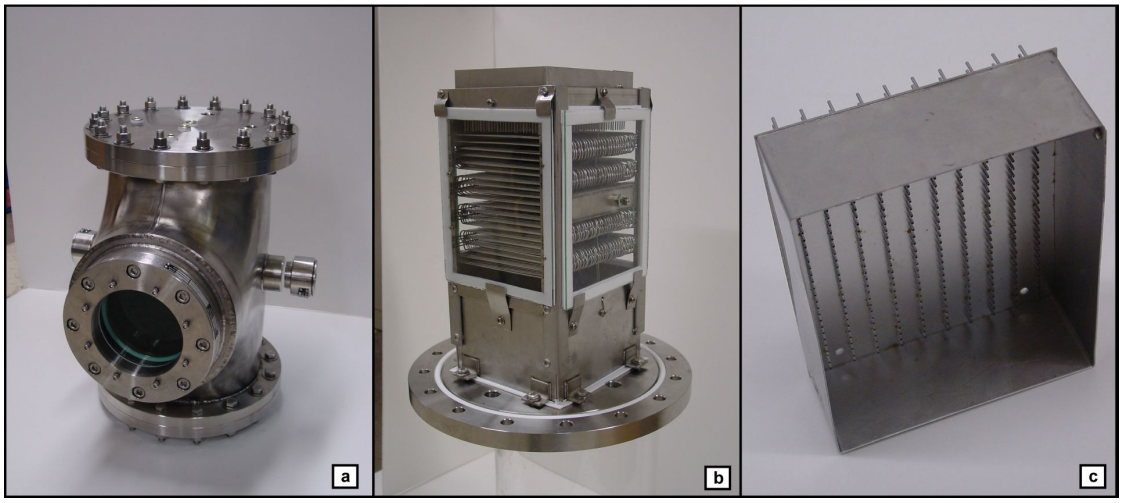

Fig. 3.3 Photograph of microchannel falling-film absorber

instead of using headers. (With the U-bends at the ends of the tubes, the overall extent of the tube array in the length direction of the tubes is 0.162 m.) The coupling fluid enters an inlet manifold, splits into two rows of tubes in parallel, flows through the sets of tube rows (10 passes) in series, and exits at the top of the array through another manifold and an outlet fitting, providing an almost pure counterflow orientation with the solution flowing downward due to gravity. A manifold is provided at the middle rows of the tube array to halve the lengths of straight sections that had to be bent in serpentine fashion. In addition, this manifold provides structural support and minimizes progressive stack-up of potential distortions in the serpentine tubes. Thus, the overall dimensions of the absorber array are approximately $0.162 \times 0.157 \times 0.150$ m, with a surface area of 0.456 m^2.

The drip tray on top of the tube array supplies dilute solution to the absorber. It consists of a stainless steel tray with perforations at a pitch of 12.7×4.76 mm, with small lengths of tubing (17 mm) placed in each of the holes of the drip tray (Fig. 3.3c.) These tubes ensure that solution droplets form directly above the coolant tubes and do not coalesce before detaching as large streams at preferential locations. In addition, the height of the tubes in the tray provides an even gravity head in the inlet solution pool above the tubes, allowing for uniform flow through the dripper tubes to the tube array. The entire absorber tube array and drip tray assembly were brazed in place before being installed into the test facility. A summary of the absorber geometry is provided in Table 3.2.

3.2.3. Absorber assembly and coupling fluid loop

The assembly consisting of the outer shell, the microchannel tube array, and the drip tray is installed in the absorption test facility. Fig. 3.4 shows a schematic of this assembly. Dilute solution enters the absorber at the top, is evenly distributed along the different tubes by the drip tray, and flows downwards due to gravity in falling-film mode around the microchannel tube bundles. Vapor is introduced at the bottom of the absorber and is absorbed as it flows upward, counter-current to the falling-film. Coupling fluid is

introduced at the bottom of the tube array, flows countercurrent to the falling-film, and exits the tube array at the top. Thermocouples are placed at the inlets of the dilute solution and refrigerant vapor entering the absorber, and at the outlet of the concentrated solution leaving the absorber. Additionally, thermocouples are placed at the inlet, outlet, and at the intermediate manifold to measure the coupling fluid temperatures. Thus, the absorber can be divided into two segments (bottom and top segments) with the state of the coupling fluid known at the inlet and outlet of each of these segments. Furthermore, thermocouples are placed in the drip tray, the solution pool at the bottom of the absorber, and at five intermediate locations in the tube banks to track the progression of the absorption process. Absolute pressure transducers are installed on the dilute solution and refrigerant vapor inlet lines just upstream of the absorber, and on the concentrated solution line just downstream of the absorber to measure the local pressures at these locations.

The heat of absorption is removed by a distilled water loop circulated by a centrifugal pump (Model TE-7-MD-HC, Little Giant), with an upstream expansion tank

Table 3.2 Microchannel falling-film absorber geometry

Tube outer diameter, mm	1.575
Tube inner diameter, mm	1.168
Tube wall material	Stainless Steel
Tube length, m	0.1397
Number of tubes per row	33
Number of rows per pass	2
Number of passes	10
Tube transverse pitch, mm	4.76
Row vertical pitch, mm	7.94
Absorber height, m	0.150
Total surface area, m^2	0.456

to provide the required head. The flow rate of the coupling fluid can be altered using a metering needle valve, and measured using a magnetic flow meter (Model 8711, Rosemount). The coupling fluid in turn transfers heat to the laboratory chilled water/glycol coolant in a plate heat exchanger (Supercharger Model UX-016-UJ-21, Tranter). The flow rate of the chilled water/glycol coolant is measured using a rotameter (VFC-143, Dwyer Instrumentation). It should be noted that energy balance on the plate heat exchanger provides an additional means to verify the accuracy of the results over and above the energy balance between the solution and the coupling fluid in the absorber.

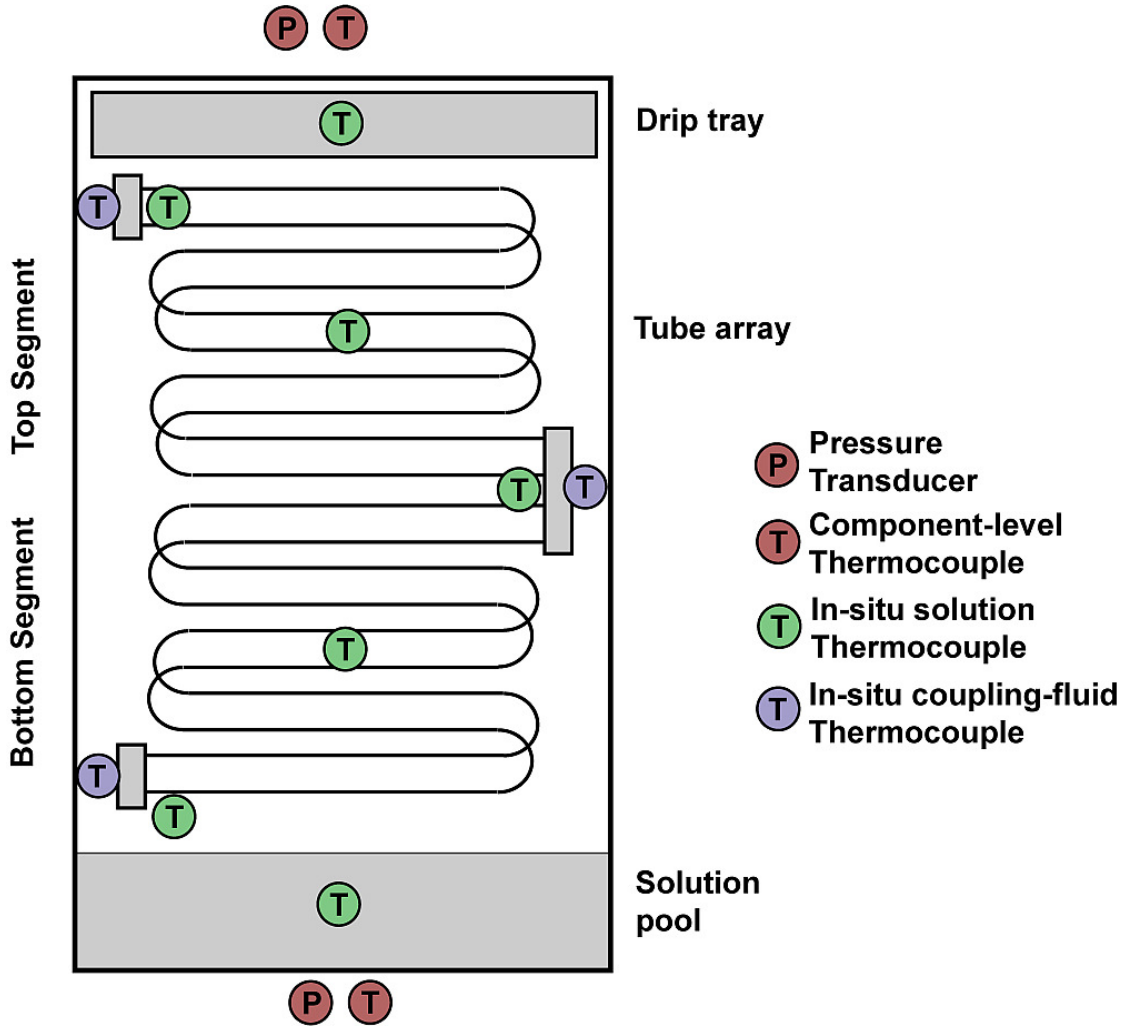

Fig. 3.4 Schematic of microchannel falling-film absorber assembly

3.3. Instrumentation and data acquisition system

3.3.1. Instrumentation

A total of 60 temperature measurements, 11 pressure measurements, and 6 flow rate measurements are recorded during each test run. T-type thermocouples (Model TMQSS-125G-6 and TMQSS-62G-36, Omega Engineering Inc.) are used to measure all the temperatures. Calibration of these thermocouples yields an accuracy of ±0.25^{o}C. Absolute pressure transducers (Model 2088 (accuracy ±0.25% of calibrated span) and 3051 (accuracy ±0.075% of calibrated span), Rosemount, and Model MMA500 (accuracy ±0.035% of span), Omega Engineering Inc.) were used to measure the pressure at 11 locations on the test loop. These include the refrigerant inlet and outlet at the condenser and evaporator, dilute solution and refrigerant vapor inlet, and concentrated solution outlet at the absorber, solution inlet and outlet at the desorber, dilute solution outlet at the separator, and reflux outlet at the rectifier. While some of these pressure transducers can measure pressures as high as 68.95 MPa, the span was reduced to the desirable range to achieve higher accuracy of the output. For example, the span of Model 3051 Rosemount pressure transducers were reset to 0 - 2048.5 kPa for an absolute uncertainty of 1.54 kPa. Additionally, dial gauges (Model 1005P (accuracy ±3% of span), Ashcroft) are used to monitor the pressure inside the absorber, condenser, and evaporator coupling fluid loops. Rotameters are used to monitor and control the flow rate of chilled water/glycol coolant from the laboratory chiller entering the test facility.

The flow rates of the dilute and concentrated solution are measured using high accuracy Coriolis flow meters (model CMF025 Elite (accuracy ±0.1% of flow), Micromotion) which can simultaneously measure the density and flow rate. The flow rate of the refrigerant is also measured using another Coriolis flow meter (CMF010 Elite (accuracy ±0.1% of flow), Micromotion). Sight glasses are installed just upstream of these flow meters to visually confirm single-phase flow. As previously discussed, the

flow rates of the absorber, evaporator, and condenser coupling fluid streams are measured using a magnetic flow meter (Model 8711, (accuracy ±0.5% of flow), Rosemount), a positive displacement flow meter (Model JVM-60KL, (accuracy ±0.5% of flow), AW Company), and a Coriolis flow meter (CMF100 (accuracy ±0.1% of flow), Micromotion), respectively. All the above instruments are directly interfaced with a PC-based data acquisition system for real-time measurement. A summary of the instrumentation for the test facility is shown in Table 3.3.

3.3.2. Data acquisition

A PC-based data acquisition system (SCXI-100, National Instruments) is used to process, display, and record measurements from the above described instruments during the experiments. Add-on cards are used to measure temperatures (SCXI-1102 and SCXI-1303, National Instruments), flow rates and pressures (SCXI-1102 and SCXI-1300, National Instruments). Signal modification is done to convert the instrument output signal (typically an electrical signal varying between 4-20 mA) to a readable voltage signal by using a 249 ohm shunt resistor. The acquisition system chassis is interfaced with the computer using Labview software (Version 8.6, National Instruments). Data acquisition rates and durations can be programmed at desired scan rates using this software. All the relevant calibration curves for the different thermocouples, pressure transducers, and flow meters are also incorporated into this software by the user.

Table 3.3 Summary of instrumentation in the falling-film absorption test facility

Parameter/ Instrument	Model	Manufacturer	Quantity	Range	Accuracy	Operating Limits
Flow meters and transmitter specifications						
Dil./ Conc. Solution	CMF025 Elite	MicroMotion Inc.	2	0 - 0.6048 kg s^{-1} 0 - 6.309 $\times 10^{-4}$ m^3 s^{-1}	±0.1% (Flow) ±0.5 kg m^{-3} (Density)	T: -240 to 350°C P: 10 MPa
Dil./ Conc. (Transducer)	RFT9739 - Rack Mounting	MicroMotion Inc.	2	0 - 5000 kg m^{-3} -240 to 450°C		T: 0 to 50°C (Ambient)
Refrigerant	CMF010 Elite	MicroMotion Inc.	1	0 - 0.03024 kg s^{-1} 0 - 3.155 $\times 10^{-5}$ m^3 s^{-1}	±0.1% (Flow) ±0.5 kg m^{-3} (Density)	T: -240 to 350°C P: 10 MPa
Refrigerant (Transducer)	1700 – Field Mounting	MicroMotion Inc.	1	0 - 5000 kg m^{-3} -240 to 450°C		T: -40 to 60°C (Ambient)
Absorber Coupling Fluid	8711	Rosemount	1	0 - 1.262×10^{-3} m^3 s^{-1}	±0.5%	T: -29 to 149°C P: 5.1MPa
Absorber Coupling Fluid (Transducer)	8712C	Rosemount	1			T: -29 to 60°C (Ambient)
Evaporator Coupling Fluid	JVM-60KL	AW Company	1	1.262×10^{-4} - 1.262×10^{-3} m^3 s^{-1}	±0.5%	P: 34.474 MPa
Evaporator Coupling Fluid (Transducer)	FEM-03	AW Company	1			
Condenser Coupling Fluid	CMF100 Elite	MicroMotion Inc.	1	0 - 7.56 kg s^{-1}	±0.1% (Flow) ±0.5 kg m^{-3} (Density)	T: -240 to 350°C P: 10 MPa
Condenser Coupling Fluid (Transducer)	RFT9739-Field Mounting	MicroMotion Inc.	1	0 – 5000 kg m^{-3} -240 to 450°C		T: 0 to 50°C (Ambient)

Table 3.3 Continued…

Parameter/ Instrument	Model	Manufacturer	Quantity	Range	Accuracy	Operating Limits
Pressure transducer and dial gauge specifications						
Absolute	2088	Rosemount	3	0 - 5.516 MPa	±0.25% of Calibrated Span	T: -40 to121^{o}C
Absolute	2088	Rosemount	1	0 - 1.034 MPa	±0.25% of Calibrated Span	T: -40 to121^{o}C
Absolute	3051	Rosemount	2	0 - 27.579 MPa	±0.075% of Calibrated Span	T: -40 to121^{o}C
Absolute	3051	Rosemount	2	0 - 68.948 MPa	±0.075% of Calibrated Span	T: -40 to121^{o}C
Absolute	MMA 500	Omega Engineering Inc.	3	0 - 3.45 MPa	±0.035% of Span	T: -45 to 121^{o}C
Dial Gauge	1005P (ABS-Black)	Ashcroft	2	0 - 689.5 kPa	±3% of Span	T: -40 to 65^{o}C
Dial Gauge	1005P (ABS-Black)	Ashcroft	1	0 - 2.068 MPa	±3% of Span	T: -40 to 65^{o}C
Thermocouple specifications						
Thermo couple	T-type	Omega Engineering Inc.	60	-270 to 240^{o}C	±0.25^{o}C	
Rotameter specifications						
Absorber	VFC-143 series	Dwyer Instrumentation	1	1.262×0^{-4} - 1.262×10^{-3} $m^3\ s^{-1}$	±2% of Full Scale	T: 49^{o}C P:690 kPa
Condenser	7530 7C-08	King Instrument Company	1	6.309×10^{-5} - 6.309×10^{-4} $m^3\ s^{-1}$	±2% of Full Scale	T: 54^{o}C P:862 kPa
Rectifier	VFB -85-EC	Dwyer Instrumentation	1	1.262×10^{-4} - 1.262×10^{-3} $m^3\ s^{-1}$	±3% of Full Scale	T: 65^{o}C P:690 kPa

Table 3.3 Continued…

Parameter/ Instrument	Model	Manufacturer	Quantity	Range	Accuracy	Operating Limits
Rectifier	VFB -86-EC	Dwyer Instrumentation	1	3.155×10^{-5} - 3.155×10^{-4} $m^3\ s^{-1}$	±3% of Full Scale	T: 65°C P:690 kPa

3.4. Test facility operational features

Several features of the test facility were designed to provide precise operational control over the test conditions. Due to the use of an intermediate fluid loop between the condenser and absorber, and the laboratory chiller, the inlet and outlet temperatures, and flow rates, of the respective coupling fluids can be adjusted to simulate heat pump operation in cooling and heating modes, over a range of ambient conditions. Similarly, the use of two independent loops for the condenser and absorber coupling fluid provides flexibility in independently setting the operating conditions for the two components. For example, the flow rates and inlet and outlet temperatures, can be adjusted to simulate both series or parallel flow configuration (or any combination of the two) of the absorber and condenser coupling fluid. Finally, the use of a variable frequency magnetic gear pump facilitates operation of the chiller over a wide range of solution and refrigerant flow rates, allowing for heat pump operation over a range of cooling/heating capacities.

3.5. Experimental procedures

3.5.1. Leak testing and charging

Ammonia is a toxic and corrosive fluid and exposure to ammonia can be dangerous to the operator. It is, therefore, important to ensure that there are no leaks in the system before charging with ammonia. Thus, extensive leak tests were performed before charging the system. The system was first charged with compressed air to a pressure of 793 kPa, and all the fittings, gaskets, welded parts, and sight glasses were

checked for leaks with soapy water. Subsequently, the system was charged with R404A up to 1379 kPa, and a refrigerant leak detector (Accuprobe^{TM} Leak Detector, sensitivity 1.7 g yr^{-1}) was used to identify all the minor leaks. Finally, the system was kept pressurized overnight. If no appreciable pressure drop was observed, the system was considered leak free.

Once the system was deemed to be leak free, evacuation was initiated. A vacuum pump (DN-200N, DV Industries) was used to evacuate the system until the system pressure was 20 Pa or lower. A vacuum gauge (Model 14571, Thermal Engineering) was used to monitor the pressure level, and pressure transducers were also used to run a pressure trace. The evacuation process removes all the non-condensable gases, and creates the necessary pressure gradient for charging both water and ammonia into the system.

The total required charge of water and ammonia is pre-determined based on the intended test conditions and the total void space in the test loop. For the test conditions considered in this study, 3-5 kg each of water and ammonia were charged into the system. First, distilled water was charged into the system. A charging container filled with distilled water was connected to the system through the charging port located at the bottom of the absorber. The hose connecting the container to the system was evacuated before opening the inlet valve to allow water into the system. The weight of the charging container was continuously monitored to determine the amount of distilled water charged into the system. Once sufficient amount of water was charged into the system, the system was prepared for charging with ammonia. Evacuated hoses were used to connect a cylinder of anhydrous ammonia to the system through the charging port. The weight of the ammonia cylinder was also continuously monitored to determine the amount of ammonia charged into the system. It should be noted that as ammonia enters the system, it is absorbed into the charged water, releasing a significant amount of heat of absorption. This could result in a rise in the system temperature and pressure beyond safety limits.

Thus, the absorber coupling fluid was circulated continuously during the charging process to ensure the system pressure was within reasonable limits.

3.5.2. Safety precautions

As previously mentioned, ammonia is a toxic substance, which if inhaled in large quantities, can cause depletion of oxygen and affect the immune system. Immediate first aid is necessary in case of exposure to sensitive organs such as the eyes. Several precautions were taken to safeguard against any possible mishaps. The main precautions are listed here.

A full face mask (Model 7600 series, Honeywell) with an ammonia/methylamine cartridge and gloves were worn whenever there was a possibility of direct or indirect contact with ammonia, especially during charging and discharging of the system. The system was located under a fume hood equipped with an exhaust fan, capable of containing and immediately removing any ammonia that might be present during charging and operation, or during plumbing modification. Chemical resistant curtains were used to enclose the whole test facility on all sides. Additionally, an ammonia monitor was installed on the wall next to the test facility. This fixed single gas monitor (SAM-NH308N, Lumidor Safety products) has a working range of 0-99 ppm and an accuracy ± 2 ppm, and was calibrated to provide a loud alarm at 25 ppm of ammonia in its vicinity to provide an alert about any accidental leaks. Protective safety wear was worn at all times during operation of the test facility, as well as during plumbing modifications.

Due to the corrosive nature of the chemical, compatibility of all the instruments and fittings with ammonia and ammonia-water mixture was ensured. For example, all O-rings were either made from Teflon or Neoprene, both of which are compatible with ammonia-water mixtures. Additionally, all sensors were made from either stainless steel or Hastelloy to prevent corrosion.

It should also be noted that all the tubing, heat exchangers, and test sections that come into contact with ammonia-water solution were fabricated from stainless steel. Although carbon steel is a cheaper alternative, in a laboratory environment, due to frequent assembly and disassembly and modification of the components and plumbing layouts, these components can frequently come into contact with air, and if fabricated from carbon steel, can corrode. Therefore, stainless steel was used to avoid these issues.

3.5.3. Experimental procedures

The ultimate heat source and heat sink for each experiment is the laboratory steam and laboratory chiller, respectively. As previously mentioned, the laboratory steam lines can supply steam up to a pressure of 1825 kPa and temperature of 208^{o}C, while the chiller can deliver a cooling capacity of 175.8 kW at temperatures as low as of -9.45^{o}C. These two limiting temperatures are controlled to achieve the desired system operating conditions.

Once the system is confirmed to be leak free and charged with the appropriate mixture of ammonia and water, the data acquisition system and Labview software are started and the different temperatures, pressures, and flow rates are monitored continuously. Then the laboratory chiller is started, and the chilled water/glycol coolant is set to the desired temperature. Next, the rotameters controlling the chilled water/glycol coolant flow rate to the absorber and condenser plate heat exchangers are adjusted to deliver the desired flow. The absorber coupling fluid pump is then started and the absorber coupling fluid flow rate is adjusted using the metering needle valve. Due to the circulating coupling fluid, the absorber cools to a lower temperature. Any accumulated non-condensable gases are bled out of the system at this point, either at the top of the absorber, or at the top of the solution tank. The solution pump is then started at a very low frequency to initiate circulation of solution between the absorber and the desorber. The expansion valve for the dilute solution is kept fully open initially to reduce any flow

restriction. Once a steady circulation is achieved, steam is slowly introduced into the desorber to initiate the desorption process. As vapor is generated in the desorber, a pressure difference between the high and the low sides starts to develop. The frequency of the solution pump motor is then increased to maintain the flow of the solution at these increasing pressure differences. The dilute solution expansion valve is then gradually closed to maintain the pressure difference between the high and low sides. Throughout this process, solution level in the separator is monitored to minimize preferential solution accumulation, so that the solution pump is never starved.

Initially, the laboratory chilled water/glycol coolant entering the rectifier is constricted to a very low flow rate to ensure that most of the vapor generated at the desorber reaches the condenser. The condenser coupling fluid pump is then started and the condenser coupling fluid flow rate is adjusted using the metering needle valve. The refrigerant rejects heat to this coupling fluid, and undergoes condensation and subsequent subcooling. The flow of the subcooled refrigerant is observed in the sight glass at the outlet of the condenser. As this refrigerant flows through the refrigerant expansion valve, it expands to the lower pressure and a correspondingly lower temperature, which is confirmed by the sudden drop in the refrigerant temperature at the inlet of the evaporator. At this point, the evaporator coupling fluid pump is started and the flow rate adjusted using the metering needle valve. Additionally, the heaters providing the heating load to the evaporator are also turned on at a low duty to provide the required heating. When this evaporated refrigerant enters the absorber, the system is fully operational.

Next, the system is adjusted to achieve the desired conditions at the absorber. The frequency of the solution pump motor is gradually increased to increase the solution pump speed so that the concentrated solution flow rate matched the target flow rate. Simultaneously, the absorber coupling fluid inlet temperature is adjusted to match the target temperature. This adjustment is done by varying the chilled glycol/water coolant flow rate in the absorber plate heat exchanger. Varying the absorber coupling fluid inlet

temperature affects the absorber operating pressure, which in turn affects the solution flow rate supplied by the solution pump. Thus, the frequency of the solution pump motor is continuously adjusted during the startup phase to maintain a uniform solution flow rate. The dilute solution needle valve is also adjusted to maintain steady operation. If solution is found to be accumulating in the separator, the dilute solution valve is opened slowly to return solution to the absorber. Alternatively, if vapor is found to be entering the absorber from the dilute solution line, the dilute solution valve is slowly closed to force single-phase flow. It should be noted that closing the solution valve typically results in a rise in the absorber pressure, and vice versa. Thus, the solution pump speed is adjusted, as appropriate, to maintain steady flow rate.

Next, the steam pressure is gradually increased to increase desorber heating and the amount of vapor generated. As the steam pressure is increased, a higher amount of water vapor is also generated at the desorber. Thus, cooling at the rectifier is increased to maintain a high purity of refrigerant circulated through the system. This adjustment is done gradually so that the refrigerant flow rate matches the target flow rate. The evaporator and condenser coupling fluid inlet temperatures are adjusted to reach the target conditions and the flow rates adjusted so that an acceptable coupling fluid temperature glide is observed. It should be noted that any of the above changes results in a variation of both the high- and the low-side pressures. Thus, the absorber coupling fluid inlet temperature and the solution pump speed are adjusted as necessary to achieve and maintain target operating conditions. Additionally, the refrigerant needle valve is adjusted to ensure that only subcooled refrigerant exits the condenser. It should be noted that, in general, closing the refrigerant valve results in an increase in the high-side pressure and decrease in the low-side pressure, and vice versa. Therefore, any adjustment to this valve is accompanied by adjustment in the solution pump speed and absorber coupling fluid inlet temperature.

The above process is continued until the targeted operating conditions are achieved throughout the test facility. Traces of the different temperatures, pressures, and flow rates are monitored to confirm that the system has reached steady state. Upon confirmation of steady state, a preliminary data point is recorded, and the energy balances across each of the components of the system are verified. If the uncertainties in the energy balances at different components are within an acceptable range (± 15%), data are recorded over a five-minute duration at a scan rate of 1 reading averaged over 2 seconds. These measurements are then averaged to define one data point.

Sometimes, during system start up, the solution pump was observed to run dry, because the solution was trapped in the absorber. This was due to an unfavorable pressure difference between the absorber and the concentrated solution tank during start up. To equalize the pressures in the absorber and the solution tank, the valve on the 6.35 mm line (dashed line in Fig. 3.5) connecting the two components was opened. This equalizes the pressure on the low side and facilitates flow of solution from the absorber to the solution tank. Once the system is operational, the valve can be closed. Similarly, to equalize pressures in the evaporator and the concentrated solution tank, the corresponding pressure

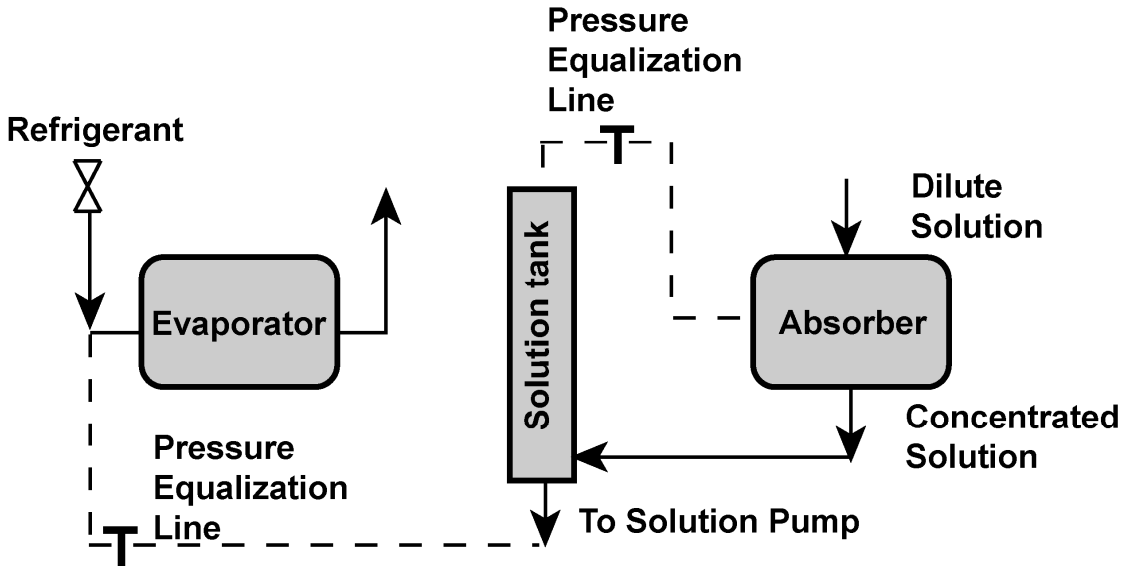

Fig. 3.5 Schematic of the pressure equalization lines

equalization line (dashed line in Fig. 3.5) was opened during start up and closed once the system was operational. The system was also found to be highly sensitive to any changes in the solution or refrigerant needle valves. Thus, the valves had to be opened or closed very slowly to ensure that the system does not destabilize. In general, if two-phase flow was observed in the dilute solution line or in the refrigerant line, the corresponding valves were closed slowly to achieve single-phase flow. However, if two-phase flow was observed in both lines, the dilute solution needle valve was closed first, followed by the refrigerant needle valve, to maintain stable operation.

3.6. Test matrix

Experiments were conducted at three nominal concentrated solution concentrations: 40, 48, and 55%. The absorber was operated at four nominal solution flow rates in the range 0.011-0.023 kg s^{-1}. Absorber coupling fluid temperatures between 20 and 40^{o}C were tested to represent a range of ambient conditions. The refrigerant fraction (ratio of the refrigerant to concentrated solution flow rate), which is representative of the cooling capacity of the system, was varied between 15 and 40%. The absorber coupling fluid flow rate was held constant at a nominal flow rate of 0.139 kg s^{-1}, which results in reasonable temperature glides that reduce error in the absorber duty measurement, as well as high coupling fluid heat transfer coefficients that reduce errors in measurement of the solution-side heat transfer coefficients. Table 3.4 shows a summary of the test matrix for this study. For each data point, the above described procedure was followed to achieve the desired steady state and record relevant data.

Data points corresponding to coupling fluid inlet temperatures ranging from 30-40^{o}C, and solution nominal concentration of 40 and 48%, represent heat pump operation in cooling mode. In this configuration, the absorber is rejecting heat to the ambient and the evaporator is cooling the conditioned space. Data points corresponding to coupling fluid inlet temperatures ranging from 20-30^{o}C, and nominal solution concentration of 48

and 55%, represent heat pump operation in heating mode. In this configuration, the absorber is heating the conditioned space, while the evaporator is gaining heat from the ambient. In each of these conditions, increasing solution and vapor flow rate represent increase in cooling/heating capacity. Details of the experiments conducted according to the above test matrix, and the modeling of the heat and mass transfer processes inside the absorber are discussed in the next chapter.

Table 3.1 Falling-film absorption test matrix

Coupling Fluid Inlet Temperature (°C)		Refrigerant Fraction (%)		Concentrated Solution Nominal Concentration											
				40%			48%				55%				
				Flow rate (kg s^{-1})			Flow rate (kg s^{-1})				Flow rate (kg s^{-1})				
				0.011	0.015	0.019	0.011	0.015	0.019	0.023	0.011	0.015	0.019	0.023
	20		25									×	×	×
			30								×	×	×	×
			35								×	×	×	×
			40								×	×	×	×
	25		25									×	×	×
			30								×	×	×	×
			35								×	×	×	×
			40								×	×	×	×
	30		15	×	×	×	×	×	×	×				
			20	×	×	×	×	×	×	×				
			25	×	×	×	×	×	×	×				
			30				×	×	×	×				
			35				×	×	×	×				
	35		15	×	×	×	×	×	×	×				
			20	×	×	×	×	×	×	×				
			25	×	×	×	×	×	×	×				
			30				×	×	×	×				
			35				×	×	×	×				
	40		15	×	×	×	×	×	×	×				
			20	×	×	×	×	×	×	×				
			25	×	×	×	×	×	×	×				
			30				×	×	×	×				
			35				×	×	×	×				

CHAPTER 4. FALLING-FILM ABSORPTION HEAT AND MASS TRANSFER ANALYSIS

As discussed in the previous chapter, pressure, temperature, and flow rate data were recorded for each test condition in the test matrix. These data are then analyzed to determine the thermodynamic state of the solution and the refrigerant at different locations in the loop, estimate component duties, and calculate heat and mass transfer rates in the absorber. This chapter starts with the description of the data reduction procedure, followed by estimation of the overall component duty, and analysis of segmental heat and mass transfer in the absorber. A representative data point with the nominal values: concentrated solution flow rate 0.0189 kg s^{-1}, refrigerant flow rate 0.0030 kg s^{-1}, concentrated solution concentration of 46.11%, and coupling fluid inlet temperature 29.6^{o}C, is chosen here to describe the analysis of the processes around the test loop and the absorber.

The thermodynamic properties of ammonia-water solution in the liquid and vapor phase were obtained from *Engineering Equation Solver* (EES) (Klein, 2011). Ammonia-water liquid phase transport properties (e.g. viscosity, conductivity, and surface tension) were estimated from curve fits of data provided by Herold *et al.* (1996). The ammonia-water liquid-phase binary diffusion coefficient was estimated using the correlation developed by Frank *et al.* (1996a). The *Chapman-Enskog Kinetic Theory* discussed in Mills (1995) was used to estimate the vapor-phase ammonia-water mixture transport properties. Additional details on the ammonia-water mixture properties are provided in Appendix A.

4.1. System level data analysis

The binary mixture of ammonia and water requires three independent properties to define its state at any location. Temperatures and pressures, which are measured at various locations around the test loop, serve as two of these three independent properties. The third property typically used for defining the state is quality or concentration. Direct measurement of ammonia-water vapor and liquid phase concentrations at multiple locations is not practical due to the difficulty in obtaining samples from a small capacity sealed system, and is associated with a high level of uncertainty. Thus, appropriate assumptions about the expected quality (e.g. saturated liquid or saturated vapor) at certain locations or other suitable equilibrium criteria around the test loop were made for the third property to define the state of the mixture. Mass and species balances are conducted in the remainder of the test loop to define the state at locations where such assumptions of quality cannot be made. Other thermodynamic properties such as enthalpy and specific volume, and overall component heat duties can be estimated once the state of the mixture is completely defined. A step-by-step procedure for such analyses was previously discussed by Lee *et al.* (2008a), and is described below for the present set of experiments.

All measurements are assumed to be uncorrelated and random, the propagated uncertainty in calculated values was estimated using the method of Taylor and Kuyatt (1993), using an uncertainty propagation tool, built into the *Engineering Equation Solver* software (Klein, 2011). Additional details on the uncertainty analysis are provided in Appendix B. In the following sections, the uncertainty associated with each calculation is reported, along with the corresponding value for the representative test condition.

Fig. 4.1 shows a schematic of the rectifier. The concentration of the refrigerant circulating through the loop was determined by assuming that the refrigerant vapor exits the rectifier as a saturated vapor (quality $q = 1$) at the measured outlet temperature and pressure. (The condenser inlet pressure was used as the rectifier outlet pressure, because there was no local pressure measurement at the rectifier vapor outlet.) The resulting

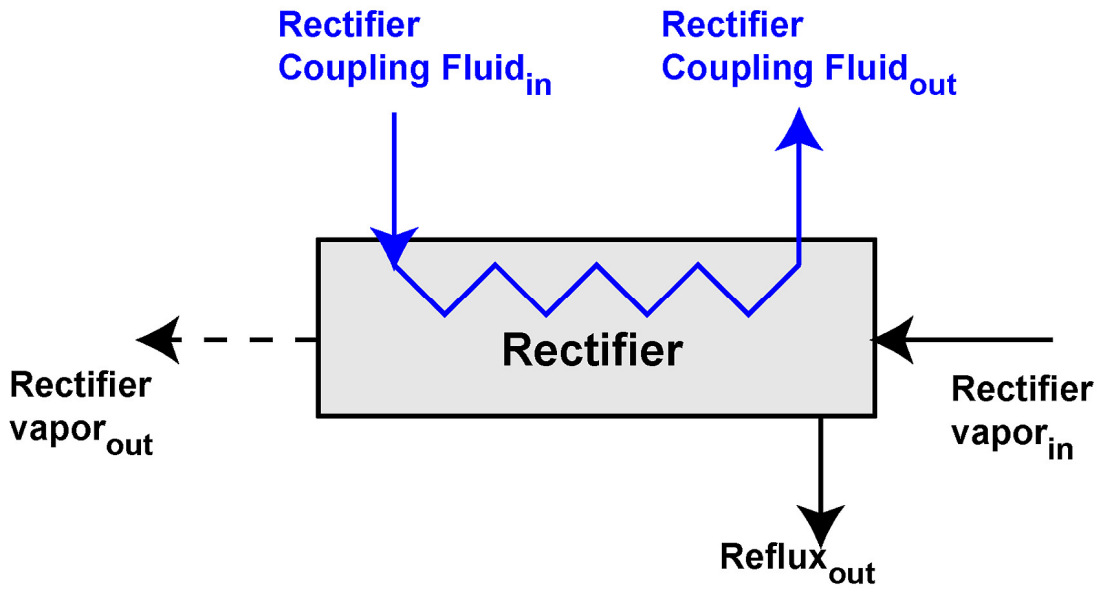

Fig. 4.1 Schematic of the rectifier

refrigerant concentration applies for the condenser, evaporator, refrigerant pre-cooler, and the absorber vapor inlet.

$$x_{\text{Rect,vap,out}} = f\left(T_{\text{Rect,vap,out}}, P_{\text{Cond,in}}, q=1\right) \tag{4.1}$$

$$x_{\text{Rect,vap,out}} = x_{\text{Ref}} = f\left(61.53\pm0.25\,^{\circ}\text{C}, 1093\pm1.5\text{kPa}, q=1\right) = 0.9937\pm0.00012 \tag{4.2}$$

The rectifier reflux concentration was estimated by assuming that the solution exits the rectifier as a saturated liquid, at the measured outlet temperature and pressure.

$$x_{\text{Reflux}} = f\left(T_{\text{Reflux}}, P_{\text{Reflux}}, q=0\right) \tag{4.3}$$

$$x_{\text{Reflux}} = f\left(37.73\pm0.25\,^{\circ}\text{C}, 1109\pm5\,\text{kPa}, q=0\right) = 0.7647\pm0.00471 \tag{4.4}$$

Fig. 4.2 shows a schematic of the separator. The concentration of the solution exiting the separator was determined by assuming that it exits the component as a saturated liquid at the measured temperature and pressure.

$$x_{\text{Sep,sol,out}} = f\left(T_{\text{Sep,sol,out}}, P_{\text{Sep,sol,out}}, q=0\right) \tag{4.5}$$

$$x_{\text{Sep,sol,out}} = f\left(98.59\pm0.25\,^{\circ}\text{C}, 1118\pm5\,\text{kPa}, q=0\right) = 0.3435\pm0.001237 \tag{4.6}$$

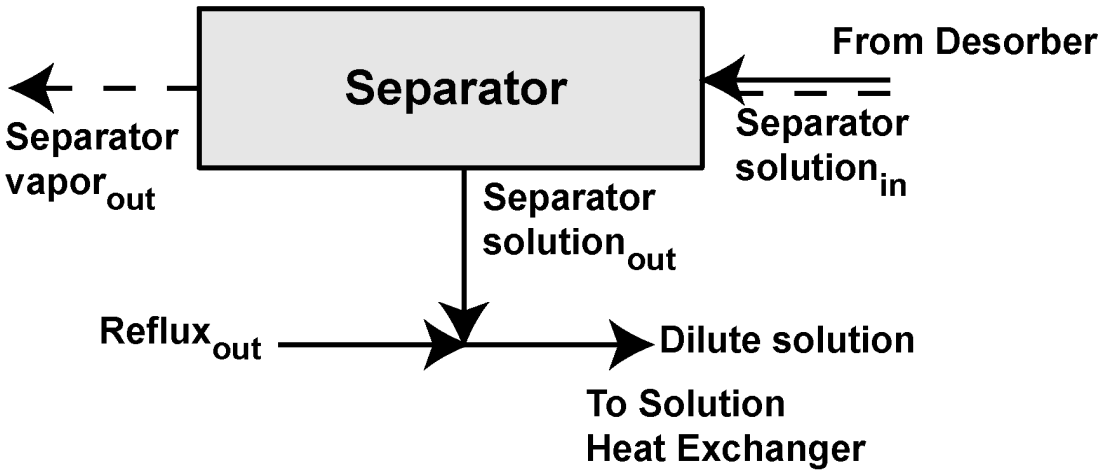

Fig. 4.2 Schematic of the separator

Similarly, the concentration of the vapor exiting the separator was determined by assuming it exits the component as a saturated vapor at the measured temperature and pressure.

$$x_{\text{Sep,vap,out}} = f\left(T_{\text{Sep,vap,out}}, P_{\text{Sep,vap,out}}, q=1\right) \tag{4.7}$$

$$x_{\text{Sep,vap,out}} = f\left(100.9\pm0.25\,^{\circ}\text{C}, 1118\pm5\,\text{kPa}, q=1\right) = 0.9370\pm0.00076 \tag{4.8}$$

It should be noted that the mass flow rate and concentration of the vapor entering the rectifier are equal to the mass flow rate and concentration of the vapor exiting the separator, respectively.

$$\dot{m}_{\text{Rect,vap,in}} = \dot{m}_{\text{Sep,vap,out}} \tag{4.9}$$

$$x_{\text{Rect,vap,in}} = x_{\text{Sep,vap,out}} = 0.9370\pm0.00076 \tag{4.10}$$

The mass flow rate of the vapor exiting the separator and entering the rectifier is determined next. The mass flow rate of the refrigerant vapor exiting the rectifier is equal to the mass flow rate of the subcooled refrigerant exiting the condenser, and is measured by the refrigerant flow meter ($\dot{m}_{\text{Rect,vap,out}} = \dot{m}_{\text{Ref}} = 0.0030\pm0.000003$ kg s^{-1}). A mass and species balance was conducted across the rectifier (Fig. 4.1) to estimate the mass flow rate of the vapor entering the rectifier and the reflux exiting the rectifier.

$$\dot{m}_{\text{Rect,vap,in}} = \dot{m}_{\text{Rect,vap,out}} + \dot{m}_{\text{Reflux}} \tag{4.11}$$

$$\dot{m}_{\text{Rect,vap,in}} = 0.0030 \pm 0.000003\,\text{kg s}^{-1} + \dot{m}_{\text{Reflux}} \tag{4.12}$$

$$\dot{m}_{\text{Reflux}} \cdot x_{\text{Reflux}} = \dot{m}_{\text{Rect,vap,in}} \cdot x_{\text{Rect,vap,in}} - \dot{m}_{\text{Rect,vap,out}} \cdot x_{\text{Rect,vap,out}} \tag{4.13}$$

$$\begin{aligned} \dot{m}_{\text{Reflux}} \cdot 0.7647 \pm 0.00471 = \dot{m}_{\text{Rect,vap,in}} \cdot 0.9370 \pm 0.00076 \\ - 0.0030 \pm 0.000003\,\text{kg s}^{-1} \cdot 0.9937 \pm 0.00012 \end{aligned} \tag{4.14}$$

$$\dot{m}_{\text{Rect,vap,in}} = 0.0040 \pm 0.000033\text{kg s}^{-1} \tag{4.15}$$

$$\dot{m}_{\text{Reflux}} = 0.0010 \pm 0.000033\text{kg s}^{-1} \tag{4.16}$$

The dilute solution circulated through the loop is a mixture of the rectifier reflux and the solution exiting the separator (Fig. 4.2). Thus, mass and species balances were applied at this location to determine the mass flow rate of the solution exiting the separator and the concentration of the dilute solution stream. The mass flow rate of the dilute solution is measured downstream of the solution heat exchanger by the dilute solution flow meter ($\dot{m}_{\text{Dil}} = 0.0154 \pm 0.0000154$ kg s^{-1}).

$$\dot{m}_{\text{Sep,sol,out}} = \dot{m}_{\text{Dil}} - \dot{m}_{\text{Reflux}} \tag{4.17}$$

$$\begin{aligned} \dot{m}_{\text{Sep,sol,out}} &= 0.0154 \pm 0.000015\,\text{kg s}^{-1} - 0.0010 \pm 0.000032\,\text{kg s}^{-1} \\ &= 0.0145 \pm 0.000036\,\text{kg s}^{-1} \end{aligned} \tag{4.18}$$

$$\dot{m}_{\text{Dil}} \cdot x_{\text{Dil}} = \dot{m}_{\text{Sep,sol,out}} \cdot x_{\text{Sep,sol,out}} + \dot{m}_{\text{Reflux}} \cdot x_{\text{Reflux}} \tag{4.19}$$

$$\begin{aligned} 0.0154 \pm 0.000015\,\text{kg s}^{-1} \cdot x_{\text{Dil}} = 0.0145 \pm 0.000036\,\text{kg s}^{-1} \cdot 0.3435 \pm 0.001237 \\ + 0.0010 \pm 0.000033\,\text{kg s}^{-1} \cdot 0.7647 \pm 0.00471 \end{aligned} \tag{4.20}$$

$$x_{\text{Dil}} = 0.3705 \pm 0.0016 \tag{4.21}$$

The concentration of the concentrated solution is the last remaining unknown. It was estimated using a species balance at the separator (Fig. 4.2). It should be noted that the total mass flow rate and concentration of the two-phase solution entering the separator is equal to the mass flow rate and bulk concentration of the concentrated solution circulated through the loop, because the desorber operates in co-current

configuration. The mass flow rate of the concentrated solution is measured downstream of the solution pump by the concentrated solution flow meter ($\dot{m}_{Conc} = \dot{m}_{Sep,sol,in} = 0.0189 \pm 0.000019$ kg s^{-1}).

$$\dot{m}_{Sep,sol,in} \cdot x_{Sep,sol,in} = \dot{m}_{Sep,sol,out} \cdot x_{Sep,sol,out} + \dot{m}_{Sep,vap,out} \cdot x_{Sep,vap,out} \tag{4.22}$$

$$\begin{aligned} 0.0189 \pm 0.000019\,\mathrm{kg\,s^{-1}} \cdot x_{Sep,sol,in} = \\ 0.0145 \pm 0.000036\,\mathrm{kg\,s^{-1}} \cdot 0.3435 \pm 0.001237 \\ + 0.0040 \pm 0.000032 \cdot 0.9370 \pm 0.00076 \end{aligned} \tag{4.23}$$

$$x_{Sep,sol,in} = x_{Conc} = 0.4611 \pm 0.00143 \tag{4.24}$$

Thus, the concentrations of the refrigerant, and dilute and concentrated solutions circulating through the loop were determined. These concentrations can be used as the third independent property in determining the state of the refrigerant and the solution circulating through the other system components.

4.1.1. Concentration range

Table 4.1 shows a summary of the ranges of calculated concentrations for the dilute and concentrated solution and refrigerant streams in this study. It should be noted for each nominal concentrated solution test condition, the system was charged with an appropriate mixture of ammonia and water in the concentrated solution tank. As solution is circulated through the loop, the resulting concentrations of the refrigerant, dilute, and concentrated solution streams depend upon the amount of heat supplied at the desorber and heat rejected at the rectifier. Thus, there is some deviation between the nominal charged concentration and the actual measured concentrations of the concentrated solution stream (a similar spread is expected during operation of a real system.)

It can also be seen that as the nominal solution concentration increases, the refrigerant concentration increases. At higher solution concentrations, the amount of water desorbed at the desorber is lower, resulting in the generation of vapor with a higher fraction of ammonia. Subsequent rectification in the rectifier results in a high purity

Table 4.1 Summary of range of concentrations investigated

	Concentrated solution nominal flow rate			
	0.011	**0.015**	**0.019**	**0.023**
	Concentrated solution nominal concentration: 40%			
x_{Conc} (%)	38.15 - 46.12	37.28 - 42.3	36.75 - 40.21	
x_{Dil} (%)	27.59 - 32.63	24.63 - 29.48	23.45 - 27.39	
x_{Ref} (%)	94.79 - 98.71	92.63 - 98.46	90.37 - 97.88	
	Concentrated solution nominal concentration: 48%			
x_{Conc} (%)	44-74 - 51.73	44.94 - 51.73	45.72 - 50.01	45.91 - 48.03
x_{Dil} (%)	29.09 - 38.9	29.25 - 37.41	26.96 - 37.35	28.68 - 36.35
x_{Ref} (%)	95.54 - 99.54	94.88 - 99.51	94.89 - 99.39	95.97 - 99.32
	Concentrated solution nominal concentration: 55%			
x_{Conc} (%)	52.86 - 56.86	53.36 - 58.22	53.30 - 57.39	52.89 - 55.88
x_{Dil} (%)	32.34 - 37.27	33.04 - 38.48	31.49 - 39.21	31.01 - 38.25
x_{Ref} (%)	97.86 - 99.38	97.71 - 99.47	97.00 - 99.58	96.92 - 99.27

refrigerant circulated through the loop. As the desorber duty is increased, a greater amount of vapor is generated, and the resulting dilute solution is of a lower concentration. Thus, a wide spread is observed in the dilute solution concentration, with the higher concentrations observed at the lower refrigerant fractions, and the lower concentrations observed at the higher refrigerant fractions.

4.2. Absorber analysis

With the state of the solution/refrigerant known at every location in the loop, the individual heat exchanger duties can be estimated from energy balances using the known mass flow rates and specific enthalpies at the inlets and outlets of each component. For the hydronically coupled components, i.e., the evaporator, the condenser, and the absorber, component duties can also be estimated from an energy balance on the coupling fluid side, using the measured coupling fluid flow rate, and inlet and outlet temperatures. For each test condition in the test matrix, energy balances were established not just at the absorber, but for all components in the test loop. This is important because the flow rates and concentrations at the absorber depend on system-wide state points, as can be seen from the above system level analysis. The following section discusses the procedure

adopted to estimate the overall absorber duty. A similar analysis was conducted for other components around the test loop. This is followed by the discussion of analyses conducted to estimate the overall and solution-side heat transfer coefficients.

4.2.1. Absorber heat duty calculations

Fig. 4.3 shows a schematic of the absorber. The enthalpy of the dilute solution and refrigerant entering the absorber, and the concentrated solution exiting the absorber were determined using the locally measured temperature, pressure, and the concentrations estimated as described above.

$$h_{\text{Abs,sol,in}} = f\left(T_{\text{Abs,sol,in}}, P_{\text{Abs,sol,in}}, x_{\text{Abs,sol,in}}\right) \tag{4.25}$$

$$\begin{aligned} h_{\text{Abs,sol,in}} &= f\left(61.5 \pm 0.25\,^{\circ}\text{C}, 537.3 \pm 1.5\,\text{kPa}, 0.3705 \pm 0.0016\right) \\ &= 51.46 \pm 1.18\,\text{kJ kg}^{-1} \end{aligned} \tag{4.26}$$

$$h_{\text{Abs,vap,in}} = f\left(T_{\text{Abs,vap,in}}, P_{\text{Abs,vap,in}}, x_{\text{Abs,vap,in}}\right) \tag{4.27}$$

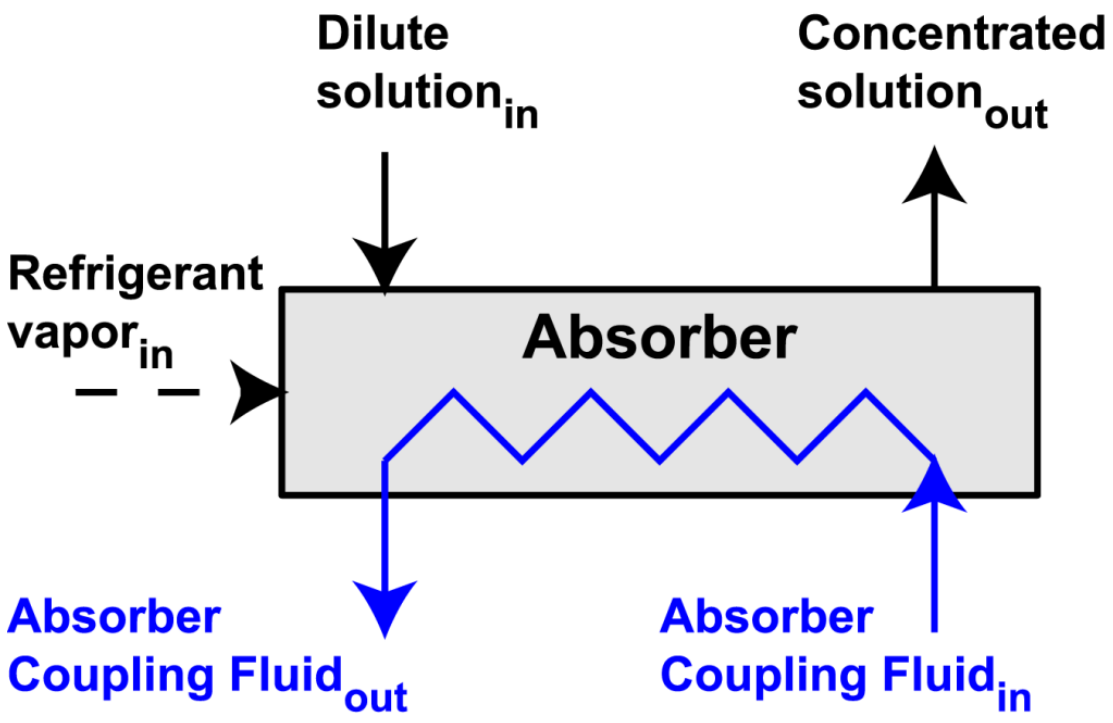

Fig. 4.3 Schematic of the absorber

$$h_{\text{Abs,vap,in}} = f\left(8.12 \pm 0.25\,^{\circ}\text{C}, 540.5 \pm 1.5\,\text{kPa}, 0.9937 \pm 0.00012\right) = 1164 \pm 17.31\,\text{kJ kg}^{-1} \tag{4.28}$$

$$h_{\text{Abs,sol,out}} = f\left(T_{\text{Abs,sol,out}}, P_{\text{Abs,sol,out}}, x_{\text{Abs,sol,out}}\right) \tag{4.29}$$

$$h_{\text{Abs,sol,out}} = f\left(37.84 \pm 0.25\,^{\circ}\text{C}, 534.1 \pm 2.6\,\text{kPa}, 0.4611 \pm 0.00142\right) = -69.11 \pm 1.12\,\text{kJ kg}^{-1} \tag{4.30}$$

With these enthalpies known, the absorber duty on the solution side was estimated as follows:

$$Q_{\text{Abs,sol}} = \dot{m}_{\text{Abs,sol,in}} \cdot h_{\text{Abs,sol,in}} + \dot{m}_{\text{Abs,vap,in}} \cdot h_{\text{Abs,vap,in}} - \dot{m}_{\text{Abs,sol,out}} \cdot h_{\text{Abs,sol,out}} \tag{4.31}$$

$$\begin{aligned} Q_{\text{Abs,sol}} &= 0.0154 \pm 0.000015\,\text{kg s}^{-1} \cdot 51.46 \pm 1.18\,\text{kJ kg}^{-1} \\ &\quad + 0.0030 \pm 0.000003\,\text{kg s}^{-1} \cdot 1164 \pm 17.31\,\text{kJ kg}^{-1} \\ &\quad - 0.0189 \pm 0.000019\,\text{kg s}^{-1} \cdot -69.11 \pm 1.12\,\text{kJ kg}^{-1} \\ &= 5.605 \pm 0.059\,\text{kW} \end{aligned} \tag{4.32}$$

The flow rate of the coupling fluid (distilled water) circulated through the absorber was measured by the absorber coupling fluid flow meter ($\dot{m}_{\text{Abs,CF}}$ = 0.1375±0.00068 kg s^{-1}). The absorber duty on the coupling fluid side was calculated using this flow rate, the average specific heat, and the measured inlet and outlet temperatures.

$$Cp_{\text{Abs,CF}} = f\left(T_{\text{Abs,CF,avg}}, P_{\text{Abs,CF,avg}}\right) \tag{4.33}$$

$$Cp_{\text{Abs,CF}} = f\left(34.22\,^{\circ}\text{C},\ 178\,\text{kPa}\right) = 4.18\,\text{kJ kg}^{-1}\,\text{K}^{-1} \tag{4.34}$$

$$Q_{\text{Abs,CF}} = m_{\text{Abs,CF}} \cdot Cp_{\text{Abs,CF}} \cdot \left(T_{\text{Abs,CF,out}} - T_{\text{Abs,CF,in}}\right) \tag{4.35}$$

$$\begin{aligned} Q_{\text{Abs,CF}} &= 0.1375 \pm 0.00068\,\text{kg s}^{-1} \cdot 4.18\,\text{kJ kg}^{-1}\,\text{K}^{-1} \\ &\quad \cdot \left(38.87 \pm 0.25\,^{\circ}\text{C} - 29.56 \pm 0.25\,^{\circ}\text{C}\right) = 5.349 \pm 0.205\,\text{kW} \end{aligned} \tag{4.36}$$

The average absorber duty for this representative case was calculated as follows:

$$Q_{\text{Abs,avg}} = \left(\frac{Q_{\text{Abs,sol}} + Q_{\text{Abs,CF}}}{2}\right) = 5.477 \pm 0.107\,\text{kW} \tag{4.37}$$

The difference between the two heat duties was calculated as follows:

$$\%\Delta Q_{\text{Abs}} = \left(\frac{Q_{\text{Abs,avg}} - Q_{\text{Abs,CF}}}{Q_{\text{Abs,avg}}} \right) \cdot 100\% = 2.34\% \tag{4.38}$$

In the entire data set of 103 points, 39 points showed energy balances within 0-5%, 61 points within 5-10%, and 3 points withing10-15%, for an average deviation of 5.85%. Similar analyses were conducted to estimate the evaporator and the condenser duties. A summary of energy balances for these three components is shown in Table 4.2.

4.2.2. Absorber segmental analysis

Fig. 4.4 shows a schematic of the different regions in the absorber (drip tray, tube array, and solution pool) and the locations of the various temperature and pressure measurements. Concentrated solution from the tube array accumulates in a pool below the tube array at the bottom of the absorber shell before flowing to the solution pump. As previously discussed, the absorber coupling fluid temperature is measured at an intermediate location inside the absorber. This intermediate temperature measurement allows the heat duty to be calculated for the top and bottom segments of the absorber. It should be noted that both these segments have the same total transfer area. Dilute solution entering the absorber is typically subcooled as it exchanges heat with concentrated solution in the solution heat exchanger. Inside the absorber, the solution bulk remains subcooled as it flows over the tube array, absorbing the refrigerant vapor. This is confirmed by the temperature measurements obtained along the tube array, which

Table 4.2 Summary of energy balances on the absorber, condenser, and evaporator

Component	Number of data points within			Average absolute deviation (%)
	±(0-5)%	±(5-10)%	±(10-15)%	
Absorber	39	61	3	5.85
Condenser	3	80	20	8.20
Evaporator	18	17	68	10.10

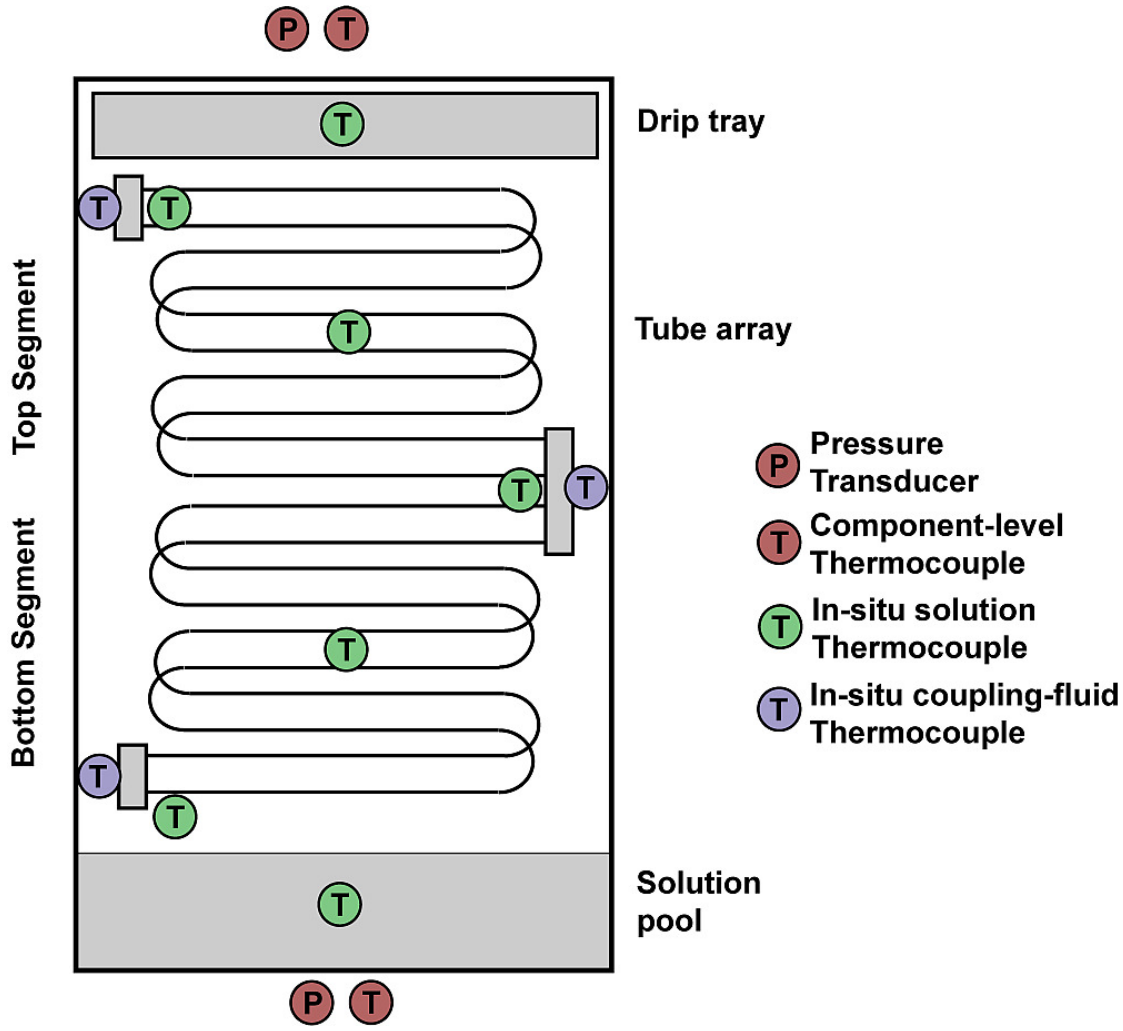

Fig. 4.4 Schematic of microchannel falling-film absorber assembly

indicate a degree of subcooling ranging between 5-20^{o}C. A similar observation was made by Lee *et al.* (2008a), who also conducted experiments under realistic operating conditions. Chen and Christensen (2000) previously observed that the absorption process can be decomposed into two basic processes: absorption due to subcooling of liquid solution in the absence of external cooling, and absorption into saturated solution cooled externally at the wall. In the following sections, a heat and mass transfer model that accounts for both of these effects is discussed.

It should also be noted that as solution flows over the tube banks, the installed thermocouples can sometimes measure the temperature of the vapor stream flowing

upward, as opposed to the solution flowing downward. Thus, these temperature measurements are only used as a guide to monitor the progression of the absorption process, and not actually used in the absorber heat and mass transfer analysis. The thermodynamic state and mass flow rate of the concentrated solution leaving, and the refrigerant vapor entering the bottom segment of the absorber are known from direct measurements. The state of the dilute solution flowing from the top segment to the bottom segment, and the vapor flowing from the bottom segment to the top segment of the absorber cannot be explicitly measured as the local temperature measurements are only used as guide. The state of the solution and vapor at intermediate locations in the absorber, as well as the heat and mass transfer rates, are therefore determined by conducting a segmental heat and mass transfer analysis on the absorber.

The heat and mass transfer model is based on an earlier model developed by Garimella (1999) for analysis of similar geometries. The basic approach was documented by Price and Bell (1974), who in turn used the technique developed by Colburn and Drew (1937), for the condensation of a binary vapor with a miscible condensate. Other investigators (Kang and Christensen, 1994, 1995; Kang *et al.*, 1997; Goel and Goswami, 2005) have also adopted a similar technique for the design of ammonia-water absorbers, as mentioned in Chapter 2.

Refrigerant inlet

The refrigerant flowing through the condenser and the evaporator is a non-azeotropic mixture of mostly ammonia and a small amount of water. This results in a temperature glide during evaporation. The refrigerant exiting the evaporator is still in two-phase, as some amount of refrigerant is not evaporated due to the temperature glide. This is particularly true for the off-design cases where relatively impure refrigerant enters the refrigerant circuit, resulting in large glides in the evaporator. When this two-phase refrigerant enters the bottom of the absorber, the liquid phase mixes with the solution

pool at the bottom, while the vapor phase moves upwards and is absorbed into the dilute solution flowing down the tube array. Fig. 4.5 shows a schematic of these interactions near the solution pool. The liquid and vapor phases of the two-phase refrigerant entering the absorber are expected to be in equilibrium with each other. Thus, the concentration of the liquid and vapor phases can be determined as follows:

$$x_{\text{Abs,ref,l,in}} = f\left(P_{\text{abs}}, T_{\text{Abs,ref,in}}, q_{\text{Abs,ref,l,in}} = 0\right) \tag{4.39}$$

$$x_{\text{Abs,ref,l,in}} = f\left(537.3 \pm 1.5\,\text{kPa}, 8.12 \pm 0.25\,^{\circ}\text{C}, 0\right) = 0.9235 \pm 0.01017 \tag{4.40}$$

$$x_{\text{Abs,ref,v,in}} = f\left(P_{\text{abs}}, T_{\text{Abs,ref,v,in}}, q_{\text{Abs,ref,v,in}} = 1\right) \tag{4.41}$$

$$x_{\text{Abs,ref,v,in}} = f\left(537.3 \pm 1.5\,\text{kPa}, 8.12 \pm 0.25\,^{\circ}\text{C}, 1\right) = 0.9999 \pm 0.000004 \tag{4.42}$$

The absorber pressure, P_{abs}, is the average of the pressure measured at the dilute solution and vapor inlet, and the solution outlet of the absorber. The mass flow rates of

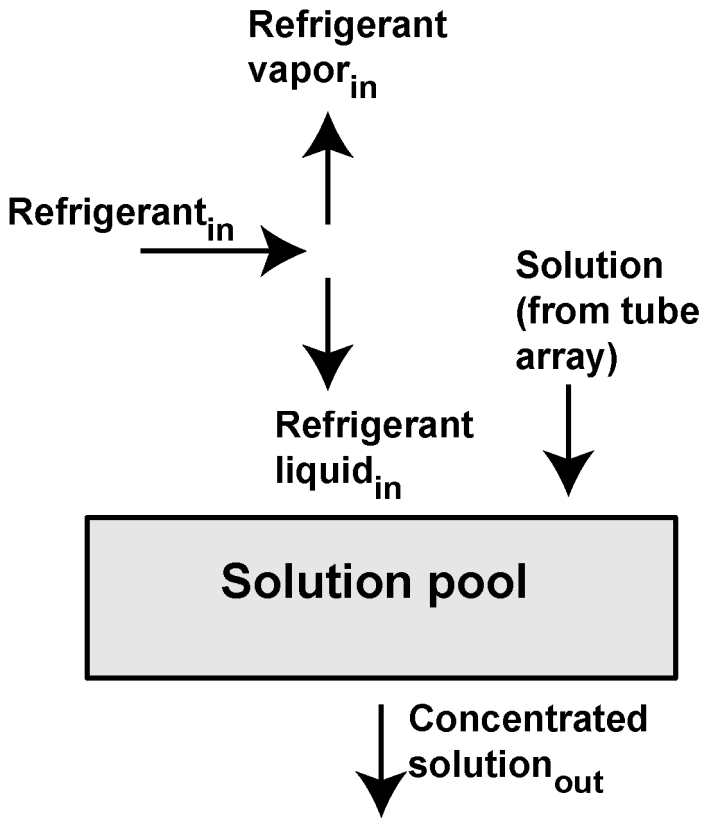

Fig. 4.5 Schematic of absorber solution pool

the individual phases were determined using mass and species balance equations.

$$\dot{m}_{\text{Abs,ref,v,in}} = \dot{m}_{\text{Abs,ref,in}} - \dot{m}_{\text{Abs,ref,l,in}} \tag{4.43}$$

$$\dot{m}_{\text{Abs,ref,v,in}} = 0.0030 \pm 0.000003\,\text{kg s}^{-1} - \dot{m}_{\text{Abs,ref,l,in}} \tag{4.44}$$

$$\dot{m}_{\text{Abs,ref,v,in}} \cdot x_{\text{Abs,ref,v,in}} = \dot{m}_{\text{Abs,ref,in}} \cdot x_{\text{Abs,ref,in}} - \dot{m}_{\text{Abs,ref,l,in}} \cdot x_{\text{Abs,ref,l,in}} \tag{4.45}$$

$$\begin{aligned} \dot{m}_{\text{Abs,ref,v,in}} \cdot 0.9999 \pm 0.000004 = {} & 0.0030 \pm 0.000003\,\text{kg s}^{-1} \cdot 0.9937 \pm 0.00012 \\ & - \dot{m}_{\text{Abs,ref,l,in}} \cdot 0.9235 \pm 0.01017 \end{aligned} \tag{4.46}$$

$$\dot{m}_{\text{Abs,ref,v,in}} = 0.0028 \pm 0.00003\,\text{kg s}^{-1} \tag{4.47}$$

$$\dot{m}_{\text{Abs,ref,l,in}} = 0.0002 \pm 0.00003\,\text{kg s}^{-1} \tag{4.48}$$

A similar mass and species balance was applied to determine the mass flow rate and state of the solution leaving the tube array.

$$\dot{m}_{\text{TA,sol,out}} = \dot{m}_{\text{Abs,sol,out}} - \dot{m}_{\text{Abs,ref,l,in}} \tag{4.49}$$

$$\begin{aligned} \dot{m}_{\text{TA,sol,out}} &= 0.0189 \pm 0.00002\,\text{kg s}^{-1} - 0.0002 \pm 0.00003\,\text{kg s}^{-1} \\ &= 0.0187 \pm 0.00004\,\text{kg s}^{-1} \end{aligned} \tag{4.50}$$

$$\dot{m}_{\text{TA,sol,out}} \cdot x_{\text{TA,sol,out}} = \dot{m}_{\text{Abs,sol,out}} \cdot x_{\text{Abs,sol,out}} - \dot{m}_{\text{Abs,ref,l,in}} \cdot x_{\text{Abs,ref,l,in}} \tag{4.51}$$

$$x_{\text{TA,sol,out}} = \left(\frac{\begin{array}{l} 0.0189 \pm 0.00002\,\text{kg s}^{-1} \cdot 0.4611 \pm 0.00141 \\ -0.0002 \pm 0.00003\,\text{kg s}^{-1} \cdot 0.9235 \pm 0.01017 \end{array}}{0.0187 \pm 0.00004\,\text{kg s}^{-1}} \right) = 0.4550 \pm 0.00177 \tag{4.52}$$

The state and flow rate of the solution leaving and vapor entering the tube array calculated here are used as inputs to the heat and mass transfer analysis of the two segments of the tube array, which is discussed next.

Regions of absorption

The absorption process can be described as the progression of ammonia and water from the vapor bulk to the vapor-liquid interface, and finally into the liquid film. As these species move, they pass through several regions of absorption shown schematically in

Fig. 4.6. As the name suggests, the "vapor bulk" is a region representative of the bulk of the vapor. In this region, the vapor exists at nearly uniform temperature and concentration, and in a segment is typically considered to be the average of the inlet and outlet conditions. Ammonia and water fractions that undergo absorption travel to the vapor-liquid interface from the vapor bulk through a very thin region adjacent to the interface, called the "vapor film" region. It is assumed that all the resistance to heat and mass transfer in the vapor phase lies in this thin film (or boundary layer), and as a result, the vapor temperature and concentration undergo a change from the bulk value to interface value through this region. The heat and mass transfer processes are strongly

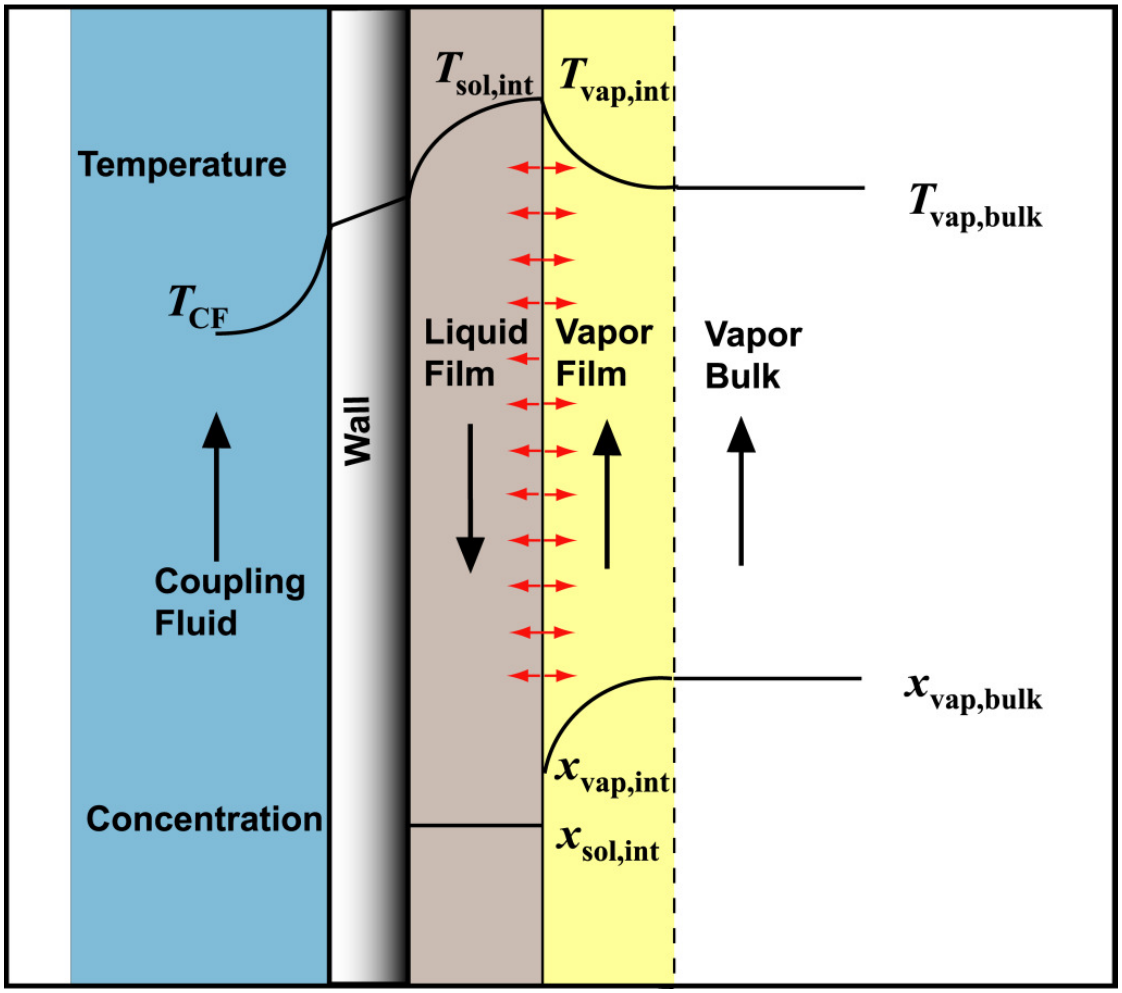

Fig. 4.6 Schematic of the regions of absorption

coupled in this region, as will be discussed later. Latent heat of absorption is released at the interface as the ammonia and water fractions undergo phase change from vapor to liquid. This heat can propagate through the liquid film, through the wall and eventually to the coupling fluid, or propagate back into the vapor bulk depending upon the local temperature gradients. A temperature gradient in the liquid film facilitates transfer of heat from the interface to the wall.

At any location, the vapor and solution are assumed to be in equilibrium with each other only at the interface, while non-equilibrium conditions exist in the respective bulk regions. To estimate the absorption rates in a segment, the solution and vapor bulk and interface conditions were first determined. These conditions were then used to determine the mass transfer rate of individual components in the vapor phase. Using these mass transfer rates, the overall absorption rates, heat transfer into the coupling fluid, and sensible cooling/heating of the solution and vapor bulk in a segment were determined. The equations presented in the following sections are strongly coupled and cannot be solved explicitly. Thus, an iterative procedure is used. However, for ease of understanding, the calculated values for the representative data point are shown when the corresponding equation is introduced. The sample calculations reported in the following sections correspond to the bottom segment of the absorber.

Solution and vapor, bulk and interface conditions

The average solution conditions in a segment were calculated using a simple arithmetic mean of the inlet and the outlet conditions.

$$x_{\text{sol,avg}} = \left(\frac{x_{\text{sol,in}} + x_{\text{sol,out}}}{2} \right) \tag{4.53}$$

$$x_{\text{sol,avg}} = \left(\frac{0.3935 + 0.4550}{2} \right) = 0.4243 \pm 0.00249 \tag{4.54}$$

$$T_{\text{sol,avg}} = \left(\frac{T_{\text{sol,in}} + T_{\text{sol,out}}}{2} \right) \tag{4.55}$$

$$T_{\text{sol,avg}} = \left(\frac{53.20^{\circ}\text{C} + 37.57^{\circ}\text{C}}{2} \right) = 45.39 \pm 0.40^{\circ}\text{C} \tag{4.56}$$

The solution inlet conditions are not explicitly known at this point and are calculated later in the model. The solution flows as a film around the horizontal tubes, and flows from one tube row to another as droplets. Details of these flow mechanisms are discussed later. Very thin films are formed on the microchannel tubes, because the total solution flow is distributed over several tubes. In addition, due to the detachment of the droplets from the previous row and impact on the subsequent row, there is intense mixing in the film. Thus, the liquid film is assumed to be well mixed, which is justified by the expected flow mechanisms (Garimella, 1999; Meacham and Garimella, 2004). A similar assumption was made by several other authors for falling-film absorption (Price and Bell, 1974; Kang and Christensen, 1994, 1995; Kang *et al.*, 1997). Thus, the concentration of the solution at the interface was assumed to be equal to the solution bulk concentration.

$$x_{\text{sol,int}} = x_{\text{sol,avg}} = 0.4243 \pm 0.00249 \tag{4.57}$$

The solution at the interface was assumed to be in equilibrium with the adjacent vapor. Thus, the interface temperature was estimated by assuming that the solution is at saturation conditions.

$$T_{\text{sol,int}} = f\left(P_{\text{abs}}, x_{\text{sol,int}}, q_{\text{sol,int}} = 0\right) \tag{4.58}$$

$$T_{\text{sol,int}} = f\left(537.3 \pm 1.5\,\text{kPa}, 0.4243 \pm 0.00249, 0\right) = 54.8 \pm 0.47^{\circ}\text{C} \tag{4.59}$$

Refrigerant vapor enters the tube array at the bottom and flows upward counter-current to the falling solution. The vapor bulk conditions for a segment were assumed to be at the average of the inlet and outlet conditions.

$$x_{\text{vap,bulk}} = \left(\frac{x_{\text{vap,in}} + x_{\text{vap,out}}}{2} \right) \tag{4.60}$$

$$x_{\text{vap,bulk}} = \left(\frac{0.9999 + 0.9835}{2} \right) = 0.9917 \pm 0.00091 \tag{4.61}$$

$$T_{\text{vap,bulk}} = \left(\frac{T_{\text{vap,in}} + T_{\text{vap,out}}}{2} \right) \tag{4.62}$$

$$T_{\text{vap,bulk}} = \left(\frac{8.12\,^{\circ}\text{C} + 68.17\,^{\circ}\text{C}}{2} \right) = 38.15 \pm 2.45\,^{\circ}\text{C} \tag{4.63}$$

$$\dot{m}_{\text{vap,bulk}} = \left(\frac{\dot{m}_{\text{vap,in}} + \dot{m}_{\text{vap,out}}}{2} \right) \tag{4.64}$$

$$\dot{m}_{\text{vap,bulk}} = \left(\frac{0.0028\,\text{kg s}^{-1} + 0.0009\,\text{kg s}^{-1}}{2} \right) = 0.0018 \pm 0.00006\,\text{kg s}^{-1} \tag{4.65}$$

As noted above, the vapor outlet conditions are not known explicitly at this point in the analysis and the relevant values are shown below the equations for illustrative purposes.

Based on the equilibrium assumption above, the temperature of the vapor at the interface is equal to the temperature of the solution at the interface.

$$T_{\text{vap,int}} = T_{\text{sol,int}} = 54.80 \pm 0.47\,^{\circ}\text{C} \tag{4.66}$$

Also, the interface concentration is obtained assuming that the vapor is at saturation conditions.

$$x_{\text{vap,int}} = f\left(P_{\text{abs}}, T_{\text{vap,int}}, q_{\text{vap,int}} = 1\right) \tag{4.67}$$

$$x_{\text{vap,int}} = f\left(537.3\,\text{kPa}, 54.80\,^{\circ}\text{C}, 1\right) = 0.9872 \pm 0.00041 \tag{4.68}$$

A summary of the inlet, outlet, bulk, and interface conditions for the representative test condition are shown schematically in Fig. 4.7.

Vapor mass transfer

The transport of species to the interface is due to a combination of convection and diffusion, governed by the convective mass transfer coefficient in the vapor phase, and

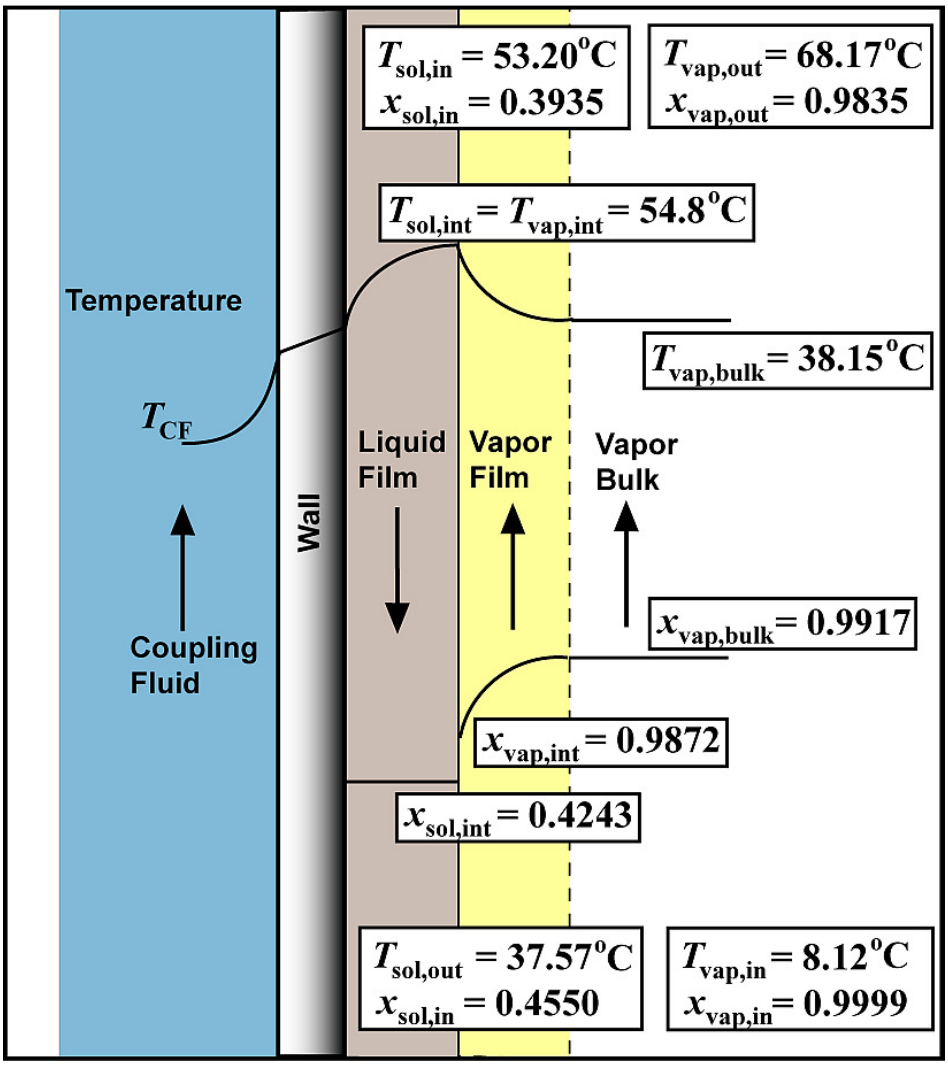

Fig. 4.7 Schematic of the solution and vapor bulk and interface conditions

the concentration gradient between the bulk vapor and the vapor-liquid interface. The molar flux of the vapor being absorbed into the liquid film is given by the following equation.

$$\dot{n}_{\mathrm{T}} = \beta_{\mathrm{vap}} \cdot C_{\mathrm{T}} \cdot \ln\left(\frac{\tilde{z} - \tilde{x}_{\mathrm{vap,int}}}{\tilde{z} - \tilde{x}_{\mathrm{vap,bulk}}}\right) \tag{4.69}$$

The driving molar concentration difference in the above equation is a function of the molar concentration of the condensing flux, $\tilde{z}$, the bulk molar concentration of the vapor, $\tilde{x}_{\mathrm{vap,bulk}}$, and the equilibrium molar vapor concentration, $\tilde{x}_{\mathrm{vap,int}}$, at the interface. The bulk and interface molar concentrations can be calculated from the mass-based bulk

and interface concentrations, which were presented above. In the above equation, β_{vap} is the vapor mass transfer coefficient, and C_T is the bulk molar concentration. The vapor mass transfer coefficient can be calculated from the vapor Sherwood number, Sh_{vap}, which in turn can be calculated from the vapor Nusselt number, Nu_{vap}, using the heat and mass transfer analogy.

$$Sh_{vap} = \frac{\beta_{vap} \cdot D_o}{D_{aw,vap}} \tag{4.70}$$

$$\left(\frac{Sh_{vap}}{Nu_{vap}} \right) = \left(\frac{Sc_{vap}}{Pr_{vap}} \right)^{1/3} \tag{4.71}$$

In the above equations, D_o is the tube outer diameter, $D_{aw,vap}$ is the vapor diffusion coefficient, and Sc_{vap} and Pr_{vap} represent the vapor Schmidt number and the vapor Prandtl number, respectively. The vapor Nusselt number was calculated from a correlation for cross-flow over a cylindrical tube developed by Sparrow *et al*. (2004), with a correction for flow across tube banks given in Mills (1995). The correlation by Sparrow *et al.* (2004) is as follows:

$$Nu_{Sparrow} = 0.25 + \left(0.4 \cdot Re_{vap}^{1/2} + 0.06 \cdot Re_{vap}^{2/3} \right) \cdot Pr_{vap}^{0.37} \cdot \frac{\mu_{vap,int}}{\mu_{vap,int}}; \quad 1 \le Re_{vap} \le 10^5 \tag{4.72}$$

The corrected vapor Nusselt number is given by

$$Nu_{vap} = \Phi \cdot Nu_{Sparrow} \tag{4.73}$$

For aligned tube rows, the arrangement factor Φ is given by

$$\Phi = 1 + \frac{0.7}{\psi^{1.5}} \cdot \frac{S_L/S_T - 0.3}{\left(S_L/S_T - 0.7 \right)^2} \tag{4.74}$$

In the above equation, S_L and S_T are the longitudinal and transverse pitches of the tube array, and ψ is given by

$$\psi = 1 - \frac{\pi}{4 \cdot P_T} \tag{4.75}$$

The above equation is valid for $P_L \geq 1$, where $P_T = S_T/D_o$ and $P_L = S_L/D_o$. For the representative test condition being discussed here, the Nusselt number calculated using the Sparrow correlation (Sparrow *et al.*, 2004) was 2.054 and the correction factor (Mills, 1995) was 1.268. Because a correlation from the literature was used to estimate the vapor Nusselt and Sherwood numbers, a conservative uncertainty of 25% was assigned to this calculation and propagated through the rest of the analysis. Thus, the vapor Nusselt number was estimated as follows:

$$Nu_{vap} = 1.268 \cdot 2.054 = 2.605 \pm 0.651 \tag{4.76}$$

The vapor Sherwood number and the vapor mass transfer coefficient were estimated as follows:

$$Sh_{vap} = 2.605 \cdot \left(\frac{0.505}{0.826}\right)^{1/3} = 2.211 \pm 0.550 \tag{4.77}$$

$$\beta_{vap} = \frac{5.773\times10^{-6}\ \mathrm{m^2\,s^{-1}} \cdot 2.211}{1.575\times10^{-3}\ \mathrm{m}} = 8.106\times10^{-3} \pm 2.1\times10^{-3}\ \mathrm{m\,s^{-1}} \tag{4.78}$$

It should be noted that all the above calculations were conducted at the bulk vapor conditions. The bulk molar concentration was calculated using the ideal gas equation as follows:

$$\begin{aligned} C_T &= \frac{P_{abs}}{R_{gas} \cdot \left(T_{vap,bulk} + 273.17\right)} = \frac{537.3\,\mathrm{kPa}}{8.314\,\mathrm{kJ\,kg^{-1}\,K^{-1}} \cdot \left(38.15 + 273.15\,\mathrm{K}\right)} \\ &= 0.2076 \pm 0.0017\,\mathrm{kmol\,m^{-3}} \end{aligned} \tag{4.79}$$

The molar flux of the vapor being absorbed in the liquid film was estimated to be

$$\begin{aligned} n_T &= 8.106\times10^{-3}\ \mathrm{m\,s^{-1}} \cdot 0.2076\,\mathrm{kmol\,m^{-3}} \cdot \ln\left(\frac{1.007 - 0.9879}{1.007 - 0.9922}\right) \\ &= 4.213\times10^{-4} \pm 0.242\times10^{-4}\ \mathrm{kmol\,m^{-2}\,s^{-1}} \end{aligned} \tag{4.80}$$

The molar concentration of the condensing flux, $\tilde{z}$, is not explicitly known at this point, and is calculated iteratively later in the model. The eventual value is shown here for convenience. It is also interesting to note that the value of $\tilde{z}$ is greater than 1,

indicating that that direction of transfer of water is opposite to the direction of transfer of ammonia. The individual ammonia and water condensing fluxes were determined from the total condensing flux as follows.

$$\dot{n}_{\mathrm{A}} = \tilde{z} \cdot \dot{n}_{\mathrm{T}} \tag{4.81}$$

$$\dot{n}_{\mathrm{A}} = 1.007 \cdot 4.213\times10^{-4}\ \mathrm{kmol\,m^{-2}\,s^{-1}} = 4.224\times10^{-4} \pm 0.239\times10^{-4}\ \mathrm{kmol\,m^{-2}\,s^{-1}} \tag{4.82}$$

$$\dot{n}_{\mathrm{W}} = \left(1 - \tilde{z}\right) \cdot \dot{n}_{\mathrm{T}} \tag{4.83}$$

$$\begin{aligned} \dot{n}_{\mathrm{w}} &= \left(1-1.007\right) \cdot 4.213\times10^{-4}\ \mathrm{kmol\,m^{-2}\,s^{-1}} \\ &= -3.139\times10^{-6} \pm 0.436\times10^{-6}\ \mathrm{kmol\,m^{-2}\,s^{-1}} \end{aligned} \tag{4.84}$$

It should be noted that the molar fluxes and mass flow rates reported in this section are for the whole tube bank in the segment and not for a single tube or tube row. Using these molar fluxes, the mass fluxes or mass flow rates of each component absorbed into the solution, as well as the total mass absorbed per time, can be estimated.

$$\dot{m}_{\mathrm{abs,A}} = M_{\mathrm{A}} \cdot \dot{n}_{\mathrm{A}} \cdot A_{\mathrm{int}} \tag{4.85}$$

$$\begin{aligned} \dot{m}_{\mathrm{abs,A}} &= 17.03\,\mathrm{kg\,kmol} \cdot 4.224\times10^{-3}\ \mathrm{kmol\,m^{-2}\,s^{-1}} \cdot 0.2602\,\mathrm{m^2} \\ &= 0.00188 \pm 0.00011\,\mathrm{kg\,s^{-1}} \end{aligned} \tag{4.86}$$

$$\dot{m}_{\mathrm{abs,W}} = M_{\mathrm{W}} \cdot \dot{n}_{\mathrm{W}} \cdot A_{\mathrm{int}} \tag{4.87}$$

$$\begin{aligned} \dot{m}_{\mathrm{abs,W}} &= 18.02\,\mathrm{kg\,kmol} \cdot -3.139\times10^{-6}\ \mathrm{kmol\,m^{-2}\,s^{-1}} \cdot 0.2602\,\mathrm{m^2} \\ &= -1.47\times10^{-5} \pm 0.205\times10^{-5}\ \mathrm{kg\,s^{-1}} \end{aligned} \tag{4.88}$$

$$\dot{m}_{\mathrm{abs}} = \dot{m}_{\mathrm{abs,A}} + \dot{m}_{\mathrm{abs,W}} \tag{4.89}$$

$$\dot{m}_{\mathrm{abs}} = 0.00188\,\mathrm{kg\,s^{-1}} - 1.47\times10^{-5}\ \mathrm{kg\,s^{-1}} = 0.00187 \pm 0.00011\,\mathrm{kg\,s^{-1}} \tag{4.90}$$

In the above equations, M_{A} and M_{W} are the molar masses of ammonia and water, respectively, and A_{int} is the area available for mass transfer at the vapor-liquid interface. This is different from the tube side transfer area, A_{seg}, since there is some additional transfer area presented due to the presence of the film, which is estimated as follows:

$$A_{\text{int}} = \left(\frac{D_{\text{o}} + 2 \cdot \delta_{\text{l,avg}}}{D_{\text{o}}} \right) \cdot A_{\text{seg}} \tag{4.91}$$

$$A_{\text{int}} = \left(\frac{1.575\times10^{-3}\,\text{m} + 2 \cdot 1.109\times10^{-4}\,\text{m}}{1.575\times10^{-3}\,\text{m}} \right) \cdot 0.2281\,\text{m}^2 = 0.2602 \pm 0.00009\,\text{m}^2 \tag{4.92}$$

Here, the average film thickness was calculated from the average linear mass flux, using the definition for Nusselt condensation given in Bird *et al.* (2002) as follows.

$$\Gamma_{\text{l,avg}} = \frac{\dot{m}_{\text{l,avg}}}{N_{\text{tube,pr}} \cdot L_{\text{tube}} \cdot 2} \tag{4.93}$$

$$\Gamma_{\text{l,avg}} = \frac{0.01771\,\text{kg s}^{-1}}{33 \cdot 0.1397\,\text{m} \cdot 2} = 1.92\times10^{-3} \pm 0.006\times10^{-3}\,\text{kg m}^{-1}\,\text{s}^{-1} \tag{4.94}$$

In the above equation, the average solution mass flow rate was divided by 2 to account for flow of solution around two sides of the tube. The average film thickness was calculated using the following equations.

$$\delta_{\text{l,avg}} = \left(\frac{3 \cdot \mu_{\text{l,avg}} \cdot \Gamma_{\text{l,avg}}}{g \cdot \rho_{\text{l,avg}}^2} \right)^{1/3} \cdot \frac{2}{\pi} \cdot \int_0^{\pi/2} \sin^{-1/3}\theta \cdot d\theta \tag{4.95}$$

$$\delta_{\text{l,avg}} = \left(\frac{3 \cdot \mu_{\text{l,avg}} \cdot \Gamma_{\text{l,avg}}}{g \cdot \rho_{\text{l,avg}}^2} \right)^{1/3} \cdot \frac{2}{\pi} \cdot 2.103 \tag{4.96}$$

$$\begin{aligned} \delta_{\text{l,avg}} &= \left(\frac{3 \cdot 6.81\times10^{-4}\,\text{kg m}^{-1}\,\text{s}^{-1} \cdot 1.92\times10^{-3}\,\text{kg m}^{-1}\,\text{s}^{-1}}{9.81\,\text{m s}^{-2} \cdot \left(838.8\,\text{kg m}^{-3}\right)^2} \right)^{1/3} \cdot \frac{2}{\pi} \cdot 2.103 \\ &= 1.109\times10^{-4} \pm 0.0003\times10^{-4}\,\text{m} \end{aligned} \tag{4.97}$$

Overall heat and mass transfer

Fig. 4.8 shows the schematic of the mass and species interactions in a control volume or segment (in the present case, the bottom segment). As vapor flows upwards in this segment, some of the ammonia vapor is absorbed into the counter-current solution. As previously mentioned, water vapor can travel in either direction at the interface

depending on the liquid and vapor bulk conditions and therefore, is shown as a dotted line. The vapor outlet flow rate and concentration can be determined for each segment using the mass transfer rates estimated above.

$$\dot{m}_{\text{vap,out}} = \dot{m}_{\text{vap,in}} - \dot{m}_{\text{abs}} \tag{4.98}$$

$$\dot{m}_{\text{vap,out}} = 0.00277\,\text{kg s}^{-1} - 0.00187\,\text{kg s}^{-1} = 0.00090 \pm 0.00011\,\text{kg s}^{-1} \tag{4.99}$$

$$x_{\text{vap,out}} = \frac{\dot{m}_{\text{vap,in}} \cdot x_{\text{vap,in}} - \dot{m}_{\text{abs,A}}}{\dot{m}_{\text{vap,out}}} \tag{4.100}$$

$$x_{\text{vap,out}} = \frac{0.00277 \cdot 0.9999 - 0.00188}{0.00090} = 0.9835 \pm 0.00184 \tag{4.101}$$

It should be noted that the outlet vapor mass flow rate and concentration used previously to estimate the bulk vapor conditions are actually calculated at this point. A mass and species balance between the vapor and liquid phases can be employed to

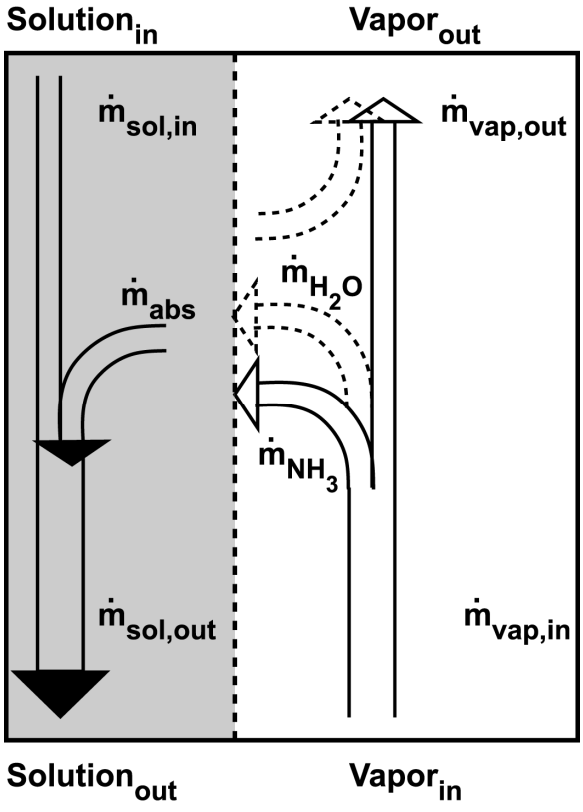

Fig. 4.8 Control volume for mass and species balance

provide closure to the system of equations, calculate the absorption rates for each incremental segment, and estimate the solution inlet flow rate and concentration.

$$\dot{m}_{\text{sol,in}} = \dot{m}_{\text{sol,out}} + \dot{m}_{\text{vap,out}} - \dot{m}_{\text{vap,in}} \tag{4.102}$$

$$\begin{aligned} \dot{m}_{\text{sol,in}} &= 0.01865\,\text{kg s}^{-1} + 0.00090\,\text{kg s}^{-1} - 0.00277\,\text{kg s}^{-1} \\ &= 0.01678 \pm 0.00011\,\text{kg s}^{-1} \end{aligned} \tag{4.103}$$

$$\dot{m}_{\text{sol,in}} \cdot x_{\text{sol,in}} = \dot{m}_{\text{sol,out}} \cdot x_{\text{sol,out}} + \dot{m}_{\text{vap,out}} \cdot x_{\text{vap,out}} - \dot{m}_{\text{vap,in}} \cdot x_{\text{vap,in}} \tag{4.104}$$

$$\begin{aligned} x_{\text{sol,in}} &= \frac{0.01865\,\text{kg s}^{-1} \cdot 0.455 + 0.00090\,\text{kg s}^{-1} \cdot 0.9835 - 0.00277\,\text{kg s}^{-1} \cdot 0.9999}{0.01678\,\text{kg s}^{-1}} \\ &= 0.3935 \pm 0.00405 \end{aligned} \tag{4.105}$$

Because the solution is assumed to be well mixed, the solution interface concentration at the inlet is necessarily the same as the concentration of the bulk solution at the inlet, which was calculated above. Additionally, the solution interface is assumed to be in equilibrium with the vapor phase. Thus, the state of the solution at the interface at the inlet of the segment can be defined and the inlet interface temperature estimated.

$$T_{\text{sol,in,int}} = f\left(P_{\text{abs}}, x_{\text{sol,in}}, q_{\text{sol,in,int}} = 0\right) \tag{4.106}$$

$$T_{\text{sol,in,int}} = f\left(537.3\,\text{kPa}, 0.3935, 0\right) = 60.49 \pm 0.78\,^{\circ}\text{C} \tag{4.107}$$

To find an alternative estimate of the bulk solution temperature at the inlet to the segment, the local flow configuration was considered. Fig. 4.9 shows a schematic of the solution flowing around a single tube. The tangential velocity of the flow is given by:

$$u\left(y\right) = \frac{\rho_{\text{sol}} \times g}{\mu_{\text{sol}}} \times \left(\delta_{\text{l}} \times y - \frac{y^2}{2}\right) \times \sin\theta \tag{4.108}$$

In the above equation, y is distance from the tube wall along the radial direction, δ_{l} is the local film thickness, and θ is the local angle along the tube as shown in Fig. 4.9. Because the film is very thin, a linear profile can be assumed for the solution temperature between the interface and the wall. The mean solution temperature can therefore be calculated as follows:

$$T_{\text{sol,mean}} = \frac{\int_0^{\delta_l} T_{\text{sol}} \times u \times dy}{\int_0^{\delta_f} u \times dy} = \frac{3}{8} \times T_{\text{wall}} + \frac{5}{8} \times T_{\text{int}} \tag{4.109}$$

The above equation was applied to the solution inlet to obtain an estimate for bulk solution temperature. This bulk solution temperature is used to calculate the liquid film transport properties and in the definition of liquid film heat transfer coefficient, discussed below.

$$T_{\text{sol,in}} = \frac{3}{8} \times T_{\text{wall,in}} + \frac{5}{8} \times T_{\text{sol,in,int}} \tag{4.110}$$

$$T_{\text{sol,in}} = \frac{3}{8} \times 41.04\,^{\circ}\text{C} + \frac{5}{8} \times 60.49\,^{\circ}\text{C} = 53.2 \pm 0.75\,^{\circ}\text{C} \tag{4.111}$$

It should be noted that the wall temperature at the segment inlet is not explicitly known at this point and is calculated later. The state of the solution at the inlet can be

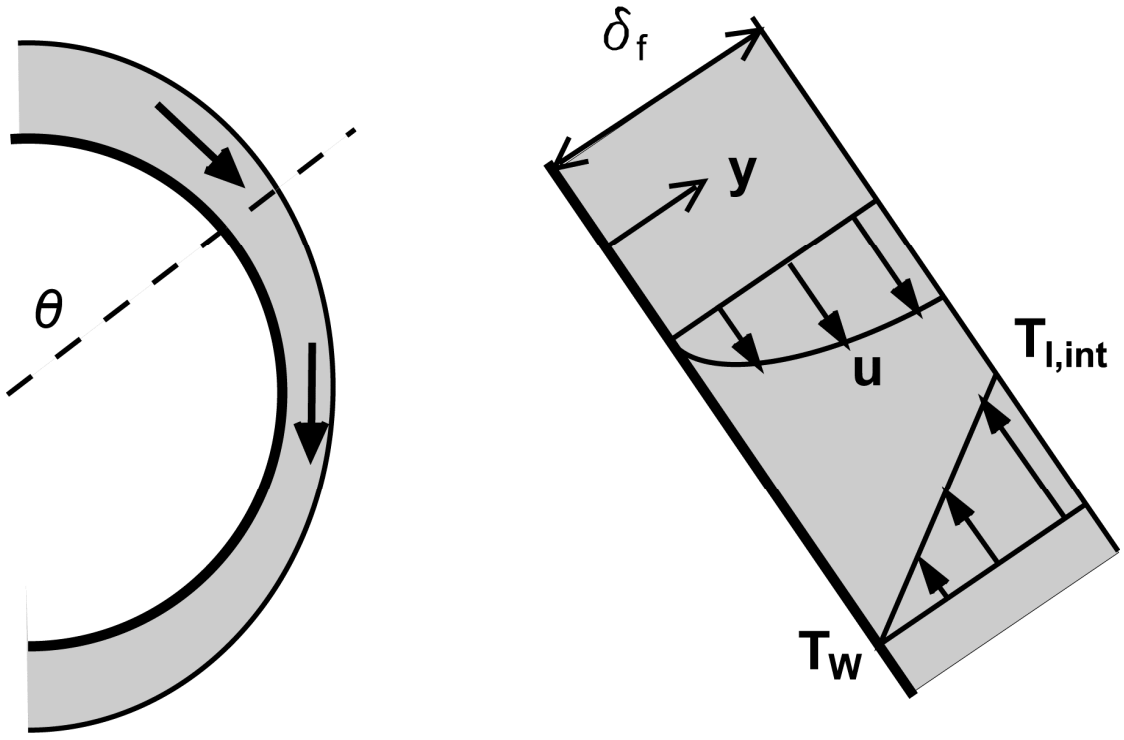

Fig. 4.9 Schematic of solution flow around a single tube

defined using the mean solution temperature, concentration, and the absorber pressure. The inlet solution mass flow rate, temperature, and concentration used previously to estimate the average solution conditions are actually calculated at this point. The enthalpy of the solution at the inlet of the segment is determined as follows:

$$h_{\text{sol,in}} = f\left(P_{\text{abs}}, T_{\text{sol,in}}, x_{\text{sol,in}}\right) \tag{4.112}$$

$$h_{\text{sol,in}} = f\left(537.3\,\text{kPa}, 53.2\,^{\circ}\text{C}, 0.3935\right) = 9.161 \pm 3.43\,\text{kJ kg}^{-1} \tag{4.113}$$

The vapor state at the outlet of the segment is determined from the sensible heat transfer between the liquid film and the vapor. The sensible heat transfer rate is calculated as follows:

$$Q_{\text{vap}} = \alpha_{\text{vap}} \cdot \left(\frac{\phi_{\text{T}}}{1 - e^{-\phi_{\text{T}}}}\right) \cdot A_{\text{int}} \cdot LMTD_{\text{vap}} \tag{4.114}$$

In the above equation, α_{vap} is the vapor heat transfer coefficient and $LMTD_{\text{vap}}$ is the logarithmic mean temperature difference between the vapor bulk and the vapor-liquid interface. The term within the parentheses is the correction factor for the heat transfer coefficient due to mass transfer. The parameter, ϕ_{T}, is defined as follows:

$$\phi_{\text{T}} = \frac{\left(\dot{n}_{\text{A}} \cdot \tilde{C}p_{\text{A}}\right) + \left(\dot{n}_{\text{W}} \cdot \tilde{C}p_{\text{W}}\right)}{\alpha_{\text{vap}}} \tag{4.115}$$

Here $\tilde{C}p_{\text{A}}$ and $\tilde{C}p_{\text{W}}$ represent the molar specific heats of the ammonia and water vapor, respectively. The vapor heat transfer coefficient is determined from the previously calculated bulk vapor Nusselt number.

$$\alpha_{\text{vap}} = \frac{Nu_{\text{vap}} \cdot k_{\text{vap}}}{D_{\text{o}}} \tag{4.116}$$

$$\alpha_{\text{vap}} = \frac{2.605 \cdot 0.0307\,\text{W m}^{-1}\,\text{K}^{-1}}{1.575 \times 10^{-3}\,\text{m}} = 50.74 \pm 13.05\,\text{W m}^{-2}\,\text{K}^{-1} \tag{4.117}$$

The parameter, ϕ_{T}, is calculated to be

$$\phi_T = \frac{\left(4.244\times10^{-3}\ \text{kmol m}^{-2}\ \text{s}^{-1}\cdot 33.26\ \text{kJ kmol}^{-1}\ \text{K}^{-1}\right)+\left(-3.139\times10^{-6}\ \text{kmol m}^{-2}\ \text{s}^{-1}\cdot 33.26\ \text{kJ kmol}^{-1}\ \text{K}^{-1}\right)}{50.74\times10^{-3}\ \text{kW m}^{-2}\ \text{K}^{-1}} = 0.2761\pm0.054 \quad (4.118)$$

$LMTD_{vap}$ is calculated as follows:

$$LMTD_{vap} = \frac{\left(T_{vap,in} - T_{sol,out,int}\right)-\left(T_{vap,out} - T_{sol,in,int}\right)}{\ln\left(\frac{T_{vap,in} - T_{sol,out,int}}{T_{vap,out} - T_{sol,in,int}}\right)} \quad (4.119)$$

The vapor outlet temperature is unknown and was calculated iteratively by matching the vapor sensible heat transfer rate calculated previously with the vapor sensible heating estimated using the equation below.

$$Q_{vap} = \dot{m}_{vap,bulk}\cdot Cp_{vap,bulk}\cdot\left(T_{vap,in} - T_{vap,out}\right) \quad (4.120)$$

The vapor outlet temperature, $LMTD_{vap}$, and the vapor sensible heat transfer rate were calculated to be

$$T_{vap,out} = 68.17\pm4.9\,^{\circ}\text{C} \quad (4.121)$$

$$LMTD_{vap} = \frac{\left(8.12\,^{\circ}\text{C} - 49.4\,^{\circ}\text{C}\right)-\left(68.17\,^{\circ}\text{C} - 60.49\,^{\circ}\text{C}\right)}{\ln\left(\frac{8.12\,^{\circ}\text{C} - 49.4\,^{\circ}\text{C}}{68.17\,^{\circ}\text{C} - 60.49\,^{\circ}\text{C}}\right)} = -16.8\pm2.5\ \text{K} \quad (4.122)$$

$$Q_{vap} = 50.74\ \text{W m}^{-2}\ \text{K}^{-1}\cdot\left(\frac{0.2761}{1-e^{-0.2761}}\right)\cdot 0.2602\ \text{m}^2\cdot -16.8\ \text{K} = -253.9\pm21.6\ \text{W} \quad (4.123)$$

$$\begin{aligned} Q_{vap} &= 0.0018\ \text{kg s}^{-1}\cdot 2.308\times10^{3}\ \text{J kg}^{-1}\ \text{K}^{-1}\cdot\left(8.12\,^{\circ}\text{C} - 68.17\,^{\circ}\text{C}\right) \\ &= -253.9\pm21.6\ \text{W} \end{aligned} \quad (4.124)$$

The calculated vapor sensible heat transfer rate can be positive or negative, depending on whether the vapor temperature is higher or lower than the interface temperature. In the present case, the heat transfer rate was negative since the vapor temperature was lower than the interface temperature, resulting in the transfer of heat from the interface to the bulk. The state of the vapor at the outlet of the segment is defined using the absorber pressure, the iteratively estimated temperature above, and the

previously estimated concentration. The outlet vapor temperature used previously to estimate the bulk vapor temperature is actually calculated at this point. The enthalpy of the vapor leaving the segment is estimated as follows:

$$h_{\text{vap,out}} = f\left(P_{\text{abs}}, T_{\text{vap,out}}, x_{\text{vap,out}}\right) \tag{4.125}$$

$$h_{\text{vap,out}} = f\left(537.3\,\text{kPa}, 68.17\,^{\circ}\text{C}, 0.9835\right) = 1446 \pm 11.87\,\text{kJ kg}^{-1} \tag{4.126}$$

The total absorption heat duty is calculated from an energy balance between the liquid and vapor streams as follows:

$$Q_{\text{abs}} = \dot{m}_{\text{sol,in}} \cdot h_{\text{sol,in}} + \dot{m}_{\text{vap,in}} \cdot h_{\text{vap,in}} - \dot{m}_{\text{sol,out}} \cdot h_{\text{sol,out}} - \dot{m}_{\text{vap,out}} \cdot h_{\text{vap,out}} \tag{4.127}$$

$$\begin{aligned} Q_{\text{abs}} &= 0.0168\,\text{kg s}^{-1} \cdot 9.2\,\text{kJ kg}^{-1}\,\text{K}^{-1} + 0.0028\,\text{kg s}^{-1} \cdot 1280\,\text{kJ kg}^{-1}\,\text{K}^{-1} \\ &\quad - 0.0187\,\text{kg s}^{-1} \cdot -69.8\,\text{kJ kg}^{-1}\,\text{K}^{-1} - 0.0009\,\text{kg s}^{-1} \cdot 1446\,\text{kJ kg}^{-1}\,\text{K}^{-1} \\ &= 3.69 \pm 0.204\,\text{kW} \end{aligned} \tag{4.128}$$

The above equation accounts for both the sensible duty associated with the heating or cooling of the vapor and liquid, as well the latent heat of absorption. As previously mentioned, in the above equations, the value of $\tilde{z}$ is required to calculate the absorption rate. This is determined iteratively by equating the absorption duty calculated above to the experimentally estimated absorption duty on the coupling fluid side for the segment.

$$Q_{\text{abs}} = \dot{m}_{\text{CF}} \cdot Cp_{\text{CF}} \cdot \left(T_{\text{CF,out}} - T_{\text{CF,in}}\right) \tag{4.129}$$

$$Q_{\text{abs}} = 0.1375\,\text{kg s}^{-1} \cdot 4.18\,\text{kJ kg}^{-1}\,\text{K}^{-1} \cdot \left(35.99\,^{\circ}\text{C} - 29.56\,^{\circ}\text{C}\right) = 3.69 \pm 0.204\,\text{kW} \tag{4.130}$$

The overall heat transfer coefficient that can support this heat transfer rate from the solution to the coupling fluid is calculated as follows.

$$Q_{\text{abs}} = U \cdot A_{\text{seg}} \cdot LMTD_{\text{T}} \tag{4.131}$$

Here, A_{seg} is the outer surface area of the tube array in the segment under consideration, and $LMTD_{\text{T}}$ is the total logarithmic mean temperature difference between the bulk solution temperature and the coupling fluid temperature (as seen in Fig. 4.10).

As previously discussed, since the bulk of the solution remains subcooled during absorption, the solution bulk temperature is more representative of the driving temperature difference.

$$LMTD_T = \frac{\left(T_{sol,in} - T_{CF,out}\right) - \left(T_{sol,out} - T_{CF,in}\right)}{\ln\left(\frac{T_{sol,in} - T_{CF,out}}{T_{sol,out} - T_{CF,in}}\right)} \tag{4.132}$$

$$LMTD_T = \frac{\left(53.20\,^{\circ}\mathrm{C} - 35.99\,^{\circ}\mathrm{C}\right) - \left(37.57\,^{\circ}\mathrm{C} - 29.56\,^{\circ}\mathrm{C}\right)}{\ln\left(\frac{53.20\,^{\circ}\mathrm{C} - 35.99\,^{\circ}\mathrm{C}}{37.57\,^{\circ}\mathrm{C} - 29.56\,^{\circ}\mathrm{C}}\right)} = 12.03 \pm 0.41\,\mathrm{K} \tag{4.133}$$

$$U = \frac{3.69 \times 10^3\ \mathrm{W}}{0.2281\,\mathrm{m}^2 \cdot 12.03\,\mathrm{K}} = 1346 \pm 54.25\,\mathrm{W\,m^{-2}\,K^{-1}} \tag{4.134}$$

It should be noted that for heat transfer from the solution to the tube wall, the relevant transfer area is the outer surface area of the tube array in the segment, A_{seg}. This is different from the area for mass transfer, which is the transfer area at the vapor-liquid interface, A_{int}, calculated above. Therefore for heat transfer calculations on the solution

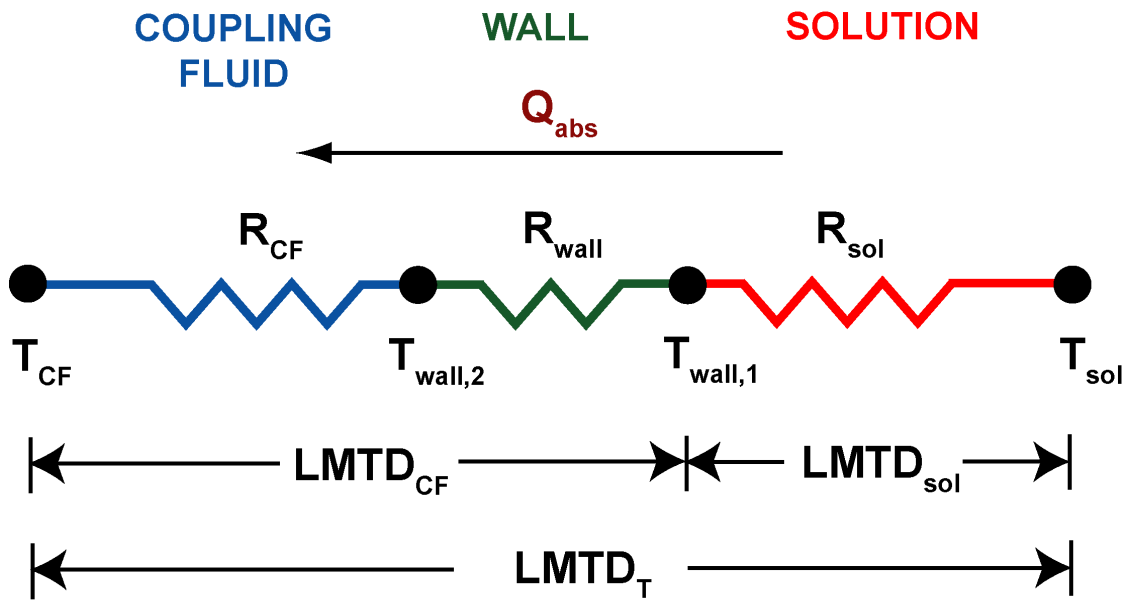

Fig. 4.10 Schematic of resistance network and *LMTD* definitions

side, the outer surface area of the tube array in the segment is considered. The solution heat transfer coefficient can be estimated using a simple 1-D resistance network between the solution and the coupling fluid sides (Fig. 4.10).

$$\frac{1}{U} = \frac{D_o}{D_i \cdot \alpha_{CF}} + R_{wall} + \frac{1}{\alpha_{sol}} \tag{4.135}$$

It should be noted that the total heat transfer area on the solution side is the total outer surface area of the tube bank in the segment, while the total heat transfer area on coupling-fluid side is the total inner surface of the tube bank in the segment. To account for this difference, the first term on the right hand side of the above equation is multiplied by the ratio of the outer and inner diameters. Additionally, in the above equation, α_{CF}, the coupling fluid heat transfer coefficient, was calculated using the correlation developed by Churchill for forced convective single-phase flow inside circular tubes (Churchill, 1977b, a) and was estimated to be 6519 W m^{-2} K^{-1}. A conservative uncertainty of 25% was assigned to this calculated value and propagated through the rest of the calculation. Thus, an uncertainty of ±1630 W m^{-2} K^{-1} in the coupling fluid heat transfer coefficient was used for the present test condition. R_{wall} is the wall thermal resistance per unit area.

$$R_{wall} = \frac{D_i}{2 \cdot k_{wall}} \cdot \ln\left(\frac{D_o}{D_i}\right) \tag{4.136}$$

$$\begin{aligned} R_{wall} &= \frac{1.168\times10^{-3}\ \text{m}}{2 \cdot 15.16\ \text{W m}^{-1}\ \text{K}^{-1}} \cdot \ln\left(\frac{1.575\times10^{-3}\ \text{m}}{1.168\times10^{-3}\ \text{m}}\right) \\ &= 1.15 \pm 0.0001\times10^{-5}\ \text{K m}^2\ \text{W}^{-1} \end{aligned} \tag{4.137}$$

The solution heat transfer coefficient was estimated to be

$$\begin{aligned} \alpha_{sol} = &\frac{1}{\dfrac{1}{1346\ \text{W m}^{-2}\ \text{K}^{-1}} - \dfrac{1.575\times10^{-3}\ \text{m}}{1.168\times10^{-3}\ \text{m} \cdot 6519\ \text{W m}^{-2}\ \text{K}^{-1}}} \\ &- 1.15\times10^{-5}\ \text{K m}^2\ \text{W}^{-1} \\ = &\ 1906 \pm 186.1\ \text{W m}^{-2}\ \text{K}^{-1} \end{aligned} \tag{4.138}$$

It should be noted that the thermal resistance ratio, R_{sol}/R_{CF}, is 2.54. Because the overall thermal resistance is dominated by the thermal resistance on the solution side, the uncertainty associated with the solution heat transfer coefficient is not very significant. The uncertainty associated with the solution heat transfer coefficient for all test conditions is reported later. The wall temperatures at the inlet and outlet of the segment can be estimated by using the same resistance network and evaluating the *LMTD*s between the solution and the wall ($LMTD_{sol}$), and the wall and the coupling fluid ($LMTD_{CF}$).

$$Q_{abs} = \alpha_{sol} \cdot A_{seg} \cdot LMTD_{sol} \tag{4.139}$$

$$LMTD_{sol} = \frac{3.69\times10^{3}\ \mathrm{W}}{1906\ \mathrm{W\,m^{-2}\,K^{-1}} \cdot 0.2281\ \mathrm{m^{2}}} = 8.50 \pm 0.74\ \mathrm{K} \tag{4.140}$$

$$Q_{abs} = U_{CF\text{-}Wall} \cdot A_{seg} \cdot LMTD_{CF} \tag{4.141}$$

$$LMTD_{CF} = \frac{3.69\times10^{3}\ \mathrm{W}}{6179\ \mathrm{W\,m^{-2}\,K^{-1}} \cdot 0.2281\ \mathrm{m^{2}} \cdot \dfrac{1.168\times10^{-3}\ \mathrm{m}}{1.575\times10^{-3}\ \mathrm{m}}} = 3.53 \pm 0.87\ \mathrm{K} \tag{4.142}$$

In the above equation, $U_{CF\text{-}Wall}$ is the overall heat transfer coefficient for heat transfer from the outer surface of the tube wall to the coupling fluid, given by the following equation.

$$\frac{1}{U_{CF\text{-}Wall}} = \frac{D_o}{D_i \cdot \alpha_{CF}} + R_{wall} \tag{4.143}$$

The two *LMTD*s (Fig. 4.10) are defined as follows, which in turn were used to determine the wall temperature at the solution inlet, $T_{wall,inlet}$, and solution outlet, $T_{wall,outlet}$.

$$LMTD_{sol} = \frac{\left(T_{sol,in} - T_{wall,inlet}\right) - \left(T_{sol,out} - T_{wall,outlet}\right)}{\ln\left(\dfrac{T_{sol,in} - T_{wall,inlet}}{T_{sol,out} - T_{wall,outlet}}\right)} \tag{4.144}$$

$$LMTD_{CF} = \frac{\left(T_{wall,inlet} - T_{CF,out}\right) - \left(T_{wall,outlet} - T_{CF,in}\right)}{\ln\left(\frac{T_{wall,inlet} - T_{CF,out}}{T_{wall,outlet} - T_{CF,in}}\right)} \quad (4.145)$$

$$T_{wall,inlet} = 41.04 \pm 1.37\,^{o}C \quad (4.146)$$

$$T_{wall,outlet} = 31.92 \pm 0.55\,^{o}C \quad (4.147)$$

With the wall temperatures at the solution inlet, previously used to determine the solution inlet temperature, calculated at this point, all the necessary equations are available to close the model. To analyze the absorber, this model was first applied to the bottom segment, and then to the top segment, to determine the solution and vapor state at intermediate locations, as well as the absorption rates in each segment. All the calculations for the system level data reduction, and component level heat and mass transfer analysis were solved iteratively using the *Engineering Equation Solver* software (Klein, 2011) platform. The approach described above was applied to each test condition in the present work, and the results of this analysis are discussed in the following sections.

4.3. Results and discussion

4.3.1. Overall absorber component

Table 4.3 shows the range of absorber duties, overall heat transfer coefficients,

Table 4.3 Summary of calculated uncertainties

Parameter	Range	Uncertainty range (absolute)	Uncertainty range (%)	Average uncertainty (%)
Q_{Abs}	2.89 - 10.09 kW	0.10 - 0.48 kW	1.53 - 6.15	2.38
U_{abs}	1065-2031 W m^{-2} K^{-1}	25.07-261.4 W m^{-2} K^{-1}	1.91 – 12.87	3.92
α_{sol}	1461-3430 W m^{-2} K^{-1}	89.16-939 W m^{-2} K^{-1}	5.39 - 28.20	11.34

and solution heat transfer coefficients obtained from the data using the analyses described above, and the associated uncertainty in each parameter. The uncertainties associated with the measurement of the absorber duty and the overall heat transfer coefficient are less than 6.15 and 12.87%, respectively. The uncertainty associated with the solution heat transfer coefficient measurement is higher, but still less than 28.2% for all test condition with an average uncertainty of 11.34%. This higher uncertainty is largely due to the conservative uncertainty assigned to the coupling fluid heat transfer coefficient.

Fig. 4.11 shows the absorber duty as a function of the concentrated solution flow

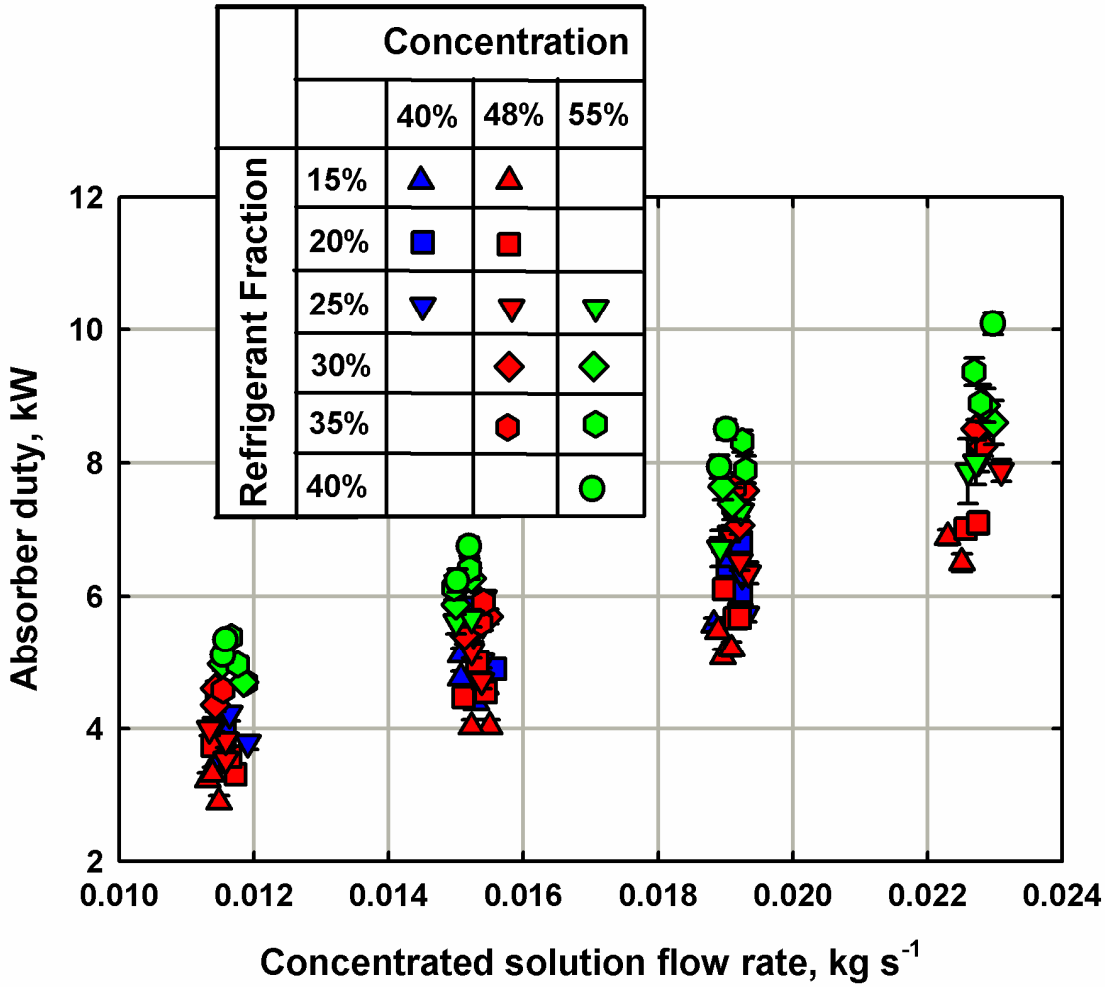

Fig. 4.11 Absorber duty as a function of concentrated solution flow rate (all data points)

rate for all 103 data points taken in this study, categorized by the nominal solution concentration and refrigerant fraction for each test case. Fig. 4.12 shows the same information for the nominal concentrated solution concentration of 48% for different coupling fluid inlet temperatures and refrigerant fractions. It should be noted that the absorber was tested over a wide range of conditions at this nominal concentration, and therefore this plot can be used to study the influence of the coupling fluid operating conditions on absorber performance. The absorber duties were found to range from 2.89 - 10.09 kW over the range of test conditions in this study.

It can be seen from both Figs. 4.11 and 4.12 that the absorber duty increases with

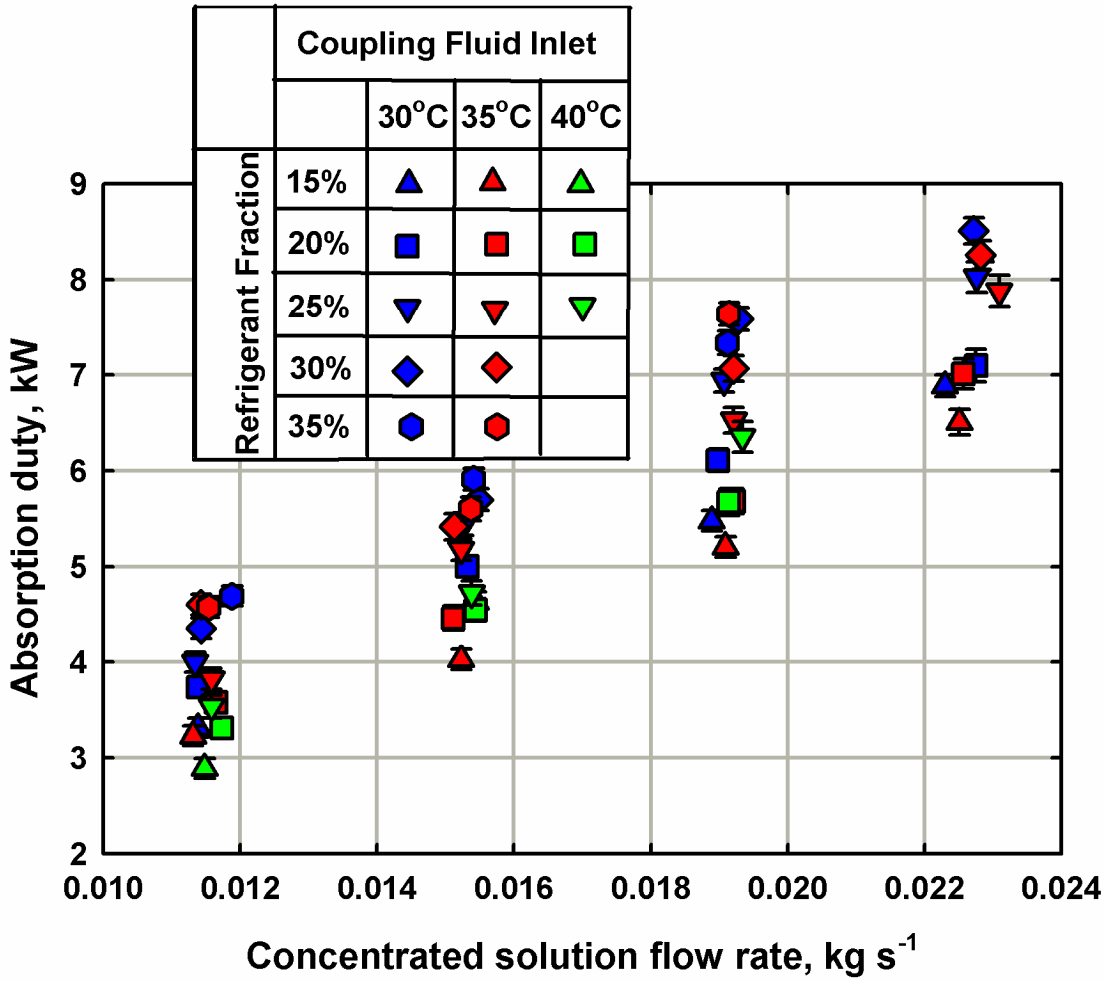

Fig. 4.12 Absorber duty as a function of concentrated solution flow rate (48% case)

an increase in the solution flow rate and refrigerant fraction. For example, the absorber duty increased from 3.2 - 6.5 kW when the solution flow rate was increased from 0.011 - 0.023 kg s^{-1}, while keeping the refrigerant fraction and coupling fluid inlet temperature at 15% and 35°C, respectively. Similarly, the absorber duty increased from 5.2 - 7.6 kW when the refrigerant fraction was increased from 15 - 35% while keeping the concentrated solution flow rate and coupling fluid inlet temperature constant at 0.019 kg s^{-1} and 35°C, respectively. As previously discussed, the absorber duty is a combination of the sensible cooling of the solution and vapor streams, and the latent heat of absorption of the vapor. Thus, the absorption duty increases with an increase in either of these parameters. The total absorption duty remains largely independent of the nominal concentration of the concentrated solution, although the higher concentration cases result in slightly higher duties. It can be seen in Fig. 4.12 that the absorption duty is generally higher for the lower coupling fluid inlet temperatures. This is an expected result because the lower coupling fluid temperatures provide a larger driving temperature difference, leading to larger heat transfer rates.

Fig. 4.13 shows the mass of vapor absorbed in the bottom and top segments of the absorber as a function of the concentrated solution mass flow rate. It can be seen that the bulk of the vapor is absorbed in the bottom segment of the absorber. As the refrigerant is introduced at the bottom of the absorber, the upward moving vapor is first absorbed in the bottom rows. A large part of the vapor is already absorbed by the time it reaches the upper segment. Thus, despite favorable heat and mass transfer conditions at the top segment of the absorber, the absorption duties are low. This also indicates that the absorber is capable of transferring higher heat duties than those reported here. Thus, this microchannel falling-film absorber configuration enables the transfer of large absorption duties in a compact geometry, similar to the findings of Meacham and Garimella (Meacham and Garimella, 2002, 2004) in experiments on this geometry when they tested it in a single-pressure facility.

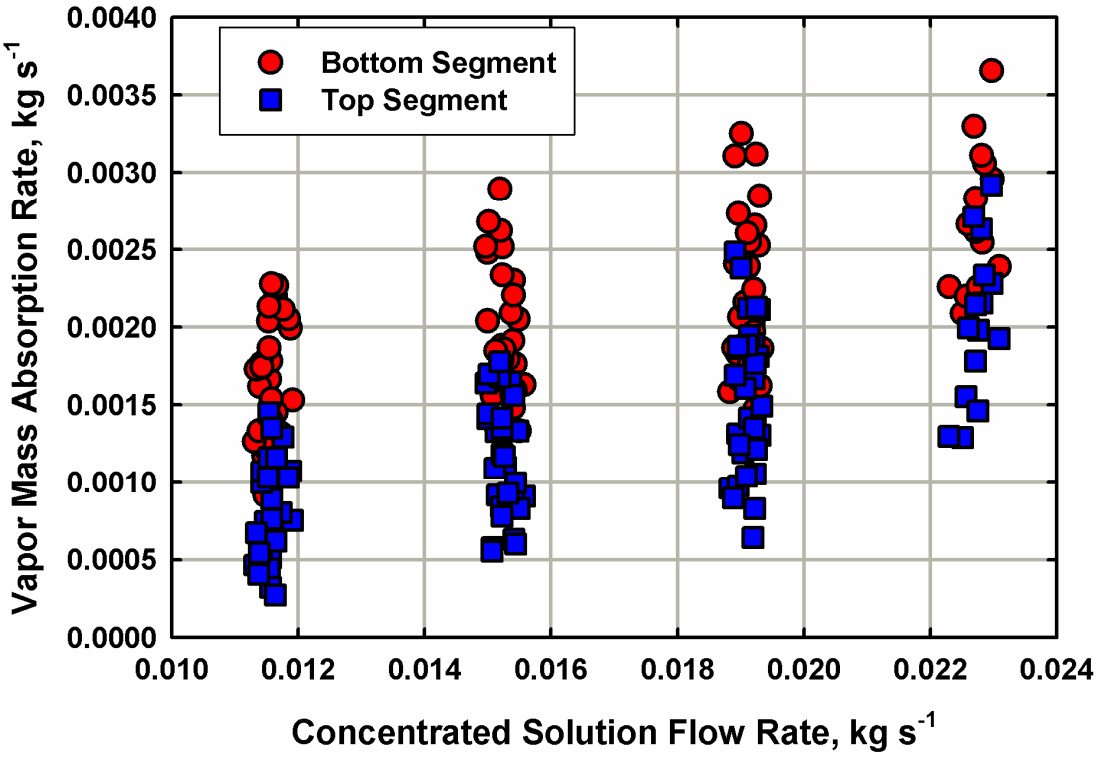

Fig. 4.13 Segmental absorption rate as a function of concentrated solution flow rate

4.3.2. Solution heat transfer coefficient

While the absorber duty was discussed above in terms of the concentrated solution flow rate, the overall and solution heat transfer coefficients are presented as a function of the more representative average linear mass flux based on the tube length. As discussed previously, the average linear mass flux is given by $\Gamma_{\text{sol,avg}} = \dot{m}_{\text{sol,avg}} / \left(N_{\text{tube}} \cdot L_{\text{tube}} \cdot 2 \right)$, and the factor of 2 in the denominator is used to account for the flow of solution on both sides of the tube. Fig. 4.14 shows a plot of the overall heat transfer coefficient (U) as a function of the average linear mass flux based on the tube length for the bottom segment of the absorber. Because most of the absorption occurred in the bottom segment of the absorber, there is a possibility that a part of the top

segment does not participate appreciably in the absorption process due to insufficient vapor flow rate in this segment. Thus, only the bottom segment is considered here while analyzing the solution heat transfer coefficient. Table 4.3 also shows a summary of the *U* values and the associated experimental uncertainties. The values for *U* vary between 1065 - 2031 W m^{-2} K^{-1}, with an average value of 1424 W m^{-2} K^{-1}. Except for 3 test conditions (nominal solution concentration 48%, concentrated solution flow rate of 0.011 kg s^{-1}, coupling fluid inlet temperature 40°C, and refrigerant fraction 15-25%), the *U* was found to generally increase with an increase in the solution mass flux, though the increase

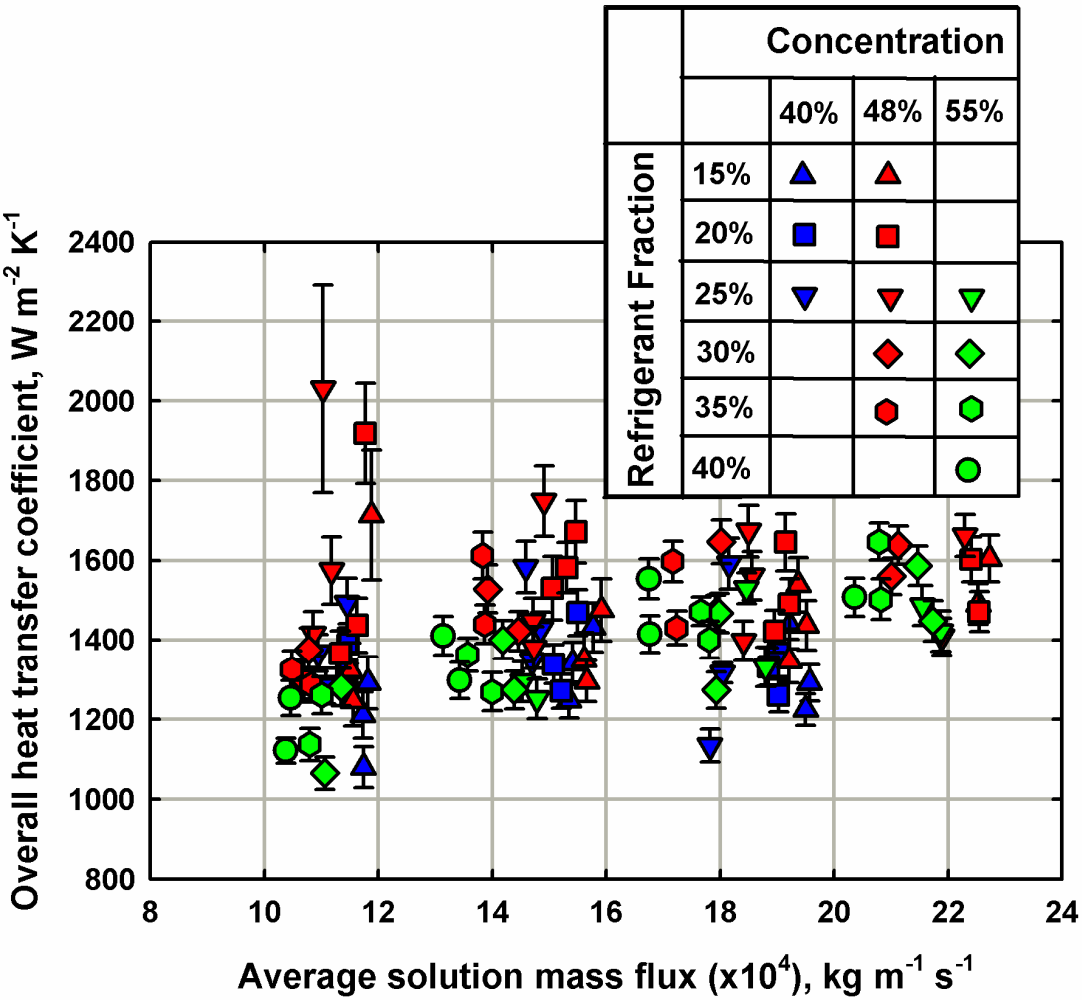

Fig. 4.14 Overall heat transfer coefficient as a function of average solution mass flux

is not very significant. The U is a function of the tube-side and the solution-side phenomena, and therefore more insight into the process can be achieved by considering only the solution heat transfer coefficient.

Fig. 4.15 shows the solution heat transfer coefficient as a function of the average linear mass flux based on the tube length for the bottom segment of the absorber. Table 4.3 also shows a summary of the solution heat transfer coefficient values and the

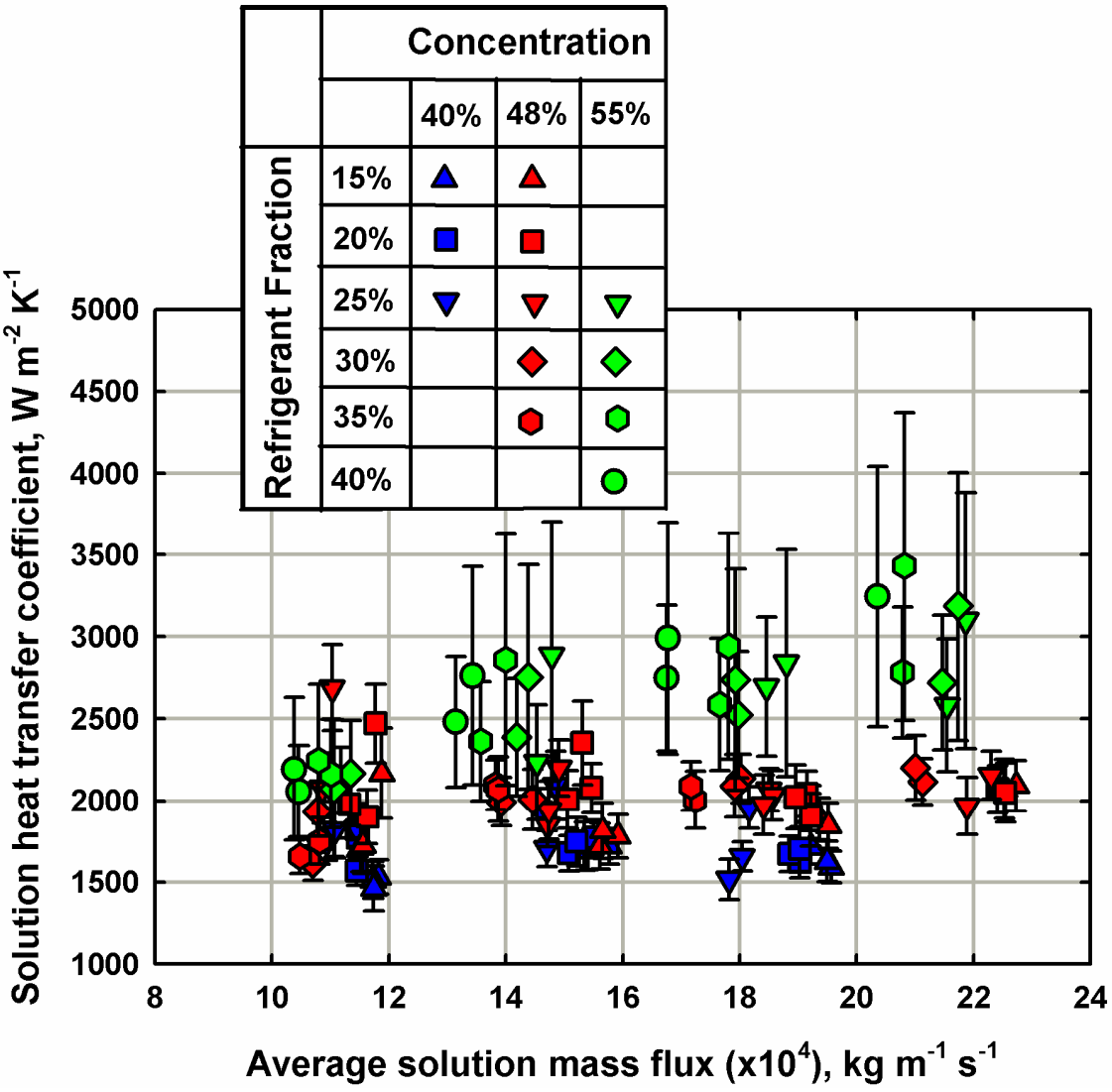

Fig. 4.15 Solution heat transfer coefficient as a function of average solution mass flux

associated experimental uncertainties. The heat transfer coefficients vary between 1461 - 3430 W m^{-2} K^{-1}, with an average value of 2110 W m^{-2} K^{-1}. The coupling fluid Reynolds numbers were found to vary between 2431 - 3748, indicating that the fluid is in transition between laminar and turbulent flow. The coupling fluid heat transfer coefficients were found to vary between 3032 - 13407 W m^{-2} K^{-1}, with an average value of 7888 W m^{-2} K^{-1}. The assigned uncertainty of ±25% in the coupling fluid heat transfer coefficient was found to be the highest contributor to the uncertainty of the calculated solution heat transfer coefficient. For example, the uncertainty associated with the solution heat transfer coefficient for the representative data point increased from ±99.11 to ±186.1 W m^{-2} K^{-1} (±5.2 to ±9.8%) as the uncertainty associated with the coupling fluid heat transfer coefficient was increased from 0 - 25%.

The higher uncertainties were observed for the test cases yielding higher solution heat transfer coefficients, where the resistance to heat transfer on the coupling fluid was significant, resulting in a higher uncertainty in the measured solution heat transfer coefficient. It should also be noted that a similar 25% uncertainty was assigned to the predictions from the correlation for the vapor heat transfer coefficient (Sparrow *et al.*, 2004) used in the heat and mass transfer analysis above. The contribution from this uncertainty to the uncertainty associated with the solution heat transfer coefficient was found to be marginal, with the uncertainty for the representative data point increasing from ±186.0 to ±186.1 W m^{-2} K^{-1} (±9.76% to ±9.75%) as the vapor heat transfer coefficient uncertainty was increased from 0 - 25%.

Higher solution heat transfer coefficients were generally observed for the higher solution concentration cases, although the refrigerant fractions were also higher for these cases. The vertical spread at any solution mass flux is due to an increasing vapor flow rate, and this spread increases with increasing solution mass flux. As the vapor flow rate increases, absorption duties also increase, resulting in higher solution heat transfer rates.

Also, with increasing vapor flow rate, countercurrent to the falling liquid, interfacial shear at the liquid film boundary probably increases, resulting in higher transfer rates.

Comparison with the literature

Fig. 4.16 shows a comparison of the solution heat transfer coefficient with values reported in similar studies from the literature. Table 4.4 shows a summary of these studies. It should be noted, however, that there are few studies in the literature that provide correlations for Nusselt numbers in the horizontal tube falling-film configuration specifically for ammonia-water absorption. In addition, there are no correlations

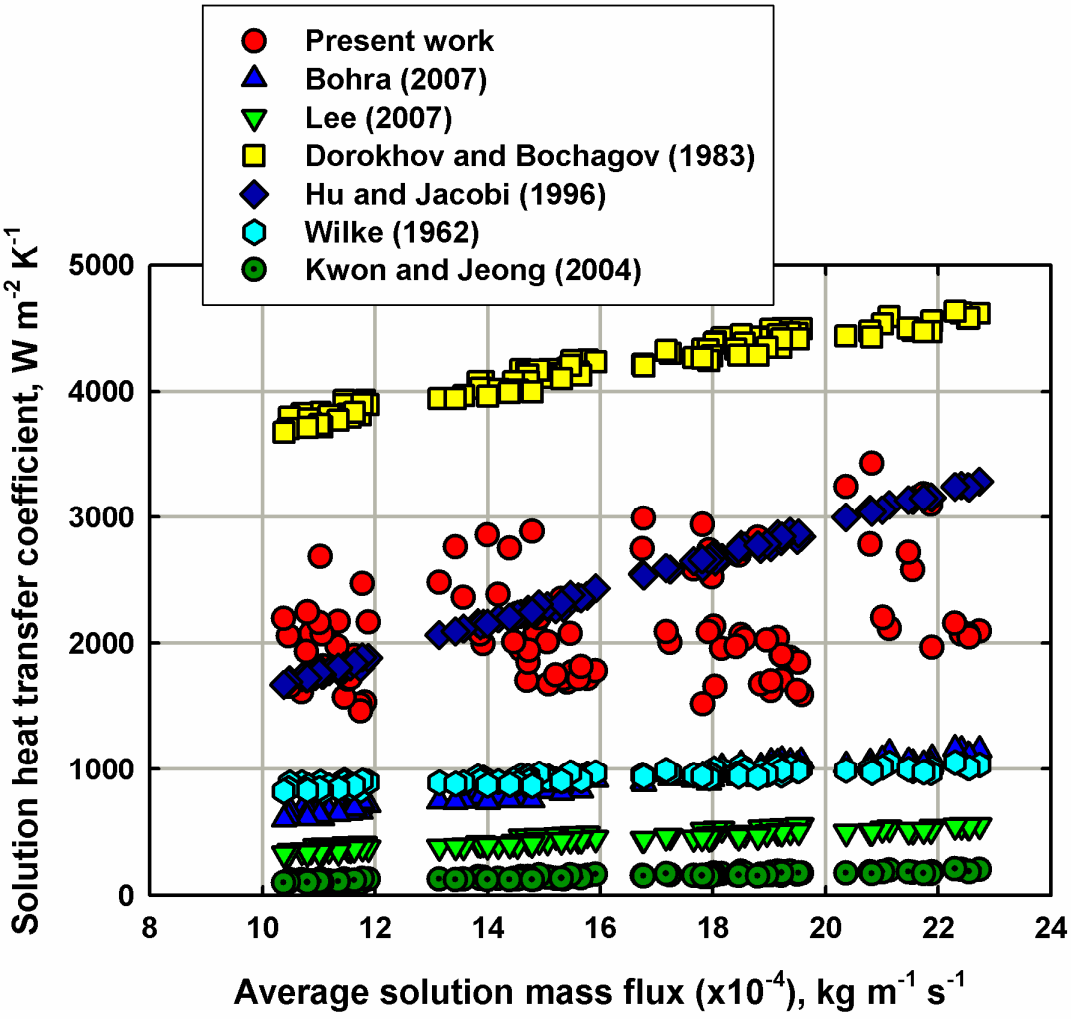

Fig. 4.16 Comparison of solution heat transfer coefficient with literature

developed for flow over microchannel tubes, which involve relatively thin films at low mass fluxes. Therefore, correlations or models for geometries and working fluids with at least some similarities to the present study are presented here. Because each of these studies has its own definition of dimensionless parameters, solution heat transfer coefficients predicted from each of the correlations are compared here *on a common basis*. The solution heat transfer coefficients are calculated according to the corresponding Nusselt number definitions in Table 4.4, while the average solution linear mass flux is calculated as $\Gamma_{\text{sol,avg}} = \dot{m}_{\text{sol,avg}} \big/ \left(N_{\text{tube}} \cdot L_{\text{tube}} \cdot 2 \right)$, where the factor of 2 in the denominator is used to account for the flow of solution on both sides of the tube. The correlation by Bohra (2007) was developed for falling-film absorption on 9.5 mm diameter horizontal tubes in a quiescent refrigerant vapor ambient, based on a segmental study. Lee (2007) developed a correlation for the whole absorber based on the same experimental study. Both these correlations under predict the solution heat transfer coefficient calculated in the present study. This is attributed to the fact that their study was conducted on larger diameter tubes, with thicker films and more developed boundary layers than is the case for the present microchannel configuration. Also, their study involved a quiescent vapor, with correspondingly low vapor-phase transport. The study by Dorokhov and Bochagov (1983) was conducted for water-LiBr absorption at low absorber pressures, leading to an over prediction of the present data by their correlation. Hu and Jacobi (1996b) and Wilke (1962) developed correlations based on water-glycol mixtures and other fluids in the absence of absorption for horizontal and vertical tube falling films, respectively. The disagreement of the present work with the correlation by Wilke (1962) is attributed to the differences in the flow configurations and working fluids between the two studies. Fluid properties, such as thermal conductivity and specific heat significantly influence the heat transfer process, and thus, these results must also be investigated in terms of dimensionless parameters such as Nusselt number and Reynolds number. These discussions are presented in the following chapter. The correlation by Hu

and Jacobi (1996b) predicts the present work reasonably well. However, their study does not have any vapor absorption, and therefore cannot predict the spread observed in the present work due to vapor flow. Kwon and Jeong (2004) developed a correlation for ammonia-water absorption on a 12.7 mm tube helical coil. Their correlation significantly under predicts the data from the present work. This is due to two main reasons: differences in the driving temperature difference and flow geometry. Their study was conducted when the solution flowed at near saturation temperature around the coil. Also, the flow mechanisms involved in the present study are different from those expected in their study. In a helical coil, the liquid phase flows along the coil in addition to flowing downwards across adjacent coils. This results in a very different film- and droplet-flow mechanism in comparison to the current geometry and thus, the resulting liquid phase mixing and associated heat and mass transfer rates are different.

Table 4.4 Summary of relevant heat transfer studies

	Type and Fluid	Mass Transfer /Phase Change	Geometry	Γ_l (kg m^{-1} s^{-1})	Film Thickness δ (m)	Re_l	Nu_l	Applicability
Present work	Horizontal Tube (NH_3/ H_2O)	Yes	Tube Length: 0.137 m Tube OD: 1.575 mm	$\frac{\dot{m}}{N_{t,pr} \cdot L_t \cdot 2}$	$\left[\frac{3 \cdot \mu_l \cdot \Gamma_l}{g \cdot \rho_l^2}\right]^{1/3} \cdot \frac{2}{\pi} \cdot \int_0^{\pi/2} \sin^{-1/3}\theta \cdot d\theta$			
Bohra (2007)	Horizontal Tube (NH_3/ H_2O)	Yes	Tube Length: 0.292 m Tube OD: 9.5 mm	$\frac{\dot{m}}{N_{t,pr} \cdot L_t \cdot 2}$	$\left[\frac{3 \cdot \mu_l \cdot \Gamma_l}{g \cdot \rho_l^2}\right]^{1/3} \cdot \frac{2}{\pi} \cdot \int_0^{\pi/2} \sin^{-1/3}\theta \cdot d\theta$	$\frac{4 \cdot \Gamma}{\mu}$	$7.589\times10^{-3} \cdot Re^{1.043} \cdot Pr^{0.455} \cdot \left(\frac{P_{abs}}{345\,kPa}\right)^{-0.145}$	$26 < Re < 157$ $2.2 < Pr < 10.4$
Lee (2007)	Horizontal Tube (NH_3/ H_2O)	Yes	Tube Length: 0.292 m Tube OD: 9.5 mm	$\frac{\dot{m}}{N_{t,pr} \cdot L_t \cdot 2}$	$\left[\frac{3 \cdot \mu_l \cdot \Gamma_l}{g \cdot \rho_l^2}\right]^{1/3} \cdot \frac{2}{\pi} \cdot \int_0^{\pi/2} \sin^{-1/3}\theta \cdot d\theta$	$\frac{4 \cdot \Gamma}{\mu}$	$3.22\times10^{-3} \cdot Re^{0.945} \cdot Pr^{0.743} \cdot \left(\frac{P_{abs}}{345\,kPa}\right)^{-0.269}$	$26 < Re < 157$ $2.2 < Pr < 10.4$
Kwon and Jeong (2004)	Helical Coil (NH_3/ H_2O)	Yes	OD: 12.7 Coil OD: 82.7 Coil Windings: 30	$\frac{\dot{m}}{N_{t,pr} \cdot L_t}$	$\left(\frac{\nu^2}{g}\right)^{\frac{1}{3}}$	$\frac{2 \cdot \Gamma}{\mu}$	$1.975\times10^{-3} \cdot Re^{0.6895} \cdot \tau^{-0.02}$	Parallel Flow $10 < Re < 250$

Table 4.4 Continued...

	Type and Fluid	Mass Transfer /Phase Change	Geometry	Γ_l (kg m^{-1} s^{-1})	Film Thickness δ (m)	Re_l	Nu_l	Applicability
Wilke (1962)	Vertical Tube (H_2O/ Glycol mixture)	No	Tube Length: 2.5 m Tube OD: 42 mm	$\frac{\dot{m}}{N_{t,pr} \cdot L_t \cdot 2}$	$\left[\frac{3 \cdot \mu_l \cdot \Gamma_l}{g \cdot \rho_l^2}\right]^{1/3} \cdot \frac{2}{\pi} \cdot \int_0^{\pi/2} \sin^{-1/3}\theta \cdot d\theta$	$\frac{\Gamma}{\mu}$	$0.0614 \cdot Re^{8/15} \cdot Pr^{0.344}$ $0.00122 \cdot Re^{6/15} \cdot Pr^{0.344}$ $0.0066 \cdot Re^{14/15} \cdot Pr^{0.344}$	$Re < 400$ $400 < Re < 800$ $Re > 800$
Dorokhov and Bochagov (1983)	Horizontal Tube (H_2O/ LiBr)	Yes	Tube OD: 19 mm Tube Length: 240 mm Tube Spacing: 28.12 mm	$\frac{\dot{m}}{N_{t,pr} \cdot L_t \cdot 2}$	$\left[\frac{3 \cdot \mu_l \cdot \Gamma_l}{g \cdot \rho_l^2}\right]^{1/3} \cdot \frac{2}{\pi} \cdot \int_0^{\pi/2} \sin^{-1/3}\theta \cdot d\theta$	$\frac{\Gamma}{\mu}$	$1.03 \cdot \left(2 \cdot Pe \cdot \frac{\delta}{\pi \cdot D_o}\right)^{0.44}$	$1 < \frac{2 \cdot Pe \cdot \delta}{\pi \cdot D_o} < 20$

Table 4.4 Continued...

	Type and Fluid	Mass Transfer /Phase Change	Geometry	Γ_l (kg m^{-1} s^{-1})	Film Thickness δ (m)	Re_l	Nu_l	Applicability
Hu and Jacobi (1996b)	Horizontal Tube (H_2O and Glycol and mixtures)	No	Tube OD:15.88, 19.05, 22.22 Tube Spacing: 5–50 Groove Depth : 0.51, 0.76 Groove Width : 2.54, 0.81 Height: 0.15 m Absorber Area: 0.45m^2	$\frac{\dot{m}}{N_{t,pr} \cdot L_t}$	$\left(\frac{\nu^2}{g}\right)^{\frac{1}{3}}$	$\frac{2 \cdot \Gamma}{\mu}$	$0.113 \cdot Re^{0.85} \cdot Pr^{0.85} \cdot Ar^{-0.27} \cdot \left(\frac{S_L}{D_o}\right)^{0.04}$	Droplet mode

4.4. Summary

This chapter presented the methodology used to determine the thermodynamic state of the solution and refrigerant around the test loop, the heat duties of each component, and the heat and mass transfer rates in the absorber from the measured experimental data. The microchannel absorber was found to transfer duties in excess of 10 kW in a compact envelope. The bulk of the absorption was found to occur in the lower half of the absorber, indicating that the absorber was capable of transferring larger duties under different operating conditions. Solution heat transfer coefficients were found to vary between 1461 - 3430 W m^{-2} K^{-1}. The calculated heat transfer coefficients were also compared with relevant correlations from the literature. The applicability of these correlations to the present study is limited due to significant differences in working fluid pair, and/or absorber geometry and the associated flow mechanisms, and operating conditions. In particular, none of these studies was conducted on microchannel tubes, where the heat transfer and flow mechanisms are different from those observed on large tubes. While solution flows around horizontal microchannel tubes as thin films, it progresses from one tube row to another as droplets. These local flow phenomena significantly affect the absorption process, and thus models are needed to account for the underlying mechanism for the falling film, as well as the evolving droplets in the inter-tube region. Development of such models is discussed in the next chapter.

CHAPTER 5. MODELING OF LOCAL HEAT AND MASS TRANSFER RATES

Several flow modes (or flow structures) have been observed when liquid films fall over a vertical row of horizontal tubes. While liquid typically flows as a film over the tube, the flow between successive tube rows exhibits several modes, such as uniform sheets, columns, and droplets. These flow regimes have been studied in the past and were found to affect the heat and mass transfer characteristics significantly (Hu and Jacobi, 1996a, b). Mitrovic (2005) presented a summary of the studies on flow transitions between different flow modes observed during falling-film flow around horizontal round tubes, and developed correlations for flow transition criteria based on the liquid Reynolds number and the Kapitza number. The transition from one mode to another depends upon the liquid flow rate, the liquid physical properties, tube geometry, and surface properties. At very low liquid flow rates, the flow between consecutive tube rows is in the form of droplets. This is often called the "droplet mode" flow. As the liquid flow rate increases, columns or jets are observed to form between successive tube rows. This is called the "droplet-column" or "droplet-jet mode" flow, where both droplets and jets exist between successive tube rows. Droplets completely cease to exist as the liquid flow rate is further increased, resulting in transition to "column" or "jet mode" flow. Partial sheets are formed when the liquid flow rate is further increased indicating transition to "column-sheet" or "jet-sheet mode" flow. At very high liquid flow rates, the flow between successive tube rows is in the form of sheets, which is called "sheet mode" flow.

The droplet mode is the preferred flow mode for absorber applications because the thin films on the tube (due to low solution flow rates) promote high heat transfer rates, while the formation and impact of droplets on tubes provides additional surface area for absorption and promotes mixing of solution on the tube surface, facilitating high mass transfer rates. Droplet formation is a phenomenon related to Rayleigh instabilities

(Carey, 1992). The formation, detachment, and fall of droplets in horizontal tube banks was described by Killion and Garimella (2003). Instabilities in the liquid film around the tube are initially driven by surface tension forces. As liquid accumulates at the bottom of the tube, resulting in local thickening of the film, buoyancy or gravity forces amplify these instabilities, resulting in the creation of droplet formation sites. These droplet formation sites are formed near the so-called most dangerous wavelength. As liquid accumulates at these sites, gravity pulls the droplet further away from the tube resulting in elongation of the droplet. As the droplet continues to grow due to fresh supply of liquid from the film, it reaches a critical volume beyond which it is unstable. Gravitational forces start to become significant (due to increasing mass), pulling the droplet further away from the tube, resulting in the formation of a neck in the liquid bridge between the droplet and the film. Depending upon the tube spacing, the droplet can break away from the film resulting in a free-falling droplet. Several factors influence the formation and break up of droplets. For example, the incidence of a droplet impacting from a tube above often leads to local excess of liquid that can initiate a new droplet formation site directly under the impact site. Additionally, when the primary droplet detaches from a tube, a significant portion of liquid is left behind which often results in the formation of secondary droplets. Furthermore, due to propagating waves on the underside of the tube, local excess of liquid can be developed at certain locations resulting in formation of new droplet sites.

Fig. 5.1 shows a photograph of the progression of the flow of solution over successive tube rows including the liquid film, droplet formation, growth and detachment, and redistribution of liquid. This figure was taken from the study conducted by Meacham and Garimella (2004), who visualized the flow mechanisms associated with the absorption process on microchannel tube arrays. High speed video was taken of the flow and each image in the figure was sampled at 10 ms time intervals. Local thickening of the film on the underside of the tube and creation of a droplet formation site is

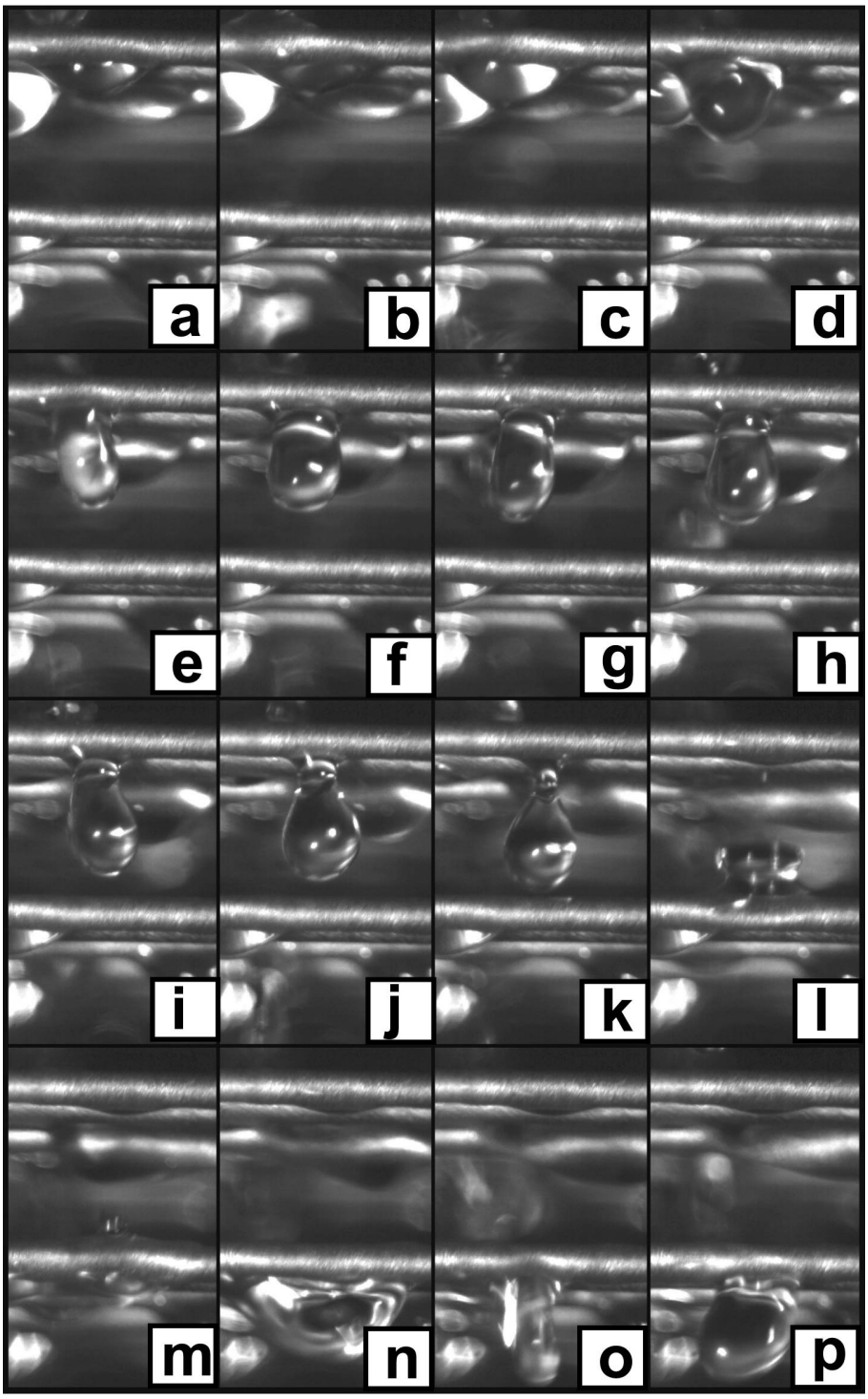

Fig. 5.1 Flow progression over the microchannel tubes at 10 ms intervals (Meacham and Garimella, 2004)

apparent in Fig. 5.1a. As more liquid is supplied to this site, the droplet starts to grow (Figs. 5.1b-f). The first signs of necking can be seen in Fig. 5.1g and droplet detachment

occurs just after the instance seen in Fig 5.1k. It is interesting to observe that the shape of the droplet at the instant of detachment is that of a hemisphere with a conical top. Killion and Garimella (2003) observed that, for large tubes (12.7 mm outer diameter), at the time of detachment, the droplet was is the shape of a nearly complete sphere with a thin cylindrical liquid bridge connecting the sphere and the tube. The present observation might be due to the use of the smaller diameter microchannel tubes (1.575 mm outer diameter), which result in formation of smaller droplets where the influences of surface tension and gravity are different. Droplet free-fall can be seen in Fig. 5.1l, and as expected, the duration is very short. Redistribution of liquid due to impact of droplet can be seen in Fig. 5.1m, indicating rapid and intense mixing of the solution, which is highly favorable for the absorption process. Subsequent thickening of the film and formation of a new droplet site can be seen in Figs. 5.1o-p.

The following sections present the development of a simplified hydrodynamic model that captures these flow mechanisms in both the liquid film and the evolving droplet. This hydrodynamic model is then coupled with the heat and mass transfer model, to account for the influence and estimate the contribution to the absorption process from each flow mechanism.

5.1. Droplet formation, growth, and break up

The droplet mode was visually observed to be the primary flow mode for flow between successive tube rows during the absorption experiments conducted on the microchannel absorber in the present study. This was also demonstrated in the visual data obtained by Meacham and Garimella (2004) for similar geometries and flow rates. Additionally, the solution Reynolds number was compared with the transition criteria developed by Mitrovic (1986) and Hu and Jacobi (1996a), presented on a *common basis* in Mitrovic (2005).

$$Re_{\text{sol,cr,Mitrovic}} = 0.34 \cdot Ka^{1/4} \tag{5.1}$$

$$Re_{\text{sol,cr,Hu\&Jacobi}} = 0.037 \cdot Ka^{0.302} \tag{5.2}$$

In the above relations, $Re_{\text{sol,cr}}$ was the critical solution Reynolds number for transition from droplet to jet mode flow and Ka was the Kapitza number defined as follows:

$$Ka = \frac{\sigma_{\text{sol}}^3 \cdot \rho_{\text{sol}}}{\mu_{\text{sol}}^4 \cdot g} \tag{5.3}$$

The solution Reynolds number for flow over the tube banks was defined as follows:

$$Re_{\text{sol}} = \frac{4 \cdot \Gamma_{\text{sol}}}{\mu_{\text{sol}}} \tag{5.4}$$

In the above equation, the solution linear mass flux is calculated as $\Gamma_{\text{sol}} = \dot{m}_{\text{sol}} / \left(N_{\text{tube}} \cdot L_{\text{tube}} \cdot 2 \right)$, where the factor of 2 in the denominator is used to account for the flow of solution on both sides of the tube. For the representative test condition considered in the previous chapter, the solution Kapitza number was calculated to be 1.24×10^{10}, and the critical solution Reynolds numbers were $Re_{\text{sol,cr,Mitrovic}}$ = 113.3 and $Re_{\text{sol,cr,Hu\&Jacobi}}$ = 41.30. For the representative test condition, the solution Reynolds number, Re_{sol}, is 11.3, which is well below the critical solution Reynolds number predicted by both correlations. For the entire set of test conditions, $Re_{\text{sol,cr,Mitrovic}}$ varied between 104.9 – 130.1 and $Re_{\text{sol,cr,Hu\&Jacobi}}$ varied between 37.6 – 48.8, while the Re_{sol} varied between 6.1 – 14.9, indicating that the solution Reynolds number was well below the critical Reynolds number predicted by both the transition criteria, confirming that the dominant flow mechanism between successive tube rows is the droplet mode.

To model the hydrodynamics of the droplet mode flow, a representative primary droplet was considered. All droplets in a segment were assumed to be similar to this primary droplet and secondary droplets were neglected. The spacing between adjacent droplets was estimated by considering the most dangerous wavelength, and the effects of

droplet impact from previous tube row and waves on underside of the tubes were neglected. Several droplet characteristics such as droplet mass, spacing, frequency, and transfer area can be estimated using these assumptions, which are discussed below. All the sample calculations reported in the following sections correspond to the bottom segment of the absorber.

5.1.1. Primary droplet

Yung *et al.* (1980) developed a correlation for the diameter of the primary droplet, detaching from a tube of diameter 38 mm, which is based only on the solution properties.

$$D_{\text{drop}} = 3 \cdot \left(\frac{\sigma}{\rho \cdot g} \right)^{1/2} \tag{5.5}$$

They observed that the primary droplet at the instant of detachment was in the shape of a nearly complete sphere with a thin cylindrical liquid bridge connecting the sphere and the tube. A similar shape was described later by Killion and Garimella (2003) for 12.7 mm diameter tubes (discussed above). It should be noted that in both the above studies, the tube diameters were larger than the diameter of the primary droplet. The diameter of the droplet calculated from the above correlation for the representative test case was 5.85×10^{-3} m. This droplet diameter is nearly 4 times the diameter of the microchannel tube under consideration in the present study. Because the supply of liquid to the droplet is from the film on the tube surface, it is expected that the maximum possible diameter of the primary droplet will be equal to the total diameter of the tube (including the additional film thickness.) For large diameter tubes, the correlation by Yung *et al.* (1980) predicts, acceptable primary droplet diameter values. However, for microchannels tubes, the tube diameter becomes important, and thus their correlation cannot accurately predict the primary droplet diameter. In addition, as discussed previously, the shape of the primary droplet at the instant of detachment is that of a hemisphere with a conical top (Fig. 5.1k) which is significantly different from the shape

observed in their study. Thus, for microchannel tubes, the following methodology was developed to determine the various primary droplet characteristics.

Fig. 5.2 shows a schematic of this primary droplet just before detachment from the tube. As the droplet starts evolving, the hemispherical section is first created. Liquid is supplied to this section from the film around the microchannel tube. Thus, the diameter of the hemispherical section is equal to the sum of the diameter of the tube and twice the film thickness in the Feed region.

$$D_{\text{hem}} = D_{\text{o}} + 2 \cdot \delta_{\text{f,feed}} \tag{5.6}$$

$$D_{\text{hem}} = 1.575 \times 10^{-3}\ \text{m} + 2 \times 1.766 \times 10^{-4}\ \text{m} = 1.928 \times 10^{-3}\ \text{m} \tag{5.7}$$

The feed region is the region directly above the droplet formation site, which essentially feeds all the liquid into the droplet. The flow in this region is discussed in further detail later. The thickness of the film in this region is different from the average thickness of the film calculated previously, and is also calculated later. However, for

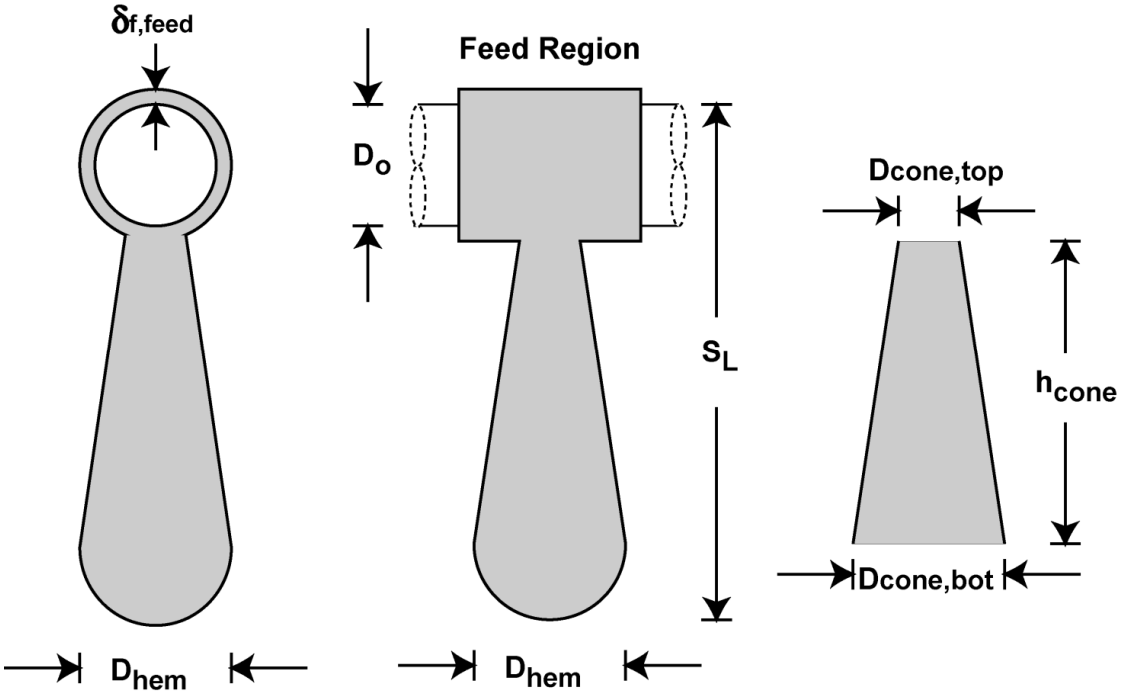

Fig. 5.2 Schematic of primary droplet

convenience, the value is shown below the equations.

The diameter of the bottom of the conical section is equal to the diameter of the hemispherical section.

$$D_{\text{cone,bot}} = D_{\text{hem}} = 1.928\times10^{-3}\ \text{m} \tag{5.8}$$

The total height of the droplet was assumed to be equal to the spacing between successive tube rows. Thus, the height of the conical section can be estimated as follows:

$$h_{\text{cone}} = S_{\text{L}} - D_{\text{o}} - \frac{1}{2}D_{\text{hem}} = 5.401\times10^{-3}\ \text{m} \tag{5.9}$$

At the instant of detachment, the weight of the droplet is equal to the surface tension acting at the circumference of the neck. Thus, the diameter of the top of the conical section was estimated by balancing the gravity forces with the surface tension forces. The surface tension force acting at the circumference of the neck was calculated as follows:

$$F_{\text{ST}} = \sigma\cdot\left(\pi\cdot D_{\text{cone,top}}\right) \tag{5.10}$$

The weight of the droplet was calculated as follows:

$$W_{\text{drop}} = \rho_{\text{sol}}\cdot\left(V_{\text{hem}} + V_{\text{cone}}\right)\cdot g \tag{5.11}$$

In the above equation, V_{hem} and V_{cone} are the volumes of the hemispherical and conical sections, respectively, which were calculated as follows:

$$V_{\text{hem}} = \frac{2}{3}\cdot\pi\cdot\left(\frac{D_{\text{hem}}}{2}\right)^3 \tag{5.12}$$

$$V_{\text{cone}} = \frac{1}{3}\cdot\pi\cdot\left(h_{\text{cone,max}}\cdot\frac{D_{\text{cone,bot}}^2}{4} - \left(h_{\text{cone,max}} - h_{\text{cone}}\right)\cdot\frac{D_{\text{cone,top}}^2}{4}\right) \tag{5.13}$$

In the above equation, $h_{\text{cone,max}}$ is the maximum cone height, which was calculated based on the principles of similar triangles using the following equation.

$$h_{\text{cone,max}} = \frac{D_{\text{cone,bot}}}{D_{\text{cone,top}}}\cdot h_{\text{cone}} \tag{5.14}$$

For the representative data point, the surface tension force and weight of the droplet were iteratively calculated to be 8.82×10^{-5} N. The diameter of the top of the conical section was calculated to be 8.98×10^{-4} m, and the maximum cone height was estimated to be 1.01×10^{-2} m. The volume of the hemispherical section, the conical section, and the whole droplet were estimated to be 1.877×10^{-9}, 8.843×10^{-9}, and 1.072×10^{-8} m^3, respectively. Thus, the characteristics of the droplet at the instant of detachment from the tube are known. Next the spacing between such primary droplets is estimated.

5.1.2. Droplet spacing and frequency

Droplet formation sites were assumed to be equally spaced on the tube underside, with the spacing dictated by the Taylor instabilities. The spacing between adjacent droplets was assumed to be approximately equal to the so-called most dangerous wavelength, λ_{drop}. Armbruster and Mitrovic (1998) presented a modified equation for the most dangerous wavelength by accounting for the influence of liquid flow.

$$\lambda_{drop} = \frac{2\cdot\pi\cdot\sqrt{2}}{\sqrt{\frac{g\cdot\Delta\rho}{\sigma}\left(1+\left(\frac{Re_{sol}}{Ka^{0.25}}\right)^{0.8}\right)+\frac{2}{D_o^2}}} \tag{5.15}$$

In the above equation, $\Delta\rho$ is difference between the densities of the solution and vapor. The most unstable wavelength for the representative test condition was calculated to be 8.558×10^{-3} m. The total number of droplet formation sites at any row was estimated as follows:

$$N_{drop,pr} = \frac{N_{tube,pr}\cdot L_{tube}}{\lambda_{drop}} \tag{5.16}$$

In the above equation, $N_{tube,pr}$ is the number of tubes per row (33 for the present absorber), and L_{tube} is the tube length. For the representative test condition, the number of droplet sites per tube row was approximately 539. While this number provides the

number of droplets on a tube row at any instant, several droplets might be created at the same location per second. The total number of droplets in any tube row per second can be estimated from the solution mass flow rate as follows:

$$N_{\text{drop,ps}} = \frac{\dot{m}_{\text{sol}}}{m_{\text{drop}}} \tag{5.17}$$

$$N_{\text{drop,ps}} = \frac{1.772\times10^{-2}\ \text{kg s}^{-1}}{8.99\times10^{-6}\ \text{kg}} = 1971\,\text{s}^{-1} \tag{5.18}$$

In the above equation, m_{drop}, is the mass of the primary droplet just before detachment, as calculated above. Thus, while there were 539 active droplet formation sites at any tube row, a total of 1971 droplets were created every second. Thus, the droplet formation time was calculated as follows:

$$t_{\text{drop}} = \frac{N_{\text{drop,pr}}}{N_{\text{drop,ps}}} = 0.273\,\text{s} \tag{5.19}$$

Based on the above estimates, for the representative test condition, nearly 4 droplets are created each second at each droplet formation site. For the 103 data points considered in this study, the droplet formation time ranged between 0.235-0.462 s, with an average formation time of 0.333 s. This result compares well with the visual data obtained previously by Meacham and Garimella (2004) where the droplet formation time was 0.2 s (for a slightly higher solution flow rate).

5.1.3. Droplet surface area

The droplet volume calculated above is the volume of the droplet at the time of detachment. The volume and the surface area of the droplet as it is evolving vary with time. Thus, an average droplet surface area was defined, and estimated over the formation time of the droplet, which can be incorporated into heat and mass transfer models described in a subsequent section.

Killion and Garimella (2004a) quantitatively analyzed the motion of a pendant droplet on horizontal tube banks and plotted the variation of droplet volume with time. In their work, the droplet volume growth rate was nearly constant until the instant of detachment. Thus, to simplify the hydrodynamic model, the droplet was assumed to grow at a uniform rate. Fig. 5.3 shows a schematic of the evolving droplet at various instants of time. As previously discussed, as liquid starts accumulating at the droplet formation site, the hemispherical section is first created. At time $t = t_{hem}$, the hemispherical section is completely evolved, and the formation of the conical section is initiated. The conical section continues to grow until detachment, which occurs at time $t = t_{drop}$. It can be seen

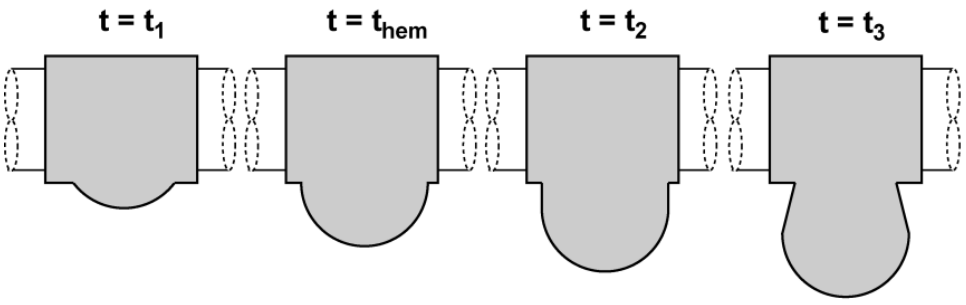

a. Hemisphere formation stage

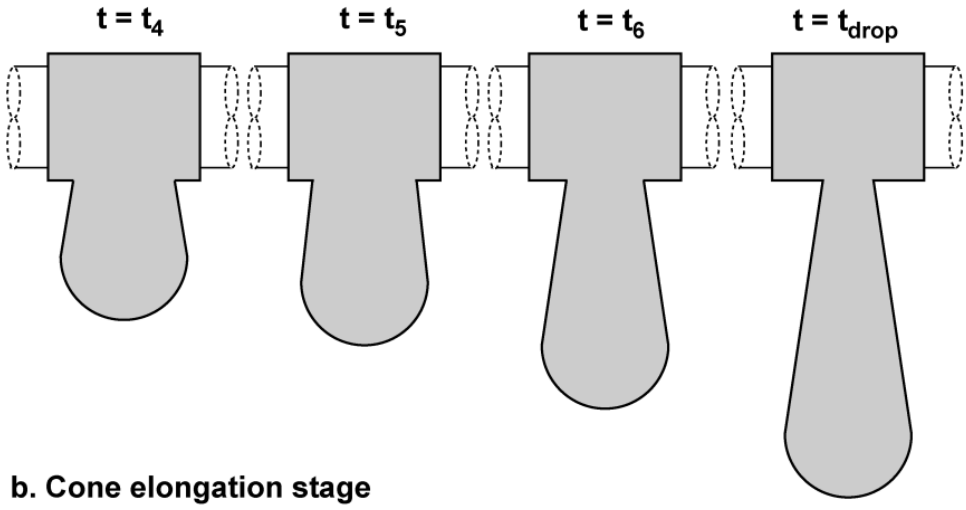

b. Cone elongation stage

Fig. 5.3 Schematic of evolving droplet

in Fig. 5.1 that the shape of the hemispherical section does change during the formation time of the conical section; however, this change is relatively small. Therefore, for simplicity, it is assumed that the shape of the hemispherical section remains the same during this time. Because uniform droplet growth rate was assumed, the formation time for the hemispherical and conical sections of the droplet can be estimated based on their volumes as follows.

$$t_{\text{hem}} = \frac{V_{\text{hem}}}{V_{\text{drop}}} \cdot t_{\text{drop}} \tag{5.20}$$

$$t_{\text{hem}} = \frac{1.88\times10^{-9}\ \text{m}^3}{1.07\times10^{-8}\ \text{m}^3} \cdot 0.2734\,\text{s} = 0.0479\,\text{s} \tag{5.21}$$

$$t_{\text{cone}} = t_{\text{drop}} - t_{\text{hem}} = 0.2255\,\text{s} \tag{5.22}$$

The surface area of a section of the hemisphere and the cone at any instant of time can be calculated based on geometric principles. The average surface area of the hemispherical section during its formation can be calculated by taking an average over the hemisphere formation time as follows.

$$\overline{A}_{\text{hem}} = \frac{\int_0^{t_{\text{hem}}} A_{\text{hem}}(t) \cdot dt}{t_{\text{hem}}} = \frac{5}{4} \cdot \pi \cdot \frac{D_{\text{hem}}^2}{4} \tag{5.23}$$

Similarly, the average surface area of the conical section during its formation can be estimated by taking an average over the cone formation time as follows.

$$\begin{aligned} \overline{A}_{\text{cone}} &= \frac{\int_0^{t_{\text{cone}}} A_{\text{cone}}(t) \cdot dt}{t_{\text{cone}}} \\ &= \frac{\pi}{4 \cdot \sin\theta} \cdot \left(D_{\text{cone,bot}}^2 - \frac{3}{5} \frac{D_{\text{cone,bot}}^4 \cdot h_{\text{cone,max}} - D_{\text{cone,top}}^4 \cdot \left(h_{\text{cone,max}} - h_{\text{cone}}\right)}{D_{\text{cone,bot}}^2 \cdot h_{\text{cone,max}} - D_{\text{cone,top}}^2 \cdot \left(h_{\text{cone,max}} - h_{\text{cone}}\right)} \right) \end{aligned} \tag{5.24}$$

In the above equation, θ is the half angle of the cone (shown in Appendix C). Further details on the estimation of instantaneous and average transfer areas of the hemispherical and conical sections are provided in Appendix C. The average surface area

of the whole droplet over its formation time is equal to the weighted average of the contribution from the hemispherical and the conical sections and was calculated as follows:

$$\bar{A}_{\text{drop}} = \frac{\bar{A}_{\text{hem}} \cdot t_{\text{hem}} + \left(A_{\text{hem}} + \bar{A}_{\text{cone}} \right) \cdot t_{\text{cone}}}{t_{\text{drop}}} \tag{5.25}$$

In the above equation, A_{hem} is the surface area of the hemisphere, which is completely formed while the conical section is evolving. For the representative test condition, the maximum surface area of the hemispherical and conical sections were calculated to be $A_{\text{hem}} = 5.84\times10^{-6}$ m^2 and $A_{\text{cone}} = 2.41\times10^{-5}$ m^2. The average surface areas were calculated to be $\bar{A}_{\text{hem}} = 3.65\times10^{-6}$ m^2, $\bar{A}_{\text{cone}} = 1.07\times10^{-5}$ m^2, and $\bar{A}_{\text{drop}} = 1.43\times10^{-5}$ m^2. The total surface area of the droplet at the moment of detachment is the sum of the total surface areas of the hemispherical and conical sections, and was equal to be 2.99×10^{-5} m^2. All the above calculations for the droplet characteristics were conducted at the average segment conditions. The characteristics of the film upon impact of this primary droplet on the tube surface are discussed next.

5.2. Film formation and spreading

Most studies on falling films in the literature assume tube surfaces to be completely wet with a uniform laminar film. However, several visual studies have confirmed that, particularly in droplet mode flow between successive tube rows, the characteristics of the film over the tube surface are significantly different (Killion and Garimella, 2003; Bohra, 2007). When a droplet first falls on the tube, the bulk of the liquid accumulates locally at the top surface of the tube. The impact of the droplet on the tube surface also induces rapid mixing due to the dramatic change in the momentum of the liquid in the droplet, which often results in the formation of waves. At the instant of droplet impact, the tube surface is covered with a small inventory of liquid. As the liquid spreads, it starts to wet the tube surface, and the film flow can be idealized as a “stretched

triangle" on the tube surface. Additionally, the thickness of the film varies along the tube surface, with the thickest film observed close to the droplet impact region and thinning out away from it. Thus, it can be seen that due to the intermittent nature of the droplet mode flow between successive tube rows, the wet region of the tube varies with time and the thickness of the film varies with both time and location. These characteristics indicate that a uniform laminar film assumption for the flow over the tube surface is not adequate. To address these flow mechanisms, a mathematical model for spreading of the liquid film on the tube surface is described next.

Fig. 5.4 shows a schematic of the solution film and droplet at an instant of time during the droplet evolution. The film on the tube surface can be classified into three regions: the Feed region, the Spread region, and the Inactive region. Feed region is defined as the region directly above the droplet which supplies liquid to the evolving droplet (indicated by the dashed region in Fig. 5.4). The liquid film is typically thickest in this region due to accumulation of liquid locally near the droplet formation/impact site, as previously discussed. Solution is supplied to the film by an impinging droplet on the upper surface of the tube. While some of this solution flows through the Feed region and enters the droplet, a larger fraction spreads horizontally along the tube surface on either side of the Feed region as a stretching triangle, as discussed earlier. This region can be considered as the Spread region (indicated by the shaded triangular region). The surface area of the Spread region is continuously changing as the wave propagates along the tube

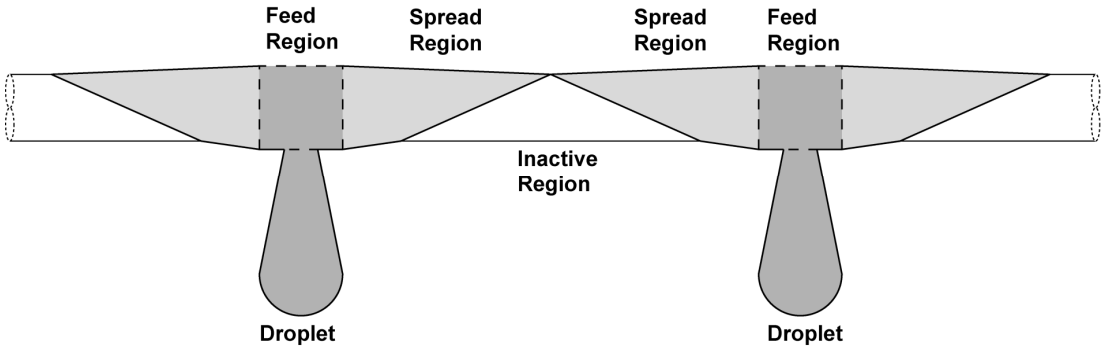

Fig. 5.4 Schematic of film and droplet at an instant of time

surface. In addition, the thickness of the film in this region varies with both time and location. The region ahead of the propagating wave front in the Spread region is termed the Inactive region. The Inactive region is continuously decreasing in surface area as the spread region grows. This region typically contains liquid left over from previous waves or very little liquid, and is considered inactive from a heat and mass transfer perspective. Vapor cannot undergo condensation in this region because the tube wall temperature is higher than the saturation temperature of the vapor (the saturation temperature is ~5^{o}C, while the wall temperature is ~40^{o}C.) Furthermore, any leftover liquid from previous waves in this region is at a higher concentration, and therefore the absorption rate is expected to be much lower than in the other two regions. This region might contribute to some sensible heat transfer with the vapor bulk, but as previously discussed, the total vapor sensible duty was found to be very low compared to the total absorption duty. Therefore, for simplicity, heat and mass transfer interactions in this region are neglected.

5.2.1. Feed region

Fig. 5.5 shows a closer view of the different film regions. The width of the Feed region was assumed to be constant and equal to the diameter of the hemispherical section of the droplet, throughout the droplet evolution process. This is equal to the maximum width of the primary droplet. Because the droplet was assumed to grow at a uniform rate, the flow rate of solution in this region is equal to the flow rate of solution into the droplet. Thus, the thickness of the film can be calculated as follows:

$$\delta_{\text{feed}} = \frac{\dot{V}_{\text{drop}}}{2 \cdot W_{\text{feed}} \cdot \overline{u}_{\text{film,feed}}} \tag{5.26}$$

In the above equation, the denominator is multiplied by 2 to account for flow on both sides of the tube. $\dot{V}_{\text{drop}}$ is the rate of increase of droplet volume and $\overline{u}_{\text{film,feed}}$ is the average film velocity in the Feed region, which was estimated by integrating the tangential velocity over the film thickness and the tube curvature.

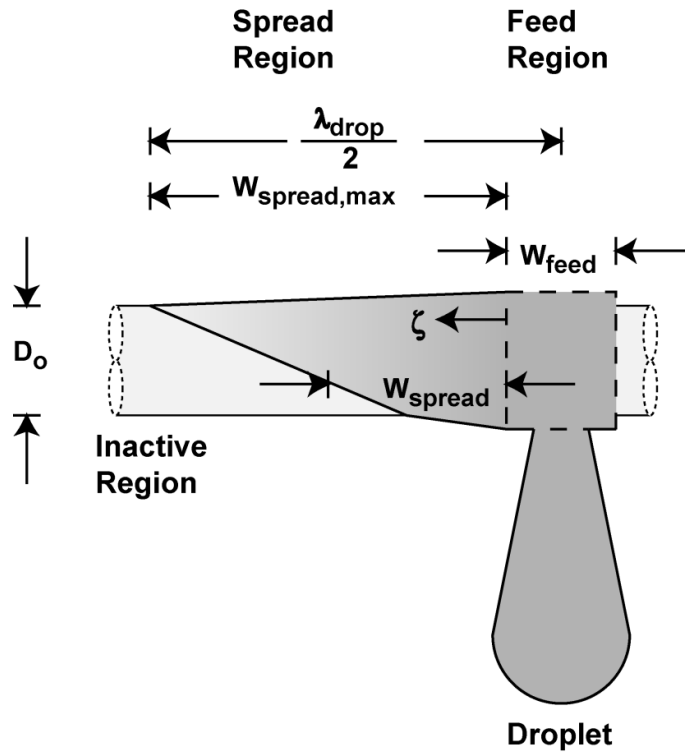

Fig. 5.5 Schematic of film regions

$$u(y,\theta) = \frac{\rho_{sol} \cdot g}{\mu_{sol}} \cdot \left(\delta_{feed} \cdot y - \frac{y^2}{2} \right) \cdot \sin\theta \tag{5.27}$$

$$\overline{u}_{film,feed} = \iint u(y,\theta) \cdot dy \cdot d\theta \tag{5.28}$$

Simplifying this equation in terms of known parameters results in the following equation:

$$\overline{u}_{film,feed} = \frac{1}{3} \cdot \left(\frac{\rho_{sol} \cdot g}{\mu_{sol}} \right)^{1/3} \cdot \left(\frac{3 \cdot \dot{V}_{drop}}{2 \cdot D_o} \right)^{1/3} \cdot \frac{2}{\pi} \cdot 1.294 \tag{5.29}$$

It should be noted that in the present work, the duration of the droplet in free-fall between successive tube rows was found to be very short (Fig. 5.1). Therefore, in this analysis, this time duration is neglected and the droplets are assumed to be forming continuously at any droplet formation site. In reality however, there will be short interval between successive droplet formations, in which the detached droplet is falling.

For the representative test condition, the rate of increase of droplet volume was calculated to be 3.91×10^{-8} m^3 s^{-1}, the average film velocity in the Feed region to be 0.07 m s^{-1}, and the thickness of the film in the Feed region to be 1.766×10^{-4} m.

5.2.2. Spread region

Fig. 5.6 shows a schematic of the film spreading in the Spread region. As can be seen in this schematic, the Spread region is approximated as a triangle or a trapezoid at any instant of time. Initially, it is a very narrow triangular region right near the top of the tube. As the film spreads over the tube surface, two ends of the triangle at the top of the tube are held fixed, while the third end (the moving end) of the triangle continues to move downward with increasing time, stretching the triangle and spreading the fluid over the tube surface. Once this end of the triangle reaches the bottom of the tube, the film spreading is captured by assuming that the third end of the triangle continues to move downward in a hypothetical space (indicated by the dotted lines in Fig. 5.6.) It should be

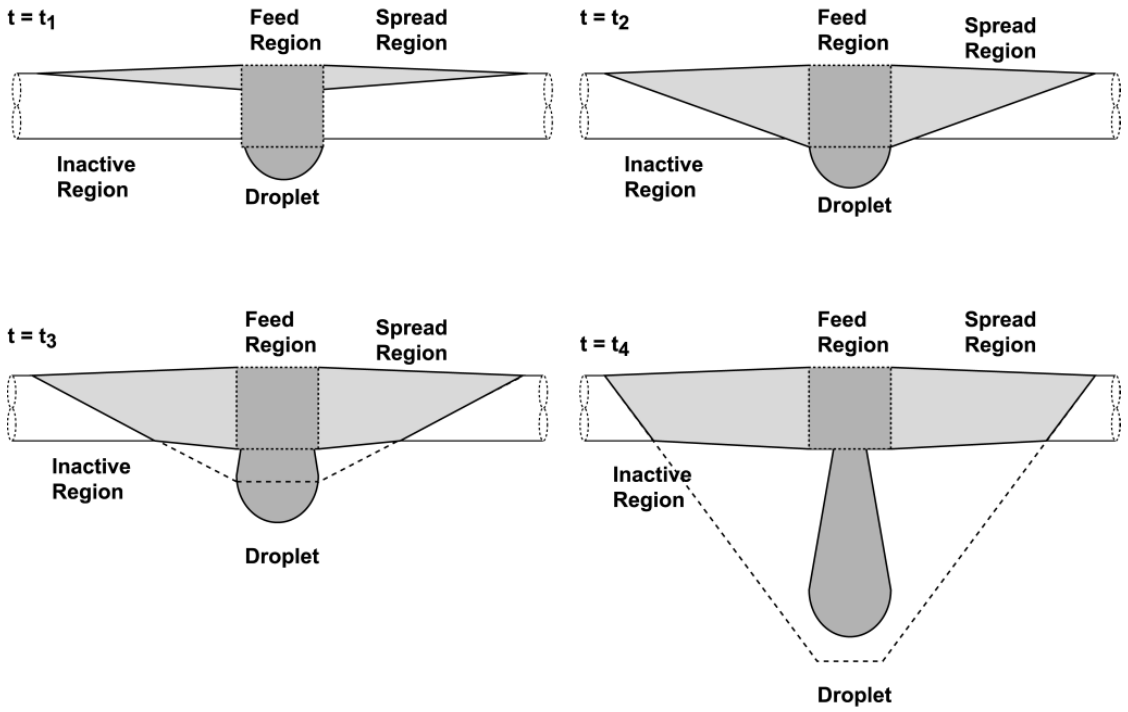

Fig. 5.6 Schematic of film spreading

noted that when fluid near the moving end of the triangle reaches the bottom of the tube, the droplet formation site restricts the movement of fluid, forcing it to enter the Feed region and consequently the droplet. However, fluid motion in the remaining part of the Spread region is still idealized as film behavior without the presence of the droplet. This results in the formation of a trapezoidal shaped film in the Spread region (A similar shape was reported in previous visualization studies (Killion and Garimella, 2003; Bohra, 2007). Spreading of the film continues until the end of the droplet formation time. As the Spread region expands, the inactive region becomes smaller, resulting in better wetting of the tube surface.

Because the moving end of the Spread region is in contact with the liquid in the Feed region, the velocity of this end is equal to the average film velocity in the Feed region. Thus, the vertical distance between the top of the tube and the moving end, S_{edge}, at any instant of the droplet formation time can be estimated as follows:

$$S_{\text{edge}}(t) = \overline{u}_{\text{film.feed}} \cdot t \tag{5.30}$$

Flow around each primary droplet is assumed to be symmetric. The width of the Spread region at the top of the tube is also constant (because the corresponding ends of the triangle were assumed to be fixed) and is equal to half the distance between successive Feed regions.

$$w_{\text{spread,max}} = \frac{\lambda_{\text{drop}} - D_o}{2} \tag{5.31}$$

The maximum width in the Spread region for the representative test case was calculated to be 3.5×10^{-3} m. The width of the Spread region at any other location on the tube, and at any instant of time, $w_{\text{spread}}(s, t)$ (see Fig. 5.5), can estimated by using similar triangles.

$$w_{\text{spread}}(s,t) = \frac{S_{\text{edge}}(t) - s}{S_{\text{edge}}(t)} \cdot w_{\text{spread,max}} \tag{5.32}$$

In the above equation, s is the distance along the tube circumference (arc length) from the top of the tube. It can be seen from the above equation that the width of the Spread region varies with both location and time. At any instant of time, the width of the Spread region decreases from the top to the bottom of the tube. Similarly, at any location on the tube surface, the width of the Spread region increases with increasing time.

Additionally, the thickness of the film is expected to vary across the Spread region, from a maximum near the end of the Feed region, to a minimum near the Inactive region. For simplicity this is approximated to a linear variation as follows.

$$\delta_{spread}\left(\zeta,s,t\right)=\left(1-\frac{\zeta}{w_{spread}\left(s,t\right)}\right)\cdot\delta_{feed} \tag{5.33}$$

In the above equation ζ is the distance along the axial direction from the boundary of the Spread and Feed regions (Fig. 5.5). The above equation indicates that the thickness of the film in the Spread region varies with location (both along the circumference and in the axial direction), and with time. This variation with location and time indicates a "wave-like" behavior. If the Feed region and the two adjoining Spread regions are considered (Fig. 5.6), the film is thickest right in the middle corresponding to the Feed region, and gradually thins out in the Spread region. The shape of the overall wave is very similar to the "saddle wave" structure previously reported by Killion and Garimella (2003). Thus, the above model provides a reasonable approximation for the formation of waves and spreading of film over horizontal round tubes, upon droplet impact. The instantaneous and time averaged heat and mass transfer areas relevant to the absorption process are calculated next.

5.2.3. Average transfer area

The time taken by the moving end of the triangle to reach the bottom of the tube is calculated as follows.

$$t_{\text{film,bot}} = \frac{\pi \cdot D_{\text{o}}}{2 \cdot \overline{u}_{\text{film,feed}}} \tag{5.34}$$

For the representative case, this was equal to 0.035 s. Between time $t = 0$ and $t = t_{\text{film,bot}}$, the film in the Spread region is in a triangular shape, while between time $t = t_{\text{film,bot}}$ and $t = t_{\text{drop}}$, the film in the Spread region is in a trapezoidal shape. To estimate the average transfer area in the Spread region, time averaged areas in both time durations were calculated separately. For the duration 0-$t_{\text{film,bot}}$, the area of the triangular region at any instant of time is given by the following equation.

$$A_{\text{spread,tri}}(t) = \frac{1}{2} \cdot w_{\text{spread,max}} \cdot \overline{u}_{\text{film,feed}} \cdot t \tag{5.35}$$

The time averaged area for the triangular shape during this duration was calculated as follows:

$$\overline{A}_{\text{spread,tri}} = \frac{\int_0^{t_{\text{film,bot}}} A_{\text{spread,tri}}(t) \cdot dt}{t_{\text{film,bot}}} = \frac{1}{4} \cdot w_{\text{spread,max}} \cdot \frac{\pi \cdot D_{\text{o}}}{2} \tag{5.36}$$

Similarly, for the duration $t_{\text{film.bot}}$ - t_{drop}, the area of the trapezoidal region at any instant of time is given by the following equation.

$$A_{\text{spread,trap}}(t) = \frac{1}{2} \cdot \frac{\pi \cdot D_{\text{o}}}{2} \cdot \left(w_{\text{spread,max}} + w_{\text{spread}}\left(\frac{\pi \cdot D_{\text{o}}}{2}, t \right) \right) \tag{5.37}$$

The time averaged area of for the trapezoidal region was calculated as follows:

$$\overline{A}_{\text{spread,trap}} = \frac{\int_{t_{\text{film,bot}}}^{t_{\text{drop}}} A_{\text{spread,trap}}(t) \cdot dt}{t_{\text{drop}} - t_{\text{film,bot}}} = \frac{\pi \cdot D_{\text{o}}}{2} \cdot w_{\text{spread,max}} \left(1 - \frac{\pi \cdot D_{\text{o}} \cdot ln\left(\frac{t_{\text{drop}}}{t_{\text{film,bot}}} \right)}{4 \cdot \overline{u}_{\text{film,feed}} \cdot \left(t_{\text{drop}} - t_{\text{film,bot}} \right)} \right) \tag{5.38}$$

Additional details on the instantaneous and average transfer area in the spread region are provided in Appendix C. Thus, for the Spread region, the time averaged transfer area during the total formation time can be calculated as follows:

$$\overline{A}_{\text{spread}} = \frac{\overline{A}_{\text{spread,tri}} \cdot t_{\text{film,bot}} + \overline{A}_{\text{spread,trap}} \cdot \left(t_{\text{drop}} - t_{\text{film,bot}} \right)}{t_{\text{drop}}} \tag{5.39}$$

For the representative test condition, the average transfer areas were calculated to be $\overline{A}_{\text{spread,tri}} = 2.16\times10^{-6}$ m^2, $\overline{A}_{\text{spread,trap}} = 7.33\times10^{-6}$ m^2, and $\overline{A}_{\text{spread}} = 6.67\times10^{-6}$ m^2. The maximum transfer area in the Spread region was calculated to be 8.64×10^{-6} m^2, which occurs right before detachment of the droplet. The Feed region on the other hand was assumed to be fully wet due to continuous formation and impact of droplets in this region. The area of the Feed region on one side of the tube was calculated as follows:

$$\overline{A}_{\text{feed}} = \frac{\pi \cdot D_{\text{o}}^2}{2} \tag{5.40}$$

The average area in the Feed region for the representative test condition was calculated to be 3.90×10^{-6} m^2. The average transfer area of the film around a single droplet is the sum of the average transfer areas in the Feed and Spread regions.

$$\overline{A}_{\text{film,drop}} = 2 \cdot \left(\overline{A}_{\text{feed}} + 2 \cdot \overline{A}_{\text{spread}} \right) \tag{5.41}$$

In the above expression, area of the Spread region was multiplied by 2 to account for Spread regions on either side of the Feed region, and the whole expression was multiplied by 2 to account for both sides of the tube. The average transfer area of the film in the segment can be calculated by multiplying the above expression with the total number of droplets in the segment.

$$\overline{A}_{\text{film}} = N_{\text{row}} \cdot N_{\text{drop,pr}} \cdot \overline{A}_{\text{film,drop}} \tag{5.42}$$

For the representative test condition, the average transfer area of the film was calculated to be 0.1857 m^2. The total available tube-side transfer area in the segment, A_{seg}, was calculated to be 0.2281 m^2. Thus, an average wetting ratio can be defined as follows:

$$WR = \frac{\overline{A}_{\text{film}}}{A_{seg}} \tag{5.43}$$

It should be noted that the Inactive region is neglected in the above definition. For the representative test condition, the wetting ratio was calculated to be 81.4%. Thus, as the solution spreads around the tubes, on an average, only about 81.4% of the total transfer area is wet, and therefore actively participating in the absorption process. It should be noted that this transfer area corresponds to the transfer area at the tube wall on the solution-side. To estimate the transfer area at the vapor-liquid interface, the slightly larger area presented due to the film thickness should also be estimated. The average film thickness was estimated by taking a weighted average the film thickness in the Feed and Spread regions.

$$\delta_{\text{film,avg}} = \frac{2 \cdot \overline{A}_{\text{spread}} \cdot \delta_{\text{spread}} + \overline{A}_{\text{feed}} \cdot \delta_{\text{feed}}}{2 \cdot \overline{A}_{\text{spread}} + \overline{A}_{\text{feed}}} \tag{5.44}$$

In the above equation δ_{spread} is the average film thickness in the Spread region which is equal to half the film thickness in the feed region. For the representative test condition, $\delta_{\text{film,avg}}$ was calculated to be 1.08×10^{-4} m. The average transfer area at the vapor-liquid interface was calculated as follows:

$$\overline{A}_{\text{film,int}} = \overline{A}_{\text{film}} \cdot \left(1 + \frac{2 \cdot \delta_{\text{film,avg}}}{D_{\text{o}}} \right) \tag{5.45}$$

This equation accounts for the different transfer areas at the vapor-liquid interface in the Film and Spread region due to different film thicknesses. For the representative test condition, the average transfer area at the interface was calculated to be 0.2112 m^2. All the above calculations were conducted at the average solution conditions of the bottom segment. The respective transfer areas in the droplet, film interface, and tube surface will be used to estimate the local heat and mass transfer rates.

5.3. Hydrodynamic model results and discussion

5.3.1. Droplet characteristics

Table 5.1 shows a summary of the most unstable wavelength λ_{drop}, the number of droplet formation sites per row $N_{drop,pr}$, and the total number of droplets in a tube row per second $N_{drop,ps}$, for all data points in the present work. The solution flow rate was found to have a weak influence upon the most unstable wavelength. Eq. 5.15 is used to calculate the most unstable wavelength, which is reproduced here for convenience.

$$\lambda_{drop} = \frac{2 \cdot \pi \cdot \sqrt{2}}{\sqrt{\frac{g \cdot \Delta\rho}{\sigma}\left(1+\left(\frac{Re_{sol}}{Ka^{0.25}}\right)^{0.8}\right)+\frac{2}{D_o^2}}} \tag{5.46}$$

This is because, the term $\left(Re_{sol}/Ka\right)^{0.25}$ which accounts for the influence of the solution flow rate, ranged between 0.018-0.040 for all data points in the present study, and thus, did not affect the denominator of the above equation significantly. Furthermore, while the density of the solution and vapor did vary over the range of operating conditions considered in this study, the value of the denominator was dominated by the tube diameter. For the representative test condition, the first term in the denominator of the above equation, which depends upon the fluid properties and flow conditions was calculated to be 2.719×10^5 m^{-2}, while the second term in the denominator of the above equation, which depends upon the tube geometry, was calculated to be 8.062×10^5 m^{-2}, nearly three times the value of the first term. In comparison, the second term in the denominator of the above equation for a larger diameter tube (9.5 mm) would be equal to

Table 5.1 Summary of droplet spacing and number of droplets

Nominal solution concentration	λ_{drop} (mm)	$N_{drop,pr}$	$N_{drop,ps}$
40%	8.60 - 8.64	533 - 536	1235 - 2065
48%	8.54 - 8.58	538 - 540	1195 - 2293
55%	8.52 - 8.56	539 - 541	1168 - 2184

2.216×10^4 m^{-2}, which is an order of magnitude lower than the first term. Therefore, in such geometries, the influence of solution and flow properties on the most unstable wavelength is more significant, and a wider range of values for λ_{drop} are observed. For the present work however, the values for λ_{drop} varied over a relatively small range of 8.52 - 8.64 mm over a wide range of solution flow rates, concentrations, and vapor flow rates.

Because the spacing between droplets remains largely the same, the number of droplet formation sites per tube row also remains nearly uniform (533 - 541). Higher solution concentrations yielded slightly smaller values for the λ_{drop}, and therefore, slightly higher values for the $N_{drop,pr}$. These analyses and the present data on microchannel tubes (large diameter tubes were not tested in this study) point toward an interesting conclusion: as the tube diameter decreases, the most unstable wavelength becomes shorter, and the dependence on flow conditions is relatively small. Thus, for microchannel tube geometries, the spacing between successive droplets can be assumed to be a constant value over a fairly wide range of operating conditions.

The total number of droplets in a tube row per second strongly depends upon the mass flow rate of the solution, which in turn varies over a wide range of values. Thus, the values for $N_{drop,ps}$ were observed to vary over a wide range of values between 1168-2293 droplets per second. Also, as can be seen in Table 5.2, the droplet formation times also varied over a wide range of values between 0.235 - 0.462 s. A corresponding range was also observed in the formation times of the hemispherical and conical sections. This indicates that while the number droplets formation sites in each tube row remain largely the same, the formation times of these droplets vary significantly with the flow rate. It

Table 5.2 Summary of droplet formation times

Nominal solution concentration	t_{hem} (s)	t_{cone} (s)	t_{form} (s)
40%	0.048 - 0.077	0.211 - 0.357	0.259 - 0.434
48%	0.041 - 0.077	0.194 - 0.374	0.235 - 0.451
55%	0.043 - 0.079	0.205 - 0.383	0.248 - 0.462

should also be noted that this formation time affects the spreading of the liquid film over the tube surface and thus, affects the film transfer area and the overall absorption process.

Table 5.3 shows a summary of the maximum droplet volume, surface area, and average droplet surface area for test conditions in the present study. The droplet volume at the instant of detachment is a function of the surface tension force. At a representative temperature of 40^{o}C, the surface tension was found to decrease from 0.0326 - 0.0281 N m^{-2}, as the concentration increased from 40 - 55%. At higher solution concentrations where the surface tension forces are lower, the diameter of the top of the conical section is larger to provide the necessary surface tension to support the droplet weight. This also resulted in a slightly larger overall droplet volume. Thus, the droplet volumes were found to range from 9.43 - 11.19×10^{-9} m^{3}, with higher droplet volumes observed at the higher solution concentrations. Correspondingly, higher maximum and average droplet areas were observed at higher concentrations due to the larger droplet volumes. The total droplet transfer area available in a segment for absorption was also higher at higher solution concentrations, due to larger number of droplet formation sites and primary droplet area.

5.3.2. Film characteristics

Fig. 5.7 shows a plot of the width of the Spread region, w_{spread}, as a function of time, at four equidistant locations below the top of the tube (s = $\pi D_o/8$, $\pi D_o/4$, $3\pi D_o/8$, $\pi D_o/2$), for the representative test condition. At t = 0, the instant at which the droplet falls on the tube, all the liquid is accumulated at the top of the tube and no liquid is present in

Table 5.3 Summary of droplet volume and surface area characteristics

Nominal solution concentration	Maximum droplet volume (×10^{-9} m^{3})	Maximum droplet area (×10^{-5} m^{2})	Average droplet area (×10^{-5} m^{2})
40%	9.43 - 10.14	2.79 - 2.90	1.31 - 1.37
48%	9.66 - 10.94	2.83 - 3.03	1.34 - 1.45
55%	9.96 - 11.19	2.88 - 3.06	1.37 - 1.47

the Spread region. As the solution starts flowing around the tube bank, the triangular wave starts propagating, introducing solution to the Spread region. It takes the triangular wave about 0.035 s to reach the bottom of the tube, about 13% of the total spread time of 0.2734 s. At each location, the width of the spread region was found to increase rapidly initially for a short duration. After this duration, the rate of increase in the width of the spread region decreases dramatically, and eventually, the width remains nearly constant until the end of the spreading time. It should be noted that while the simplified model presented here does not consider the influence of momentum balances, these observations of the predicted flow patterns are consistent with the expected flow patterns of the film around round tubes. Right after droplet impact, the liquid contains a lot of momentum due to the potential energy gained during the fall from the previous tube, which results in

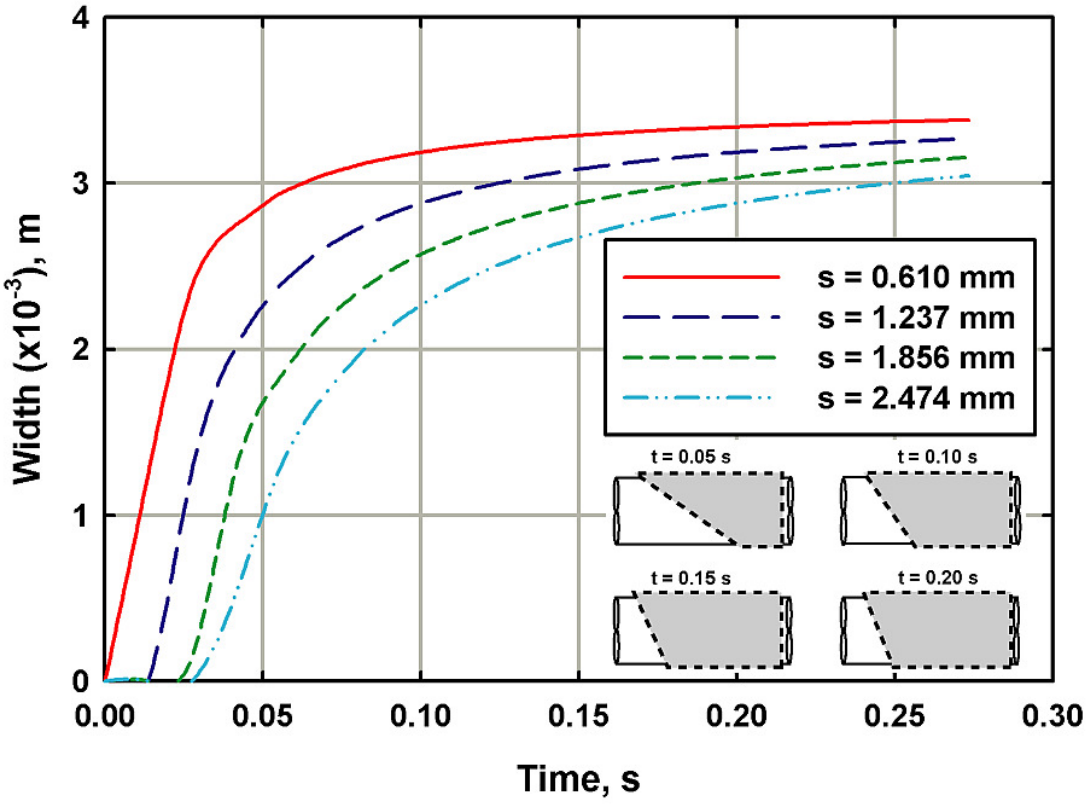

Fig. 5.7 Width of the Spread region as a function of time

rapid spreading of the film initially. With time, the drag forces on the tube surface reduce the liquid momentum, resulting in slower rates of film spreading in the Spread region.

Fig. 5.8 shows a plot of the film thickness as a function of time at six locations on the tube surface. Two axial locations (ζ = 1, 2 mm away from feed region) were chosen for each of the three equidistant locations from the top of the tube (s = $\pi D_o/8$, $\pi D_o/4$, $3\pi D_o/8$). These six locations are also shown schematically in Fig. 5.8. All these locations lie outside the Feed region, and initially at time t = 0 lie in the Inactive region. Correspondingly, the film thickness is zero at time t = 0 at all these locations. As solution spreads over the tube surface, these locations transition into the Spread region, and the thickness of the film starts to increase. As previously noted, the film thickness varies with time and location (in both circumferential and axial directions) in the Spread region, which is confirmed by Fig. 5.8. The film thickness at each of the six locations was found

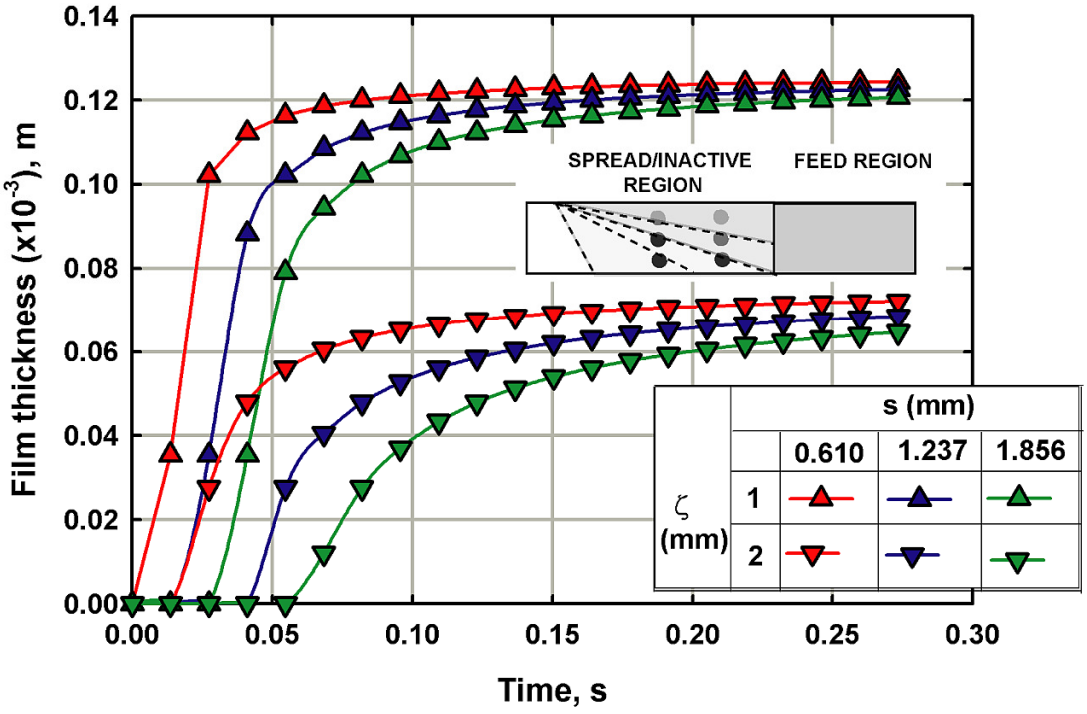

Fig. 5.8 Film thickness on tube surface (Spread and Inactive regions) as a function of time

to rapidly rise initially for a short duration. After this duration, the rate of increase in the thickness of the film was found to decrease dramatically, with near-asymptotic film thickness values observed towards the end of the spread time. While the simplified model presented here does not consider momentum balances, it is interesting to the note that this predicted behavior is consistent with the flow of a wave, where, the movement of the wave-front results in a rapid increase in the local film thickness at any location. Once the wave-front has passed this location, the film thickness is generally uniform indicating asymptotic behavior. Similarly, the film thickness was found to vary with location, where, at any instant of time, the film thickness decreased toward the bottom of the tube in the circumferential direction, or away from the feed region in the axial direction (the combination of these two results in a decrease in the diagonal direction.) This is an expected trend because the solution is introduced to the tube from the falling droplet at the top of the tube near the Feed region, and lesser fluid reaches regions away from this location resulting in thinner films.

Table 5.4 shows a summary of the film thickness in the Feed region and the average film thickness. The film thickness in the Feed region, δ_{feed}, depends upon the rate of increase of the droplet volume and the flow velocity in the feed region, which in turn depends upon the formation time of the droplet. As previously noted, the droplet formation times were found to vary over a wide range of values, which in turn resulted in variation of δ_{feed} over a wide range of values (1.398 – 1.847×10^{-4} m). Higher film thickness values in the feed region were observed at higher solution flow rates, where higher volume flow rates were necessary to support the growth of the droplet. Also, the

Table 5.4 Summary of film thickness characteristics

Nominal solution concentration	δ_{feed} ($\times10^{-4}$ m)	δ_{spread} ($\times10^{-4}$ m)	$\delta_{film,avg}$ ($\times10^{-4}$ m)	$\delta_{l,avg}$ ($\times10^{-4}$ m)
40%	1.442 - 1.751	0.721 - 0.876	0.881 - 1.074	0.902 - 1.096
48%	1.398 - 1.834	0.699 - 0.917	0.854 - 1.125	0.877 - 1.150
55%	1.445 - 1.849	0.723 - 0.925	0.883 - 1.134	0.907 - 1.161

value of δ_{feed} was found to be relatively independent of the nominal solution concentration. The average film thickness, $\delta_{film,avg}$, depends upon δ_{feed}, and thus, varied over a range of values between 0.854 – 1.134×10^{-4} m. As with the thickness in the feed region, the average film thickness was found to be higher at higher solution flow rates to accommodate the higher volume of liquid flowing over the tube. The $\delta_{film,avg}$ values were compared with the equation for the film thickness, $\delta_{l,avg}$, presented in Bird *et al.* (2002) and discussed in the previous chapter. While that equation assumes uniform flow around the tube bank, and the idealization used here considers the different regions of the film, the average values predicted from both definitions compared well.

Table 5.5 shows a summary of the average transfer area at the tube wall on the solution-side, $\overline{A}_{film}$, and at the vapor-liquid interface, $\overline{A}_{film,int}$. While the film thickness values were found to vary over a wide range, $\overline{A}_{film}$ was found to be relatively constant, varying over a relatively small range of 0.1840 - 0.1897 m^2. As previously noted, the width of the Spread region remains relatively constant after the initial rapid rise. Thus, the resulting average transfer area at the tube wall on the solution side also remains relatively constant over a range of solution flow rates. Consequently, the wetting ratios were found to remain relatively constant, only ranging between 0.807 - 0.832. It should be noted that in a study conducted for water-LiBr absorption by Jeong and Garimella (2002), the authors reported a wetting ratio between 0.6-0.8 for experiments conducted by Nomura *et al.* (1994a). While that study was conducted for a different working fluid pair and for different tube diameters, the range of wetting ratios is comparable. The

Table 5.5 Summary of film transfer area characteristics

Nominal solution concentration	$\overline{A}_{film}$ (m^2)	$\overline{A}_{film,int}$ (m^2)	*WR*
40%	0.1840 - 0.1881	0.2086 - 0.2094	0.807 - 0.825
48%	0.1850 - 0.1897	0.2099 - 0.2117	0.811 - 0.832
55%	0.1856 - 0.1894	0.2104 - 0.2124	0.814 - 0.830

values for $\bar{A}_{film,int}$ were found to vary over a relatively larger range of 0.2086 - 0.2124 m^2. This is because the interfacial area depends upon the film thickness, which was found to vary over a wide range of values, as discussed above.

5.4. Heat and mass transfer modeling

The heat and mass transfer model described in the previous chapter was next coupled with the above described hydrodynamic model for the film and droplet, to estimate the local heat and mass transfer rates. As solution flows over horizontal tube banks, absorption can occur in the film region around the tube, in the evolving droplet on the underside of the tube, and in the free-falling droplet between successive tubes. Jeong and Garimella (2002) observed that during water-LiBr absorption, the contribution to overall absorption from the free-falling droplet was negligible in comparison to the other two flow modes. The residence time in this flow regime is very small in comparison to the residence time in the evolving droplet, which is confirmed by Fig. 5.1. Bohra *et al.* (2008) also reported similar observations and neglected free-falling droplets in their analysis. Thus, absorption in the free-falling droplet was neglected in the following calculations.

Additionally, there is a large pool of subcooled solution at the bottom of the absorber. This region provides a large surface area for interaction with the vapor and can be a region for absorption. Thus, in addition to the droplet and film regions, the solution pool is also considered while modeling the local heat and mass transfer rates. The following sections detail the methodology developed for each region starting with the solution pool.

5.4.1. Solution pool

Absorption of vapor into the solution pool is adiabatic. The heat of absorption released at the vapor-liquid interface propagates back into the vapor bulk and/or into

solution pool. Fig. 5.9 shows a schematic of the vapor flow around the solution pool. Vapor is introduced at the bottom of the absorber through a vapor inlet header just above the solution pool. This vapor interacts with the top layer of the solution pool, which in turn receives fresh solution from the tube array located above it. Because there are no external forcing mechanisms, heat transfer between the solution pool and the vapor was modeled as natural convection.

$$Q_{\text{vap,pool}} = \alpha_{\text{vap,NC}} \cdot A_{\text{pool}} \cdot \left(T_{\text{sol,pool,in}} - T_{\text{vap,pool,avg}} \right) \tag{5.47}$$

In the above equation, A_{pool} is the area of the top surface interacting with the vapor, $T_{\text{vap,pool,avg}}$ is the average of the inlet and outlet vapor temperatures, and $T_{\text{sol,pool,in}}$ is the solution temperature at the inlet of the solution pool. It should be noted that as solution drips down from the tube array, the top layer of the solution has solution at the outlet conditions of the tube array. It is this solution that interacts with the vapor, as it is present at the vapor-liquid interface, and is termed the solution inlet to the solution pool. The solution that is removed from the bottom of the absorber to the solution pump is

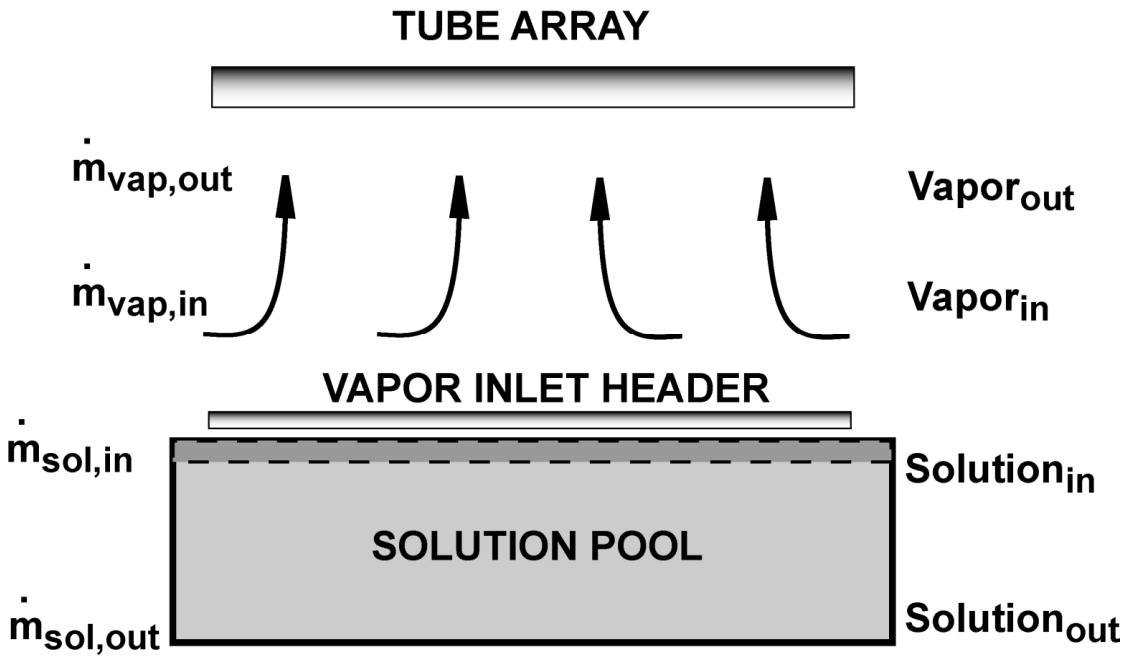

Fig. 5.9 Schematic of the solution pool

termed the solution outlet of the solution pool. The vapor heat transfer coefficient was calculated using the Nusselt number correlation for natural convection over a heated surface given in Incropera *et al.* (2007).

$$\begin{aligned} Nu_{\text{vap,NC}} &= 0.54 \cdot Ra_{\text{vap}}^{1/4}, 10^4 \le Ra_{\text{vap}} \le 10^7 \\ &= 0.15 \cdot Ra_{\text{vap}}^{1/3}, 10^7 \le Ra_{\text{vap}} \le 10^{11} \end{aligned} \tag{5.48}$$

$$\alpha_{\text{vap,NC}} = \frac{Nu_{\text{vap,NC}} \cdot k_{\text{vap,avg}}}{L_{pool}} \tag{5.49}$$

In the above equation, Ra_{vap} is the Rayleigh number and L_{pool} is the length scale for natural convection, which is calculated using the pool surface area and perimeter, Per_{pool}.

$$L_{\text{pool}} = \frac{4 \cdot A_{\text{pool}}}{Per_{\text{pool}}} \tag{5.50}$$

For the representative test condition, Ra_{vap}, Nu_{vap}, and α_{vap} were calculated to be 8.97×10^7, 67.15, and 12.55 W m^{-2} K^{-1}, respectively. The heat transfer rate to the vapor was calculated as follows.

$$Q_{\text{vap,pool}} = 12.55\,\text{W m}^{-2}\,\text{K}^{-1} \cdot 0.0226\,\text{m}^2 \cdot \left(37.99\,^{\circ}\text{C} - 11.11\,^{\circ}\text{C}\right) = 7.63\,\text{W} \tag{5.51}$$

It should be noted that the average vapor temperature and solution inlet temperature are unknown at this point, and are calculated later. Heat transfer within the liquid solution pool was also modeled as natural convection.

$$Q_{\text{sol,pool}} = \alpha_{\text{sol,NC}} \cdot A_{\text{pool}} \cdot \left(T_{\text{sol,pool,in}} - T_{\text{sol,pool,out}}\right) \tag{5.52}$$

The natural convection solution heat transfer coefficient was calculated using the Nusselt number correlation for natural convection under a heated surface given in Incropera *et al.* (2007).

$$Nu_{\text{sol,NC}} = 0.27 \cdot Ra_{\text{sol}}^{1/4} \tag{5.53}$$

$$\alpha_{\text{sol,NC}} = \frac{Nu_{\text{sol,NC}} \cdot k_{\text{sol,avg}}}{L_{\text{pool}}} \tag{5.54}$$

For the representative test condition, Ra_{sol}, $Nu_{\text{sol,NC}}$, $\alpha_{\text{sol,NC}}$ were calculated to be 9.89×10^{7}, 26.92, and 98.15 W m^{-2} K^{-1}, respectively. The experimentally measured $T_{\text{sol,pool,out}}$ was 37.57°C, which yields a $Q_{\text{sol,pool}}$ of 0.93 W. It should be noted that while $\alpha_{\text{sol,NC}}$ is higher than $\alpha_{\text{vap,NC}}$, the temperature difference for heat transfer in the vapor is 26.88 K compared to a temperature difference of 0.42 K in the solution. This results in a significantly higher heat transfer rate into the vapor.

As vapor is absorbed at the vapor-liquid interface, the latent heat released at the interface is propagated to the vapor and solution bulk. The latent heat of phase change at the vapor-liquid interface is equal to the enthalpy difference between the average vapor conditions and the interface liquid conditions, and was calculated as follows:

$$\Delta h_{\text{pool,int}} = h_{\text{vap,avg}} - h_{\text{sol,in}} \tag{5.55}$$

For the representative test condition, $\Delta h_{\text{pool,int}}$ was calculated to be 1356 kJ kg^{-1}. It should be noted that the average vapor and inlet solution enthalpies are currently unknown at this stage of the calculation and will be known once the local state is determined. The heat released due to phase change at the interface, $Q_{\text{pool,int}}$, is calculated using the following equation.

$$Q_{\text{pool,int}} = \dot{m}_{\text{abs,pool}} \cdot \Delta h_{\text{pool,int}} \tag{5.56}$$

In the above equation, $\dot{m}_{\text{abs,pool}}$ is the mass of vapor absorbed at the interface, which is calculated by equating the heat of absorption with the sum of the heat transfer rates into the vapor and liquid phases.

$$Q_{\text{pool,int}} = Q_{\text{sol,pool}} + Q_{\text{vap,pool}} \tag{5.57}$$

$$Q_{\text{pool,int}} = 0.93 + 7.63 = 8.56\,\text{W} \tag{5.58}$$

For the representative test condition, $\dot{m}_{\text{abs,pool}}$ was calculated to be 6.31×10^{-6} kg s^{-1}. This indicates that the absorption rate in the solution pool is relatively low, which is

understandable because the heat of absorption in the solution pool is removed by natural convection processes and not by a separate coupling fluid. The mass flow rate of the vapor leaving the solution pool region and entering the tube array was estimating by applying a mass balance equation as follows:

$$\dot{m}_{\text{vap,pool,out}} = \dot{m}_{\text{vap,pool,in}} - \dot{m}_{\text{abs,pool}} \tag{5.59}$$

The mass flow rate of the solution entering the solution pool was calculated by applying mass balances between the vapor and solution streams.

$$\dot{m}_{\text{sol,pool,in}} = \dot{m}_{\text{vap,pool,out}} + \dot{m}_{\text{sol,pool,out}} - \dot{m}_{\text{vap,pool,in}} \tag{5.60}$$

For the representative test condition, the mass flow rates of the vapor entering and exiting the solution pool were determined to be 2.765×10^{-3} kg s^{-1} and 2.759×10^{-3} kg s^{-1}, respectively. The mass flow rate of the solution entering and exiting the solution pool were calculated to be 1.864×10^{-2} kg s^{-1} and 1.865×10^{-2} kg s^{-1}, respectively. The temperature of the vapor exiting the solution pool was determined by comparing the heat transfer to the vapor with the sensible heating load of the average vapor.

$$Q_{\text{vap,pool}} = \left(\frac{m_{\text{vap,pool,in}} + m_{\text{vap,pool,out}}}{2} \right) \cdot Cp_{\text{vap,pool,avg}} \cdot \left(T_{\text{vap,pool,out}} - T_{\text{vap,pool,in}} \right) \tag{5.61}$$

For the representative test condition, the inlet temperature of the vapor was experimentally determined to be 8.12°C, while the outlet temperature of the vapor was calculated to be 14.1°C. It is interesting to note that while the solution pool does not accomplish appreciable absorption, it does significantly increase the temperature of the vapor entering the tube array. The average vapor temperature used previously is the average of these two inlet and outlet temperatures. Due to the flow associated with natural convection, vapor leaving the solution pool region is assumed to be in equilibrium with the solution. The concentration of the vapor at the outlet of the solution pool was calculated using the outlet temperature, absorber pressure, and saturated vapor

assumption. The concentration of the vapor leaving the solution pool is calculated as follows:

$$x_{\text{vap,pool,out}} = f\left(P_{\text{abs}}, T_{\text{vap,pool,out}}, q_{\text{vap,pool,out}} = 1\right) \tag{5.62}$$

For the representative test condition, the concentration of the vapor at the outlet of the solution pool was calculated to be 0.9998. The concentration of the vapor at the inlet of the solution pool was previously determined to be 0.9999.

Species and energy balance equations between the solution and vapor are used to calculate the solution concentration and enthalpy at the inlet to the solution pool, respectively.

$$\dot{m}_{\text{sol,pool,in}} \cdot x_{\text{sol,pool,in}} + \dot{m}_{\text{vap,pool,in}} \cdot x_{\text{vap,pool,in}} = \dot{m}_{\text{sol,pool,out}} \cdot x_{\text{sol,pool,out}} + \dot{m}_{\text{vap,pool,out}} \cdot x_{\text{vap,pool,out}} \tag{5.63}$$

$$\dot{m}_{\text{sol,pool,in}} \cdot h_{\text{sol,pool,in}} + \dot{m}_{\text{vap,pool,in}} \cdot h_{\text{vap,pool,in}} = \dot{m}_{\text{sol,pool,out}} \cdot h_{\text{sol,pool,out}} + \dot{m}_{\text{vap,pool,out}} \cdot h_{\text{vap,pool,out}} \tag{5.64}$$

For the representative test condition, the solution concentration and enthalpy at the inlet to the solution pool were calculated to be 0.4548 and -67.91 kJ kg^{-1}, respectively. The state of the solution at the top of the solution pool was calculated using the above determined concentration, enthalpy, and the absorber operating pressure. The temperature of the solution at the top of the solution pool, which was used previously is calculated here.

$$T_{\text{sol,pool,in}} = f\left(P_{\text{abs}}, h_{\text{sol,pool,in}}, x_{\text{sol,pool,in}}\right) = 37.99\,^{\circ}\text{C} \tag{5.65}$$

Thus, the state of the vapor leaving the solution pool (and entering the tube array) and solution entering the solution pool (and leaving the tube array) are now completely known, and estimation of the heat and mass transfer rates in the solution pool region is complete.

Modeling of the heat and mass transfer in the tube array is conducted next, first considering the droplet mode and then considering film-mode flow. The bulk vapor and

average solution conditions for both regimes were calculated by averaging the inlet and outlet conditions, similar to what was described in Chapter 4. The interface condition for each regime was determined by considering local flow, heat, and mass transfer mechanisms.

5.4.2. Droplet absorption

Fig. 5.10 shows a schematic of the regions of the absorption near the droplet. Absorption into the droplet is assumed to be adiabatic since it is away from the tube surface, which is cooled by the circulating coupling fluid. The heat released at the vapor-liquid interface propagates both into the solution bulk and vapor bulk. As previously described, all the resistance to heat and mass transfer in the vapor phase was assumed to

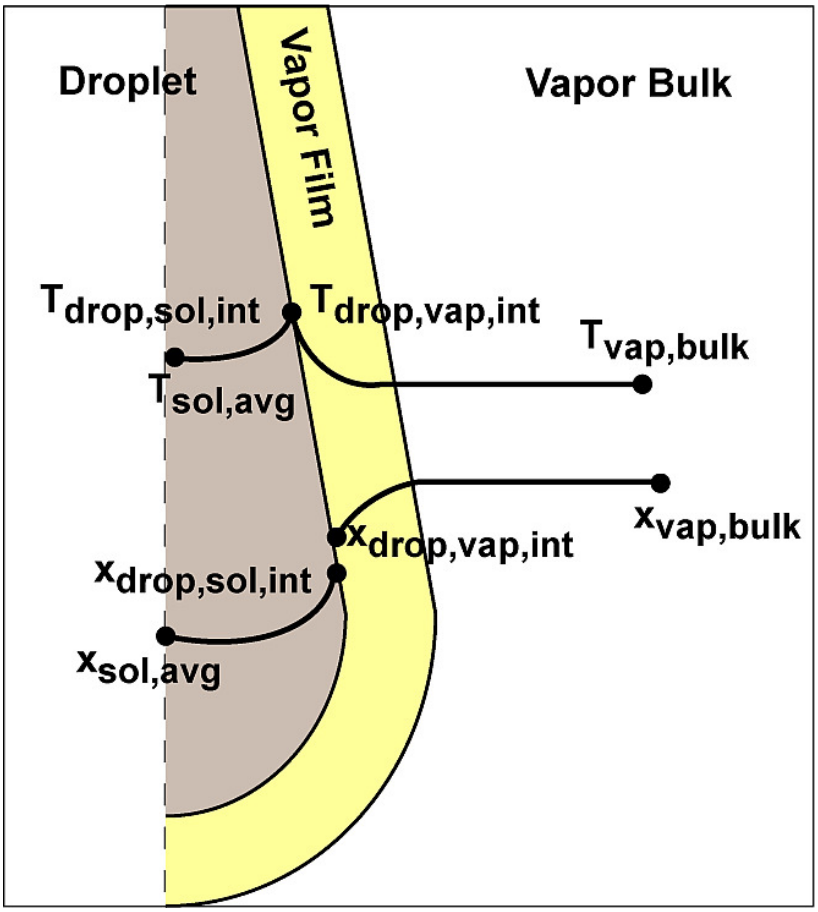

Fig. 5.10 Schematic of the droplet absorption regions

be in a narrow region adjacent to the vapor-liquid interface, called the vapor film. Both concentration and temperature gradients are observed in this region. Additionally, the ammonia and water vapor species that undergo phase change at the vapor-liquid interface induce a concentration and temperature gradient in the droplet bulk. Unlike the solution in the film, solution in the droplet cannot be assumed to be well mixed because there are no mechanisms such as droplet impingement to induce mixing. Thus, concentration gradients in the solution in the droplet were considered.

The molar flux of the vapor being absorbed into the droplet is given by the following equation.

$$\dot{n}_{\mathrm{T,drop}} = \beta_{\mathrm{vap}} \cdot C_{\mathrm{T}} \cdot \ln\left(\frac{\tilde{z}_{\mathrm{drop}} - \tilde{x}_{\mathrm{vap,drop,int}}}{\tilde{z}_{\mathrm{drop}} - \tilde{x}_{\mathrm{vap,bulk}}} \right) \tag{5.66}$$

In the above equation, $\tilde{x}_{\mathrm{vap,drop,int}}$ is the vapor concentration at the droplet interface, which is determined using the droplet interface temperature, and $\tilde{z}_{\mathrm{drop}}$ is the molar concentration of the condensing flux into the droplet, which is determined iteratively using the following equations. The heat released per unit mass when vapor molecules undergo phase change at the interface can be estimated as follows:

$$\Delta h_{\mathrm{drop,int}} = h_{\mathrm{vap,drop,int}} - h_{\mathrm{sol,drop,int}} \tag{5.67}$$

This heat released can also be calculated by considering the latent heat of condensation of individual components, and the heat of mixing (and dilution) of the condensed components.

$$\Delta h_{\mathrm{drop,int}} = z_{\mathrm{drop}} \cdot h_{\mathrm{fg,NH_3}} + \left(1 - z_{\mathrm{drop}}\right) \cdot h_{\mathrm{fg,H_2O}} + \Delta h_{\mathrm{mix}} \tag{5.68}$$

$$\Delta h_{\mathrm{mix}} = z_{\mathrm{drop}} \cdot h_{\mathrm{f,NH_3}} + \left(1 - z_{\mathrm{drop}}\right) \cdot h_{\mathrm{f,H_2O}} - h_{\mathrm{sol,drop,int}} \tag{5.69}$$

In the above equations, z_{drop} is the mass-based concentration of the condensing flux, h_{fg} and h_{f} indicate the latent heat of phase change and saturated liquid enthalpy of each component at the operating pressure. For the representative test condition, the mass

and molar based concentrations of the condensing flux are calculated from the above equations to be 0.9282 and 0.9319, respectively. $\Delta h_{\text{drop,int}}$ is calculated to be 1416 kJ kg^{-1}. It should be noted that for these calculations, the reference state for calculation of the enthalpy of the saturated liquid must be standardized to the same reference state as the ammonia-water mixtures.

The molar flux of the vapor being absorbed was calculated to be

$$\begin{aligned}\dot{n}_{\text{T,drop}} &= 0.00817\,\text{m s}^{-1} \cdot 0.2067\,\text{kmol m}^{-3} \cdot \ln\left(\frac{0.9319 - 0.9939}{0.9319 - 0.9930}\right) \\ &= 2.49\times10^{-5}\,\text{kmol m}^{-2}\,\text{s}^{-1}\end{aligned} \tag{5.70}$$

It should be noted that the concentration of the vapor at the interface is not known explicitly at this point and is calculated later. The individual ammonia and water condensing fluxes, and mass absorption rates were determined from the total condensing flux as follows:

$$\dot{n}_{\text{A,drop}} = \tilde{z}_{\text{drop}} \cdot \dot{n}_{\text{T,drop}} \tag{5.71}$$

$$\dot{m}_{\text{abs,A,drop}} = M_{\text{A}} \cdot \dot{n}_{\text{A,drop}} \cdot N_{\text{row}} \cdot N_{\text{drop,pr}} \cdot \overline{A}_{\text{drop}} \tag{5.72}$$

$$\dot{n}_{\text{W,drop}} = \left(1 - \tilde{z}_{\text{drop}}\right) \cdot \dot{n}_{\text{T,drop}} \tag{5.73}$$

$$\dot{m}_{\text{abs,W,drop}} = M_{\text{W}} \cdot \dot{n}_{\text{W,drop}} \cdot N_{\text{row}} \cdot N_{\text{drop,pr}} \cdot \overline{A}_{\text{drop}} \tag{5.74}$$

For the representative test conditions, molar fluxes of ammonia and water were estimated to be 2.32×10^{-5} and 1.70×10^{-6} kmol m^{-2} s^{-1}. The corresponding mass absorption rates for ammonia and water were estimated to be 3.04×10^{-5} and 2.22×10^{-6} kg s^{-1}, respectively. The mass absorption rate into the droplet is the sum of the two individual component absorption rates, and was calculated to be 3.23×10^{-5} kg s^{-1}.

The temperature of the droplet vapor-liquid interface is calculated iteratively by estimating the heat transfer rates into the vapor bulk and the solution bulk in the droplet. The heat released at the interface due to phase change is calculated as follows:

$$Q_{\text{drop,int}} = \dot{m}_{\text{abs,drop}} \cdot \Delta h_{\text{drop,int}} = 0.046\,\text{kW} \tag{5.75}$$

This heat released propagates both to the solution bulk and the vapor bulk. The heat transfer rate to the vapor bulk was calculated using the vapor heat transfer coefficient, and the vapor interface and bulk temperatures, as follows:

$$Q_{\text{vap,drop}} = \alpha_{\text{vap}} \cdot \left(\frac{\phi_{\text{T,drop}}}{1 - e^{-\phi_{\text{T,drop}}}} \right) \cdot N_{\text{row}} \cdot N_{\text{drop,pr}} \cdot \bar{A}_{\text{drop}} \cdot \left(T_{\text{vap,drop,int}} - T_{\text{vap,bulk}} \right) \tag{5.76}$$

$$\phi_{\text{T,drop}} = \frac{\left(\dot{n}_{\text{A,drop}} \cdot \tilde{C}p_{\text{A}} \right) + \left(\dot{n}_{\text{W,drop}} \cdot \tilde{C}p_{\text{W}} \right)}{\alpha_{\text{vap}}} \tag{5.77}$$

The vapor heat transfer coefficient is calculated using the correlation developed by Sparrow *et al.* (2004) with a correction factor for the tube bundles, as discussed in the previous chapter. In the above equation, the expression in the parenthesis involving $\phi_{\text{T,drop}}$ is the parameter that accounts for the correction to the heat transfer due to mass transfer in the vapor phase.

Heat transfer into the liquid bulk was modeled as transient conduction into a semi-infinite body as discussed in Nellis and Klein (2009). It should be noted that in the present case, droplet formation times are very short (0.2734 s for the representative test conditions.) The corresponding diffusion time (time for the temperature at the center of the droplet to experience any change) is 2.6 s, which is nearly 9.5 times the total droplet formation time. Therefore, for such short formation times, the heat transfer process is dominated by transient condition and can be approximated as conduction into a semi-infinite body. The average penetration depth of the thermal wave was calculated using the following equation.

$$l_{\text{semi,inf}} = 2 \cdot \left(\frac{k_{\text{sol,avg}} \cdot t_{\text{drop}}}{2 \cdot \rho_{\text{sol,avg}} \cdot Cp_{\text{sol,avg}}} \right)^{1/2} \tag{5.78}$$

The heat transfer rate into the liquid bulk was calculated using this penetration depth, the droplet thermal conductivity, and the interface and bulk temperatures as follows:

$$Q_{\text{sol,drop}} = k_{\text{l,avg}} \cdot N_{\text{row}} \cdot N_{\text{drop,pr}} \cdot \bar{A}_{\text{drop}} \cdot \left(\frac{T_{\text{sol,drop,int}} - T_{\text{sol,avg}}}{l_{\text{semi,inf}}} \right) \tag{5.79}$$

At the droplet vapor-liquid interface, the solution temperature is equal to the vapor temperature. This temperature can be calculated by equating the total heat released at the interface to the sum of the heat transfer rates into the solution and vapor bulk.

$$Q_{\text{drop,int}} = Q_{\text{vap,drop}} + Q_{\text{sol,drop}} \tag{5.80}$$

For the representative test condition, the heat released at the interface was calculated to be 0.046 kW, while $Q_{\text{vap,drop}}$ and $Q_{\text{sol,drop}}$ were calculated to be 0.036 and 0.010 kW, respectively. These results are for the whole segment. The temperature of the vapor-liquid interface was calculated to be 45.61°C, and $l_{\text{semi,inf}}$ was estimated to be 2.85×10^{-4} m. It should be noted that in typical water-LiBr absorption studies, heat transfer rate into the vapor is expected to be much lower than heat transfer rate into the solution. In water-LiBr absorption, heat transfer in the large vapor space is better approximated as being quiescent, akin to natural convection. However, in the present work, vapor is in forced-convective flow, which results in higher heat transfer coefficients, and therefore might explain the non-negligible heat transfer rate into the vapor bulk. Further discussion on the heat transfer rates into the solution and vapor bulk follows in later sections.

At the droplet vapor-liquid interface, the solution and vapor are assumed to be in equilibrium with each other. Thus, the concentration of the vapor at the interface was calculated using the interface temperature, absorber pressure, and saturated vapor assumption.

$$x_{\text{vap,drop,int}} = f\left(P_{\text{abs}}, T_{\text{vap,drop,int}}, q_{\text{vap,drop,int}} = 1\right) \tag{5.81}$$

$$x_{\text{vap,drop,int}} = f\left(537.3\,\text{kPa}, 45.7\,^{\circ}\text{C}, 1\right) = 0.9936 \tag{5.82}$$

The concentration of the vapor at the droplet interface which was used previously was calculated here. Similarly the concentration of the solution at the interface was

calculated using the interface temperature, absorber pressure, and saturated liquid assumption.

$$x_{\text{sol,drop,int}} = f\left(P_{\text{abs}}, T_{\text{sol,drop,int}}, q_{\text{sol,drop,int}} = 0\right) \tag{5.83}$$

$$x_{\text{sol,drop,int}} = f\left(537.3\,\text{kPa}, 45.61^{\circ}\text{C}, 0\right) = 0.4777 \tag{5.84}$$

Thus, the concentration of solution at the interface is slightly higher than the concentration of the solution in the bulk of the droplet (0.4244), indicating concentration gradients in the droplet. It should be noted though that this gradient is expected to occur in a very thin region, adjacent to the vapor-liquid interface, as previously reported by Jeong and Garimella (2002). With the interface temperature and concentrations in both the vapor and solution known, the terms required to estimate the absorption rates in the droplet are known. Heat and mass transfer rates in the film region are calculated next, before summing these absorption rates over the entire segment.

5.4.3. Film absorption

Fig. 5.11 shows a schematic of the regions of absorption near the film. As is the case with droplet absorption, all the resistance to heat and mass transfer in the vapor phase is assumed to be in a narrow region adjacent to the vapor-liquid interface, called the vapor film. Both concentration and temperature gradients are observed in this region. The heat of absorption liberated at the film interface is removed by the circulating coupling fluid inside the microchannel tube. A temperature gradient is established in the film as this heat transfers from the interface to the coupling fluid. Additionally, the solution is assumed to be well mixed in the film due to the impact of droplets from the previous row, as discussed previously. The solution at the interface is assumed to be in equilibrium with the adjacent vapor. The solution temperature at the interface is estimated using the absorber pressure, average solution concentration, and saturated liquid assumption as follows.

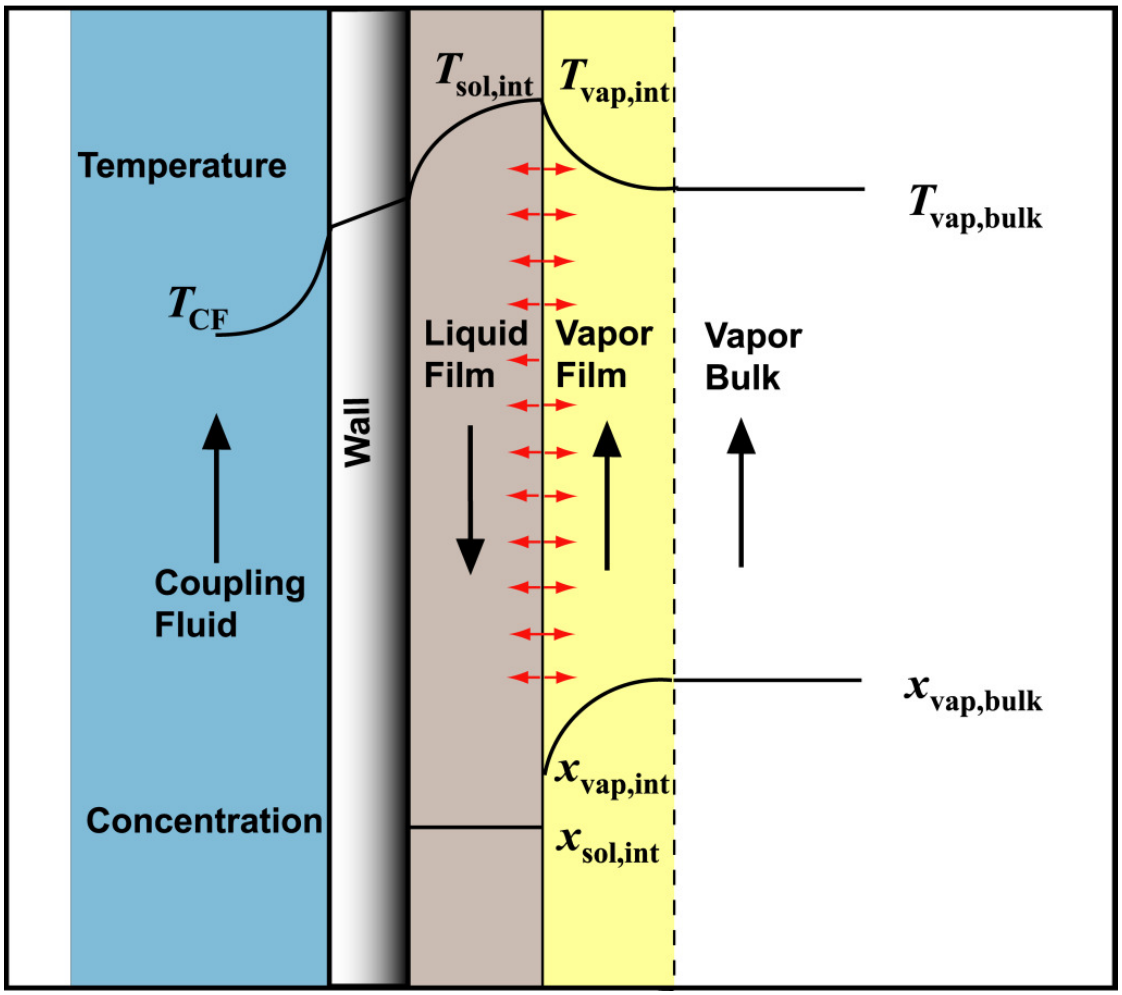

Fig. 5.11 Schematic of falling-film absorption regions

$$T_{\text{sol,film,int}} = f\left(P_{\text{abs}}, x_{\text{sol,avg}}, q_{\text{sol,film,int}} = 0\right) \tag{5.85}$$

$$T_{\text{sol,film,int}} = f\left(537.3\,\text{kPa}, 0.4244, 0\right) = 54.78\,^{\circ}\text{C} \tag{5.86}$$

It should be noted that the corresponding bulk solution temperature was 45.55°C as reported previously. The vapor temperature at the film interface is equal to the solution temperature at the film interface. The concentration of the vapor at the interface was calculated by assuming the vapor is at saturation conditions at the absorber pressure and interface temperature.

$$x_{\text{vap,film,int}} = f\left(P_{\text{abs}}, T_{\text{vap,film,int}}, q_{\text{vap,film,int}} = 1\right) \tag{5.87}$$

$$x_{\text{vap,film,int}} = f\left(537.3\,\text{kPa}, 54.78\,^{\circ}\text{C}, 1\right) = 0.9872 \tag{5.88}$$

The molar flux of the vapor being absorbed into the film is given by the following equation.

$$\dot{n}_{\text{T,film}} = \beta_{\text{vap}} \cdot C_{\text{T}} \cdot \ln\left(\frac{\tilde{z}_{\text{film}} - \tilde{x}_{\text{vap,film,int}}}{\tilde{z}_{\text{film}} - \tilde{x}_{\text{vap,bulk}}}\right) \tag{5.89}$$

$$\begin{aligned}\dot{n}_{\text{T,film}} &= 0.00817\,\text{m s}^{-1} \cdot 0.2067\,\text{kmol m}^{-3} \cdot \ln\left(\frac{1.008 - 0.9879}{1.008 - 0.9926}\right) \\ &= 5.06\times10^{-4}\,\text{kmol m}^{-2}\,\text{s}^{-1}\end{aligned} \tag{5.90}$$

In the above equation, $\tilde{x}_{\text{vap,film,int}}$ is the vapor concentration at the film interface, and $\tilde{z}_{\text{film}}$ is the molar concentration of the condensing flux into the film, which is calculated iteratively later in the model. It is interesting to note that molar flux of the vapor being absorbed into the film is nearly an order of magnitude higher than the molar flux of the vapor being absorbed into the droplet (2.49×10^{-5} kmol m^{-2} s^{-1}). This is due to the different local concentration gradients in the vapor film region, and the concentration of the condensing flux.

The individual ammonia and water condensing fluxes, and mass absorption rates were determined from the total condensing flux as follows:

$$\dot{n}_{\text{A,film}} = \tilde{z}_{\text{film}} \cdot \dot{n}_{\text{T,film}} \tag{5.91}$$

$$\dot{m}_{\text{abs,A,film}} = M_{\text{A}} \cdot \dot{n}_{\text{A,film}} \cdot \bar{A}_{\text{film,int}} \tag{5.92}$$

$$\dot{n}_{\text{W,film}} = \left(1 - \tilde{z}_{\text{film}}\right) \cdot \dot{n}_{\text{T,film}} \tag{5.93}$$

$$\dot{m}_{\text{abs,W,film}} = M_{\text{W}} \cdot \dot{n}_{\text{W,film}} \cdot \bar{A}_{\text{film,int}} \tag{5.94}$$

For the representative test conditions, molar fluxes of ammonia and water were estimated to be 5.09×10^{-4} and -3.93×10^{-6} kmol m^{-2} s^{-1}. The corresponding mass absorption rates for ammonia and water were estimated to be 1.83×10^{-3} and -1.49×10^{-5} kg s^{-1}, respectively. The negative absorption rate for water indicates transfer of water from

the interface to the vapor bulk, which is expected since $\tilde{z}_{film}$ was greater than 1. The mass absorption rate into the film is the sum of the two individual component absorption rates, and calculated to be 1.82×10^{-3} kg s^{-1}. All the above mass transfer calculations were conducted for the complete segment. A summary of the mass transfer characteristics in the droplet and film is provided in Table 5.6.

The absorption rate in the film is nearly two orders of magnitude higher than absorption into the droplet. This is because both the molar condensing flux and the total transfer area are greater for the film than for the droplet. The average transfer area of the film in the bottom segment is 0.2112 m^2, which is nearly 3 times the average droplet transfer area of 0.0768 m^2. The higher absorption rate in the film region is understandable because this region is being cooled continuously, and is able to rapidly remove the heat of absorption liberated at the interface. Furthermore, due to the formation of thin films and fluid mixing on the tube surface, the associated resistances to heat and mass transfer are also low. For the representative test condition, 1.76% of the total absorption in the bottom half of the absorber occurred at the droplets, while 0.34% occurred at the solution pool. Absorption in these regions was adiabatic. The remaining 97.90% of absorption occurred at the film. The contribution of droplets to the overall absorption varied across the different data points on the test matrix. These aspects are discussed in detail later.

5.4.4. Overall heat and mass transfer

To determine the overall heat and mass transfer rates, and the solution and vapor conditions at the top of the absorber segment, the cumulative heat and mass transfer to both the film and the droplet were considered. The mass flow rate and concentration of

Table 5.6 Summary of droplet and film mass transfer characteristics

	$\tilde{z}$	$\tilde{x}_{vap,int}$	$\dot{n}_T$ (kmol m^{-2} s^{-1})	$\dot{m}_T$ (kg s^{-1})
Droplet	0.9319	0.9939	2.49×10^{-5}	3.26×10^{-5}
Film	1.008	0.9879	5.06×10^{-4}	1.81×10^{-3}

the vapor stream leaving the absorber segment can be calculated using the absorption rate of the vapor in the droplet and film regions as follows.

$$\dot{m}_{\text{vap,TA,out}} = \dot{m}_{\text{vap,TA,in}} - \dot{m}_{\text{abs,drop}} - \dot{m}_{\text{abs,film}} \tag{5.95}$$

$$x_{\text{vap,TA,out}} = \frac{\dot{m}_{\text{vap,TA,in}} \cdot x_{\text{vap,TA,in}} - \dot{m}_{\text{abs,A,drop}} - \dot{m}_{\text{abs,A,film}}}{\dot{m}_{\text{vap,TA,out}}} \tag{5.96}$$

It should be noted that the mass flow rate and concentration of the vapor entering the tube array are known previously from the analysis of the solution pool. For the representative test condition, the mass flow rate and concentration of the vapor leaving the tube array for the bottom segment were calculated to be 9.09×10^{-4} kg s^{-1} and 0.9855, respectively. Similarly, the mass flow rate and concentration of the solution entering the absorber segment can be calculated by applying mass and species balances between the solution and vapor.

$$\dot{m}_{\text{sol,TA,in}} = \dot{m}_{\text{sol,TA,out}} + \dot{m}_{\text{vap,TA,out}} - \dot{m}_{\text{vap,TA,in}} \tag{5.97}$$

$$\dot{m}_{\text{sol,TA,in}} \cdot x_{\text{sol,TA,in}} = \dot{m}_{\text{sol,TA,out}} \cdot x_{\text{sol,TA,out}} + \dot{m}_{\text{vap,TA,out}} \cdot x_{\text{vap,TA,out}} - \dot{m}_{\text{vap,TA,in}} \cdot x_{\text{vap,TA,in}} \tag{5.98}$$

It should be noted that the mass flow rate and concentration of the solution exiting the tube array are known previously from the analysis of the solution pool. For the representative test condition, the mass flow rate and concentration of the solution entering the tube array were calculated to be 1.679×10^{-2} kg s^{-1} and 0.394, respectively.

The interface temperature at the inlet of the tube array was determined by assuming that the solution at the interface was in equilibrium with the vapor phase. Since the solution is assumed to be well mixed, the concentration of the solution at the interface is equal to the concentration of the solution in the bulk. Thus, the interface temperature can be calculated as follows:

$$T_{\text{sol,TA,in,int}} = f\left(P_{\text{abs}}, x_{\text{sol,TA,in}}, q_{\text{sol,TA,in,int}} = 0\right) \tag{5.99}$$

For the representative test condition, the interface temperature was calculated to be 60.41°C. As discussed in the previous chapter, the bulk temperature of the solution

was calculated by assuming a linear temperature profile in the film. It should be noted that several other temperature profiles were considered to model the temperature variation in the film, including polynomial and exponential profiles. However, the difference in the bulk temperature, and the corresponding effect on the heat and mass transfer rates was found to be minimal with any of these choices. This is understandable because the film is very thin around the microchannel tube banks and thus, a linear temperature profile closely approximates any of the other profiles. The temperature of the bulk solution at the inlet was calculated using the interface and wall temperatures as follows.

$$T_{\text{sol,TA,in}} = \frac{3}{8} \times T_{\text{wall,in}} + \frac{5}{8} \times T_{\text{sol,TA,in,int}} \tag{5.100}$$

$$T_{\text{sol,TA,in}} = \frac{3}{8} \times 40.92^{\circ}\text{C} + \frac{5}{8} \times 60.41^{\circ}\text{C} = 53.1^{\circ}\text{C} \tag{5.101}$$

It should be noted that the temperature of the wall at the inlet is unknown at this stage of the analysis, and will be calculated later by matching the heat transfer rates on the solution and coupling fluid sides. The state of the solution at the inlet can be defined using the mean solution temperature, concentration, and absorber pressure. The enthalpy of the solution at the inlet of the segment was determined as follows:

$$h_{\text{sol,TA,in}} = f\left(P_{\text{abs}}, T_{\text{sol,TA,in}}, x_{\text{sol,TA,in}}\right) \tag{5.102}$$

For the representative test condition, $h_{\text{sol,TA,in}}$ was calculated to be 8.624 kJ kg^{-1}.

The temperature of the vapor leaving the absorber segment was determined by estimating the sensible heat transfer between the vapor bulk and the vapor-liquid interface. The vapor sensible heat transfer rate was calculated as follows:

$$Q_{\text{vap,TA}} = \alpha_{\text{vap}} \cdot \left(\begin{array}{l} \left(\dfrac{\phi_{\text{T,drop}}}{1 - e^{-\phi_{\text{T,drop}}}} \right) \cdot N_{\text{row}} \cdot N_{\text{drop,pr}} \cdot \overline{A}_{\text{drop}} \cdot LMTD_{\text{vap,drop}} \\ + \left(\dfrac{\phi_{\text{T,film}}}{1 - e^{-\phi_{\text{T,film}}}} \right) \cdot \overline{A}_{\text{film,int}} \cdot LMTD_{\text{vap,film}} \end{array} \right) \tag{5.103}$$

In the above equation, the two terms in the parenthesis represent heat transfer between the vapor bulk and the vapor-liquid interface in the droplet and film regions, respectively. $LMTD_{vap,drop}$ and $LMTD_{vap,film}$ represent the logarithmic mean temperature difference between the vapor bulk and the vapor-liquid interface at the droplet and the film, respectively and are defined as follows:

$$LMTD_{vap,drop} = \frac{\left(T_{vap,TA,in} - T_{sol,drop,out,int}\right) - \left(T_{vap,TA,out} - T_{sol,drop,in,int}\right)}{\ln\left(\frac{T_{vap,TA,in} - T_{sol,drop,out,int}}{T_{vap,TA,out} - T_{sol,drop,in,int}}\right)} \tag{5.104}$$

$$LMTD_{vap,film} = \frac{\left(T_{vap,TA,in} - T_{sol,TA,out,int}\right) - \left(T_{vap,TA,out} - T_{sol,TA,in,int}\right)}{\ln\left(\frac{T_{vap,TA,in} - T_{sol,TA,out,int}}{T_{vap,TA,out} - T_{sol,TA,in,int}}\right)} \tag{5.105}$$

The parameter $\phi_{T,film}$ was calculated as follows:

$$\phi_{T,film} = \frac{\left(\dot{n}_{A,film} \cdot \tilde{C}p_A\right) + \left(\dot{n}_{W,film} \cdot \tilde{C}p_W\right)}{\alpha_{vap}} \tag{5.106}$$

The vapor heat transfer coefficient was determined using the methodology described in the previous chapter, and was calculated to be 50.03 W m^{-2} K^{-1} for the representative test condition. The values for $LMTD_{vap,drop}$ and $LMTD_{vap,film}$ were calculated to be -9.32 and -11.70 K, respectively, while the correction factors $\phi_{T,drop}$ and $\phi_{T,film}$ were calculated to be 0.017 and 0.336, respectively. It should be noted that in the above calculations, the vapor outlet temperature is not explicitly known, which is determined by iteratively matching the vapor sensible heat transfer rate calculated previously with the vapor sensible cooling estimated using the equation below.

$$Q_{vap,TA} = \dot{m}_{vap,TA,bulk} \cdot Cp_{vap,bulk} \cdot \left(T_{vap,TA,in} - T_{vap,TA,out}\right) \tag{5.107}$$

For the representative test condition, the vapor sensible heat transfer rate was calculated to be -0.1817 kW, with a corresponding vapor outlet temperature of 58.35°C. The state of the vapor at the outlet of the segment was defined using the absorber

pressure, the iteratively estimated temperature above, and the previously estimated concentration. Enthalpy of the vapor leaving the segment was estimated as follows:

$$h_{\text{vap,TA,out}} = f\left(P_{\text{abs}}, T_{\text{vap,TA,out}}, x_{\text{vap,TA,out}}\right) \tag{5.108}$$

For the representative test condition, the enthalpy of the vapor at the outlet of the segment was calculated to be 1420 kJ kg^{-1}.

The absorption duty on the solution side can be calculated by considering the mass flow rate and enthalpy of the solution and vapor streams entering and exiting the absorber segment.

$$\begin{aligned} Q_{\text{abs}} = {} & \dot{m}_{\text{sol,TA,in}} \cdot h_{\text{sol,TA,in}} + \dot{m}_{\text{vap,TA,in}} \cdot h_{\text{vap,TA,in}} \\ & - \dot{m}_{\text{sol,TA,out}} \cdot h_{\text{sol,TA,out}} - \dot{m}_{\text{vap,TA,out}} \cdot h_{\text{vap,TA,out}} \end{aligned} \tag{5.109}$$

For the representative test condition, the absorption duty on the solution side was calculated to be 3.69 kW. The molar concentration of the condensing flux in the film region, $\tilde{z}_{\text{film}}$, which was used previously to determine the absorption rate in the film region, was iteratively calculated by matching this absorption duty with the experimentally measured absorption duty on the coupling-fluid side of the segment.

$$Q_{\text{abs}} = \dot{m}_{\text{CF}} \cdot Cp_{\text{CF}} \cdot \left(T_{\text{CF,out}} - T_{\text{CF,in}}\right) \tag{5.110}$$

The molar concentration of the condensing flux, $\tilde{z}_{\text{film}}$, was calculated to be 1.008. The state of the solution entering and the state of the vapor leaving the absorber segment are completely known at this point. Additionally, the absorption rates in the film and droplet region, and the associated heat transfer rates are also known. The overall heat transfer coefficient that can support this heat transfer rate from the solution-side to the coupling fluid-side was calculated as follows:

$$Q_{\text{abs}} = U \cdot A_{\text{seg}} \cdot LMTD_{\text{T}} \tag{5.111}$$

$$LMTD_{\text{T}} = \frac{\left(T_{\text{sol,TA,in}} - T_{\text{CF,out}}\right) - \left(T_{\text{sol,TA,out}} - T_{\text{CF,in}}\right)}{\ln\left(\dfrac{T_{\text{sol,TA,in}} - T_{\text{CF,out}}}{T_{\text{sol,TA,out}} - T_{\text{CF,in}}}\right)} \tag{5.112}$$

It should be noted that in the above equation, A_{seg} based on the outer tube wall was used as a representative area for the overall heat transfer coefficient. In reality, on the solution side, the heat transfer area is the film area, while on the coupling-fluid side, the heat transfer area is the inner tube area. Thus, the respective transfer areas must be considered when estimating the film heat transfer coefficient. For the representative test condition, the overall heat transfer coefficient was calculated to be 1321 W m^{-2} K^{-1}, while $LMTD_T$ was calculated to be 12.26 K. The film heat transfer coefficient was calculated by using a simple 1-D resistance network between the solution and the coupling fluid side.

$$\frac{1}{U} = \frac{D_o}{D_i \cdot \alpha_{CF}} + R_{wall} + \frac{1}{\alpha_{film}} \cdot \frac{A_{seg}}{\bar{A}_{film}} \tag{5.113}$$

The above equation accounts for the different transfer areas for the film and the coupling fluid. As in the previous chapter, the coupling fluid heat transfer coefficient was calculated using the correlation developed by Churchill for forced convective single-phase flow inside circular tubes (Churchill, 1977b, a). For the representative test condition, this was estimated to be 6519 W m^{-2} K^{-1}, while the wall thermal resistance was calculated to be 1.15×10^{-5} K m^2 W^{-1}. The film heat transfer coefficient was calculated to be 2280 W m^{-2} K^{-1}.

The wall temperatures at the inlet and outlet of the segment were estimated by using a similar resistance network and evaluating the *LMTD*s between the film and the wall ($LMTD_{film}$), and the wall and the coupling fluid ($LMTD_{CF}$), as discussed in the previous chapter.

$$Q_{abs} = \alpha_{film} \cdot \bar{A}_{film} \cdot LMTD_{film} \tag{5.114}$$

$$Q_{abs} = U_{CF\text{-}wall} \cdot A_{seg} \cdot LMTD_{CF} \tag{5.115}$$

In the above equation, $U_{\text{CF-Wall}}$ is the overall heat transfer coefficient for heat transfer from the outer surface of the tube wall to the coupling fluid, given by the following equation.

$$\frac{1}{U_{\text{CF-Wall}}} = \frac{D_{\text{o}}}{D_{\text{i}} \cdot \alpha_{\text{CF}}} + R_{\text{wall}} \tag{5.116}$$

The two *LMTD*s are defined as follows, which in turn were used to determine the wall temperature at the solution inlet and outlet.

$$LMTD_{\text{film}} = \frac{\left(T_{\text{sol,TA,in}} - T_{\text{wall,in}}\right) - \left(T_{\text{sol,TA,out}} - T_{\text{wall,out}}\right)}{\ln\left(\frac{T_{\text{sol,TA,in}} - T_{\text{wall,in}}}{T_{\text{sol,TA,out}} - T_{\text{wall,out}}}\right)} \tag{5.117}$$

$$LMTD_{\text{CF}} = \frac{\left(T_{\text{wall,in}} - T_{\text{CF,out}}\right) - \left(T_{\text{wall,out}} - T_{\text{CF,in}}\right)}{\ln\left(\frac{T_{\text{wall,in}} - T_{\text{CF,out}}}{T_{\text{wall,out}} - T_{\text{CF,in}}}\right)} \tag{5.118}$$

For the representative test condition, the wall temperatures at the solution inlet and outlet, $T_{\text{wall,in}}$ and $T_{\text{wall,out}}$, were calculated to be 40.92 and 31.99°C, respectively. The model is now complete with the hydrodynamics of the fluid flow around tube banks, and heat and mass transfer in the solution pool, droplet and film known. This model was applied to the entire data recorded from all the test conditions in the test matrix, and the relevant and heat and mass transfer rates were determined. As discussed in Chapter 4, a major portion of the absorption was found to occur in the bottom segment. Vapor is introduced at the bottom of the absorber, and is first absorbed in the bottom segment. Excess vapor that is not absorbed in this segment is absorbed in the top segment. As seen from the segmental results in the previous chapter, there is a possibility that a part of the top segment did not participate appreciably in the absorption process, because most of the vapor absorbed upstream of this location. The bottom segment on the other hand completely participates in the absorption process. Therefore, only the bottom segment of

the absorber was considered in this analysis. The results of this analysis are discussed in detail later in this chapter.

5.5. Definition of dimensionless numbers

The primary dimensionless numbers pertinent to the heat transfer phenomena in falling-films are the film Nusselt, Reynolds, and Prandtl numbers. Additionally, in the present study, vapor flows counter-current to the falling film and thus, the Weber number and the vapor Reynolds number become important. In the conventional definition of the film Reynolds number, the tube is assumed to be fully wet. However, as previously observed, as solution spreads over the tube surface, it is not fully wet, thus necessitating a revised definition for the linear solution mass flux, taking into account the wetting ratio.

$$\Gamma_{\text{film}} = \Gamma_{\text{l}} \cdot \frac{A_{\text{seg}}}{A_{\text{film}}} = \frac{m_{\text{sol}}}{N_{\text{tube.pr}} \cdot L_{\text{tube}} \cdot 2} \cdot \frac{1}{WR} \tag{5.119}$$

This definition accounts for the fact that a higher amount of fluid is flowing through a reduced amount of area as the tube is not fully wet. Using this revised definition for Γ_{film}, the film Reynolds number is defined as follows:

$$Re_{\text{film}} = \frac{4 \cdot \Gamma_{\text{film}}}{\mu_{\text{sol}}} \tag{5.120}$$

The film Prandtl number depends only on the solution properties and is defined as follows:

$$Pr_{\text{film}} = \frac{\mu_{\text{sol}} \cdot Cp_{\text{sol}}}{k_{\text{sol}}} \tag{5.121}$$

The film Nusselt number, which is the dimensionless film heat transfer coefficient, requires a characteristic length for its definition. Several authors have previously proposed using the tube diameter, D_{o}, or combination of solution properties, $\left(\nu^2/g\right)^{1/3}$, as the characteristic length (Hu and Jacobi, 1996b). In this study, for

consistency with the definition of the film Reynolds number, the average film thickness is considered to be the characteristic length.

$$Nu_{\text{film}} = \frac{\alpha_{\text{film}} \cdot \delta_{\text{film,avg}}}{k_{\text{sol}}} \tag{5.122}$$

The vapor Reynolds number definition is taken from the definition presented in Mills (1995) for vapor in cross-flow across a tube bank. The average vapor velocity across a tube row is calculated based on the free flow area of the tube row and the tube pitch.

$$u_{vap} = u_{vap,min} \cdot \frac{S_T}{S_T - \frac{\pi \cdot D_{\text{o}}}{4}} \tag{5.123}$$

Where $u_{\text{vap,min}}$ is at a location in the banks between tube rows. It should be noted that u_{vap} is the average velocity within the tube bank, and not the maximum velocity, which occurs at the centerline of the tube row. The vapor Reynolds number is defined using the tube outer diameter as the characteristic length, as follows:

$$Re_{\text{vap}} = \frac{\rho_{\text{vap}} \cdot u_{\text{vap}} \cdot D_{\text{o}}}{\mu_{\text{vap}}} \tag{5.124}$$

Finally, the Weber number for the flow is defined as follows:

$$We = \frac{\rho_{\text{vap}} \cdot u_{\text{vap}}^2 \cdot D_{\text{o}}}{\sigma_{\text{sol}}} \tag{5.125}$$

5.6. Heat and mass transfer results and discussion

5.6.1. Solution pool

Table 5.7 shows a summary of the interface heat duty, $Q_{\text{pool,int}}$, the heat transfer rates to the vapor and solution bulk, $Q_{\text{vap,pool}}$ and $Q_{\text{sol,pool}}$, and the vapor absorption rate at the solution pool, $\dot{m}_{\text{abs,pool}}$. The heat transfer rate to the vapor bulk was found to range from 3.95 - 14.57 W, while the heat transfer rate to the solution bulk was found to range

Table 5.7 Summary of solution pool heat and mass transfer

Nominal solution concentration	$Q_{sol,pool}$ (W)	$Q_{vap,pool}$ (W)	$Q_{pool,int}$ (W)	$\dot{m}_{abs,pool}$ ($\times 10^{-5}$ kg s^{-1})
40%	0 - 0.34	3.95 - 14.57	3.95 - 14.88	0.28 - 1.14
48%	0.11 - 1.30	6.83 - 14.09	7.59 - 14.38	0.55 - 1.08
55%	0.12 - 0.31	7.20 - 8.00	6.51 - 8.22	0.47 - 0.60

from 0 - 1.30 W. While the natural convection heat transfer coefficients were higher in the liquid phase in comparison to the vapor phase, the heat transfer rate to the vapor bulk was higher due to the greater temperature difference between the interface and the average vapor. Also, higher vapor heat transfer rates were observed at lower nominal solution concentrations. This is because experiments involving lower solution concentrations were conducted at higher coupling fluid temperatures, resulting in a larger temperature difference between the interface and the average vapor near the solution pool. The interface heat duty was found to range between 3.95 - 14.88 W, with higher duties observed at lower solution concentration. This is due to the higher vapor heat transfer rate and favorable concentration difference between the vapor and the solution facilitating better absorption. The mass of vapor absorbed in the solution pool ranged between $0.28 - 1.14 \times 10^{-5}$ kg s^{-1}, which is a small fraction of the total absorption in the absorber. As previously noted, absorption into the solution pool is adiabatic and thus the absorption rates are lower. However, since absorption in the pool influences the vapor inlet conditions to the tube array, it is important to consider this phenomenon.

5.6.2. Droplet

Table 5.8 shows a summary of the heat transfer rates to the vapor bulk, $Q_{vap,drop}$, and solution in the droplet, $Q_{sol,drop}$, from the droplet vapor-liquid interface, and the latent heat released at the droplet interface $Q_{drop,int}$. Heat transfer rates into the vapor bulk were found to range between 12.4 - 61.5 W, while the heat transfer rates into the solution were found to range between -90.9 - 96.8 W. The negative values for heat transfer rates in the

Table 5.8 Summary of droplet heat transfer

Nominal solution concentration	$Q_{vap,drop}$ (W)	$Q_{sol,drop}$ (W)	$Q_{drop,int}$ (W)
40%	12.8 - 58.9	-90.9 - 92.7	-65 - 143.2
48%	12.4 - 61.5	-46.8 - 86.9	-18.5 - 122.1
55%	30.3 - 59.2	-51.6 - 96.8	-6.3 - 56.5

solution indicate transfer of heat from the droplet bulk to the interface. At these test conditions, the droplet bulk temperature is higher than the interface temperature. As seen previously, absorption of vapor into the droplet is governed by a coupled heat and mass transfer process. Due to the local concentration profiles in the vapor film next to the droplet, and the concentration of the condensing flux, transfer of species can be both towards and away from the vapor-liquid interface. In cases where species transfer away from the interface, heat is transferred from the droplet bulk to the vapor-liquid interface, supplying the necessary duty for phase change of the liquid molecules, and eventually into the vapor bulk. In the present work, only positive values for the heat transfer rates into the vapor bulk were observed, which indicates that the vapor bulk, which is at a lower temperature than the interface, is effectively cooling the droplet. It should be noted that heat can also transfer from the vapor bulk to the vapor-liquid interface if the vapor bulk is at higher temperature that the interface, which will result in negative values for $Q_{vap,drop}$.

The heat released at the droplet interface, $Q_{drop,int}$, was found to be range between -65 - 143.2 W. While the negative values of $Q_{drop,int}$ indicate transfer of species away from the interface, the positive values of $Q_{drop,int}$ indicate absorption of vapor into the droplet. Unlike absorption into the solution film, where the bulk of the heat is expected to transfer towards the coupling fluid, there is no preferred path for heat transfer in droplet absorption, and thus, the eventual direction depends upon the local concentration and temperature gradients near the vapor-liquid interface. In general, higher values of $Q_{sol,drop}$ were observed in comparison to $Q_{vap,drop}$. This is due to two reasons. Because the

penetration depth of the thermal wave is very short (1-3×10^{-4} m for a majority of the test conditions) due to the brief droplet formation times, even a small temperature difference between the interface and the solution bulk results in a sharp temperature gradient. This gradient coupled with the high thermal conductivity of the solution results in higher values for $Q_{sol,drop}$.

Table 5.9 shows a summary of the absorption rates of the vapor, $\dot{m}_{abs,drop}$, and the constituent ammonia, $\dot{m}_{abs,A,drop}$, and water, $\dot{m}_{abs,W,drop}$, at the droplet interface. The vapor absorption rates were found to vary from -4.6 – 10.2×10^{-5} kg s^{-1}. As previously discussed, the negative values indicate transfer of species away from the interface. For all test conditions, the molar concentration of the condensing flux, $\tilde{z}_{drop}$, was found to be less than 1, indicating that both ammonia and water species were transferring in the same direction. For test conditions with nominal solution concentrations 40%, 48%, and 55%, this value was found to range from 0.8970 - 0.9107, 0.9210 - 0.9312, 0.9398 - 0.9444, respectively. Thus, as the solution concentration increased, the concentration of the condensing flux increased, resulting in a smaller fraction of water in the absorbing vapor, as reflected in the smaller water mass transfer rates in Table 5.9. As noted previously, $\tilde{z}_{drop}$ depends upon the latent heat of phase change of ammonia and water, and the heat of mixing. The heat of mixing of the condensed constituents varies with the solution concentration, which in turn affects $\tilde{z}_{drop}$, thereby affecting the overall absorption rates of constituent ammonia and water.

Table 5.9 Summary of droplet mass transfer

Nominal solution concentration	$\dot{m}_{abs,A,drop}$ (×10^{-5} kg s^{-1})	$\dot{m}_{abs,W,drop}$ (×10^{-5} kg s^{-1})	$\dot{m}_{abs,drop}$ (×10^{-5} kg s^{-1})
40%	-4.2 - 9.2	-0.4 - 1.0	-4.6 - 10.2
48%	-1.2 - 8.1	-0.09 - 0.7	-1.3 - 8.8
55%	-0.4 - 3.8	-0.02 - 0.2	-0.5 - 4.0

5.6.3. Film

Table 5.10 shows a summary of the absorption rates of the vapor, $\dot{m}_{abs,film}$, and the constituent ammonia, $\dot{m}_{abs,A,film}$, and water, $\dot{m}_{abs,W,film}$, at the film interface. The vapor absorption rates in the film ranged between 8.6 - 36.4×10^{-4} kg s^{-1} which is significantly higher than the absorption rates observed in the solution pool and the droplet. This is an expected trend, because the film is actively being cooled by the circulating coupling fluid. The molar concentration of the condensing flux in the film, $\tilde{z}_{film}$, was usually slightly greater than 1 for most test conditions. This is reflected in the negative values for the mass transfer rates of water. As refrigerant enters the bottom of the tube array, it is almost pure ammonia after interactions with the solution pool. Thus, the absorption rate is high initially, resulting in release of a substantial amount of heat at the interface. If sufficient heat transfer between the film and the coupling fluid to support this heat release does not occur, the excess heat at the interface will locally desorb water at the interface. However, the amount of water desorbed is very small, typically almost 2 orders of magnitude less than the amount of ammonia absorbed into the film.

Table 5.11 shows a summary of the absorption rates in the solution pool, droplet, and film, as percentages of the total absorption rate. As expected, the major portion of the absorption was found to occur in the film, ranging from 92.37 - 101.8%. Values greater than 100% indicate test conditions where mass is transferred away from the droplet vapor-liquid interface, resulting in an increase in the vapor mass to be absorbed into the solution film. Absorption into the droplet comes next, ranging from -2.07 - 6.89%,

Table 5.10 Summary of film mass transfer

Nominal solution concentration	$\dot{m}_{abs,A,film}$ (×10^{-5} kg s^{-1})	$\dot{m}_{abs,W,film}$ (×10^{-5} kg s^{-1})	$\dot{m}_{abs,film}$ (×10^{-5} kg s^{-1})
40%	112.6 - 233.5	-6.8 - 0.05	110.5 - 231.5
48%	87.7 - 257.9	-4.9 - -0.6	86.0 - 253.4
55%	201.8 - 366.5	-2.5 - -0.9	200.7 - 364.1

Table 5.11 Summary of absorption in each region

Nominal solution concentration	Pool absorption (%)	Droplet absorption (%)	Film absorption (%)
40%	0.22 - 0.77	-2.07 - 6.89	92.37 - 101.8
48%	0.25 - 0.85	-0.86 - 4.86	94. 29 - 100.2
55%	0.14 - 0.27	-0.15 - 1.53	98.25 - 99.98

followed by absorption into the solution pool, ranging from 0.14 - 0.85%. As can be seen in Fig. 5.12, the contribution of droplet mode absorption to the total absorption rate was higher at lower solution concentrations, which can be attributed to the favorable concentration differences between the vapor and solution. Bohra *et al.* (2008) reported that the droplet mode contributed to a maximum of 6% of the total absorption for a majority of their cases. At very low solution concentrations (5-15%), higher absorption rates in the droplet were observed. They also observed that as the solution concentration decreases, the absorption rate in droplet mode increases, a trend which is consistent with the observations in the present study. Subramaniam and Garimella (2009) also reported a contribution of about 4.4% from droplet absorption to the overall absorption for the water-LiBr fluid pair. However, previous modeling studies conducted on water-LiBr absorption reported absorption rates as high as 50% in the droplet mode (Kirby and Perez-Blanco, 1994; Jeong and Garimella, 2002, 2005). Bohra *et al.*(2008) argued that ammonia-water mixtures have higher liquid-phase diffusivities and smaller surface tension forces, which result in more rapid absorption rates in the film in comparison to water-LiBr absorption. In addition to these explanations, it should also be noted that the droplets generated in the microchannel tube array are inherently smaller in size with a very short residence time, and thus, the overall contribution to absorption is relatively lower.

While the contribution to absorption from the droplet mode is limited, it is important to consider this flow mode for several reasons. As the solution concentration decreases, the contribution to absorption from the droplet mode increases. Further, there

is also the possibility of desorption of vapor from the droplet which can increase the absorption load on the film. The flow of solution in the droplets is closely linked with the flow of solution as a film around the tube banks. As reported by Subramaniam and Garimella (2009), the impact of droplets produces substantial perturbation in the flow patterns in the film, generating waves and mixing the solution, which results in much higher absorption rates in the film. Thus, it is important to consider both the hydrodynamics, and the associated heat and mass transfer, to obtain a representative picture of the absorption process in horizontal tube banks.

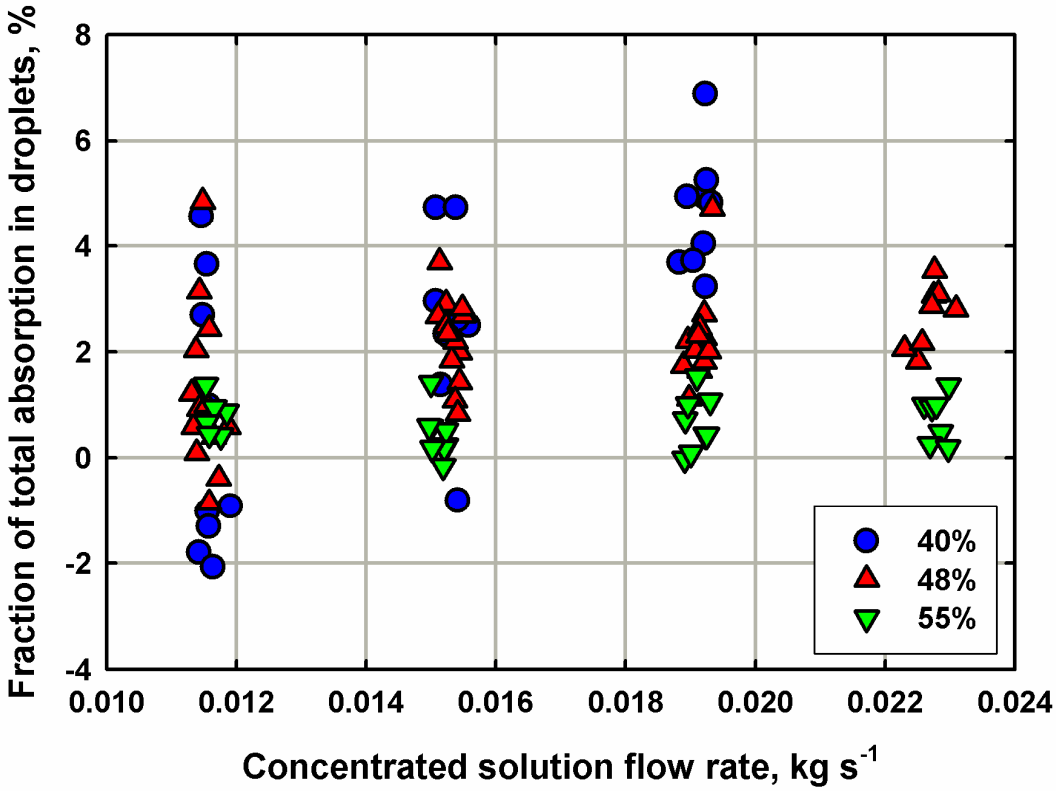

Fig. 5.12 Contribution of droplet mode absortpion as a function of concentrated solution flow rate

5.6.4. Heat transfer coefficient and Nusselt number

Fig. 5.13 shows a plot of film heat transfer coefficient as a function of the modified linear solution mass flux, Γ_{film}. The heat transfer coefficients vary from 1788 – 4179 W m^{-2} K^{-1}, with an average value of 2537 W m^{-2} K^{-1}. As discussed in the previous chapter, the coupling fluid Reynolds numbers and heat transfer coefficients were found to vary from 2431-3748 and 3032-13407 W m^{-2} K^{-1}, respectively. Higher heat transfer coefficients were generally observed for the higher solution concentration cases, although

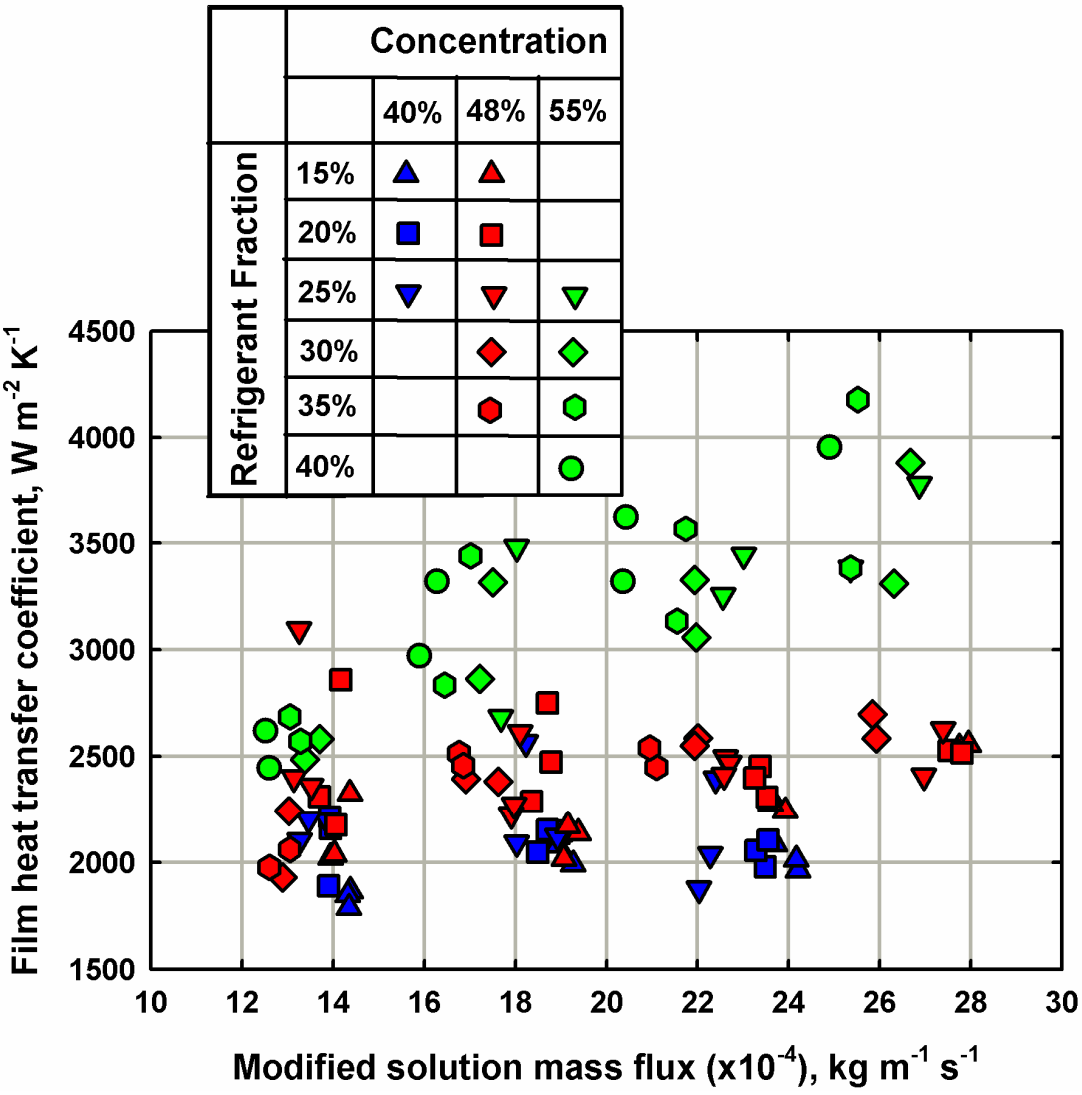

Fig. 5.13 Film heat transfer coefficient as a function of modified solution mass flux

it should be noted that the refrigerant fractions were also higher for the higher solution concentration cases. As explained previously, the vertical spread at any solution mass flux is due to an increasing vapor flow rate, which results in higher absorption duties, necessitating higher heat transfer rates. This spread increases with increasing solution mass flux. Some authors have previously reported a similar observation when they studied the effect of gas flow on falling-films (Hu and Jacobi, 1996b; Kwon and Jeong, 2004). As the vapor flow rate increases, the absorption duties also increase, resulting in higher solution heat transfer coefficients. Also, with increasing vapor flow rate, counter-current to the falling liquid, interfacial shear at the liquid film boundary probably increases, resulting in higher transfer rates.

To understand the effects of different flow parameters, and the solution and vapor properties, dimensionless numbers are compared next. Fig. 5.14 shows a plot of the film Nusselt number as a function of the film Reynolds number. The film Nusselt number varied from 0.2944 - 0.8545, while the film Reynolds number varied from 7.41 - 18.35. At a nominal temperature of 40^{o}C, the viscosity of the solution decreases from 7.86 - 5.84×10^{-4} kg m^{-1} s^{-1} with an increase in solution concentration from 40-55%. Thus, the increase in the film Reynolds number is due to a combination of the increase in solution linear mass flux and decrease in solution viscosity. Similarly, at a nominal temperature of 40^{o}C, the thermal conductivity of the solution decreases marginally from 0.5564 – 0.5282 W m^{-1} K^{-1}. Additionally, as previously noted, over the range of experiments conducted in this study, the average film thickness varies between 0.877 – 1.161×10^{-4} m. The film Nusselt number depends upon both of these parameters, and increases with a decrease in thermal conductivity of the solution and increase in thickness of the film. Lower thermal conductivity values are observed at higher solution concentrations and thicker films are observed at higher solution flow rates.

As can be seen from Fig. 5.14, higher film Nusselt numbers were observed for higher solution concentrations. For the same α_{film} lower thermal conductivity and thicker

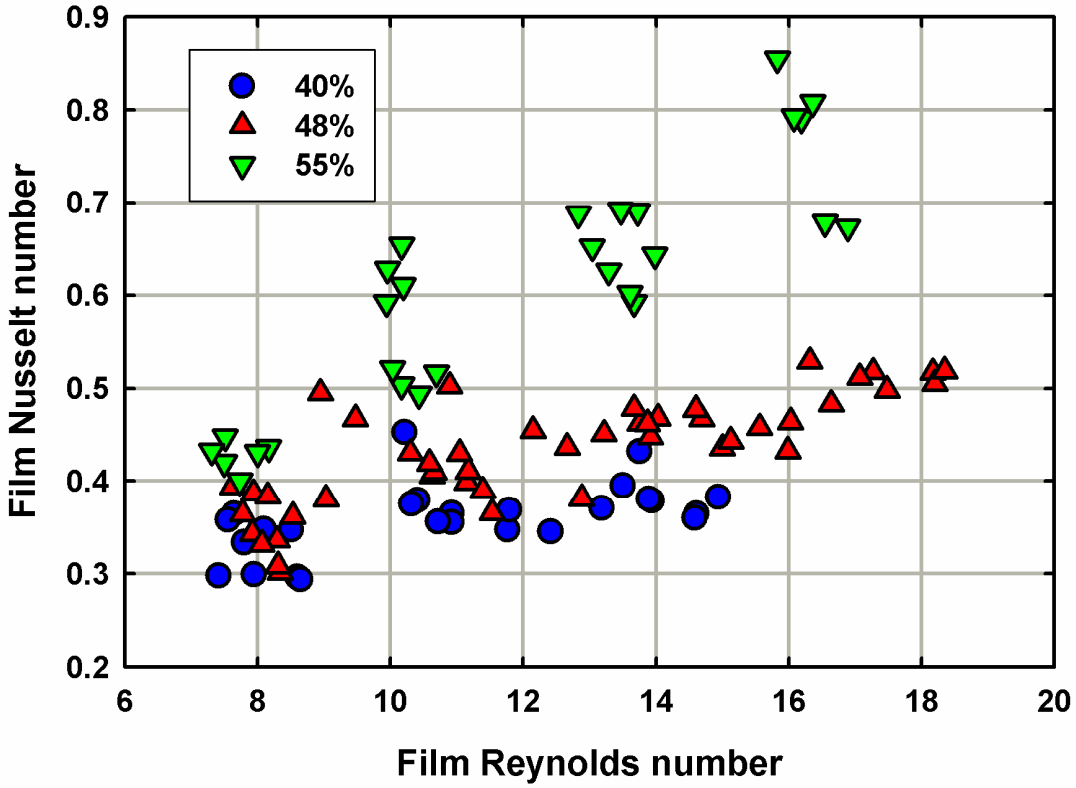

Fig. 5.14 Film Nusselt number as a function of film Reynolds number

films correspond to higher values of Nu_{film} The higher film heat transfer coefficient values at the higher solution concentrations are reflected in higher Nu_{film} at these concentrations. Additionally, the vertical spread at any film Reynolds number is due to an increasing vapor flow rate (correspondingly increasing vapor Reynolds number), and this spread increases with increasing film Reynolds number. Overall, a general increasing trend is observed in the film Nusselt number with increasing film Reynolds number.

In addition to the solution viscosity and thermal conductivity, the specific heat of the solution is also an important property. To understand the effect of these solution properties, Fig. 5.15 shows a plot of the film Nusselt number as a function of the film Prandtl number. While variation is observed in the film Nusselt number values, there is

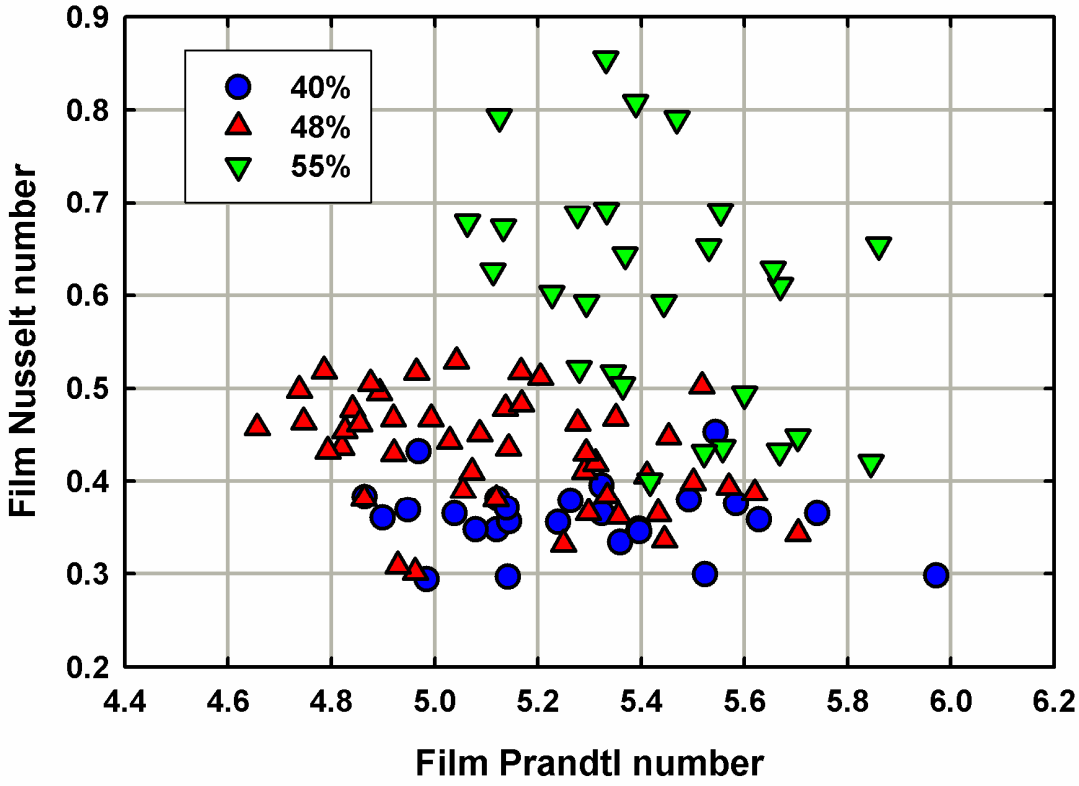

Fig. 5.15 Film Nusselt number as a function of film Prandtl number

no noticeable trend. In general, higher values were observed at higher Prandtl numbers, although it should be noted that the range of Prandtl numbers is small.

To understand the combined influence of the flow and fluid property related parameters, the film Nusselt number is plotted as a function of the product of the film Reynolds and Prandtl numbers, or the film Peclet number (Fig. 5.16). A more discernible and systematic increasing trend is observed in the film Nusselt number with increasing film Peclet number. Thus, increasing Reynolds and Prandtl numbers together contribute to the increasing Nusselt number. The vertical spread at any specified Peclet number is again attributed to the increasing vapor flow rate, which induces shear at the vapor-liquid interface and enhances the heat transfer rate. Hu and Jacobi (1996b) suggested that the

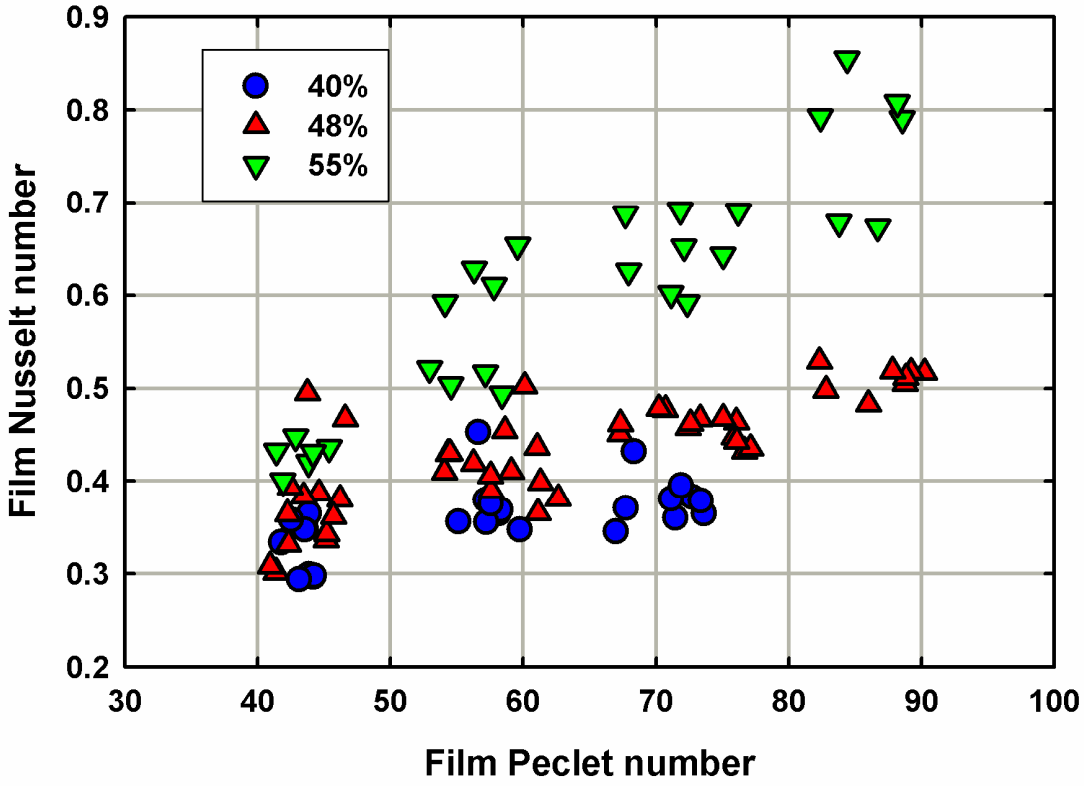

Fig. 5.16 Film Nusselt number as a function of the film Peclet number

Weber number might be an important parameter in falling-film heat transfer in the presence of a moving vapor, and this aspect is investigated next.

Figs. 5.17 and 5.18 show plots of the film Nusselt number as a function of the Weber number and the vapor Reynolds number, respectively. The Weber number increases with increase in the solution concentration, and with increases in the vapor velocity (or the vapor flow rate.) Similarly, the vapor Reynolds number increases with increases in the vapor velocity. Thus, an increase in vapor velocity results in an increase in both of these dimensionless numbers. A clear increasing trend is observed in the film Nusselt number with increasing Weber number and vapor Reynolds numbers. This confirms that the vertical spread observed in the plots of the film Nusselt number with

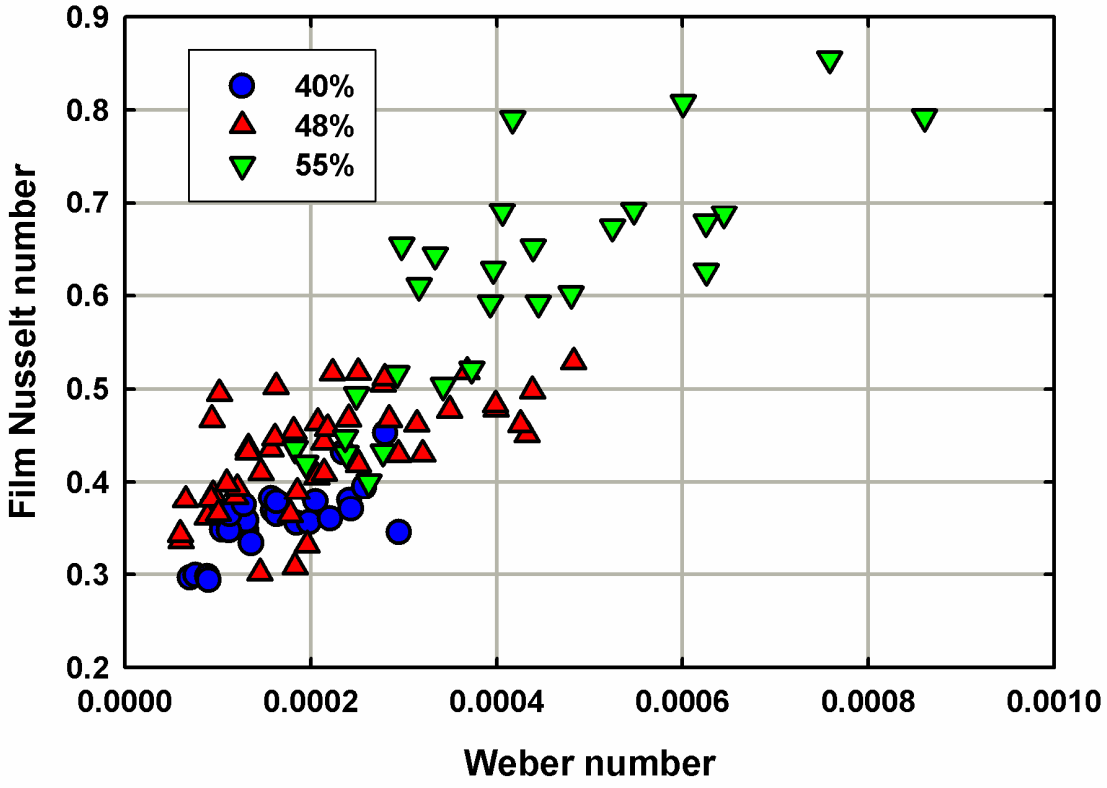

Fig. 5.17 Film Nusselt number as a function of Weber number

respect to the film Reynolds and Peclet numbers is due to the increasing vapor flow rate, which enhances the heat transfer rate by increasing shear at the interface.

For the representative test condition, the momentum rates of the vapor flowing upward ($\dot{m}_{vap} \cdot u_{vap}$) and solution flowing downward ($\dot{m}_{sol} \cdot u_{sol}$) were calculated to be 5.3×10^{-5} and 4.6×10^{-4} kg m s^{-2}, respectively. Thus, the vapor momentum rate is approximately 12% of the solution momentum rate. For the test conditions in this study, the vapor momentum rate ranged from 7-45% of the solution momentum rate. A similar range was observed for the kinetic energy rate ($(1/2)\cdot\dot{m}\cdot u^2$) for the test conditions in this study (5-52%). Therefore, the momentum and kinetic energy of the vapor stream does constitute a non-negligible fraction of the corresponding values for the solution stream, particularly at higher vapor flow rates, indicating that there may be some influence of the

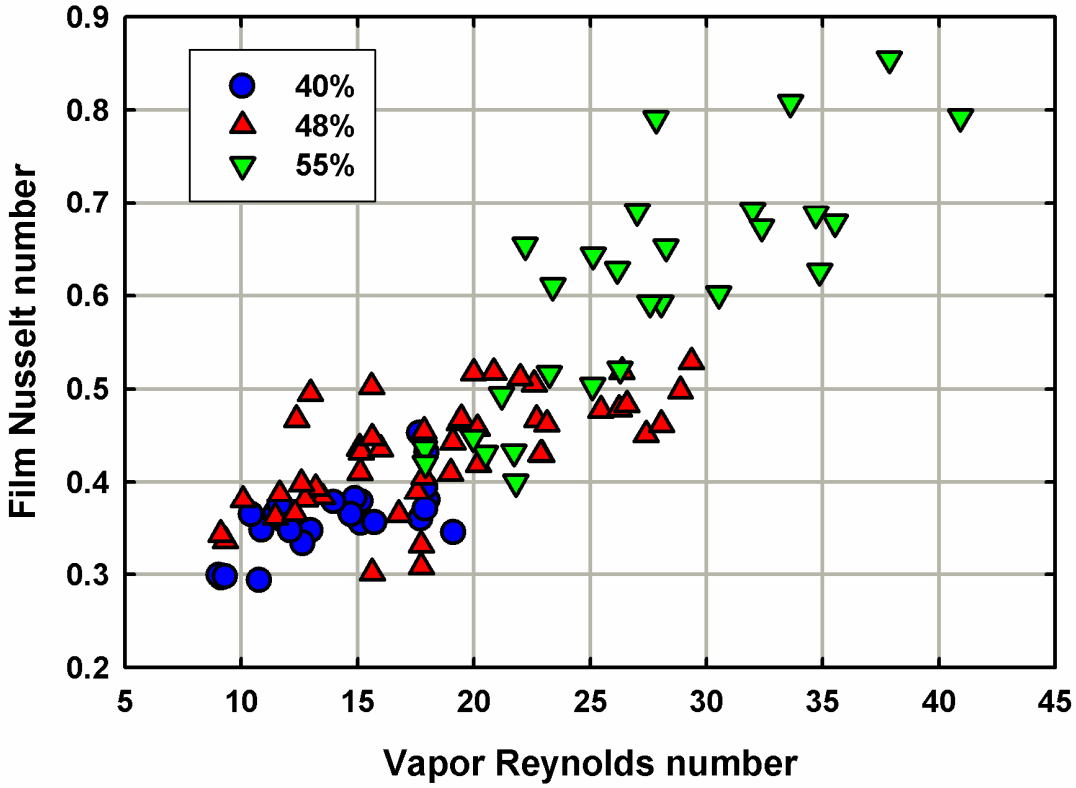

Fig. 5.18 Film Nusselt number as a function of vapor Reynolds number

shear at the vapor-liquid interface. These observations further support the trends seen in Figs. 5.17 and 5.18.

5.7. Nusselt number correlation development

As can be seen from the above discussion, the film Nusselt number was influenced by the flow rate through the film Reynolds number, fluid properties by the film Reynolds and Prandtl number, and the vapor flow enhancement through the vapor Reynolds number. Vapor Reynolds number instead of Weber number was chosen because of the convenience in calculating this parameter (as it is independent of the solution conditions) and because Re_{vap} was found to vary over a wider range of values, which resulted in reasonable exponents for the correlation. Based on these observations, the following form was adopted to develop a correlation for the present data.

$$Nu_{\text{film}} = a \cdot Re_{\text{film}}^{\text{b}} \cdot Pr_{\text{film}}^{\text{c}} \cdot \left(1 + Re_{\text{vap}}^{\text{d}}\right) \tag{5.126}$$

In the above equation, the constant *a*, and the exponents b, c, and d are determined using regression analysis. It can be seen in the above formulation that as the vapor flow rate approaches zero, the influence of the last term tends to 1, indicating falling-film flow in the absence of vapor flow. The regression analysis yields the following Nusselt number correlation.

$$Nu_{\text{film}} = 0.0071 \cdot Re_{\text{film}}^{0.6} \cdot Pr_{\text{film}}^{0.6} \cdot \left(1 + Re_{\text{vap}}^{0.5}\right) \tag{5.127}$$

Fig. 5.19 shows a comparison of the measured and predicted film Nusselt numbers along with ±25% error bands. The absolute uncertainty in the prediction from the film Nusselt number correlation is given by:

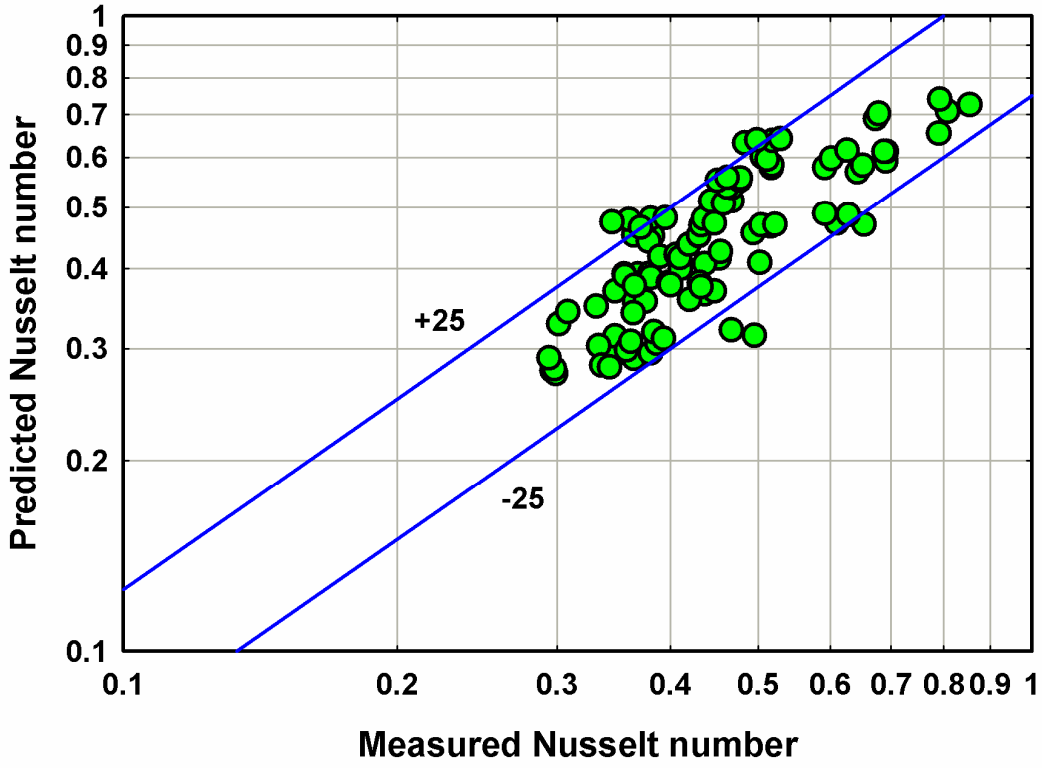

Fig. 5.19 Comparison of measured and predicted Nusselt numbers

$$\Delta Nu = \left| \frac{Nu_{\text{film,measured}} - Nu_{\text{film,predicted}}}{Nu_{\text{film,measured}}} \right| \cdot 100[\%] \qquad (5.128)$$

As can be seen from Fig. 5.19, the above correlation is able to predict the experimentally measured film Nusselt number fairly accurately. The absolute uncertainty in the prediction of the film Nusselt number for all the test conditions studied here was 0.5-37.7% with an average value of 12.9%. A total of 94 of the 103 data points were predicted within ±25%.

5.7.1. Parametric evaluation of film Nusselt number correlation

The film Nusselt number correlation developed above can be used to study the influence of various parameters on the film absorption heat transfer process. Fig. 5.20

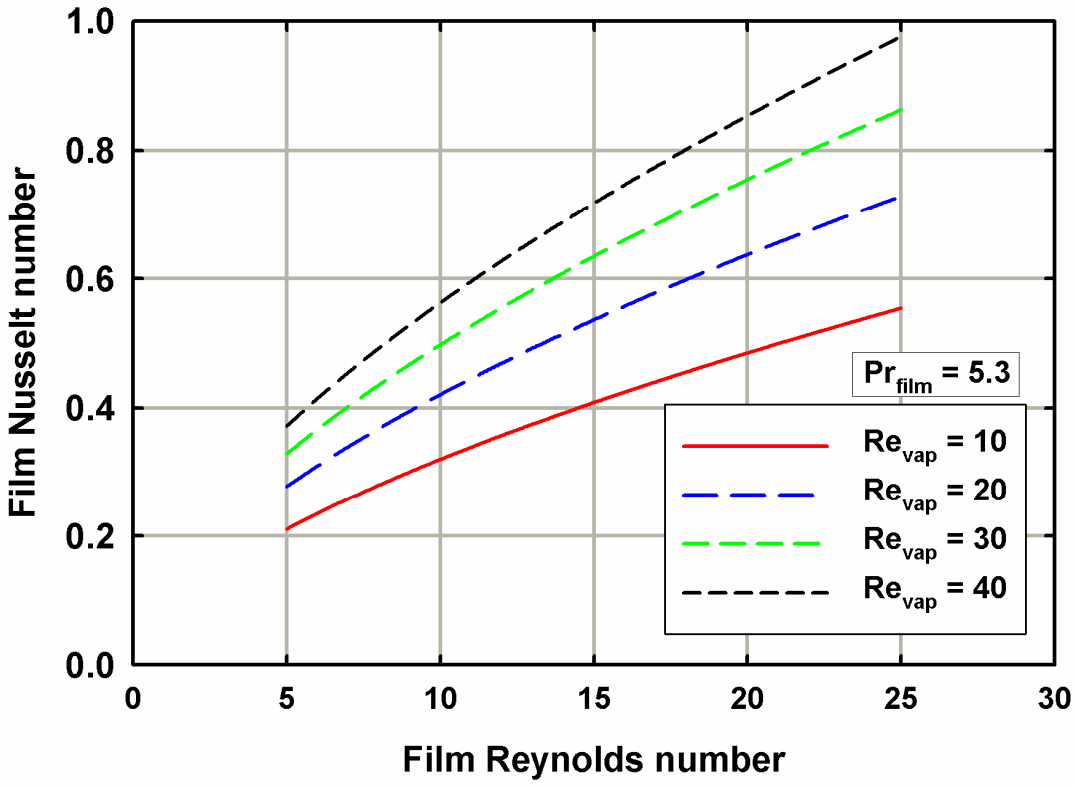

Fig. 5.20 Effect of Re_{film} and Re_{vap} on Nu_{film}

shows a plot of the film Nusselt number as a function of the film Reynolds number for different vapor Reynolds numbers. The film Prandtl number was held constant at 5.3 (representative of the average Prandtl number in the present work) for all calculations. The film Nusselt number was found to increase with an increase in the film Reynolds number at any fixed vapor Reynolds number. Similarly, the film Nusselt number increased with an increase in the vapor Reynolds number at any fixed film Reynolds number. These trends are expected, because increasing solution mass flux and vapor flow rate was found to enhance the heat transfer coefficient.

Fig. 5.21 shows a plot of the film Nusselt number as a function of the film Reynolds number for different film Prandtl numbers. The vapor Reynolds number is held constant at 20 for all calculations. This plot also indicates an increasing trend in the film

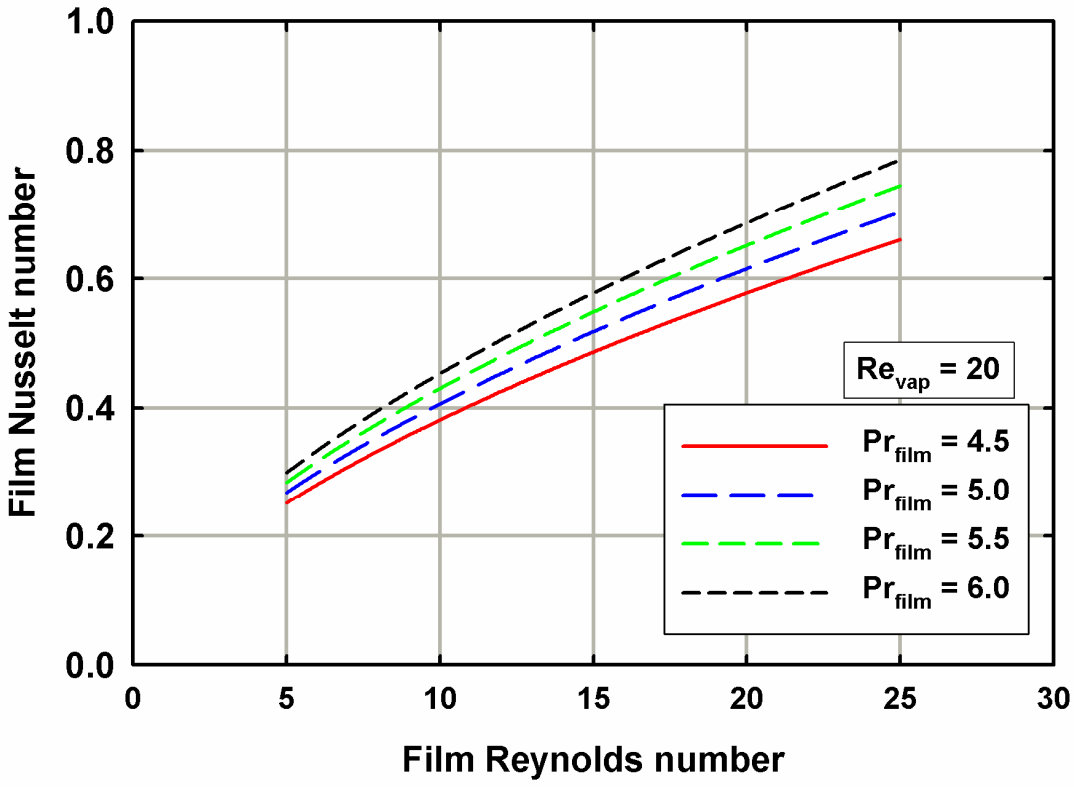

Fig. 5.21 Effect of Re_{film} and Pr_{film} on Nu_{film}

Nusselt number with the film Prandtl number, which is expected from Eq. 5.127.

While these trends demonstrate the capability of the correlation to predict film absorption heat transfer characteristics, the effect of operating conditions on the heat transfer process are not explicitly observed. To study this further, the effect of solution properties on the dimensionless numbers was explored. Table 5.12 shows a summary of the film Prandtl and Reynolds numbers at a representative solution temperature of 40°C, linear solution mass flux Γ_{film} of 2.5×10^{-3} kg m^{-1} s^{-1}, for solution concentrations ranging from 40-60%. As can be seen from this table, at a fixed solution temperature, the film Prandtl number decreases with an increase in solution concentration. Therefore according to Fig. 5.21, the film Nusselt number should decrease with increased solution concentration, which is contrary to the previous observations. However, it can also be seen from Table. 5.12 that as the solution concentration increases, for the same linear solution mass flux, Γ_{film}, the film Reynolds number increases. Thus, the combined effect of both these terms must be considered to address the true effect of the operating conditions. A closer look at Eq. 5.127 reveals this dependence.

$$Nu_{film} = 0.0071 \cdot Re_{film}^{0.6} \cdot Pr_{film}^{0.6} \cdot \left(1 + Re_{vap}^{0.5}\right) \tag{5.129}$$

$$Nu_{film} = 0.0071 \cdot \left(\frac{4 \cdot \Gamma_{film}}{\mu_{sol}}\right)^{0.6} \cdot \left(\frac{\mu_{sol} \cdot Cp_{sol}}{k_{sol}}\right)^{0.6} \cdot \left(1 + Re_{vap}^{0.5}\right) \tag{5.130}$$

$$Nu_{film} = 0.0071 \cdot \left(4 \cdot \Gamma_{film}\right)^{0.6} \cdot \left(\frac{Cp_{sol}}{k_{sol}}\right)^{0.6} \cdot \left(1 + Re_{vap}^{0.5}\right) \tag{5.131}$$

Table 5.12 Variation of film characteristics with solution concentration

Nominal solution concentration	T_{sol} (°C)	Pr_{film}	Γ_{sol} (kg m- s^{-1})	Re_{film}	$Cp_{sol}\, k_{sol}^{-1}$ (m s kg^{-1})
40%	40	6.216	2.5×10^{-3}	12.73	7912
50%	40	5.523	2.5×10^{-3}	15.15	8364
60%	40	4.438	2.5×10^{-3}	19.19	8833

From the above equation, at a constant Γ_{film} and Re_{vap}, the Nu_{film} increases with increase in the value of the ratio $\left(Cp_{sol}/k_{sol}\right)$. As can be seen in Table 5.12, this ratio increases with an increase in the solution concentration, resulting in an increase in the film Nusselt number. This is confirmed by Fig. 5.22, which shows an increase in Nu_{film} with an increase in the solution concentration.

It should be noted that in these calculations, the Re_{vap} was held constant. Due to the coupled nature of the heat and mass transfer process during absorption, the average vapor mass flow rate in any segment is significantly affected by the film heat transfer coefficient. Thus, not only is the Re_{vap} dependent upon the vapor properties (μ_{vap}), which in turn depend on the operating conditions (P_{abs}, Q_{Evap}), it is also dependent on the mass flow rate, which depends upon the local absorption process. This coupled relationship

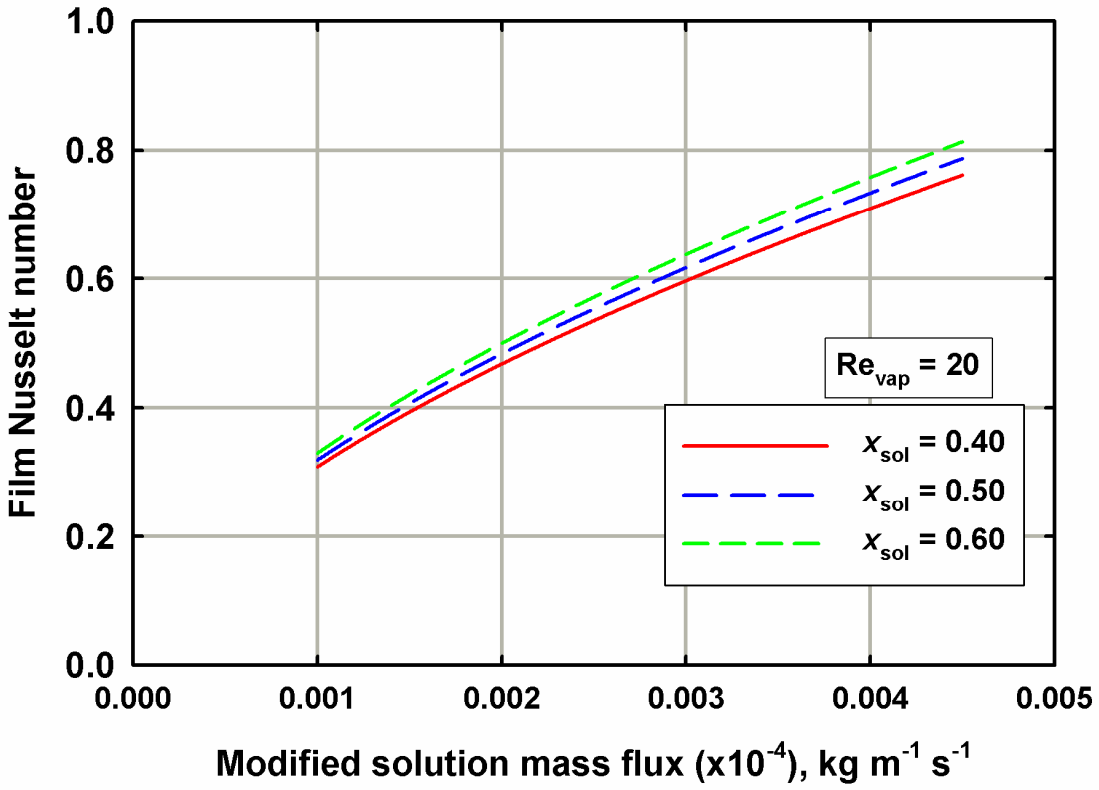

Fig. 5.22 Effect of Γ_{film} and solution concentration on Nu_{film}

further emphasizes the need to study both heat and mass transfer simultaneously when considering ammonia-water absorption. In general, at a given solution mass flux, any increase in the Re_{vap} will result in an increase in the Nu_{film}, as seen in the previous results.

Another interesting observation from Eq. 5.131 is that the Nu_{film} appears to be independent of the solution viscosity. While this is true, it should be noted that the film heat transfer coefficient, α_{film}, depends on the solution viscosity. In the definition of Nu_{film}, the characteristic length adopted is the average film thickness, $\delta_{film,avg}$, which depends on parameters such as droplet spacing, droplet volume, droplet evolution time, and droplet volume growth rate, which are inherently related to the solution viscosity. Thus, while the film Nusselt number correlation does not readily show this dependence, the heat transfer coefficient is dependent upon the solution viscosity, and therefore the operating temperature and concentration, via the definition of $\delta_{film,avg}$.

5.7.2. Comparison of film Nusselt number correlation with literature

The functional form of the correlation developed by Hu and Jacobi (1996b) for sensible heat transfer in droplet mode flow compares well with the correlation developed in the present study.

$$Nu_{sol,Hu\&Jacobi} = 0.113 \cdot Re_{sol}^{0.85} \cdot Pr_{sol}^{0.85} \cdot A_{sol}^{-0.27} \cdot \left(\frac{S_L}{D_o} \right)^{0.04} \tag{5.132}$$

Their study was conducted in the absence of vapor flow and for large tube diameters. Due to the absence of vapor flow in their experiments, there is no dependence on the vapor Reynolds number in their correlation. In addition, their correlation shows a slight dependence on the Archimedes number (Ar_{sol}) and the tube spacing. However, the Nusselt number is strongly dependent on the solution Reynolds and Prandtl numbers, and while the degree of dependence is different for each parameter, the order of magnitude of these dependences is comparable. Also, it is interesting to note that the exponents of the Reynolds and Prandtl numbers are equal, which indicates that their Nusselt number

prediction is independent of the fluid viscosity. However, as previously discussed, the heat transfer coefficient is dependent upon the solution viscosity through the definition of the characteristic length.

The functional form and the dependence on the flow parameters (solution Reynolds and Prandtl numbers) in the segmental correlation developed by Bohra *et al.* (2008) also compares well with the correlation developed in the present study.

$$Nu_{\text{sol,Bohra}} = 7.589\times10^{-3}\cdot Re_{\text{sol}}^{1.043}\cdot Pr_{\text{sol}}^{0.455}\cdot\left(\frac{P_{\text{abs}}}{345\,\text{kPa}}\right)^{-0.145} \tag{5.133}$$

It should be noted that their study involved ammonia-water absorption in a quiescent vapor over large diameter (9.5 mm) tubes, for a wide range of solution concentrations and flow rates. While their correlation shows a dependence on the absorber operating pressure, it should be noted that its influence is small in comparison to the other flow parameters. Also, while the degree of dependence on these flow parameters was different, the order of magnitude of these dependencies is still comparable.

It should be noted that while developing the above correlation, Bohra *et al.* assumed that the tubes were fully wet with a laminar film, and did not consider the influence of spreading of solution on the tube surface. Thus, for a true comparison between the two studies, the effect of film spreading on the overall heat and mass transfer process must be included. For this purpose, the hydrodynamic model described above was applied to the flow in their study, and the revised heat transfer coefficients were calculated according the new definition presented in this study. These calculations are described briefly here.

The tube array in the absorber studied by Bohra *et al.* (2008) was divided into 3 segments. It should be noted that in addition to the tube array, they also considered 3 other segments where adiabatic absorption could occur. Fig. 5.23 shows a schematic of

these different segments in their absorber (figure taken from Bohra *et al.* (2008)). Only segments 3, 4, and 5, which correspond to the tube array, are considered here.

The hydrodynamic model was first applied to each of these segments to determine the spreading of the film, and calculate relevant transfer areas. In the visualization study of films falling over 9.5 mm diameter tubes, Bohra (2007) observed that the size of the primary droplet was predicted well by the correlation developed by Yung *et al.* (1980). Thus, the size of the primary droplet was calculated using Eq. 5.5. Once the droplet size is determined, other parameters such as the droplet spacing, and the droplet formation time were calculated according to the equations described in the hydrodynamic model described above. Based on these parameters, the relevant average transfer areas in the Feed, Spread, and Inactive regions of the tube were calculated. The width of the Feed region was assumed to be equal to the diameter of the primary droplet since this is the

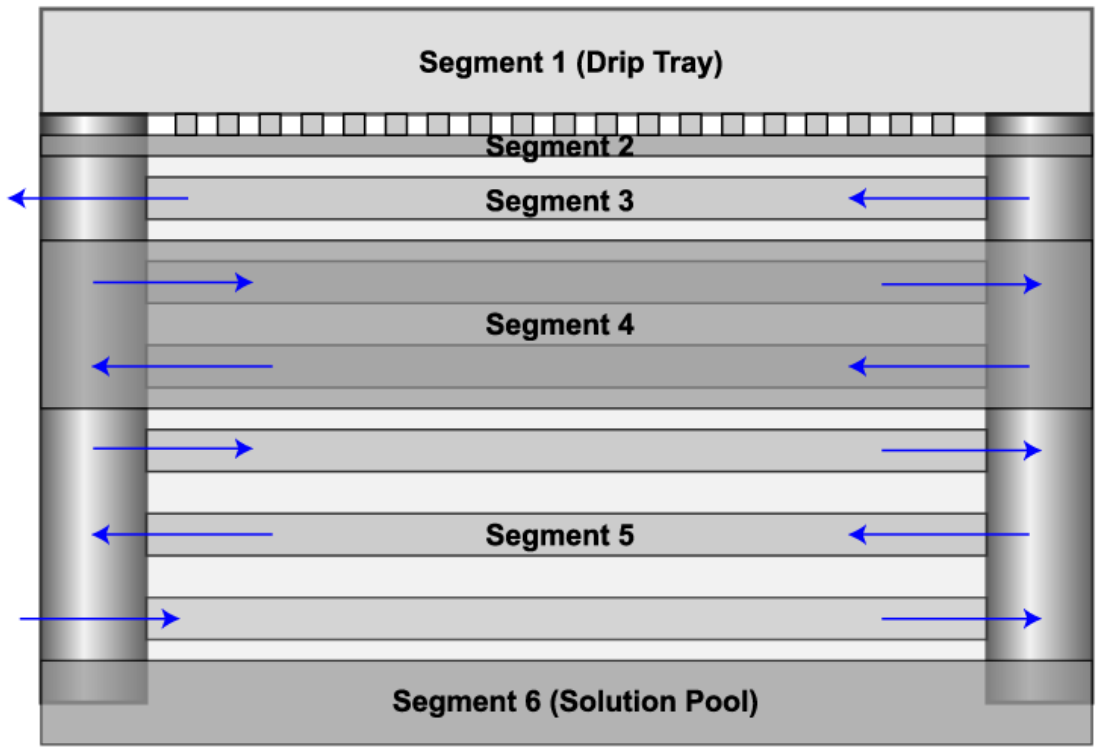

Fig. 5.23 Absorber segments considered by Bohra *et al.* (2008) (souce: Bohra *et al.* (2008))

maximum horizontal expanse of the droplet. The average film transfer area on the tube in each segment was calculated using Eq. 5.42, while accounting for the average transfer area in the Spread and the Feed regions. It should be noted that based on the above hydrodynamic model, the wetting ratios for their study were found to range from 0.58-0.70, indicating that the larger tubes do not wet as well as the microchannel tubes. It is also interesting to note that these predictions are still within the range of wetting ratios predicted by Jeong and Garimella (2002), as discussed previously. Next, the average film thickness over the tube was also calculated, which is used as the characteristic length for the film Nusselt number. Once the relevant transfer areas are known for each test condition, the film heat transfer coefficient was estimated from the overall heat transfer coefficient values calculated by Bohra *et al.* (2008) for each segment.

In their study, Bohra *et al.* (2008) utilized the following 1-D resistance network formulation to determine the film heat transfer coefficient.

$$\frac{1}{U} = \frac{D_o}{D_i \cdot \alpha_{CF}} + R_{wall} + \frac{1}{\alpha_{film}} \tag{5.134}$$

However, this equation assumes that the tube is fully wet, which is not the case. Thus, the following revised equation was utilized to estimate the film heat transfer coefficient while considering the reduced wetting on the tube side.

$$\frac{1}{U} = \frac{D_o}{D_i \cdot \alpha_{CF}} + R_{wall} + \frac{1}{\alpha_{film}} \cdot \frac{1}{WR} \tag{5.135}$$

It should be noted that the above equation is the same as Eq. 5.112, and accounts for the reduced transfer area at the tube wall on the solution side due to incomplete wetting. It is this film heat transfer coefficient that can be compared with the heat transfer coefficient predicted using the correlation developed in this study.

The film Reynolds number is defined using the modified solution linear mass flux, Γ_{film} discussed previously, as is the film Prandtl number. The vapor Reynolds number is defined using the average mass flow rate of vapor in each segment and the tube

diameter. Bohra *et al.* (2008) had a large shell around the tube bank resulting in a quiescent vapor. Thus, the dominant mode of vapor flow is natural convection, where vapor moves from the colder regions at the bottom of the absorber to the warmer regions at the top of the absorber. The mass of vapor moving upwards is assumed to be equal to the mass of vapor absorbed in the tube array, and the average value in each segment is used to define the vapor Reynolds number. The characteristic length for the definition of film Nusselt number was taken to be the average film thickness, which is according the definition in the present work.

Fig. 5.24 shows the comparison of the measured heat transfer coefficient with the predicted heat transfer coefficient from the film Nusselt number correlation developed in the present work for segment 5. Two sets of data are plotted: the uncorrected data, which

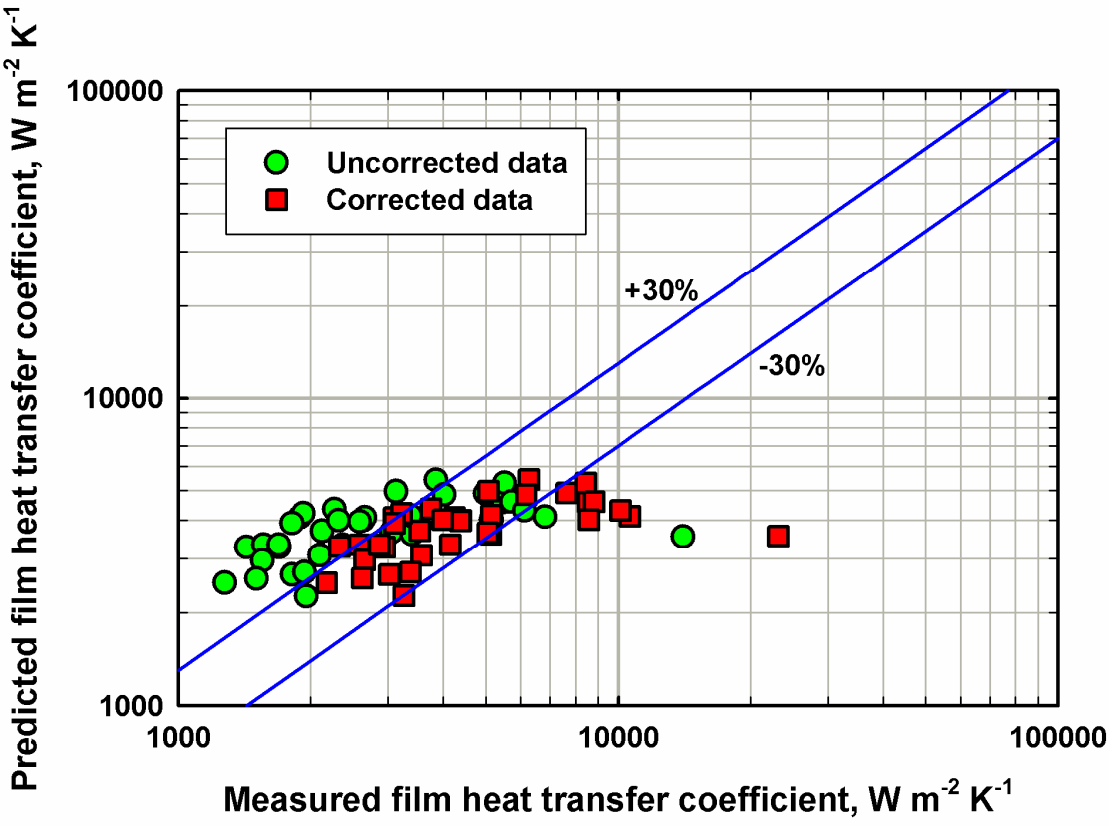

Fig. 5.24 Comparison of measured and predicted film heat transfer coefficients for segment 5 of Bohra et al. (2008)

are the heat transfer coefficient values reported by Bohra *et al.* (2008) where complete tube wetting was assumed, and the corrected data, which are the heat transfer coefficient values predicted using the modified resistance network accounting for the wetting ratio (Eq. 5.135). Segment 5 is the bottommost segment in the tube array, accounting for 3 of the 6 tube rows in the absorber, and is similar to the bottom segment in the present work. It can be seen from Fig. 5.24 that without accounting for the reduced tube-side heat transfer area, the present correlation over-predicts the measured heat transfer coefficients (only 13 of 35 data points were predicted within ±30%.) However, by accounting for the variation in the tube-side heat transfer area, the present correlation was able to predict 23 of the 35 data points within ±30%. Bohra *et al.* (2008) studied falling-film absorption on tubes of diameter 9.5 mm, which are significantly larger than the microchannel tubes, of diameter 1.575 mm, utilized in the present study. Solution flow over larger tube diameters often results in formation of thicker films (because there are lesser tubes in each row to distribute the solution over), which in turn results in higher film Reynolds numbers. Also, their study involved dilute solution of nominal concentration ranging from 5 - 40%, which is lower than the concentration range studied in the present work. The only overlap in solution concentration lies around the 40% solution concentration region. Considering these differences between the two studies, the present correlation is able to predict these measured heat transfer coefficients reasonably well.

Table 5.13 shows a summary of the accuracy of the prediction of the measured heat transfer coefficient measured by Bohra *et al.* (2008) using the present correlation. As

Table 5.13 Summary of accuracy of prediction of Bohra *et al.* (2008) heat transfer coefficients

Average solution concentration	Number of measurements	Number of prediction within ±30%
35-45%	10	9
25-35%	16	11
15-25%	9	3

can be seen from this table, the accuracy of the correlation is excellent at higher solution concentrations. However, as the solution concentration decreases, the accuracy of the correlation decreases. In general, the correlation under-predicted heat transfer coefficients at the lower solution concentrations, while the predictions at higher solution concentrations were within reasonable limits.

Figs. 5.25 and 5.26 show the plots of the heat transfer coefficient measured by Bohra *et al.* (2008) and those predicted by the present correlation as a function of the modified linear solution mass flux, Γ_{film}, and the film Reynolds number, Re_{film}. Fig. 5.25 shows that the present correlation is able to predict their measured heat transfer coefficients at higher solution concentrations reasonably well, even though their values of Γ_{film} are significantly higher than those tested in the present study (12 – 28×10^{-4} kg m^{-1} s^{-}

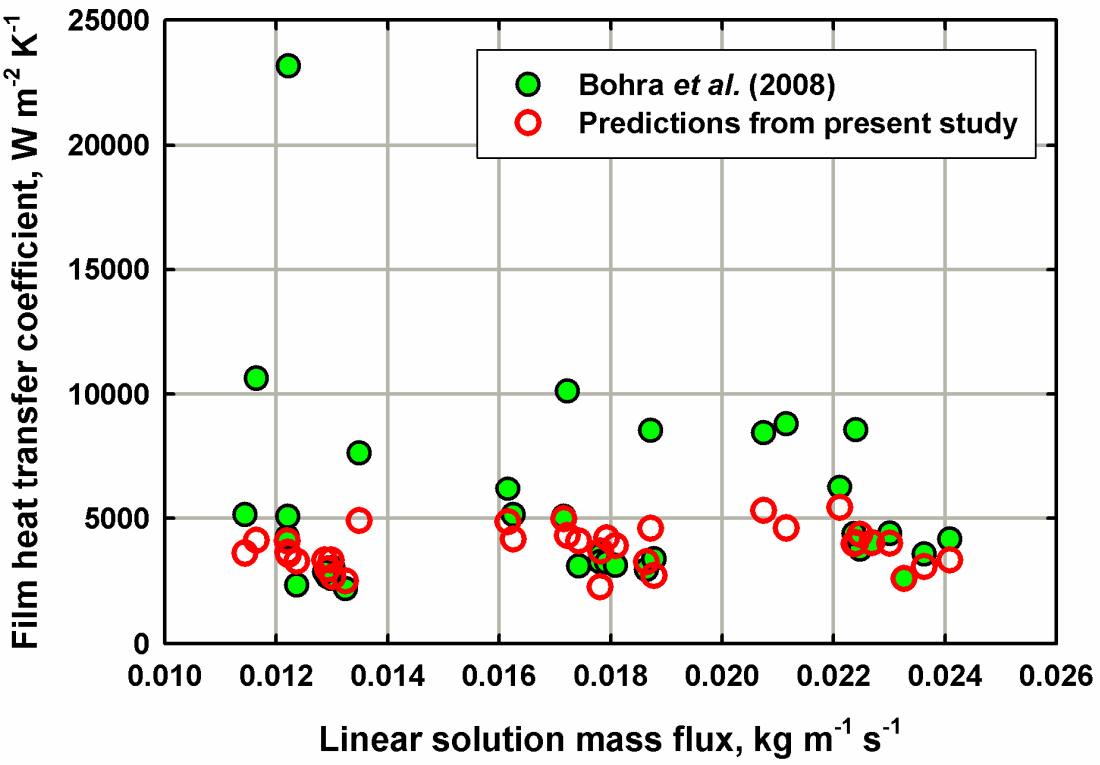

Fig. 5.25 Comparison of measured and predicted film heat transfer coefficients for segment 5 of Bohra et al. (2008) as a function of linear solution

[1]). The correlation under-predicts the measured heat transfer coefficients at lower concentrations. It should however be noted that, as the film heat transfer coefficient increases, the uncertainty associated with this measurement also increases (Bohra, 2007). Thus, larger uncertainties are expected at these higher heat transfer coefficient values, generally observed at the lower solution concentrations, and thus, the predictions from the present correlation might still be within the limits of experimental uncertainty in their study.

Fig. 5.26 shows that while the Re_{film} values in the present work were below 40, the correlation developed is able to predict a major portion of the measured heat transfer coefficients at higher solution concentrations fairly accurately up to a Re_{film} of ~100. At lower solution concentrations, the predictions are not very accurate even for Re_{film} less

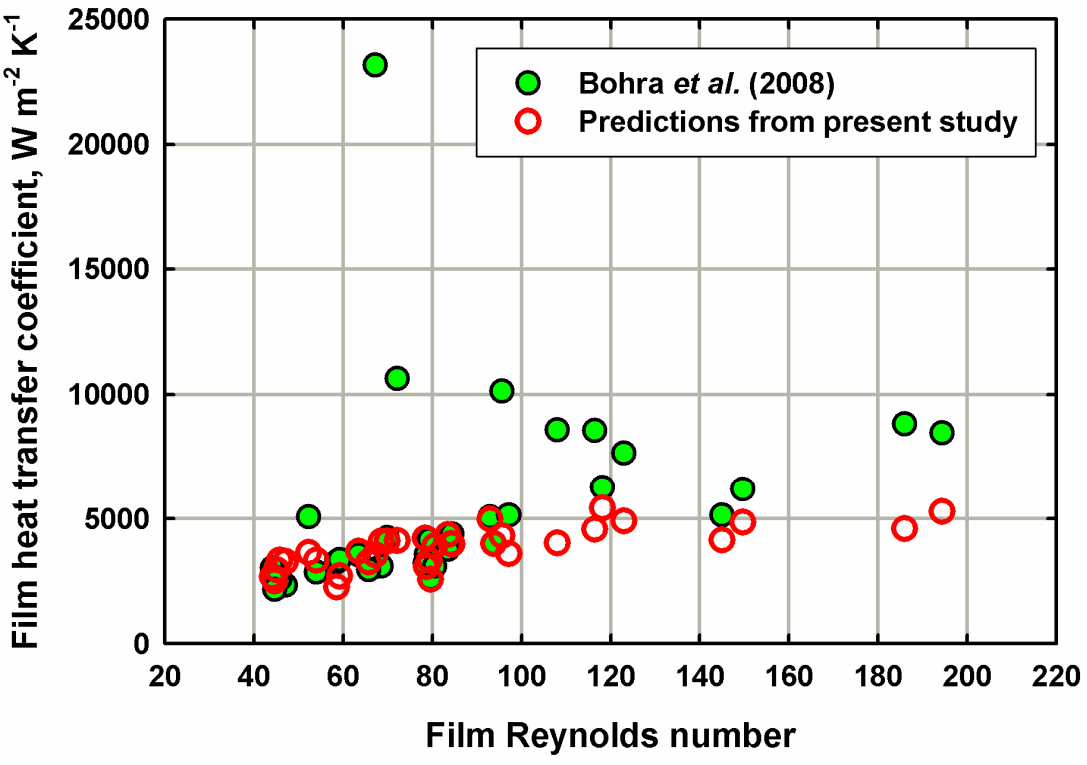

Fig. 5.26 Comparison of measured and predicted film heat transfer coefficient for segment 5 of Bohra et al. (2008) as a function of film Reynolds number

than 100 (Table 5.13). Beyond a Re_{film} of 100, the correlation under-predicts the experimentally measured heat transfer coefficients. It is possible that at higher Reynolds numbers, the solution flow between successive tube rows might be transitioning to "droplet-jet" mode, which can significantly affect the tube wetting process and yield different values for the measured heat transfer coefficients. This could be one possible explanation for the poor performance of the correlation at the higher film Reynolds numbers.

Meacham and Garimella (2004) experimentally demonstrated ammonia-water falling-film absorption on microchannel tube arrays in a single-pressure test facility. In their study, the absorber was studied over a range of solution and vapor flow rates, and overall performance of the absorber component was measured. The hydrodynamic and heat and mass transfer model developed here was applied to data from their study to calculate and compare the measured film heat transfer coefficients.

Fig. 5.27 shows the comparison of the measured heat transfer coefficient with the heat transfer coefficient predicted by the film Nusselt number correlation developed in the present work for the bottom segment of the microchannel absorber studied by Meacham and Garimella (2004). The correlation developed in the present work was able to predict 30 of the 46 data points within ± 30%. As previously noted, Meacham and Garimella (2004) evaluated the absorber in a single-pressure test facility, and therefore, the operating conditions at the absorber were different from those observed during typical heat pump operation. Furthermore, their experiments were conducted to demonstrate the capability of the microchannel concept to transfer large absorption duties. Consequently, good control over the uncertainties associated with the measurement of the film heat transfer coefficients could not be exercised by them across the test matrix. For the entire set of test conditions their experimental uncertainties ranged between 7.3 and 47.2%, with an average uncertainty of 22.4%. Considering these aspects, the present correlation is able to predict the measured heat transfer coefficients reasonably well.

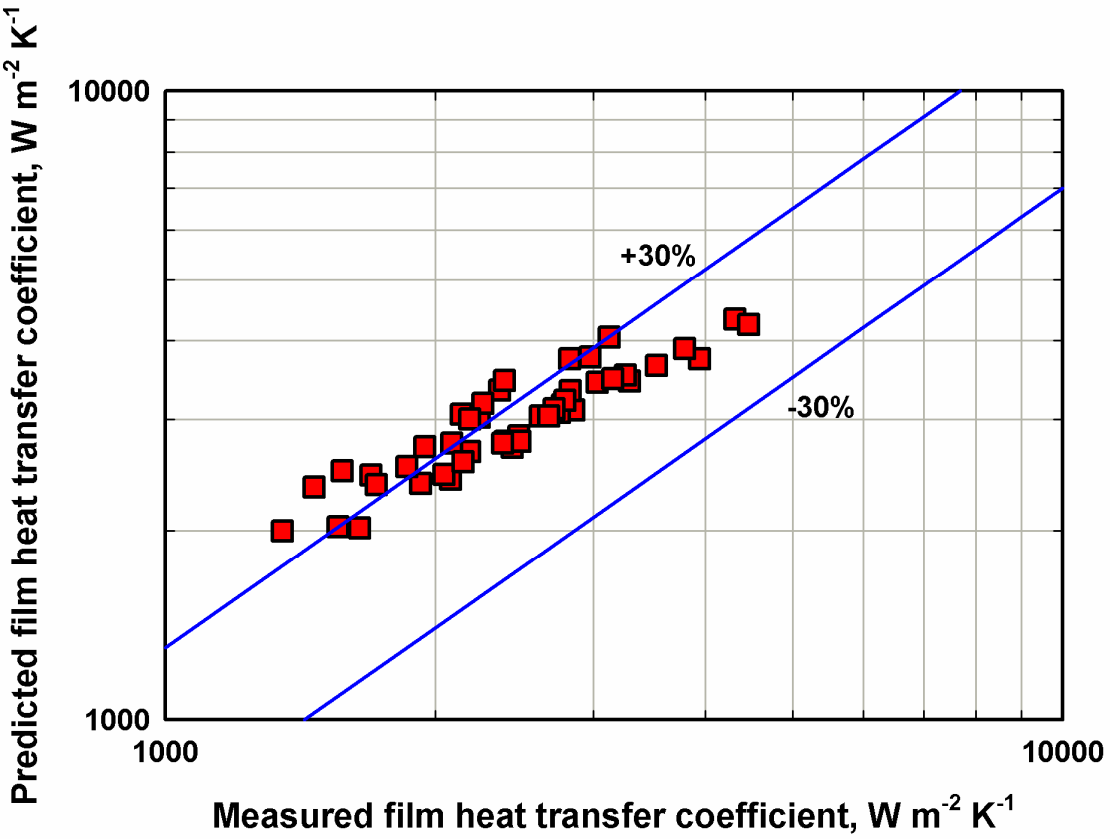

Fig. 5.27 Comparison of measured and predicted film heat transfer coefficient for bottom segment of Meacham and Garimella (2004)

Fig. 5.28 shows a plot of the heat transfer coefficients measured by Meacham and Garimella (2004) and those predicted by the correlation from the present study as a function of the film Reynolds number, Re_{film}. It can be seen that while the present correlation generally over-predicts their measured film heat transfer coefficients, most of the predictions lie within the uncertainty ranges of the experiments. The predictions compare well with the measured data at higher Re_{film}. At lower solution flow rates, corresponding to lower Re_{film}, it is possible there is solution mal-distribution which can result in lower measured heat transfer coefficients. In general, the present correlation is able to predict the measured heat transfer coefficients from Meacham and Garimella (2004) within reasonable uncertainty limits, despite their experiments being conducted on a single-pressure test facility.

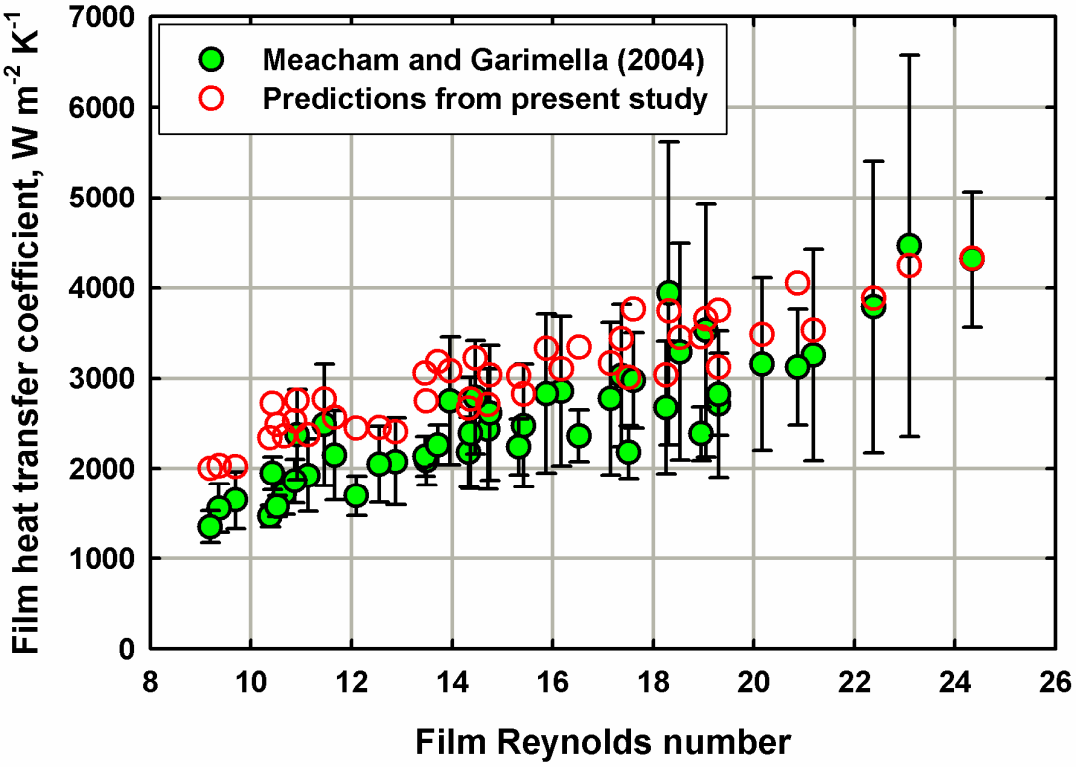

Fig. 5.28 Comparison of the measured and predicted heat transfer coefficient for Meacham and Garimella (2004) as a function of film Reynolds number

5.8. Summary

This chapter presents the development of a coupled hydrodynamic and heat and mass transfer model to estimate local absorption rates during falling-film ammonia-water absorption. The hydrodynamic model developed for the flow of solution over the horizontal tube banks considered the development and growth of droplets, the subsequent impact of these droplets on these tube rows, and the associated spreading of film over the tube surface. The spacing between adjacent droplet formation sites was estimated by considering the most dangerous wavelength. The volume of primary droplet was estimated by balancing the surface tension force with the droplet weight at the instant of detachment. The droplet formation time was determined by applying mass conservation

and assuming uniform droplet growth rate. Average transfer area of the droplet was calculated by time averaging the droplet surface area over the droplet formation time. The film on the tube surface was classified into three regions: the Feed region, the Spread region, and the Inactive region. The Feed region was located above the droplet formation site and supplied solution to the droplet. The spreading of liquid film in the Spread region was modeled as the "stretching" of a triangle over the tube surface. The width of the Spread region and the thickness of the film were found to vary with both location and time. The flow of the film over the tube surface was found to be similar to the spread of a saddle wave over the tube surface. The tube wetting ratios were found to range from 0.807 – 8.32 for the entire range of test conditions.

This hydrodynamic model was coupled with the heat transfer model to estimate the local absorption rates. Three regions in the absorber were considered for absorption of vapor: absorption at the solution pool, absorption into the droplets, and absorption into the film. Absorption in the solution pool and the droplet was assumed to be adiabatic, while the heat of absorption in the film was removed by circulating coupling fluid. Most of the absorption was found to occur in the film region, while up to ~ 7% of the absorption was found to occur in the droplet. A small amount of vapor was also found to desorb from the droplets at certain operating conditions. The contribution to absorption from the solution pool was relatively low. Heat transfer coefficients in the film were evaluated using the above model for all test conditions in the test matrix, and were found to range from 1788-4179 W m^{-2} K^{-1}. These heat transfer coefficients were presented in terms of dimensionless Nusselt numbers based on the film thickness, and the effects of the operating conditions on this parameter were discussed. Based on these insights, an empirical correlation was developed for the film Nusselt number in terms of the film Reynolds number, Prandtl number, and the vapor Reynolds number. The applicability of this correlation is limited to the range of parameters shown in Table 5.14. This

correlation, in conjunction with the coupled hydrodynamic and heat and mass transfer model presented above, can be used to design microchannel falling-film absorbers.

Table 5.14 Range of applicability of Nusselt number correlation

Absorber pressure	
Absorber	321.3 - 721.9 kPa
Absorber mass flow rate	
Dilute solution	$0.84 - 1.99\times10^{-2}$ kg s^{-1}
Concentrated solution	$1.06 - 2.20\times10^{-2}$ kg s^{-1}
Vapor inlet	$1.65 - 6.57\times10^{-3}$ kg s^{-1}
Absorber concentration	
Dilute solution	0.2877 - 0.4489
Concentrated solution	0.3561 - 0.5458
Vapor inlet	0.9982 - 0.9999
Absorber temperature	
Dilute solution	47.85 - 65.51°C
Concentrated solution	28.57 - 46.85°C
Vapor inlet	9.72 - 22.35°C
Dimensionless numbers	
Film Reynolds number	7.3 - 18.4
Film Prandtl number	4.7 - 6.0
Vapor Reynolds number	9.0 - 40.9

CHAPTER 6. MICROSCALE FORCED-CONVECTIVE ABSORPTION

In the previous chapters, ammonia-water absorption in external falling films was discussed. A complementary treatment of absorption in internal forced-convective mode through microscale geometries is discussed here. This study starts with the development of a microscale heat and mass exchange miniaturization concept, followed by the design and fabrication of test sections for an absorber application. A breadboard test facility was fabricated to experimentally demonstrate microscale forced-convective absorption in these geometries as part of a miniature absorption chiller using diesel engine waste heat as the source. Data collected during these experiments were then analyzed to estimate the heat and mass transfer in forced-convective absorption.

6.1. Microscale forced-convective absorption concept

An exploded view of the subject miniaturization technology for heat and mass exchangers for absorption heat pumps is shown in Fig. 6.1. This technology provides a compact, modular, versatile design architecture that can be applied for high flux heat and mass transfer not only in individual components, but also the overall heat pump assembly. The focus of the present work is on the development of an absorber for an ammonia-water absorption heat pump; however, the technology can also be used for other fluid pairs with nonvolatile and volatile absorbents, as well as the other components of the absorption heat pump.

As shown in Fig 6.1, the absorber consists of an array of alternating sheets with integral microscale features, fluid inlet and outlet passages, and vapor-liquid spaces, enclosed between cover plates. The microscale features on the sheets include microchannel arrays for the flow of solution, vapor, and coupling fluid, and the inlet and outlet headers for the distribution of these fluids into the microchannel arrays. The

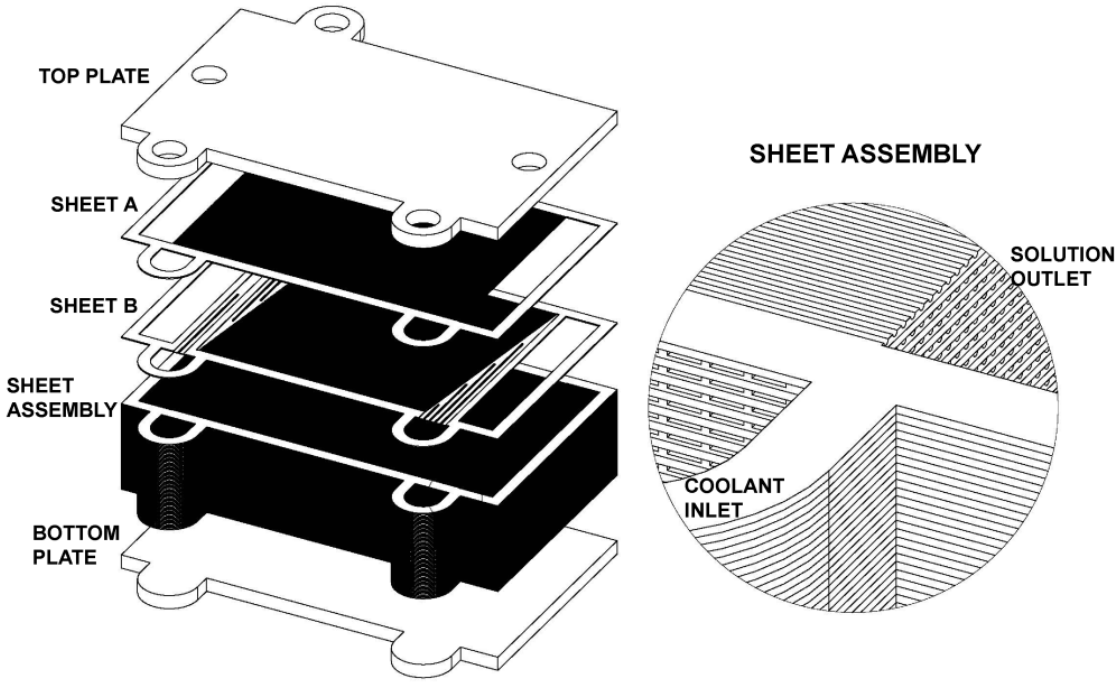

Fig. 6.1 Schematic of microscale absorber concept

microscale features in the sheets can assume square, semi-circular, triangular or other cross-sections to enable fluid flow in single- or two-phase state, as necessary. In the present study, semi-circular and semi-elliptical cross-sections are studied. The microscale cross-section shape and dimensions are determined based on heat and mass transfer requirements, operating pressures, structural strength of the assembled unit, and manufacturing constraints for dimensional tolerances and bonding. Hydraulic diameters (D_h) of the microscale passages in the 200-700 μm range yield high heat and mass transfer coefficients $\left(\alpha = (Nu \bullet k)/D_h;\quad D_h \to 0 \Rightarrow \alpha \to \infty\right)$ on both the working fluid and the coupling fluid side, thereby lowering thermal resistances on both sides, and resulting in extremely low surface area requirements. Counterflow operation possible in each of the components further improves heat transfer performance for a given surface area. Parallel flow of fluids through short channel lengths in the laminar regime due to the

microscale passages allows high heat and mass transfer rates with low pressure drops and thus, low parasitic power requirements. Low volumes of the working fluid contained within this assembly reduce fluid inventories several fold over conventional heat pumps of similar capacities.

Schematics of representative alternating Sheets A and B are shown in Figs. 6.2 and 6.3. Dilute solution enters Sheet A through the solution inlet void C, flows through the channel array from the left to right, and exits Sheet A through the solution outlet void D. Coupling fluid enters Sheet B through the coupling fluid inlet void A, and flows through the angled coupling fluid inlet header, which uniformly distributes the flow among the different channels in the microchannel array. Coupling fluid flows from right to left in these microchannels (in counter-current configuration with the solution), through the angled coupling fluid outlet header and into the coupling fluid outlet void B, where it is collected and removed from Sheet B. The angled coupling fluid inlet and

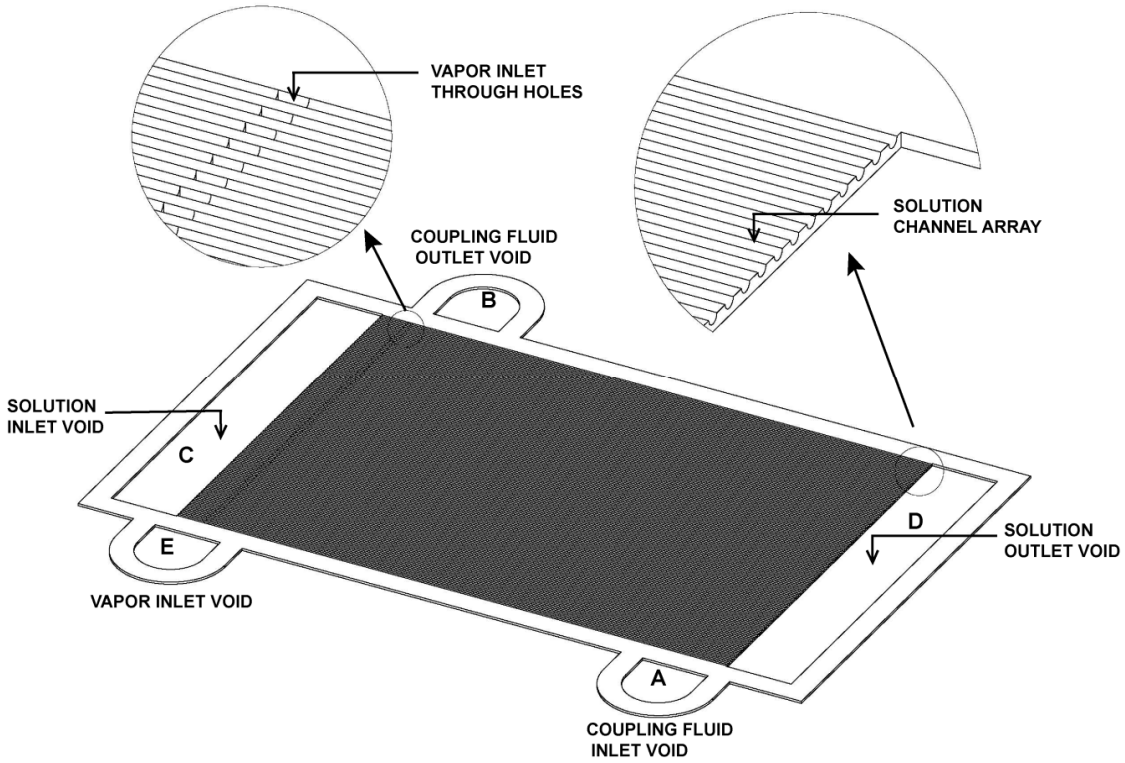

Fig. 6.2 Schematic of Sheet A

outlet headers are subdivided into several sections by means of positioning ribs along the flow direction. These ribs serve as guide vanes, ensuring that the flow is distributed uniformly to the various microscale passages. In single-phase flow, potential maldistribution can be addressed better through these design features in the headers. A detailed flow distribution model was developed to account for pressure drop in each portion of the inlet and outlet headers and the channels. Flow and pressure drop balancing analyses led to the conclusion that with these design features, there would be less than 1% variation in the flow rate through the channels in the array. The ribs also provide structural strength in the manufacturing process and facilitate better bonding.

Vapor enters Sheet B through vapor inlet void E, and flows through the vapor inlet header where it is introduced to the solution stream via small through holes located on Sheet A (Fig. 6.4). The vapor inlet header can also be subdivided into two or more channels with the use of the previously described ribs. A close-up view of the vapor inlet

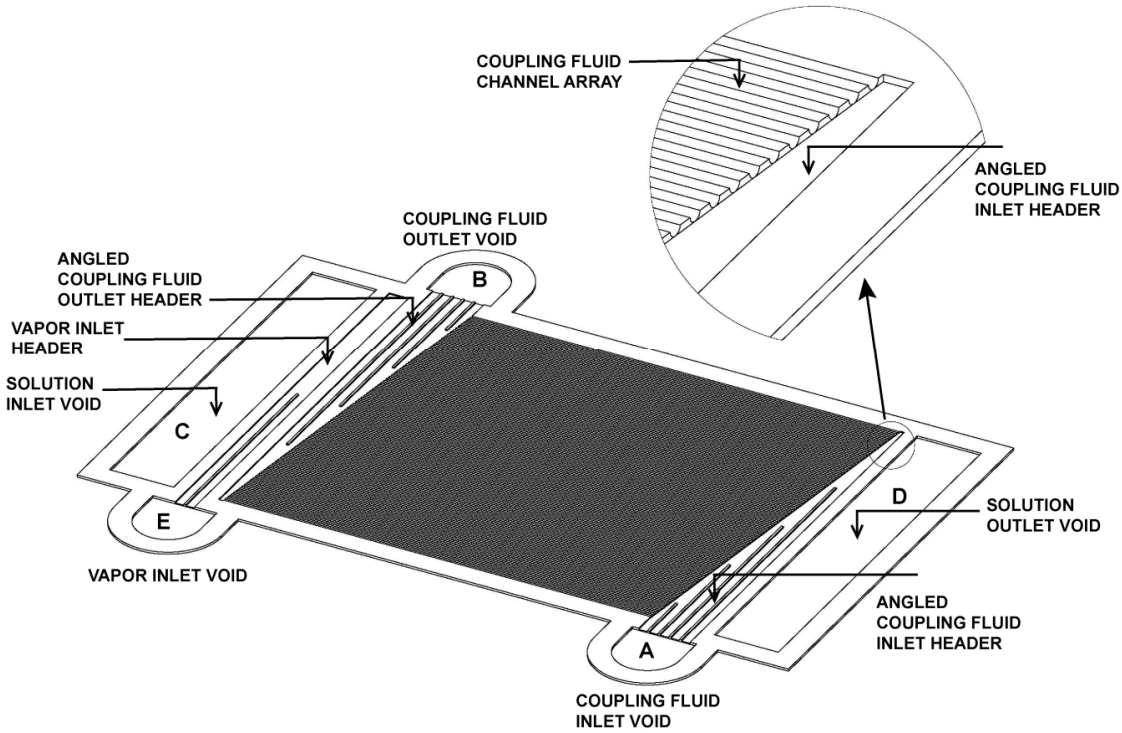

Fig. 6.3 Schematic of Sheet B

arrangement is shown in Fig. 6.4. The inlet and outlet headers created by an assembly of these sheets and integral voids are seen in Fig 6.1. Due to the design features of these sheets, coupling fluid cannot enter Sheet A through voids A or B. Similarly, ammonia-water solution cannot enter Sheet B through voids C or D. Vapor flows through the absorber in a restricted path that allows distribution into the solution channels while ensuring no leakage into the coupling fluid channels. The vapor enters Sheet B through void E, but is restricted from entering the coupling fluid channels due to the design of the vapor header. Similarly, vapor enters Sheet A and the dilute solution channels only through the vapor orifices holes, but is restricted from entering through void E. As can be seen from the above description, vapor and dilute solution are mixed locally in each channel. It should be noted that while most test sections were fabricated using this concept, a separate absorber test section was also fabricated, where vapor and dilute solution were mixed upstream of the absorber, and the resulting two-phase mixture was distributed into the microscale channels. Details of this revised design are discussed later.

Sets of two sheets constitute building blocks (a single functional unit) of an absorber, duplicated in numbers required to accomplish the desired cooling or heating. Modularity in heat duties is achieved by varying the channel dimensions, number of channels, length and width of the sheets, and number of sheet assemblies while maintaining aspects such as flow rate per channel constant, thereby ensuring scalable hydrodynamics and heat and mass transfer performance. The sheet geometry can be fabricated using photochemical etching, with eventual mass production also possible through processes such as stamping, micromachining, reel-to-reel etching, etc. The plate assemblies can be sealed using diffusion bonding, and in large quantities, using vacuum or controlled atmosphere brazing.

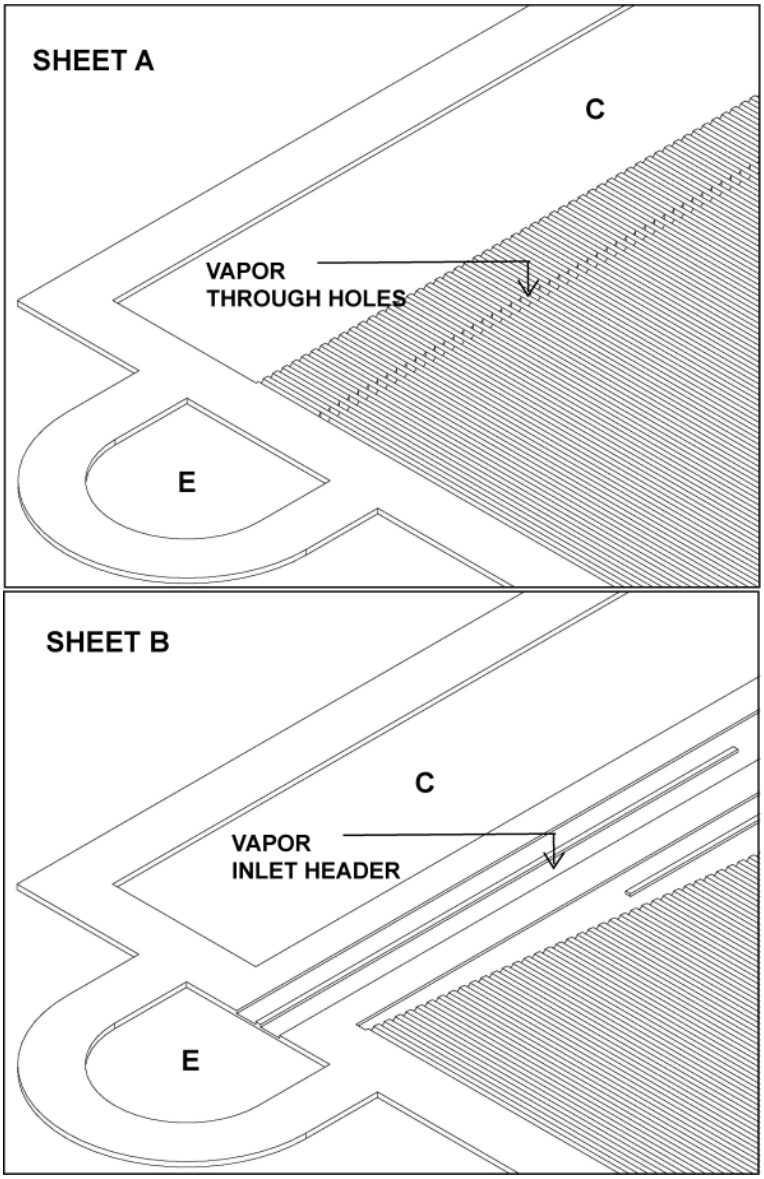

Fig. 6.4 Schematic of vapor inlet arrangement

6.2. Segmental heat and mass transfer model

To obtain estimates of the miniaturization possible from the use of the above geometry, a segmental heat and mass transfer model was developed for a hydronically cooled absorber. The model adapts the falling-film heat and mass transfer analysis described previously to the forced-convective configuration. The whole absorber is divided into several segments, and the heat and mass transfer model is applied in each

segment to determine the state of the vapor and solution at each location, local absorption rates, overall heat transfer rates, and the necessary transfer area to accomplish complete absorption. For the present study, the absorber was divided into 10 segments of equal absorption duty.

Fig. 6.5 shows a schematic of the regions of absorption, while Fig. 6.6 shows a schematic of the flow of vapor, solution, and coupling fluid. It should be noted that solution, vapor, and coupling fluid flow horizontally, and Fig. 6.5 has been rotated by 90 to display the temperatures and concentration profiles conveniently.

Unlike the falling-film absorption, in this forced-convective absorption geometry,

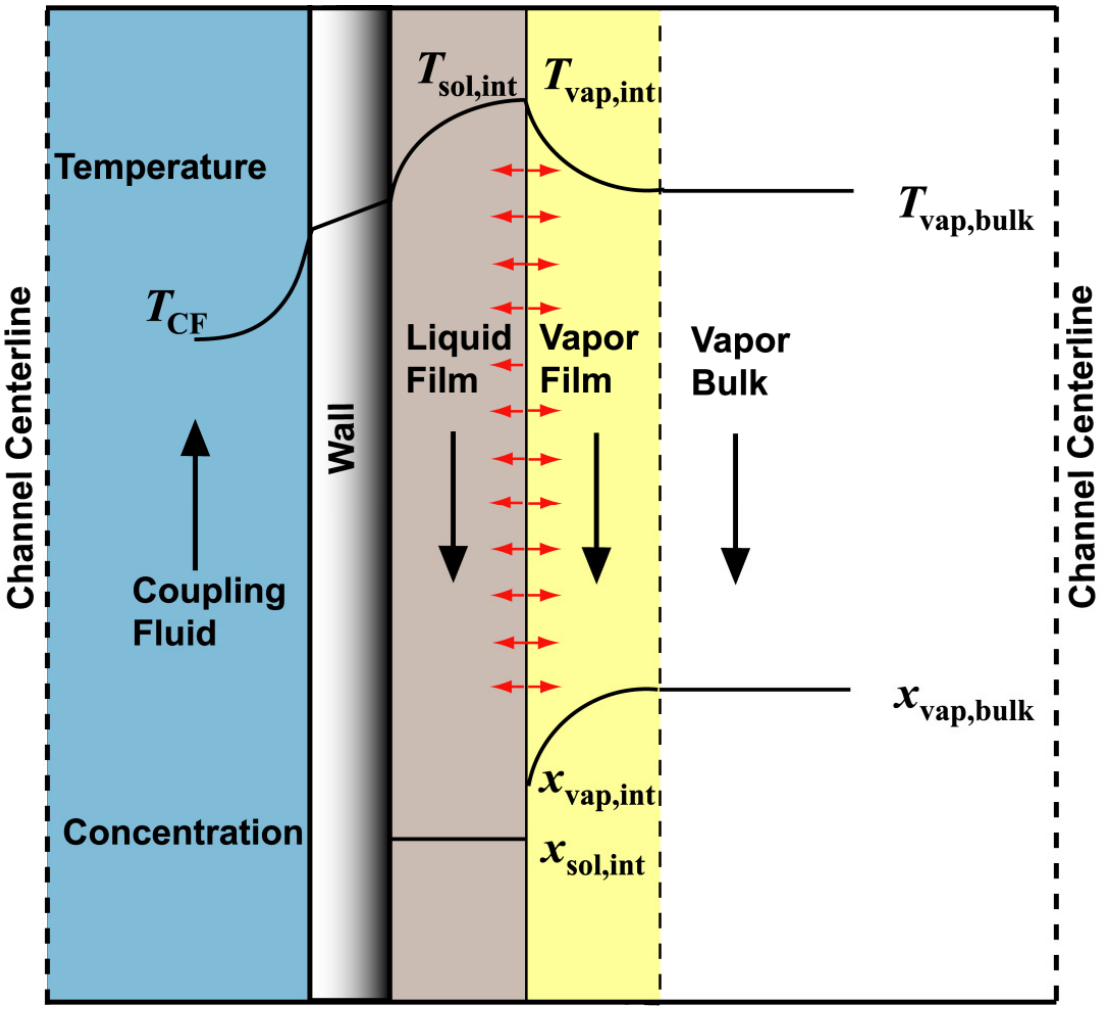

Fig. 6.5 Schematic of the regions of absorption

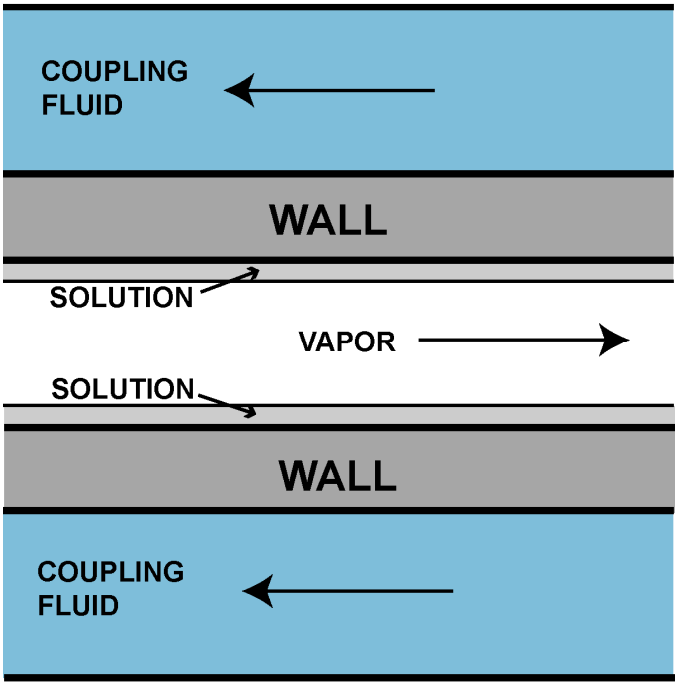

Fig. 6.6 Schematic of flow of vapor, solution, and coupling fluid

solution and vapor flow in co-current configuration inside the microchannels. Due to the relatively high specific volume of the vapor, the solution is expected to flow as a thin film close to the wall. This is confirmed by identifying the flow regime using the Taitel-Dukler flow map (Taitel and Dukler, 1976), which indicated annular flow regime through most of the absorber. In addition, while it is expected that there will be some waves at the vapor-liquid interface due to shear between the two phases, they have been neglected in this model for simplicity. The vapor, at bulk conditions, flows through the core of the channel and occupies most of the void space in the channel. As previously discussed, all resistance to heat and mass transfer in the vapor phase is expected to occur in a small region, adjacent to the vapor-liquid interface, called the "vapor film" region. Both concentration and temperature gradients are observed in this region. The latent heat of absorption released at the vapor-liquid interface can propagate through the liquid film, through the wall, and eventually to the coupling fluid, or propagate back into the vapor bulk, depending upon the local temperature gradients.

6.2.1. Solution and vapor, bulk and interface conditions

As discussed in Chapter 4, the bulk vapor and average solution conditions for each segment are calculated by averaging the inlet and outlet conditions. Thus, the average solution and vapor concentrations are calculated as follows:

$$x_{\text{sol,avg}} = \frac{x_{\text{sol,in}} + x_{\text{sol,out}}}{2} \tag{6.1}$$

$$x_{\text{vap,bulk}} = \frac{x_{\text{vap,in}} + x_{\text{vap,out}}}{2} \tag{6.2}$$

As with falling-film absorption, the liquid film in forced-convective absorption is assumed to be well mixed, which is well justified due to the forced-convective flow mechanism in the absorber. Thus, the concentration of the solution at the interface is equal to the bulk solution concentration. The solution at the interface was assumed to be in equilibrium with the adjacent vapor. The solution temperature at the film interface was estimated by assuming the solution is at saturation conditions.

$$T_{\text{sol,int}} = f\left(P_{\text{abs}}, x_{\text{sol,avg}}, q_{\text{sol,int}} = 0\right) \tag{6.3}$$

The vapor temperature at the vapor-liquid interface is equal to the solution interface temperature. Also, because the vapor at the interface is assumed to be in equilibrium with the adjacent solution, the concentration of the vapor at the interface is calculated by assuming the vapor is at saturation conditions.

$$T_{\text{vap,int}} = T_{\text{sol,int}} \tag{6.4}$$

$$x_{\text{vap,int}} = f\left(P_{\text{abs}}, T_{\text{vap,int}}, q_{\text{vap,int}} = 1\right) \tag{6.5}$$

These interface and bulk concentrations and temperatures are used to determine the heat and mass transfer rates in the vapor phase.

6.2.2. Vapor mass transfer

In each segment, the absorption of vapor into the dilute solution, which is in convective flow, is governed by the mass transfer coefficient in the vapor phase, and the

concentration gradient between the bulk vapor and the vapor-liquid interface. The molar flux of the vapor being absorbed into the liquid film is given by the following equation:

$$\dot{n}_{\mathrm{T}} = \beta_{\mathrm{vap}} \cdot C_{\mathrm{T}} \cdot \ln\left(\frac{\tilde{z} - \tilde{x}_{\mathrm{vap,int}}}{\tilde{z} - \tilde{x}_{\mathrm{vap,bulk}}} \right) \tag{6.6}$$

In the above equation, β_{vap} is the vapor mass transfer coefficient, and C_{T} is the bulk molar concentration, which is calculated using the ideal gas equation. The driving molar concentration difference in the above equation is a function of the molar concentration of the condensing flux, $\tilde{z}$, the bulk molar concentration of the vapor $\tilde{x}_{\mathrm{vap,bulk}}$, and the equilibrium molar vapor concentration at the interface $\tilde{x}_{\mathrm{vap,int}}$. The vapor mass transfer coefficient can be calculated from the vapor Sherwood number, Sh_{vap}, which in turn can be calculated from the vapor Nusselt number, Nu_{vap}, using the heat and mass transfer analogy.

$$Sh_{\mathrm{vap}} = \frac{\beta_{\mathrm{vap}} \cdot D_{\mathrm{h}}}{D_{\mathrm{aw,vap}}} \tag{6.7}$$

$$\left(\frac{Sh_{\mathrm{vap}}}{Nu_{\mathrm{vap}}} \right) = \left(\frac{Sc_{\mathrm{vap}}}{Pr_{\mathrm{vap}}} \right)^{1/3} \tag{6.8}$$

In the above equations, D_{h} is the hydraulic diameter of the channel, $D_{\mathrm{aw,vap}}$ is the vapor diffusion coefficient, and Sc_{vap} and Pr_{vap} represent the vapor Schmidt number and the vapor Prandtl number, respectively. The corresponding Nusselt number for the vapor flow is calculated using the correlation for laminar single-phase flow in semicircular channels developed by Sparrow and Haji-Sheikh (1965) as cited in Kakac *et al.* (1987).

$$Nu_{\mathrm{vap}} = 2.0705 \cdot \left(1 + 2.2916 \cdot \theta - 2.5682 \cdot \theta^2 + 1.4815 \cdot \theta^3 - 0.3338 \cdot \theta^4 \right) \tag{6.9}$$

In the above equation, 2θ is the angle of the circular sector duct and is equal to π for semicircular ducts. The individual ammonia and water condensing fluxes are determined from the total condensing flux as follows:

$$\dot{n}_{\mathrm{A}} = \tilde{z} \cdot \dot{n}_{\mathrm{T}} \tag{6.10}$$

$$\dot{n}_{W} = \left(1 - \tilde{z}\right) \cdot \dot{n}_{T} \tag{6.11}$$

Using these molar fluxes, the mass of each component absorbed into the solution, as well as the total mass absorbed can be estimated as follows:

$$\dot{m}_{abs,A} = M_{A} \cdot \dot{n}_{A} \cdot A_{seg} \tag{6.12}$$

$$\dot{m}_{abs,W} = M_{W} \cdot \dot{n}_{W} \cdot A_{seg} \tag{6.13}$$

$$\dot{m}_{abs} = \dot{m}_{abs,A} + \dot{m}_{abs,W} \tag{6.14}$$

In the above equation, A_{seg} is the area available for absorption in the segment. Once the mass transfer rate in the vapor phase in each segment is known, the overall heat and mass transfer rates in a segment can be estimated as described below.

6.2.3. Overall heat and mass transfer rates

Using the previously estimated absorption rates, the outlet vapor flow rate and concentration for each segment can be estimated using a simple mass conservation equation as follows:

$$\dot{m}_{vap,out} = \dot{m}_{vap,in} - \dot{m}_{abs} \tag{6.15}$$

$$x_{vap,out} = \frac{\dot{m}_{vap,in} \cdot x_{vap,in} - \dot{m}_{abs,A}}{\dot{m}_{vap,out}} \tag{6.16}$$

A mass and species balance between the vapor and solution can be employed to determine the solution outlet mass flow rate and concentration, and complete the computation of the absorption rates for each incremental segment.

$$\dot{m}_{sol,out} + \dot{m}_{vap,out} = \dot{m}_{sol,in} + \dot{m}_{vap,in} \tag{6.17}$$

$$\dot{m}_{sol,out} \cdot x_{sol,out} + \dot{m}_{vap,out} \cdot x_{vap,out} = \dot{m}_{sol,in} \cdot x_{sol,in} + \dot{m}_{vap,in} \cdot x_{vap,in} \tag{6.18}$$

The total absorption heat duty can be calculated using an energy balance between the solution and vapor streams as follows:

$$Q_{abs,seg} = \dot{m}_{sol,in} \cdot h_{sol,in} + \dot{m}_{vap,in} \cdot h_{vap,in} - \dot{m}_{sol,out} \cdot h_{sol,out} - \dot{m}_{vap,out} \cdot h_{vap,out} \tag{6.19}$$

This equation accounts for both latent heat of absorption and the sensible cooling of the stream. The relevant vapor and solution outlet mass flow rates are established using the mass transfer and mass balance equations outlined above. The vapor and solution inlet conditions are known from heat and mass transfer calculations of the previous segment (and for the first segment, from the inlet design condition). The solution outlet enthalpy is calculated using the relevant equilibrium conditions. The vapor outlet enthalpy must be determined from the sensible heat transfer between the liquid film and the vapor. This sensible heat transfer rate can be calculated as follows:

$$Q_{\text{vap}} = \alpha_{\text{vap}} \cdot \left(\frac{\phi_{\text{T}}}{1 - e^{-\phi_{\text{T}}}} \right) \cdot A_{\text{seg}} \cdot LMTD_{\text{vap}} \tag{6.20}$$

In the above equation, α_{vap} is the vapor heat transfer coefficient and $LMTD_{\text{vap}}$ is the logarithmic mean temperature difference between the vapor bulk and the vapor-liquid interface. The term within the parentheses is the correction factor for the heat transfer coefficient due to mass transfer. The parameter, ϕ_{T}, is defined as follows:

$$\phi_{\text{T}} = \frac{\left(\dot{n}_{\text{A}} \cdot \tilde{C}p_{\text{A}} \right) + \left(\dot{n}_{\text{W}} \cdot \tilde{C}p_{\text{W}} \right)}{\alpha_{\text{vap}}} \tag{6.21}$$

Here $\tilde{C}p_{\text{A}}$ and $\tilde{C}p_{\text{W}}$ represent the molar specific heats of the ammonia and water vapor, respectively. The vapor heat transfer coefficient is calculated using the correlation for laminar single-phase flow in semicircular channels developed by Sparrow and Haji-Sheikh (1965) cited in Kakac *et al.* (1987), as described above. The outlet temperature of the uncondensed vapor was calculated by matching the heat transfer rate estimated above, with the sensible cooling of the average vapor as follows:

$$Q_{\text{vap}} = \dot{m}_{\text{vap,bulk}} \cdot Cp_{\text{vap}} \cdot \left(T_{\text{vap,in}} - T_{\text{vap,out}} \right) \tag{6.22}$$

This heat transfer rate can be positive or negative, based on whether the vapor temperature is higher or lower than the interface temperature, as previously discussed in Chapter 4.

It should be noted that in the above equations, the value of $\tilde{z}$, is required to calculate the absorption rate. This was determined using the heat transfer rate from the solution to the coupling fluid that can be supported by the overall heat transfer coefficient. The overall heat transfer coefficient for heat transfer to the coupling fluid can be calculated by employing a simple resistance network model between the solution and the coupling fluid. Fig. 6.7 shows the representative arrangement of the sheets used for this model. The absorber is modeled as two sets of fins extending into two different fluid streams, separated by a solid wall. The thermal resistance of the fin array was calculated as follows:

$$R_{\mathrm{FA}} = \frac{1}{\eta_{\mathrm{T}} \cdot \alpha \cdot A_{\mathrm{T}}} \tag{6.23}$$

Here, α is the fluid heat transfer coefficient, A_{T} is the total fin array heat transfer area, and η_{T} is the total fin array efficiency, which can be calculated from the individual

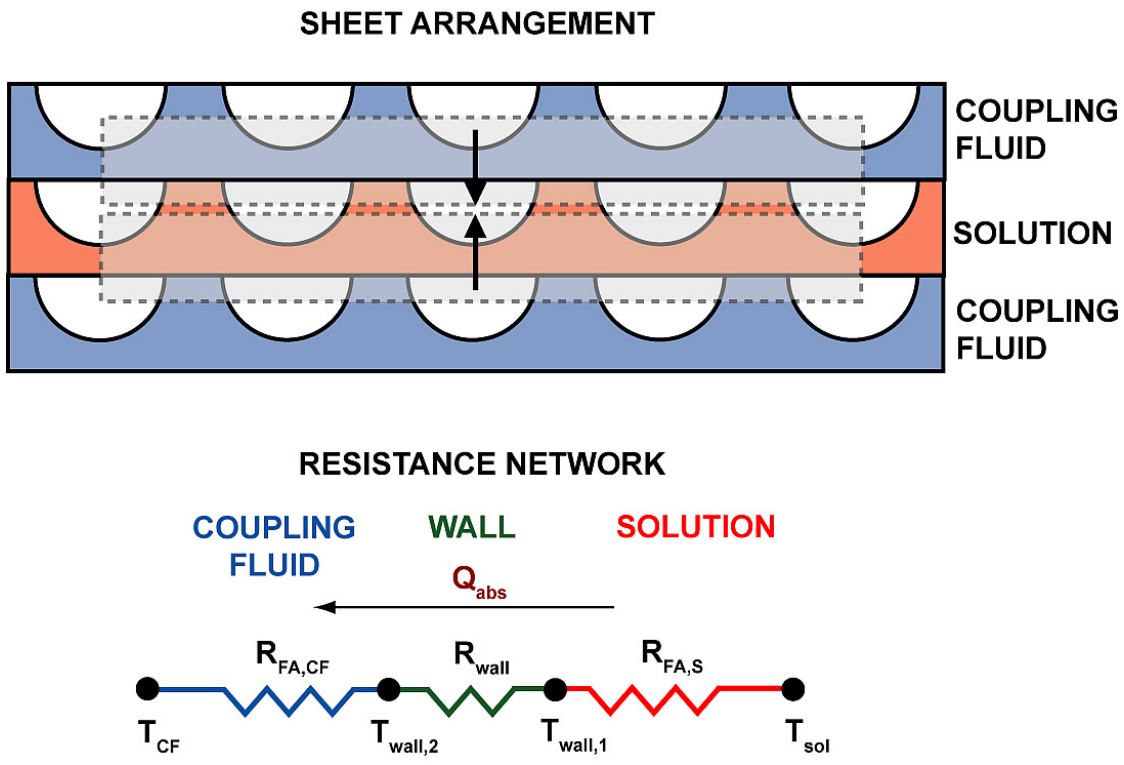

Fig. 6.7 Schematic of sheet arrangement and resistance network

fin efficiency, η_f, and is given by

$$\eta_T = 1 - \frac{N \cdot A_f}{A_T}\left(1 - \eta_f\right) \tag{6.24}$$

Here N is the number of fins and A_f is the area of each fin. The total thermal resistance of the system is the sum of the individual thermal resistances of the solution, the coupling fluid and the wall.

$$R_T = R_{FA,sol} + R_{wall} + R_{FA,CF} \tag{6.25}$$

Here $R_{FA,S}$ and $R_{FA,C}$ are the thermal resistances of the fin array in the solution and coupling fluid streams, respectively, and R_{wall} is the thermal resistance of the wall (Fig. 6.7.)

The fluid heat transfer coefficient on the solution-side was estimated using the Shah (1979) correlation. The heat transfer coefficient on the coupling fluid-side was calculated using the single phase correlation for laminar flow in semicircular channels (Sparrow and Haji-Sheikh, 1965) cited in Kakac *et al.* (1987). The overall heat transfer coefficient can be related to the overall thermal resistance as follows:

$$\frac{1}{U_{seg} \cdot A_{seg}} = R_T \tag{6.26}$$

With the overall heat transfer coefficient known, the heat transfer rate to the coupling fluid, which was previously calculated, can be related to the logarithmic mean temperature difference ($LMTD_T$) between the solution and coupling fluid as

$$Q_{abs,seg} = U_{seg} \cdot A_{seg} \cdot LMTD_T \tag{6.27}$$

This heat duty should equal the change in the enthalpy of the coupling fluid.

$$Q_{abs,seg} = \dot{m}_{CF} \cdot Cp_{CF} \cdot \left(T_{CF,out} - T_{CF,in}\right) \tag{6.28}$$

The value of $\tilde{z}$ was iteratively calculated by matching the Q_{abs} calculated in Eq. 6.27 and 6.28 with that calculated using Eq. 6.19. All the heat and mass transfer equations are satisfied once this criterion is met.

Pressure drop on the solution side was calculated using the Lockhart-Martinelli correlation (1949). The pressure drop on the coupling fluid side was calculated using the friction factor for laminar flow in semicircular channels (Sparrow and Haji-Sheikh, 1965) cited in Kakac *et al.* (1987).

6.3. Absorber test sections

6.3.1. Design conditions

Absorber test sections were designed for two representative test conditions using the heat and mass transfer model described above. The first absorber (Microscale Absorber 1) was designed as part of a single-effect absorption chiller of cooling capacity 2.5 kW, with a co-current desorber. The second absorber (Microscale Absorber 2) was designed as part of a single-effect absorption chiller of cooling capacity 2 kW, with a counter-current desorber. It should be noted that flow configuration inside the desorber is critical to the operation of an ammonia-water absorption chiller. In a co-current desorber, vapor and solution exit the desorber as a two-phase mixture, in equilibrium with each other. Thus, the vapor exiting the desorber has a high percentage of water in it, which results in a relatively impure refrigerant circulating through the condenser and the evaporator, and eventually entering the absorber. In a counter-current desorber, the generated vapor flows counter-current to the solution, which causes local rectification of the vapor stream, and results in vapor of higher concentration exiting the component. Thus, the refrigerant circulated through the condenser and the evaporator, and eventually entering the absorber is of a higher purity. This results in different operating conditions at the absorber, which in turn results in different required transfer areas. Thus, two separate absorbers were designed and fabricated for experimental evaluation.

Table 6.1 shows a summary of the operating conditions for the absorber for the 2.5 kW cooling capacity chiller (Microscale Absorber 1), and for the absorber for the 2 kW cooling capacity chiller (Microscale Absorber 2). These conditions are known from system level thermodynamic models developed for operation of the relevant absorption chillers. The absorber duty and inlet pressure of the Microscale Absorbers 1 and 2 were 3.6 and 3.2 kW, and 482.3 and 497.5 kPa, respectively. Additionally, Microscale Absorber 1 was designed with water as the coupling fluid while Microscale Absorber 2 was designed with propylene glycol/water (25% mixture by mass) as the coupling fluid.

6.3.2. Design constraints

In addition to these operating conditions, there are several other constraints that should be considered while designing an absorber test section. For example, the pressure drop in the solution and coupling fluid passages should be limited. High pressure drops in the solution will result in a decrease in the solution saturation temperature, which reduces the driving temperature between the solution and coupling fluid. The lower driving temperature differences require increased area to transfer the same absorption duty, resulting in larger components. Similarly, high pressure drops in the coupling fluid

Table 6.1 Design conditions for Microscale Absorbers 1 and 2

	Microscale Absorber 1		**Microscale Absorber 2**	
	Inlet	**Outlet**	**Inlet**	**Outlet**
Pressure (kPa)	**482.3**	476.1	**497.5**	495.9
Solution flow rate (kg s^{-1})	**0.0070**	0.0092	**0.0038**	0.0056
Solution concentration	**0.3502**	0.5035	**0.2459**	0.4896
Solution Temperature (^{o}C)	**45.55**	37.7	**60.20**	40.22
Vapor flow rate (kg s^{-1})	**0.0023**	0	**0.0018**	0
Vapor concentration	**0.9800**	N/A	**0.9986**	N/A
Vapor Temperature (^{o}C)	**37.65**	N/A	**43.70**	N/A
Coupling fluid flow rate (kg s^{-1})	**0.0862**			
Coupling fluid temperature (^{o}C)	35	**45**	37.36	**49.93**
Absorber Heat Duty (kW)	3.6			
Note: Bold quantities are model inputs, other values are calculated results.				

require a bigger pump to circulate the fluid. This would mean higher parasitic power requirements, in addition to the larger overall volume required to accommodate the bigger pump. Thus, these constraints govern length of channels, passage dimensions, and number of sheets used in the microscale forced-convective absorber.

The number of channels that can be accommodated on a single sheet are constrained by two factors: flow distribution and fabrication. As the number of channels on a single sheet increase, the header necessary to evenly distribute fluid among these channels becomes larger, and the risk of maldistribution of solution increases. Additionally, fabrication constraints limit the spacing between adjacent channels, which affects the width of the sheets, and consequently, the size of the header. Thus, to provide the necessary area for absorption, the number of sheets in the component assembly was adjusted, while the number of channels per sheet and the length of each channel were held within design limits imposed by the pressure drop constraints discussed above.

The thickness of the sheets and the geometry of the channel and header are also governed by material properties and fabrication constraints. Any large unsupported void spaces in the header may experience mechanical failure or rupturing due to the large pressure differential between the solution-side (operating pressure ~495 kPa) and the coupling fluid-side (operating pressure ~101 kPa). Also, fabrication constraints limit the hydraulic diameter of the channel that can be machined or etched on the sheet surface. Finally, the bonding process used to join the sheet assembly also limits the size of the sheets, and the height of the sheet assembly, and may require additional features to support the fabrication process. With these constraints in mind, an iterative process was used to design and fabricate the test sections to address the requirements imposed by system thermal operation, and the constraints imposed by fabrication capabilities.

6.3.3. Fabrication techniques

As previously mentioned, the microscale absorption test sections were fabricated using a two-step process. In the first step, microscale features are machined on the sheet surface, while in the second step, the sheet array is joined together to form a hermetic seal between the different fluid streams. A photochemical etching process was used to chemically machine the microscale features on stainless steel sheet stock. The process starts with cleaning of the stainless steel sheet with hydrochloric acid to remove any scales or oxides on the surface. Next, a photoresist and a template containing the image of the required microscale features on either side of the sheet are applied to both sides of the sheet. Fig. 6.8 shows a photograph of this sheet with the photoresist and template applied on the top surface. The sheet is then exposed to UV light which cures the surface, and hardens the photoresist. The template prevents exposure of the underlying photoresist to the UV radiation, and therefore avoids hardening. Fig. 6.9 shows a photograph of the developed sheet. The unexposed photoresist is then removed and the sheet is exposed to acid, which removes the exposed metal forming the channels and other features. Fig. 6.10 shows a photograph the final etched sheet. Further details of the etching process used in

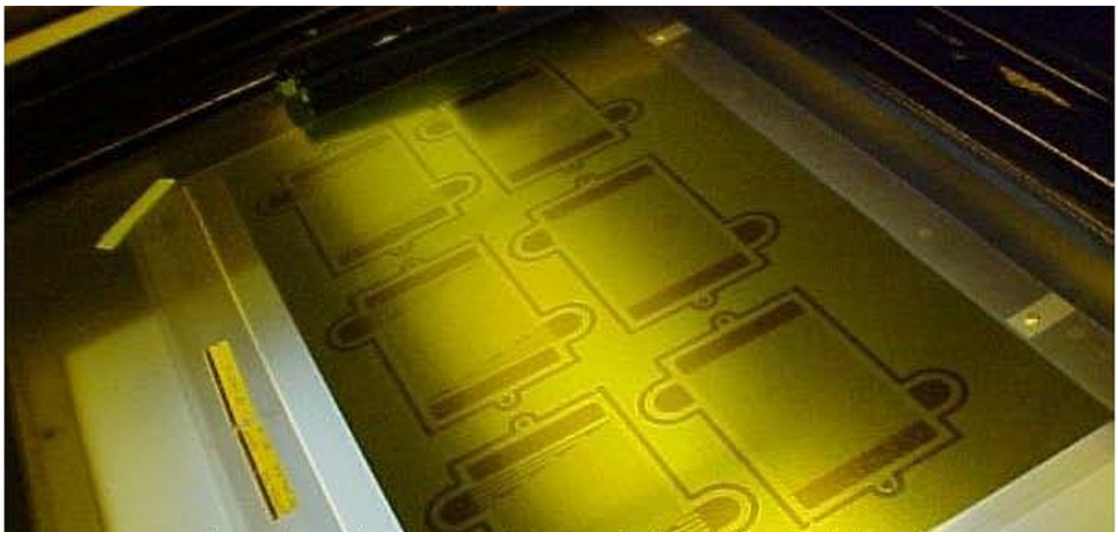

Fig. 6.8 Photograph of the photoresist and template applied on the sheet surface

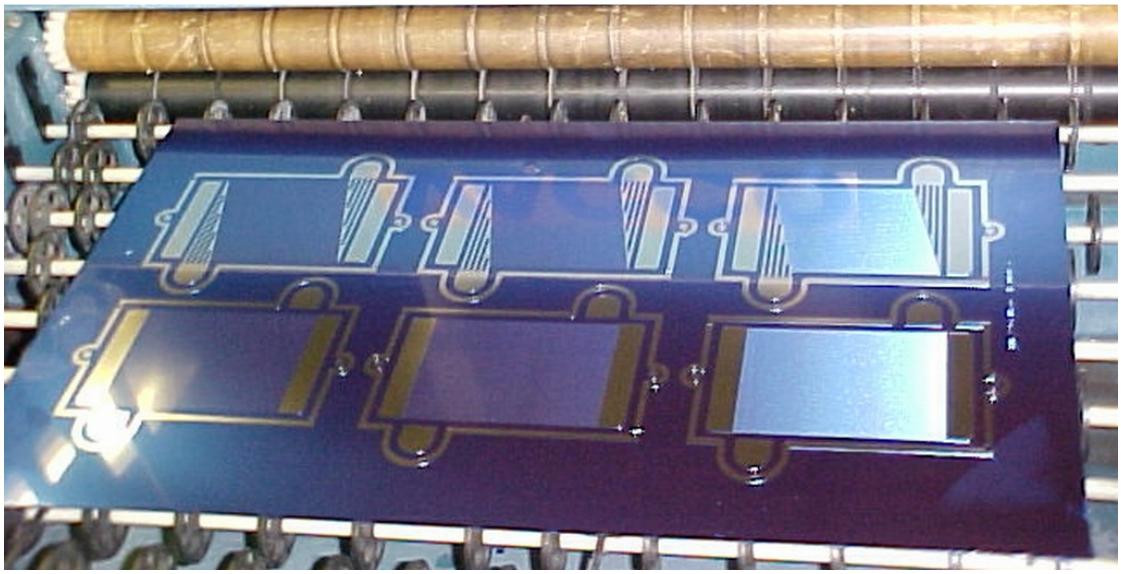

Fig. 6.9 Photograph of the developed sheet

this study are available in Determan (2008).

Two different processes were used to join the etched sheet assemblies together: diffusion bonding and vacuum brazing. The test section for Microscale Absorber 1 was fabricated using diffusion bonding, while test sections for Microscale Absorber 2 were fabricated using vacuum brazing. Both processes begin with cleaning of the sheets, followed by inspection to ensure no burrs or foreign materials are located on the sheet surface. The sheets are then coated with nickel plating by an electroless nickel plating procedure. The thickness of the deposited nickel varies depending on the features requiring bonding, and the bonding process used, with slightly thicker films used for vacuum brazing.

The plated sheets and end plates are then arranged in the correct order and proper alignment confirmed. For diffusion bonding, alignment pins are used to ensure that stack of sheets and end plates does not deform when a compressive force is applied during the bonding process. The assembly was then placed under a hot press in a vacuum furnace at an elevated temperature of (~1000^{o}C), and a load is applied to raise the interfacial stress between adjoining sheets to the required values (~10 MPa) (Fig. 6.11). The system is

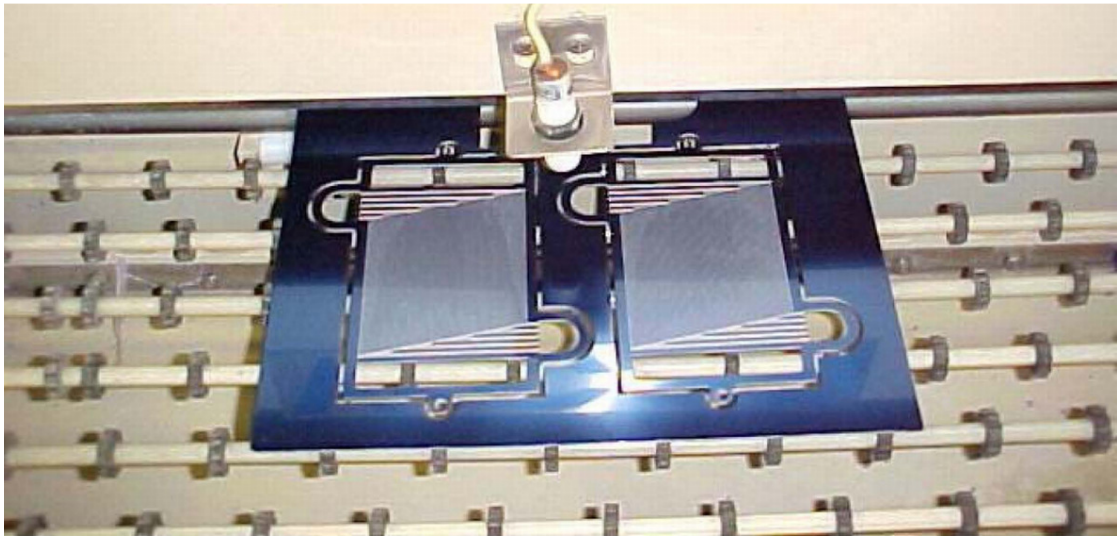

Fig. 6.10 Photograph of the final etched sheets

then maintained at these conditions for a sufficient amount of time, for the bonding process to occur (~5 hours). During the diffusion bonding process, the surface asperities on contacting surfaces begin to deform plastically, until the pores between the surfaces are eliminated. This is followed by diffusion of atoms across the interface resulting in a reorganization of the grain boundaries in the interface region. The resulting bond has the yield strength of the bulk material.

For vacuum brazing, a fixture is created to house and align the sheet array and the end plate assembly. A compressive force on the sheet assembly is achieved by tightening the ends of the fixture (this force is much smaller for vacuum brazing compared to diffusion bonding.) Fig. 6.12 shows a photograph of a representative fixture. This assembly is then introduced into an evacuated furnace, and kept at an elevated temperature (~1000^{o}C) for sufficient time for the bonding to occur completely. During vacuum brazing, the plated braze material melts at the elevated temperatures, and flows via capillary action along the joints. While the base material does not melt, it can still form an alloy at the joint due to diffusion of material at the interface. Unlike the diffusion bonding process, the strength of the joint during brazing is different from the bulk material, and so care must be taken to choose the right material to form the joint. Furnace

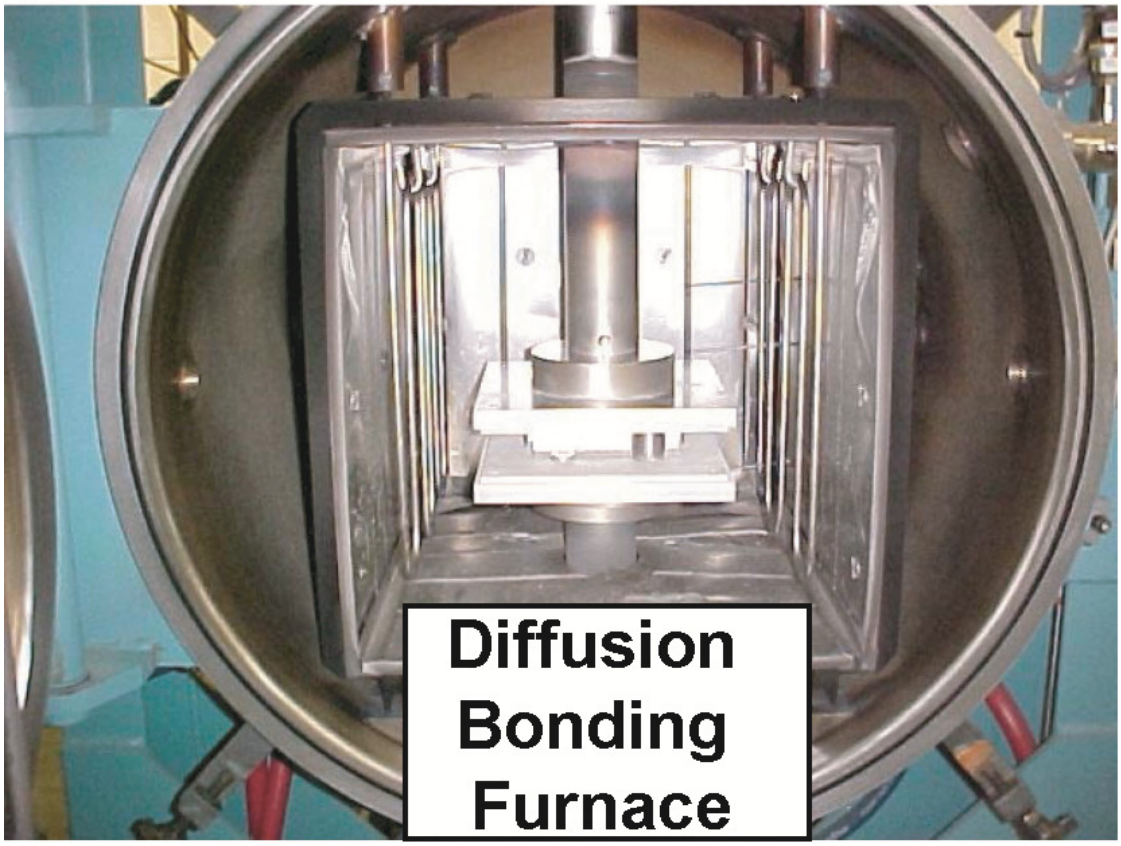

Fig. 6.11 Photograph of the diffusion bonding furnace

temperature, time at various temperatures, and braze material are varied to suit the needs to braze a particular component.

6.3.4. Representative absorber test sections

The heat and mass transfer model described above was applied to each of the absorber operating conditions described in Table 6.1. Details of the results from the heat and mass transfer model are discussed later. For Microscale Absorber 1, the diffusion bonding process was used to join the sheets that were chemically machined by photochemical etching. Due to fabrication constraints, the etched channels were of semi-circular cross-section, with a hydraulic diameter of 306 μm (Fig. 6.13). A summary of the resulting absorber geometry from the heat and mass transfer model is provided in Table

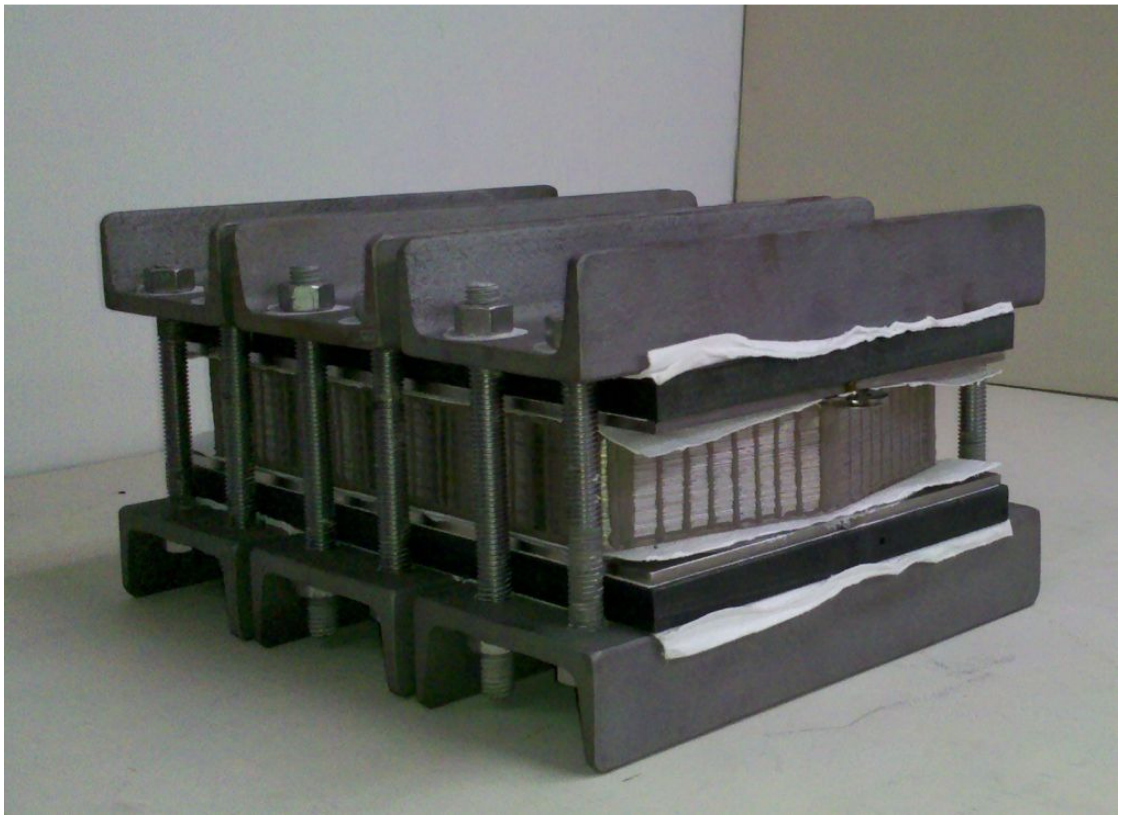

Fig. 6.12 Photograph of brazing fixture

6.2, and a single test section was fabricated using the fabrication processes described above. This test section was fabricated by Vacco Industries.

The schematic of Sheets A and B of this test section are similar to Figs. 6.2 and 6.3, respectively. Sheet A consists of 90 semicircular channels of length 176 mm each, and hydraulic diameter 306 μm. The channel pitch is 1 mm. Solution enters these channels through rectangular voids at the end. Voids 15 mm wide and 90 mm long are chosen for the present design. Sheet B consists of 90 semicircular channels of length 142 mm each, and hydraulic diameter 306 μm. The channel pitch is 1 mm; thus, a coupling fluid channel lies directly above and below each solution channel. Coupling fluid is supplied to, and removed from, this component through an angled header. A 90 mm long header tapering from 18 mm to 1 mm was chosen. The header was divided into five sections by four 2 mm wide ribs. The variation in flow distribution between channels with such a configuration was estimated to be less than 2% of the mean value. The vapor

Table 6.2 Microscale Absorber 1 geometry

	Sheet A	Sheet B
Sheet material	Stainless Steel 316L	
Sheet thickness (mm)	0.5	0.5
Number of sheets each	25	25
Number of channels per sheet	90	90
Channel Pitch (mm)	1	1
Coupling fluid channel length (mm)	176	142
Channel hydraulic diameter (mm)	0.306	0.306
End Plate thickness (mm)	13, 6	
Total Transfer Area (m^2)	0.4107	
Microchannel Array (mm × mm × mm)	216 × 100 × 25	
Overall Envelope (mm × mm × mm)	216 × 100 × 44	

inlet header is 6 mm wide and 90 mm long, and is split into two channels by a supporting rib (2 mm thick and 50 mm long).

For Microscale Absorber 2, vacuum brazing was used to join the sheets that were chemically machined by photochemical etching. Due to fabrication constraints, the etched channels were of semi-elliptical cross-section, with a hydraulic diameter of 442 µm (Fig. 6.13). A slightly larger feature size was used for these test sections due to the constraints imposed by vacuum brazing. The cross-section of the channel is approximated to half an ellipse, where two 350 µm quarter-circular sections are separated by a 50×350 µm rectangular section to form the channel. Two test sections (Microscale Absorber 2a and Microscale Absorber 2b) were designed and fabricated for this absorber, the designs varying in the inlet mechanism for the solution and the vapor. The sheets for these test sections were etched by AME Industries and vacuum brazing was done by ARS Solutions. In the first test section (Microscale Absorber 2a), vapor and solution are premixed upstream of the absorber test section and introduced through a common header as shown in Sheet A in Fig. 6.14. The two-phase solution then distributes across the array of channels, exchanging heat with coupling fluid circulated in Sheet B, flowing counter-current to the solution flow. As a result, the additional distribution header for the vapor is absent in this test section, resulting in a smaller overall component size.

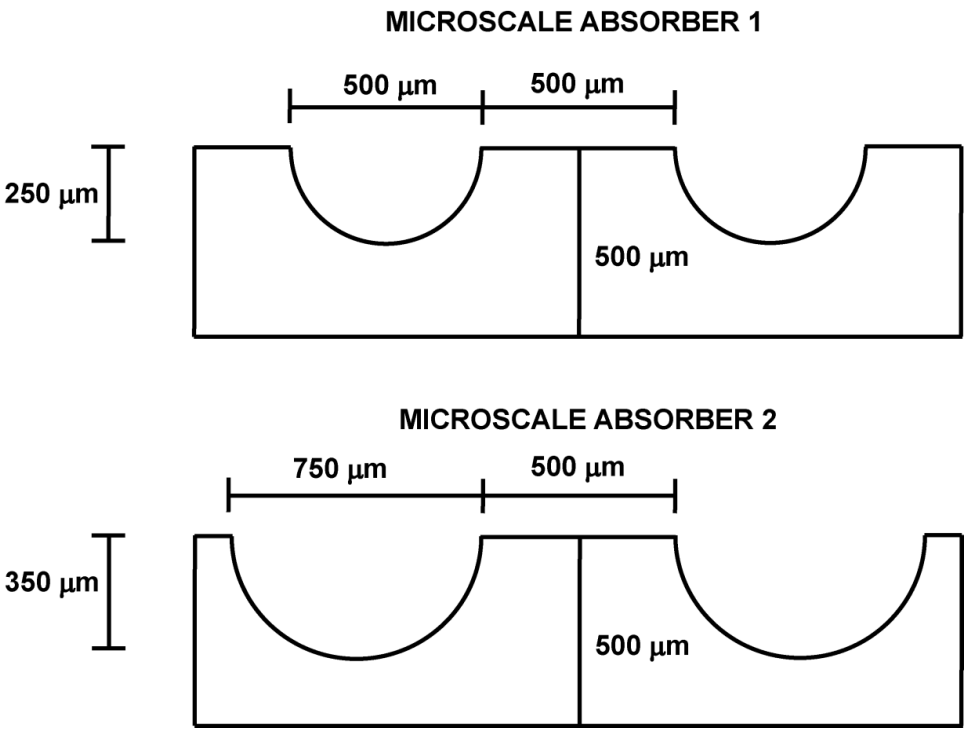

Fig. 6.13 Schematic of channel geometries

The design of the microscale features on each sheet of the second test section (Microscale Absorber 2b) is similar to that of Microscale Absorber 1, involving a separate vapor header to distribute vapor directly inside solution channels as seen Fig. 6.15. A summary of the resulting absorber geometries for Microscale Absorber 2a and 2b is provided in Tables 6.3 and 6.4, respectively.

For both test sections, Sheet B consists of 55 channels of length 152.4 mm each and hydraulic diameter 442 μm. The channel pitch is 1.25 mm. Coupling fluid is supplied to, and removed, from this component through an angled header. For Microscale Absorber 2a, a 68.3 mm long header tapering from 25.4 mm to 4 mm was chosen. Several small circular studs (or bosses) are located along the flow path in this header to create the necessary pressure drop, and distribute fluid evenly though the microchannel array. Additionally, these studs (or bosses), when brazed together, provide structural support for the void space in the header. For Microscale Absorber 2b, a similar 68.3 mm long header was chosen. The header was divided into four sections by three 2 mm wide

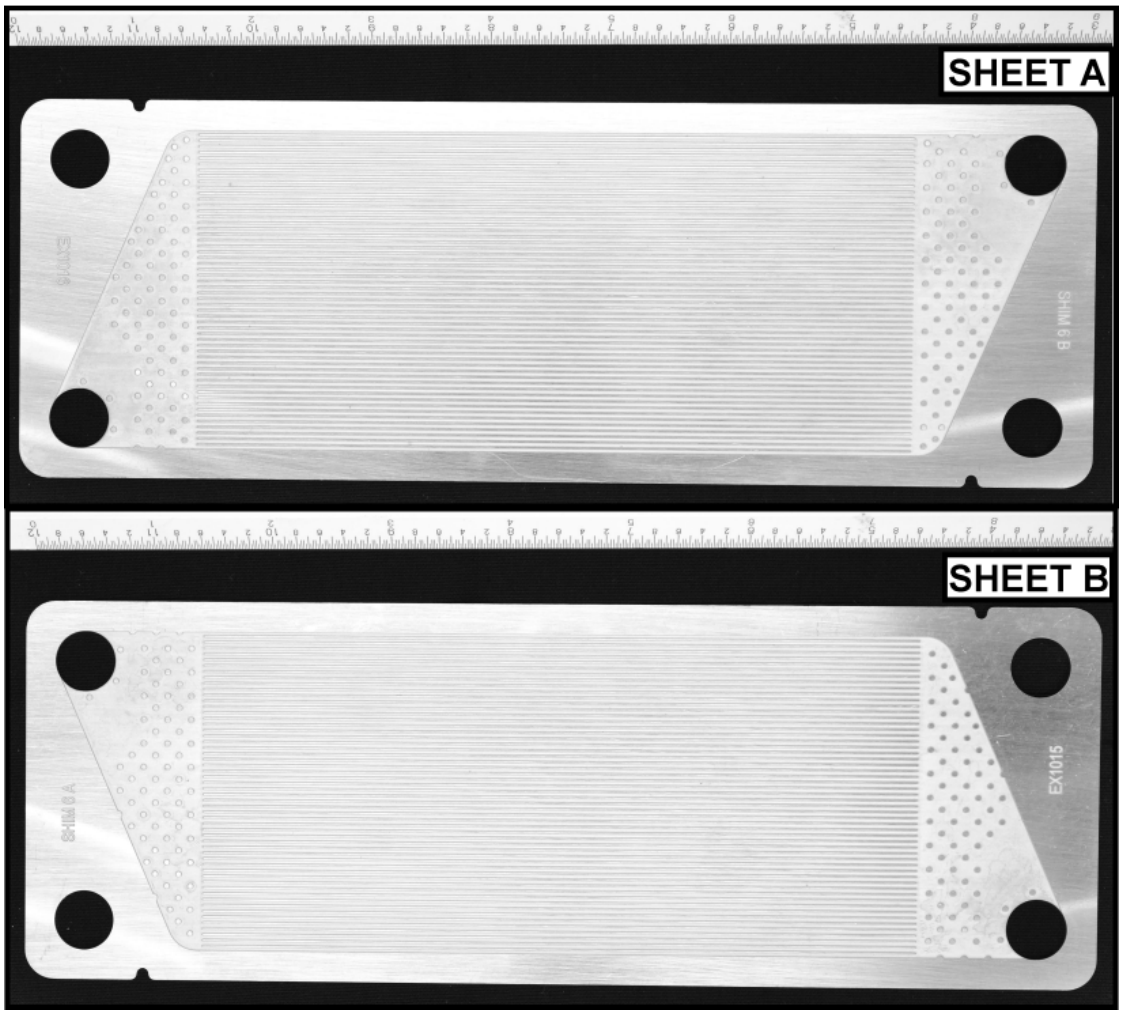

Fig. 6.14 Photograph of Sheets A and B for Microscale Absorber 2a

ribs. The vapor inlet header is 10.2 mm wide and 68.3 mm long, and is split into two channels by a supporting rib (2 mm thick and 34.2 mm long).

Sheet A of Microscale Absorber 2a is a mirror image of Sheet B, and has the same dimensions and number of channels. Sheet A of Microscale Absorber 2b consists of 55 channels of length 213.1 mm and hydraulic diameter of 442 μm. As mentioned previously, the presence of the vapor header results in longer solution channels in the Microscale Absorber 2b test section. The channel pitch is 1.25 mm. Solution enters these channels through a rectangular void at the end. Voids 16 mm wide and 68.3 mm long are chosen for the present design.

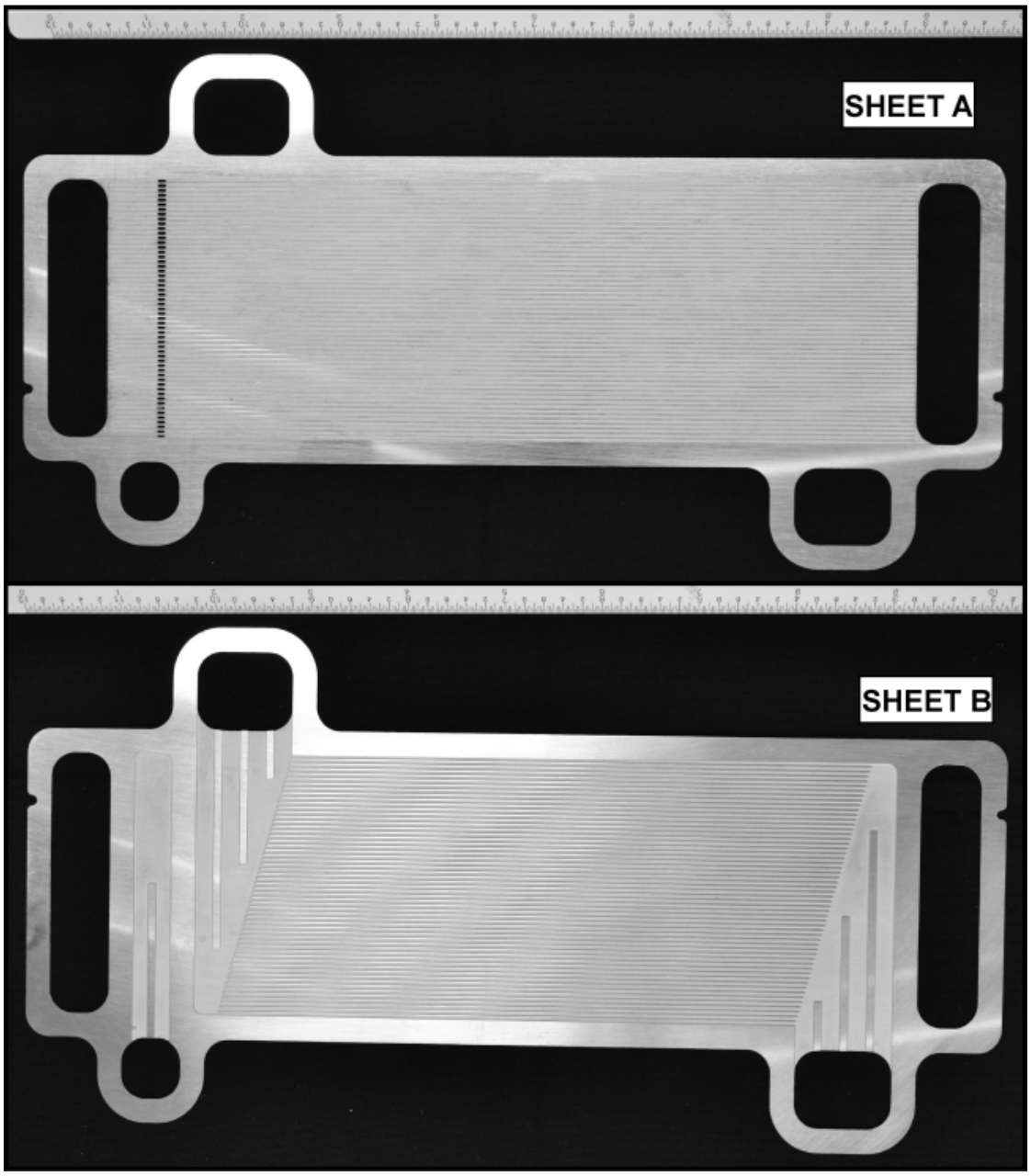

Fig. 6.15 Photograph of Sheets A and B for Microscale Absorber 2b

6.4. Segmental heat and mass transfer model predictions

6.4.1. Overall results

The heat and mass transfer calculations described above were conducted using *Engineering Equation Solver* software (Klein, 2011). The absorber was divided into

Table 6.3 Microscale Absorber 2a geometry

	Sheet A	**Sheet B**
Sheet material	Stainless Steel 304L	
Sheet thickness (mm)	0.5	0.5
Number of sheets each	20	20
Number of channels per sheet	55	55
Channel Pitch (mm)	1.25	1.25
Coupling fluid channel length (mm)	152.4	152.4
Channel hydraulic diameter (mm)	0.442	0.442
End Plate thickness (mm)	3.05	
Total Transfer Area (m^2)	0.3185	
Microchannel Array (mm × mm × mm)	228.6 × 81 × 20	
Overall Envelope (mm × mm × mm)	228.6 × 81 × 26.1	

Table 6.4 Microscale Absorber 2b geometry

	Sheet A	**Sheet B**
Sheet material	Stainless Steel 304L	
Sheet thickness (mm)	0.5	0.5
Number of sheets each	22	22
Number of channels per sheet	55	55
Channel Pitch (mm)	1.25	1.25
Coupling fluid channel length (mm)	213.1	152.4
Channel hydraulic diameter (mm)	0.442	0.442
End Plate thickness (mm)	3.05	
Total Transfer Area (m^2)	0.3504	
Microchannel Array (mm × mm × mm)	257.8 × 81 × 20	
Overall Envelope (mm × mm × mm)	257.8 × 81 × 26.1	

several segments of equal absorption duty and iterative calculations were initiated at the dilute solution inlet of the absorber. The dilute solution and refrigerant vapor conditions at the inlet of the first segment are known from the design conditions. The outlet conditions for the segment calculated from the above model serve as inlet conditions for the succeeding segment. Coupling fluid inlet and outlet conditions at each segment are known from the heat duty requirements. These conditions and the respective resistances are used to calculate the required channel length for each segment. A summary of these

calculations for a representative segment for Microscale Absorber 2 is shown in Appendix D.

For Microscale Absorber 1, the liquid-only Reynolds number of the solution for the design case was calculated to be 18.7. The Reynolds number of the vapor bulk was found to vary between 16.7 and 236.8, while the Reynolds number of the coupling fluid varied between 168.8 and 198.1 along the length of the absorber. Therefore, all fluid streams are in laminar flow inside the heat and mass exchanger. The corresponding heat and mass transfer coefficients of the vapor bulk were calculated to be 410.3-423.1 W m^{-2} K^{-1} and 0.073-0.077 m s^{-1}, respectively. The solution and coupling fluid heat transfer coefficients ranged from 1352-4612 and 8336-8496 W m^{-2} K^{-1}, respectively.

For Microscale Absorber 2, the liquid-only Reynolds number of the solution for the design case was calculated to be 16.5. The Reynolds number of the vapor bulk varied between 13.8 and 272.2, while the Reynolds number of the coupling fluid varied between 88.4 and 110.9 along the length of the absorber. It should be noted that the lower Reynolds number values for the coupling fluid are due to the use of propylene glycol/water as the coupling fluid, which has a higher viscosity than water at the operating temperature. All fluid streams are in laminar flow inside the heat and mass exchanger. The corresponding heat and mass transfer coefficients of the vapor bulk were calculated to be 287.4-297.2 W m^{-2} K^{-1} and 0.049-0.054 m s^{-1}, respectively. The solution and coupling fluid heat transfer coefficients were found to range from 823-4092 and 4460-4586 W m^{-2} K^{-1}, respectively.

6.4.2. Segmental results

The variation of temperature, concentration, and flow rate of solution and vapor, as well local absorption characteristics are considered next. While the local absorption rates and the relevant transfer areas were different, the trends in each segment were found to be similar for all the microscale absorbers. Thus for brevity, only absorption

characteristics of Microscale Absorber 2 are discussed here (both Microscale Absorber 2a and 2b have the same characteristics.)

Fig. 6.16 shows a plot of the solution and vapor superficial velocities inside a representative channel for Microscale Absorber 2, superimposed on the Taitel-Dukler flow regime map (1976). As can be seen from this plot, the flow inside the channels is mostly in the annular-disperse flow regime. Towards the end of the absorption process, the flow starts to transition into the intermittent flow regime. Based on this plot, the annular flow configuration assumed in the development of the design model above is justified.

Fig. 6.17 shows the variation of the mass flow rate of the solution and the vapor as function of channel length, while Fig. 6.18 shows the corresponding solution and vapor concentrations. It should be noted that the channel length represented here is the

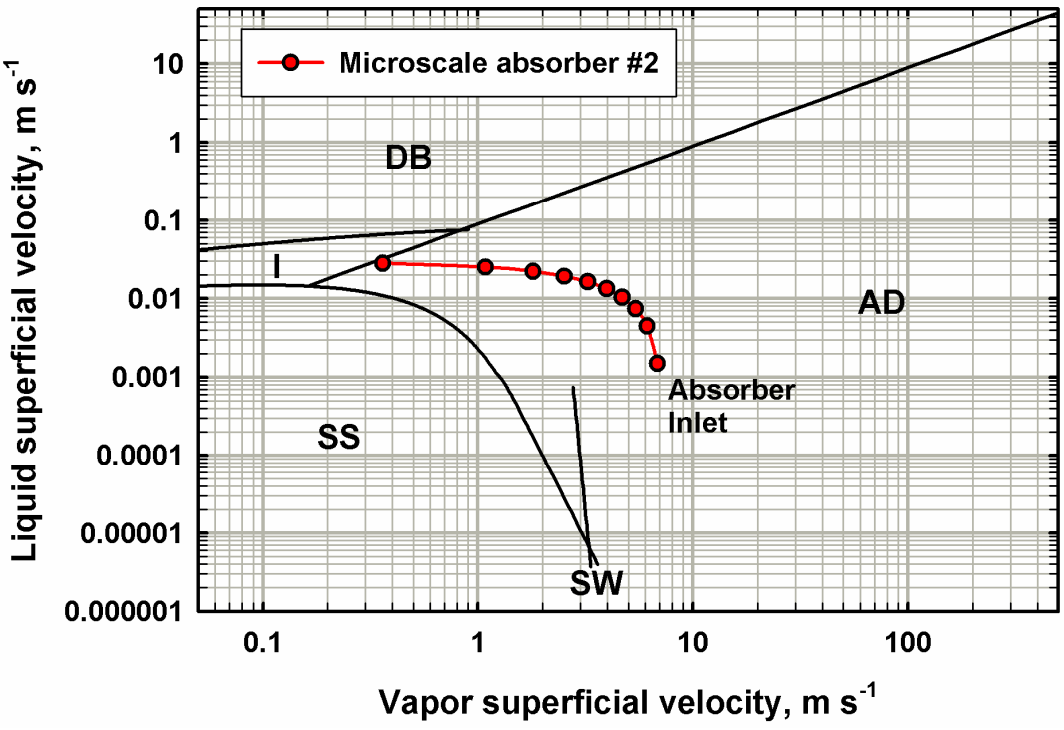

Fig. 6.16 Plot of the solution and vapor superficial velocities superimposed on the Taitel-Dukler flow regime map (Microscale Absorber 2)

microchannel array portion, in which the solution and coupling fluid are in thermal contact with each other, i.e., lengths of the inlet and outlet headers are not included. It can be seen from Fig. 6.17 that the absorption rate is quite high near the inlet, resulting in a steep increase in the solution mass flow rate and a corresponding decrease in the vapor mass flow rate. In fact, more than one-half of the vapor flow rate is absorbed within the first 20% of the channel length. This observation is explained based on the profiles seen in Figs. 6.18 and 6.19. As can be seen in Fig. 6.18, the large concentration difference between the vapor and solution near the inlet initially promotes a high mass transfer rate. In addition, the large temperature difference between the solution and the coupling fluid (Fig. 6.19) in this region yields a high local heat transfer rate. Both these factors contribute to the large absorption rates observed in initial part of the absorber.

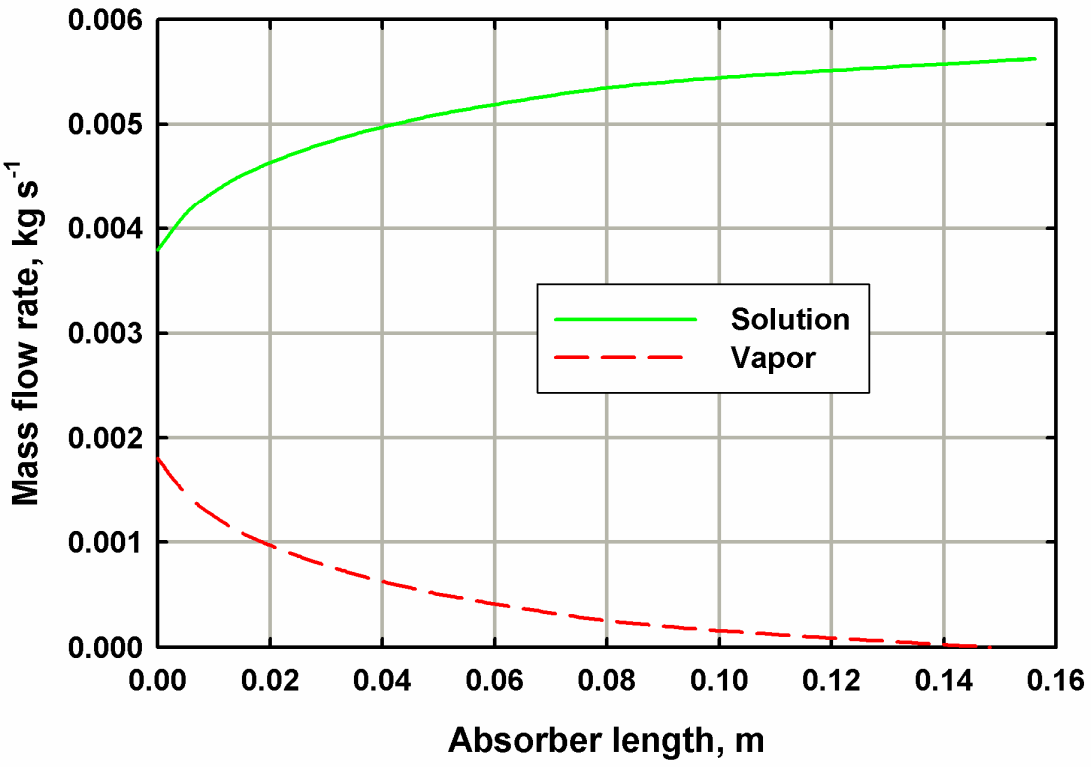

Fig. 6.17 Solution and vapor mass flow rate as a function of absorber length

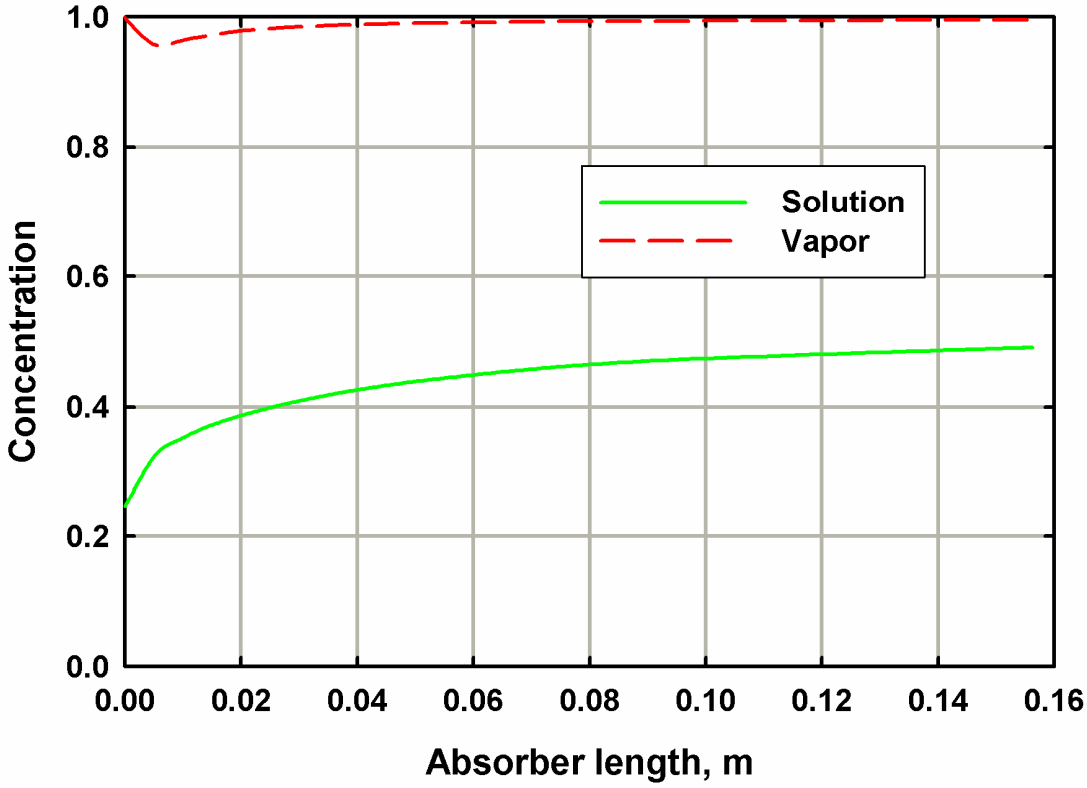

Fig. 6.18 Solution and vapor concentration as a function of absorber length

Fig. 6.18 also shows that the concentration of the solution increases continuously along the absorber length. On the other hand, concentration of the vapor decreases initially, followed by a gradual increase, eventually approaching a near constant value. In the initial absorber segments, the molar concentration of the condensing flux $\tilde{z} \geq 1$. This indicates local absorption of the ammonia from the vapor to the solution and desorption of water from solution to the vapor. Due to the local desorption of water, the concentration of the vapor decreases in the initial segments. In succeeding segments, the values of $\tilde{z}$ are smaller than the vapor concentration, resulting in an increase in the vapor concentration. This observation is further substantiated by Fig. 6.20, which shows the rate of cumulative absorption of the refrigerant vapor and its individual components (ammonia and water) as a function of absorber length. It can be seen that water is initially

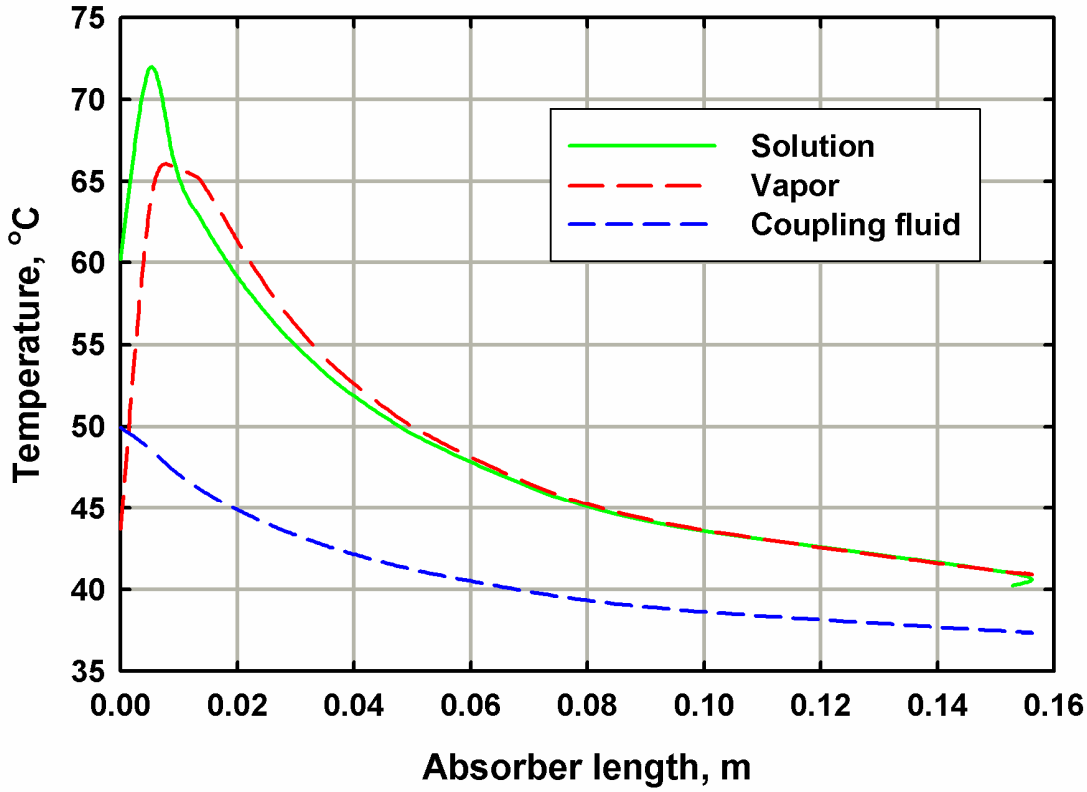

Fig. 6.19 Temperature as a function of absorber length

desorbed (indicated by a negative value), followed by absorption through the remainder of the absorber length.

The temperature of the coupling fluid is observed to decrease continuously along the length of the absorber (Fig. 6.19). It should be noted that the coupling fluid is flowing counter-current to the solution, and thus the absorber length of 0 corresponds to the coupling fluid outlet. The temperature of the solution and vapor, however, initially increases, followed by a monotonic decrease. The dilute solution entering the absorber is highly subcooled by exchanging heat with the colder concentrated solution in the solution heat exchanger. As previously observed, a large amount of heat is released in the initial segments of the absorber due to the high initial absorption rate. While most of this heat is transferred to the coupling fluid, some of the heat is used for sensible heating of the

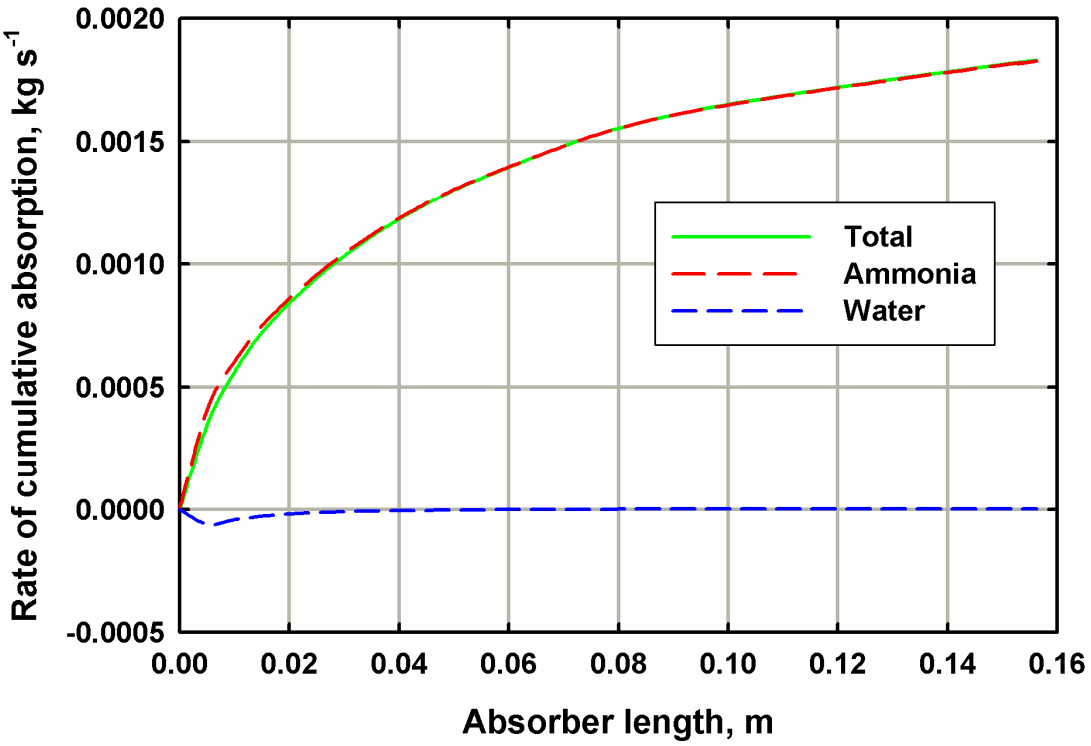

Fig. 6.20 Rate of cumulative absorption as a function of absorber length

subcooled solution. Additionally, in the initial segments, the vapor-liquid interface temperature is greater than the vapor bulk temperature, resulting in heating of the vapor bulk by heat transfer from the interface to the vapor bulk. This explains the initial rise in the vapor bulk temperature.

In contrast, in the later segments of the absorber, where the temperature of the bulk vapor is greater than the temperature of the vapor-liquid interface, the vapor undergoes sensible cooling, resulting in a decrease in its temperature through the rest of the absorber. This is confirmed by Fig. 6.21 which shows negative values for vapor sensible cooling in the initial segments, followed by a positive value in the succeeding segments.

Fig. 6.22 shows the cumulative absorber heat duty as a function of absorber length. As stated above, nearly 50% of the total absorber heat duty is exchanged within

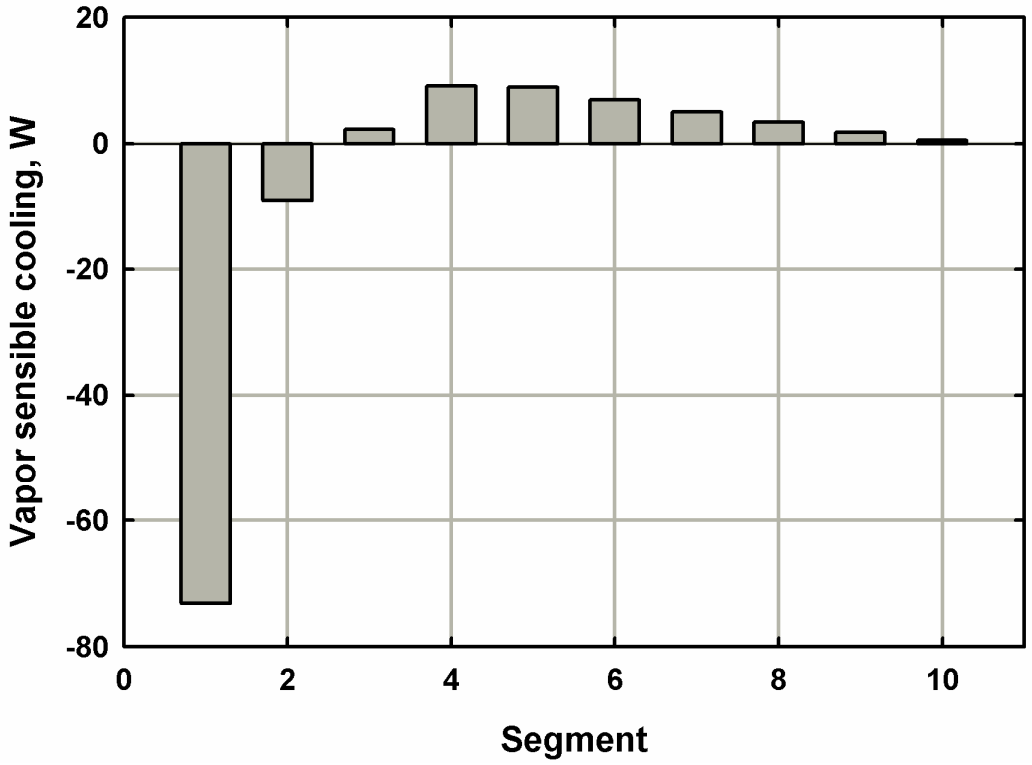

Fig. 6.21 Vapor sensible heat duty as a function of absorber segment

the first 20% of the absorber length, due to large driving temperature and concentration differences in this region. Fig. 6.23 shows the solution and coupling fluid pressure drops as a function of absorber length. The total pressure drops in both the solution and coupling fluid are within reasonable design limits. These low pressure drops are due to distribution of the total flow into several parallel channels, with laminar flow in each channel over short flow lengths. Thus, the parasitic losses in the present design are expected to be low.

Fig. 6.24 shows the variation of the overall, coupling fluid-side, and solution-side thermal resistances per unit length for a single representative sheet. The solution- and coupling-fluid side resistances are comparable in the initial segments. In fact, in the initial segments, the coupling fluid-side resistance is slightly greater than the solution-side resistance. However towards the outlet of the absorber, the solution-side resistance is

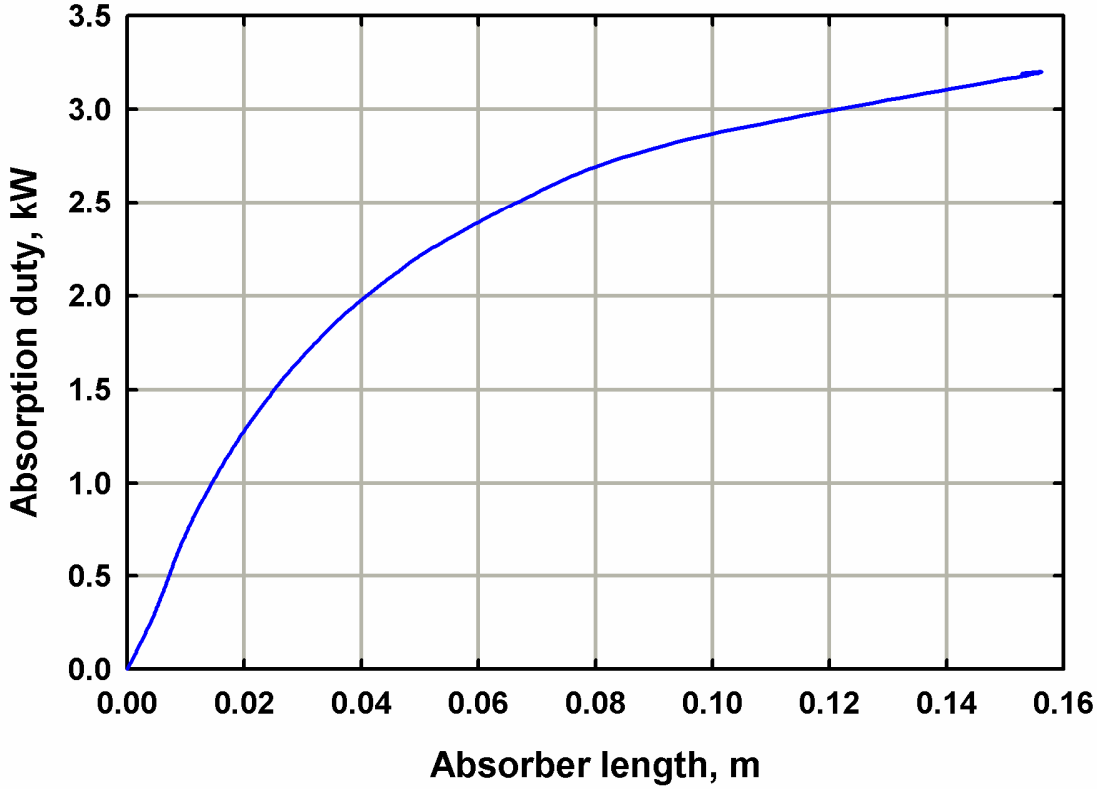

Fig. 6.22 Absorption heat duty as a function of absorber length

significantly greater than the coupling-fluid side resistance. This is because the solution flow rate is considerably lower than the coupling fluid flow rate, and towards the outlet of the absorber, with most of the vapor having been absorbed in the upstream segments, almost the entire solution flow is in liquid phase, with low velocities. In the last segment, the solution-side thermal resistance is an order of magnitude greater than the coupling fluid-side thermal resistance, thus dominating the overall heat transfer resistance. Due to the large thermal resistances in the segments near the outlet, and lower driving temperature differences, larger segment lengths are required to transfer the same amount of heat (Fig. 6.25).

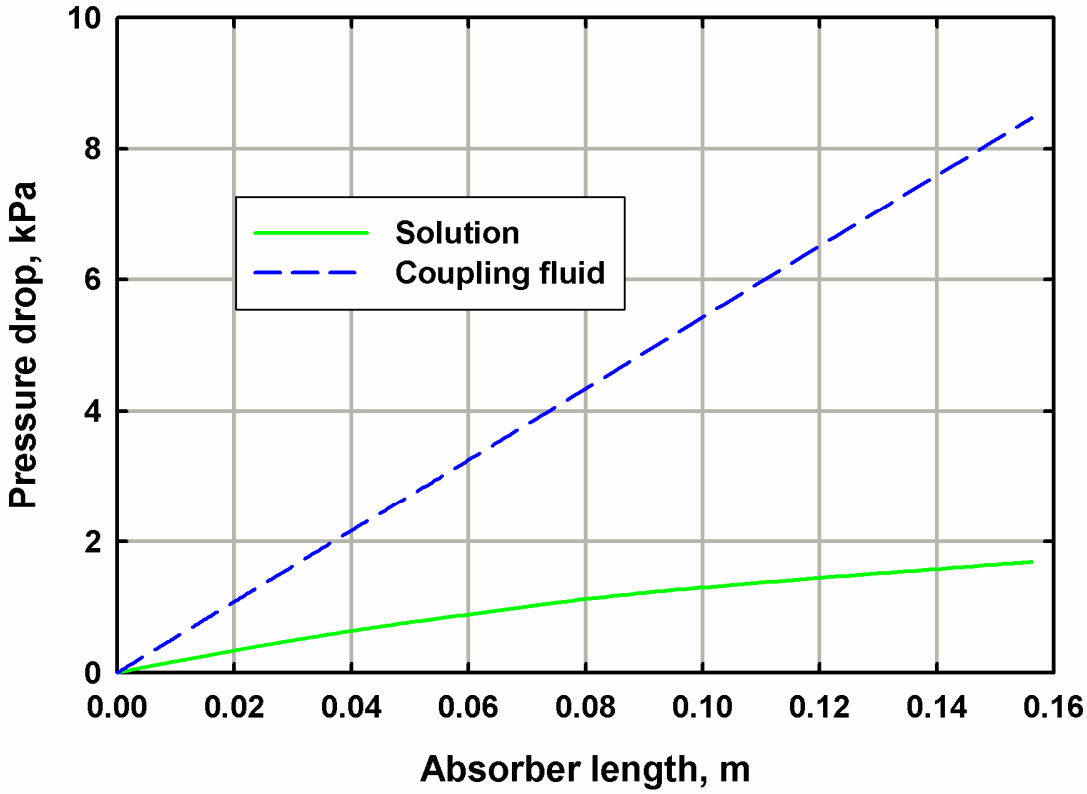

Fig. 6.23 Pressure drop as a function of absorber length

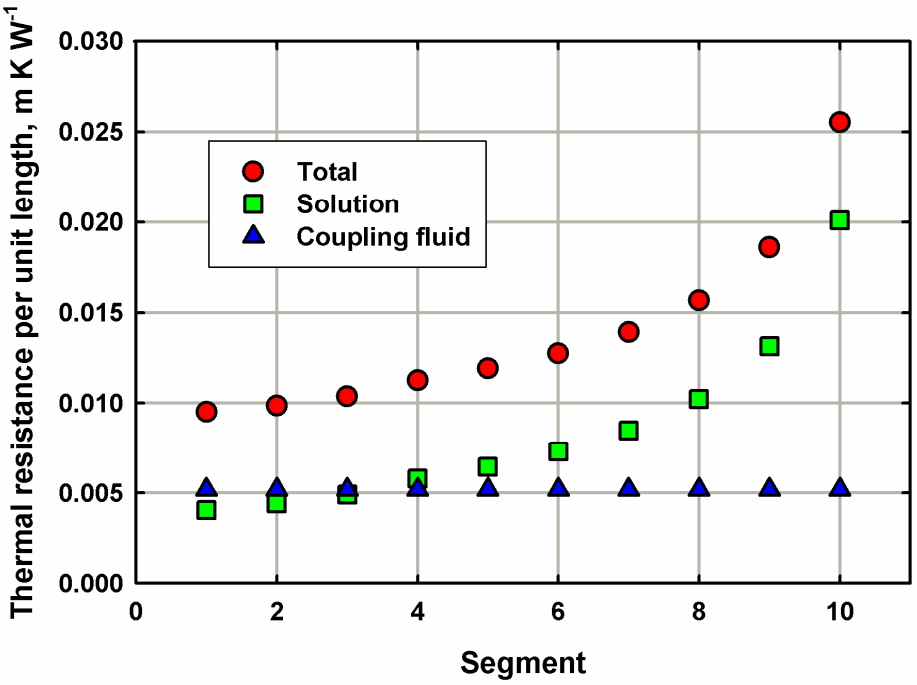

Fig. 6.24 Thermal resistance per unit length as a funtion of absorber segment

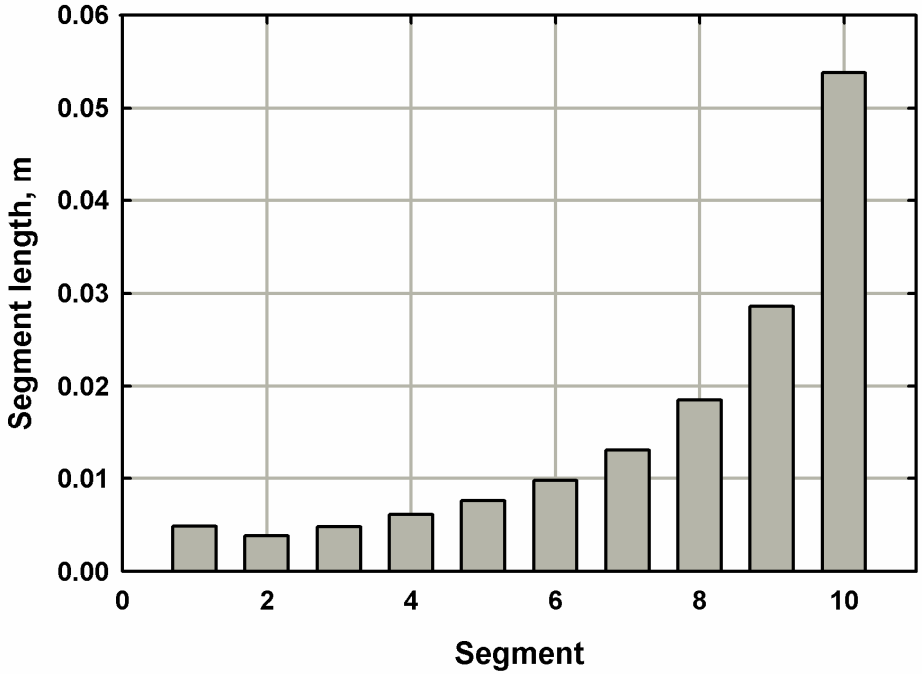

Fig. 6.25 Absorber segment lengths

6.5. Summary

This chapter presents the development of a microscale heat and mass exchange miniaturization concept, and a design model for an absorber application. The absorber consists of an array of alternating sheets with integral microscale features, enclosed between cover plates. The microscale features on the sheets include microchannel arrays for the flow of solution, vapor, and coupling fluid, and the inlet and outlet headers for the distribution of these fluids into the microchannel arrays. Test sections were fabricated for two conditions: an absorber as part of a single-effect absorption chiller of cooling capacity 2.5 kW, with a co-current desorber, and an absorber as part of a single-effect absorption chiller of cooling capacity 2 kW, with a counter-current desorber. Photochemical etching was used to chemically machine the microscale features on individual sheets, and diffusion bonding or vacuum brazing were used to join the sheet array. Test sections also differed in terms of the inlet header configuration adopted to distribute various fluid streams. Heat and mass transfer modeling of the absorption process shows that this concept has the potential for the development of extremely small absorption system components. Results from the analysis of the absorber for the 2 kW cooling capacity chiller were presented. A bulk of the absorption was found to occur near the inlet of the absorber due to favorable concentration and temperature gradients at this location. In addition, local desorption of water was also predicted in these initial segments, due to the large of amount of heat generated because of rapid absorption. Overall system level penalties, resulting from pressure drops in various fluid streams, were found to be low due to distribution of the total flow into several parallel channels, where flow in each channel is laminar, and is through short flow lengths. In addition to the absorber (and other absorption system components) application discussed here, the present concept can be adopted in a variety of other industrial applications involving multi-component fluid, single-phase and phase-change heat and mass transfer processes.

CHAPTER 7. DEMONSTRATION OF ABSORPTION COOLING USING MICROSCALE GEOMETRIES

In the previous chapter, a microscale forced-convective heat and mass exchanger concept was described, and a coupled heat and mass transfer model was developed for absorber applications. Test sections were designed and fabricated using microfabrication techniques, for absorbers that were part of a 2.5 kW cooling capacity chiller with a co-current desorber, and a 2 kW cooling capacity chiller with a counter-current desorber. To demonstrate microscale forced-convective absorption in these test sections, a breadboard test facility was designed and fabricated. The absorber test sections were installed in this test facility, along with all other components of a single-effect ammonia-water absorption chiller. All the other principal absorption chiller components i.e. the desorber, rectifier, condenser, evaporator, solution heat exchanger, and refrigerant pre-cooler were also fabricated using similar microscale geometries and microfabrication techniques. The following sections present a summary of the absorption system components, development of the test facility, experimental demonstration of absorption cooling using convective flow components, and system and component-level analysis of the data.

7.1. Microchannel system components

Two sets of microchannel absorption system components were designed and fabricated to develop the two chiller configurations (2.5 kW cooling capacity with a co-current desorber, and a 2 kW cooling capacity with a counter-current desorber.) Microscale Absorber 1 was tested as part of the 2.5 kW cooling capacity chiller, while Microscale Absorbers 2a and 2b were tested as part of the 2 kW cooling capacity system. As previously mentioned, a system level thermodynamic model was developed to determine the operating conditions at the inlet and outlet of each component. A modified

version of the heat and mass transfer model developed in the previous chapter was then used to size these other supporting components to meet the target design conditions.

7.1.1. 2.5 kW cooling capacity chiller

Table 7.1 shows a summary of the design conditions for the system components of the 2.5 kW cooling capacity absorption chiller, as predicted by the thermodynamic model. Table 7.2 shows the summary of a corresponding component geometries based on the predictions from the heat and mass transfer model. It is interesting to note that while the refrigerant pre-cooler transfers a very small duty of 0.35 kW, the predicted size is comparable to that of the condenser and the evaporator, which transfer much higher duties. This is because the refrigerant exiting the evaporator is almost completely vapor, and the resulting heat transfer coefficient is much lower than the refrigerant heat transfer coefficient in the evaporator or the condenser. Similarly, the desorber was found to be smaller than the condenser or the evaporator, in spite of transferring a higher heat duty. This is due to a combination of higher heat transfer coefficients because of higher solution flow rates in each channel, and a higher driving temperature difference between the desorber coupling fluid and the solution.

Fig. 7.1 shows a schematic of the representative sheets (Sheet A and B) used to fabricate each of the system components, except the desorber and the rectifier, for the 2.5 kW cooling capacity chiller. The design of these sheets is similar to the design of the microscale heat and mass exchanger concept described in the previous chapter, with a minor modification. Since only one fluid stream enters and exits on each side of the system components, there is no need for a separate vapor header. Similar to the flow inside the microscale heat and mass exchanger concept described in the previous chapter, one fluid stream enters Sheet A through the rectangular void on the left, flows from left to right in the array of parallel channels, and is removed from the sheet through the rectangular void on the right. The second fluid stream enters Sheet B through the

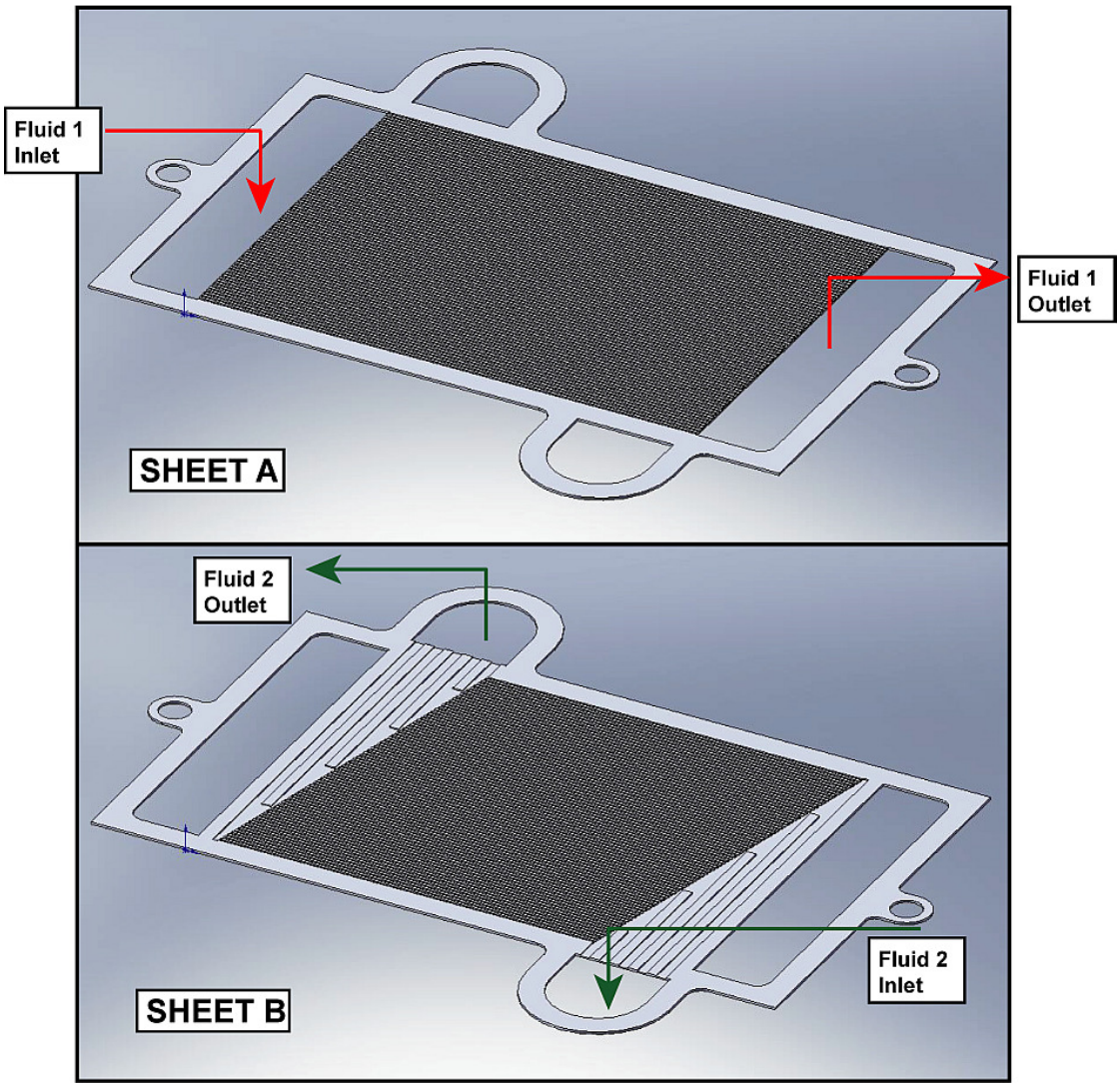

Fig. 7.1 Schematic of representative sheets for 2.5 kW cooling capacity absorption chiller

semicircular void on the right, and flows through the angled header which facilitates distribution into the array of parallel channels. The fluid then flows from right to left, exchanging heat with the fluid stream flowing in counterflow orientation in Sheet A. The fluid exiting the channel array flows through the angled headers, and is collected in the semicircular void on the left, before being removed from Sheet B. As previously mentioned, because of the design of the headers and flow passages, the fluid stream flowing through Sheet A does not mix with fluid stream flowing through Sheet B.

In the evaporator and the condenser, the refrigerant flowed through Sheet A, while the coupling fluid flowed through Sheet B. In the refrigerant pre-cooler and solution heat exchanger, the low-pressure refrigerant and the dilute solution flowed through Sheet A, respectively, while the high-pressure refrigerant and the concentrated solution flowed through Sheet B, respectively. Similar to the fabrication procedures used for the development of Microscale Absorber 1, the microscale features on each individual sheet were chemically machined using a photochemical etching process, and the sheet array was bonded together using a diffusion bonding process.

Fig. 7.2 shows a schematic of the sheets used to fabricate the desorber and rectifier. It should be noted that both components were integrated into the same sheet, with the rectifier located directly above the desorber. Concentrated solution enters the component at the bottom rectangular header, is distributed into the array of parallel channels in Sheet A, and flows vertically upwards. The desorber coupling fluid flows counter-current to the solution, entering the component through the semicircular void located on the right in the middle of the component, and exiting the component through the semicircular void located at the bottom of the component on the left. Due to the design of the various flow passages, the coupling fluid enters only Sheet B, and is routed to the array of channels via the angular headers.

The desorber coupling fluid provides the necessary heat to desorb vapor from the concentrated solution, and the resulting vapor and dilute solution flow in a co-current configuration. The dilute solution is removed from the component at the top of the desorber channel array, while the vapor continues to move upwards into the rectifier. Unlike the desorber, in the rectifier, vapor and coupling fluid streams flow through both sheets. However, they are routed through separate channels in each sheet which are designed such that the fluid streams do not mix with each other (Fig. 7.2). The rectifier coupling fluid enters the rectifier through four different semicircular voids located at the top of the component, flows downward through both Sheet A and Sheet B, and is

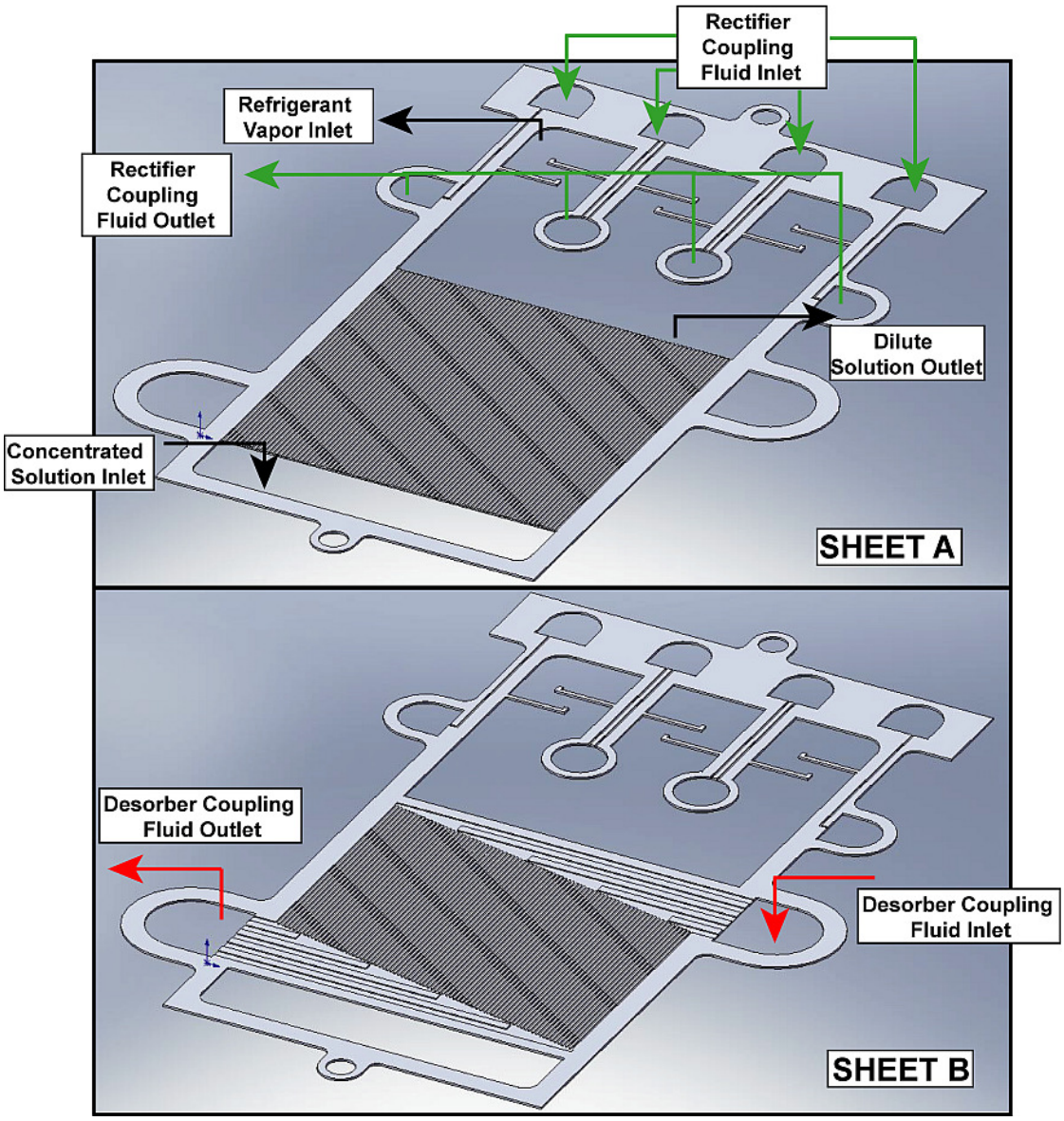

Fig. 7.2 Schematic of desorber and rectifier sheets for 2.5 kW cooling capacity absorption chiller

removed from two semicircular voids, and two circular voids located at the bottom of the rectifier section. As the vapor flows upwards through both Sheet A and Sheet B, water is preferentially condensed, and the resulting vapor, which has a higher purity of ammonia, is removed from the top of the rectifier section.

Table 7.1 Summary of component design conditions for 2.5 kW cooling capacity absorption chiller

Component	Line	Temperature (^oC)		Flow rate (kg s^{-1})		Concentration (%)		Pressure (kPa)		Duty (kW)
		Inlet	Outlet	Inlet	Outlet	Inlet	Outlet	Inlet	Outlet	
Condenser	Refrigerant	93.42	46	0.0023	0.0023	98.0	98.0	1892	1892	2.82
	Coupling Fluid	35	45	0.0675	0.0675	-	-	-	-	
Evaporator	Refrigerant	3.72	9.72	0.0023	0.0023	98.0	98.0	482.8	482.8	2.50
	Coupling Fluid	12.78	7.22	0.1127	0.1127	15.0	15.0	-	-	
Desorber	Solution	90.71	121.5	0.0092	0.0092	50.4	50.4	1892	1892	4.50
	Coupling Fluid	126.5	116.5	0.1513	0.1513	90.0	90.0	-	-	
Rectifier	Vapor	121.5	93.42	0.0025	0.0023	92.32	98	1892	1892	0.61
	Reflux	-	116.5	-	0.0002	-	37.2	-	1892	
	Coupling Fluid	35	45	0.0146	0.0146	-	-	-	-	
Solution HX	Conc. Solution	36.51	90.71	0.0092	0.0092	50.4	50.4	1892	1892	2.39
	Dil. Solution	121.3	45.28	0.0069	0.0069	35.0	35.0	1892	1892	
Refrigerant Pre-cooler	High Pressure	46	13.47	0.0023	0.0023	98.0	98.0	1892	1892	0.35
	Low Pressure	9.72	37.65	0.0023	0.0023	98.0	98.0	482.8	482.8	

Table 7.2 Summary of component geometries for 2.5 kW cooling capacity absorption chiller

	Evaporator	Condenser	Desorber	Rectifier	Solution heat exchanger	Refrigerant pre-cooler
Sheet thickness (mm)	0.5	0.5	0.5	0.5	0.5	0.5
Number of sheets (Sheet A)	20	20	20	20	20	20
Number of sheets (Sheet B)	20	20	20	20	20	20
Number of channels per sheet	76	76	80	6	40	81
Channels pitch (mm)	1	1	1	1	1	1
Channel length (mm)	76	79	54	30	41	85
Channel hydraulic diameter (mm)	0.306	0.306	0.306	0.306	0.306	0.306
End plate thickness (mm)	13, 6	13, 6	13, 6	13, 6	13, 6	13, 6
Total transfer area (m^2)	0.1485	0.1544	0.1111	0.0024	0.0422	0.1770
Overall envelope (mm × mm × mm)	161 × 86 × 44	164 × 86 × 44	205 × 90 × 44		122 × 50 × 44	170 × 91 × 44

7.1.2. 2 kW cooling capacity chiller

Table 7.3 shows a summary of the design conditions for the system components of the 2 kW cooling capacity absorption chiller, as predicted by the thermodynamic model. Table 7.4 shows a summary of the corresponding component geometries based on the predictions from the heat and mass transfer model. From these tables, it can be seen that the transfer area required for the refrigerant pre-cooler for this design is lesser than the transfer area of the evaporator and the condenser, which is due to a higher driving temperature difference (5.6 K) between the high- and low-pressure refrigerant streams compared to the driving temperature difference (3.8 K) for the 2.5 kW design.

Fig. 7.3 shows a photograph of the representative sheets (Sheet A and B) used to fabricate each of the system components, except the desorber and the rectifier, for the 2 kW cooling capacity chiller. The design of these sheets is similar to the design of the Microscale Absorber 2a described in the previous chapter. Similar to the flow inside the Microscale Absorber 2a, one fluid stream enters Sheet A through the circular void on the bottom left corner, and flows through the angled header which facilitates distribution into the array of parallel channels. The fluid exiting the channel array flows through the angled headers and is collected in the circular void on the top right corner before being removed from Sheet A. The second fluid stream enters Sheet B through the circular void on the bottom right corner, and flows through the angled header which facilitates distribution into the array of parallel channels. The fluid then flows from right to left, exchanging heat with the fluid stream in Sheet A in countercurrent orientation. The fluid exiting the channel array flows through the angled headers and is collected in the circular void on the top left corner before being removed from Sheet B. Similar to the fabrication procedures used for the development of Microscale Absorber 2a and 2b, the microscale features on each individual sheet were chemically machined using a photochemical

etching process, and the sheet array was bonded together using a vacuum brazing process.

Two desorber and rectifier configurations were developed for the 2 kW cooling capacity system: a vertical column desorber-rectifier and a branched tray desorber-rectifier. Similar to the 2.5 kW cooling capacity chiller, the desorber and rectifier components of the present chiller were integrated into a single component. The integration is done either at the sheet level, where both components are etched on the same sheet, or at the assembly level, where separate assemblies for the desorber and

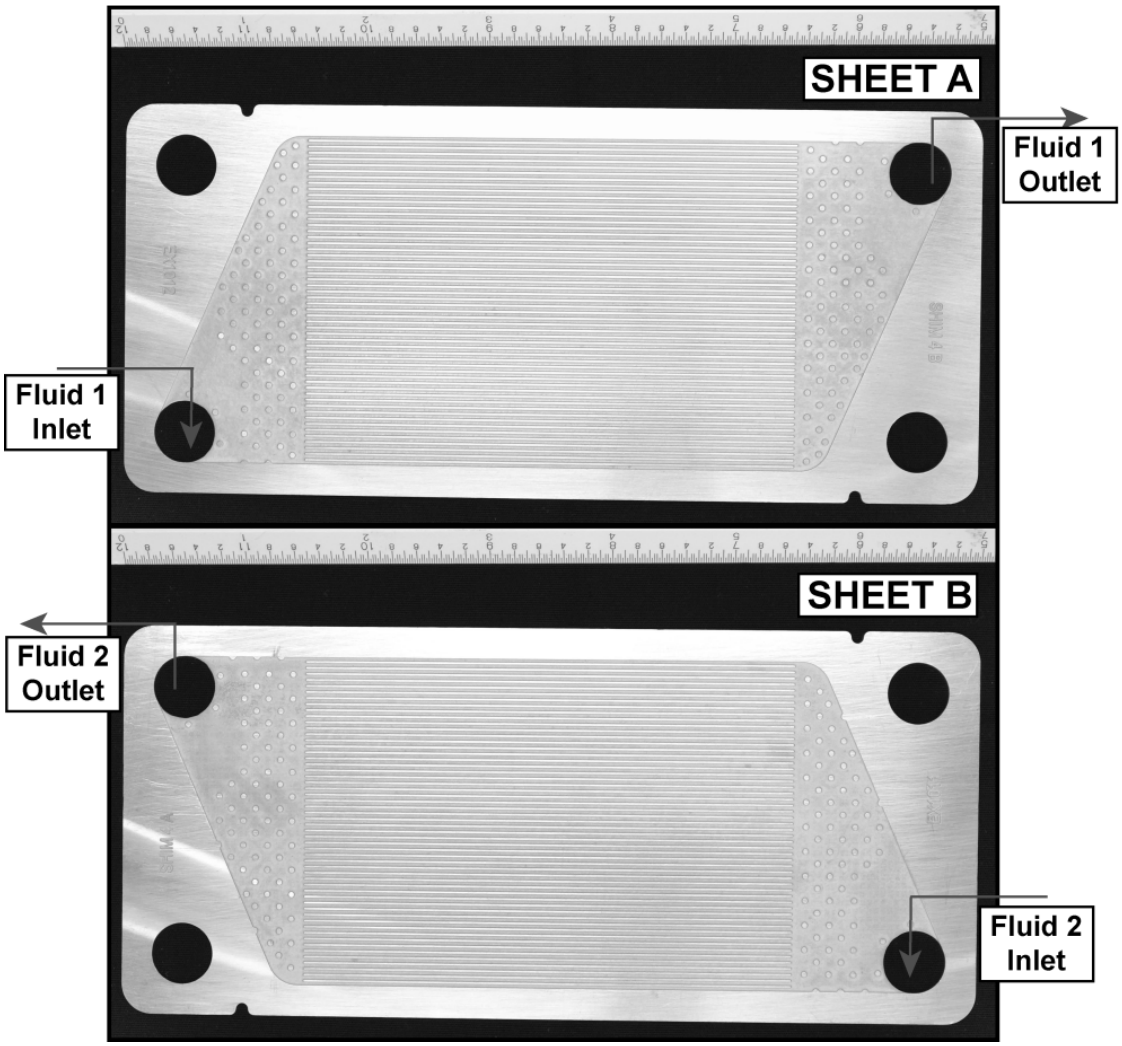

Fig. 7.3 Photograph of representative sheets for 2 kW cooling capacity absorption chiller

rectifier are developed and integrated together. In both configurations, the desorber is located below the rectifier. Concentrated solution is introduced at the top of the desorber, while the generated vapor flows upward, counter-current to the downward flowing solution. This vapor flows up further into the rectifier, where water is selectively condensed out, and the ammonia rich refrigerant is removed from the component at the top of the rectifier.

Fig. 7.4 shows a schematic of the sheets used to fabricate the vertical column desorber-rectifier component. It consists of three sheets: Sheet A of thickness 0.5 mm and Sheet B of thickness 2 mm for solution flow, and Sheet C of thickness 0.5 mm for coupling fluid flow. Sheet A consists of 5 channels of width 25.4 mm that were formed by completely etching the sheet to a depth of 0.5 mm. The top 101.6 mm of this channel comprises the rectifier component, while the bottom 76.2 mm of this channel comprises the desorber component. Two such sheets were stacked on top of Sheet B to form deeper channels for counter-current flow of solution and vapor. Sheet B consists of etched channels of depth 1 mm and width 25.4 mm in the desorber section, and several small surface formations in the rectifier section to enhance the heat and mass transfer process. Sheet C consists of an array of microchannels used to for the desorber coupling fluid, the rectifier coupling fluid, as well as the inlet header for the concentrated solution. The assembly of two Sheet As, one Sheet B, and one Sheet C is termed a unit, because these sheets together act as a self-contained building block for the desorber-rectifier assembly.

Concentrated solution is introduced into the desorber through this concentrated solution inlet header, and introduced into Sheet B via the solution through holes (similar to the vapor inlet mechanism in Microscale Absorber 1 and 2b.) This solution flows downward as a thin film due to gravity on the surface of Sheet B, while the desorbed vapor flows upwards, counter-current to the solution flow. The heat for desorption is supplied by the circulating coupling fluid in Sheet C.

The generated vapor flows upwards to the rectifier, where it is cooled by the circulating rectifier coupling fluid in Sheet C. The ammonia-rich refrigerant is collected

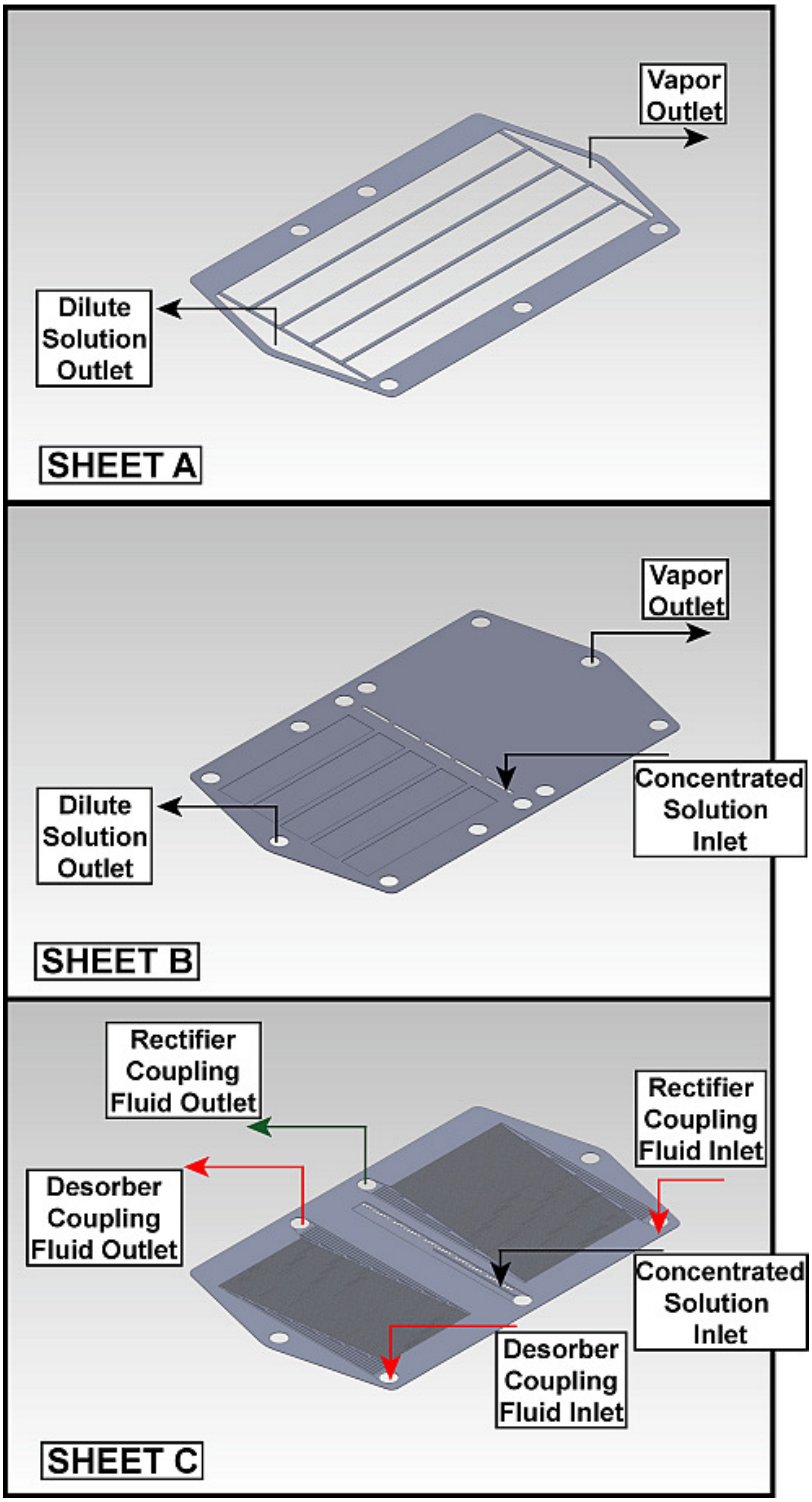

Fig. 7.4 Schematic of vertical column desorber and rectifier sheets

and removed from the circular void located at the top of the Sheets A and B. A small section between the desorber and rectifier components is provided for adiabatic heat and mass exchange between the solution and the vapor. This section is called the analyzer and is used to ensure that the vapor entering the rectifier is as close to equilibrium as possible with the concentrated solution entering the desorber. All the features on the sheets were chemically machined using photochemical etching, and the sheet array was bonded using vacuum brazing. Table 7.5 shows a summary of the vertical column desorber and rectifier geometries.

Fig. 7.5 shows a schematic of the plates used to fabricate the branched tray desorber and rectifier. It consists of 2 sets of plates: Plate A, for the flow of solution and vapor, and Plate B, for the flow of the coupling fluid streams. These two plates act as building blocks for the desorber and rectifier assemblies. Plate A of the desorber consists of 2 channels of width 61.6 mm that were formed by machining the plate to a depth of 5.7 mm. These channels have four equidistant trays, located along the length of the channel, that facilitate mixing of the solution and enhance the heat and mass transfer process. Plate B consists of an array of microchannels for the flow of the desorber coupling fluid, as well as the inlet header for the concentrated solution. These features were machined using photochemical etching.

Concentrated solution is introduced into the desorber through this concentrated solution inlet header, and introduced into Plate A via the solution through holes (similar to the vapor introduction mechanism in Microscale Absorbers 1 and 2b.) This solution flows downward in a serpentine fashion, while the desorbed vapor flows upwards around these trays, counter-current to the solution flow. The presence of these trays increases vapor-solution interaction inside the desorber, and facilitates better heat and mass transfer. Additionally, the presence of these trays results in desorption due to pool boiling, in addition to the falling-film heat transfer that occurs between successive trays. The heat of desorption is supplied by the circulating coupling fluid in Sheet C. A small

section at the top of the desorber called the analyzer is provided for adiabatic heat and mass exchange between the solution and the vapor.

The generated vapor in the desorber flows upwards and is removed from the vapor outlet ports located at the top of this component. These outlet ports are aligned with the vapor inlet ports in the rectifier, and the desorbed vapor is introduced into Plate A of the rectifier through these ports. Several surface features (vertical bosses) as seen in Fig. 7.5 are machined on the plate surface, which enhance the heat and mass transfer process in the rectifier. The vapor in the rectifier is cooled by the circulating rectifier coupling fluid in Plate B. The ammonia-rich refrigerant is collected and removed from the vapor outlet void located at the top of the Plate A. The sheet array for the desorber and rectifier, and the whole assembly, were bonded using vacuum brazing. Table 7.6 shows a summary of the branched tray desorber and rectifier geometries.

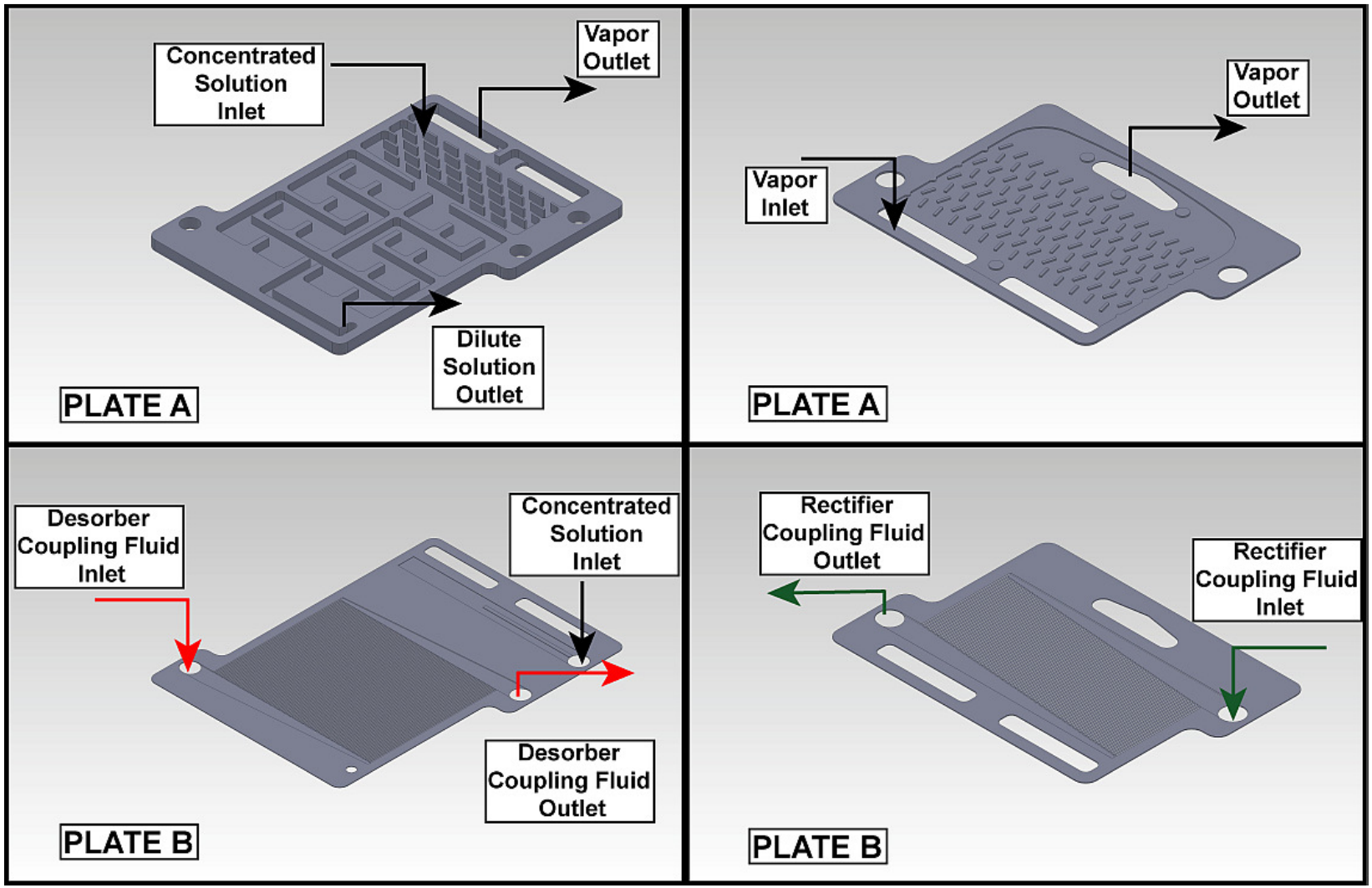

Fig. 7.5 Schematic of branched tray desorber and rectifier plates

Table 7.3 Summary of component design conditions for 2 kW cooling capacity absorption chiller

Component	Line	Temperature (^oC)		Flow rate (kg s^{-1})		Concentration (%)		Pressure (kPa)		Duty (kW)
		Inlet	Outlet	Inlet	Outlet	Inlet	Outlet	Inlet	Outlet	
Condenser	Refrigerant	59.52	45.01	0.0018	0.0018	99.86	99.86	1964	1964	2.02
	Coupling Fluid	37.35	45.33	0.0635	0.0635	25%	25%	-	-	
Evaporator	Refrigerant	4.88	6.38	0.0018	0.0018	99.86	99.86	485.3	485.3	2.09
	Coupling Fluid	12.78	7.41	0.0983	0.0983	25%	25%	-	-	
Desorber	Solution	99.58	147.9	0.0056	0.0038	48.88	24.56	1964	1964	3.11
	Vapor	-	104.2	-	0.0019	-	96.61	-	1964	
	Coupling Fluid	174.1	150	0.0500	0.0500	-	-	-	-	
Rectifier	Vapor	104.2	59.69	0.0019	0.0018	96.61	99.86	1964	1964	0.45
	Reflux	-	101.2	-	0.0001	-	45.11	-	1964	
	Coupling Fluid	40.17	57.92	0.0056	0.0056	48.88	48.88	1964	1964	
Solution HX	Conc. Solution	57.92	99.58	0.0056	0.0056	48.88	48.88	1964	1964	1.49
	Dil. Solution	147.9	60.1	0.0038	0.0038	24.56	24.56	1964	1964	
Refrigerant Pre-cooler	High Pressure	45.01	20.67	0.0018	0.0018	99.86	99.86	1964	1964	0.21
	Low Pressure	6.38	43.60	0.0018	0.0018	99.86	99.86	485.3	485.3	

Table 7.4 Summary of component geometries for 2 kW cooling capacity absorption chiller

	Evaporator	Condenser	Solution heat exchanger	Refrigerant pre-cooler
Sheet thickness (mm)	0.5	0.5	0.5	0.5
Number of sheets (Sheet A)	20	20	6	11
Number of sheets (Sheet B)	21	20	6	11
Number of channels per sheet	55	55	55	55
Channels pitch (mm)	1.25	1.25	1.25	1.25
Channel length (mm)	101.6	152.4	101.6	101.6
Channel hydraulic diameter (mm)	0.442	0.442	0.442	0.442
End plate thickness (mm)	3.05	3.05	3.05	3.05
Total transfer area (m^2)	0.2123	0.3184	0.0637	0.1168
Overall envelope (mm × mm × mm)	177.8 × 81 × 26.1	228.6 × 81 × 26.1	177.8 × 81 × 12.1	177.8 × 81 × 17.1

Table 7.5 Summary of vertical column counter-current desorber geometry

Coupling Fluid Channels	
Sheet thickness (mm)	0.5
Number of sheets in assembly	18
Number of desorber channels per sheet	112
Number of rectifier channels per sheet	112
Channel hydraulic diameter (mm)	0.442
Channel pitch (mm)	1.25
Desorber channel length (mm)	76.2
Rectifier channel length (mm)	101.6
Refrigerant/Solution Channels	
Number of desorber channels per unit	5
Number of rectifier channels per unit	5
Number of units in assembly	9
Channel width (mm)	25.4
Desorber channel depth (mm)	2.0
Rectifier channel depth (mm)	1.0
Desorber hydraulic diameter (mm)	3.76
Rectifier hydraulic diameter (mm)	1.99
Channel pitch (mm)	28.6
Assembly Specifications	
Material	304L Stainless Steel
Endplate thickness (mm)	3
Overall Envelope (mm × mm × mm)	313.7 × 190.5 × 47.2

Table 7.6 Summary of branched tray counter-current desorber geometry

Coupling Fluid Channels	
Sheet thickness (mm)	0.5
Number of desorber sheets in assembly	8
Number of rectifier sheets in assembly	11
Number of rectifier channels per sheet	75
Number of desorber channels per sheet	100
Channel hydraulic diameter (mm)	0.442
Desorber channel pitch (mm)	1.25
Rectifier channel pitch (mm)	1.68
Rectifier channel length (mm)	50.8
Desorber channel length (mm)	101.6
Refrigerant/Solution Channels	
Desorber plate thickness (mm)	7.9
Rectifier plate thickness (mm)	1.2
Number of desorber plates in assembly	4
Number of rectifier plates in assembly	10
Channel width (mm)	61.6
Channel depth (mm)	5.7
Assembly Specifications	
Material	304L Stainless Steel
Endplate thickness (mm)	3
Overall Envelope (mm × mm × mm)	310.5 ×171.5 × 53.4

7.2. Breadboard test facility

A breadboard test facility was designed and fabricated to install the system components discussed above and experimentally evaluate the absorber test sections. Fig. 7.6 shows a schematic of the microscale absorption breadboard test facility. This test facility consists of one closed solution loop, four closed coupling fluid loops (absorber, condenser, evaporator, and desorber), and steam and chilled water loops. The absorber and the condenser coupling fluid loops are used to reject heat from the solution loop, while the desorber and evaporator coupling fluid loops are used to supply heat to the solution loop. The chilled water/glycol coolant and laboratory steam loops act as the ultimate heat sink and source for the heat pump, respectively. The details of each of these loops are given below.

7.2.1. Coupling fluid loops

Two closed coupling fluid loops, with distilled water as the coupling fluid, are used to remove the heat of absorption and condensation from the absorber and condenser, respectively, and transfer this heat to the laboratory chilled water/glycol coolant open loop (cooled by a 50 RT Carrier AquaSnap Chiller). Two independent loops, instead of one single loop to cool both absorber and condenser components, are incorporated to facilitate better control over the operating conditions of the test loop during the testing process. As previously mentioned, in such a configuration, the flow arrangements, flow rates and inlet and outlet temperatures can be adjusted to simulate series or parallel flow configurations for the coupling fluid. A centrifugal pump (Model TE-6-MD-HC, Little Giant), with an upstream expansion tank to provide the necessary head, is used to circulate the coupling fluid in each loop. For the absorber coupling fluid loop, a plate heat exchanger (Model MPN5X12-10, Flat Plate) is used as the auxiliary heat exchanger that facilitates heat exchange between coupling fluid and laboratory chilled water/glycol

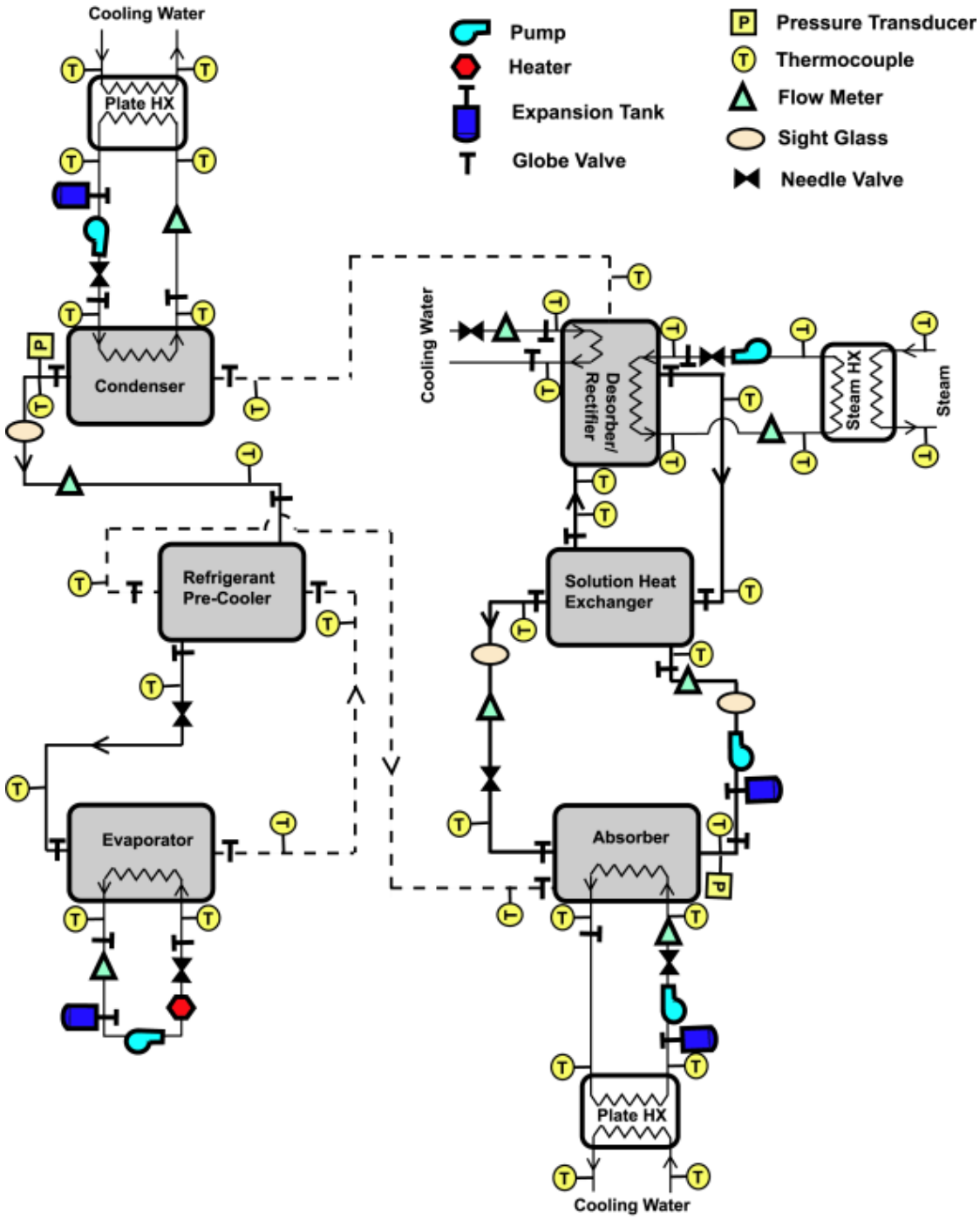

Fig. 7.6 Schematic of microscale convective absorption breadboard test facility

coolant. For the condenser coupling fluid loop, a tube-in-tube heat exchanger (Model 00528, Exergy Inc.) is used as the auxiliary heat exchanger. For both loops, most of the plumbing for the closed loop lines is fabricated using 12.7 mm nominal O.D. copper and

stainless steel tubes to minimize pressure drop in the lines. Similarly for each loop, the coupling fluid flow is regulated using a needle valve, and measured using a magnetic flow meter (Model FMG-220-NPT, Omega Engineering Inc.) Chilled water flow rates are regulated using a needle valve, and measured using rotameters (Absorber: Model FL4302, Omega Engineering Inc., and Condenser: Model FL4301, Omega Engineering Inc.) Thermocouples are used to measure the temperature of the coupling fluid and the laboratory chilled water/glycol coolant at the inlet and outlet of the absorber, condenser, and the absorber and condenser auxiliary heat exchangers. As previously discussed in Chapter 3, energy balances on the auxiliary heat exchangers provide an additional means to verify the accuracy of the results, over and above the energy balance between the solution and the coupling fluid at the absorber and the condenser.

A closed loop, with propylene glycol-water mixture (25% by mass) as the fluid, is used to provide the necessary heat duty to the evaporator. The coupling fluid is heated by an immersion rod heater (Model L9EX11A, Firerod), and the heating rate is controlled using a solid state, variable potential controller. A centrifugal pump (Model TE-6-MD-HC, Little Giant), with an upstream expansion tank to provide the necessary head, is used to circulate the coupling fluid. Most of the plumbing for the closed loop lines is fabricated using 12.7 mm nominal O.D. copper and stainless steel tubes to minimize pressure drop in the lines. The coupling fluid flow is regulated using a needle valve, and measured using a Coriolis flow meter (Model CMF025, Micromotion.) Thermocouples are used to measure the temperature of the coupling fluid at the inlet and outlet of the evaporator.

Another closed loop, with Paratherm NF (Paratherm Corporation) as the heat transfer fluid, is used to provide the heat of desorption to the desorber from the laboratory steam loop. A high temperature centrifugal pump (Model AC4STS1, Finnish Thompson) and a high temperature gear pump (Model 4104-V-C-7, Tuthill), with an upstream expansion tank to provide the necessary head, are used to circulate the coupling fluid, for

low and high coupling fluid flow rates, respectively. A tube-in-tube heat exchanger (Model 00528, Exergy Inc.) is used as the auxiliary heat exchanger to facilitate heat exchange between desorber coupling fluid and laboratory steam. Most of the plumbing for the closed loop lines is fabricated using 12.7 mm nominal O.D. stainless steel tubes, suitable for high temperature applications, to minimize pressure drop in the lines. The coupling fluid flow is regulated using a variable speed controller, and measured using a positive displacement flow meter (Model JVM-30KG-50, AW Company.) Thermocouples are used to measure the temperature of the coupling fluid and steam at the inlet and outlet of the desorber and the desorber auxiliary heat exchanger.

7.2.2. Solution loop

As previously mentioned, the test facility replicates a thermally activated single-effect absorption chiller. The system operates at two different nominal pressure levels: high pressure at the condenser, rectifier and desorber, and low pressure at the absorber, and evaporator. The solution loop is a closed loop with three principal fluid lines: the concentrated solution line, the dilute solution line, and the refrigerant line.

High pressure refrigerant vapor exits the rectifier after water is preferentially condensed from the vapor generated in the desorber. For the chiller of cooling capacity 2.5 kW with the co-current desorber, the rectifier is coupled to the laboratory chilled water/glycol coolant. The flow rate of the rectifier coupling fluid is regulated using a needle valve, and measured using a rotameter (Model FL4202, Omega Engineering Inc.) For the chiller of cooling capacity 2 kW with a counter-current desorber, the rectifier is cooled by the concentrated solution exiting the solution pump. To regulate the flow rate of the solution cooling the rectifier, a by-pass line with a valve is installed to route excess flow directly to the solution heat exchanger. Such a configuration is important for operation at lower cooling capacities, where excessive cooling at the rectifier can result in condensation of excessive amounts of ammonia, reducing the refrigerant flow rate and

the cooling capacity of the system. High pressure refrigerant exiting the rectifier undergoes condensation and subsequent subcooling in the condenser. The flow rate of the subcooled refrigerant is measured using a Coriolis flow meter (RHM015, Rheonik, GE Sensing.) To visually confirm that the refrigerant exiting the condenser is subcooled, a sight glass is installed at the outlet of the condenser (Bulls Eye ¼'' NPT, Pressure Products.) Additionally, a refrigerant tank is installed at the outlet of the condenser. This tank provides a small reservoir to hold the condensed refrigerant, which helps in damping out fluctuations in the system during operation.

The high-pressure refrigerant exiting the refrigerant flow meter is further subcooled in the refrigerant pre-cooler, after exchanging heat with the low-pressure refrigerant exiting the evaporator. The cooled high pressure refrigerant is expanded to the low pressure through a needle valve (Model SS-4MG-MH, Swagelok), before entering the evaporator. The low pressure refrigerant is evaporated in the evaporator while exchanging heat with the evaporator coupling fluid. The evaporated refrigerant exiting the evaporator is further heated in the refrigerant pre-cooler, before being routed to the absorber. This vapor is mixed with the dilute solution either upstream of the absorber inlet or directly inside the absorber, depending upon the absorber test section being investigated.

Dilute solution exiting the desorber exchanges heat with the concentrated solution in the solution heat exchanger. The flow rate of the dilute solution is measured at the outlet of the solution heat exchanger, using a Coriolis flow meter (RHM030, Rheonik, GE Sensing.) To visually confirm that the dilute solution exiting the solution heat exchanger is subcooled, a sight glass is installed at the exit of the solution heat exchanger (Bulls Eye ¼'' NPT, Pressure Products.) A dilute solution tank is installed at the desorber dilute solution outlet to provide a small reservoir to hold the dilute solution, which helps in damping out fluctuations in the system during operation. Dilute solution exiting the

solution heat exchanger is expanded to the low pressure through a needle valve (Model SS-4MG-MH, Swagelok), before being routed to the absorber.

A concentrated solution tank is installed at the outlet of the absorber, just upstream of the solution pump, which acts as the reservoir for most of the solution inventory in the solution loop. This tank ensures that the pump never runs dry, and helps in damping out fluctuations during system operation. The flow rate of the concentrated solution is measured at the outlet of the solution pump, using a Coriolis flow meter (RHM030, Rheonik, GE Sensing.) To visually confirm that the concentrated solution exiting the solution pump is subcooled, a sight glass is installed at the exit of the pump (Bulls Eye ¼'' NPT, Pressure Products.) The concentrated solution exiting the flow meter flows into the solution heat exchanger, before being introduced into the desorber. A variable frequency magnetic gear pump (Model TXS2.6 series, Tuthill) and a variable speed piston pump (Stone Mountain Technologies Inc.) are used separately as the solution pump for low and high differential pressure test conditions, respectively. Thermocouples are used to measure the temperatures of the refrigerant, and the dilute and concentrated solution streams, at the inlets and outlets of all system components.

7.2.3. Instrumentation and data acquisition

All temperatures are measured using T-type thermocouples (Model TMQSS-125G-6, Omega Engineering Inc.) High-side pressure on the solution loop is measured using an absolute pressure transducer (Model MMA500 (accuracy ±0.035% of span), Omega Engineering Inc.) at the outlet of the condenser, while the low-side pressure is measured using an absolute pressure transducer (Model MMA100 (accuracy ±0.035% of span), Omega Engineering Inc.) at the outlet of the absorber. Additionally, the pressure of the refrigerant entering the evaporator is measured using an absolute pressure transducer (Model 2088 (accuracy ±0.25% of calibrated span), Rosemount.) Dial gauges (Model 1005P (accuracy ±3% of span), Ashcroft) are used to monitor the pressure inside the

absorber, desorber, condenser, and evaporator coupling fluid loops. As previously mentioned, Coriolis flow meters are used to measure the refrigerant, dilute and concentrated solution, and evaporator coupling fluid flow rates, while magnetic flow meters are used to measure the absorber and condenser coupling fluid flow rates, and a positive displacement flow meter is used to measure the desorber coupling fluid flow rate. Rotameters are used to measure the flow rates of the absorber and condenser laboratory chilled water/glycol coolant as well as the coolant supplied to the rectifier.

A PC-based data acquisition system (National Instruments SCXI-100) is used to process, display, and record the signals received from the different measurement devices. Add-on cards (SCXI-1102 and SCXI-1303, National Instruments) are used to measure temperatures, flow rates, and pressures. Signal modification is done to convert the instrument output signal (typically an electrical signal varying from 4-20 mA) to a readable voltage signal by using a 249 ohm shunt resistor. The acquisition system chassis is interfaced with the computer using the software Labview (Version 8.6, National Instruments.) Data acquisition rates and durations can be programmed at desired scan rates using this software. All the relevant calibration curves for the different thermocouples, pressure transducers, and flow meters are also incorporated in this software by the user.

A total of 41 thermocouples, 3 pressure transducers, and 7 flow meters are used to measure the relevant data on this test facility. A summary of these instruments is shown in Table 7.7. Five pumps are used to circulate the solution and coupling fluids. All pumps are controlled through a locally installed electric utility box. The same utility box is used to route the power supply to the data acquisition system, flow meters, and pressure transducers. Fig. 7.7 shows a photograph of the test facility. It should be noted that the ammonia-water system heat exchangers are installed in a self-contained area in the test loop, referred to here as the “system block”, which represents the components required for the eventual field-installed waste-heat-driven cooling system. Fig. 7.8 shows a closer

view of the system block. The rest of the test facility primarily serves to provide the conditioning of high, medium, and low temperature sources and sinks to the absorption system. Plumbing and wiring is run from this system block to the different coupling fluid lines, solution pump, and instrumentation, discussed above.

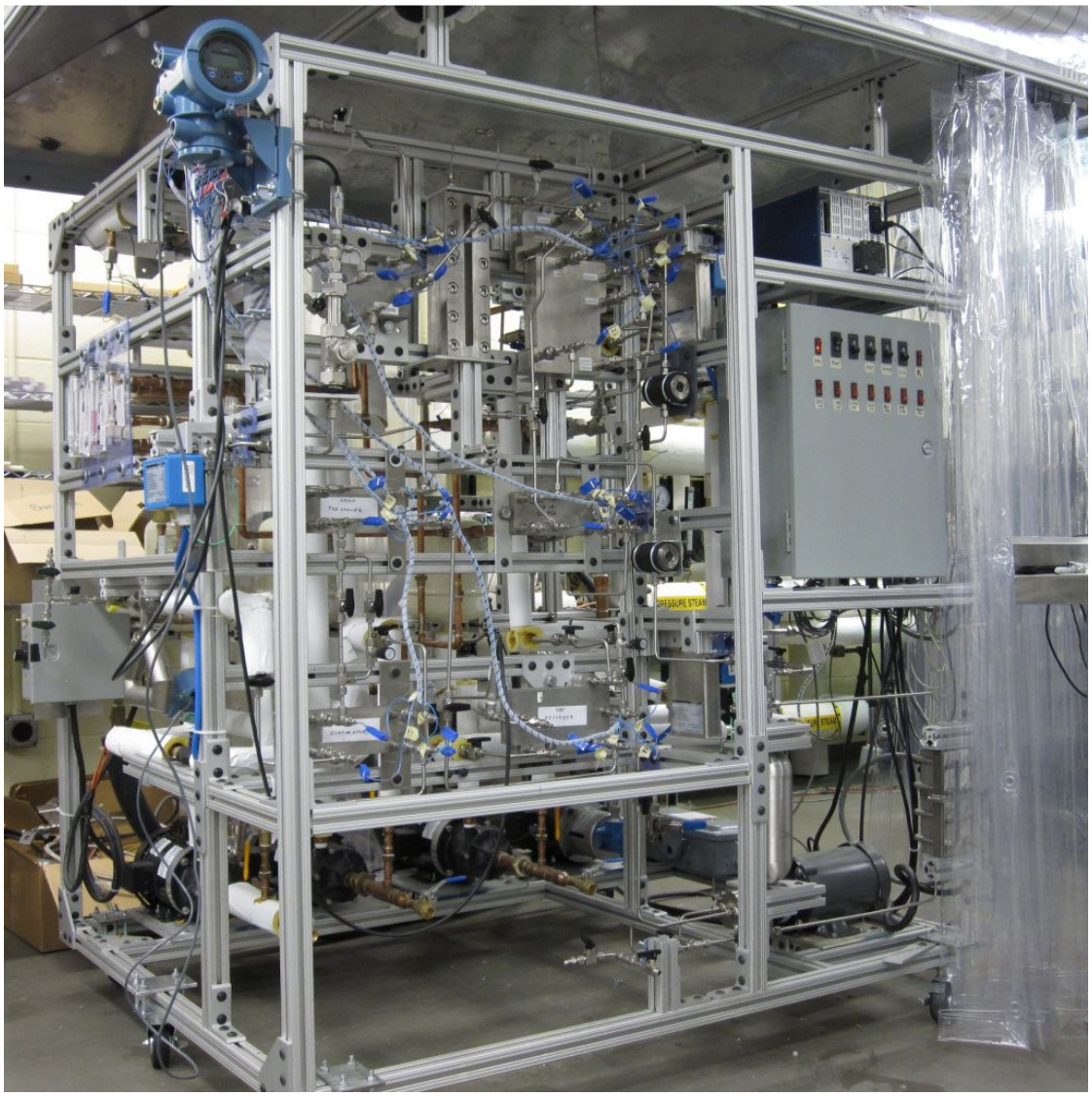

Fig. 7.7 Photograph of breadboard test facility

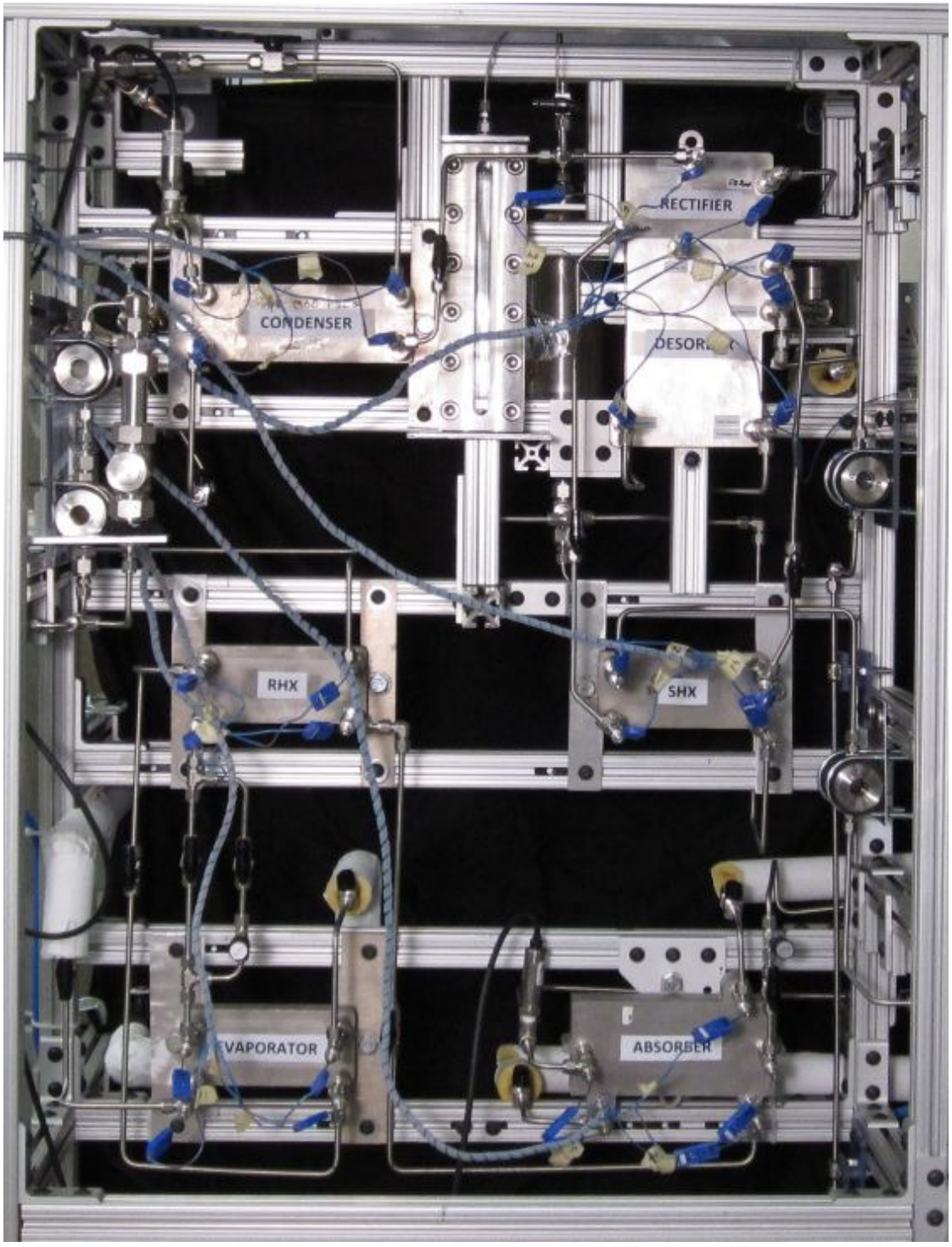

Fig. 7.8 Photograph of system block

Table 7.7 Summary of instrumentation on the breadboard test facility

Parameter/ Instrument	Model	Manufacturer	Quantity	Range	Accuracy	Operating Limits
Flow meters and transmitter specifications						
Dil/ Conc Solution	RHM030	Rheonik. GE Sensing	2	0 - 0.083 kg s^{-1}	±0.1%	T: -20 to 120°C P: 20 MPa
Dil/ Conc Solution (Trans)	RHM030	Rheonik. GE Sensing	2			T: -40 to 65°C
Refrigerant	RHM015	Rheonik/GE Sensing	1	0 - 0.010 kg s^{-1}	±0.1%	T: -20 to 120°C P: 20 MPa
Refrigerant (Trans)	RHM030	Rheonik. GE Sensing	1			T: -40 to 65°C
Absorber/ Condenser Coupling Fluid	FMG220-NPT	Omega Engineering Inc.	2	1.89-18.9×10^{-5} m^3 s^{-1}	±0.5%	T: 0 to 85°C P: 1.0 MPa
Evaporator Coupling Fluid	CMF025 Elite	MicroMotion Inc.	2	0 - 0.6048 kg s^{-1} 0 - 6.309 ×10^{-4} m^3 s^{-1}	±0.1% (Flow) ±0.5 kg m^{-3} (Density)	T: -240 to 350°C P: 10 MPa
Evaporator Coupling Fluid (Trans)	1700 – Field Mounting	MicroMotion Inc.	1	0-5000 kg m^{-3} -240 to 450°C		T: -40 to 60°C (Ambient)
Desorber Coupling Fluid	JVM-30KG-50	AW Company	1	1.89-44.2×10^{-5} m^3 s^{-1}	±0.5%	T: 0 to 204°C P: 34.5 MPa
Pressure transducers and dial gauges specifications						
Absolute	2088	Rosemount	1	0-1.034 MPa	±0.25% of Calibrated Span	T: -40 to121°C
Absolute	MMA 100	Omega Engineering Inc.	1	0-0.69 MPa	±0.035% of Span	T: -45 to 121°C
Absolute	MMA 500	Omega Engineering Inc.	1	0-3.45 MPa	±0.035% of Span	T: -45 to 121°C
Dial Gauge	1005P (ABS-Black)	Ashcroft	4	0-689.5 kPa	±3% of Span	T: -40 to 65°C
Thermocouples and RTDs specifications						

Table 7.7 Continued…

Parameter/ Instrument	Model	Manufacturer	Quantity	Range	Accuracy	Operating Limits
Thermo couple	T-type	Omega Engineering Inc.	41	-270 to 240°C	±0.25°C	
Rotameters specifications						
Absorber Chilled Coolant	FL4302	Omega Engineering Inc.	1	$1.262 - 12.62 \times 10^{-5}$ m^3/s	±4% of Full Scale	T: 54°C P: 862 kPa
Condenser Chilled Coolant	FL4301	Omega Engineering Inc.	1	$6.309 - 63.09 \times 10^{-5}$ m^3/s	±4% of Full Scale	T: 54°C P: 862 kPa
Rectifier Chilled Coolant	FL4202	Omega Engineering Inc.	1	$1.262 - 12.62 \times 10^{-6}$ m^3/s	±4% of Full Scale	T: 54°C P: 862 kPa

7.3. Experimental procedures

7.3.1. Component and system leak testing, and system charging

All absorption system components were tested for cross leaks between the two fluid streams, as well as leaks to the ambient. Each side of the heat exchanger was pressurized to 2758 kPa using a hydrostatic pump, and the pressure monitored for several minutes. In case any leaks were observed, the bonding process was repeated until a good seal is achieved and the component passes the leak test. These tests confirmed that the components were leak free, and could withstand the pressures seen during absorption heat pump operation. Upon installation of these components into the breadboard test facility, system-level leak testing procedures were employed, as discussed in Chapter 3.

Upon confirmation that the system is leak free, the system is prepared for charging with the appropriate mixture of ammonia and water. The procedure used for evacuating the system, and charging with distilled water and anhydrous ammonia is similar to the procedure described in Chapter 3.

7.3.2. Safety precautions

All the safety precautions described in Chapter 3 were followed during fabrication and modification of the breadboard, charging of working fluid mixture, and operation of the system. Similar to the test facility for the microchannel falling-film absorber, this breadboard test facility is placed under a fume hood with a fan and a vent at the top, and curtains on the sides, to isolate it from the rest of the laboratory space, in case of accidental ammonia leaks. Additionally, ammonia sensors with alarms were installed to detect accidental leaks during system charging, discharging, and operation. Further details about the safety precautions are found in Chapter 3.

7.3.3. Experimental procedures

The experimental procedures used to initiate and control each experiment are similar to the procedures described in Chapter 3. However, due to lower fluid inventory in the system, some modifications are made to the procedure to ensure that the solution pump does not run dry during start up. The data acquisition system and the Labview software were started first to monitor the various temperatures, pressures, and flow rates. Then the laboratory chiller was started, and the chilled water/glycol coolant was set to the desired temperature. Next, the metering valve controlling the chilled water/glycol coolant flow rate to the absorber auxiliary heat exchanger was adjusted to deliver the desired flow. The absorber coupling fluid pump was then started, and the absorber coupling fluid flow rate was adjusted using the metering needle valve. At this point, laboratory steam was slowly introduced into the desorber auxiliary heat exchanger, and the desorber coupling fluid pump was started to circulate the heat transfer fluid. Due to cooling of the absorber, and heating of the desorber, a pressure difference was created across the refrigerant and solution expansion valves. Because of this pressure difference, most of the solution inventory in the loop accumulates in the concentrated solution tank, thus mitigating the risk of the solution pump running dry during start up. At this point, the

solution pump was started to circulate solution between the absorber and the desorber. Circulating the desorber heat transfer fluid before the solution is the main modification to the startup procedure described in Chapter 3 for the falling-film test facility. Once circulation of solution between the absorber and the desorber was established, the remaining steps to achieve the desired operating conditions were similar to those described in Chapter 3.

7.4. Absorber testing

Experimental evaluation of the absorber test sections was conducted over a range of solution and vapor flow rates for each test section. Temperature, pressure, and flow rate data were recorded for each experiment, and these data were analyzed to determine the state of the solution and refrigerant at various locations in the loop, estimate component duties, and determine relevant heat and mass transfer rates in the absorber. A brief description of these analyses follows.

7.4.1. System-level analysis

As mentioned in Chapter 4, the working fluid, a binary mixture of ammonia and water, requires three independent properties to define its state at any location. Temperature and pressure, which are measured at various locations around the test loop, serve as two of these three independent properties. The third property typically used for defining the state is quality or concentration. The steps used to determine this thermodynamic property is similar to those described in Chapter 4 for the falling-film absorption test facility. The principal steps are described below briefly, along with the changes implemented for analyzing the counter-current desorber.

1. Vapor is assumed to exit the rectifier in a saturated condition. This yields the concentration of the refrigerant leaving the rectifier, and therefore the

concentration of the refrigerant circulating through the condenser, refrigerant pre-cooler, and evaporator.

2. For the co-current desorber, the two-phase mixture leaving the desorber is assumed to be in equilibrium. This yields the concentration of the dilute solution leaving the desorber and vapor entering the rectifier. For the counter-current desorber, the dilute solution exiting the desorber is assumed to be at saturation conditions, yielding the concentration of the dilute solution circulating through the solution heat exchanger and entering the absorber. The vapor entering the rectifier is assumed to be at saturation conditions at the measured temperature, yielding the concentration of the vapor stream exiting the desorber and entering the rectifier.
3. The reflux from the rectifier is assumed to be a saturated liquid at the measured outlet temperature of the rectifier. This yields the concentration of the reflux stream mixing with the dilute solution leaving the desorber.
4. Mass and species balances at the absorber are applied to determine the concentration of the concentrated solution leaving the absorber, flowing through the solution heat exchanger and entering the desorber.

With the state of the solution/refrigerant known at every location in the loop, the relevant component duties are estimated on the working-fluid side. For the hydronically coupled components, i.e. the evaporator, condenser, desorber, and absorber, component duties are also estimated on the coupling-fluid side, using the measured coupling fluid inlet and outlet temperatures and flow rates. As with the analysis described in Chapter 4, for each test condition on the test matrix, energy balances are evaluated not just at the absorber, but also for all components in the test loop, which is important because the flow rates and concentrations at the absorber depend on system-wide state points. The component duties were estimated according to the methodology described in Chapter 4.

Because the primary focus of this study is the absorber, only the results corresponding to this component are discussed here.

Fig. 7.9 shows a plot of the absorber duty as a function of concentrated solution flow rate for all three absorption test sections. Duties for Microscale Absorber 1 were between 1.1 and 1.8 kW. The absorber duties for Microscale Absorber 2a and 2b were found to range from 1.4 – 3.3 kW, and 1.8 – 3.5 kW, respectively. It should be noted that Microscale Absorber 1 was tested over much lower vapor flow rates than Microscale Absorber 2a and 2b. As discussed in Chapter 4, the absorber duty is due to a combination of sensible cooling of the solution and vapor streams, and latent heat of absorption of the vapor. The low vapor flow rates supplied led to lower absorption duties for Microscale Absorber 1. In general, the absorption duty was found to increase with an increase in

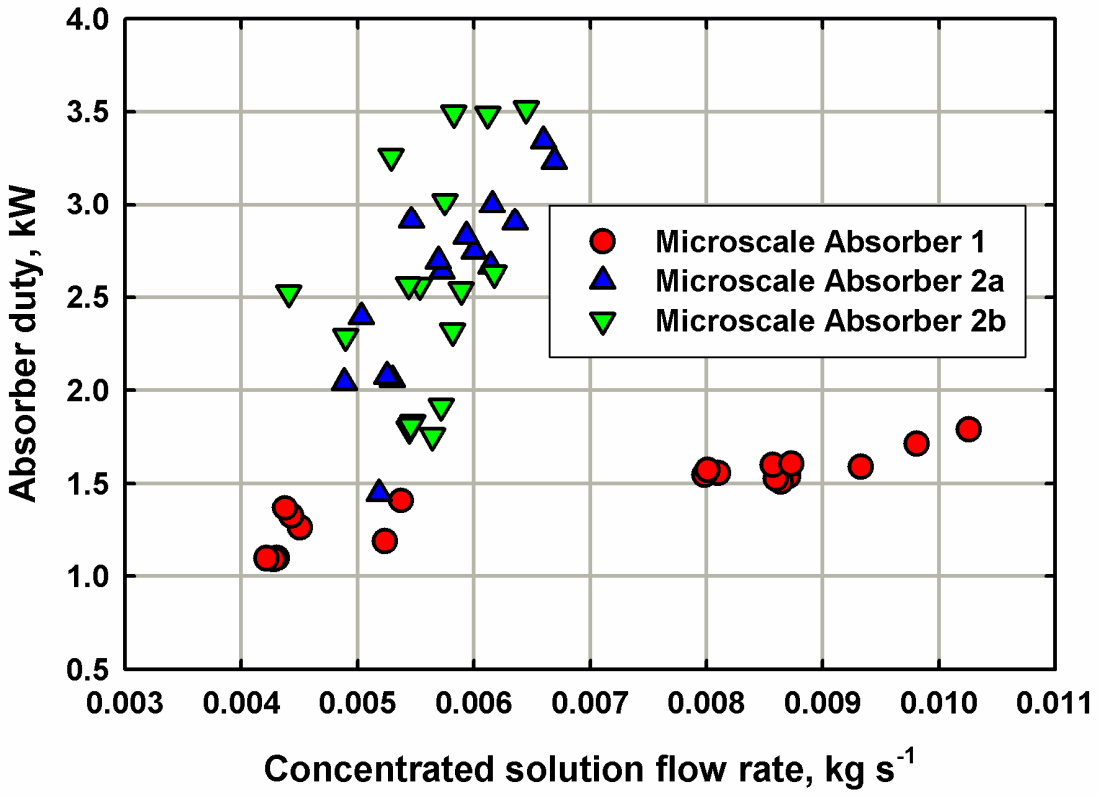

Fig. 7.9 Absorber duty as a function of concentrated solution flow rate

solution flow rate, which is due to an increase in the sensible load. The vertical spread in absorber duty at any solution flow rate was due to an increase in the vapor flow rate, which results in an increase in the latent heat of absorption of the vapor.

7.4.2. Microscale absorber analysis

As-Fabricated channel flow areas

A nickel alloy plating material was used to plate all sheets before either of the bonding processes (diffusion bonding and vacuum brazing) was initiated. This plating material liquefies and causes bonding at elevated temperatures in the furnace/oven. However, it also introduces the possibility of blockage in some channels because of accumulation of this plating material. Due to the very small feature sizes, the liquid plating material can wick into the microchannels. Upon cooling, this material can solidify and block the channels. It is important to estimate the number of channels that are blocked, because such channels reduce the total effective flow and transfer area, and affect the overall heat and mass transfer process.

To estimate this channel blockage, a series of laminar pressure drop experiments was conducted. Water was circulated through the solution and coupling-fluid sides of each absorber test section, and the resulting pressure drop across the component was measured for a range of flow rates. The pressure drop associated with just the channel array was calculated by subtracting the minor losses associated with contraction and expansion of the fluid in the header, and change in the direction of flow. The channel array pressure drop values estimated from the above analysis and compared with theoretical predictions to estimate the possible blockage in each component. Details of these analyses are provided in Appendix E.

It should be noted that as the plating material spreads, it can occupy a part of or the entire channel cross section over a portion of the channel length. The extent of

blockage in a single channel need not be uniform throughout the channel length. To identify the exact distribution of these blockages, the test sections should be cut at several locations, and each channel examined individually. However, with the laminar pressure drop experiments, some idealized possibilities for the distribution of the channel blockages can be identified. These scenarios are discussed below.

Three scenarios were considered while estimating the channel blockages in each of the test sections (Fig. 7.10). In the first scenario (Scenario 1), all channels are assumed to be partially blocked. While all channels are operational, braze material accumulates evenly over each channel, causing a reduction in the effective hydraulic diameter. The resulting hydraulic diameter of each channel is assumed to be uniform. In the second and third scenarios, channels are assumed to be either fully open or fully blocked, with the blocked channels uniformly distributed over each sheet. In the second scenario (Scenario 2), the hydraulic diameter of the open channels is assumed to be equal to the design

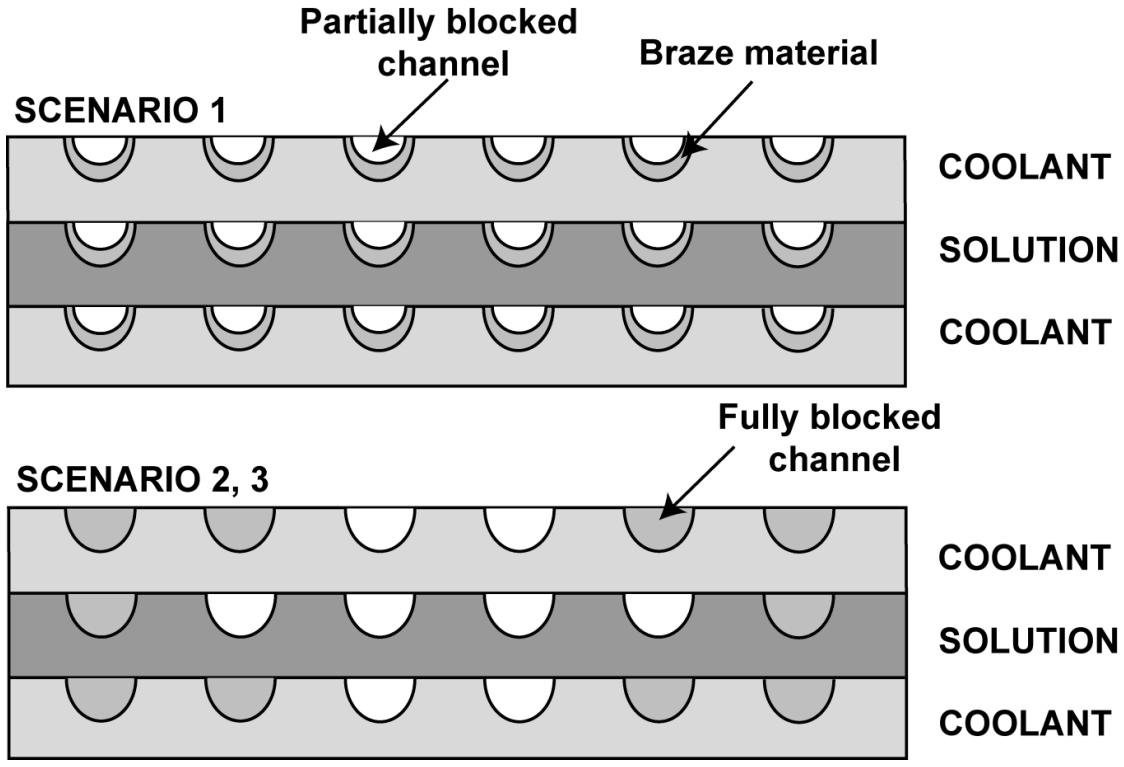

Fig. 7.10 Schematic of channel blockage

hydraulic diameter. In the third scenario (Scenario 3), the hydraulic diameter of the open channels is assumed to be equal to the smallest diameter dictated by the dimensional tolerances of the photochemical etching process. The tolerance specification provided by the vendor for the etching process was ±0.051 mm. Table 7.8 shows a summary of the blockages for the three test sections according to the three scenarios discussed above, and the corresponding design values for comparison.

Table 7.8 shows that there could either be significant shrinkage in the channel hydraulic diameter due to ingress of braze material as indicated by the hydraulic diameter values in Scenario 1, or significant number of blocked channels as indicated in Scenarios 2 and 3 or a combination. For Microscale Absorber 1, the percentage of blocked channels for Scenario 3 decreases significantly from Scenario 2, because the channel hydraulic diameter while considering the dimensional tolerances for Scenario 3 is comparable with the effective hydraulic diameter calculated in Scenario 1. The percentage of blocked channels for Microscale Absorber 2a and 2b range between 40-77% for both Scenarios 2 and 3. Correspondingly, there is significant shrinkage in the channel diameter for Scenario 1 for both absorber test sections. In general, slightly higher channels blockages are observed in Microscale Absorber 2a and 2b test sections, which could be attributed to the vacuum brazing process used to join these assemblies. A graphical summary of the channel blockage in the different absorbers is shown in Fig. 7.11.

As previously noted, the scenarios discussed above are idealizations. In reality, the blockage of the channels inside the test sections is probably a combination of these three scenarios. It should also be noted that with so much blockage in the microchannels, even flow distribution is probably not accomplished. The distribution of the open/active channels could also be uneven, which can result in additional wall resistance, or even contact resistance between the solution and the coupling fluid streams if the blockages on the solution side are in different locations than those on the coupling-fluid side.

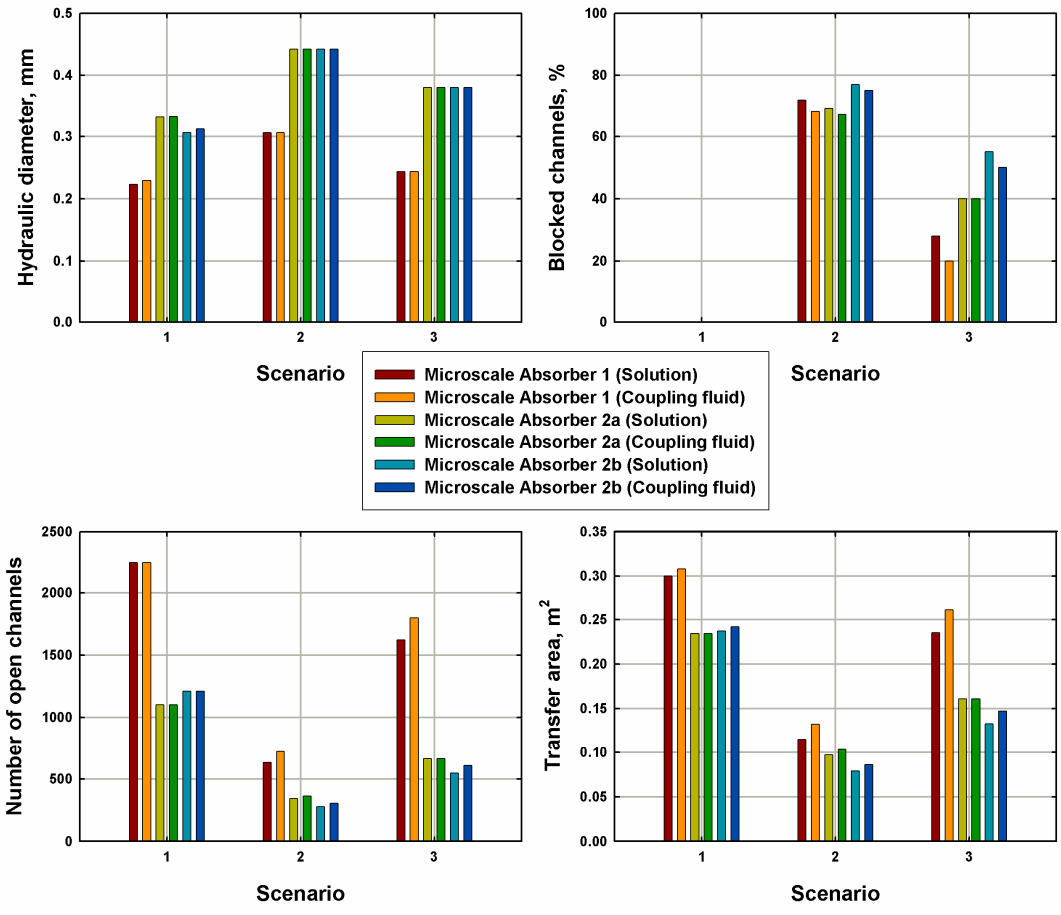

Fig. 7.11 Summary of test section blockage

Table 7.8 Summary of test section blockage

Microscale Absorber 1											
Scenario	**Hydraulic diameter (mm)**			**% of channels blocked**		**Number of open channels**			**Total flow area (m^2)**		
	Design	*Solution*	*Coupling Fluid*	*Solution*	*Coupling Fluid*	*Design*	*Solution*	*Coupling Fluid*	*Design*	*Solution*	*Coupling Fluid*
#1	0.306	0.223	0.229	0	0	2250	2250	2250	2.2×10^{-4}	1.2×10^{-4}	1.2×10^{-4}
#2	0.306	0.306	0.306	72%	68%	2250	630	720	2.2×10^{-4}	6.2×10^{-5}	7.1×10^{-5}
#3	0.306	0.243	0.243	28%	20%	2250	1620	1800	2.2×10^{-4}	1.0×10^{-4}	1.1×10^{-4}
Microscale absorber 2a											
Scenario	**Hydraulic diameter (mm)**			**% of channel blocked**		**Number of open channels**			**Total flow area (m^2)**		
	Design	*Solution*	*Coupling Fluid*	*Solution*	*Coupling Fluid*	*Design*	*Solution*	*Coupling Fluid*	*Design*	*Solution*	*Coupling Fluid*
#1	0.442	0.331	0.332	0	0	1100	1100	1100	2.3×10^{-4}	1.3×10^{-4}	1.3×10^{-4}
#2	0.442	0.442	0.442	69%	67%	1100	341	363	2.3×10^{-4}	7.2×10^{-5}	7.6×10^{-5}
#3	0.442	0.380	0.380	40%	40%	1100	660	660	2.3×10^{-4}	1.0×10^{-4}	1.0×10^{-4}
Microscale Absorber 2b											
Scenario	**Hydraulic diameter (mm)**			**% of channels blocked**		**Number of open channels**			**Total flow area (m^2)**		
	Design	*Solution*	*Coupling Fluid*	*Solution*	*Coupling Fluid*	*Design*	*Solution*	*Coupling Fluid*	*Design*	*Solution*	*Coupling Fluid*
#1	0.442	0.306	0.312	0	0	1210	1210	1210	2.5×10^{-4}	1.2×10^{-4}	1.2×10^{-4}
#2	0.442	0.442	0.442	77%	75%	1100	278	303	2.5×10^{-4}	5.8×10^{-5}	6.4×10^{-5}
#3	0.442	0.380	0.380	55%	50%	1100	545	608	2.5×10^{-4}	8.3×10^{-5}	9.2×10^{-5}

Heat and mass transfer analysis

Vapor and dilute solution flow in a co-current configuration in each of the microscale absorber test sections. The concentrated solution exiting the test section is typically subcooled. Thus, the absorber can be divided into two segments: the two-phase segment, which is located in the first part of the absorber, where both vapor and solution flow, followed by the single-phase segment, where there is only subcooled solution flow. The state of the solution at the exit of the two-phase segment and at the inlet of the single-phase segment can be determined by assuming that the solution at this location is at saturation conditions. The temperature and enthalpy of the solution at this location can be estimated as follows:

$$T_{\text{Abs,sol,sat}} = f\left(P_{\text{Abs}}, x_{\text{Abs,sol,out}}, q_{\text{Abs,sol,sat}} = 0\right) \tag{7.1}$$

$$h_{\text{Abs,sol,sat}} = f\left(P_{\text{Abs}}, x_{\text{Abs,sol,out}}, q_{\text{Abs,sol,sat}} = 0\right) \tag{7.2}$$

The absorption duties in the two-phase segment, $Q_{\text{abs,sat}}$, and single-phase segment, $Q_{\text{abs,sub}}$, of the absorber were determined using the following equations.

$$Q_{\text{Abs,sat}} = m_{\text{Abs,sol,in}} \cdot h_{\text{Abs,sol,in}} + m_{\text{Abs,vap,in}} \cdot h_{\text{Abs,vap,in}} - m_{\text{Abs,sol,out}} \cdot h_{\text{Abs,sol,sat}} \tag{7.3}$$

$$Q_{\text{Abs,sub}} = m_{\text{Abs,sol,out}} \cdot h_{\text{Abs,sol,sat}} - m_{\text{Abs,sol,out}} \cdot h_{\text{Abs,sol,out}} \tag{7.4}$$

The temperature of the coupling fluid at the exit of the single-phase segment, and entering the two-phase segment, $T_{\text{abs,CF,sat}}$, was determined as follows:

$$Q_{\text{Abs,sub}} = m_{\text{Abs,CF}} \cdot Cp_{\text{Abs,CF}} \cdot \left(T_{\text{Abs,CF,sat}} - T_{\text{Abs,CF,in}}\right) \tag{7.5}$$

To analyze the heat and mass transfer process inside each of the absorber test sections, both these segments were considered independently. In the laminar pressure drop analysis conducted to determine the number of blocked channels in Scenarios 2 and 3, it was assumed that the blocked channels were distributed evenly among each sheet. Also, for the heat and mass transfer analysis, all the open channels were assumed to be located in the middle of the sheet (as shown in Fig. 7.10). Thus, there is direct thermal

contact between the solution and the coupling fluid channels, and additional conductive resistance due to the presence of a blocked channel between consecutive solution and coupling fluid channels can be neglected. The single-phase segment of the test section is considered first. The total thermal resistance in this segment, $R_{T,sub}$, can be determined from the overall heat transfer conductance values ($U_{sub} \cdot A_{sub}$), which in turn can be determined from the duty in this segment as follows:

$$R_{T,sub} = \frac{1}{U_{sub} \cdot A_{sub}} \tag{7.6}$$

$$U_{sub} \cdot A_{sub} = \frac{Q_{Abs,sub}}{LMTD_{sub}} \tag{7.7}$$

In the above equation, $LMTD_{sub}$ is the logarithmic mean temperature difference between the solution and coupling fluid, which is determined using the following equation.

$$LMTD_{sub} = \frac{\left(T_{Abs,sol,sat} - T_{Abs,CF,sat}\right) - \left(T_{Abs,sol,out} - T_{Abs,CF,in}\right)}{\ln\left(\frac{T_{Abs,sol,sat} - T_{Abs,CF,sat}}{T_{Abs,sol,out} - T_{Abs,CF,in}}\right)} \tag{7.8}$$

As single-phase fluid flows through the solution and coupling fluid channels in this segment, the corresponding heat transfer coefficients can be determined using the correlation developed by Sparrow and Haji-Sheikh (1965) and presented in Kakac *et al.* (1987). Thus, the thermal resistance on the solution- and the coupling-fluid sides can be determined using the methodology used for estimating the resistance of an array of parallel fins that was discussed in Chapter 6.

$$R_{FA} = \frac{1}{\eta_T \cdot \alpha \cdot A_T} \tag{7.9}$$

$$\eta_T = 1 - \frac{N \cdot A_f}{A_T}\left(1 - \eta_f\right) \tag{7.10}$$

In the above equations, α is the fluid heat transfer coefficient, A_T is the total fin array heat transfer area, and η_T is the total fin array efficiency which is calculated from

the individual fin efficiency, η_f. N is the number of fins (which is equal to the number of open channels in a sheet), and A_f is the area of each fin. It should be noted that in the above equation, the total fin area is unknown because the channel length required to accomplish absorption is unknown, and this area differs on the solution and the coupling-fluid sides, because the number of active channels may be different (see Fig. 7.10). These fin areas can be determined using the following equations:

$$R_{T,sub} = R_{FA,sol,sub} + R_{wall} + R_{FA,CF,sub} \tag{7.11}$$

$$\frac{A_{T,sol}}{A_{T,CF}} = \frac{N_{sol}}{N_{CF}} \tag{7.12}$$

In the above equation, N_{sol} and N_{CF}, represent the number of open channels, in the solution and coupling fluid sheets, respectively. Because the length of the segment is equal on both the solution- and coupling-fluid sides, the corresponding effective surface areas are given by the ratio of the number of open channels. The length of the single-phase segment can be determined from the fin area on the solution side, the number of open channels, and the perimeter of the fin on the solution side $Per_{f,sol}$, using the following equation.

$$l_{sub} = \frac{A_{T,sol}}{N_{sol} \cdot Per_{f,sol}} \tag{7.13}$$

The two-phase segment is considered next. The length of this segment is calculated as follows:

$$l_{sat} = l_{ch} - l_{sub} \tag{7.14}$$

The total transfer area available on the solution- and coupling-fluid sides in this segment can be determined using the segment length calculated above. For each test condition, the inlet conditions of the solution and vapor are known from the system level analysis conducted on each test condition. Similarly, the coupling fluid inlet and outlet conditions are also known. Thus, the heat and mass transfer model for microscale forced-

convective absorption discussed in Chapter 6 can be applied to this segment. This model can be used to determine the absorption rates in this segment, and calculate the solution-side heat transfer coefficient. It should be noted that in the design model discussed in Chapter 6, Shah (1979) correlation was used to determine the solution heat transfer coefficient for design purposes. In the present analysis, the heat transfer area in the segment calculated above was used to determine the experimental solution heat transfer coefficient. Similar to the design model, the heat transfer coefficient in the coupling fluid and vapor (needed for the coupled heat and mass transfer analysis in the Colburn-Drew (1937) approach) in the present analysis were determined using the correlation developed by Sparrow and Haji-Sheikh (1965) and presented in Kakac et al. (1987). The vapor mass transfer coefficient was determined using the heat and mass transfer analogy from the vapor heat transfer coefficient calculated above.

This heat and mass transfer analysis was conducted for all experiments on the three microscale absorption test sections (Microscale Absorber 1, 2a, and 2b) for the three channel blockage scenarios discussed above (Scenarios 1, 2, and 3.) For all three absorption test sections, the length of the subcooled segment ranged from 2 – 25 mm, for all test conditions. Fig. 7.12 shows plots of the solution heat transfer coefficient as a function of the concentrated solution mass flow rate per channel in the two-phase segment, for the channel blockage Scenario 1. The solution heat transfer coefficients for Microscale Absorber 1, 2a, and 2b were found to vary from 25.5-155.6, 168.4-295.6, and 99.5-248.6 W m^{-2} K^{-1}, respectively. It should be noted that while total concentrated solution flow rate values for Microscale Absorber 1 were higher than those for Microscale Absorber 2a and 2b, the number of active channels in the former test section is significantly higher than the latter test sections, resulting in lower flow rates per channel. In general, the solution heat transfer coefficient was found to increase with increase in solution flow rate per channel. As the solution flow rate increases, the

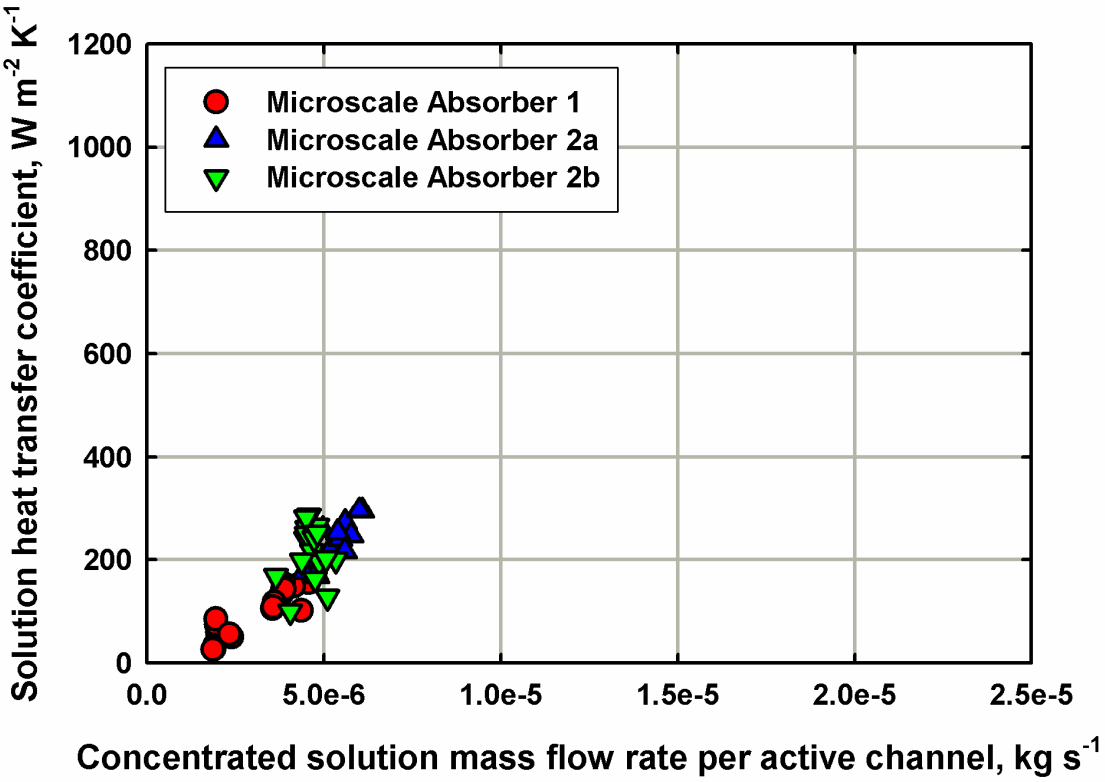

Fig. 7.12 Solution heat transfer coefficient as a function of concentrated solution flow rate per active channel for Scenario 1

convective forces increase, resulting in thinner boundary layers in the solution, which yield higher heat transfer rates.

Figs. 7.13 and 7.14 show plots of the solution heat transfer coefficient as a function of the concentrated solution flow rate per active channel in the two-phase segment, for channel blockage Scenarios 2 and 3, respectively. Because the percentage of blocked channels is higher for Scenario 2 in comparison to the percentage in Scenario 3, for the same concentrated solution flow rate, the solution mass flow rate per channel is higher for Scenario 2 in comparison to Scenario 3. The concentrated solution mass flow rate per active channel for both these scenarios is higher than for Scenario 1, because Scenario 1 assumes that all channels are open, albeit at a lower cross sectional area per channel. The solution heat transfer coefficients for Microscale Absorber 1, 2a, and 2b

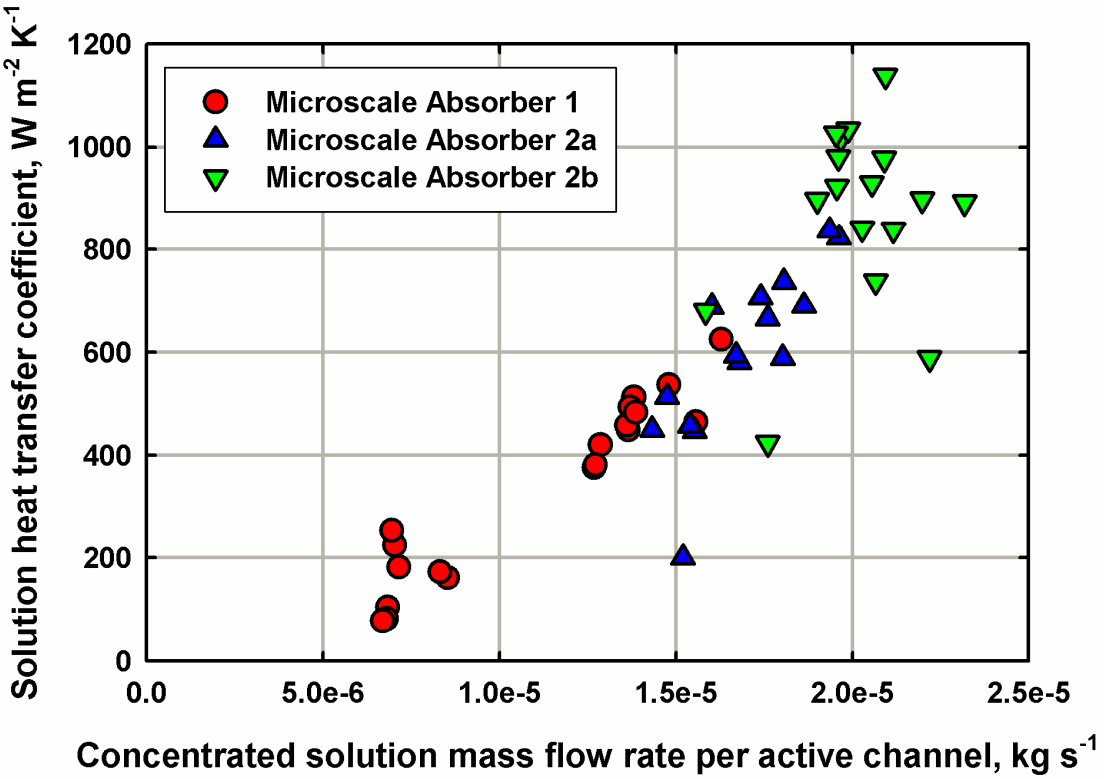

Fig. 7.13 Solution heat transfer coefficient as a function of concentrated solution flow rate per active channel for Scenario 2

were found to vary from 77.4-625.7, 199.6-837.6, and 423.5-1138 W m^{-2} K^{-1}, respectively for Scenario 2. The solution heat transfer coefficient for Microscale Absorber 1, 2a, and 2b varied from 33.3-210.7, 247.1-441.8, and 204.9-554.3 W m^{-2} K^{-1}, respectively for Scenario 3.

As with Scenario 1, the solution heat transfer coefficient was found to increase with an increase in solution flow rate per channel. Higher solution heat transfer coefficient values were observed for Scenario 2 compared to those in Scenario 3, which is due to the higher solution mass flow rates observed in each channel. Slightly higher solution heat transfer coefficients were also observed for Microscale Absorber 2b compared to those for Microscale Absorber 2a for both scenarios, although higher solution flow rates were observed in each channel of Microscale Absorber 2b due to

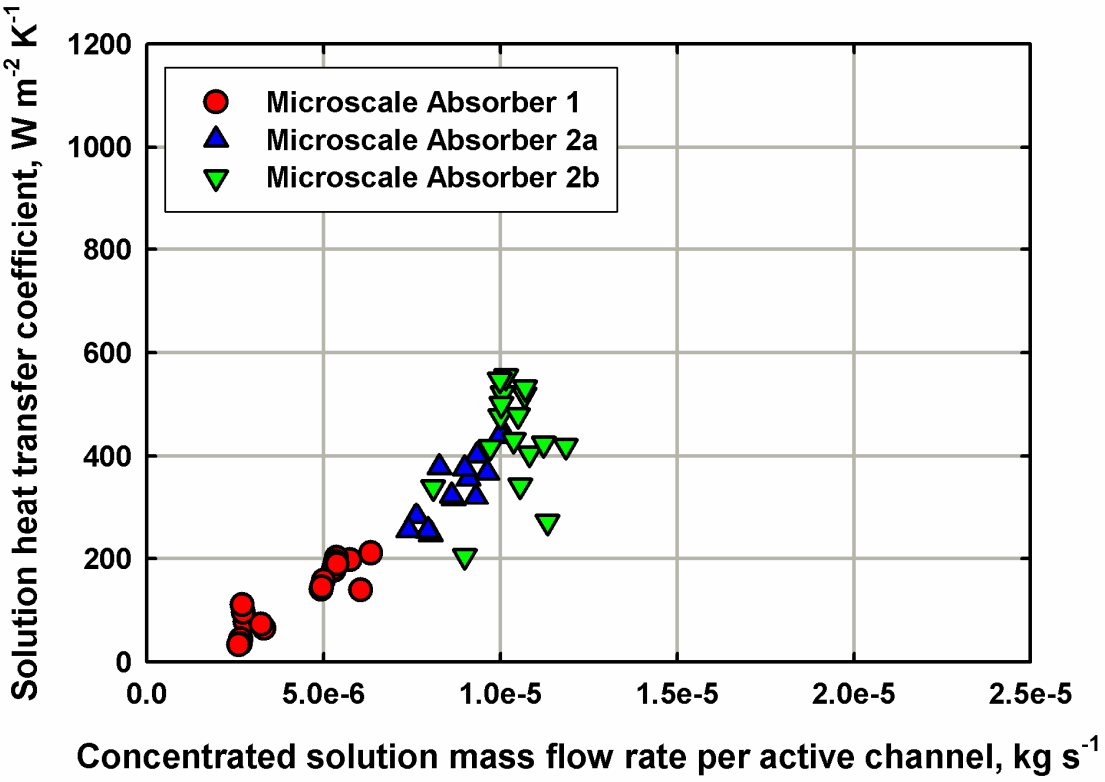

Fig. 7.14 Solution heat transfer coefficient as a function of concentrated solution flow rate per active channel for Scenario 3

higher channel blockage. The heat transfer coefficients in Microscale Absorber 1 were the lowest for all three channel blockage scenarios.

Fig. 7.15 shows a graph of the solution heat transfer coefficient as a function of concentrated solution flow rate per active channel for all Scenarios. As previously observed, the solution heat transfer coefficient increased with an increase in the solution mass flow rate per channel. The highest heat transfer coefficient values were predicted for Scenario 2, while the lowest values were predicted for Scenario 1, for all microscale absorbers. The solution mass fluxes in each active channel for Microscale absorbers 1, 2a, and 2b ranged from 35.8 – 87.2, 38.6 – 52.9, and 35.6 – 52.1 kg m^{-2} s^{-1}, respectively for Scenario 1, from 68.0 – 165.4, 69.7 – 95.5, and 77.1 – 112.8 kg m^{-2} s^{-1}, respectively for Scenario 2, and from 41.9 – 102.0, 48.7 – 66.8, and 53.3 – 78.0 kg m^{-2} s^{-1},

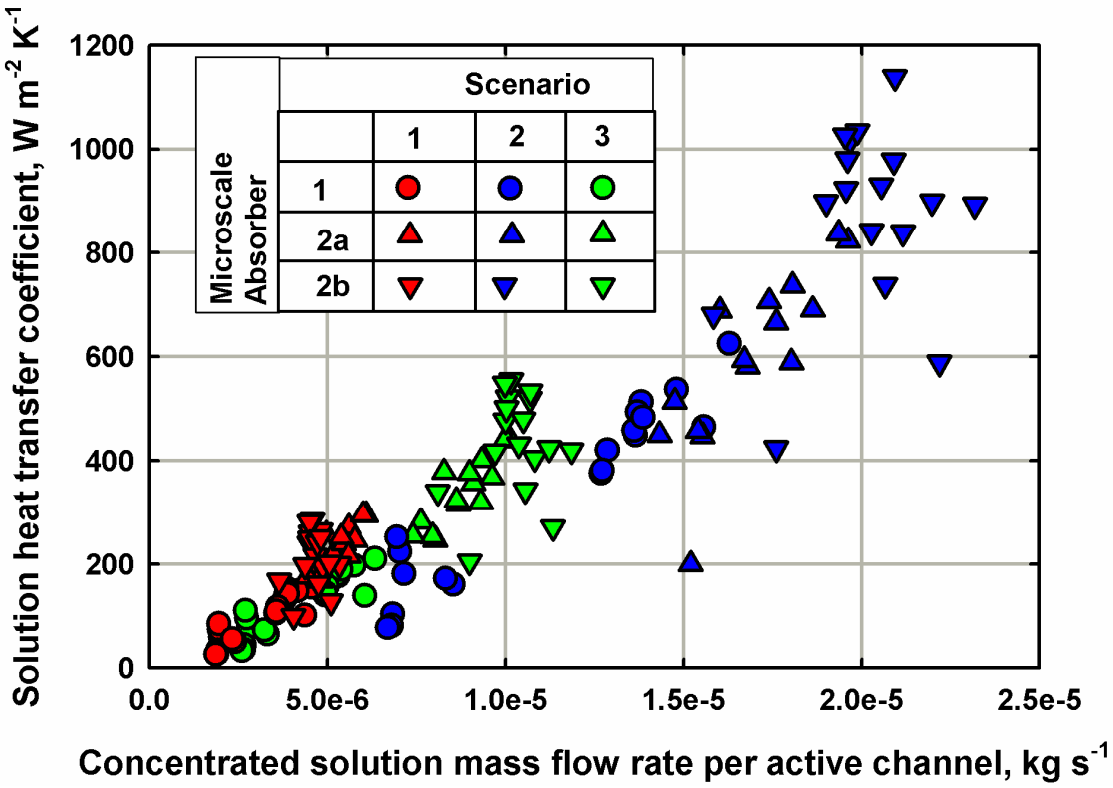

Fig. 7.15 Solution heat transfer coefficient as a function of concentrated solution flow rate for all Scenarios

respectively for Scenario 3. As expected, the highest mass fluxes were observed for Scenario 2, while the lowest mass fluxes were observed for Scenario 1.

In the design model developed in Chapter 6, as previously mentioned, the correlation developed by Shah (1979) was used to estimate the solution heat transfer coefficient. The solution heat transfer coefficients calculated above were compared with the corresponding predictions from this correlation. For this purpose the following ratio of the measured and predicted heat transfer coefficients is defined:

$$HT_{\text{ratio}} = \frac{\alpha_{\text{sol}}}{\alpha_{\text{Shah}}} \tag{7.15}$$

Table 7.9 shows a summary of these ratios for the three absorption test sections, according to the three channel blockage scenarios considered above. All the ratios were considerably less than 1. The HT_{ratio} values for Microscale Absorber 1 were the lowest, ranging from 0.01-0.09 for the three scenarios. The HT_{ratio} for Microscale Absorber 2a and 2b were relatively higher, ranging from 0.05-0.14 and 0.03-0.20, respectively. In general, HT_{ratio} values were highest for Scenario 2 and lowest for Scenario 1.

7.5. Discussion of convective absorber performance

Microscale forced-convective absorption in three absorber test sections, as part of two separate absorption chillers, was measured and analyzed above. The test sections were studied over a range of solution and vapor flow rates, and the measured data were analyzed to estimate the local heat and mass transfer rates. These analyses, however, involved several assumptions that should be examined further.

Channel blockage scenarios discussed above are idealizations, and the blockage in a real test section is a combination of these three scenarios. This is confirmed by Fig. 7.16, which shows a photograph of a sample heat exchanger that was sectioned using wire EDM at one axial location. As can be seen from this photograph, some channels appear to be fully blocked, while others appear to be partially blocked or fully open. In addition, the shapes of the channels are different from the originally designed semi-circular or semi-oval shapes, and are not consistent. This indicates that the correlations used to calculate the friction factor, and laminar heat transfer coefficient may not be

Table 7.9 Ratios of measured and predicted solution heat transfer coefficients

Scenario	Microscale absorber #1	Microscale absorber #2a	Microscale absorber #2b
#1	0.01-0.04	0.05-0.07	0.03-0.09
#2	0.02-0.09	0.05-0.14	0.07-0.20
#3	0.01-0.05	0.06-0.09	0.05-0.13

completely valid for the as-fabricated absorber geometries. It should be noted that these observations are for the location that was sectioned. The channel blockage scenario could be different upstream and downstream of this location. In Particular, a channel that appears to be fully or partially open at this location might be fully blocked at some other upstream or downstream location. From a flow, and heat and mass transfer perspective, such a channel is completely inactive. Thus, to get a true picture of the channel blockage and channel shapes, each test section has to be sectioned into several small sections, and the channels in each section should be examined. The laminar pressure drop analysis discussed above is only a guide for the determination of actual channel geometries of these absorbers.

In the heat and mass transfer analysis conducted above, adjacent solution and coupling fluid channels were assumed to be in direct thermal contact with each other. However, it can be seen from Fig. 7.16 that there is a possibility that a blocked channel may lie in the thermal path between a solution and coupling fluid channel. This results in a higher wall thermal resistance, because the heat transfer path between the two fluids is longer. The overall thermal resistance in a segment calculated for each data point remains the same for any distribution of blocked channels, and is dictated by the duty and the *LMTD* between the solution and coupling fluid sides.

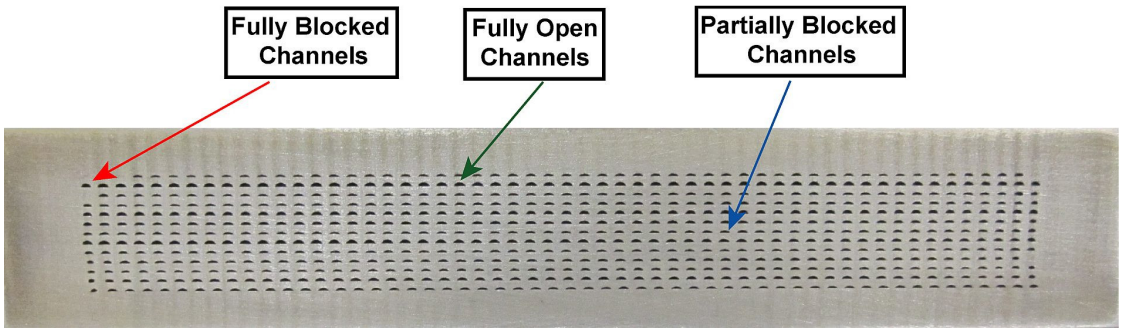

Fig. 7.16 Photograph of the channel array at an intermediate location along the channel length

$$R_{\mathrm{T}} = \frac{1}{U_{\mathrm{seg}} \cdot A_{\mathrm{seg}}} = \frac{LMTD_{\mathrm{T}}}{Q_{\mathrm{seg}}} \tag{7.16}$$

The thermal resistance on the solution-side, on the other hand, depends upon the definition of the thermal resistance of the wall and the coupling fluid.

$$R_{\mathrm{FA,sol}} = R_{\mathrm{T}} - R_{\mathrm{wall}} - R_{\mathrm{FA,CF}} \tag{7.17}$$

Thus, the predicted film thermal resistance for an experimental data point decreases with an increase in the wall thermal resistance. The wall thermal resistance values calculated in the above heat and mass transfer analysis are the lowest possible values for any channel blockage scenario, because the solution and coupling fluid channels were assumed to be in direct thermal contact with each other. Thus, the predicted solution heat transfer coefficients are the worst-case-scenario values, because any increase in the wall thermal resistance will result in a decrease in the solution-side thermal resistance, and correspondingly an increase in the solution heat transfer coefficients. This also indicates that while very low values for HT_{ratio} were predicted, in reality, these values might be higher, depending on the actual channel blockage distribution, and the predictions summarized in Table 7.9 are for worst-case-scenarios. It is possible that the actual channel blockage scenario inside the absorber test sections is a combination of Scenarios 2 and 3. In such a scenario, both completely blocked and partial blocked channels exist, and the blocked channels are randomly distributed, resulting in a significant increase in the wall thermal resistance.

Channel blockages also affect flow distribution. While the original absorber sheet designs were developed assuming even flow distribution, blockage or uneven shrinkage of some channels introduces additional pressure drop for a given flow rate, which in turn results in mal-distribution of fluid in the channel array. Even fluid distribution is critical to the effective operation of such components. If excess vapor flows into a channel, the vapor is not completely absorbed in the channels, and two-phase solution exits the absorber. On the other hand, if too little vapor flows through a channel, the solution is

significantly subcooled, and the transfer area available for the absorption process is not effectively utilized. It should be noted that the sheet design for Microscale Absorber 2b should yield better distribution of the vapor and solution inside the channel array, compared to the distribution resulting from the sheet design for Microscale Absorber 2a. This is reflected in the slightly better performance of Microscale Absorber 2b, which transfers higher absorption duties at higher solution heat transfer coefficients. However, due to the significant channel blockages in this component, the flow is still expected to be mal-distributed, which is detrimental to the performance of the component.

To address this issue, new sheet designs for microscale forced-convective absorption were developed (Fig. 7.17). The design of Sheet B is similar to the design of the Sheet B for Microscale Absorber 1 and 2b. The solution inlet and outlet headers, and the vapor through holes in Sheet A are also similar to the design for Microscale Absorbers 1 and 2b. The primary difference between the two sheet designs is in the microchannel geometry. In the revised design, several breaks in the channel walls are introduced along length of the channel, with space provided for mixing of the fluid stream at intermediate location in the channel array. These channel breaks serve several purposes. The space near the channel breaks facilitates mixing and redistribution of the solution and vapor, such that the resulting flow in the channels downstream of these breaks is more uniform. Additionally, if a channel is blocked in a certain region of the sheet but open at upstream and downstream locations, the open sections can still be utilized for heat and mass transfer due to the presence of mixing sections at several locations. These breaks are located at more frequent intervals toward the beginning of the channels, where there is higher vapor flow. The frequency of these breaks decreases along the flow direction, with no breaks located towards the end of the absorber, where vapor flow rate is very low. This revised design is used for the comparative assessment study conducted in the next chapter.

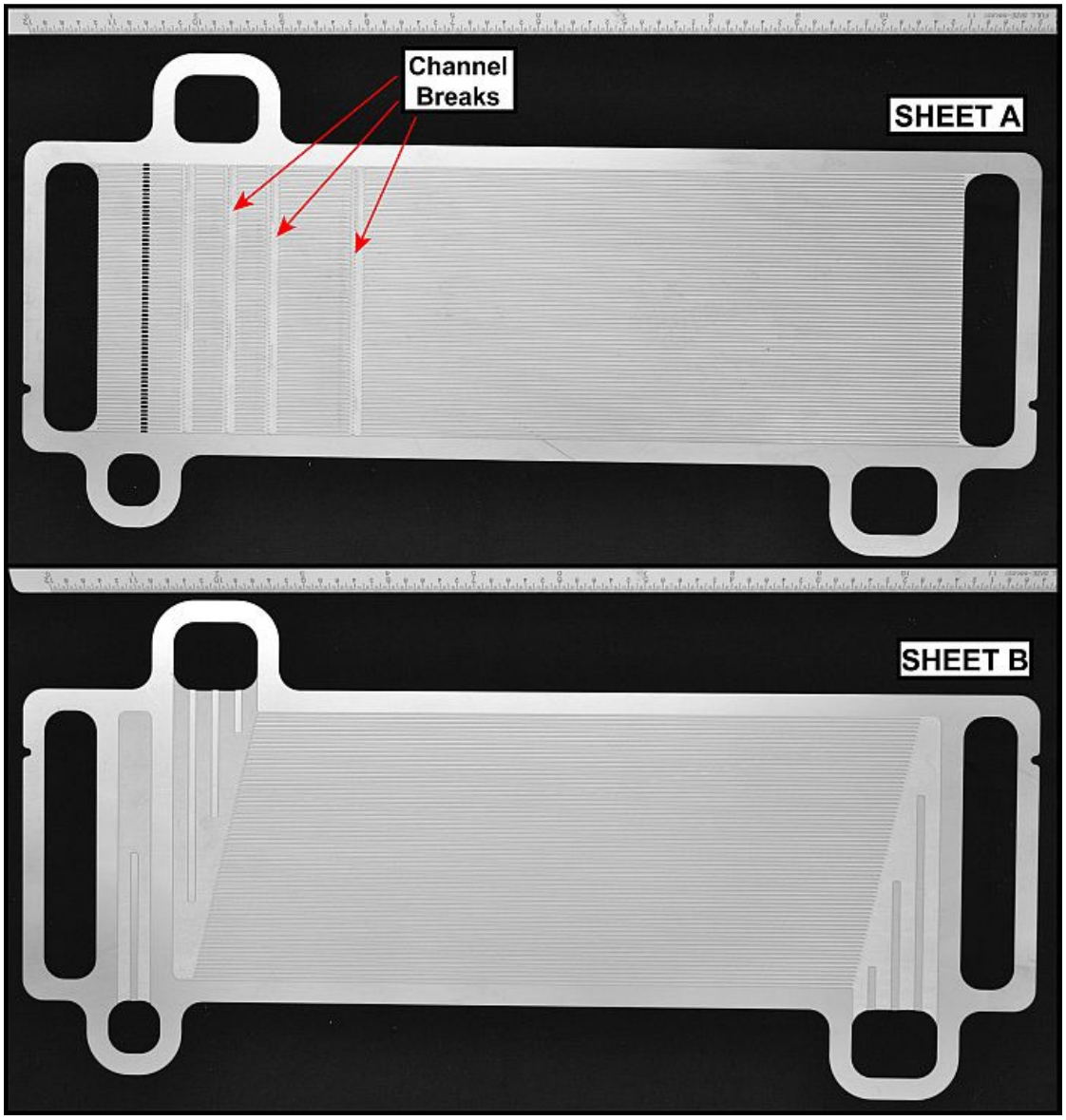

Fig. 7.17 Photograph of absorber sheets for revised microscale forced-convective absorber

It should be noted that while these design modifications are expected to improve the performance of the absorption test sections, it is critical that the fabrication process be improved and channel blockages be minimized. In both diffusion bonding and vacuum brazing, the nickel plating facilitates bonding of the sheet array, but also presents the problem of channel blockage. If the thickness of the plating is reduced, the amount of material entering the channels can be reduced, but the risk of not forming a hermetic seal

increases. Thus, several fabrication trials are necessary to develop the expertise required to bond these test sections effectively without blocking the channels significantly.

7.6. Summary

This chapter presents the experimental demonstration of absorption cooling using microscale geometries. The three test sections developed in the previous chapter were tested as part of two absorption chillers: a 2.5 kW absorption chiller with a co-current desorber, and a 2 kW absorption chiller with a counter-current desorber. All the absorption system components, such as the desorber, rectifier, condenser, evaporator, solution heat exchanger, and refrigerant pre-cooler, were designed and fabricated using the same microfabrication technologies used to develop the absorption test sections. A breadboard test facility was developed to install these components, and provide the necessary fluid streams at the required operating conditions. The test sections were evaluated over a wide range of solution and vapor flow rates. Data analysis procedures from Chapter 4 were modified to analyze these data, and determine the state of the solution and vapor at various locations in the test loop. The relevant component duties were also estimated, and the absorber duty was found to range between 1.1 – 3.5 kW for the three test sections. The heat and mass transfer design model for microscale convective flow absorption discussed in Chapter 6 was adapted to estimate the measured solution heat transfer coefficients. While these heat transfer coefficient values were much lower than the predictions from the correlation developed by Shah (1979), these estimates are for the worst-case-scenario and are highly dependent upon the assumptions used to analyze as-fabricated channel geometries and the flow in the absorber. Channel blockage, and the resulting vapor-liquid mal-distribution was identified as a major cause of the poor performance of the absorbers. To address this challenge, a revised absorber sheet design was proposed. However, effective fabrication of test components with minimum channel blockage remains critical for success of this technology.

CHAPTER 8. COMPARATIVE ASSESSMENT OF FALLING-FILM AND FORCED-CONVECTIVE ABSORPTION

Two absorption modes are investigated in the present study: falling-film absorption around horizontal microchannel tube banks, and forced forced-convective absorption inside microscale channels. A microchannel falling-film absorber was experimentally investigated over a wide range of operating conditions in a test facility replicating a single-effect ammonia-water absorption chiller. The absorption duties were found to range from 2.89 – 10.09 kW over the range of test conditions. A coupled hydrodynamic and heat and mass transfer model was developed to analyze the falling-film absorption process, and a correlation for the film heat transfer coefficient was developed. A complementary study on forced-convective absorption in microscale geometries was conducted, and three absorption test sections were fabricated using microfabrication techniques. These test sections were installed in a breadboard test facility along with other components of a single-effect ammonia-water absorption chiller, and the absorption process was studied over a range of solution and coupling fluid flow rates. The absorption duties were found to range between 1.1 – 3.5 kW over the range of test conditions. Experimentally measured heat transfer coefficients were compared with predictions from a correlation from the literature.

The analyses on the two absorption modes were conducted over significantly different component sizes and system duties. For a valid comparison between the two modes, their performance must be assessed at similar operating conditions. Under such operating conditions, a comparison can be made between the two absorption modes in terms of the heat and mass transfer rates, temperature and concentration profiles, overall component size and weight, and fabrication aspects. Therefore, a target cooling capacity of 10.5 kW (3 RT) was chosen, which is representative of cooling requirements in a residential application. The heat and mass transfer models developed for each mode in

the previous chapters were employed to design prototype absorbers to satisfy this cooling duty.

8.1. Design conditions and constraints

8.1.1. Absorber operating conditions

Table 8.1 shows a summary of the operating conditions for the absorber. These operating conditions were determined from a system level thermodynamic model, developed for a cooling capacity of 10.5 kW. The corresponding absorber duty was calculated to be 16.9 kW. The absorber is hydronically cooled with distilled water acting as the coupling fluid. The absorber coupling fluid in turn rejects heat to the ambient at a temperature of 35^{o}C, in an air-coupled heat exchanger. The hydronically coupled evaporator operates in air-conditioning mode, where the coupling fluid enters at a temperature of 12.78^{o}C and exits at a temperature of 7.21^{o}C.

8.1.2. Design constraints

As discussed in Chapter 6, in addition to the constraints imposed by the operating conditions, there are several other constraints that should be considered while designing these absorbers. These can be broadly classified into operational constraints and

Table 8.1 Design conditions for the absorber (10.5 kW cooling capacity)

	Inlet	Outlet
Pressure, kPa	503.3	503.3
Solution flow rate, kg s^{-1}	0.01997	0.02925
Solution concentration	0.2374	0.4789
Solution temperature, ^{o}C	65.6	41.27
Vapor flow rate, kg s^{-1}	0.00929	0
Vapor concentration	0.9984	N/A
Vapor temperature, ^{o}C	47.92	N/A
Coupling fluid flow rate, kg s^{-1}	0.336	
Coupling fluid temperature, ^{o}C	40.57	52.6
Absorber heat duty, kW	16.9	

fabrication constraints.

Operational constraints include constraints imposed due to pressure drop on the solution- and coupling-fluid side, fluid distribution, and structural strength limits. Fabrication constraints include constraints imposed by the different features sizes, header shapes, and assembly of building units. Because the pressure drop on the solution-side should be limited since excessive pressure drop will result in a reduction in the saturation temperature, which in turn results in the requirement of a larger transfer area to achieve the same absorption duty. Similarly, high pressure drops in the coupling fluid will require a bigger pump to circulate the fluid, which results in higher parasitic losses. For the present designs, the pressure drops on the solution- and coupling-fluid sides were conservatively limited to 7 kPa and 15 kPa, respectively.

Several fabrication constraints associated forced-convective absorbers were discussed in Chapter 6. The fabrication constraints associated for falling-film absorbers are relatively less stringent. The most significant constraint is the spacing between adjacent tubes, and successive tube rows. If the tube rows can be packed closer together, a higher transfer area can be packed into the same volume. However, as the tube rows get closer, flow mechanisms such as the evolving droplet and droplet impact do not occur as desired, which can result in a significant reduction in the performance of the absorber. Thus for the microchannel falling-film absorber, the diameter of the tube sections, and the transverse and longitudinal pitch of the tube array are assumed to be equal to that of the absorber tested earlier. Similarly, for the microscale forced-convective absorber, the channel hydraulic diameter, channel shape, and channel pitch are assumed to be equal to those of Microscale Absorber 2b. The absorber designs for comparative assessment are developed while considering these constraints, as well as the other constraints discussed in Chapter 6.

8.2. Absorber designs and variants

8.2.1. Microchannel falling-film absorbers

The falling-film absorption hydrodynamic and heat and mass transfer model discussed in Chapter 5 was applied to the design conditions in Table 8.1 to develop several absorber design variants. Similar to the design of the absorber discussed earlier, several stainless steel tube segments of 1.575 mm OD, 0.2 mm thick tube wall, and 0.140 m length were arranged parallel to each other, to form a single tube row. Headers are located at either end of the tube segments to provide structural stability to the tube rows and facilitate distribution of the coupling fluid. The number of tube segments in each row, and the number of tube rows in each pass were varied in each of the variants. The number of passes was adjusted to provide the necessary transfer area for complete absorption. For the present design variants, the number of tube rows was varied between 40, 50, and 60, and the number of rows per pass was varied between 6, 8, and 10. It should be noted that there were 33 tubes per row, and 2 rows per pass in the microchannel absorber discussed in Chapter 5. The transverse and longitudinal pitch of the tube array was held constant and equal to 4.76 and 7.94 mm, respectively.

Table 8.2 shows a summary of the predicted absorber sizes for the different tube row and pass configurations. It can be seen from this table that for a fixed number of tubes per row, as the number of rows per pass increases the required number of passes for complete absorption decreases. This is expected because as the number of the tube rows per pass increases, a higher amount of transfer area is available in each pass, resulting in a reduction in the required number of passes for complete absorption. A similar trend was observed for the required number of passes as the number of tubes per row was increased, for a fixed number of tube rows per pass.

It is interesting to note however, that as the number of tubes per row is increased, the required transfer area on the solution side also increased, for a fixed number of tube

rows per pass. It should be noted that the dilute and concentrated solution flow rates for all designs are the same. Thus, as the number of tubes per row increased, the linear solution mass flux, Γ_{film}, decreased, resulting in a reduction in the film Reynolds number, Re_{film}. This in turn results in a decrease in the film heat transfer coefficient (based on the Nusselt number correlations developed in Chapter 5) and correspondingly, a reduction in the absorption rate. Similarly, as the number of tube rows per pass increased, the required transfer area on the solution side also increased, for a fixed number of tubes per row. As the number of tube rows per pass increases, the coupling fluid Reynolds number decreases, which in turn results in a decrease in the coupling fluid heat transfer coefficient. The reduction in the coupling fluid heat transfer coefficient results in an increase in the overall heat transfer resistance, and correspondingly an increase in the required area for complete absorption.

Fig. 8.1 shows a schematic of the microchannel falling-film absorber. As discussed in Chapter 3, the tube array of the microchannel falling-film absorber was assembled and brazed in place. Series flow between passes of the absorber was achieved by bending the tubes instead of using headers, and an intermediate manifold was installed to provide structural support. However, the required number of tube segments and tube rows are much higher for the absorber variants designed here because the required absorption duty is also higher. Thus, two headers are installed at both ends of the tube segments to facilitate the distribution of the coupling fluid, and provide structural support to the tube array. Each tube segment therefore requires two braze joints, one on either end, to form a hermetic seal between the solution and coupling fluid sides. Table 8.2 shows a summary of the number of braze joints for each absorber variant. As the required transfer area for the absorber increased, the number of tube segments increased, and correspondingly, the number of braze joints also increased.

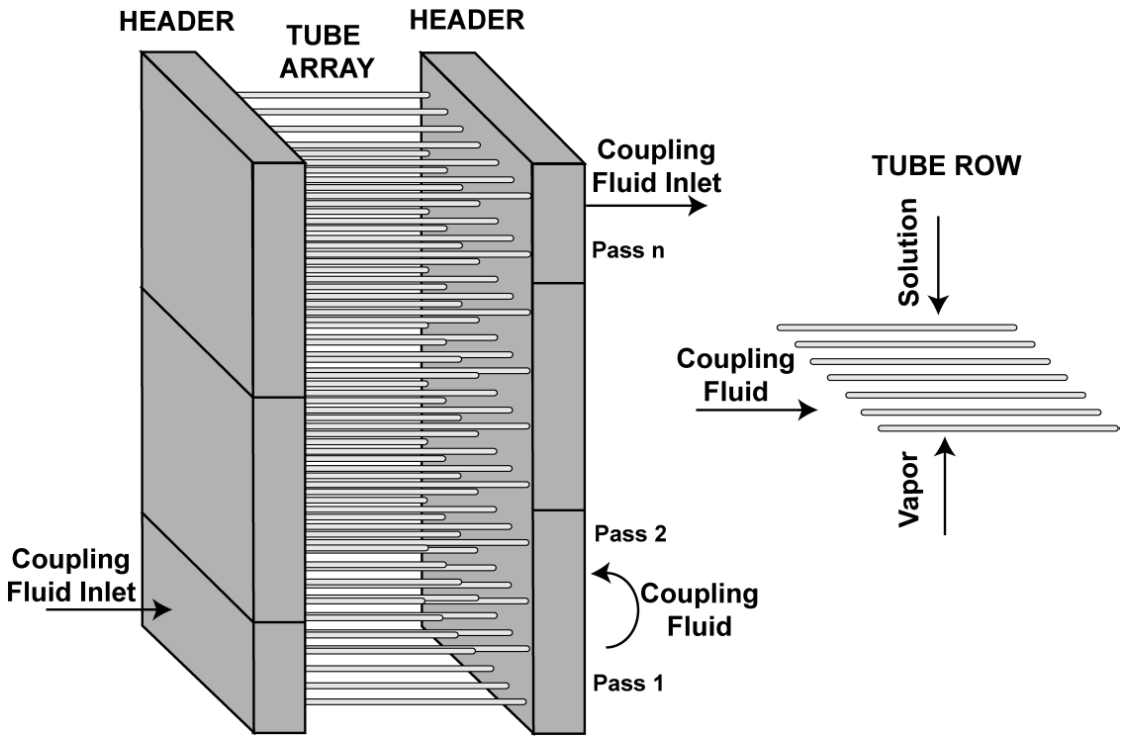

Fig. 8.1 Schematic of microchannel falling-film absorber

Table 8.2 also shows a summary of the predicted pressure drop on the coupling-fluid side in the tube array. For the absorber variants designed with 6 tube rows per pass, the coupling fluid pressure drop was always higher than the design limit discussed above. The pressure drop decreased with increase in the number of tubes per row, due to a reduction in the mass flow rate of coupling fluid in each tube. However, the resulting pressure drop was still higher than the design limit. The coupling fluid pressure drop for two of the three design variants designed with 8 tube rows per pass, and all three design variants designed with 10 tube rows per pass was found to be below the design limit of 15 kPa. Among these, variant 5 was found to have the least transfer area, and correspondingly require the least number of tube segments and braze joints. It has a total solution-side transfer area of 2.21 m^2, arranged in 8 passes of 8 rows each, and a total of 50 tubes per row. This variant was chosen as the prototype design for comparison with

the corresponding forced-convective absorber prototype design. Fig. 8.2 shows a graphical summary of the microchannel falling-film absorber variants.

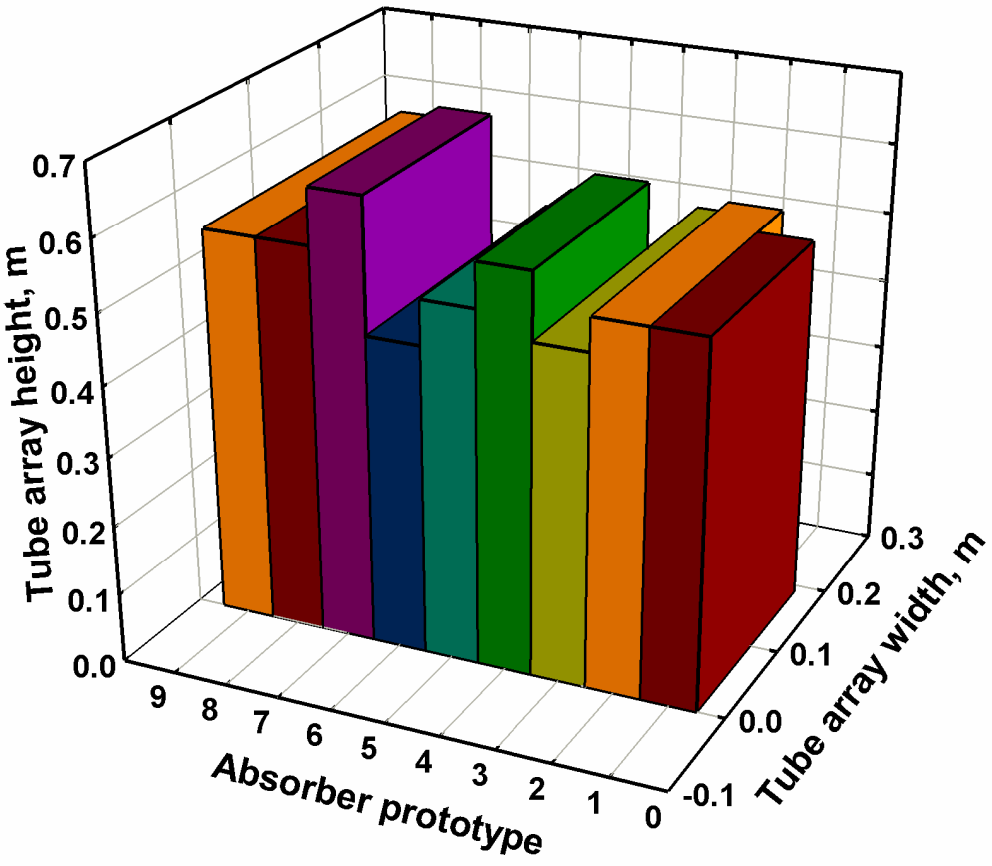

Fig. 8.2 Summary of microchannel falling-film absorber variants

Table 8.2 Summary of microchannel falling-film absorber variants

Variant	Number of tube rows per pass	Number of tubes per row	Number of passes	Coupling fluid pressure drop (kPa)	Number of tube segments	Tube array width (m)	Tube array height (m)	Transfer area (m^2)	Number of braze joints
1	6	40	11	40.3	2640	0.1904	0.5240	1.82	5280
2	6	50	11	23.3	3300	0.2380	0.5240	2.28	6600
3	6	60	10	17.5	3600	0.2856	0.4764	2.49	7200
4	8	40	9	17.7	2880	0.1904	0.5717	1.99	5760
5	**8**	**50**	**8**	**12.5**	**3200**	**0.2380**	**0.5082**	**2.21**	**6400**
6	8	60	7	9.2	3360	0.2856	0.4446	2.32	6720
7	10	40	8	12.6	3200	0.1904	0.6352	2.21	6400
8	10	50	7	8.9	3500	0.2380	0.5558	2.42	7000
9	10	60	7	7.5	4200	0.2856	0.5558	2.90	8400
Note: Variant 5 was selected for comparison									

8.2.1. Microscale forced-convective absorbers

The microscale forced-convective absorption heat and mass transfer model discussed in Chapter 6 was applied to the design conditions in Table 8.1 to develop several absorber design variants. The hydraulic diameter of the channel was fixed at 442 μm, similar to the D_h used for Microscale Absorbers 2a and 2b. The design of the absorber sheets (Sheet A and Sheet B) is similar to the design of the revised absorber sheets, discussed in Chapter 7. In this design, several breaks are located along the length of the solution channels on Sheet A, to increase mixing of the solution and vapor and enhance absorption. In the microscale forced-convective absorber design model, the correlation developed by Shah (1979) was used to estimate the solution heat transfer coefficient. However, as discussed in Chapter 7, the measured solution heat transfer coefficients were found to be lower than the predictions from this correlation. Thus, a multiplying factor of 0.25 was applied to the predictions from the Shah (1979) correlation to estimate the solution heat transfer coefficient based on the HT_{ratio} in Chapter 7 varying from 0.03-0.20, under worst case scenario assumptions. Also, the revised absorber sheet design is expected to enhance the absorption process with better mixing of the solution and vapor streams, and improvements in the fabrication process will result in a reduction in the channel blockages and mal-distribution and correspondingly an improvement in the flow distribution and the overall absorption process.

The number of channels per sheet, as well as the number of sheets in an assembly was varied in each of the variants. The required channel length was adjusted to provide the necessary transfer area for complete absorption. For the present design variants, the number of channels per sheet was varied between 50, 70, and 90, and the number of sheets in an assembly was varied between 100, 150, and 200. The number of sheets here corresponds to the number of each individual sheets (Sheet A or Sheet B). For Microscale Absorber 2b, there were 55 channels per sheet and 22 individual sheets in the assembly.

The pitch of the channel array was held constant and equal to 1.25 mm, and stainless steel was chosen as the sheet material.

Table 8.3 shows a summary of the predicted absorber sizes for different combinations of the number of channels per sheet and the number of sheets in an assembly. It can be seen from this table that for a fixed number of channels per sheet, as the number of sheets in an assembly increases the required channel length for complete absorption decreases. This is expected because as the number of sheets in an assembly increases, a higher amount of transfer area is available per unit channel length, resulting in a reduction in the required channel length for complete absorption. A similar trend was observed for the required channel length as the number of channels per sheet was increased, for a fixed number of sheets in an assembly.

It is interesting to note however, that as the number of channels per sheet increased, the required transfer area on the solution side also increased, for a fixed number of sheets in an assembly. A similar finding was previously observed for microchannel falling-film absorption, where the required heat transfer area increased with increase in the number of tubes per row, for a fixed number of tube rows per pass. As discussed previously, the dilute and concentrated solution flow rates for all designs are the same. As the number of channels per sheet increases, the mass flux of solution through each individual channel decreases, resulting in a decrease in the solution heat transfer coefficient and the overall absorption rate. Similarly, as the number of sheets in an assembly increases, the required heat transfer area also increases, for a fixed number of channels per sheet, which is again attributed to the reduction in the solution heat transfer coefficient.

To form a hermetic seal between the solution and vapor streams, and the coupling fluid streams, the seal has to be made at 13 locations on Sheet A, and 16 locations on Sheet B. These locations are identified in Fig. 8.3. Thus, each combination of Sheets A and B must be bonded at 29 locations, corresponding to 29 braze joints. Table 8.3 shows

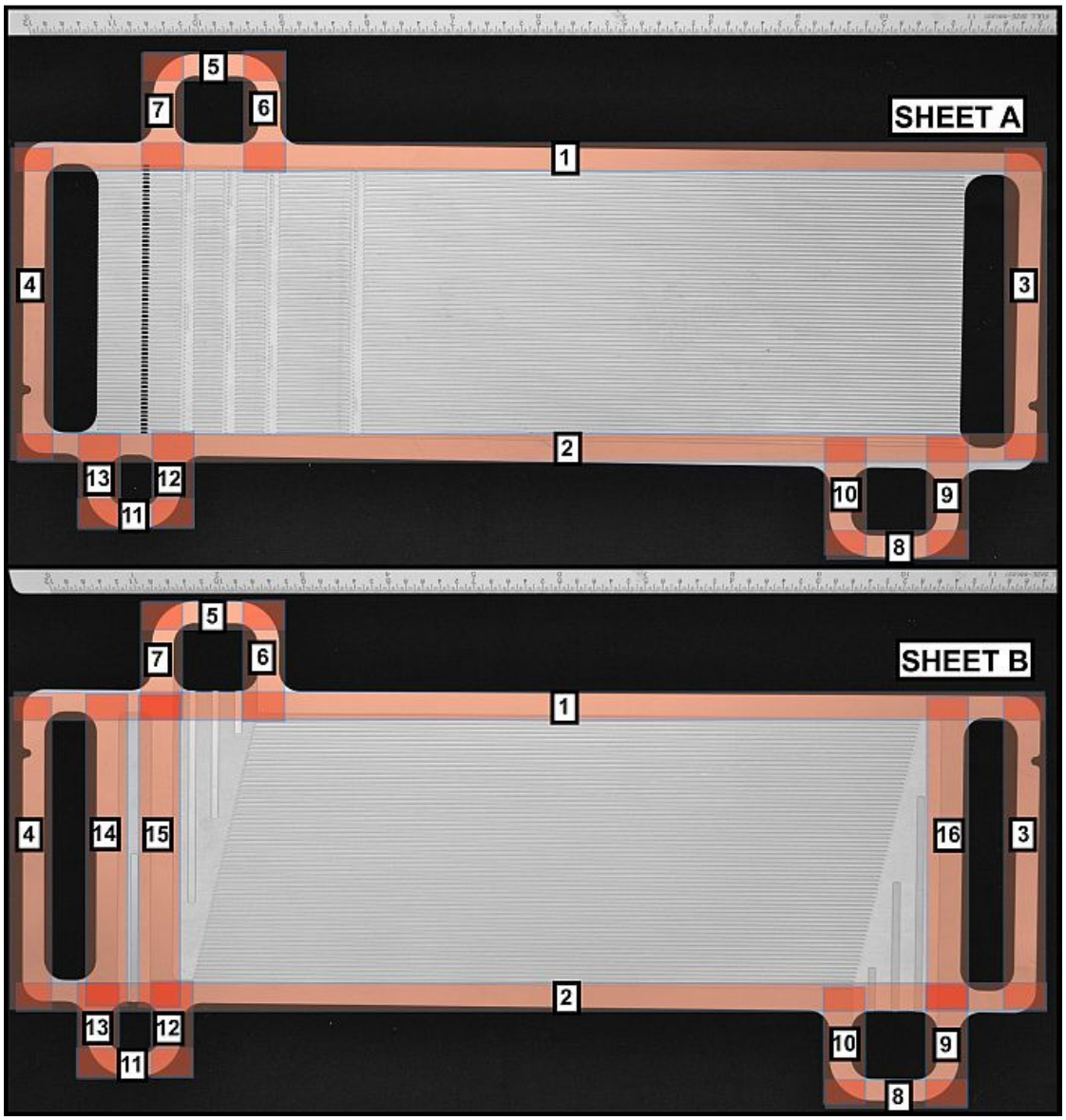

Fig. 8.3 Schematic of braze joints for the microscale forced-convective absorber

a summary of the number of braze joints for each absorber variant. The number of braze joints depend upon the number of sheets, but are independent of the number of channels per sheet, or the length of the channels. While the surfaces between adjacent channels in the same sheet are also bonded, these joints are not critical for a hermetic seal between the two sides of the heat and mass exchanger. The 29 joints identified above are the critical joints, where failure can lead to either cross leakage between the two fluid streams or leakage from the heat and mass exchanger to the outside. It should be noted

that while the number of braze joints for the microscale forced-convective absorber variants are lower than the number of braze joints for the microchannel falling-film absorber variants, these joints are much longer and present a more significant challenge from a bonding perspective, as discussed previously.

Table 8.3 shows a summary of the pressure drop on the coupling fluid- and solution-side in the channel array. Both the solution and coupling fluid pressure drops for two of the three design variants with 50 channels per sheets, and all three design variants with 70 and 90 channels per sheets were found to be below the design limits of 7 and 15 kPa, respectively. Among these, variant 4 was found to have the least transfer area, and also required the least number of brazed joints. It has a total solution-side transfer area of 8.15 m^2, fabricated from 100 sheets each of Sheet A and Sheet B, with 70 channels per sheet. This variant was chosen as the prototype design for comparison with the corresponding microchannel falling-film absorber prototype design discussed above. Fig. 8.4 shows a graphical summary of the microscale forced-convective absorber variants.

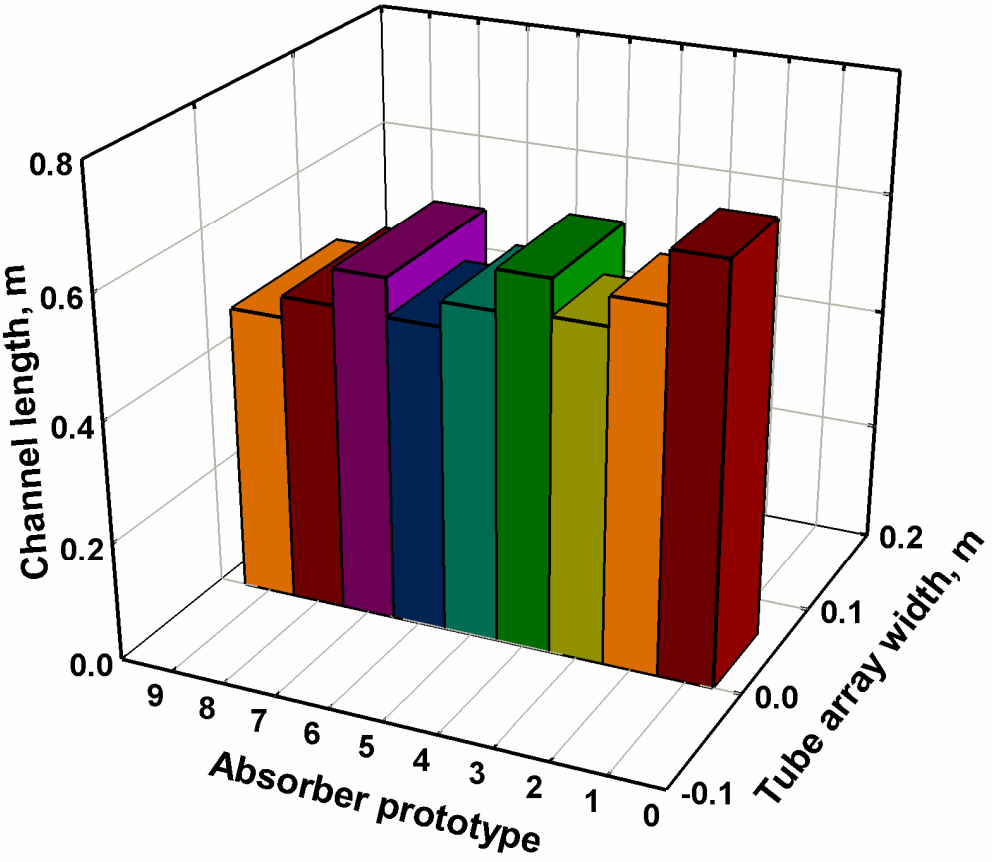

Fig. 8.4 Summary of microscale forced-convective absorber variants

Table 8.3 Summary of microscale forced-convective absorber variants

Variant	Number of channels per sheet	Number of sheets	Channel length (m)	Coupling fluid pressure drop (kPa)	Solution pressure drop (kPa)	Channel array width (m)	Sheet array height (m)	Transfer area (m^2)	Number of braze joints
1	50	100	0.685	22.1	7.4	0.063	0.10	6.50	2900
2	50	150	0.601	12.9	4.3	0.063	0.15	8.56	4350
3	50	200	0.554	8.9	3.0	0.063	0.20	10.52	5800
4	**70**	**100**	**0.613**	**14.1**	**4.7**	**0.088**	**0.10**	**8.15**	**2900**
5	70	150	0.548	8.4	2.8	0.088	0.15	10.92	4350
6	70	200	0.508	5.9	2.0	0.088	0.20	13.51	5800
7	90	100	0.571	10.2	3.4	0.113	0.10	9.75	2900
8	90	150	0.512	6.1	2.1	0.113	0.15	13.13	4350
9	90	200	0.478	4.3	1.4	0.113	0.20	16.33	5800
Note: Variant 4 was selected for comparison									

8.3. Comparative assessment

8.3.1. Heat and mass transfer characteristics

It can be seen from Tables 8.2 and 8.3 that the necessary transfer area on the solution-side for complete absorption for the falling-film and forced-convective absorbers is 2.25 and 8.15 m^2, respectively. Thus, it appears that the microchannel falling-film absorber configuration is significantly more efficient than microscale forced-convective absorber configuration in transferring the same absorption load. It should be noted that in the design of the microscale forced-convective absorber, a multiplication factor of 0.25 was applied to prediction of the solution heat transfer coefficient from the Shah correlation (Shah, 1979). If this multiplying factor is increased to 0.5, the required transfer area for complete absorption decreases to 3.37 m^2, which is comparable to the transfer area of the microchannel falling-film absorber. A more detailed study is warranted on forced forced-convective absorption inside microchannels, so that models and correlations can be developed to estimate the solution heat transfer coefficient accurately, similar to the analysis conducted on falling-film absorption in the present study. However, based on the approximate design models and tests on channels with blockages and their effects, the correction factor employed here can provide a conservative estimate of the required transfer area.

Fig. 8.5 shows a plot of the solution and vapor bulk temperatures as a function of dimensionless length for the two absorbers. Because the channel length of the microscale forced-convective absorber is different from the array height of the microchannel falling-film absorber, for comparison purposes, a dimensionless length is defined as follows:

$$l' = \frac{l}{L_T} \tag{8.1}$$

In the above equation, l represents the distance from the dilute solution inlet, and L_T represents the total distance the solution travels. In the microchannel falling-film

absorber, this corresponds to the total height of the tube array, and in the microscale forced-convective absorber, this corresponds to the length of the microchannel array in which the solution and coupling fluid are in thermal contact with each other. For the falling-film absorber, the dilute solution enters at location $l' = 0$, and vapor enters at location $l' = 1$. For the forced-convective absorber, both the dilute solution and the vapor enter at location $l' = 0$.

For both absorption modes, the temperature of the solution bulk undergoes a rise initially. The rise is sharper in forced-convective absorption, in comparison to falling-film absorption. As reported in Chapter 6, rapid absorption occurs near the inlet of the forced-convective absorber due to favorable heat and mass transfer mechanisms, resulting in a release of a large amount of heat, which results in an increase in the dilute

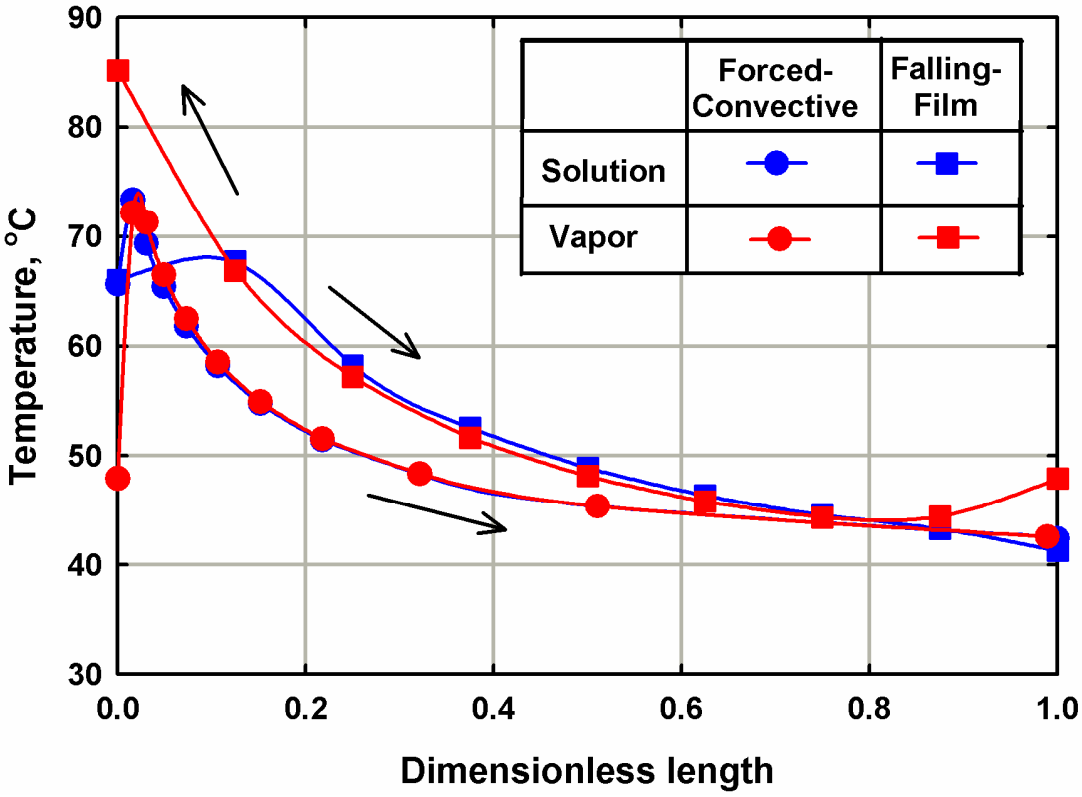

Fig. 8.5 Temperature as a function of absorber length

solution temperature in the initial segments. A similar phenomenon is expected in falling-film absorption. However, because the vapor is in counter-current flow, the vapor flow rate at the topmost pass of the absorber is lower, resulting in a lower absorption rate, and correspondingly, a lower temperature rise. The temperature of the solution monotonically decreases along the rest of the absorber length for both absorption modes, and the vapor temperature closely follows the solution temperature. Cooling of the vapor bulk is also observed at the bottom of the falling-film absorber. Warm vapor from the refrigerant pre-cooler is introduced into the absorber at $l' = 1$. As this vapor comes into contact with the cooler solution, it cools down rapidly in the bottommost pass, and subsequently, closely follows the solution temperature through the rest of the absorber. At the top most pass, because of rapid local absorption due to favorable concentration and temperature gradients, the vapor is heated, resulting in a rise in the vapor temperature. Furthermore, due to the low vapor mass flow rate near the top of the absorber, a small heat transfer rate can cause a significant change in the vapor bulk temperature.

Fig. 8.6 shows a plot of the solution and vapor mass flow rate as a function of the dimensionless length for the two absorbers. It should be noted that while it appears that vapor mass flow rate is increasing along the absorber length for the microchannel falling-film absorber, the vapor is actually flowing counter-current to the solution. Thus, vapor flow rate at the bottom of the absorber is equal to the flow rate of the vapor entering the absorber. The rapid absorption rate observed in the initial segments of the forced-convective absorber results in a dramatic reduction in the vapor flow rate initially. On the other hand, the absorption rate at the top passes of the falling-film absorber is not as rapid, although it should be noted that nearly 50% of the vapor is absorbed in the top 2 passes, while 6 further passes are required to absorb the remaining vapor. Similar to the latter segments of the forced-convective absorber, in the lower passes of the falling-film absorber, the concentration difference between the vapor bulk and the solution is lower, resulting in a lower driving potential for mass transfer. Furthermore, the temperature

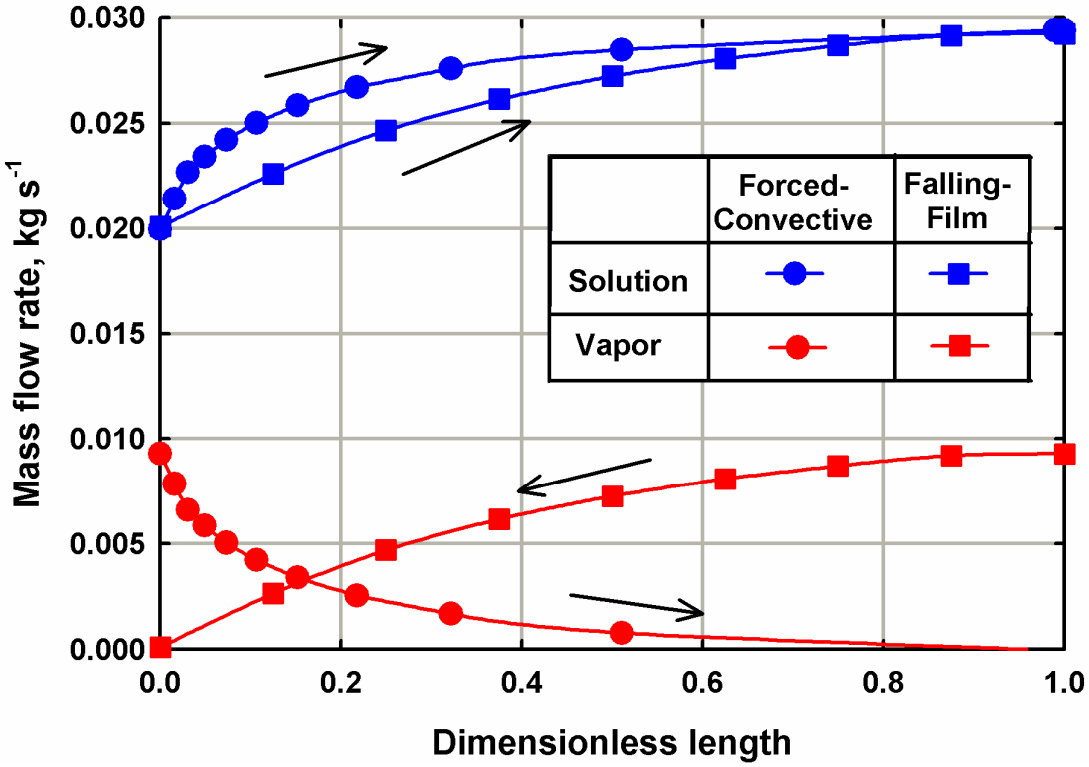

Fig. 8.6 Mass flow rate as a function of absorber length

difference between the solution bulk and the coupling fluid is small, resulting in higher heat transfer resistance, and effectively requiring larger transfer area to absorb the same amount of vapor.

Fig. 8.7 shows a plot of the absorption duty as a function of the dimensionless length of the two absorbers. This plot confirms the higher absorption rates observed in the forced-convective absorber, in comparison to the falling-film absorber, near the beginning of the absorption length. However, as previously discussed, because the vapor is flowing counter-current to the solution in the falling-film absorber, the amount of unabsorbed vapor near the topmost pass is lesser, resulting in a lower absorption rate. The absorption rate in the forced-convective absorber decreases dramatically towards the latter part of the channel, indicating that the heat and mass transfer resistance to

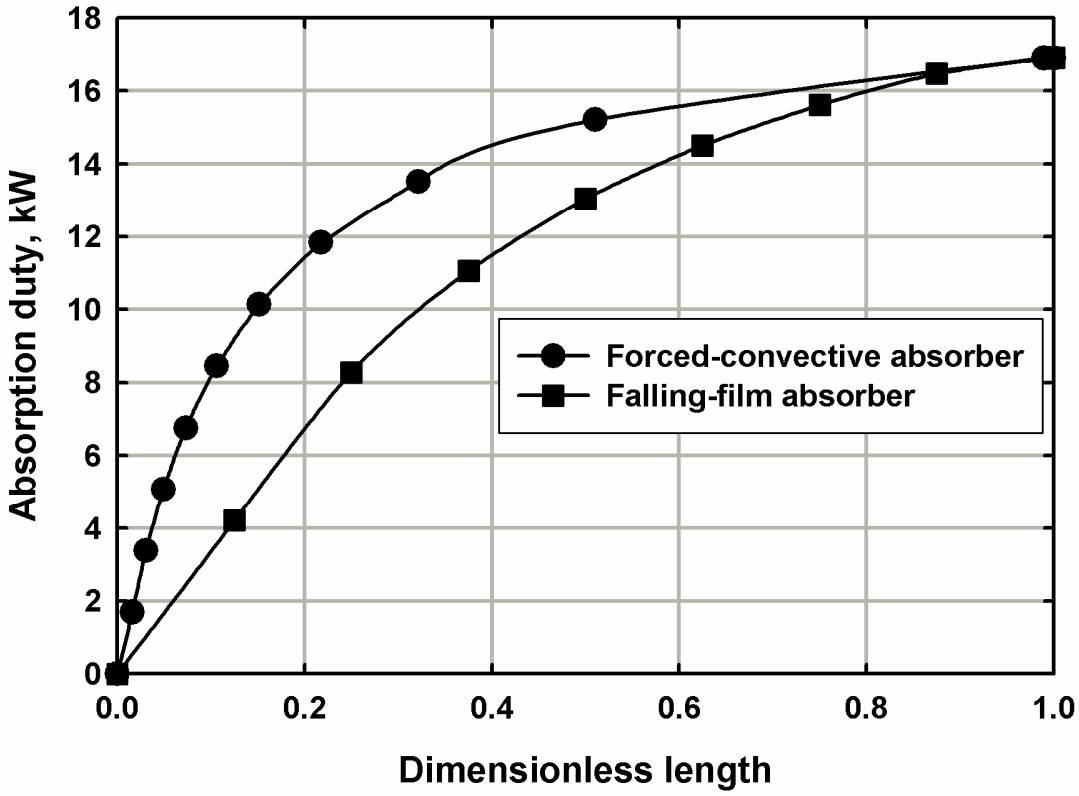

Fig. 8.7 Absorber duty as a function of absorber length

absorption here is higher than the corresponding resistance to absorption in the falling-film absorber.

As can be seen from the above discussion, as well as the discussions in Chapters 4, 5, 6, and 7, ammonia-water absorption in both absorption modes is due to a combination of several transport processes. To study the influence of the individual transfer coefficients on the overall absorption rate, a multiplication factor was applied to each of them, and its effect on the necessary transfer area for complete absorption was calculated for each of the prototype absorbers. Table 8.4 shows the summary of this analysis. As can be seen from this table, the solution heat transfer coefficient strongly affects the absorption process. For the microchannel falling-film absorber, an extra pass was required if the solution heat transfer coefficient was decreased by 20%. On the other

Table 8.4 Summary of influence of individual transport process

Fluid stream	Multiplication factor	Microchannel falling-film absorber (Tube rows)	Microscale convective flow absorber (Channel length, m)
Solution heat transfer coefficient	80%	72	0.765
	100%	64	0.613
	120%	57	0.514
Vapor heat transfer coefficient	80%	64	0.612
	100%	64	0.613
	120%	64	0.614
Coupling fluid heat transfer coefficient	80%	72	0.621
	100%	64	0.613
	120%	57	0.608

hand, an increase of 20% in the solution heat transfer coefficient resulted in a decrease in the required transfer area by almost a whole pass. The coupling fluid heat transfer coefficient was also found to have a similar influence on the required area for complete absorption. The vapor heat transfer coefficient (and correspondingly the vapor mass transfer coefficient from the heat and mass transfer analogy) was found to have negligible influence on the required absorption area. This indicates that the overall process is not limited by the vapor transport process, and that the solution and coupling fluid heat transfer processes significantly influence the absorption process.

In microscale forced-convective absorption, a decrease of 20% in the solution heat transfer coefficient resulted in an increase in the required channel length for complete absorption by ~25%. Correspondingly, an increase of 20% in the solution heat transfer coefficient resulted in a decrease in the required channel length by ~16%. The reduced influence of the coupling fluid heat transfer coefficient was reflected in the channel lengths increasing and decreasing by 1.3 and 0.8%, with decrease and increase of the coupling fluid heat transfer coefficient by 20%, respectively. Similar to the falling-film absorber, the influence of the vapor transport process was found to be marginal on the required channel length for complete absorption. Thus, for the forced-convective

absorber, absorption is not significantly limited by the vapor transport process. The solution heat transfer coefficient strongly influences absorption, while the influence of the coupling fluid heat transfer coefficient is relatively low. Fig. 8.8 shows a graph of the influence of individual transport processes on the necessary absorption length for complete absorption.

8.3.2. Fabrication and packaging aspects

Table 8.5 shows a summary of the overall volume, weight, and transfer area for the two absorber prototypes. In estimating the overall size of the microchannel falling-film absorber, the additional volume occupied by the headers, the drip tray on top of the tube array, and the solution pool at the bottom of the tube array was considered. Furthermore, a shell of thickness 5 mm was also considered to house the microchannel tube array. A shell of this thickness can withstand pressures above 1 MPa. Similarly in estimating the overall size of the microscale forced-convective absorber, the additional volume occupied by the solution, vapor, and coupling fluid headers was also considered. End plates of 3 mm thickness were chosen to contain the channel array. Fig. 8.9 shows a comparative schematic of the two prototype absorbers.

It can be seen from Table 8.5 that the overall envelope volume of the microscale forced-convective absorber is only about 17% of the volume of the microchannel falling-film absorber even though the corresponding solution-side transfer area is nearly 4 times higher. This highlights the improved miniaturization achieved by the microscale forced-convective heat and mass exchange concept. In the microchannel falling-film absorber, there are several void spaces between adjacent tube segments, which are necessary for the various flow mechanisms that affect absorption. However, no such spaces are necessary in the microscale forced-convective absorber, thus facilitating a much denser packing of the transfer area. This is highlighted by the transfer area per unit volume parameter, which is nearly two orders of magnitude higher for the microscale forced-convective

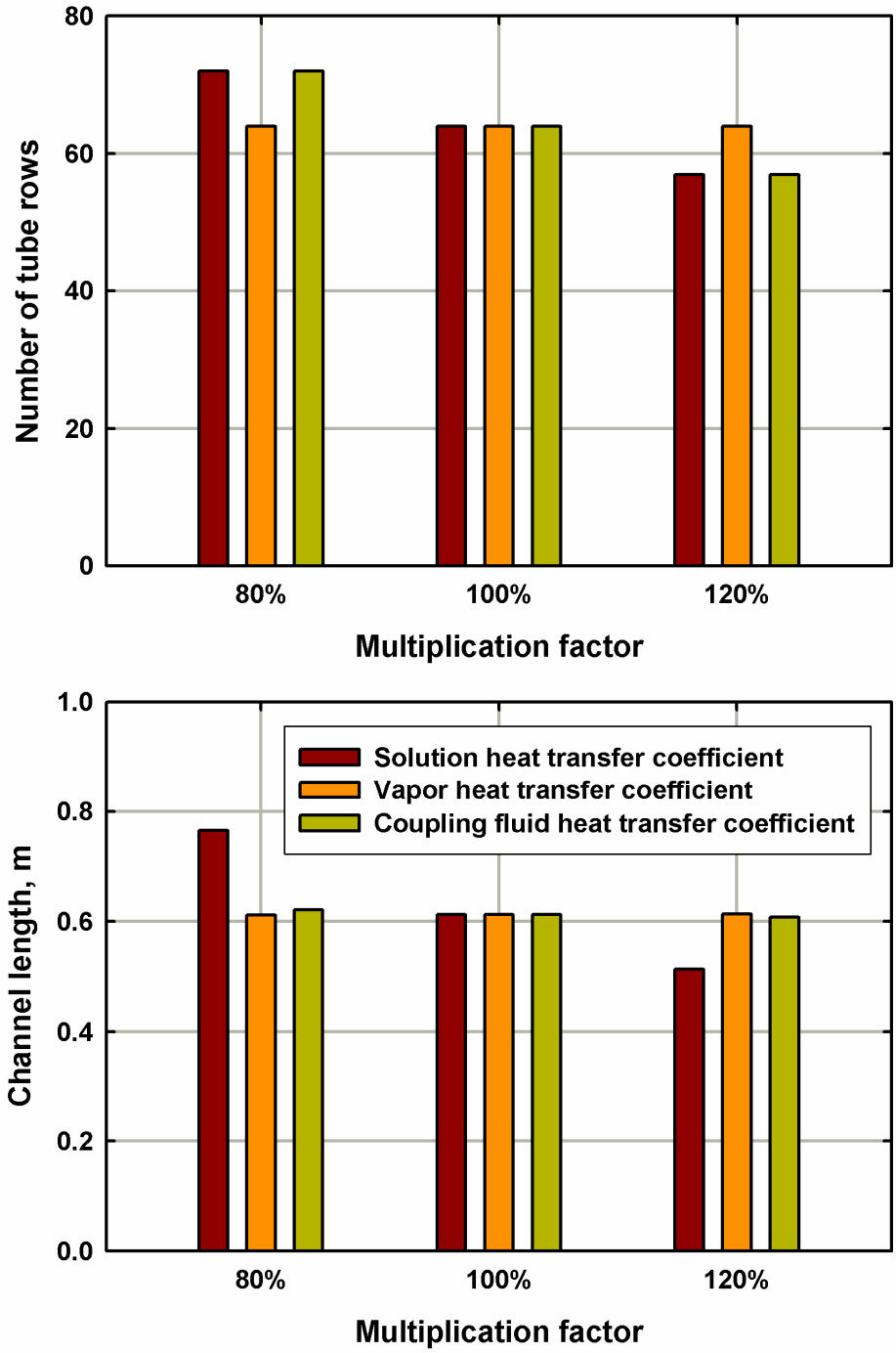

Fig. 8.8 Summary of influence of individual transport process

absorber, compared to the microchannel falling-film absorber. As previously mentioned, any improvement in the solution heat transfer coefficient in the forced-convective

absorber will result in a reduction in the necessary transfer area, and a corresponding reduction in the overall component volume.

The mass of the microchannel falling-film absorber is lower that the mass of the microscale forced-convective absorber, even though it is nearly 6 times bigger in the overall volume, which is again attributed to the dense packing in the forced-convective absorber. However, it should be noted that the microscale forced-convective absorber has a lower component mass per unit transfer area, as seen in Table 8.5. Thus, for a fixed transfer area, the convective flow absorber has a smaller mass than the falling-film absorber by ~54%.

In general, the microscale forced-convective absorber is expected to have a much smaller overall volume, compared to the microchannel falling-film absorber, and is ideally suited for applications where space is at a premium. However, the mass of this component is higher, and so applications where lower weight is critical, the microchannel falling-film absorber might be more appropriate. The microscale forced-convective absorber has a lower component mass per unit transfer area, and thus any improvement in

Table 8.5 Comparison of geometry characteristics

Characteristic	Microchannel falling-film absorber	Microscale convective flow absorber
Length (m)	0.29	0.76
Width (m)	0.29	0.10
Height (m)	0.71	0.11
Envelope volume (m^3)	0.047	0.008
Transfer area (m^2)	2.21	8.15
Transfer area per unit volume (m^2 m^{-3})	36.8	1018.8
Weight (kg)	26.1	44.2
Component weight per unit volume (kg m^{-3})	435	5525
Duty per unit volume (active transfer area) (kW m^{-3})	1000.9	3132.9
Duty per unit volume (overall) (kW m^{-3})	359.6	2112.5

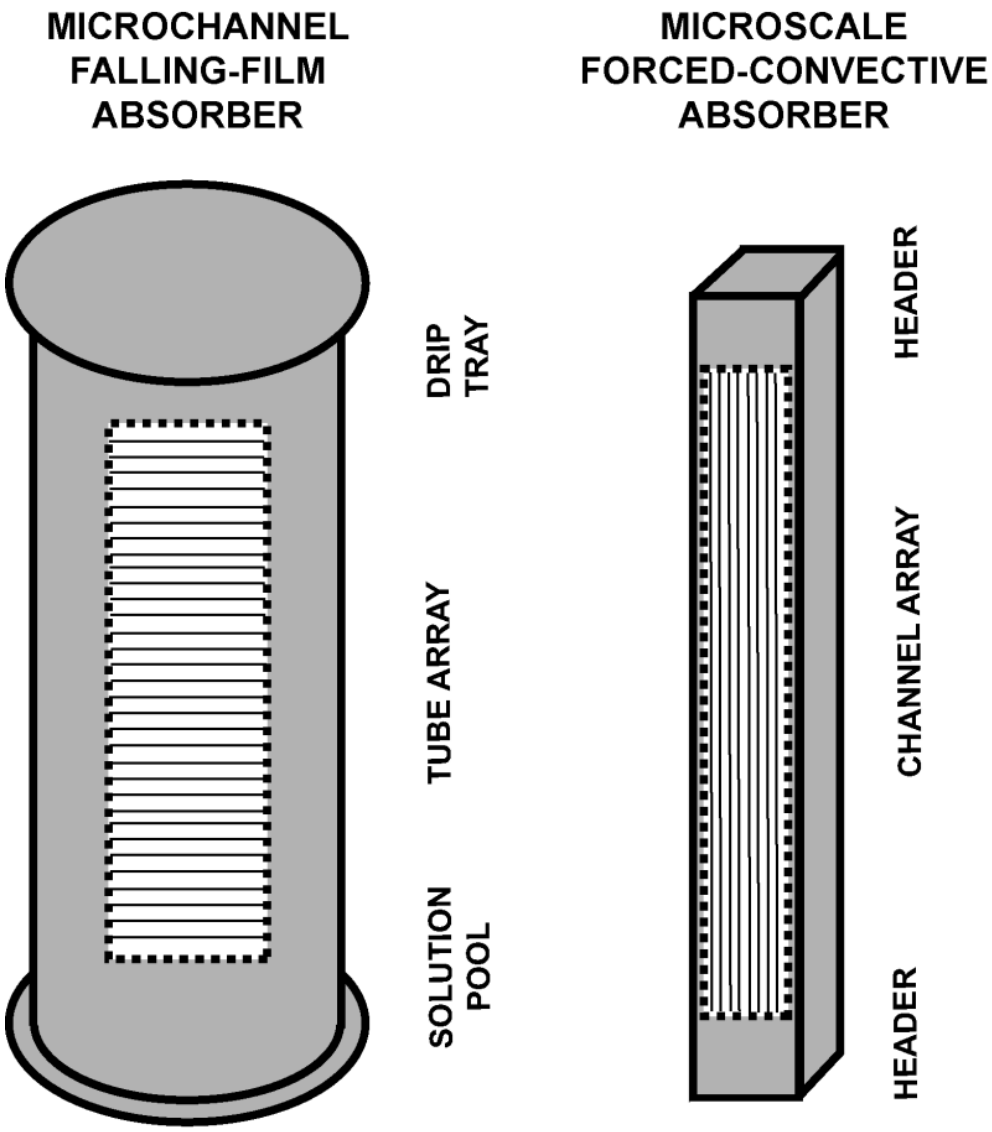

Fig. 8.9 Schematic of protoytpe absorbers

the solution heat transfer coefficient will result in a reduction in the necessary transfer area, and correspondingly the mass of the overall component. Thus, the microscale forced-convective absorber can also be competitive in applications where weight is at a premium.

As previously mentioned, the microchannel tube array in the falling-film absorber is bonded to the coupling fluid headers, by brazing the assembly in place. Welding process is used to bond the other joints at the headers and the shell. The tube segments

are typically fabricated by a drawing process. For the microscale forced-convective absorber, the microscale features are machined using photochemical etching, and the sheet array and end plates are bonded using vacuum brazing or diffusion bonding. The individual sheets used to develop the sheets are typically fabricated using a rolling process. Thus, two processes are used in fabrication of both components: vacuum brazing and welding for the falling-film absorber, and photochemical etching and diffusion bonding/vacuum brazing for the forced-convective absorber. The number of braze joints for the microchannel falling-film absorber (6400) are significantly higher than the number of braze joints for the microscale forced-convective absorber (2900). However, as previously mentioned, the length of the braze joints is much higher for the latter, making the fabrication process more complicated. Furthermore, as noted in Chapters 6 and 7, there is a possibility that the nickel alloy plating material used to bond the sheets might occupy parts of the microscale features, resulting in blockage of channels. The possibility of such blockage in the vacuum brazing process or the welding process used for the falling-film absorber is lower. Thus, in general the fabrication of the microchannel falling-film absorber is simpler than the microscale forced-convective absorber.

8.4. Summary

A comparative assessment of the two absorption modes, microchannel falling-film absorption and microscale forced-convective absorption, was conducted in this chapter. The heat and mass transfer models developed in the previous chapters were applied to design an absorber that is part of a 10.5 kW cooling capacity chiller for residential applications. Several design variants were developed for each absorption mode, and the optimal designs were identified based on several design and operational constraints.

The heat and mass transfer characteristics in both these prototype designs were studied. While the local absorption rate and the required transfer area for complete

absorption were different for the two modes, the overall heat and mass transfer trends were comparable. The fabrication and packaging characteristics of the two prototype absorbers were also studied. While a higher number of braze joints is necessary for the microchannel falling-film absorber, the overall fabrication process is expected to be simpler than the fabrication process for the microscale forced-convective absorber. The microscale forced-convective absorber was found to be more favorable for applications where space is at a premium, while the microchannel falling-film absorber was found to be more favorable for applications where overall mass is important. However, with improvement in the solution heat transfer coefficient, the microscale forced-convective absorber can also be competitive in applications where component weight is critical.

CHAPTER 9. CONCLUSIONS AND RECOMMENDATIONS

9.1. Conclusions

A detailed investigation of ammonia-water absorption at the microscales was conducted. Two absorption configurations were studied: falling-film absorption around horizontal microchannel tube bundles, and forced-convective absorption inside microscale channels. Falling-film absorption was first investigated, where a microchannel absorber was installed in a test facility replicating a single-effect ammonia-water absorption heat pump, and investigated over a range of concentrated solution flow rates (0.011 – 0.023 kg s^{-1}) and concentrations (40 – 55%), refrigerant fractions (15 – 40%), and coupling fluid inlet temperatures (20 – 40^{o}C). These operating conditions represent operation of the heat pump in both cooling and heating mode, over a range of capacities, and ambient conditions unlike those typically achievable in simple benchtop, single component test rigs. The measured temperatures, pressures, and flow rates were analyzed to determine the state of the solution and vapor at various locations around the test loop, obtain the relevant component duties, and estimate the segmental absorption rates and the overall and solution heat transfer coefficients.

The microchannel falling-film absorber was found to transfer duties ranging from 2.89 – 10.09 kW in a compact envelope. A significant portion of the absorption was found to occur in the lower half of the absorber, and only a small portion of the inlet vapor reached the top half of the absorber. Thus, it is likely that the microchannel falling-film absorber is capable of transferring duties larger than those observed in the present study. The solution heat transfer coefficients were found to range between 1461 – 3430 W m^{-2} K^{-1}, and in general were found to increase with increase in the solution flow rate, solution concentration, and vapor flow rate. The calculated heat transfer coefficients were also compared with relevant correlations from the literature. The applicability of these correlations to the present study is limited due to differences in working fluid pair, and/or

absorber geometry and the associated flow mechanisms, and operating conditions. In particular, none of these studies was conducted on microchannel tubes, where the heat transfer and flow mechanisms are different from those observed on large tubes, and so the comparison was found to be poor, warranting a more detailed study of the flow mechanisms and development of new heat and mass transfer correlations.

In the horizontal tube absorber considered here, solution flows from one tube row to another as droplets. As these droplets fall on the tube, a film is formed, which spreads over the tube surface similar to a wave. Droplet-mode flow was modeled by considering a representative primary droplet, evolving at specific droplet formation sites on each tube row. The shape of the droplet at the instant of detachment was found to be similar to a hemisphere with a conical top. Various droplet characteristics, such as droplet spacing, droplet evolution time, and instantaneous volume and surface area, were also modeled. The droplet formation times were found to range from 0.235 – 0.462 s, which compared well with the experimentally estimated formation times from previous visualization studies on similar geometries (Meacham and Garimella, 2004). Upon detachment and impact of this droplet on the subsequent tube row, the spreading of liquid over the tube surface was modeled by considering three regions of the film: Feed region, Spread region, and Inactive region. The Feed region was located directly above the droplet formation site and supplied the solution to the droplet. The spreading of the liquid film in the Spread region was modeled as "stretching" of a triangle over the tube surface. The film flow over the tube surface was found to have a "wave like" behavior, where the width of the spread region (and correspondingly the wave) and the thickness of the film were found to vary with both location and time. Film characteristics such as average film thickness, film spreading, and tube wetting were also estimated. The wetting ratio of the tube surface was found to range from 0.807 – 0.830 over the experiments conducted in this study.

This hydrodynamic model was coupled with the heat and mass transfer model to estimate the local absorption rates in each flow mode. Three regions in the absorber were considered for the absorption of vapor: absorption at the solution pool, absorption into the droplets, and absorption into the film. Absorption in the solution pool and the droplet was assumed to be adiabatic, while the heat of absorption in the film was removed by the circulating coupling fluid. Relevant concentration and temperature profiles were estimated in each region to estimate the local heat and mass transfer rates. Most of the absorption was found to occur in the film region, while up to ~ 7% of the absorption occurred in the droplet. A small amount of vapor was also found to desorb from the droplets at certain operating conditions. While the contribution to absorption from the droplets is low, the flow mechanisms associated with these droplets significantly affect the absorption process in the film region. Thus, considering both flow modes is critical to analyzing the absorption process. The contribution to absorption from the solution pool under the tube array was found to be relatively low. The film heat transfer coefficients ranged between 1788-4179 W m^{-2} K^{-1}. The corresponding film Nusselt numbers were affected by both the fluid properties and flow parameters, and the following correlation for heat transfer in the film mode over the surface of the tube was developed based on the solution Reynolds and Prandtl numbers, and vapor Reynolds number.

$$Nu_{\text{film}} = 0.0071 \cdot Re_{\text{film}}^{0.6} \cdot Pr_{\text{film}}^{0.6} \cdot \left(1 + Re_{\text{vap}}^{0.5}\right) \tag{9.1}$$

The functional form of this correlation was found to compare well with other correlations developed for fluid flow over horizontal tube banks. In addition, this correlation was able to predict the experimentally measured heat transfer coefficients from the study of Bohra *et al.* (2008) reasonably well for Reynolds numbers lower than 100 and at solution concentrations comparable to those studied in the present work, even though their absorption study was conducted over larger tube diameters in a quiescent vapor. Furthermore, this correlation was able to predict the experimentally measured heat

transfer coefficients from the study of Meacham and Garimella (2004) within the limits of experimental uncertainty, even though their study was conducted on a single-pressure component test facility at conditions that may not be representative of heat pump operation.

A complementary study of binary fluid coupled heat and mass transfer in internal microscale forced-convective absorption was also conducted. A miniaturization concept using microscale heat and mass exchange was presented, consisting of an array of alternating sheets with integral microscale features, enclosed between cover plates. These microscale features on the sheet include microchannel arrays for the flow of solution, vapor, and coupling fluid, and inlet and outlet headers for distribution of these fluids into the microchannel arrays. A segmental heat and mass transfer model was developed to obtain estimates of the miniaturization possible from the use of the above geometry for a hydronically cooled absorber. The model adapted the falling-film heat and mass transfer model developed previously to the co-current convective-flow configuration, and predicted potential for the development of extremely small absorption system components. In an absorber application, a bulk of the absorption was found to occur in the initial segments of the absorber due to favorable concentration and temperature gradients at these locations. The overall system level penalties due to pressure drop in the respective streams were predicted to be low due to distribution of the flow into several parallel channels, where the flow was laminar and extended over a short length.

Test sections were fabricated for two conditions: an absorber as part of a single-effect absorption chiller of cooling capacity 2.5 kW with a co-current desorber, and an absorber as part of a single-effect waste-heat driven absorption chiller of cooling capacity 2 kW with a counter-current desorber. Photochemical etching was used to machine the microscale features on individual sheets, and diffusion bonding and vacuum brazing were used to join the sheet array. Test sections also differed in terms of the inlet header configuration used to distribute various fluid streams. These test sections were tested as a

part of their corresponding chillers, where all the absorption system components, the desorber, rectifier, condenser, evaporator, solution heat exchanger, and refrigerant pre-cooler were also designed and fabricated using similar microfabrication technologies. An absorption breadboard test facility was developed to install these components and provide the necessary fluid streams at operating conditions representative of absorption heat pump operation. The microscale forced-convective absorption test sections were tested over a range of solution and vapor flow rates, and the measured temperature, pressure, and flow rate data were analyzed to determine the state of the solution and vapor at various locations in the test loop, and calculate the relevant component duties. The absorber duty was found to range from 1.1 – 3.5 kW for the three test sections.

Because nickel plating is used to facilitate bonding of the sheet array and the end plates in both, the diffusion bonding and vacuum brazing processes, some channel blockage is expected in each of the test sections, due to flow and redistribution of this plating material at elevated temperatures. A laminar flow pressure drop analysis was conducted to estimate the amount of channel blockage for three idealized scenarios. The actual channel blockage distribution in each test section is expected to be a combination of these three scenarios. Heat and mass transfer analyses were conducted for the three test sections based on each of these channel blockage scenarios. The calculated solution heat transfer coefficients were found to range from 25.5 – 1138 W m^{-2} K^{-1}. While the heat transfer coefficient values were much lower than the predictions from the correlation developed by Shah (1979), these estimates are for the worst-case-scenario, and are highly dependent upon the assumptions used to analyze the flow and thermal paths in the absorber. Channel blockage was identified as a major issue in the operation of the absorber, leading to reductions in flow and transfer areas, and also to exacerbate two-phase flow mal-distribution. A revised sheet design was proposed to mitigate some of these problems. However, effective fabrication of system components with minimum channel blockage remains critical for the success of this technology.

Finally, a comparative assessment between the two absorption modes was conducted. Because the test sections developed for microchannel falling-film absorption and microscale forced-convective absorption were evaluated over different range of absorption duties and solution and vapor flow rates, the heat and mass transfer models developed for each configuration were used to design a representative absorber for a 10.5 kW cooling capacity chiller for residential applications. Several variants were designed for each absorption mode, and two optimized prototypes were identified for comparison among these variants based on several design, operational, and fabrication constraints. The local absorption rate and the required transfer area for complete absorption were estimated for the two modes. The vapor transport processes were found to have the least significant influence, while the solution heat transfer coefficient was found to have the most significant influence on the overall absorption process. The influence of the coupling fluid heat transfer coefficient was found to be lower in forced-convective absorption, in comparison to falling-film absorption. The microchannel falling-film absorber was found to be more efficient in transferring the same absorption duty, requiring a solution-side transfer area of 2.21 m^2, in comparison to the microscale forced-convective absorber, which required a transfer area of 8.15 m^2. Absorption in the forced-convective absorber was limited on the solution side, and doubling the solution heat transfer coefficient decreased the required transfer area for complete absorption to 3.37 m^2, i.e., a reduction of 59% The overall volume of the microscale forced-convective absorber (0.008 m^3) was found to be nearly 6 times smaller than the microchannel falling-film absorber (0.047 m^3). However, the mass of the microscale forced-convective absorber (44.2 kg) was nearly 1.6 times more than the microchannel falling-film absorber (26.1 kg). In general, the microscale forced-convective absorber was found to be suited for applications where space is at a premium, while the microchannel falling-film absorber was found to be suited for applications where component weight is critical. However, with improvement in the solution heat transfer coefficient, the microscale

forced-convective absorber can also be competitive in applications where component weight is critical. On the other hand, fabrication of microchannel falling-film absorbers is expected to be simpler than fabrication of the microscale forced-convective absorbers.

9.2. Recommendations

Ammonia-water absorption is a complex, coupled heat and mass transfer process, which strongly depends upon the operating conditions and the component geometry. The theory based, experimentally validated models developed for the coupled heat and mass transfer process in the present study have helped in improving the understanding of the ammonia-water absorption process at the microscales. While several insights were gained from this study, there are still unresolved issues in understanding the process, as well as fabricating components based on these insights. The following are some recommendations that will enhance the understanding of the absorption process, and assist in the development of compact heat and mass exchangers for miniaturized absorption heat pumps.

9.2.1. Local level measurements

The driving concentration and temperature gradients in each phase can vary significantly with changes in the operating conditions. Thus, in the present work, full absorption systems were developed to simulate realistic operating conditions at the absorber for both flow configurations. However, controlling and adjusting a full system to reach the desired operating conditions is a challenging task. As a result, only limited experimental analysis could be conducted at the local level, while maintaining operation of the absorption heat pump at the system level. More detailed measurements can be made at the local level if the absorber test sections are studied in a simpler, single-pressure test facility, with specific focus on capturing the local phenomena. Such measurements would supplement the experimental results and the models from the

present work and increase the accuracy of prediction of the entire process. The recommended local level measurements for each flow configuration are provided below.

Falling-film absorption

During the absorption experiments conducted on the microchannel falling-film absorber, while temperature measurements were taken on the solution-side at intermediate tube rows, they were only used to get an approximate gauge of the overall progression of the absorption process, and not in the eventual heat and mass transfer analyses. Due to the dynamic behavior of the solution and vapor flow, it is quite possible that the thermocouples alternately measure solution and vapor temperatures, introducing considerable uncertainty in the measured temperatures. While it is difficult to dynamically adjust the location of the thermocouple during the experiments, several thermocouples can be installed on the underside of the tubes to provide a more representative estimate of the solution temperature. Additionally, some thermocouples can be welded onto the tube surface, to measure the tube wall temperature, which in turn can be used to calculate the solution bulk temperature.

In the present study, the coupling fluid temperature was measured at only one intermediate location in the absorber tube array. A significant amount of information on the local absorption characteristics can be gained if the coupling fluid temperatures are measured at the inlet and outlet of each tube row. Headers at each end of the tube row, similar to the prototype microchannel falling-film absorber developed in Chapter 8, can be used to fabricate test sections that enable this measurement.

Forced-convective absorption

Similar to the experiments on the microchannel falling-film absorber, no temperature measurements were taken at intermediate locations in the channel array on either the solution- or the coupling-fluid side. Thermocouples can be welded onto the

channel surface at intermediate locations on both the solution and coupling fluid sheets to obtain internal temperature profiles. However, this could be a challenging task considering the small feature sizes. An alternative set of experiments can be conducted to study the local phenomena in forced-convective absorption.

In these experiments, instead of evaluating the whole absorber, only a segment of the total channel length is studied. The test section is either a short channel, or a short channel array. Solution, vapor, and coupling fluid streams can be introduced into this test section to simulate the inlet conditions of a certain segment in the forced-convective absorber. The measured outlet conditions can be used to estimate the local level absorption characteristics inside this segment. Several such segments can be assembled to form the complete length of the absorber channels. Thus, local level heat and mass transfer characteristics, as well as component level absorber performance characteristics can be studied simultaneously using such experiments. Analogous experiments should also be conducted for binary mixture phase-change processes, such as condensation, evaporation, and desorption, where the influence of high temperature glides and mass transfer resistances is critical in determining transfer rates compared to those in pure component phase change.

9.2.2. Flow visualization studies

Falling-film absorption

In the present study, a hydrodynamic model was developed for the evolution, growth, and impact of a droplet, and the subsequent spreading of the film on the tube surface. This evolution should be studied in more detail through quantitative visualization studies, where the different droplet and film characteristics such as the droplet volume, surface area, frequency, formation time, film thickness, surface area, and wetting ratio can be measured and compared with model predictions. In addition, in the development

of the hydrodynamic model, several flow mechanisms such as formation of secondary droplets and waves on the underside of tube rows were neglected, and the influence of droplet impact on subsequent droplet formation sites was ignored. These assumptions need not always be valid and thus, there is a need to quantitatively estimate the uncertainty introduced by these assumptions on the overall absorption process. The flow of solution over the tube surface was idealized as stretching of a triangle. There is a need to further study and refine this model by considering the momentum balances in the flow and the associated redistribution of the species as the film spreads on the tube surface. Furthermore, the flow (and the associated heat and mass transfer) in the Inactive region should also receive more attention. Improvement of the hydrodynamic model presented in this study, with insights from a detailed visualization study, can vastly improve the analysis of the coupled heat and mass transfer process.

Forced-convective absorption

In the present study, the flow inside the microscale channels was assumed to be in the annular flow regime. However, in reality, depending upon the channel geometry, and fluid properties and flow parameters, the flow regimes could also be in stratified, intermittent, or dispersed flow. The thickness of the film also need not be uniform around the channel, and there is a possibility of waves on the surface of the film due to shear between the vapor and solution. Thus, there is a need to conduct a detailed visualization study to identify the specific flow regimes observed during the absorption process, and quantify the relevant absorption characteristics. Insights from this study can be used to develop a detailed hydrodynamic model that can be coupled with the heat and mass transfer model developed in the present study, to develop a more rigorous model of forced-convective absorption inside microscale channels. Fluid mal-distribution was identified as a major challenge in microscale forced-convective absorption. Detailed visualization studies of the flow inside these microscale features can provide valuable

information about the distribution of the solution and mixing of vapor inside each channel. Strategies to address mal-distribution and enhance solution-vapor mixing can be developed based on such studies.

9.2.3. Computational treatments

The primary nature of this study is experimental. A complementary study can be conducted, where the governing mass, momentum, and energy conservation equations are solved to simulate the flow mechanisms, and determine the local heat and mass transfer rates during the absorption process. In this respect, the study conducted by Subramaniam and Garimella (2009) on water-LiBr absorption can be extended to the ammonia-water fluid pair, by considering the concentration and temperature gradients in the vapor phase. Such a study can further refine our understanding of the absorption process at the local level, and develop insights about possible flow features that will enhance the absorption process.

9.2.4. System level studies

In the present study, two miniaturization concepts were studied for binary mixture heat and mass exchangers. As previously discussed, these concepts can be extended to the development of other components of the absorption heat pump. While the principal objective of the present study was to study the absorber, system level studies can be conducted on the miniaturized heat pumps fabricated from these heat and mass exchanger concepts. These heat pumps can be utilized for space-conditioning (cooling or heating) or water heating. System level studies will provide the necessary insights to refine the design and operation of the heat pumps, and facilitate deployment of these technologies in the future.

9.2.5. Microscale component fabrication

In the present study, several fabrication challenges were faced in the development of the microscale forced-convective absorption test sections. Thus, there is a need to develop a better understanding of the fabrication process, through several fabrication trials. Trials must be conducted to determine the optimal thickness of the nickel alloy plating and the temperature schedules and fixturing that can successfully bond the sheets, but not cause channel blockage. Also, trials must be conducted to determine the optimal channel geometry and pitch that can successfully fabricated. Also, studies must be conducted to optimize the fabrication process, and the required number of steps to facilitate inexpensive mass production of these components, in eventual field application.

APPENDIX A. AMMONIA-WATER MIXTURE PROPERTIES

A.1. Thermodynamic properties

All the thermodynamic properties of ammonia-water mixtures in both liquid and vapor phases were obtained from the *Engineering Equation Solver* software (Klein, 2011). Properties in this software platform are calculated from the correlations provided by Ibrahim and Klein (1993). Separate equations are used to determine the individual pure component properties, and combined to determine the mixture properties. In the work of Ibrahim and Klein (1993), for the vapor phase, the mixture is assumed to behave as an ideal gas, while for the liquid phase, the excess Gibbs energy is used to account for the departure from the ideal solution behavior. The Gibbs free energy of a fluid can be obtained using the following equation.

$$G = h_o - T \cdot s_o + \int_{T_o}^{T} Cp \cdot dT - \int_{P_o}^{P} v \cdot dP - \int_{T_o}^{T} \frac{Cp}{T} \cdot dT \tag{A.1}$$

In the above equation, empirical correlations developed by Ziegler and Trepp (1984) were used to determine the specific volume (v) and the specific heat capacity (Cp) as a function of temperature (T) and pressure (P). For the liquid phase, the empirical correlations were of the following form.

$$v_{liq} = a_1 + a_2 \cdot P + a_3 \cdot T + a_4 \cdot T^2 \tag{A.2}$$

$$Cp_{liq} = b_1 + b_2 \cdot T + b_3 \cdot T^2 \tag{A.3}$$

For the vapor phase, the empirical correlations were of the following form.

$$v_{vap} = \frac{R \cdot T}{P} + c_1 + \frac{c_2}{T^3} + c_3 \cdot T^{11} + c_4 \cdot \frac{P^2}{T^{11}} \tag{A.4}$$

$$Cp_{vap} = d_1 + d_2 \cdot T + d_3 \cdot T^2 \tag{A.5}$$

The molar specific enthalpy, entropy, and volume can be obtained from the Gibbs free energy as follows:

$$h = -R_{\text{gas}} \cdot T_{\text{B}} \cdot T_{\text{r}}^2 \cdot \left[\frac{\partial}{\partial T_{\text{r}}} \left(\frac{G_{\text{r}}}{T_{\text{r}}} \right) \right]_{P_{\text{r}}} \tag{A.6}$$

$$s = -R_{\text{gas}} \cdot \left[\frac{\partial G_{\text{r}}}{\partial T_{\text{r}}} \right]_{P_{\text{r}}} \tag{A.7}$$

$$v = -\frac{R_{\text{gas}} \cdot T_{\text{B}}}{P_B} \cdot \left[\frac{\partial G_{\text{r}}}{\partial P_{\text{r}}} \right]_{T_{\text{r}}} \tag{A.8}$$

In the above equations, T_{r}, P_{r}, G_{r}, h_{r}, s_{r}, v_{r} represent the reduced parameters, according to the reference state T_{B} = 100 K, P_{B} = 10 bar. R_{gas} is the universal gas constant and is equal to 8.314 kJ kmol^{-1} K^{-1}. Once the properties of the individual components are known, mixing rules are applied to determine the mixture properties. Because the ideal gas assumption is made for the vapor phase, a mass fraction weighted average is used to estimate the mixture properties. Thus, the relevant properties are determined using the following relations.

$$h_{\text{vap,NH3-H2O}} = x_{\text{vap}} \cdot h_{\text{vap,NH3}} + \left(1 - x_{\text{vap}}\right) \cdot h_{\text{vap,H2O}} \tag{A.9}$$

$$s_{\text{vap,NH3-H2O}} = x_{\text{vap}} \cdot s_{\text{vap,NH3}} + \left(1 - x_{\text{vap}}\right) \cdot s_{\text{vap,H2O}} \tag{A.10}$$

$$v_{\text{vap,NH3-H2O}} = v_{\text{vap}} \cdot h_{\text{vap,NH3}} + \left(1 - v_{\text{vap}}\right) \cdot h_{\text{vap,H2O}} \tag{A.11}$$

Because the ideal solution assumption cannot be made for the liquid phase, the excess Gibbs energy is calculated to account for the deviation from ideal conditions. Ibrahim and Klein (1993) used the equation presented by Ziegler and Trepp (1984), but refined the empirical coefficients by including data from Gillespie (1987).

$$G_{\text{liq,excess}} = \left(F_1 + F_2 \cdot \left(2 \cdot x_{\text{liq}} - 1\right) + F_3 \cdot \left(2 \cdot x_{\text{liq}} - 1\right)^2 \right) \cdot \left(1 - x_{\text{sol}}\right) \tag{A.12}$$

The coefficients, F_1, F_2, and F_3 were in turn calculated from the reduced pressure and temperature using correlations of the following form.

$$F_1 = E_1 + E_1 \cdot P_r + \left(E_3 + E_4 \cdot P_r\right) \cdot T_r + \frac{E_5}{T_r} + \frac{E_6}{T_r^2} \tag{A.13}$$

$$F_2 = E_7 + E_8 \cdot P_r + \left(E_9 + E_{10} \cdot P_r\right) \cdot T_r + \frac{E_{11}}{T_r} + \frac{E_{12}}{T_r^2} \tag{A.14}$$

$$F_3 = E_{13} + E_{14} \cdot P_r + \frac{E_{15}}{T_r} + \frac{E_{16}}{T_r^2} \tag{A.15}$$

The excess Gibbs energy calculated from the above equations is substituted in Eqs. A.6-A.8, and the excess specific enthalpy, entropy, and volume, respectively, are calculated. The relevant mixture properties in the liquid phase can then be determined using the following equations.

$$h_{\text{liq,NH3-H2O}} = x_{\text{liq}} \cdot h_{\text{liq,NH3}} + \left(1 - x_{\text{liq}}\right) \cdot h_{\text{liq,H2O}} + h_{\text{liq,excess}} \tag{A.16}$$

$$s_{\text{liq,NH3-H2O}} = x_{\text{liq}} \cdot s_{\text{liq,NH3}} + \left(1 - x_{\text{liq}}\right) \cdot s_{\text{liq,H2O}} + s_{\text{liq,excess}} \tag{A.17}$$

$$v_{\text{liq,NH3-H2O}} = v_{\text{liq}} \cdot h_{\text{liq,NH3}} + \left(1 - v_{\text{liq}}\right) \cdot h_{\text{liq,H2O}} + h_{\text{liq,excess}} \tag{A.18}$$

The above correlations are valid over a pressure range of 20 – 11000 kPa, and a temperature range of -43 – 327^{o}C. All the experiments conducted in the present study lie within this range.

A.2. Transport properties

A.2.1. Vapor phase

Similar to the thermodynamic properties, separate equations are used to determine the individual pure component transport properties, and combined to determine the mixture transport properties. The transport properties for pure components are calculated using the Chapman-Enskog kinetic theory (Mills, 1995), and for the ammonia-water mixtures using the mixture rules of Wilke (1950). The validity of the properties estimated using this methodology, and the associated uncertainties have been discussed in detail by Bohra (2007).

Pure components

The viscosities of ammonia and water are determined using a Lennard-Jones potential model using the following equation.

$$\mu_{\text{vap}} = 2.67\times10^{-6}\cdot\frac{\sqrt{M\cdot T_{\text{vap}}}}{\sigma_{\text{vap}}^{2}\cdot\Omega_{\mu,\text{vap}}} \tag{A.19}$$

In the above equation, σ_{vap} is the collision diameter at zero potential energy expressed in angstroms, $\Omega_{\mu,\text{vap}}$ is the collision integral which is a function of temperature, and the maximum energy of attraction. T_{vap} is the temperature in K of each component in the vapor phase, and M is the molecular mass.

The thermal conductivities of ammonia and water are calculated using the relationship between the thermal conductivity and the viscosity of monatomic gases, and a modified Eucken correction to account for the rotation and vibrational modes caused by nonlinearity of polyatomic ammonia and water vapor.

$$k_{\text{vap,translational}} = \frac{5}{2}\cdot Cv_{\text{vap}}\cdot\mu_{\text{vap}} \tag{A.20}$$

$$k_{\text{vap}} = k_{\text{vap,translational}} + 1.32\cdot\left(Cp_{\text{vap}} - \frac{5}{2}\cdot\frac{R_{\text{gas}}}{M}\right)\cdot\mu_{\text{vap}} \tag{A.21}$$

In the above equations, $Cv_{\text{vap}} = \frac{3}{2}\cdot\frac{R_{\text{gas}}}{M}$, $Cp_{\text{vap}} = (5+N_{\text{r}})\cdot\left(\frac{1}{2}\cdot\frac{R_{\text{gas}}}{M}\right)$, and N_{r} is the rotational degrees of freedom for each molecule. For both ammonia and water molecules, there are three degrees of freedom.

Mixtures

The mixtures rules of Wilke (1950) are used to determine the viscosity and thermal conductivity of the ammonia-water mixture vapor as follows:

$$\mu_{12,\text{vap}} = \sum_{\text{i=1}}^{2}\frac{x_{\text{i,vap}}\cdot\mu_{\text{i,vap}}}{\sum_{\text{j=1}}^{2}x_{\text{j,vap}}\cdot\Phi_{\text{ij,vap}}} \tag{A.22}$$

$$k_{12,vap} = \sum_{i=1}^{2} \frac{x_{i,vap} \cdot k_{i,vap}}{\sum_{j=1}^{2} x_{j,vap} \cdot \Phi_{ij,vap}} \tag{A.23}$$

$$\Phi_{ij,vap} = \frac{\left[1 + \left(\frac{\mu_{i,vap}}{\mu_{j,vap}}\right)^{1/2} \cdot \left(\frac{M_j}{M_i}\right)^{1/4}\right]^2}{\sqrt{8} \cdot \left[1 + \left(\frac{M_i}{M_j}\right)\right]^{1/2}} \tag{A.24}$$

In the above equations, 1 and 2 refer to ammonia and water, respectively. The vapor-phase binary diffusion coefficient is calculated using the following equation.

$$D_{12,vap} = 1.86 \times 10^{-7} \cdot \frac{\sqrt{T_{vap}^3 \cdot \left(\frac{1}{M_1} + \frac{1}{M_2}\right)}}{\sigma_{12,vap}^2 \cdot \Omega_{D,vap} \cdot P_{vap}} \tag{A.25}$$

$$\sigma_{12,vap} = \frac{1}{2} \cdot \left(\sigma_{1,vap} + \sigma_{2,vap}\right) \tag{A.26}$$

$$\varepsilon_{12,vap} = \sqrt{\varepsilon_{1,vap} \cdot \varepsilon_{2,vap}} \tag{A.27}$$

In the above equation, P_{vap} is the vapor pressure expressed in atmospheres, $\Omega_{D,vap}$ is the collision integral for diffusion (which is different from $\Omega_{\mu,vap}$ calculated previously.) Finally, the specific heat of the ammonia-water mixture can be calculated from the enthalpy change observed due to a temperature change of 1°C, at the temperature of interest, and at the given pressure and concentration.

A.2.2. Liquid phase

Herold et al. (1996) provide the liquid-phase viscosity, thermal conductivity, and surface tension data for ammonia-water mixtures in graphical form. Using these data, empirical correlations as a function of solution temperature and concentration are developed (Meacham, 2002). The liquid-phase viscosity (expressed in cP) is calculated using the following equations, where T_{sol} is expressed in °F.

For T_{sol} < 145°F (63°C)

$$\mu_{sol} = 2.5210 + 1.0675 \cdot x_{sol} + 2.2685 \times 10^{-3} \cdot T_{sol} - 0.0322 \cdot (1 - x_{sol}) \cdot T_{sol} - 5.2229 \cdot x_{sol}^2 + 112.90 \times 10^{-6} \cdot (1 - x_{sol})^2 \cdot T_{sol}^2 - 0.8639 \cdot x_{sol}^3 + 2.4387 \cdot x_{sol}^4 \quad \text{(A.28)}$$

For 145°F (63°C) < T_{sol} < 195°F (91°C)

$$\mu_{sol} = 1.0816 - 0.2202 \cdot x_{sol} - 2.1732 \times 10^{-3} \cdot T_{sol} - 1.9322 \times 10^{-3} \cdot (1 - x_{sol}) \cdot T_{sol} - 0.3905 \cdot x_{sol}^2 \quad \text{(A.29)}$$

For T_{sol} > 195°F (91°C)

$$\mu_{sol} = 0.5279 + 0.1654 \cdot x_{sol} - 1.8905 \times 10^{-3} \cdot T_{sol} + 734.47 \times 10^{-6} \cdot (1 - x_{sol}) \cdot T_{sol} \quad \text{(A.30)}$$

The viscosity of the solution can be expressed in SI units (kg m^{-1} s^{-1}) using the following equation.

$$\mu_{sol,SI} = 0.001 \cdot \mu_{sol} \quad \text{(A.31)}$$

The liquid-phase thermal conductivity of ammonia-water (expressed in W m^{-1} K^{-1}) is calculated using the following equation, where T_{sol} is expressed in °C.

$$k_{sol} = 0.5727 + 1.7021 \times 10^{-3} \cdot T_{sol} - 0.0541 \cdot x_{sol} - 5.8359 \times 10^{-6} \cdot T_{sol}^2 + 8.49 \times 10^{-9} \cdot x_{sol}^2 - 3.341 \times 10^{-3} \cdot T_{sol} \cdot x_{sol} \quad \text{(A.32)}$$

The liquid-phase surface tension (expressed in dyne cm^{-2}) can be calculated using the following equation, where T_{sol} is expressed in °F.

$$\sigma_{sol} = 1.1211 \times 10^{-6} \cdot T_{sol}^3 - 1.1955 \times 10^{-3} \cdot T_{sol}^2 + 0.2970413 \cdot T_{sol} - 6.2041 \times 10^{1} \cdot x_{sol}^3 + 103.3571 \cdot x_{sol}^2 - 4.8571 \times 10^{1} \cdot x_{sol} + 39.92207 + 1.9450 \times 10^{-4} \cdot x_{sol}^2 \cdot T_{sol}^2 + 0.1851776 \cdot x_{sol}^2 \cdot T_{sol} + 1.40568 \times 10^{-3} \cdot x_{sol} \cdot T_{sol}^2 - 7.0072 \times 10^{-1} \cdot x_{sol} \cdot T_{sol} \quad \text{(A.33)}$$

The surface tension can be expressed in SI units (N m^{-2}) using the following equation.

$$\sigma_{sol,SI} = 9.7254 \times 10^{-4} \cdot \sigma_{sol} \quad \text{(A.34)}$$

Finally, the ammonia-water binary diffusion coefficient (expressed in $m^2\ s^{-1}$) in the liquid-phase is obtained using the following equation suggested by Frank *et al.* (1996b).

$$D_{\mathrm{aw,sol}} = (1.65 + 2.47 \cdot x_{\mathrm{sol}}) \times 10^{-6} \cdot e^{\left(\frac{-16600}{R \cdot (T_{\mathrm{sol}} + 273.15)} \right)} \tag{A.35}$$

In the above equation, T_{sol} is expressed in ^{o}C.

APPENDIX B. UNCERTAINTY CALCULATIONS

An uncertainty propagation analysis was conducted on the data obtained in this study on the falling-film absorber. The parameters of interest are the concentrations of the various fluid streams, the absorber duty, and the solution heat transfer coefficient. The calculation of these parameters is affected by errors in estimation of various temperatures, pressures, and flow rates. Additionally, to determine the solution heat transfer coefficient, correlations were used to estimate the coupling fluid and vapor Nusselt number, which can also be sources of error. Thus, the effect of the following uncertainties is accounted for in the uncertainty calculations for the parameters of interest:

- *Working fluid side*: Pressures and temperatures at the rectifier vapor outlet and reflux, separator vapor and solution outlet, separator solution inlet, absorber vapor and dilute solution inlet, and the absorber concentrated solution outlet. Flow rates of the dilute and concentrated solution, and the refrigerant streams.
- *Coupling fluid side:* Inlet and outlet temperatures, and coupling fluid flow rate.
- *Correlations:* Coupling fluid and vapor Nusselt numbers.

As discussed in Chapter 3, absolute pressure transducers and T-type thermocouples were used to measure the pressures and temperatures, respectively, at various locations around the test loop. The flow rates of the dilute and concentrated solution, and the refrigerant streams were measured using Coriolis flow meters. The relevant uncertainties associated with of each of these instruments are also tabulated in Chapter 3.

In the calculation of the error propagated by these uncertainties, the following methodology is adopted. Consider a calculated parameter, x, which is affected by uncertainties in measurements of several other parameters (a, b, c, d … etc.)

$$x = f\left(a,b,c,d,...\right) \tag{B.1}$$

The total uncertainty associated with the calculation of parameter, x, is given by the following equation.

$$U_x^2 = \left(\frac{\partial x}{\partial a}\cdot U_a\right)^2 + \left(\frac{\partial x}{\partial b}\cdot U_b\right)^2 + \left(\frac{\partial x}{\partial c}\cdot U_c\right)^2 + \left(\frac{\partial x}{\partial d}\cdot U_d\right)^2 + ... \tag{B.2}$$

In the above equation, U_a, U_b, U_c, and U_d .. are the uncertainties associated with a, b, c, d ….

A total of 22 measured parameters were considered to determine the uncertainties in this study. Table B.1 shows a summary of the uncertainties associated with each of these parameters for the representative test condition. Additionally, a conservative uncertainty of ±25% was applied to the vapor and coupling fluid Nusselt number calculations. These uncertainties were used to calculate the uncertainties associated with the various solution and vapor concentrations, absorber duty, and solution heat transfer coefficient. The error propagation method by Taylor and Kuyatt (1993) implemented in *Engineering Equation Solver* software (Klein, 2011) was used to determine these uncertainties.

Table B.1 List of parameters included in uncertainty analysis

Parameter	Measured/calculated value ± uncertainty
Pressures	
$P_{Abs,sol,in}$ (kPa)	537.3 ± 1.54
$P_{Abs,sol,out}$ (kPa)	534.1 ± 2.59
$P_{Abs,vap,in}$ (kPa)	540.5 ± 1.54
$P_{Cond,ref,in}$(kPa)	1093 ± 1.54
P_{Reflux}(kPa)	1109 ± 5.17
$P_{Sep,sol,in}$ (kPa)	1121 ± 1.21
$P_{Sep,sol,out}$ (kPa)	1118 ± 5.17
Temperatures	
$T_{Abs,sol,in}$ (^{o}C)	61.50 ± 0.25
$T_{Abs,sol,out}$ (^{o}C)	37.84 ± 0.25
$T_{Abs,vap,in}$ (^{o}C)	8.12 ± 0.25
$T_{abs,CF,in}$ (^{o}C)	29.56 ± 0.25
$T_{Abs,CF,out}$ (^{o}C)	38.87 ± 0.25
$T_{Abs,CF,mid}$ (^{o}C)	35.99 ± 0.25
$T_{Rect,vap,out}$ (^{o}C)	61.53 ± 0.25
T_{Reflux} (^{o}C)	37.73 ± 0.25
$T_{Sep,sol,in}$ (^{o}C)	103.1 ± 0.25
$T_{Sep,sol,out}$ (^{o}C)	98.59 ± 0.25
$T_{Sep,vap,out}$ (^{o}C)	100.90 ± 0.25
Flow rates	
$\dot{m}_{Conc}\left(\mathrm{kg\,s^{-1}}\right)$	0.0189 ± 0.000019
$\dot{m}_{Dil}\left(\mathrm{kg\,s^{-1}}\right)$	0.0154 ± 0.000015

Table B.1 Continued...

Parameter	Measured/calculated value ± uncertainty
$\dot{m}_{\text{Ref}}\left(\text{kg s}^{-1}\right)$	0.0030 ± 0.000003
$\dot{m}_{\text{Abs,CF}}\left(\text{kg s}^{-1}\right)$	0.1375 ± 0.00068
Correlations	
Nu_{vap}	2.605 ± 0.651
α_{CF} (W m^{-2} K^{-1})	6519 ± 1630

Table B.2 shows a summary of the uncertainties in the main parameters of interest for the representative test condition. In addition, the partial derivatives and percent contribution to the total uncertainty from the respective measured/calculated parameters are also reported. As can be seen from this table, the biggest contributor to the uncertainty in calculation of the solution heat transfer coefficient is the uncertainty associated with the coupling fluid heat transfer coefficient. The uncertainty associated with the coupling fluid temperature measurement is the highest contributor to the uncertainty associated with the absorber duty. Finally, uncertainties in temperature measurements were found to have a higher contribution to the uncertainty associated with various fluid stream concentrations, in comparison with the uncertainty in the pressure measurements.

Table B.2 Summary of uncertainties of main parameters of interest

Partial derivative	% Uncertainty (of total)
$x_{\text{Ref}} = 0.9937 \pm 0.0001213$ (± 0.012%)	
$\frac{\partial x_{\text{Rect,vap,out}}}{\partial P_{\text{Cond,in}}} = 0.00007305$	1.84%
$\frac{\partial x_{\text{Rect,vap,out}}}{\partial T_{\text{Rect,vap,out}}} = -0.0004806$	98.16%
$x_{\text{Reflux}} = 0.7647 \pm 0.004719$ (± 0.62%)	
$\frac{\partial x_{\text{Reflux}}}{\partial P_{\text{Reflux}}} = 0.003479$	30.56%
$\frac{\partial x_{\text{Rect,vap,out}}}{\partial T_{\text{Rect,vap,out}}} = -0.01573$	69.44%
$x_{\text{Sep,sol,out}} = 0.3435 \pm 0.001237$ (± 0.36%)	
$\frac{\partial x_{\text{Sep,sol,out}}}{\partial P_{\text{Sep,sol,out}}} = 0.001209$	13.42%
$\frac{\partial x_{\text{Sep,sol,out}}}{\partial T_{\text{Sep,sol,out}}} = -0.004605$	86.58%
$x_{\text{Sep,vap,out}} = 0.9370 \pm 0.0007638$ (± 0.08%)	
$\frac{\partial x_{\text{Sep,vap,out}}}{\partial P_{\text{Sep,vap,out}}} = 0.000526$	6.67%
$\frac{\partial x_{\text{Sep,vap,out}}}{\partial T_{\text{Sep,vap,out}}} = -0.002952$	93.33%
$\dot{m}_{\text{Sep,vap,out}} = 0.0040 \pm 0.00003273\,\text{kg s}^{-1}$ (±0.82%)	
$\frac{\partial \dot{m}_{\text{Sep,vap,out}}}{\partial P_{\text{Sep,vap,out}}} = -0.00001221$	1.96%

Table B.2 Continued...

$\frac{\partial \dot{m}_{\text{Sep,vap,out}}}{\partial P_{\text{Reflux}}} = 0.00002$	21%
$\frac{\partial \dot{m}_{\text{Sep,vap,out}}}{\partial P_{\text{Cond,in}}} = 0.000001276$	0.01%
$\frac{\partial \dot{m}_{\text{Sep,vap,out}}}{\partial \dot{m}_{\text{Ref}}} = 0.01005$	1.49%
$\frac{\partial \dot{m}_{\text{Sep,vap,out}}}{\partial T_{\text{Reflux}}} = -0.00009045$	47.73%
$\frac{\partial \dot{m}_{\text{Sep,vap,out}}}{\partial T_{\text{Sep,vap,out}}} = 0.00006853$	27.40%
$\frac{\partial \dot{m}_{\text{Sep,vap,out}}}{\partial T_{\text{Rect,vap,out}}} = -0.000008396$	0.41%
$\dot{m}_{\text{Reflux}} = 0.0010 \pm 0.0000325\,\text{kg s}^{-1}\,(\pm 3.28\%)$	
$\frac{\partial \dot{m}_{\text{Reflux}}}{\partial P_{\text{Sep,vap,out}}} = -0.00001221$	1.99%
$\frac{\partial \dot{m}_{\text{Reflux}}}{\partial P_{\text{Reflux}}} = 0.00002$	21.30%
$\frac{\partial \dot{m}_{\text{Reflux}}}{\partial P_{\text{Cond,in}}} = 0.000001276$	0.01%
$\frac{\partial \dot{m}_{\text{Reflux}}}{\partial \dot{m}_{\text{Ref}}} = 0.02488$	0.09%
$\frac{\partial \dot{m}_{\text{Reflux}}}{\partial T_{\text{Reflux}}} = -0.00009045$	48.41%
$\frac{\partial \dot{m}_{\text{Reflux}}}{\partial T_{\text{Sep,vap,out}}} = 0.00006853$	27.79%

Table B.2 Continued...

$\frac{\partial \dot{m}_{\text{Reflux}}}{\partial T_{\text{Rect,vap,out}}} = -0.000008396$	0.42%
$\dot{m}_{\text{Sep,sol,out}} = 0.01445 \pm 0.0000360\,\text{kg s}^{-1}\ (\pm 2.49\%)$	
$\frac{\partial \dot{m}_{\text{Sep,sol,out}}}{\partial P_{\text{Sep,sol,out}}} = 0.00001221$	1.62%
$\frac{\partial \dot{m}_{\text{Sep,sol,out}}}{\partial P_{\text{Reflux}}} = -0.00002$	17.38%
$\frac{\partial \dot{m}_{\text{Sep,sol,out}}}{\partial P_{\text{Cond,in}}} = -0.000001276$	0.01%
$\frac{\partial \dot{m}_{\text{Sep,sol,out}}}{\partial \dot{m}_{\text{Ref}}} = -0.02488$	0.08%
$\frac{\partial \dot{m}_{\text{Sep,sol,out}}}{\partial \dot{m}_{\text{Dil}}} = 0.00756$	18.41%
$\frac{\partial \dot{m}_{\text{Sep,sol,out}}}{\partial T_{\text{Reflux}}} = 0.00009045$	39.50%
$\frac{\partial \dot{m}_{\text{Sep,sol,out}}}{\partial T_{\text{Sep,vap,out}}} = -0.00006853$	22.67%
$\frac{\partial \dot{m}_{\text{Reflux}}}{\partial T_{\text{Rect,vap,out}}} = 0.000008396$	0.34%
$x_{\text{Dil}} = 0.3705 \pm 0.001601\ (\pm 0.43\%)$	
$\frac{\partial x_{\text{Dil}}}{\partial P_{\text{Sep,sol,out}}} = 0.000798$	3.49%
$\frac{\partial x_{\text{Dil}}}{\partial P_{\text{Reflux}}} = -0.000769$	12.98%
$\frac{\partial x_{\text{Ref}}}{\partial P_{\text{Cond,in}}} = 0.00003482$	0.00%

Table B.2 Continued...

$\frac{\partial x_{\text{Dil}}}{\partial \dot{m}_{\text{Ref}}} = 0.06789$	0.03%
$\frac{\partial x_{\text{Dil}}}{\partial \dot{m}_{\text{Dil}}} = -0.01324$	0.03%
$\frac{\partial x_{\text{Dil}}}{\partial T_{\text{Reflux}}} = -0.003478$	29.51%
$\frac{\partial x_{\text{Dil}}}{\partial T_{\text{Sep,vap,out}}} = 0.00187$	8.53%
$\frac{\partial x_{\text{Dil}}}{\partial T_{\text{Rect,vap,out}}} = -0.0002291$	0.13%
$\frac{\partial x_{\text{Dil}}}{\partial T_{\text{Sep,sol,out}}} = -0.004309$	45.30%
$x_{\text{Conc}} = 0.4611 \pm 0.001427$ ($\pm$ 0.43%)	
$\frac{\partial x_{\text{Conc}}}{\partial P_{\text{Sep,sol,out}}} = 0.000652$	2.94%
$\frac{\partial x_{\text{Dil}}}{\partial P_{\text{Reflux}}} = 0.0006284$	10.91%
$\frac{\partial x_{\text{Conc}}}{\partial \dot{m}_{\text{Ref}}} = 0.4531$	1.60%
$\frac{\partial x_{\text{Conc}}}{\partial \dot{m}_{\text{Dil}}} = 0.1374$	3.87%
$\frac{\partial x_{\text{Conc}}}{\partial \dot{m}_{\text{Conc}}} = -0.1845$	10.44%
$\frac{\partial x_{\text{Conc}}}{\partial T_{\text{Reflux}}} = -0.002842$	24.79%
$\frac{\partial x_{\text{Conc}}}{\partial T_{\text{Sep,vap,out}}} = 0.001528$	7.17%

Table B.2 Continued...

$\frac{\partial x_{\text{Conc}}}{\partial T_{\text{Rect,vap,out}}} = -0.0002638$	0.21%
$\frac{\partial x_{\text{Dil}}}{\partial T_{\text{Sep,sol,out}}} = -0.003521$	38.06%
Q_{Abs} = 5.477 ± 0.1065 (± 1.94%)	
$\frac{\partial Q_{\text{Abs}}}{\partial P_{\text{Abs,sol,out}}} = -0.00003517$	0.00%
$\frac{\partial Q_{\text{Abs}}}{\partial P_{\text{Abs,vap,in}}} = -0.03507$	0.55%
$\frac{\partial Q_{\text{Abs}}}{\partial P_{\text{Cond,in}}} = 0.001992$	0.00%
$\frac{\partial Q_{\text{Abs}}}{\partial P_{\text{Reflux}}} = -0.001129$	0.01%
$\frac{\partial Q_{\text{Abs}}}{\partial P_{\text{Sep,sol,out}}} = -0.001172$	0.00%
$\frac{\partial Q_{\text{Abs}}}{\partial \dot{m}_{\text{Ref}}} = 4.588$	0.03%
$\frac{\partial Q_{\text{Abs}}}{\partial \dot{m}_{\text{Dil}}} = 0.3207$	0.00%
$\frac{\partial Q_{\text{Abs}}}{\partial \dot{m}_{\text{Conc}}} = 0.1284$	0.00%
$\frac{\partial Q_{\text{Abs}}}{\partial \dot{m}_{\text{Abs,CF}}} = 1.218$	1.58%
$\frac{\partial Q_{\text{Abs}}}{\partial T_{\text{Abs,CF,in}}} = -0.2873$	45.46%
$\frac{\partial Q_{\text{Abs}}}{\partial T_{\text{Abs,CF,out}}} = 0.2868$	45.29%

Table B.2 Continued...

$\frac{\partial Q_{\text{Abs}}}{\partial T_{\text{Abs,sol,in}}} = 0.0341$	0.64%
$\frac{\partial Q_{\text{Abs}}}{\partial T_{\text{Abs,sol,out}}} = -0.04208$	0.98%
$\frac{\partial Q_{\text{Abs}}}{\partial T_{\text{Abs,vap,in}}} = 0.09842$	5.33%
$\frac{\partial Q_{\text{Abs}}}{\partial T_{\text{Rect,vap,out}}} = -0.0131$	0.09%
$\frac{\partial Q_{\text{Abs}}}{\partial T_{\text{Reflux}}} = 0.005108$	0.01%
$\frac{\partial Q_{\text{Abs}}}{\partial T_{\text{Sep,sol,out}}} = 0.006329$	0.02%
$\frac{\partial Q_{\text{Abs}}}{\partial T_{\text{Sep,vap,out}}} = -0.002746$	0.00%
α_{sol} = 1906 ± 186.1 (± 9.76%)	
$\frac{\partial \alpha_{\text{sol}}}{\partial P_{\text{Abs,sol,out}}} = -10.84$	0.05%
$\frac{\partial \alpha_{\text{sol}}}{\partial P_{\text{Abs,vap,in}}} = -10.59$	0.02%
$\frac{\partial \alpha_{\text{sol}}}{\partial P_{\text{Cond,in}}} = 0.6084$	0.00%
$\frac{\partial \alpha_{\text{sol}}}{\partial P_{\text{Reflux}}} = 5.913$	0.06%
$\frac{\partial \alpha_{\text{sol}}}{\partial P_{\text{Sep,sol,out}}} = 6.137$	0.06%
$\frac{\partial \alpha_{\text{sol}}}{\partial \dot{m}_{\text{Ref}}} = 3930$	0.01%

Table B.2 Continued...

$\frac{\partial \alpha_{sol}}{\partial \dot{m}_{Conc}} = -1361$	0.03%
$\frac{\partial \alpha_{sol}}{\partial \dot{m}_{Abs,CF}} = -212.2$	0.02%
$\frac{\partial \alpha_{Abs}}{\partial T_{Abs,CF,in}} = -163.1$	4.80%
$\frac{\partial \alpha_{sol}}{\partial T_{Abs,CF,mid}} = 318.5$	18.31%
$\frac{\partial \alpha_{sol}}{\partial T_{Abs,sol,out}} = -160.1$	4.62%
$\frac{\partial \alpha_{Abs}}{\partial T_{Abs,vap,in}} = 3.971$	0.00%
$\frac{\partial \alpha_{sol}}{\partial T_{Rect,vap,out}} = -3.89$	0.00%
$\frac{\partial \alpha_{sol}}{\partial T_{Reflux}} = -26.74$	0.13%
$\frac{\partial \alpha_{sol}}{\partial T_{Sep,sol,out}} = -33.12$	0.20%
$\frac{\partial \alpha_{sol}}{\partial T_{Sep,vap,out}} = 14.38$	0.04%
$\frac{\partial \alpha_{sol}}{\partial \alpha_{CF}} = -629.9$	71.63
$\frac{\partial \alpha_{sol}}{\partial Nu_{vap}} = -13.26$	0.03%

APPENDIX C. DROPLET AND FILM TRANSFER AREAS

C.1. Droplet instantaneous and average surface area

C.1.1. Hemispherical section

Fig. C.1 shows a schematic of the hemispherical section of the droplet. The rate of change of volume of the hemispherical section is given by the following equation.

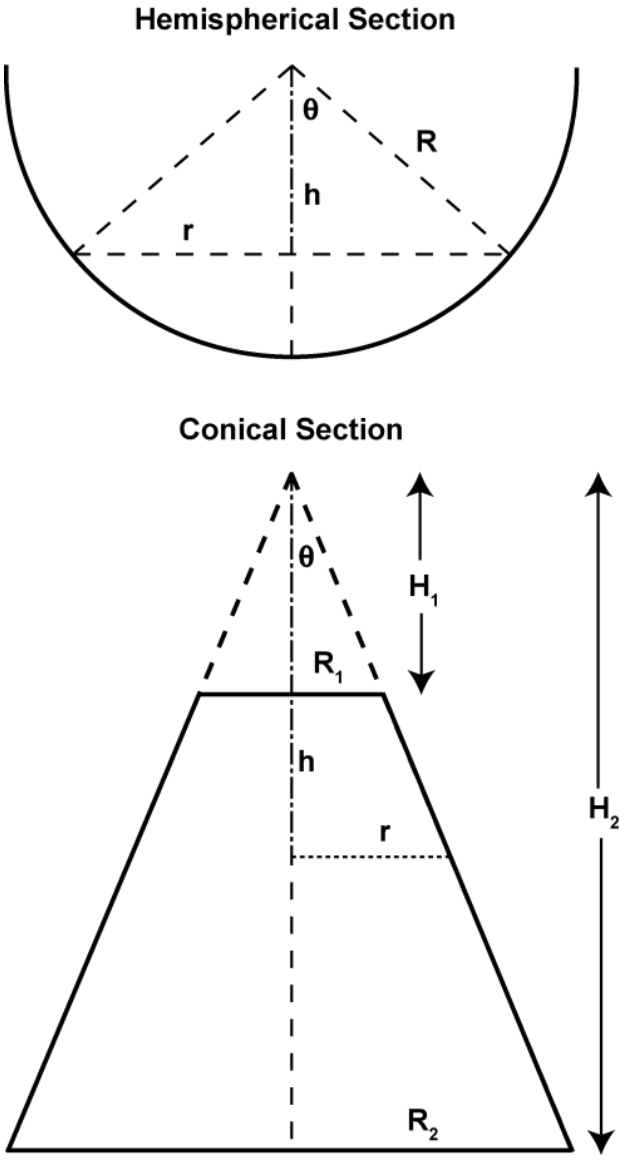

Fig. C.1 Schematic of hemispherical and conical sections of the droplet

$$\frac{dV_{\text{hem}}}{dt} = \pi \cdot \left(R^2 - h^2\right) \cdot \frac{-dh}{dt} = \dot{V} \tag{C.1}$$

In the above equation, h is the vertical distance below the center of the hemisphere, and R is the radius of the droplet. Because it is assumed that the droplet grows at a uniform rate, the right hand side of the above equation is a constant.

The infinitesimal surface area of a "ring" in the hemispherical section, a distance "h" below the center is calculated using the following equation.

$$dA_{\text{hem}} = 2 \cdot \pi \cdot r \cdot \frac{dh}{\sin\theta} = 2 \cdot \pi \cdot r \cdot \frac{dh}{\left(r/R\right)} = 2 \cdot \pi \cdot R \cdot dh \tag{C.2}$$

Integrating the above equation with respect to h, with the boundary condition that $A_{\text{hem}} = 0$ at $h = R$, results in the following equation.

$$A_{\text{hem}}\left(h\right) = \int_{R}^{h} 2 \cdot \pi \cdot R \cdot dh = 2 \cdot \pi \cdot R \cdot \left(R - h\right) \tag{C.3}$$

This is the surface area of a spherical segment located at a height, h, below the center of the hemisphere. When $h = 0$, the hemisphere is fully formed, and the resulting area is the surface area of the hemisphere.

The average transfer area over the evolution time of the hemispherical section can be calculated by using the following equation.

$$\overline{A}_{\text{hem}} = \frac{\int_{0}^{t_{\text{hem}}} A_{\text{hem}} \cdot dt}{t_{\text{hem}}} \tag{C.4}$$

Because A_{hem} is known in terms of h, Eq. C.1 can be used to express dt in terms of dh as follows:

$$dt = \frac{-\pi \cdot \left(R^2 - h^2\right) \cdot dh}{\dot{V}} \tag{C.5}$$

The expression for *dt* from the above equation can be substituted in Eq. C.4 to determine the average transfer area over the evolution time of the hemispherical section as follows:

$$\begin{aligned}\overline{A}_{\text{hem}} &= \frac{\int_{R}^{0} 2\cdot\pi\cdot R\cdot\left(R-h\right)\cdot\left(-\pi\cdot\left(R^2-h^2\right)\right)\cdot dh}{\dot{V}\cdot t_{\text{hem}}} \\ &= \frac{2\cdot\pi^2\cdot R}{\left(2/3\right)\cdot\pi\cdot R^3}\cdot\int_{0}^{R}\left(R^3-R^2h-Rh^2+h^3\right)\cdot dh \\ &= \frac{5}{4}\cdot\pi\cdot R^2\end{aligned} \tag{C.6}$$

It should be noted that in the above equation, the product $\dot{V}\cdot t_{\text{hem}}$ is the total volume of the hemispherical section.

C.1.2. Conical section

Fig. C.1 also shows a schematic of the conical section. The volume of the conical section at an instant of time is calculated using the following equation.

$$V_{\text{cone}} = \frac{1}{3}\cdot\pi\cdot\left(H_2^3-h^3\right)\cdot\tan^2\theta \tag{C.7}$$

In the above equation, *h* is the vertical distance below the top of the cone, and H_2 is the total height of the cone. The rate of change of the volume of the conical section can be estimated using the following equation.

$$\frac{dV_{\text{cone}}}{dt} = -\pi\cdot\tan^2\theta\cdot h^2\cdot\frac{dh}{dt} = \dot{V} \tag{C.8}$$

The infinitesimal surface area of a "ring" in the conical section, a distance "*h*" below the center is calculated using the following equation.

$$dA_{\text{cone}} = 2\cdot\pi\cdot r\cdot\frac{dh}{\cos\theta} = 2\cdot\pi\cdot h\cdot\tan\theta\cdot\frac{dh}{\cos\theta} = 2\cdot\pi\cdot\frac{\tan^2\theta}{\sin\theta}h\cdot dh \tag{C.9}$$

Integrating the above equation with respect to *h*, with the boundary condition that $A_{\text{cone}} = 0$ at $h = H_2$, results in the following equation.

$$A_{\text{cone}} = \pi \cdot \frac{\tan^2 \theta}{\sin \theta} \cdot \left(H_2^2 - h^2 \right) \tag{C.10}$$

This is the surface area of a conical segment located at a height, h below the top of the cone. When $h = 0$, the cone is fully formed, and the resulting area is the surface area of the cone.

The average transfer area over the evolution time of the hemispherical section can be calculated by using the following equation.

$$\overline{A}_{\text{cone}} = \frac{\int_0^{t_{\text{cone}}} A_{\text{cone}} \cdot dt}{t_{\text{cone}}} \tag{C.11}$$

Because A_{cone} is known in terms of h, Eq. C.8 can be used to express dt in terms of dh as follows:

$$dt = \frac{-\pi \cdot \tan^2 \theta \cdot h^2 \cdot dh}{\dot{V}} \tag{C.12}$$

The expression for dt from the above equation can be substituted in Eq. C.11 to determine the average transfer area over the evolution time of the conical section as follows:

$$\begin{aligned} \overline{A}_{\text{hem}} &= \frac{\tan^2 \theta}{\sin \theta} \cdot \frac{\int_{H_2}^{H_1} \pi \cdot \left(H_2^2 - h^2 \right) \cdot \left(-\pi \cdot \tan^2 \theta \cdot h^2 \right) \cdot dh}{\dot{V} \cdot t_{\text{cone}}} \\ &= \frac{\tan^4 \theta}{\sin \theta} \cdot \frac{-\pi^2}{\left(\frac{1}{3} \cdot \pi \cdot \tan^2 \theta \cdot \left(H_2^3 - H_1^3 \right) \right)} \cdot \int_{H_1}^{H_2} h^2 \cdot \left(H_2^2 - h^2 \right) \cdot dh \\ &= \frac{\pi}{\sin \theta} \cdot \left(R_2^2 - \frac{3}{5} \frac{R_2^4 \cdot H_2 - R_1^4 \cdot H_1}{R_2^2 \cdot H_2 - R_1^2 \cdot H_1} \right) \end{aligned} \tag{C.13}$$

It should be noted that in the above equation, the product $\dot{V} \cdot t_{\text{cone}}$ is the total volume of the conical section.

C.2. Film instantaneous and average surface area

C.2.1. Triangular region

Fig. C.2 shows a schematic of the triangular region in the spread region. The area of the triangular region at any instant of time is expressed in terms of the maximum width of the spread region, and the velocity of the feed region using the following equation.

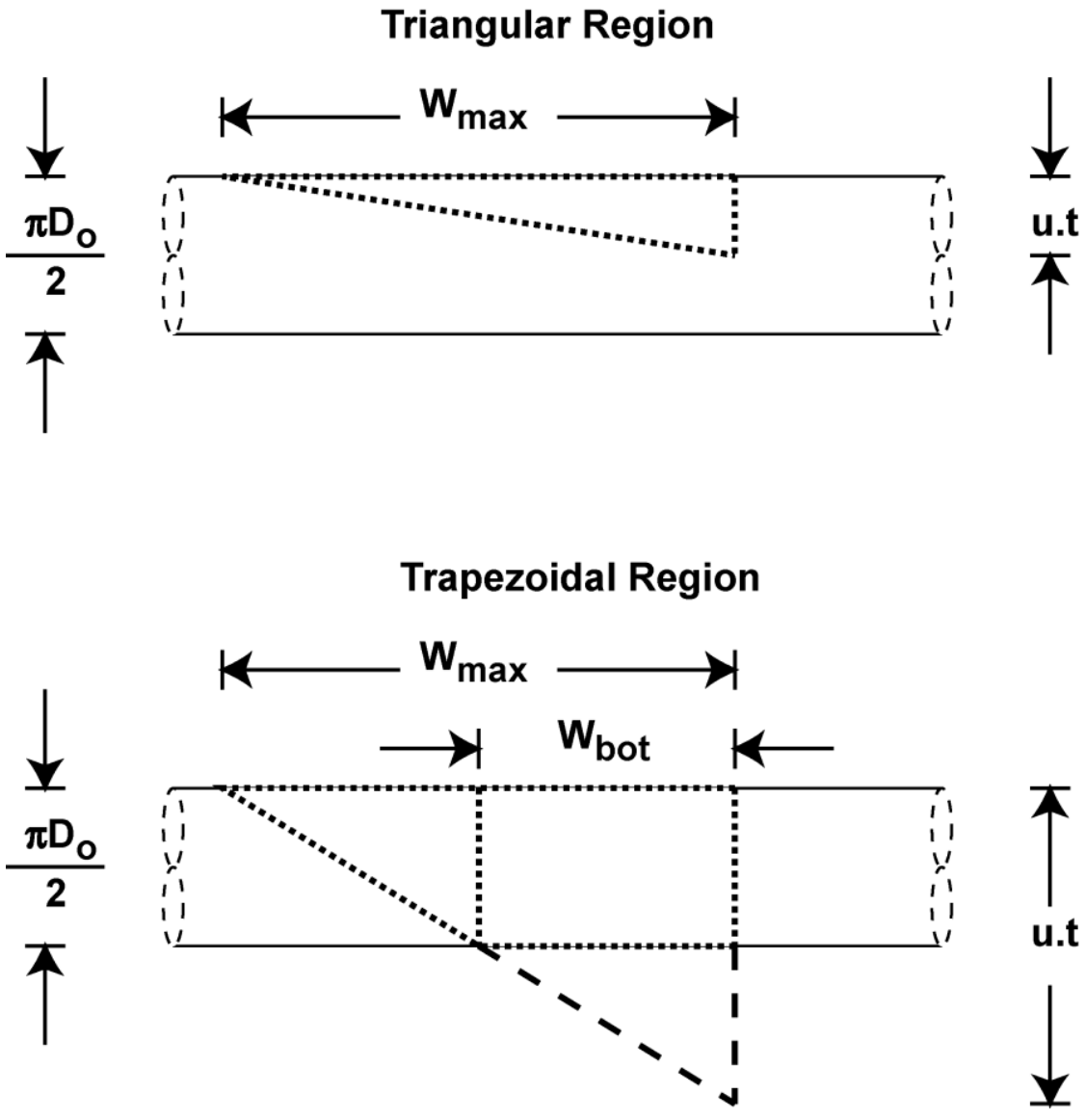

Fig. C.2 Schematic of triangular and trapezoidal regions of the film

$$A_{\text{tri}}(t) = \frac{1}{2} \cdot w_{\max} \cdot (\overline{u} \cdot t) \tag{C.14}$$

The average transfer area over the triangular region formation time is calculated using the following equation.

$$\begin{aligned} \overline{A}_{\text{tri}} &= \frac{\int_0^{t_{\text{film,bot}}} A_{\text{tri}}(t) \cdot dt}{t_{\text{film,bot}}} = \frac{1}{t_{\text{film,bot}}} \cdot \int_0^{t_{\text{film,bot}}} \frac{1}{2} \cdot w_{\max} \cdot \overline{u} \cdot t \cdot dt \\ &= \frac{1}{4} \cdot w_{\max} \cdot \overline{u} \cdot t_{\text{film,bot}} \\ &= \frac{1}{4} \cdot w_{\max} \cdot \frac{\pi \cdot D_{\text{o}}}{2} \end{aligned} \tag{C.15}$$

C.2.2. Trapezoidal region

Fig. C.2 also shows a schematic of the trapezoidal region in the spread region. The width of the spread region at the bottom of the tube at any instant of time is calculated using similar triangles and is given by the following equation.

$$w_{\text{bot}}(t) = \frac{\overline{u} \cdot t - \frac{\pi \cdot D_{\text{o}}}{2}}{\overline{u} \cdot t} \cdot w_{\max} \tag{C.16}$$

The area of the trapezoidal region at any instant of time is expressed as the sum of a rectangular and triangular region using the following equation.

$$\begin{aligned} A_{\text{trap}}(t) &= \frac{1}{2} \cdot \frac{\pi \cdot D_{\text{o}}}{2} \cdot \left(w_{\max} - w_{\text{bot}}(t) \right) + \frac{\pi \cdot D_{\text{o}}}{2} \cdot w_{\text{bot}}(t) \\ &= \frac{1}{2} \cdot \frac{\pi \cdot D_{\text{o}}}{2} \cdot \left(w_{\max} + \frac{\overline{u} \cdot t - \frac{\pi \cdot D_{\text{o}}}{2}}{\overline{u} \cdot t} \cdot w_{\max} \right) \\ &= \frac{\pi \cdot D_{\text{o}}}{2} \cdot w_{\max} - \frac{1}{8} \cdot \frac{(\pi \cdot D_{\text{o}})^2}{\overline{u} \cdot t} \cdot w_{\max} \end{aligned} \tag{C.17}$$

The average transfer area over the trapezoidal region formation time is calculated using the following equation.

$$\overline{A}_{\text{trap}} = \frac{\int_{t_{\text{film,bot}}}^{t_{\text{drop}}} A_{\text{trap}}(t)\cdot dt}{t_{\text{drop}} - t_{\text{film,bot}}}$$

$$= \frac{1}{t_{\text{drop}} - t_{\text{film,bot}}} \cdot \int_{t_{\text{film,bot}}}^{t_{\text{drop}}} \left(\frac{\pi \cdot D_{\text{o}}}{2} \cdot w_{\max} - \frac{1}{8} \cdot \frac{(\pi \cdot D_{\text{o}})^2}{\overline{u} \cdot t} \cdot w_{\max} \right) \cdot dt \qquad \text{(C.18)}$$

$$= \frac{\pi \cdot D_{\text{o}}}{2} \cdot w_{\max} \left(1 - \frac{\pi \cdot D_{\text{o}} \cdot ln\left(\frac{t_{\text{drop}}}{t_{\text{film,bot}}} \right)}{4 \cdot \overline{u} \cdot \left(t_{\text{drop}} - t_{\text{film,bot}} \right)} \right)$$

It should be noted that in the trapezoidal region, the velocity of the moving edge is assumed to be equal to the velocity of the moving edge in the triangular region. In the extreme case, if this edge is assumed to be in free fall and the corresponding average velocity is used in the above calculations, the difference in the average film area in the Spread region for the representative test condition is within 11%. The corresponding difference in the average film transfer area is within 8%. It is expected that because of fluid viscosity and surface tension, there will be significant deceleration of the film, and free-fall velocity would be the upper limit. With these considerations, the above analysis is expected to yield reasonable predictions for the average film area.

APPENDIX D. SEGMENTAL HEAT AND MASS TRANSFER MODEL SAMPLE CALCULATIONS FOR MICROSCALE FORCED-CONVECTIVE ABSORPTION

Inputs	Equations	Results
Solution and vapor, bulk and interface conditions		
$x_{sol,in} = 0.3473$ $x_{sol,out} = 0.3678$	$x_{sol,avg} = \frac{x_{sol,in} + x_{sol,out}}{2}$ $x_{sol,int} = x_{sol,avg}$	$x_{sol,avg} = 0.3576$ $x_{sol,int} = 0.3576$
$P_{sol,int} = 497.3$ kPa $x_{sol,int} = 0.3576$	$T_{sol,int} = f\left(P_{sol,int}, x_{sol,int}, q_{sol,int} = 0\right)$	$T_{sol,int} = 64.82^{o}$C
$P_{sol,int} = 497.3$ kPa $T_{sol,int} = 64.82^{o}$C	$P_{vap,int} = P_{sol,int}$ $T_{vap,int} = T_{sol,int}$ $x_{vap,int} = f\left(P_{vap,int}, T_{vap,int}, q_{vap,int} = 1\right)$	$P_{vap,int} = 497.3$ kPa $T_{vap,int} = 64.82^{o}$C $x_{vap,int} = 0.9719$
$x_{vap,in} = 0.9609$ $x_{vap,out} = 0.9696$	$x_{vap,bulk} = \frac{x_{vap,in} + x_{vap,out}}{2}$	$x_{vap,bulk} = 0.9653$
Vapor mass transfer		
$\mu_{vap,bulk} = 1.19\times10^{-5}$ kg m^{-1} s^{-1} $Cp_{vap,bulk} = 2.393$ kJ kg^{-1} K^{-1} $k_{vap,bulk} = 0.033$ W m^{-1} K^{-1} $\rho_{vap,bulk} = 3.15$ kg m^{-3} $D_{aw,vap,bulk} = 7.28\times10^{-6}$ m^2 s^{-1}	$Pr_{vap} = \frac{\mu_{vap,bulk} \cdot Cp_{vap,bulk}}{k_{vap,bulk}}$ $Sc_{vap} = \frac{\mu_{vap,bulk}}{D_{aw,vap,bulk} \cdot \rho_{vap,bulk}}$	$Pr_{vap} = 0.8574$ $Sc_{vap} = 0.5209$

Inputs	Equations	Results
$Pr_{vap} = 0.8574$ $Sc_{vap} = 0.5209$ $\theta = \frac{\pi}{2}$	$Nu_{vap} = 2.0705 \cdot \left(1 + 2.2916 \cdot \theta - 2.5682 \cdot \theta^2 + 1.4815 \cdot \theta^3 - 0.3338 \cdot \theta^4\right)$ (Sparrow and Haji-Sheikh, 1965) $\frac{Sh_{vap}}{Nu_{vap}} = \left(\frac{Sc_{vap}}{Pr_{vap}}\right)^{1/3}$	$Nu_{vap} = 4.084$ $Sh_{vap} = 3.459$
$D_h = 4.42 \times 10^{-4}$ m $k_{vap,bulk} = 0.033$ W m^{-1} K^{-1} $D_{aw,vap,bulk} = 7.28 \times 10^{-6}$ m^2 s^{-1} $Nu_{vap} = 4.084$ $Sh_{vap} = 3.459$	$\alpha_{vap} = \frac{Nu_{vap} \cdot k_{vap,bulk}}{D_h}$ $\beta_{vap} = \frac{Sh_{vap} \cdot D_{aw,vap,bulk}}{D_h}$	$\alpha_{vap} = 308$ W m^{-1} K^{-1} $\beta_{vap} = 0.0570$ m s^{-1}
$P_{vap,bulk} = 497.3$ kPa $T_{vap,bulk} = 65.54^{o}$C $R_{gas} = 8.314$ kJ kmol^{-1} K^{-1}	$C_T = \frac{P_{vap,bulk}}{R_{gas} \cdot T_{vap,bulk}}$	$C_T = 0.1766$ kmol m^{-3}

Inputs	Equations	Results
$M_A = 17.03$ kg kmol^{-1} $M_W = 18.02$ kg kmol^{-1} $x_{vap,int} = 0.9719$ $x_{vap,bulk} = 0.9653$	$\tilde{x}_{vap,int} = \frac{\frac{x_{vap,int}}{M_A}}{\frac{x_{vap,int}}{M_A} + \frac{\left(1 - x_{vap,int}\right)}{M_W}}$ $\tilde{x}_{vap,bulk} = \frac{\frac{x_{vap,bulk}}{M_A}}{\frac{x_{vap,bulk}}{M_A} + \frac{\left(1 - x_{vap,bulk}\right)}{M_W}}$	$\tilde{x}_{vap,int} = 0.9734$ $\tilde{x}_{vap,bulk} = 0.9671$
$\beta_{vap} = 0.0570$ m s^{-1} $C_T = 0.1766$ kmol m^{-3} $\tilde{x}_{vap,int} = 0.9734$ $\tilde{x}_{vap,bulk} = 0.9671$ $\tilde{z} = 0.9064$	$\dot{n}_T = \beta_{vap} \cdot C_T \cdot \ln\left(\frac{\tilde{z} - \tilde{x}_{vap,int}}{\tilde{z} - \tilde{x}_{vap,bulk}}\right)$ $\dot{n}_A = \tilde{z} \cdot \dot{n}_T$ $\dot{n}_W = \left(1 - \tilde{z}\right) \cdot \dot{n}_T$	$\dot{n}_T = 9.89 \times 10^{-4}$ kmol m^{-2} s^{-1} $\dot{n}_A = 8.97 \times 10^{-4}$ kmol m^{-2} s^{-1} $\dot{n}_w = 9.26 \times 10^{-5}$ kmol m^{-2} s^{-1}
$PM_{ch} = 0.0019$ m $N_{ch,ps} = 55$ $N_{shim} = 20$ $l_{ch} = 0.0048$ m	$A_{seg} = PM_{ch} \cdot l_{ch} \cdot N_{ch,ps} \cdot \left(N_{shim} - 1/2\right)$	$A_{seg} = 9.76 \times 10^{-3}$ m^2

Inputs	Equations	Results
$M_A = 17.03\ \text{kg kmol}^{-1}$ $M_W = 18.02\ \text{kg kmol}^{-1}$ $\dot{n}_A = 8.97\times10^{-4}\ \text{kmol m}^{-2}\ \text{s}^{-1}$ $\dot{n}_w = 9.26\times10^{-5}\ \text{kmol m}^{-2}\ \text{s}^{-1}$	$\dot{m}_{abs,A} = M_A \cdot \dot{n}_A \cdot A_{seg}$ $\dot{m}_{abs,W} = M_W \cdot \dot{n}_W \cdot A_{seg}$ $\dot{m}_{abs} = \dot{m}_{abs,A} + \dot{m}_{abs,W}$	$\dot{m}_{abs,A} = 1.49\times10^{-4}\ \text{kg s}^{-1}$ $\dot{m}_{abs,W} = 1.63\times10^{-5}\ \text{kg s}^{-1}$ $\dot{m}_{abs} = 1.65\times10^{-4}\ \text{kg s}^{-1}$
Overall heat and mass transfer rates		
$\dot{m}_{vap,in} = 1.29\times10^{-3}\ \text{kg s}^{-1}$ $\dot{m}_{abs} = 1.65\times10^{-4}\ \text{kg s}^{-1}$ $x_{vap,in} = 0.9609$	$\dot{m}_{vap,out} = \dot{m}_{vap,in} - \dot{m}_{abs}$ $x_{vap,out} = \frac{\dot{m}_{vap,in} \cdot x_{vap,in} - \dot{m}_{abs,A}}{\dot{m}_{vap,out}}$	$\dot{m}_{vap,out} = 1.13\times10^{-3}\ \text{kg s}^{-1}$ $x_{vap,out} = 0.9696$
$\dot{m}_{vap,in} = 1.29\times10^{-3}\ \text{kg s}^{-1}$ $\dot{m}_{vap,out} = 1.13\times10^{-3}\ \text{kg s}^{-1}$ $\dot{m}_{sol,in} = 4.31\times10^{-3}\ \text{kg s}^{-1}$ $x_{vap,in} = 0.9609$ $x_{vap,out} = 0.9696$ $x_{sol,in} = 0.3473$	$\dot{m}_{sol,out} + \dot{m}_{vap,out} = \dot{m}_{sol,in} + \dot{m}_{vap,in}$ $\dot{m}_{sol,out} \cdot x_{sol,out} + \dot{m}_{vap,out} \cdot x_{vap,out} = \dot{m}_{sol,in} \cdot x_{sol,in} + \dot{m}_{vap,in} \cdot x_{vap,in}$	$\dot{m}_{sol,out} = 4.47\times10^{-3}\ \text{kg s}^{-1}$ $x_{sol,out} = 0.3678$

Inputs	Equations	Results
$T_{sol,in,int} = 66.87^{o}C$ $T_{sol,out,int} = 62.8^{o}C$ $T_{vap,in} = 65.93^{o}C$ $T_{vap,out} = 65.16^{o}C$	$LMTD_{vap} = \frac{\left(T_{vap,in} - T_{sol,in,int}\right) - \left(T_{vap,out} - T_{sol,out,int}\right)}{\frac{T_{vap,in} - T_{sol,in,int}}{T_{vap,out} - T_{sol,out,int}}}$	$LMTD_{vap} = 0.7065$ K
$\alpha_{vap} = 308$ W m^{-1} K^{-1} $A_{seg} = 9.76\times10^{-3}$ m^2 $\dot{n}_A = 8.97\times10^{-4}$ kmol m^{-2} s^{-1} $\dot{n}_w = 9.26\times10^{-5}$ kmol m^{-2} s^{-1} $\tilde{C}p_A = 33.26$ kJ kmol^{-1} K^{-1} $\tilde{C}p_W = 33.26$ kJ kmol^{-1} K^{-1}	$\phi_T = \frac{\left(\dot{n}_A \cdot \tilde{C}p_A\right) + \left(\dot{n}_W \cdot \tilde{C}p_W\right)}{\alpha_{vap}}$ $Q_{vap} = \alpha_{vap} \cdot \left(\frac{\phi_T}{1 - e^{-\phi_T}}\right) \cdot A_{seg} \cdot LMTD_{vap}$	$\phi_T = 0.1068$ $Q_{vap} = 2.239$ W
$\dot{m}_{vap,in} = 1.29\times10^{-3}$ kg s^{-1} $\dot{m}_{vap,out} = 1.13\times10^{-3}$ kg s^{-1} $Q_{vap} = 2.239$ W $T_{vap,in} = 65.93^{o}C$ $Cp_{vap,bulk} = 2.393$ kJ kg^{-1} K^{-1}	$\dot{m}_{vap,bulk} = \frac{\dot{m}_{vap,in} + \dot{m}_{vap,out}}{2}$ $Q_{vap} = \dot{m}_{vap,bulk} \cdot Cp_{vap} \cdot \left(T_{vap,in} - T_{vap,out}\right)$	$\dot{m}_{vap,bulk} = 1.21\times10^{-3}$ kg s^{-1} $T_{vap,out} = 65.16^{o}C$

Inputs	Equations	Results
$P_{vap,out} = 497.3$ kPa $T_{vap,out} = 65.16^{o}C$ $x_{vap,out} = 0.9696$	$h_{vap,out} = f\left(P_{vap,out}, T_{vap,out}, x_{vap,out}\right)$	$h_{vap,out} = 1450$ kJ kg^{-1}
$P_{sol,out} = 497.3$ kPa $x_{sol,out} = 0.3678$	$h_{sol,out} = f\left(P_{sol,out}, x_{sol,out}, q_{sol,out} = 0\right)$ $T_{sol,out} = f\left(P_{sol,out}, x_{sol,out}, q_{sol,out} = 0\right)$	$h_{sol,out} = 58.25$ kJ kg^{-1} $T_{sol,out} = 62.8^{o}C$
$\dot{m}_{vap,in} = 1.29\times10^{-3}$ kg s^{-1} $\dot{m}_{vap,out} = 1.13\times10^{-3}$ kg s^{-1} $\dot{m}_{sol,in} = 4.31\times10^{-3}$ kg s^{-1} $\dot{m}_{sol,out} = 4.47\times10^{-3}$ kg s^{-1} $h_{vap,in} = 1437$ kJ kg^{-1} $h_{vap,out} = 1450$ kJ kg^{-1} $h_{sol,in} = 82.19$ kJ kg^{-1} $h_{sol,out} = 58.25$ kJ kg^{-1}	$Q_{abs} = \dot{m}_{sol,in} \cdot h_{sol,in} + \dot{m}_{vap,in} \cdot h_{vap,in} - \dot{m}_{sol,out} \cdot h_{sol,out} - \dot{m}_{vap,out} \cdot h_{vap,out}$	$Q_{abs} = 0.3165$ kW

Inputs	Equations	Results
$\dot{m}_{vap,bulk} = 1.21\times10^{-3}$ kg s^{-1} $\dot{m}_{sol,avg} = 4.39\times10^{-3}$ kg s^{-1} $k_{sol,avg}$ = 0.5617 W m^{-1} K^{-1} $D_h = 4.42\times10^{-4}$ m Re_{LO} = 24.1 $Pr_{sol,avg}$ = 3.5 $P_{sol,avg}$ = 497.3 kPa P_{cr} = 18780 kPa	$q_{avg} = \frac{\dot{m}_{vap,bulk}}{\left(\dot{m}_{vap,bulk} + \dot{m}_{sol,avg}\right)}$ $\alpha_{LO,sol} = 0.023 \cdot \frac{k_{sol,avg}}{D_h} \cdot Re_{LO}^{0.8} \cdot Pr_{sol,avg}^{0.4}$ $\alpha_{sol} = \alpha_{LO,sol} \cdot \left(\left(1-q_{avg}\right)^{0.8} + \frac{3.8 \cdot q_{avg}^{0.76} \cdot \left(1-q_{avg}^{0.04}\right)}{\left(\frac{P_{sol,avg}}{P_{cr}}\right)^{0.38}} \right)$ (Shah, 1979)	q_{avg} = 0.22 $\alpha_{LO,sol}$ = 614.8 W m^{-2} K^{-1} α_{sol} = 3375 W m^{-2} K^{-1}
$\theta = \frac{\pi}{2}$ k_{CF} = 0.4902 W m^{-1} K^{-1} $D_h = 4.42\times10^{-4}$ m	$Nu_{CF} = 2.0705 \cdot \left(1 + 2.2916 \cdot \theta - 2.5682 \cdot \theta^2 + 1.4815 \cdot \theta^3 - 0.3338 \cdot \theta^4\right)$ (Sparrow and Haji-Sheikh, 1965) $\alpha_{CF} = \frac{Nu_{CF} \cdot k_{CF}}{D_h}$	Nu_{CF} = 4.084 α_{CF} = 4530 W m^{-2} K^{-1}
Fin array thermal resistance calculations		
l_{ch} = 0.0048 m t_{fin} = 0.0005 m k_{fin} = 13.95 W m^{-1} K^{-1} α_{sol} = 3375 W m^{-2} K^{-1} α_{CF} = 4530 W m^{-2} K^{-1}	$m_{fin,sol} = \left(\frac{\alpha_{sol} \cdot 2 \cdot \left(l_{ch} + t_{fin}\right)}{k_{fin} \cdot l_{ch} \cdot t_{fin}} \right)^{1/2}$ $m_{fin,CF} = \left(\frac{\alpha_{CF} \cdot 2 \cdot \left(l_{ch} + t_{fin}\right)}{k_{fin} \cdot l_{ch} \cdot t_{fin}} \right)^{1/2}$	$m_{fin,sol}$ = 1034 m^{-1} $m_{fin,CF}$ = 1198 m^{-1}

Inputs	Equations	Results
$m_{\text{fin,sol}} = 1034\ \text{m}^{-1}$ $m_{\text{fin,CF}} = 1198\ \text{m}^{-1}$ $l_{\text{fin}} = 1.75\times10^{-4}\ \text{m}$	$\eta_{\text{fin,sol}} = \frac{tanh\left(m_{\text{fin,sol}} \cdot l_{\text{fin}}\right)}{m_{\text{fin,sol}} \cdot l_{\text{fin}}}$ $\eta_{\text{fin,sol}} = \frac{tanh\left(m_{\text{fin,sol}} \cdot l_{\text{fin}}\right)}{m_{\text{fin,sol}} \cdot l_{\text{fin}}}$	$\eta_{\text{fin,sol}} = 0.9892$ $\eta_{\text{fin,CF}} = 0.9856$
$\eta_{\text{fin,sol}} = 0.9892$ $\eta_{\text{fin,CF}} = 0.9856$ $N_{\text{ch,ps}} = 55$ $A_{\text{fin,top}} = 1.168\times10^{-6}\ \text{m}^2$ $A_{\text{fin,bot}} = 1.168\times10^{-6}\ \text{m}^2$ $A_{\text{FA,top,total}} = 2.90\times10^{-4}\ \text{m}^2$ $A_{\text{FA,bot,total}} = 2.06\times10^{-4}\ \text{m}^2$	$\eta_{\text{FA,sol,top}} = 1 - \frac{N_{\text{ch,ps}} \cdot A_{\text{fin,top}}}{A_{\text{FA,top,total}}}\left(1 - \eta_{\text{fin,sol}}\right)$ $\eta_{\text{FA,sol,bot}} = 1 - \frac{N_{\text{ch,ps}} \cdot A_{\text{fin,bot}}}{A_{\text{FA,bot,total}}}\left(1 - \eta_{\text{fin,sol}}\right)$ $\eta_{\text{FA,CF,top}} = 1 - \frac{N_{\text{ch,ps}} \cdot A_{\text{fin,top}}}{A_{\text{FA,top,total}}}\left(1 - \eta_{\text{fin,CF}}\right)$ $\eta_{\text{FA,CF,bot}} = 1 - \frac{N_{\text{ch,ps}} \cdot A_{\text{fin,bot}}}{A_{\text{FA,bot,total}}}\left(1 - \eta_{\text{fin,CF}}\right)$	$\eta_{\text{FA,sol,top}} = 0.9966$ $\eta_{\text{FA,sol,bot}} = 0.9906$ $\eta_{\text{FA,CF,top}} = 0.9954$ $\eta_{\text{FA,CF,bot}} = 0.9874$

Inputs	Equations	Results
$A_{FA,top,total} = 2.90\times10^{-4}\ m^2$ $A_{FA,bot,total} = 2.06\times10^{-4}\ m^2$	$R_{FA,sol,top} = \frac{1}{\eta_{FA,sol,top} \cdot A_{FA,top,total} \cdot \alpha_{sol}}$ $R_{FA,sol,bot} = \frac{1}{\eta_{FA,sol,bot} \cdot A_{FA,top,bot} \cdot \alpha_{sol}}$ $R_{FA,CF,top} = \frac{1}{\eta_{FA,sol,top} \cdot A_{FA,top,total} \cdot \alpha_{CF}}$ $R_{FA,CF,bot} = \frac{1}{\eta_{FA,sol,bot} \cdot A_{FA,top,bot} \cdot \alpha_{CF}}$	$R_{FA,sol,top} = 1.026\,K\,m^2\,W^{-1}$ $R_{FA,sol,bot} = 1.45\,K\,m^2\,W^{-1}$ $R_{FA,CF,top} = 0.7653\,K\,m^2\,W^{-1}$ $R_{FA,CF,bot} = 1.084\,K\,m^2\,W^{-1}$
$R_{FA,sol,top} = 1.026\,K\,m^2\,W^{-1}$ $R_{FA,sol,bot} = 1.45\,K\,m^2\,W^{-1}$ $R_{FA,CF,top} = 0.7653\,K\,m^2\,W^{-1}$ $R_{FA,CF,bot} = 1.084\,K\,m^2\,W^{-1}$ $R_{Wall} = 0.054\,K\,m^2\,W^{-1}$ $N_{shim} = 20$	$R_{FA,CF\text{-}Sol,top} = R_{FA,CF,bot} + R_{wall} + R_{FA,sol,top}$ $R_{FA,CF\text{-}Sol,bot} = R_{FA,CF,top} + R_{wall} + R_{FA,sol,bot}$ $R_{FA,N\text{-}1} = \frac{1}{N_{shim} - 1}\left(\frac{R_{FA,CF\text{-}Sol,top} \cdot R_{FA,CF\text{-}Sol,bot}}{R_{FA,CF\text{-}Sol,top} + R_{FA,CF\text{-}Sol,bot}}\right)$ $R_T = \left(\frac{R_{FA,N\text{-}1} \cdot R_{FA,CF\text{-}Sol,top}}{R_{FA,N\text{-}1} + R_{FA,CF\text{-}Sol,top}}\right)$	$R_{FA,CF\text{-}Sol,top} = 2.164\,K\,m^2\,W^{-1}$ $R_{FA,CF\text{-}Sol,bot} = 2.27\,K\,m^2\,W^{-1}$ $R_{FA,N\text{-}1} = 0.0583\,K\,m^2\,W^{-1}$ $R_T = 0.0569\,K\,m^2\,W^{-1}$

Inputs	Equations	Results
$R_T = 0.0569\,\mathrm{K\,m^2\,W^{-1}}$ $A_{seg} = 9.76\times10^{-3}\ \mathrm{m^2}$ $T_{sol,in} = 66.87^oC$ $T_{sol,out} = 62.8^oC$ $T_{CF,out} = 47.43^oC$ $T_{CF,in} = 46.19^oC$	$R_T = \frac{1}{U_{seg}\cdot A_{seg}}$ $LMTD_T = \frac{\left(T_{sol,in} - T_{CF,out}\right) - \left(T_{sol,out} - T_{CF,in}\right)}{\frac{T_{sol,in} - T_{CF,out}}{T_{sol,out} - T_{CF,in}}}$ $Q_{abs} = U_{seg}\cdot A_{seg}\cdot LMTD_T$	U_{seg} = 1802.3 W m^{-2} K^{-1} $LMTD_T$ = 17.99 K Q_{abs} = 0.3165 kW
Q_{abs} = 0.3165 kW $T_{CF,out} = 47.43^oC$ Cp_{CF} = 4.00 kJ kg^{-1} K^{-1} $\dot{m}_{CF} = 0.0635\,\mathrm{kg\,s^{-1}}$	$Q_{abs} = \dot{m}_{CF}\cdot Cp_{CF}\cdot\left(T_{CF,out} - T_{CF,in}\right)$	$T_{CF,in} = 46.19^oC$
Pressure drop calculations		
$\theta = \frac{\pi}{2}$ Re_{CF} = 98.59	$f_{CF} = \frac{48}{Re_{CF}}\left(1 + 0.5059\cdot\theta - 0.3948\cdot\theta^2 + 0.1875\cdot\theta^3 - 0.0385\cdot\theta^4\right)$ (Sparrow and Haji-Sheikh, 1965)	f_{CF} = 0.6392

Inputs	Equations	Results
$f_{CF} = 0.6392$ $\dot{m}_{CF} = 0.0635\,\text{kg s}^{-1}$ $N_{shim} = 20$ $N_{ch,ps} = 55$ $\rho_{CF} = 1008\ \text{kg m}^{-3}$ $A_{face,ch} = 2.099\times10^{-7}\ \text{m}^2$ $l_{ch} = 0.0048\ \text{m}$ $D_h = 4.42\times10^{-4}\ \text{m}$	$\Delta P_{CF} = \frac{f_{CF}}{2} \cdot \frac{\dot{m}_{CF}^2}{N_{ch,ps}^2 \cdot N_{shim}^2 \cdot \rho_{CF} \cdot A_{face,ch}^2} \cdot \frac{l_{ch}}{D_h}$ $v_{CF} = \frac{\dot{m}_{CF}}{N_{ch,ps} \cdot N_{shim} \cdot A_{face,ch} \cdot \rho_{CF}}$	$\Delta P_{CF} = 732.6\ \text{Pa}$ $v_{CF} = 0.273\ \text{m s}^{-1}$
$N_{shim} = 20$ $N_{ch,ps} = 55$ $D_h = 4.42\times10^{-4}\ \text{m}$ $A_{face,ch} = 2.099\times10^{-7}\ \text{m}^2$ $\mu_{sol,avg} = 4.452\times10^{-4}\ \text{kg m}^{-1}\ \text{s}^{-1}$ $\dot{m}_{sol,avg} = 4.39\times10^{-3}\,\text{kg s}^{-1}$ $\dot{m}_{vap,bulk} = 1.21\times10^{-3}\,\text{kg s}^{-1}$	$Re_L = \frac{\dot{m}_{sol,avg} \cdot D_h}{N_{ch,ps} \cdot N_{shim} \cdot A_{face,ch} \cdot \mu_{sol,avg}}$ $Re_V = \frac{\dot{m}_{vap,bulk} \cdot D_h}{N_{ch,ps} \cdot N_{shim} \cdot A_{face,ch} \cdot \mu_{vap,bulk}}$	$Re_L = 18.88$ $Re_v = 193.9$

Inputs	Equations	Results
$Re_L = 18.88$ $Re_V = 193.9$ $\theta = \frac{\pi}{2}$	$f_L = \frac{48}{Re_L}\left(1 + 0.5059 \cdot \theta - 0.3948 \cdot \theta^2 + 0.1875 \cdot \theta^3 - 0.0385 \cdot \theta^4\right)$ $f_V = \frac{48}{Re_{CF}}\left(1 + 0.5059 \cdot \theta - 0.3948 \cdot \theta^2 + 0.1875 \cdot \theta^3 - 0.0385 \cdot \theta^4\right)$ (Sparrow and Haji-Sheikh, 1965)	$f_L = 3.338$ $f_V = 0.3251$
$f_L = 3.338$ $f_V = 0.3251$ $N_{shim} = 20$ $N_{ch,ps} = 55$ $D_h = 4.42\times10^{-4}$ m $A_{face,ch} = 2.099\times10^{-7}$ m^2 $\rho_{sol,avg} = 845.4$ kg m^{-3} $\rho_{vap,bulk} = 3.1$ kg m^{-3} $\dot{m}_{sol,avg} = 4.39\times10^{-3}$ kg s^{-1} $\dot{m}_{vap,bulk} = 1.21\times10^{-3}$ kg s^{-1} $C = 5$ $l_{ch} = 0.0048$ m	$\frac{dP_L}{dx} = \frac{f_L}{2} \cdot \frac{\dot{m}_{sol,avg}^2}{N_{ch,ps} \cdot N_{shim} \cdot \rho_{sol,avg} \cdot A_{face,ch}^2} \cdot \frac{1}{D_h}$ $\frac{dP_V}{dx} = \frac{f_V}{2} \cdot \frac{\dot{m}_{vap,bulk}^2}{N_{ch,ps} \cdot N_{shim} \cdot \rho_{vap,bulk} \cdot A_{face,ch}^2} \cdot \frac{1}{D_h}$ $X_{mart} = \left(\frac{\frac{dP_L}{dx}}{\frac{dP_V}{dx}}\right)^{\frac{1}{2}}$ $\phi_{sol}^2 = 1 + \frac{C}{X_{mart}} + \frac{1}{X_{mart}^2}$ $\Delta P_{sol} = \phi_{sol}^2 \cdot \frac{dP_L}{dx} \cdot l_{ch}$ (Lockhart and Martinelli, 1949)	$\frac{dP_L}{dx} = 1614$ Pa m^{-1} $\frac{dP_V}{dx} = 3254$ Pa m^{-1} $X_{mart} = 0.7043$ $\phi_{sol} = 3.18$ $\Delta P_{sol} = 78.22$ Pa
$P_{sol,in} = 497.4$ kPa $\Delta P_{sol} = 78.22$ Pa	$P_{sol,out} = P_{sol,in} - \Delta P_{sol}$	$P_{sol,out} = 497.3$ kPa

APPENDIX E. PRESSURE DROP ESTIMATION IN MICROSCALE FORCED-CONVECTIVE ABSORBERS

A series of laminar pressure drop experiments were conducted in the microscale absorbers to estimate the pressure drop in the channel array. Water was circulated through the solution and coupling-fluid sides of each heat exchanger over a range flow rates, and the resulting pressure drop across the component was measured. This pressure drop includes several minor losses, such as, pressure drop due to expansion and contraction of the fluid inside the various headers, pressure drop due to friction in the connecting plumbing, and pressure drop due to change in direction of flow. Therefore, to estimate the pressure drop in just the channel array, a model was developed to estimate these minor losses. This model was applied to each test condition, and the pressure drop in just the channel array was calculated from the data. Theoretical predictions of the pressure drop for various channel blockage scenarios were then compared with this measured pressure drop in the channel array, and the necessary shrinkage in the channel hydraulic diameter and the percentage of blocked channels were estimated. The pressure drop model is discussed first.

E.1. Pressure drop model

Fig. E.1 shows a schematic of the microscale absorber and the plumbing used to route the different fluid streams into and out of the component. A total of 25 locations are considered for calculating the pressure losses and identified on the schematic. Pressure measurements are recorded at the T-fittings at locations 1 and 25. The pressure drop, ΔP, due to sudden expansion, sudden contraction, change in the flow direction, or flow through a T-fitting is calculated using the following equation.

$$\Delta P = K \cdot \frac{\rho_{liq} \cdot v_{liq}^2}{2} \tag{E.1}$$

In the above equation, ρ_{liq}, and v_{liq} are the liquid density and velocity, K is the coefficient for minor losses, which varies depending upon the flow configuration. For sudden expansions, the minor loss coefficient is calculated using the following equation.

$$K = -1.05 \cdot \left[1 - \left(\frac{D_1}{D_2} \right)^2 \right]^2 \tag{E.2}$$

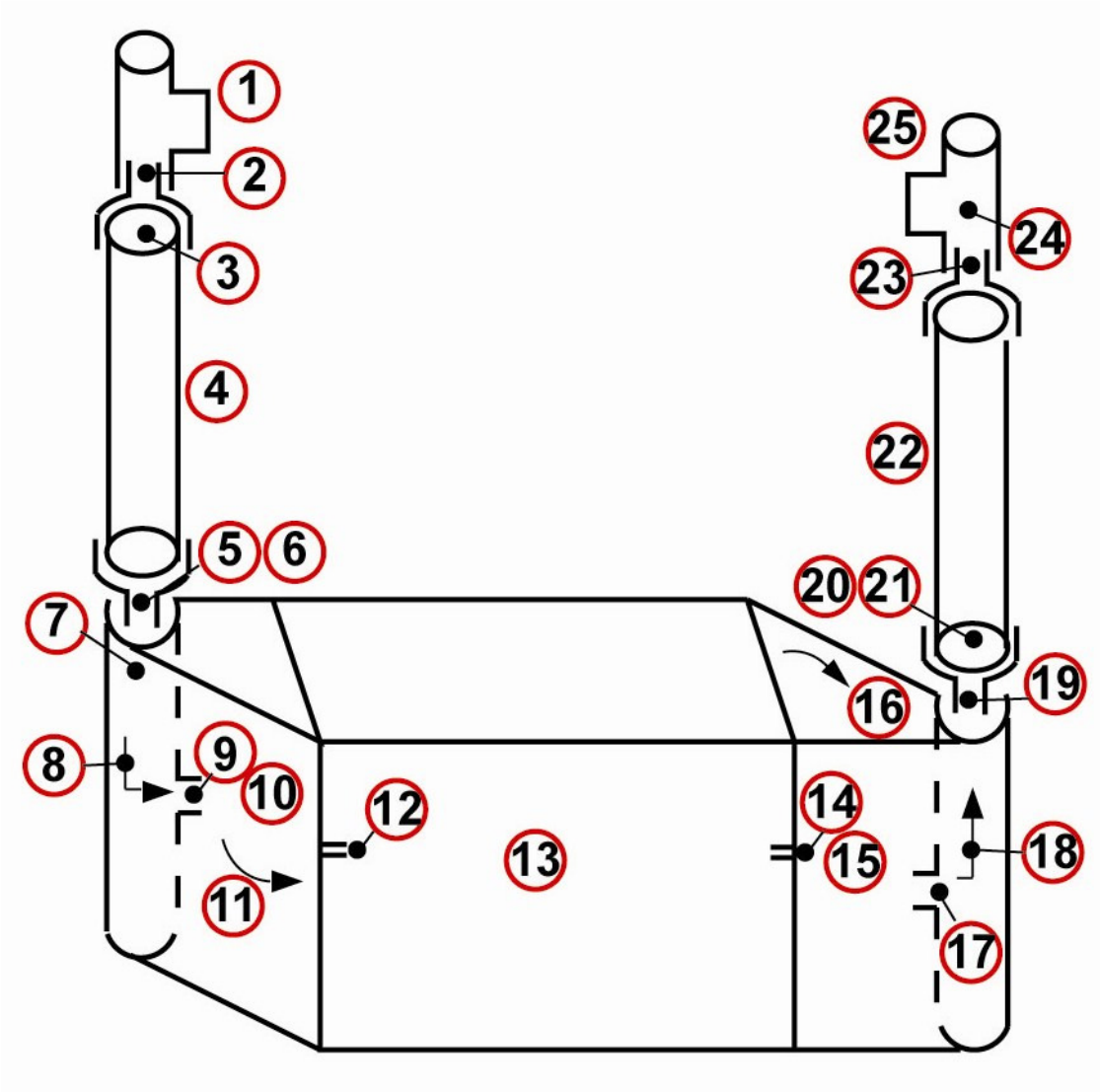

Fig. E.1 Schematic of absorber test section and plumbing

In the above equation, D_1 and D_2 are the inner diameter before and after expansion. It should be noted that sudden expansions result in a pressure recovery. Therefore, a negative sign is used in the above equation. For sudden contractions, the minor loss coefficient is estimated graphically from Cengel and Cimbala (2009) using the ratio of the diameters. For flow through T-fittings and 90^o turns, the minor loss coefficient is equal to 0.9 and 1.1, respectively (Cengel and Cimbala, 2009). Pressure drop through tube segments was estimated using the following equation.

$$\Delta P = f \frac{\rho_{liq} \cdot v_{liq}^2}{2} \cdot \frac{l}{D} \tag{E.3}$$

In the above equation, f is the friction factor which is calculated using the Churchill (1977b) correlation, l and D are the length and diameter of the tube segment, respectively.

Pressure of the fluid (water) entering the heat exchanger is measured at a T-fitting (Fig. E.1). Pressure losses are calculated from this point forward. Pressure drop at this location (Location 1) is due to flow in a T-fitting. Next, the fluid flows through a connecting fitting (Location 2), where the pressure drop is due to friction in a tube segment. This is followed by a sudden expansion into the tube stub (Location 3) connecting the fitting to the inlet of the heat exchanger. Fluid flowing through the tube stub experiences pressure drop due to friction (Location 4). As this fluid enters the tube stub at the inlet of the heat exchanger, it experiences a sudden contraction (Location 5). This is followed by friction losses due to flow in the tube stub (Location 6).

Fluid exiting the tube stub enters the inlet port to the heat exchanger. Pressure drop at this location is due to a sudden expansion (Location 7). This is followed by a 90^o turn in the flow (Location 8). After undergoing a change in direction, the fluid enters the header region in each sheet (Location 9). Pressure drop at this location is modeled as a sudden contraction. Pressure drop as the fluid flows through the header region is due friction (Location 10). As the fluid flows through the header of Microscale Absorber 2a,

it experiences some pressure drop due to flow around the circular studs or bosses. These losses are modeled as several sudden contractions and expansions (Location 11). The fluid entering the individual channels from the header undergoes a sudden contraction (Location 12). As the fluid flows through the channel array, it experiences friction pressure drop (Location 13). This is the major loss and pressure drop at this location is estimated by later.

Fluid exiting the tube array undergoes a sudden expansion (Location 14). This is followed by friction losses in the header (Location 15), and local contraction and expansion losses around the circular studs or bosses (Location 16). As the fluid exits the header region, it undergoes a sudden expansion into the outlet port (Location 17). In this port, the fluid further undergoes a 90^{o} turn (Location 18). This is followed by a sudden contraction into the tube stub (Location 19). Fluid flowing through the tube stub experiences friction (Location 20), before undergoing a sudden expansion into the tube stub (Location 21). As the fluid flows through the tube stub, it experiences friction (Location 22) followed by a sudden contraction to the connecting fitting (Location 23). Pressure drop in the connecting fitting is due to friction (Location 24). The pressure of the fluid exiting the heat exchanger is measured at a T-fitting. The pressure drop at this location (Location 25) is due to flow in a T-fitting.

For each test condition, the pressure drop due to the minor losses listed above is estimated. The pressure drop through the channel array (Location 13) is the experimentally measured pressure drop less the sum of these minor losses.

E.2. Estimation of channel blockage

The above estimated pressure drop in the channel array is compared with theoretical predictions for the various channel blockage scenarios discussed previously. Theoretical pressure drop in each channel is calculated using Eq. E.3, but the friction

factor is calculated using the correlation for laminar single-phase flow in semicircular channels developed by Sparrow and Haji-Sheikh (1965) as cited in Kakac *et al.* (1987).

In Scenario 1, all channels are assumed to be partially blocked. To determine the resulting channel hydraulic diameter, D_h is varied until the predicted pressure drop matches the experimental pressure drop in the channel array. In Scenario 2, all channels are assumed to be fully open or fully closed, and the hydraulic diameter of the open channels is assumed to be equal to the design hydraulic diameter. To determine the number of channels that are open, the number fully closed channels is varied until the predicted pressure drop matches experimental pressure drop. A similar analysis was conducted for Scenario 3, while accounting for reduced D_h for the open channels because of the fabrication tolerances. Fig, E.2 shows a graph of the experimental and predicted pressure drops in the channel arrays for different channel blockage scenarios for

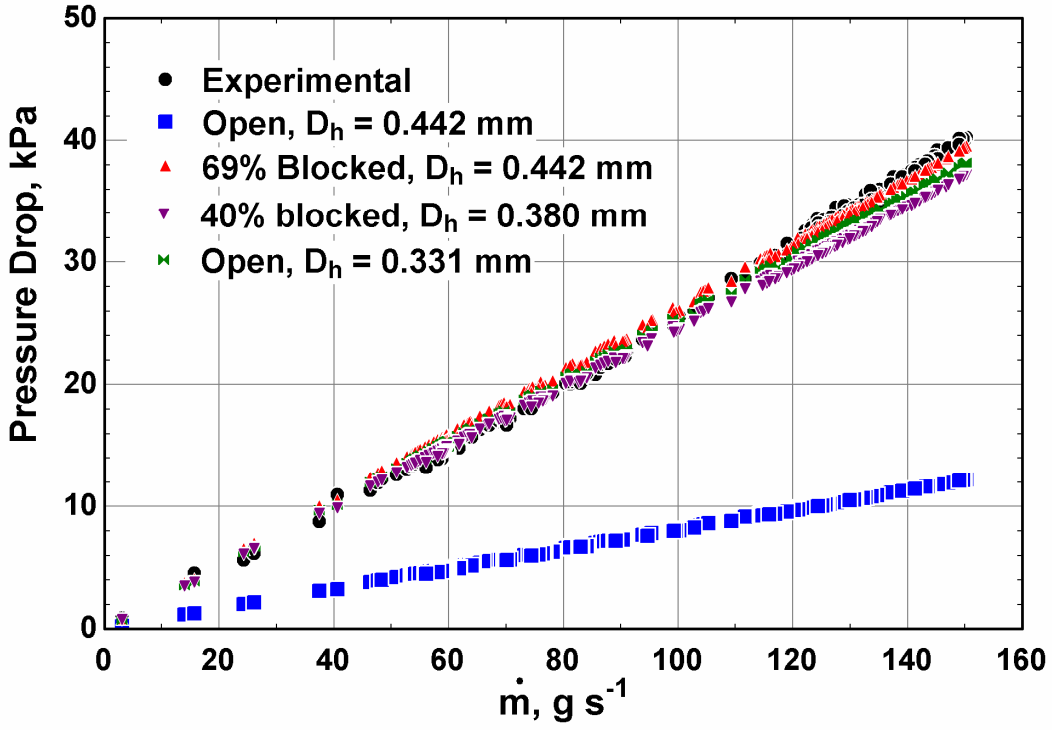

Fig. E.2 Channel pressure drop as a function of fluid flow rate for different channel blockage scenarios

Microscale Absorber 2A. As can be seen from this figure, the predicted pressure drop in the channel array according to the design for this absorber is lower than experimentally measured pressure drop. However, if the channel hydraulic diameter is adjusted (Scenario 1) or the percentage of blocked channels is adjusted (Scenarios 2 and 3), the predicted pressure drop compares very well with the experimentally measured pressure drop in the channel array. These adjusted channel hydraulic diameters and percentages of blocked channels for each absorber are used in the heat and mass transfer analysis discussed in Chapter 7.

REFERENCES

Akita, K., Yoshida, F., 1974. Bubble Size, Interfacial Area, and Liquid-Phase Mass Transfer Coefficient in Bubble Columns. Industrial & Engineering Chemistry Process Design and Development 13 (1), 84-91.

Armbruster, R., Mitrovic, J., 1998. Evaporative cooling of a falling water film on horizontal tubes. Experimental Thermal and Fluid Science 18 (3), 183-194.

Bell, K.J., Ghaly, M.A., 1972. Approximate Generalized Design Method for Multicomponent/Partial Condensers. American Institute of Chemical Engineers, Papers (24), 72-79.

Beutler, A., Ziegler, F., Alefeld, G., 1996. Falling Film Absorption with Solutions of a Hydroxide Mixture, Proceedings of the International Ab-Sorption Heat Pump Conference, Montreal, Canada, pp. 303-309.

Bhavaraju, S.M., Russell, T.W.F., Blanch, H.W., 1978. The design of gas sparged devices for viscous liquid systems. AIChE Journal 24 (3), 454-466.

Bird, R.B., Stewart, W.E., Lightfoot, E.N., 2002. Transport Phenomena, 2 ed. Wiley, New York.

Bohra, L.K., 2007. Analysis of Binary Fluid Heat and Mass Transfer in Ammonia-Water Absorption, Mechanical Engineering. Georgia Institute of Technology, Atlanta, p. 337.

Bohra, L.K., Lee, S., Garimella, S., 2008. Heat and Mass Transfer Models for Horizontal-Tube Falling-Film Ammonia-Water Absorption, Proceedings of the International Sorption Heat Pump Conference 2008, Seoul, Korea.

Brauner, N., 1989. Modelling of wavy flow in turbulent free falling films. International Journal of Multiphase Flow 15 (4), 505-520.

Cardenas, R., Narayanan, V., 2010. A numerical model for ammonia-water absorption into a constrained microscale film. International Journal of Thermal Sciences 49 (9), 1787-1798.

Carey, V.P., 1992. Liquid-vapor phase-change phenomena : an introduction to the thermophysics of vaporization and condensation processes in heat transfer equipment. Taylor & Francis Series, Hemisphere Pub. Corp., Washington, D.C.

Castro, J., Oliet, C., Rodríguez, I., Oliva, A., 2009. Comparison of the performance of falling film and bubble absorbers for air-cooled absorption systems. International Journal of Thermal Sciences 48 (7), 1355-1366.

Cengel, Y., Cimbala, J., 2009. Fluid Mechanics: Fundamental and Applications. McGraw-Hill.

Cerezo, J.s., Best, R., Bourouis, M., Coronas, A., 2010. Comparison of numerical and experimental performance criteria of an ammonia-water bubble absorber using plate heat exchangers. International Journal of Heat and Mass Transfer 53 (17-18), 3379-3386.

Cerezo, J.s., Bourouis, M., VallÃ¨s, M., Coronas, A., Best, R., 2009. Experimental study of an ammonia-water bubble absorber using a plate heat exchanger for absorption refrigeration machines. Applied Thermal Engineering 29 (5-6), 1005-1011.

Chen, J., Chang, H., Chen, S.-R., 2006. Simulation study of a hybrid absorber-heat exchanger using hollow fiber membrane module for the ammonia-water absorption cycle. International Journal of Refrigeration 29 (6), 1043-1052.

Chen, W., Christensen, R.N., 2000. Inlet subcooling effect on heat and mass transfer characteristics in a laminar film flow. International Journal of Heat and Mass Transfer 43 (2), 167-177.

Christensen, R.N., Garimella, S., Kang, Y.T., Garrabrant, M.A., 1998. Perforated fin heat and mass transfer device. Gas Research Institute (Chicago, IL), USA.

Churchill, S.W., 1977a. Comprehensive Correlating Equations for Heat, Mass and Momentum Transfer in Fully Developed Flow in Smooth Tubes. Industrial & Engineering Chemistry, Fundamentals 16 (1), 109-116.

Churchill, S.W., 1977b. Friction-Factor Equation Spans all Fluid-Flow Regimes. Chemical Engineering Progress 84 (24), 91-92.

Colburn, A.P., Drew, T.B., 1937. The Condensation of Mixed Vapours. AIChE Transactions 33, 197-212.

Conlisk, A.T., 1992. Falling film absorption on a cylindrical tube. AIChE Journal 38 (11), 1716-1728.

Dence, A.E., Nowak, C.C., Perez-Blanco, H., 1996. A novel GAX heat exchanger for cooling applications, in: Hosatte, S., Nikanpour, D. (Eds.), International Absorption Heat Pump Conference, Montreal, Canada, pp. 595-602.

Determan, M.D., 2008. Thermally Activated Miniaturized Cooling System, Mechanical Engineering. Georgia Institute of Technology, Atlanta, p. 230.

Determan, M.D., Garimella, S., 2010. A microscale monolithic absorption heat pump, 13th International Refrigeration and Air Conditioning Conference at Purdue, West Lafayette, Indiana.

Determan, M.D., Garimella, S., 2011. Ammonia-water desorption heat and mass transfer in microchannel devices. International Journal of Refrigeration 34 (5), 1197-1208.

Determan, M.D., Garimella, S., Lee, S., 2004. Experimental Demonstration of a Microchannel Desorber for Ammonia-Water Heat Pumps, Seventeenth National Heat and Mass Transfer Conference and Sixth ISHMT/ASME Heat and Mass Transfer Conference, Kalpakkam, India, pp. 453-458.

Dorokhov, A.R., Bochagov, V.N., 1983. Heat Transfer to a Falling Film over horizontal cylinders. Heat Transfer - Soviet Research 15 (2), 96-101.

Elperin, T., Fominykh, A., 2003. Four stages of the simultaneous mass and heat transfer during bubble formation and rise in a bubbly absorber. Chemical Engineering Science 58 (15), 3555-3564.

Fernández-Seara, J., Sieres, J., Rodríguez, C., Vázquez, M., 2005. Ammonia-water absorption in vertical tubular absorbers. International Journal of Thermal Sciences 44 (3), 277-288.

Fernández-Seara, J., Uhía, F.J., Sieres, J., 2007. Analysis of an air cooled ammonia-water vertical tubular absorber. International Journal of Thermal Sciences 46 (1), 93-103.

Ferreira, C.A.I., 1985. Combined momentum, heat and mass transfer in vertical slug flow absorbers. International Journal of Refrigeration 8 (6), 326-334.

Ferreira, C.A.I., Keizer, C., Machielsen, C.H.M., 1984. Heat and mass transfer in vertical tubular bubble absorbers for ammonia-water absorption refrigeration systems. International Journal of Refrigeration 7 (6), 348-357.

Frank, M.J.W., Kuipers, J.A.M., van Swaaij, W.P.M., 1996a. Diffusion Coefficients and Viscosities of CO2 + H2O, CO2 + CH3OH, NH3 + H2O, and NH3 + CH3OH Liquid Mixtures. J. Chem. Eng. Data 41 (2), 297-302.

Frank, M.J.W., Kuipers, J.A.M., van Swaaij, W.P.M., 1996b. Diffusion coefficients and viscosities of CO2+H2O, CO2+CH3OH, NH3+H2O, and NH3+CH3OH liquid mixtures. Journal of Chemical and Engineering Data 41 (2), 297-302.

Garimella, S., 1999. Miniaturized Heat and Mass Transfer Technology for Absorption Heat Pumps, Proceedings of the International Sorption Heat Pump Conference, Munich, Germany, pp. 661-670.

Garimella, S., Determan, M.D., Meacham, J.M., Lee, S., Ernst, T.C., 2011. Microchannel component technology for system-wide application in ammonia/water absorption heat pumps. International Journal of Refrigeration 34 (5), 1184-1196.

Garrabrant, M.A., Christensen, R.N., 1997. Modeling and experimental verification of a Perforated Plate-Fin Absorber for aqua-ammonia absorption systems, Proceedings of the ASME International Mechanical Engineering Congress and Exposition ASME, Fairfield, NJ, USA, Dallas, TX, USA, pp. 337-347.

Gillespie, P.C., Wilding, W.V., Wilson, G.M., 1987. Vapor-liquid Equilibrium Measurements on the Ammonia-Water system from 313 K to 589 K. AIChE Symposium Series 83 (256), 97-127.

Goel, N., Goswami, D.Y., 2005. A Compact Falling Film Absorber. Journal of Heat Transfer 127 (9), 957-965.

Goel, N., Goswami, D.Y., 2007. Experimental Verification of a New Heat and Mass Transfer Enhancement Concept in a Microchannel Falling Film Absorber. Journal of Heat Transfer 129 (2), 154-161.

Gommed, K., Grossman, G., Koenig, M.S., 2001. Numerical study of absorption in a laminar falling film of ammonia-water, ASHRAE Transactions. ASHRAE Inc., Atlanta, GA, USA, Atlanta, GA, United states, pp. 453-462.

Haselden, G.G., Malaty, S.A., 1959. Heat and mass transfer accompanying the absorption of ammonia in water. Institution of Chemical Engineers -- Transactions 37 (3), 137-146.

Herbine, G.S., Perez-Blanco, H., 1995. Model of an ammonia-water bubble absorber, Proceedings of the 1995 ASHRAE Annual Meeting, Jan 29-Feb 1 1995. ASHRAE, Atlanta, GA, USA, Chicago, IL, USA, pp. 1324-1332.

Herold, K.E., Radermacher, R., Klein, S.A., 1996. Absorption Chillers and Heat Pumps. CRC Press.

Higbie, R., 1935. The Rate of Absorption of a Pure Gas Into a Still Liquid during Short Periods of Exposure. Transactions of the AICHE 31, 365 - 389.

Hoffmann, L., Ziegler, F., 1996. Experimental Investigation of Heat and Mass Transfer with Aqueous Ammonia, International Ab-sorption Heat Pump Conference, Montreal, Canada, pp. 383-392.

Hu, X., Jacobi, A.M., 1996a. The Intertube Falling Film: Part 1---Flow Characteristics, Mode Transitions, and Hysteresis. Journal of Heat Transfer 118 (3), 616-625.

Hu, X., Jacobi, A.M., 1996b. The Intertube Falling Film: Part 2---Mode Effects on Sensible Heat Transfer to a Falling Liquid Film. Journal of Heat Transfer 118 (3), 626-633.

Ibrahim, O.M., Klein, S.A., 1993. Thermodynamic properties of ammonia-water mixtures. ASHRAE Transactions 99 (1), 1495-1502.

Incropera, F.P., Dewitt, D.P., Bergman, T.L., Lavine, A.S., 2007. Fundamentals of Heat and Mass Transfer, Sixth ed. John Wiley & Sons Inc.

Jenks, J., Narayanan, V., 2008. Effect of Channel Geometry Variations on the Performance of a Constrained Microscale-Film Ammonia-Water Bubble Absorber. Journal of Heat Transfer 130 (11), 112402-112409.

Jeong, S., Garimella, S., 2002. Falling-film and droplet mode heat and mass transfer in a horizontal tube LiBr/water absorber. International Journal of Heat and Mass Transfer 45 (7), 1445-1458.

Jeong, S., Garimella, S., 2005. Optimal Design of Compact Horizontal Tube LiBr/Water Absorbers. HVAC&R Research 11 (1), 27-44.

Jeong, S., Koo, K.-K., Lee, S.K., 1998. Heat transfer performance of a coiled tube absorber with working fluid of ammonia/water, Proceedings of the 1998 ASHRAE Winter Meeting. Part 2 (of 2). ASHRAE, Atlanta, GA, USA, San Francisco, CA, USA, pp. 1577-1583.

Kakaç, S., Shah, R.K., Aung, W., 1987. Handbook of single-phase convective heat transfer. Wiley, New York, NY.

Kang, Y.T., Akisawa, A., Kashiwagi, T., 1999. Experimental correlation of combined heat and mass transfer for NH3-H2O falling film absorption. International Journal of Refrigeration 22 (4), 250-262.

Kang, Y.T., Akisawa, A., Kashiwagi, T., 2000. Analytical investigation of two different absorption modes: falling film and bubble types. International Journal of Refrigeration 23 (6), 430-443.

Kang, Y.T., Chen, W., Christensen, R.N., 1997. Generalized component design model by combined heat and mass transfer analysis in NH_3/H_2O absorption heat pump systems, Proceedings of the ASHRAE Winter Meeting ASHRAE, Atlanta, GA, USA, Philadelphia, PA, USA, pp. 444-453.

Kang, Y.T., Christensen, R.N., 1994. Development of a counter-current model for a vertical fluted tube GAX absorber, Proceedings of the International Absorption Heat Pump Conference. ASME, New York, NY, USA, New Orleans, LA, USA, pp. 7-16.

Kang, Y.T., Christensen, R.N., 1995. Combined heat and mass transfer analysis for absorption in a fluted tube with a porous medium in confined cross flow, Proceedings of the ASME/JSME Thermal Engineering Joint Conference ASME, New York, NY, USA, Maui, HI, USA, pp. 251-260.

Kang, Y.T., Christensen, R.N., Vafai, K., 1994. Analysis of Absorption Process in a Smooth-Tube Heat Exchanger with a Porous Medium. Heat Transfer Engineering 15 (4), 42-55.

Kang, Y.T., Kashiwagi, T., Christensen, R.N., 1998. Ammonia-water bubble absorber with a plate heat exchanger, Proceedings of the 1998 ASHRAE Winter Meeting. Part 2 (of 2). ASHRAE, Atlanta, GA, USA, San Francisco, CA, USA, pp. 1565-1575.

Kang, Y.T., Nagano, T., Kashiwagi, T., 2002. Visualization of bubble behavior and bubble diameter correlation for NH3-H2O bubble absorption. International Journal of Refrigeration 25 (1), 127-135.

Killion, J.D., Garimella, S., 2001. A critical review of models of coupled heat and mass transfer in falling-film absorption. International Journal of Refrigeration 24 (8), 755-797.

Killion, J.D., Garimella, S., 2003. Gravity-driven flow of liquid films and droplets in horizontal tube banks. International Journal of Refrigeration 26 (5), 516-526.

Killion, J.D., Garimella, S., 2004a. Pendant droplet motion for absorption on horizontal tube banks. International Journal of Heat and Mass Transfer 47 (19-20), 4403-4414.

Killion, J.D., Garimella, S., 2004b. Simulation of Pendant Droplets and Falling Films in Horizontal Tube Absorbers. Journal of Heat Transfer 126 (6), 1003-1013.

Kim, H.Y., Saha, B.B., Koyama, S., 2003a. Development of a slug flow absorber working with ammonia-water mixture: part I--flow characterization and experimental investigation. International Journal of Refrigeration 26 (5), 508-515.

Kim, H.Y., Saha, B.B., Koyama, S., 2003b. Development of a slug flow absorber working with ammonia-water mixture: part II--data reduction model for local heat and mass transfer characterization. International Journal of Refrigeration 26 (6), 698-706.

Kim, J.-K., Jung, J.Y., Kang, Y.T., 2006. The effect of nano-particles on the bubble absorption performance in a binary nanofluid. International Journal of Refrigeration 29 (1), 22-29.

Kirby, M.J., Perez-Blanco, H., 1994. Design model for horizontal tube water/lithium bromide absorbers, American Society of Mechanical Engineers, Advanced Energy Systems Division (Publication) AES. ASME, Chicago, IL, USA, pp. 1-10.

Klein, S.A., 2011. Engineering Equation Solver, Academic Professional V8.881-3D ed. F-Chart Software.

Kwon, K., Jeong, S., 2004. Effect of vapor flow on the falling-film heat and mass transfer of the ammonia/water absorber. International Journal of Refrigeration 27 (8), 955-964.

Lee, J.-C., Lee, K.-B., Chun, B.-H., Lee, C., Ha, J., Kim, S., 2002a. A study of the characteristics of heat transfer for an ammonia-water bubble mode absorber in absorption heat pump systems. Korean Journal of Chemical Engineering 19 (4), 552-556.

Lee, J.-C., Lee, K.-B., Chun, B.-H., Lee, C.H., Ha, J.J., Kim, S.H., 2003. A study on numerical simulations and experiments for mass transfer in bubble mode absorber of ammonia and water. International Journal of Refrigeration 26 (5), 551-558.

Lee, K.-B., Chun, B.-H., Lee, J.-C., Park, C.-J., Kim, S.-H., 2002b. Absorption characteristics of ammonia-water system in the cylindrical tube absorber. Korean Journal of Chemical Engineering 19 (1), 87-92.

Lee, K.B., Chun, B.H., Lee, J.C., Hyun, J.C., Kim, S.H., 2002c. Comparison Of Heat And Mass Transfer In Falling Film And Bubble Absorbers Of Ammonia-Water. Experimental Heat Transfer 15 (3), 191 - 205.

Lee, K.B., Chun, B.H., Lee, J.C., Lee, C.H., Kim, S.H., 2002d. Experimental analysis of bubble mode in a plate-type absorber. Chemical Engineering Science 57 (11), 1923-1929.

Lee, S., 2007. Development of techniques for in-situ measurement of heat and mass transfer in ammonia-water absorption systems, Mechanical Engineering. Georgia Institute of Technology, Atlanta, p. 289.

Lee, S., Bohra, L.K., Garimella, S., 2008a. In-situ Measurement of Absorption Rates in Horizontal-Tube Falling-Film Ammonia-Water Absorbers: Part I - Measurement

Technique, International Refrigeration and Air Conditioning Conference at Purdue, West Lafayette, IN.

Lee, S., Bohra, L.K., Garimella, S., 2008b. In-situ Measurement of Absorption Rates in Horizontal-Tube Falling-Film Ammonia-Water Absorbers: Part II - Heat and Mass Transfer Coefficients, International Refrigeration and Air Conditioning Conference at Purdue, West Lafayette, IN.

Lockhart, R.W., Martinelli, R.C., 1949. Proposed correlation of data for isothermal two-phase, two-component flow in pipes. Chemical Engineering Progress 45 (1), 39-45.

Ma, X., Su, F., Chen, J., Bai, T., Han, Z., 2009. Enhancement of bubble absorption process using a CNTs-ammonia binary nanofluid. International Communications in Heat and Mass Transfer 36 (7), 657-660.

Meacham, J.M., 2002. An integrated experimental and analytical study of ammonia-water absorption in microchannel geometries, Mechanical Engineering. Iowa State University, Ames, p. 140.

Meacham, J.M., Garimella, S., 2002. Experimental Demonstration of a Prototype Microchannel Absorber for Space-Conditioning Systems, International Sorption Heat Pump Conference, Shanghai, China, pp. 270-276.

Meacham, J.M., Garimella, S., 2003. Modeling of local measured heat and mass transfer variations in a microchannel ammonia-water absorber. ASHRAE Transactions 109 (1), 412-422.

Meacham, J.M., Garimella, S., 2004. Ammonia-water absorption heat and mass transfer in microchannel absorbers with visual confirmation. ASHRAE Transactions 110 (1), 525-532.

Merrill, T., Setoguchi, T., Perez-Blanco, H., 1994. Compact bubble absorber design and analysis, Proceedings of the International Absorption Heat Pump Conference. ASME, New York, NY, USA, New Orleans, LA, USA, pp. 217-223.

Merrill, T.L., Perez-Blanco, H., 1997. Combined heat and mass transfer during bubble absorption in binary solutions. International Journal of Heat and Mass Transfer 40 (3), 589-603.

Mikielewicz, J., Moszynskl, J.R., 1976. Minimum thickness of a liquid film flowing vertically down a solid surface. International Journal of Heat and Mass Transfer 19 (7), 771-776.

Mills, A.F., 1995. Heat and Mass Transfer. Concord, MA, Richard D. Irwin, Inc.

Mitrovic, J., 1986. Influence of Tube Spacing and Flow Rate on Heat Transfer from a Horizontal Tube to a Falling Liquid Film, Proceedings of the 8th International Heat Transfer Conference. Hemisphere Publ Corp, Washington, DC, USA, San Francisco, CA, USA, pp. 1949-1956.

Mitrovic, J., 2005. Flow Structures of a Liquid Film Falling on Horizontal Tubes. Chemical Engineering & Technology 28 (6), 684-694.

Nellis, G., Klein, S.A., 2009. Heat transfer. Cambridge University Press, New York.

Niu, X.F., Du, K., Xiao, F., 2010. Experimental study on ammonia-water falling film absorption in external magnetic fields. International Journal of Refrigeration 33 (4), 686-694.

Nomura, T., Nishimura, N., Wei, S., Yamaguchi, S., Kawakami, R., 1994a. Heat and mass transfer mechanism in the absorber of water/LiBr convectional absorption refrigerator: Experimental examination by visualized model, Proceedings of the International Absorption Heat Pump Conference, Jan 19-21 1994. ASME, New York, NY, USA, New Orleans, LA, USA, pp. 203-208.

Nomura, T., Nishimura, N., Wei, S., Yamaguchi, S., Kawakami, R., 1994b. Heat and mass transfer mechanism in the absorber of water/LiBr convectional absorption refrigerator: Experimental examination by visualized model, Proceedings of the International Absorption Heat Pump Conference. ASME, New Orleans, LA, USA, pp. 203-208.

Nusselt, W., 1916. Die Oberflachen Kondensation des Wasserdampfes. Zeitschrift des Vereines Deutscher Ingenieure 60 (27, 28), 541-546, 569-575.

Palmer, S.C., Christensen, R.N., 1996. Experimental investigation and model verification for a GAX absorber, International Ab-Sorption Heat Pump Conference, Montreal, Canada, pp. 367-374.

Patnaik, V., Perez-Blanco, H., 1996a. Roll waves in falling films: an approximate treatment of the velocity field. International Journal of Heat and Fluid Flow 17 (1), 63-70.

Patnaik, V., Perez-Blanco, H., 1996b. A study of absorption enhancement by wavy film flows. International Journal of Heat and Fluid Flow 17 (1), 71-77.

Patnaik, V., Perez-Blanco, H., Ryan, W.A., 1993. Simple analytical model for the design of vertical tube absorbers. ASHRAE Transactions 99 (2), 69-80.

Perez-Blanco, H., 1988. A Model of an Ammonia-Water Falling Film Absorber. ASHRAE Transactions 94 (1), 467-483.

Price, B.C., Bell, K.J., 1974. Design of Binary Vapor Condensers Using the Colburn-Drew Equations. AIChE Symposium Series - Heat Transfer - Research and Design 70 (138), 163-171.

Ruhemann, M., 1947. A study of the transfer of heat and matter in an ammonia absorber. Transactions of the Institute of Chemical Engineers 25, 158-162.

Shah, M.M., 1979. A general correlation for heat transfer during film condensation inside pipes. International Journal of Heat and Mass Transfer 22 (4), 547-556.

Sparrow, E.M., Abraham, J.P., Tong, J.C.K., 2004. Archival correlations for average heat transfer coefficients for non-circular and circular cylinders and for spheres in cross-flow. International Journal of Heat and Mass Transfer 47 (24), 5285-5296.

Sparrow, E.M., Haji-Sheikh, A., 1965. Laminar Heat Transfer and Pressure Drop in Isosceles Triangular, Right Triangular, and Circular Sector Ducts. Journal of Heat Transfer 87, 426-427.

Subramaniam, V., Garimella, S., 2009. From measurements of hydrodynamics to computation of species transport in falling films. International Journal of Refrigeration 32 (4), 607-626.

Taitel, Y., Dukler, A.E., 1976. A Model for Predicting Flow Regime Transitions in Horizontal and Near Horizontal Gas-Liquid Flow. AIChE Journal 22 (1), 47-55.

Taylor, B.N., Kuyatt, C.E., 1993. Guidelines for evaluating and expressing the uncertainty of NIST measurement results. National Institute of Standards and Technology, Washington, DC, USA, p. 15.

Wassenaar, R.H., Segal, G., 1999. Numerical results of falling film absorption with water/ammonia. International Journal of Thermal Sciences 38 (11), 960-964.

Wilke, C.R., 1950. A viscosity equation for gas mixtures. Journal of Chemical Physics 18, 517-519.

Wilke, W., 1962. Heat transfer to falling liquid films: Waermeuebergang an Rieselfilme. VDI -- Forschungsheft (490), 36.

Xiaofeng, N., Kai, D., Shunxiang, D., 2007. Numerical analysis of falling film absorption with ammonia-water in magnetic field. Applied Thermal Engineering 27 (11-12), 2059-2065.

Yang, L., Du, K., Niu, X.F., Cheng, B., Jiang, Y.F., 2011. Experimental study on enhancement of ammonia-water falling film absorption by adding nano-particles. International Journal of Refrigeration 34 (3), 640-647.

Yung, D., Lorenz, J.J., Ganic, E.N., 1980. Vapor/Liquid Interaction and Entrainment in Falling Film Evaporators. Journal of Heat Transfer 102 (1), 20-25.

Ziegler, B., Trepp, C., 1984. Equation of state for ammonia-water mixtures. International Journal of Refrigeration 7 (2), 101-106.